High-Speed Multi-Modal Scattering Polarimetry for Nerve Fiber Imaging

Dissertation
zur Erlangung eines Doktorgrades (Dr. rer. nat.)

in der
Fakultät für Mathematik und Naturwissenschaften
der
Bergischen Universität Wuppertal

vorgelegt von

Franca auf der Heiden

Forschungszentrum Jülich GmbH
Institut für Neurowissenschaften und Medizin (INM-1)

1. Berichterstatter
Prof. Dr. Markus Axer
BU Wuppertal

2. Berichterstatter
Dr. Miriam Menzel
TU Delft

October 15, 2024

Abstract

Understanding the intricate structure of the human brain is a major objective in neuroscience. To image and map the connectome across various scales, neuroscience has developed a range of imaging techniques, each with distinct advantages, limitations, and variations in resolution, scale, speed, and application range.

Neuroimaging techniques such as Müller polarimetry, three-dimensional polarized light imaging (3D-PLI), diattenuation imaging (DI), and computational scattered light imaging (ComSLI) offer valuable insights into the nerve fiber architecture of the brain. All four techniques employ incoherent visible light for the investigation of long-range fiber pathways in histological brain sections and achieve a micrometer in-plane resolution. While there are ongoing efforts to optimize individual neuroimaging techniques, there is a growing need for multi-modal analysis to benefit from the strengths of multiple techniques.

The combination of Müller polarimetry, 3D-PLI, DI, and ComSLI into a single measurement device allows for unprecedented multi-modal parameter analysis and pixel-precise cross-validation of fiber orientations. This thesis presents the development of a multi-modal high-speed Scattering Polarimeter that combines these complementary imaging techniques into one automated high-speed device, enabling multi-modal, high-resolution analysis of brain fiber networks within reasonable time and leveraging the unique advantages of each technique.

Designed as wide-field Müller polarimeter in transmission mode, the Scattering Polarimeter employs a large-area light source and four voltage-controlled liquid crystal variable retarders (LCVRs) that were chosen for their superior switching speed compared to mechanically rotating optical elements. The setup was developed from scratch and transitioned from a prototype to a functional device. This development process included hardware selection, the creation of an automated measurement routine, mathematical description with a focus on error analysis, performance evaluation of each modality, and, as a proof-of-principle, various multi-modal analyses.

The Scattering Polarimeter was characterized by measuring optical elements with known properties and by comparison with reference measurements from established devices for 3D-PLI, DI, and ComSLI. Furthermore, the device performance was evaluated through error analysis based on Müller calculus and Taylor approximations for the incident and transmitted intensity, accounting for non-ideal behavior in the device components. This approach precisely identifies of the sources of systematic errors. The Scattering Polarimeter showed excellent performance for 3D-PLI and good performance for Müller polarimetry and ComSLI. Primarily, the performance was limited by the brightness of the light source. DI, as explored in this work, was constrained by minor systematic deviations, for which the causes within the optical hardware were identified and alternative measurement approaches were proposed. Aiming towards a high-speed measurement routine, the thesis successfully explored the acceleration of the multi-modal measurement by reducing the number of required

images for 3D-PLI. Furthermore, a novel high-speed illumination strategy based on compressed sensing was realized for scatterometry ComSLI. Again, the main limitation for high-speed measurement remained the brightness of the light source, which directly determined the minimum achievable exposure time.

Building on the single-mode measurements of all four modalities, the initial steps toward multi-modal parameter map analysis were successfully taken: This thesis presents a multi-modal classification of tissue types and white matter fiber configurations based on various optical properties. A multi-modal fiber orientation map (FOM) was constructed, offering improved visualization of nerve fiber orientations and crossings, demonstrating superior performance compared to the single-mode approach. Briefly, the complex relation between fiber inclination and the resulting optical properties were addressed with multi-modal parameter analysis.

A part of this thesis is dedicated to advancing ComSLI as a technique by extending its application to formalin-fixed paraffin-embedded sections, implementing a novel high-speed illumination strategy based on compressed sensing, and upgrading the measurement with a high-sensitivity camera and a custom-built scanning stage. These advancements are directly applicable to the Scattering Polarimeter.

This thesis establishes the theoretical, experimental, and technical foundation for scattering polarimetry, thereby advancing multi-modal nerve fiber imaging and contributing to a deeper understanding of the human connectome.

Acknowledgements

This doctoral thesis has been carried out during the years 2021 – 2024 in the 'Fiber Architecture' group of Prof. Dr. Markus Axer at the *Institute of Neuroscience and Medicine* (INM-1), *Forschungszentrum Jülich GmbH* (FZJ), and has been submitted to *Bergische Universität Wuppertal* (BUW) to obtain a doctorate in physics. The thesis has received funding from the *Klaus Tschira Boost Fund* of the *German Scholars Association* and from the *Deutsche Forschungsgemeinschaft* (DFG) under project no. 498596755.

First and foremost, my sincere thanks go to my supervisor and examiner, Dr. Miriam Menzel *(Imaging Physics, Technische Universiteit Delft)*, for giving me the opportunity to continue the project that began with my master's thesis. Thank you for your continuous scientific and moral support, for always having an open ear to all questions and problems, for all the opportunities to learn new things and meet new people in Delft and Stanford, for the record-speed proofreading, for giving me the chance to realize my own ideas and for encouraging me to actually finish this thing. Bedankt voor de begeleiding van mijn doctoraat, ook over de grens, het was me een genoegen! Thank you!

I extend my gratitude to my supervisor and examiner Prof. Dr. Markus Axer (INM-1, FZJ) for the opportunity to work in his team, for supporting my thesis, and also for encouraging my interest in science communication. As a group leader, he was supportive, approachable, and open to all questions and he undoubtedly contributes to the positive working atmosphere in the Fiber Architecture group. Thank you as well!

I would also like to acknowledge Prof. Dr. Katrin Amunts (director of the INM-1, FZJ and of the *C. and O. Vogt Institute of Brain Research at Heinrich Heine University Düsseldorf*) for the opportunity to work at the INM-1, for supporting my scientific career, and for giving me the opportunity to attend international conferences.

Furthermore, I would like to recognize the rest of my thesis committee, Prof. Dr. Dirk Lützenkirchen-Hecht (*Kondensierte Materie - Röntgenphysik*, BUW), and Prof. Dr. Johannes Grebe-Ellis (*Physik und ihre Didaktik*, BUW), for their time and support.

Next, a shout-out and thanks to my colleagues at the INM-1 who contributed to this thesis: Philipp Schlömer for the support with everything hardware-related, especially with the cameras and the choice of objective lenses, for proofreading, and moreover for providing the reference measurements for 3D-PLI in Chapter 5. David Gräßel – who has been part of the development of ComSLI since the early dawn of that technique –, for his boundless knowledge of anatomy, for helping with diattenuation reference measurement in Chapter 5, and also for proofreading parts of this thesis. Jan Reuter, now part of the *Institute for Advanced Simulation* (IAS), FZJ and *Jülich Supercomputing Center* (JSC), FZJ, who developed the software tools SLI ToolboX (SLIX) and ScatBox that are used throughout this thesis for the evaluation of angular and scatterometry ComSLI, and who helped with C++ troubleshooting for

the camera in Chapter 7. The laboratory team of the INM-1 for the tissue preparation and for providing the various tissue samples, and especially Markus Cremer for also proofreading the part about tissue preparation in Chapter 3. Dr. Christian Schiffer for introducing me to the institute's 3D-printer and for squeezing my projects in between the mass production of plastic brains. Stefan Schiffer for developing an advanced version of the sample holder of the XY stage. Andreas Müller (IAS/JSC, FZJ) and Martin Schober for aiding with the integration of the ComSLI measurements into the database. Oliver Münzer (previously INM-1) for taking the first steps into compressed sensing during his master thesis. Last but not least, Dr. Felix Matuschke and Nicole Schubert: In case of doubt, it was these two who always know what to do or whom to ask. Thank you all!

I would also like to thank the team at *Stanford Medicine*, particularly Dr. Marios Georgiadis and Prof. Dr. Michael Zeineh, for the collaboration in performing ComSLI on formalin-fixed paraffin-embedded tissue, for providing the tissue sections shown in Chapter 7, and for their hospitality during my short visit at Stanford.

Similar thanks go to the *Menzel Lab* at TU Delft, with special thanks to Simon van Staalduine for calculating the line profiles from the scattering patterns obtained via compressed sensing and generating the corresponding fiber orientation maps in Chapter 7. I also appreciate the lab tour during my visit and the opportunity to meet all the people from Menzel Lab in real life. Thank you for the warm welcome in the beautiful city of Delft.

Thank you to Moritz Battermann for proofreading Chapter 2 from the perspective of a laser physicist (I'm sorry there is only a minor Star Wars reference in this thesis). I would also like to recognize my other proofreaders in various stages of this thesis: René Schäfer, Rene Niewianda, Melina Kummetat, Jan Holtschneider, and Maria Häser. Thanks for the thorough literature critique!

On a personal note, I would like to thank the people from the INM-1 at the FZJ, especially from the groups "Fiber Architecture" and "Big Data Analysis", for the friendly working atmosphere, the fun conversations, the hiking and climbing trips, the boardgaming events, the coffee breaks, and the profound discussions about gaming, fantasy, and sci-fi. Thank you for all the support and fun along the way!

Special thanks to my favorite sidequests: To my amazing and hilarious D&D group, who still carries around the most obnoxious brain-in-a-jar, and to the wonderful people from the RPG Librarium, whose creativity knows no bounds.

Thank you also to my parents Birgit and Friedrich auf der Heiden for their unwavering support (seems like the "Was ist was" book collection paid off after all) and for knowing all the good stories, no matter the travel destination. Many thanks!

Finally, heartfelt thanks (once again) to Jan Holtschneider and Maria Häser for providing bardic inspiration when needed and for being true companions on every quest. Thank you!

Contents

Chapter 1

Introduction

The human brain consists of about 86×10^9 neurons and ten times as many glial cells [80]. Together, they form an intricate system in which a neuron can make up to 10^5 synaptic connections with other neurons [177]. The entirety of neural connections in the brain is called the *connectome*. Brain function is conditioned by highly complex nerve fiber pathways and connections, with *dendrites* and *axons* forming the cable-like extensions of the neuron cell body which propagate neurological information coded as electrical stimuli. Neuroscience has developed a large number of imaging techniques to map and understand the connectome from macroscopic scales to the molecular level, with each method offering advantages, drawbacks and general differences in resolution, scale, speed, and range of application. Nowadays, a multitude of techniques for mapping the nerve fiber architecture of the human brain is available. However, while there is an ongoing effort to optimize individual neuroimaging techniques, there is also a growing need for *multi-modal* analysis to leverage the strengths of complementary and compatible techniques, ideally taken from the same integrated device (*correlative microscopy*).

1.1 Neuroimaging Across all Scales

The spectrum of neuroimaging techniques relevant for mapping nerve fiber architectures spans several orders of magnitude. On a macroscopic scale, *diffusion-weighed magnetic resonance imaging* (dMRI or DWI) allows the in-vivo study of a whole brain with a resolution of about one millimeter, mainly limited by scanning time and motion artifacts. In dMRI, axons are not directly imaged but measured indirectly based on the diffusion of water molecules in biological tissue [211]. The probabilistic distribution of axonal orientations can be computed from dMRI data [173].

Macroscopic dissection methods such as *Klingler's dissection method* have been used since the 1930s [94]. Here, the white matter tracts are subsequently peeled away manually to reveal the three-dimensional anatomical fiber architecture. Klingler's method has become less relevant since the development of *microtomes* and histological techniques but is still used, in particular in medical training. Nowadays, it is common to integrate an operating microscope into Klingler's dissection. However, the dissection process is time-consuming and demanding [197, 209].

Light microscopy in neuroscience achieves resolutions down to the diffraction limit. In modern neuroscience, light microscopy benefits from advanced tissue preparation and staining methods, automation for faster image acquisition, and increased computational power [142]. Post-mortem tissue is sectioned into thin slices, usually after paraffin-embedding or when in a frozen state. *Histological stains* can label various

cell components, e.g. the radial lipid bilayer around axons, the so-called *myelin sheath*. The *modified Heidenhain-Woelcke* stain allows a better identification of white matter tracts [32]. *Luxol fast blue* stains myelin fibers in blue and Nissl bodies and mast cells in purple [35]. Silver stains include *Bodian* [27] that labels all axons, dendrites, and cell bodies, and *Gallyas* [57, 58]) that labels myelin. Lipophilic dyes, such as the fluorescent dyes *dil* and *diO*, act as post-mortem tracers [81] and allow the measurement of axonal orientations via *structure tensor analysis* (STA) [30]. When cell nuclei are Nissl-stained, STA can derive fiber orientations from cell body distributions with a resolution of 15 micrometers [170].

Fiber orientations can also be measured directly in unstained histological brain sections, even for densely packed white matter fibers. Techniques such as *Müller polarimetry*, *three-dimensional polarized light imaging* (3D-PLI) as developed by AXER ET AL. [15, 17], *diattenuation imaging* (DI) as presented by MENZEL ET AL. [118, 117], and *computational scattered light imaging* (ComSLI) as introduced by MENZEL ET AL. [121, 120] employ incoherent visible light to achieve a micrometer in-plane resolution in the investigation of long-range fiber pathways in histological brain sections. Wide-field Müller polarimetry measures all optical properties of brain tissue, i.e. diattenuation, retardance, and depolarization. Additionally, Müller polarimetry can separate circular from linear effects. 3D-PLI determines the orientation of nerve fiber bundles in dense white matter by exploiting the birefringent properties of myelin. DI – as an extension to 3D-PLI – distinguishes two tissue types by their diattenuating properties. ComSLI investigates light scattering at nerve fibers and yields the individual orientations of multiple crossing fiber bundles for each measured image pixel, which is not possible with Müller polarimetry, 3D-PLI or DI. All four techniques are presented in detail in Chapter 3, because the objective of this thesis is the combination of the four techniques within a multi-modal device.

While the aforementioned light microscopy techniques typically provide only two-dimensional information, *optical coherence tomography* (OCT) uses optical interferometry of backscattered light to image depth-resolved tissue structures at a resolution of 1 to 20 micrometers [83]. *polarization sensitive OCT* (PS-OCT) enables a polarization-sensitive detection of the backscattered light [28], currently achieving a resolution of 3.5 micrometers in-plane and 50 micrometers through-plane voxel size [200]. *Micron-scale synchrotron X-ray computed tomography* (micro-CT) is a 3D imaging technique with micrometer resolution that is however limited by the sample volume to cubes of about 1 cm^3 [54, 195].

Fluorescence microscopy (FM), and *transmission electron microscopy* (TEM) offer resolutions down to several nanometers, thereby enabling the investigation of neurofilaments and axonic myelin sheaths. When combined with super-resolution microscopy approaches, FM circumvents the diffraction limit of light microscopy [164]. FM is often combined with clearing techniques like *CLARITY* (Clear Lipid-exchanged Acrylamide-hybridized Rigid Imaging/Immunostaining/In situ hybridization - compatible Tissue-hYdrogel) [42, 101]. Axon orientations are computed from the fluorescence microscopy images with an STA. However, the sample volume is limited: Clearing solutions and dyes penetrate a rat brain but not an entire human brain. *Confocal fluorescence microscopy* (CFM) and *two-photon fluorescence microscopy* (TPFM) [164] are subtypes of FM. TEM can resolve nanometer-scale structures from tissue stained with heavy metals (typically osmium), e.g. the detailed structure of neurons or the lipid bilayers of the myelin [55, 91].

AXER & AMUNTS [14] and YENDIKI ET AL. [211] provided a detailed overview of most of the aforementioned techniques.

1.2 Aims and Objectives

Within this thesis, the construction of a multi-modal high-speed *Scattering Polarimeter* is documented. The Scattering Polarimeter combines Müller polarimetry, 3D-PLI, DI, and ComSLI into a single device to investigate long-range fiber bundles in post-mortem histological brain sections with micrometer resolution while using visible, mostly incoherent light.

The combination of these complementary imaging techniques within one setup facilitates pixelwise mapping, cross-validation of fiber orientations, and leverages the unique advantages of each technique while mitigating their limitations: From the four techniques, 3D-PLI provides the most robust results for fiber orientations, even for the much lower fiber density in gray matter, but it can neither resolve fiber crossings nor measure depolarization. In contrast, ComSLI can determine the directions of multiple crossing fiber bundles, but is more affected by statistical noise. Müller polarimetry can measure depolarization and differentiate linear and circular optical effects in tissue. Lastly, DI as an extension to 3D-PLI distinguishes between two fiber types with different attenuating properties.

The Scattering Polarimeter was developed under two premises:

- **Multi-Modality**: The setup should measure the four modalities with the best achievable performance and without compromising any modality through the requirements of the other modalities. The design needs to balance the requirements of all modalities. Pixel-precise alignment of all obtained parameter maps must be achieved.
- **High-Speed**: The measurement process should be scalable and measure an entire human brain section within a reasonable time frame, comparable to other single-mode setups. Consequently, the software and measurement routine should be automatized and fast.

The Scattering Polarimeter is realized as wide-field Müller polarimeter in transmission mode that employs a large-area light source and four voltage-controlled *liquid crystal variable retarders* (LCVRs). This configuration does not only enable Müller polarimetry but also facilitates 3D-PLI and DI by selecting appropriate polarization states. Additionally, the large-area light source can generate the oblique light incidence required for ComSLI. LCVRs are chosen for their higher switching speed compared to mechanically rotating optical elements.

The setup is developed from scratch and transitioned from a prototypical stage to a functional device. This process includes the selection of suitable hardware, the development of a fully automatic measurement routine, the qualitative and quantitative evaluation of the performance for each modality using exemplary brain tissue with characteristic fiber structures and well-known optic samples, the mathematical description of the measured modalities (particularly in the context of error analysis), and, as a proof-of-principle, a multi-modal parameter analysis.

1.3 Thesis Outline

The thesis is organized into the following chapters:

Chapter 1: Introduction illustrates neuroimaging across all size scales and places this thesis within the broader context of nerve fiber imaging.

Chapter 2: Theoretical Background provides an overview of the physical, mathematical and neurobiological theory necessary for the understanding of this thesis. Topics include light-matter interaction, Müller matrix calculus, and the optical properties of brain tissue.

Chapter 3: Methods and Materials illustrates procedures for brain tissue preparation and introduces 3D-PLI, DI, Müller Polarimetry, and ComSLI along with their respective measurement devices.

Chapter 4: The Scattering Polarimeter documents the development of the Scattering Polarimeter from the conceptual sketch to a fully operational device, covering the optical and mechanical hardware and its assembly and adjustment, the measurement software, and the characterization of the LCVRs.

Chapter 5: Single-Mode Performance investigates the performance across all four modalities qualitatively and quantitatively by measuring a set of well-known optical elements and tissue samples with characteristic fiber structures. Reference measurements and mathematical considerations provide a deep understanding of the device features from both a mathematical and an experimental perspective. Error propagation in the device is investigated using Müller calculus.

Chapter 6: Multi-Modal Parameter Analysis showcases the potential of multi-modal parameter analysis and suggests various applications for the Scattering Polarimeter. As a proof-of-principle, an automatic tissue classification is developed, a combined fiber orientation map is assembled, and the scattering properties of inclined fibers are investigated.

Chapter 7: Advancing ComSLI delves into various enhancements made to the original ComSLI setup and the measurement routine, such as the integration of an XY stage and a high-sensitivity camera, the application of ComSLI on formalin-fixed paraffin-embedded brain sections, and a novel high-speed illumination strategy based on *compressed sensing*. The advancements are directly applicable to the Scattering Polarimeter.

Chapter 8: Discussion and Outlook presents all results obtained throughout this thesis in the broader context and methodologies. Furthermore, it includes suggestions for future research on multi-modal imaging with the Scattering Polarimeter.

Chapter 9: Conclusion refers back to all achievements made within the broader context of neuroimaging of nerve fiber architecture.

Symbols and abbreviations used throughout this thesis are provided in the appendix. Figures and tables are also listed there. Appendix A includes detailed calculations that are referenced in the thesis. Appendix B contains additional figures that are not shown in the main chapters. Appendix C presents data sheets for optical components used in the Scattering Polarimeter. Appendix D details which parts of this thesis have already been published, in particular content from Chapter 7.

Chapter 2

Theoretical Background

This chapter provides an overview of the **physical, mathematical, and neurobiological theory** that is required for the understanding of this thesis. The physics of **light-matter interaction** is addressed, focusing on phenomena relevant to brain tissue such as polarization, refraction, absorption, and scattering. Additionally, the working principle of **liquid crystals** is illustrated as they are crucial polarimetric components for the construction of the Scattering Polarimeter in Chapter 4. In context of polarimetry, **Müller and Jones matrix calculus** are introduced; mathematical tools that are applied throughout the thesis. Finally, the **anatomy of the human brain** and the structure of **white matter nerve fiber tracts** are detailed, in particular the optical properties of brain tissue which are exploited in polarimetric and scattering-based neuroimaging.

2.1 Light Matter Interaction

Phenomena like refraction, birefringence, absorption and scattering can occur when an electromagnetic wave – such as visible light – propagates in matter. Investigating those effects yields information about a material's microscopic structure. The following section introduces electromagnetic phenomena and their mathematical description while focusing on non-metallic matter and visible light.

The explanations are based upon the textbooks by HECHT [74] and DEMTRÖDER [47] unless stated otherwise. Moreover, the final section of the chapter explores the physics of liquid crystal devices commonly employed in polarimetry, thereby establishing a connection to the various polarimetric methods and experimental techniques in Chapter 3.

2.1.1 Light Propagation in Matter

As a result of MAXWELL's equations [112], the propagation of an electromagnetic wave through matter is described by a differential equation of second order for the electric field $\vec{E}$ that depends on the time t and the location of the wave

$$\Delta\vec{E} = \mu\mu_0\epsilon\epsilon_0\frac{\partial^2\vec{E}}{\partial t^2} = \frac{1}{c^2}\frac{\partial^2\vec{E}}{\partial t^2} \qquad c = \frac{1}{\sqrt{\mu\mu_0\epsilon\epsilon_0}} \tag{2.1}$$

with the electric field $\vec{E}$, the permittivity of free space $\epsilon_0 \approx 8.854 \times 10^{-12}\,\mathrm{F}\cdot\mathrm{m}^{-1}$, the permeability of free space $\mu_0 \approx 1.256\,\mathrm{N}\cdot\mathrm{A}^{-2}$, the unit-less material-specific permittivity ϵ and permeability μ, and the speed of light c. In a vacuum, $\epsilon = \mu$=1 so that c

becomes the speed of light in vacuum $c_0 \approx 3 \times 10^8$ m/s. A solution for Eq. (2.1) is a plane wave that propagates in z-direction[1]

$$\vec{E}(t,z) = E_{x0}\hat{e}_x \cdot \cos(\omega t - kz + \varphi_x) + E_{y0}\hat{e}_y \cdot \cos(\omega t - kz + \varphi_y) \tag{2.2}$$

Eq. (2.2) is a linear combination of two linearly independent waves in x- and y-direction E_{x0} and E_{y0}, respectively, with $\hat{e}_x$ and $\hat{e}_y$ being unit vectors, and ω being the frequency, related to the wavelength λ via $\omega = 2\pi c/\lambda$, Furthermore, they are each characterized by a phase φ_x and φ_y. The light intensity I is given by

$$I = |\vec{E}(z,t)|^2 \tag{2.3}$$

When the two waves have a fixed relation between their amplitudes and their phases, the light is *polarized*. When the phase difference of the two wave components is fixed with $\Delta\varphi = \varphi_x - \varphi_y = m\pi$ with $m \in \mathbb{N}_0$, the polarization is *linear*. Specifically, when $E_{x0} = 0$ or $E_{y0} = 0$, the linear polarization is *vertical* or *horizontal*[2]. When $E_{x0} = \pm E_{y0}$, the polarization is called *(anti-) diagonal*. Figure 2.1 displays antidiagonal linear polarization as an example.

The polarization of a plane light wave is *circular* when the x- and y-component have the same amplitude E_{x0}=E_{y0} but the phase difference is fixed with $\Delta\varphi = (m + \frac{1}{2})\pi$ with $m \in \mathbb{N}_0$. Figure 2.1 displays *left-handed* circular polarization ($\Delta\phi = -\frac{\pi}{2}$), as opposed to *right-handed* circular polarization ($\Delta\varphi = +\frac{\pi}{2}$).

When the phase relation is fixed but the prerequisites for linear or circular polarization are not fulfilled, the wave is *elliptically polarized*. Elliptical polarization can be interpreted as a combination of linear and circular wave components. When no fixed phase relation exists, the wave is *unpolarized*. Furthermore, light can also be a linear combination of polarized and unpolarized light waves. This is called *partial polarization*.

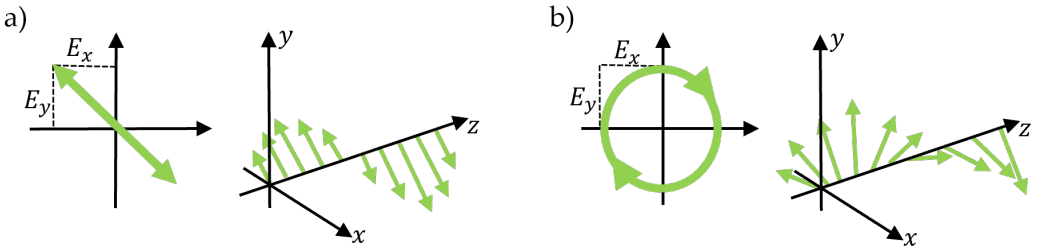

FIGURE 2.1: Linear and circular polarization. a) The polarization of a plane light wave is called linear when the phase difference between x- and y-component of the wave is fixed and a multiple of π, i.e. $\varphi_x - \varphi_y = m\pi$ with $m \in \mathbb{N}_0$. b) The polarization of a plane light wave is called circular when the x- and y-component have the same amplitude $E_{x0} = E_{y0}$ but the phase difference is fixed with $\Delta\varphi = \varphi_x - \varphi_y = (m + \frac{1}{2})\pi$ with $m \in \mathbb{N}_0$. The image displays left-circular polarization ($\Delta\varphi = -\frac{\pi}{2}$), in contrast to right-circular polarization ($\Delta\varphi = \frac{\pi}{2}$). Image inspired by DEMTRÖDER [47].

[1] Another common solution is a radial wave originating from one point.
[2] Depending on the chosen coordinate system.

2.1.2 Refraction and Birefringence

Following Eq. (2.1), the refractive index n links the speed of light in vacuum c_0 to the speed of light in matter c and is defined by the material-specific parameters ϵ and μ

$$c = \frac{1}{\sqrt{\mu\mu_0\epsilon\epsilon_0}} = \frac{c_0}{\sqrt{\mu\epsilon}} = \frac{c_0}{n} \tag{2.4}$$

The refractive index can be $n \in \mathbb{C}$ when absorption occurs (addressed later in Section 2.1.3) and also negative $n = -\epsilon\mu$ in so-called metamaterials, but is $n \in \mathbb{R}^+$ for non-absorbing regular materials. Furthermore, $\mu \approx 1$ for non-ferromagnetic materials. Therefore, the refractive index n is a scalar that is only defined by the free space permittivity ϵ:

$$n = \sqrt{\epsilon} \tag{2.5}$$

In case of a non-isotropic material, the refractive index must be written not as a scalar but as a tensor $\tilde{\epsilon}$:

$$\tilde{\epsilon} = \begin{pmatrix} \epsilon_{11} & \epsilon_{12} & \epsilon_{13} \\ \epsilon_{21} & \epsilon_{22} & \epsilon_{23} \\ \epsilon_{31} & \epsilon_{32} & \epsilon_{33} \end{pmatrix} \tag{2.6}$$

By making use of the *principal axis theorem*, i.e. finding an appropriate coordinate system, $\tilde{\epsilon}$ transforms into the diagonal tensor $\tilde{\epsilon}'$

$$\tilde{\epsilon}' = \begin{pmatrix} \epsilon_1 & 0 & 0 \\ 0 & \epsilon_2 & 0 \\ 0 & 0 & \epsilon_3 \end{pmatrix} = \begin{pmatrix} n_1^2 & 0 & 0 \\ 0 & n_2^2 & 0 \\ 0 & 0 & n_3^2 \end{pmatrix} \tag{2.7}$$

n_1, n_2 and n_3 define the main axes of the *index ellipsoid* as shown in Figure 2.2a. When $n_1 = n_2 \neq n_3$, a material is *birefringent* with an *optic axis* along the third axis $\hat{e}_3$.[3] In birefringent materials, the refractive index that a light wave experiences differs with the direction of its polarization. The transmitted light can be decomposed into two linearly independent waves where the two components are called the *slow* and the *fast ray* of the wave, referring to their different speed of light s. Eq. (2.4)).

When the incident light is already polarized, i.e. the slow and fast ray have fixed phase relation, a phase shift δ occurs between the slow and the fast ray. δ is called *retardance*. For a material thickness d and $\Delta n = n_3 - n_1$ the retardance is given by

$$\delta = \frac{2\pi d}{\lambda}\Delta n \tag{2.8}$$

It must be noted that the retardance is wavelength-dependent[4]. Typical optical components include quarter-wave plates and half-wave plates. A quarter-wave plate has a retardance of $\delta(d = \pm\frac{\lambda}{4}) = \pm\frac{\pi}{2}$ and changes linear polarization into left-handed or right-handed circular polarization (depending on the sign) and vice versa. Correspondingly, a half-wave plate has a retardance of $\delta(d = \pm\frac{\lambda}{2}) = \pi$ and rotates the angle of linear polarization around 90° or changes right-handed circular polarization into left-handed circular polarization. The working principle of a quarter-wave plated is depicted in Figure 2.2b.

[3] A famous example for a birefringent materials is the calcite crystal as depicted in many textbooks.

[4] Which is why polarimetry usually relies on light sources with a narrow wavelength spectrum, as introduced in Chapter 3 and constructed in Chapter 4

Furthermore, the retardance depends on the angle of incident light with the optic axis[5] α_{inc} via [15]

$$\delta = \frac{2\pi d}{\lambda} \Delta n \cos^2(\alpha_{\text{inc}}) \tag{2.9}$$

The phenomenon of *optical activity* or *circular birefringence* occurs in materials with a chirality and refers to the ability of a material to rotate the polarization direction ρ of incident linear polarized light according to

$$\Delta\rho = \Psi \cdot d \tag{2.10}$$

where d is the material thickness and Ψ a material-specific coefficient. Optical acitivity can also be observed in fluids such as sugar solution or lactid acid.

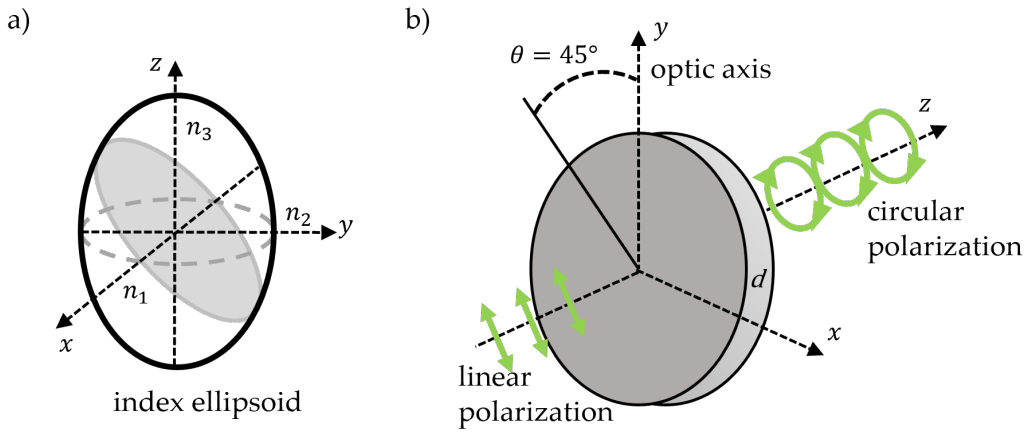

FIGURE 2.2: Birefringence in non-isotropic materials. a) The index ellipsoid represents the direction-dependent refractive indices in a non-isotropic material. When two of the three refractive indices are the same, a material is birefringent and the optic axis is defined as the axis along which the different refractive index occurs. b) A quarter-wave plate (QWP) introduces a phase shift of $\delta = \pm\frac{\lambda}{4} = \pm\frac{\pi}{2}$ between the slow and the fast ray. The QWP changes linear polarization into left-handed or right-handed circular polarization (depending on the sign) and vice versa. Image inspired by DEMTRÖDER [47].

2.1.3 Absorption, Attenuation, Dichroism and Diattenuation

In general, the refractive index n as introduced in Eq. (2.4) is a complex number

$$n = n_{\text{real}} - i\kappa \qquad \in \mathbb{C} \tag{2.11}$$

When an electromagnetic wave is traveling through a material with $n \in \mathbb{C}$, the imaginary component κ leads to an exponentially diminishing amplitude of the wave. Thus, $n \in \mathbb{C}$ contains not only the refractive properties but also the absorption.

The intensity of light undergoing absorption while traveling a distance Δz is expressed by the Lambert-Beer law of absorption

$$I = I_0 \cdot e^{-\mu_{\text{abs}}\Delta z} \tag{2.12}$$

[5] α_{inc} is referred to as the *inclination angle* in the next chapters as it represents the angle between an inclined nerve fiber with the direction of light incidence.

with the absorption coefficient μ_{abs} as

$$\mu_{\text{abs}} = \frac{4\pi\kappa}{\lambda_0} = 2k_0\kappa \tag{2.13}$$

with $k_0 = \frac{2\pi}{\lambda_0}$ being the wave number in vacuum. In addition, light scattering can also lead to a diminished intensity. The *attenuation* coefficient μ_{att} (synonymous to the *extinction* coefficient μ_{ext}) sums up μ_{abs} and the scattering coefficient μ_{scat}

$$I = I_0 \cdot e^{-\mu_{\text{att}}\Delta z} = I_0 \cdot e^{-(\mu_{\text{scat}}+\mu_{\text{abs}})\Delta z} \tag{2.14}$$

Just as birefringence is the polarization-dependent refraction, *dichroism* is the polarization-dependent absorption, and the direction-dependent attenuation is called *diattenuation*. The diattenuation D and the average transmittance τ are defined by the minimum and maximum transmittance T_{min} and T_{max}

$$D = \frac{T_{\text{max}} - T_{\text{min}}}{T_{\text{max}} + T_{\text{min}}} \qquad -1 \leq D \leq 1 \tag{2.15}$$

$$\tau = \frac{T_{\text{max}} + T_{\text{min}}}{2} \qquad 0 \leq \tau \leq 1 \tag{2.16}$$

The most extreme example of a diattenuating optical element is an ideal linear polarization filter: Here, the transmission of one linear polarization direction is zero whereas the orthogonal polarization is transmitted with no attenuation at all. When an ideal polarization filter is placed in a polarized light beam, the intensity I_{out} that passes through the filter is given by the angle $\Delta\rho$ between the polarization and the axis of the polarization filter. The relation is described by *Malus' law*

$$I_{\text{out}} = I_{\text{in}} \cos^2(\Delta\rho) \tag{2.17}$$

where I_{in} is the intensity of the original polarized light wave.

2.1.4 Scattering of Electromagnetic Waves

So far, attenuation has been described macroscopically. VAN DE HULST [84] provided an overview of light scattering at small particles: Scattering effects depend on the wavelength of the scattered light compared to the size of the scattering objects, as expressed by the size parameter $\frac{2\pi r}{\lambda}$ with r as the particle radius and λ the wavelength.

Geometric scattering occurs in the macroscopic regime where $\frac{2\pi r}{\lambda} \gg 1$. *Rayleigh scattering* as described by RAYLEIGH [151] occurs when $\frac{2\pi r}{\lambda} \ll 1$. Rayleigh scattering is highly dependent on the wavelength. *Mie scattering* occurs for $\frac{2\pi r}{\lambda} \approx 1$. MIE [126] provides the mathematical description of Mie scattering.[6]

ALERSTAM ET AL. [5] linked the microscopic direction-dependent diffusion to macroscopic scattering phenomena and established a direction-dependent scattering coefficient

$$\mu_{\text{scat}} = \begin{pmatrix} \mu_{xx} & 0 & 0 \\ 0 & \mu_{yy} & 0 \\ 0 & 0 & \mu_{zz} \end{pmatrix} \tag{2.18}$$

[6] However, only for scattering at spheres; Therefore, the analytical solution to Mie scattering is only valid for spheres, and with some modifications, for spheroids and ellipsoids. Elsewhere, a finite elements approach has to be applied.

Light traveling in a random medium can be classified into ballistic light, quasi-ballistic light and diffuse light, depending on the amount of scattering events. *Ballistic* light travels unscattered on its original path, quasi-ballistic light undergoes near-forward scattering, and diffuse photons are scattered multiple times, as summarized by MUJUMDAR ET AL. [132].

VAN DER LAAN ET AL. [96, 97] conducted Monte-Carlo simulations for Mie and Rayleigh scattering and a high number of scattering events. They revealed that the circularly polarized light maintains its degree of polarization better than linearly polarized light in the visible and infrared range. SAKAMOTO ET AL. [163] experimentally explored the influence of wavelength and polarization of illuminating light on polarization imaging for birefringent objects concealed behind scattering structures for visible and infrared light. They found that the birefringent object was more clearly visualized using longer wavelengths combined with circularly polarized light.

An example of an optical element where scattering is desired is the *diffuser plate* that depolarizes and homogenizes light.

2.1.5 Diffraction of Electromagnetic Waves

Diffraction is the spreading of a wave into the geometrical shadow behind an obstacle [24, 74]. The mechanism is based on the *Huygens-Fresnel principle* as proposed by HUYGENS [85] and expanded by FRESNEL [56]. The Huygens-Fresnel principle states that every point on a wavefront is the source of a spherical wavelet. The sum of these spherical wavelets forms a new wavefront.

Often, the term "diffraction" is used to describe a scattering phenomenon in which the scattered waves propagate in forward direction to create a diffraction pattern [24]. An optical diffraction pattern arises when *coherent* light waves (i.e. light waves with a constant relative phase relation, e.g. a laser beam) scatter off an object and interfere with each other. This interference results in regions of light and darkness in the observed diffraction pattern, where the waves constructively or destructively interfere.

The *Fraunhofer diffraction equation* applies when the diffraction pattern is observed in the far field. Then, the *Fraunhofer condition* is fulfilled with

$$l \gg \frac{d^2}{\lambda} \tag{2.19}$$

where l is the distance between the diffracting object or aperture and the observation plane, d the size of the diffracting aperture or object, and λ the wavelength. In the context of this thesis, all measurements fulfill this condition. Conversely, in the near field, the diffraction pattern is described by *Fresnel diffraction*. The Fresnel and Fraunhofer equations are approximations in the near field and far field, respectively, of the more general *Kirchhoff equation*.

Common diffraction scenarios include diffraction by a single slit, by circular or rectangular apertures, by double slits as in the double-slit experiment by YOUNG [212] as depicted in Figure 2.3a and – particularly relevant in the context of light scattering by nerve fibers – diffraction by a grating as depicted in Figure 2.3b

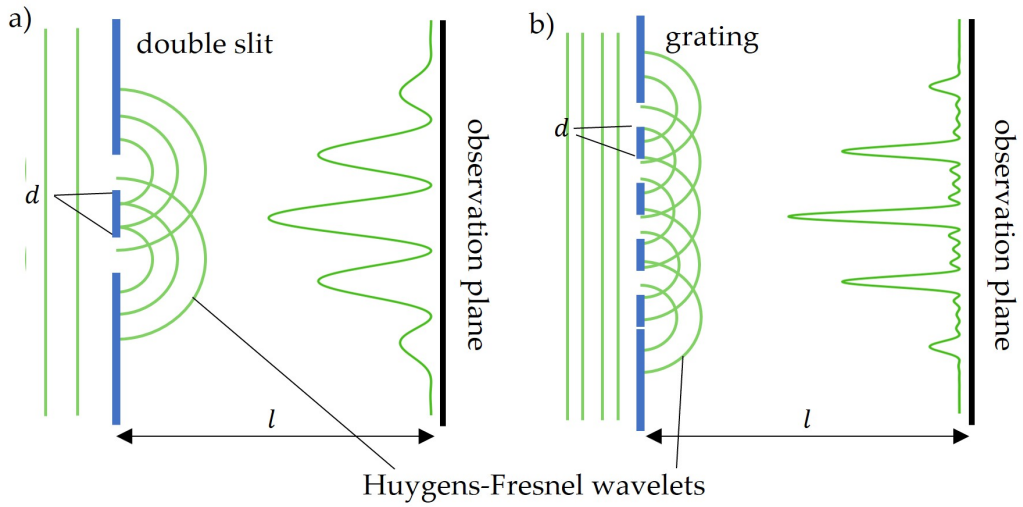

FIGURE 2.3: Huygens-Fresnel principle in two diffracting settings. Every point on a wavefront is the source of a spherical wavelet. The sum of these spherical wavelets forms a new wavefront. The Fraunhofer diffraction equation applies when $l \gg d^2/\lambda$ with λ the wavelength of the incident coherent light. a) Diffraction by a double slit with a periodic pattern of constructive and destructive interference. b) Diffraction by a grating. An increased number of slits results in interference peaks with a smaller width. Image inspired by [152].

2.1.6 Liquid Crystal Variable Retarders

In the recent years, *liquid crystals* have gained importance as optical elements. Unlike classical wave plates, the retardance of a liquid crystal device is not fixed but variable through the variation of an applied electrical field. The content of this section follows DE GENNES & PROST [60], LUCKHURST & DUNMUR [90], MUŠEVIČ [133] and ANDRIENKO ET AL. [8].

A liquid crystal is a fluid with the anisotropic properties typically associated with a solid crystal. A majority of liquid crystals known as calamitic liquid crystals consist of rod-like molecules. The long- and short-range order of the molecules determines the phase of the liquid crystal. The isotropic phase has neither orientation nor translation order. When the rod-like molecules have an orientation order, the liquid crystal is its nematic phase, the most common phase in electro-optical applications. The molecules have a preferred orientation direction (the "director") but no long-range translation order, i.e. the molecules do not group into layers.

The nematic phase is stable within a certain temperature range. Above the clearing point T_c, the nematic liquid crystal turns into an isotropic fluid. A phase transition into the more solid-like smectic A phase occurs with lower temperatures[7]. The molecular orientations of liquid crystal are displayed in Figure 2.4a.

When a liquid crystal is subjected to an electrical field, the orientation of the molecules changes with the voltage as shown in Figure 2.4b. Depending on the orientation of the molecules, the electro-optical properties of the liquid crystal change, rendering it birefringent due to the optical anisotropy of the rod-like molecules. Therefore, a liquid crystal acts like a retarder. The size and material of the molecules determines

[7] Furthermore, the smectic C phase can occur, which resembles the smectic A phase with the molecules tilted in their layers.

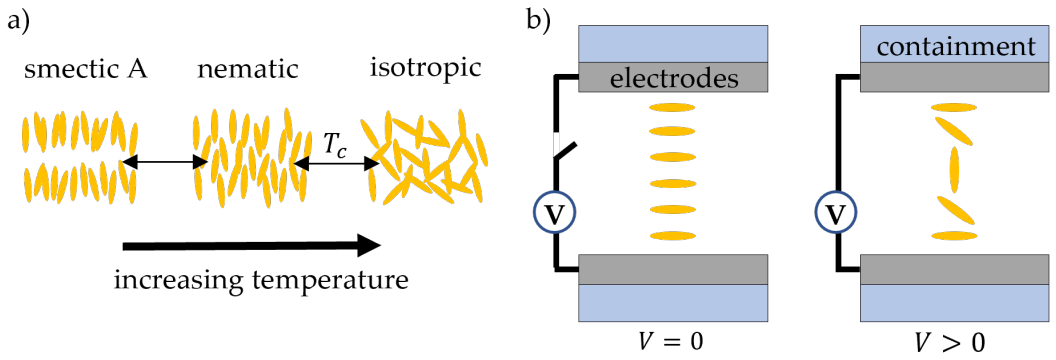

FIGURE 2.4: Working principle of liquid crystals. a) The isotropic phase has no longe-range order of the rod-like molecules. Liquid crystals for electro-optical applications are usually in the nematic phase, where the molecules have a preferred orientation direction but no translation order as they would in the smectic A phase. The phase changes with temperature. Image inspired by MUŠEVIČ [133]. b) When a liquid crystal is subjected to an electrical field, the orientation of the molecules changes with the voltage. To avoid charge built-ups, liquid crystal cells are usually not driven with a static electric field but with an alternating square wave. Image inspired by LUCKHURST & DUNMUR [90].

the wave length spectrum for which the liquid crystal retarder can be used. The retardance is wavelength-dependent. Thus, a liquid crystal retarder cell (also called a variable retarder) can act like a quarter-wave plate, a half-wave plate, an optical element with no retardance at all[8] or anything in-between. The dependence of the retardance and voltage is given by non-linear curve and usually determined by a measurement between crossed polarization filters. PALMER [144] investigated charge build-ups in liquid crystal cells caused by static electromagnetic fields. As those charge build-ups can interrupt or even damage the liquid crystal cell, liquid crystals are usually driven by an alternating square wave.

Liquid crystal cells can be used in the construction of a Müller polarimeter as demonstrated e.g. by DE MARTINO ET AL. [46], LAUDE-BOULESTEIX ET AL. [99] or LÓPEZ-TÉLLEZ & BRUCE [108]. The theoretical construction of a Müller polarimeter and the experimental measurement of the Müller matrix are addressed in Section 2.2.2 and Section 3.4, respectively.

2.2 Matrix Calculus in Polarimetry

Polarimetry refers to the measurement and analysis of the polarization exhibited by transverse waves, particularly electromagnetic waves, and investigates either the intrinsic properties of light waves or the optical properties of materials interacting with light through transmission or reflection. A system comprising polarizing optical elements can be represented through sequentially multiplied matrices, with each optic element characterized by a matrix. The order of matrix multiplication follows the path of light trough the system.

Jones matrix calculus is based on 2×2 matrices that operate on the polarization, absorption and retardation of a 2×1 vector representing the x- and y-amplitude of an electromagnetic wave. Müller matrix calculus employs 4×4 matrices. The

[8] In theory. Practically, a correction of residual retardance is required in real liquid crystal retarders.

corresponding 4×1 vector represents not the amplitude but the measurable intensity of linearly independent polarization states.

2.2.1 Jones Calculus

The explanations follow the textbooks by GOLDSTEIN [71], CHIPMAN [40] and PEDROTTI [145] unless stated otherwise.

In 1941, JONES [86, 87] formulated a mathematical description of polarized light[9]. A 2×1 vector represents an electromagnetic wave $\vec{E}$ through its linearly independent x- and y-component E_x and E_y, each characterized by its amplitude $E_{0,x}$ and $E_{0,y}$ and its phase φ_x and φ_y

$$\vec{E} = \begin{pmatrix} E_x \\ E_y \end{pmatrix} = \begin{pmatrix} E_{0x} e^{i\varphi_x} \\ E_{0y} e^{i\varphi_y} \end{pmatrix} \tag{2.20}$$

When $\vec{E}$ is normalized, the *Jones vector* $\vec{J}$ is defined by

$$\vec{J} = \begin{pmatrix} J_x \\ J_y \end{pmatrix} = \frac{1}{|\vec{E}|} \begin{pmatrix} E_{0x} e^{i\varphi_x} \\ E_{0y} e^{i\varphi_y} \end{pmatrix} \tag{2.21}$$

Typical basic polarization states can be written as linear combinations of the linear independent basic vectors $\vec{J}_\mathrm{H}$ (horizontal polarization) and $\vec{J}_\mathrm{V}$ (vertical polarization)

$$\vec{J}_\mathrm{H} = \begin{pmatrix} 1 \\ 0 \end{pmatrix} \qquad \vec{J}_\mathrm{V} = \begin{pmatrix} 0 \\ 1 \end{pmatrix} \tag{2.22a}$$

$$\vec{J}_\mathrm{D} = \frac{1}{\sqrt{2}} \begin{pmatrix} 1 \\ 1 \end{pmatrix} \qquad \vec{J}_\mathrm{A} = \frac{1}{\sqrt{2}} \begin{pmatrix} 1 \\ -1 \end{pmatrix} \tag{2.22b}$$

$$\vec{J}_\mathrm{R} = \frac{1}{\sqrt{2}} \begin{pmatrix} 1 \\ i \end{pmatrix} \qquad \vec{J}_\mathrm{L} = \frac{1}{\sqrt{2}} \begin{pmatrix} 1 \\ -i \end{pmatrix} \tag{2.22c}$$

For example, $\vec{J}_\mathrm{D}$ and $\vec{J}_\mathrm{A}$ are the Jones vectors for diagonal and antidiagonal polarization, respectively, i.e. a linear electromagnetic wave swinging in along the (anti-) diagonal axis of the Cartesian coordinate system. $\vec{J}_\mathrm{R}$ and $\vec{J}_\mathrm{L}$ refer to right- and left-circular polarization as introduced in Section 2.1.1.

The *Jones matrix* for a general optical element reads

$$M = \begin{pmatrix} m_{11} & m_{12} \\ m_{21} & m_{22} \end{pmatrix} \qquad m_{ij} \in \mathbb{C} \tag{2.23}$$

Table 2.1 shows the Jones matrices for typical optical elements used within the scope of this thesis. The azimuthal rotation of an optical element M around the angle θ is realized by

$$M(\theta) = R(\theta) \cdot M(0) \cdot R(-\theta) \tag{2.24}$$

with the rotation matrix $R(\theta)$

$$R(\theta) = \begin{pmatrix} \cos\theta & -\sin\theta \\ \sin\theta & \cos\theta \end{pmatrix} \tag{2.25}$$

[9] Jones calculus assumes full polarization and cannot treat depolarization, unlike Müller calculus. However, Jones calculus is sufficient for many applications when depolarization can be neglected.

TABLE 2.1: Jones matrices for common optic components. Matrices as given by PEDROTTI [145] for ideal behavior.

optical component	**Jones matrix**
horizontal linear polarizer ($\theta = 0°$)	$\begin{pmatrix} 1 & 0 \\ 0 & 0 \end{pmatrix}$
vertical linear polarizer ($\theta = 90°$)	$\begin{pmatrix} 0 & 0 \\ 0 & 1 \end{pmatrix}$
phase retarder ($\theta = 0°$)	$\begin{pmatrix} e^{i\varphi_x} & 0 \\ 0 & e^{i\varphi_y} \end{pmatrix} = \begin{pmatrix} 1 & 0 \\ 0 & e^{i\delta} \end{pmatrix}$
phase retarder ($\theta = 45°$)	$e^{i\frac{\delta}{2}} \begin{pmatrix} \cos(\delta/2) & i\sin(\delta/2) \\ i\sin(\delta/2) & \cos(\delta/2) \end{pmatrix}$
quarter-wave plate (fast axis horizontal)	$\begin{pmatrix} 1 & 0 \\ 0 & e^{+i\frac{\pi}{2}} \end{pmatrix}$
quarter-wave plate (fast axis vertical)	$\begin{pmatrix} 1 & 0 \\ 0 & e^{-i\frac{\pi}{2}} \end{pmatrix}$

Most commonly, experimental setups cannot measure the Jones vector itself but the intensity, i.e. the squared absolute value of the amplitude, s. Section 2.1.1.

2.2.2 Müller Calculus

The explanations follow the textbooks by GOLDSTEIN [71], CHIPMAN [40] and PEDROTTI [145] unless stated otherwise.

In 1852, STOKES [179] established a mathematical way of describing polarized light only in terms of observable quantities. Any polarization state of light can be completely described by only four *Stokes parameters* S_0 to S_3 (in literature sometimes also denoted with S_1 to S_4) that represent the intensity of light rather than the amplitude as in Jones calculus. In contrast to Jones calculus, Stokes calculus also describes unpolarized or partially polarized light. The parameter S_0 expresses the total intensity of the light. The following three parameters describe the polarization state, with S_1 being the dominance of horizontal linear polarization H over vertical linear polarization V, S_2 being the dominance of diagonal linear polarization D over antidiagonal linear polarization A, and S_3 being the dominance of right circular polarization R over left circular polarization L. It must be emphasized that D and A are no linear combinations of H and V because they represent intensity. While amplitudes would

in fact be a linear combination, intensities as the squared amplitudes are not. S_0 to S_3 make up the *Stokes vector* $\vec{S}$. The normalized Stokes vector is given by

$$\vec{S} = \frac{1}{S_0}\begin{pmatrix} S_0 \\ S_1 \\ S_2 \\ S_3 \end{pmatrix} = \begin{pmatrix} 1 \\ \mathrm{H}-\mathrm{V} \\ \mathrm{D}-\mathrm{A} \\ \mathrm{R}-\mathrm{L} \end{pmatrix} = \frac{1}{\langle E_x^2 + E_y^2 \rangle}\begin{pmatrix} \langle E_x^2 + E_y^2 \rangle \\ \langle E_x^2 - E_y^2 \rangle \\ \langle 2E_x E_y \cos(\delta) \rangle \\ \langle 2E_x E_y^2 \sin(\delta) \rangle \end{pmatrix} \tag{2.26}$$

The normalized polarization states H, V, D, A, R, and L written as Stokes vectors read

$$\vec{S}_\mathrm{H} = \begin{pmatrix} 1 \\ 1 \\ 0 \\ 0 \end{pmatrix} \qquad \vec{S}_\mathrm{V} = \begin{pmatrix} 1 \\ -1 \\ 0 \\ 0 \end{pmatrix} \tag{2.27a}$$

$$\vec{S}_\mathrm{D} = \begin{pmatrix} 1 \\ 0 \\ 1 \\ 0 \end{pmatrix} \qquad \vec{S}_\mathrm{A} = \begin{pmatrix} 1 \\ 0 \\ -1 \\ 0 \end{pmatrix} \tag{2.27b}$$

$$\vec{S}_\mathrm{R} = \begin{pmatrix} 1 \\ 0 \\ 0 \\ 1 \end{pmatrix} \qquad \vec{S}_\mathrm{L} = \begin{pmatrix} 1 \\ 0 \\ 0 \\ -1 \end{pmatrix} \tag{2.27c}$$

and are depicted in Figure 2.5a. A tool to visualize polarization states in Stokes calculus is the *Poincaré sphere*[10] introduced by POINCARÉ [147], as depicted in Figure 2.5b [43]. The three axes form the three linearly independent vectors in Stokes calculus. $\vec{S_\mathrm{H}}$ and $\vec{S_\mathrm{V}}$ are found at the location ± 1 on the first axis, $\vec{S_\mathrm{D}}$ and $\vec{S_\mathrm{A}}$ are found at the location ± 1 of the second axis etc. A change in polarization corresponds to rotating and/or shortening/lengthening a vector within the border of the Poincaré sphere. Vectors with the length of the radius of the sphere represent complete polarization. Shorter vectors represent partially unpolarized light. Completely depolarized light is depicted as a vector with no length in the origin of the coordinate system, i.e. $\vec{S} = (0,0,0,0)^T$.

Any polarization state always satisfies the Cauchy Schwarz's inequality [73], i.e. the normalized vector is never longer than the radius of the Poincaré sphere

$$\sqrt{S_1^2 + S_2^2 + S_3^2} \leq S_0 \tag{2.28}$$

In case of completely polarized light, the two sides are equal. In case of partial depolarization, the left side is smaller. In case of completely unpolarized light, there is no dominance of any polarization and the left side becomes 0. The *degree of polarization (DOP)* can be expressed as

$$DOP = \frac{\sqrt{S_1^2 + S_2^2 + S_3^2}}{S_0} \in [0,1] \tag{2.29}$$

The four Stokes parameters for monochromatic light of an unknown polarization can

[10] Mathematically, the Poincaré sphere is identical to the *Bloch sphere* in quantum mechanics [135].

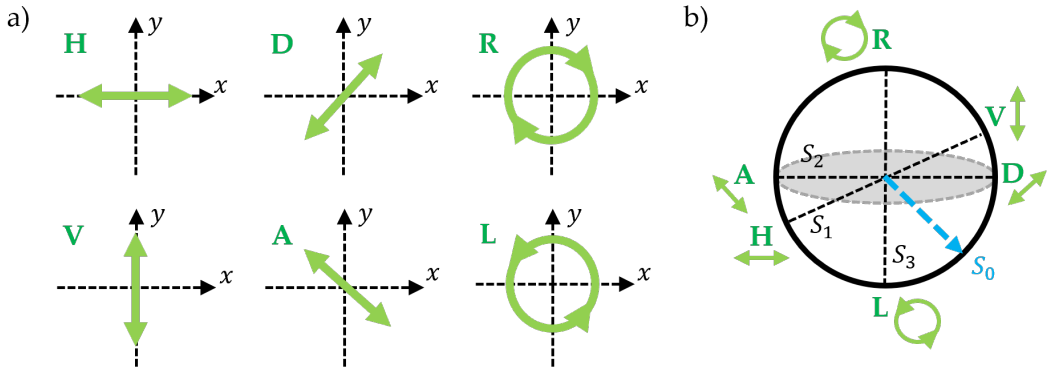

FIGURE 2.5: Basic polarization states and the Poincaré sphere. a) Schematic depiction of polarization states of a transverse wave: Horizontal Linear (H), Vertical Linear (V), Diagonal Linear (D), Antidiagonal Linear (A), Right-handed Circular (R) and Left-handed Circular Polarization (L). b) The basic states visualized on the Poincaré sphere. A change in polarization corresponds to rotating and/or shortening/lengthening the Stokes vector within the borders of the Poincaré sphere. Vectors with the length of the radius of the sphere represent complete polarization. Shorter vectors represent partially unpolarized light. Image inspired by COLLETT [43].

be measured using a retarder with a retardance δ followed by a linear polarization filter with its transmitting axis at angle θ

$$I(\theta,\delta) = \frac{1}{2}\left(S_0 + S_1\cos(2\theta) + S_2\cos(\delta)\sin(2\theta) + S_3\sin(\delta)\sin(2\theta)\right) \tag{2.30}$$

The whole derivation was presented by GOLDSTEIN [71]. Four measurements suffice to obtain the Stokes vector

$$I(\theta = 0°,\delta = 0°) = \frac{1}{2}\left(S_0 + S_1\right) \qquad I(\theta = 45°,\delta = 0°) = \frac{1}{2}\left(S_0 + S_2\right) \tag{2.31a}$$

$$I(\theta = 90°,\delta = 0°) = \frac{1}{2}\left(S_0 - S_1\right) \qquad I(\theta = 45°,\delta = 90°) = \frac{1}{2}\left(S_0 + S_3\right) \tag{2.31b}$$

The variable retarders in Chapter 4 employ those settings, flexibly serving as linear polarization filers and quarter-wave plates.

The Stokes formalism was rediscovered in the midth of the 20th century by CHANDRASEKHAR [38] in the context of astrophysics; but also by MÜLLER [131] who developed the *Müller matrix* formalism to describe all polarizing (or depolarizing) properties of any material within a single 4×4 matrix

$$M = \begin{pmatrix} m_{00} & m_{01} & m_{02} & m_{03} \\ m_{10} & m_{11} & m_{12} & m_{13} \\ m_{20} & m_{21} & m_{22} & m_{23} \\ m_{30} & m_{31} & m_{32} & m_{33} \end{pmatrix} \tag{2.32}$$

Material symmetries can lead to a reduction of independent matrix entries down to 10, 8 or only 6 independent parameters as discussed by VAN DE HULST [84, 166]. Multiple optical elements can be described by a multiplication of Müller matrices in the order of light propagation. Table 2.2 shows the Müller matrices of various optical elements that are used in the scope of this thesis. The derivations are detailed by GOLDSTEIN [71]. Additionally, the azimuthal rotation $R(\theta)$ around an angle θ is

given by the transformation

$$M(\theta) = R(\theta) \cdot M(0) \cdot R(-\theta) \tag{2.33}$$

with the rotation matrix

$$R(\theta) = \begin{pmatrix} 1 & 0 & 0 & 0 \\ 0 & \cos(2\theta) & -\sin(2\theta) & 0 \\ 0 & \sin(2\theta) & \cos(2\theta) & 0 \\ 0 & 0 & 0 & 1 \end{pmatrix} \tag{2.34}$$

TABLE 2.2: Müller matrices for common optical components. The derivations of the matrices were given by GOLDSTEIN [71]. The diattenuator/retarder $M(D_L, \delta)$ is calculated by CHENAULT & CHIPMAN [39] and represents a sample whose axes of linear diattenuation D_L (as introduced in Section 2.2.4) and retardance δ are coincident.

optical element	**Müller matrix**
horizontal linear polarizer ($\theta = 0°$)	$\frac{1}{2}\begin{pmatrix} 1 & +1 & 0 & 0 \\ +1 & 1 & 0 & 0 \\ 0 & 0 & 0 & 0 \\ 0 & 0 & 0 & 0 \end{pmatrix}$
vertical linear polarizer ($\theta = 90°$)	$\frac{1}{2}\begin{pmatrix} 1 & -1 & 0 & 0 \\ -1 & 1 & 0 & 0 \\ 0 & 0 & 0 & 0 \\ 0 & 0 & 0 & 0 \end{pmatrix}$
variable retarder ($\theta = 45°$)	$\begin{pmatrix} 1 & 0 & 0 & 0 \\ 0 & \cos(\delta) & 0 & -\sin(\delta) \\ 0 & 0 & 1 & 0 \\ 0 & \sin(\delta) & 0 & \cos(\delta) \end{pmatrix}$
variable retarder ($\theta = 0°$)	$\begin{pmatrix} 1 & 0 & 0 & 0 \\ 0 & 1 & 0 & 0 \\ 0 & 0 & \cos(\delta) & \sin(\delta) \\ 0 & 0 & -\sin(\delta) & \cos(\delta) \end{pmatrix}$
diattenuator/retarder ($\theta = 0°$)	$\begin{pmatrix} 1 & D_L & 0 & 0 \\ D_L & 1 & 0 & 0 \\ 0 & 0 & \sqrt{1-D_L^2}\cos(\delta) & \sqrt{1-D_L^2}\sin(\delta) \\ 0 & 0 & -\sqrt{1-D_L^2}\sin(\delta) & \sqrt{1-D_L^2}\cos(\delta) \end{pmatrix}$

A *complete polarimeter* determines all 16 elements of Müller matrix for an unknown sample using reflected or transmitted light. Accordingly, a complete polarimeter is also called a *Müller polarimeter*. The optical elements before the sample generate the in-going polarization state and are called the *polarization state generator (PSG)*. Analogously, the *polarization state analyer (PSA)* after the sample analyzes the outgoing polarization state.

When the incident state of polarization S_{in} and the transmitted state of polarization S_{out} are both known, finding the Müller matrix elements for an unknown sample comes down to solving a linear equation system with 16 unknown parameters. The most intuitive approach is to generate and analyze combinations of the 6 polarization states $\vec{S_{\text{H}}}$, $\vec{S_{\text{V}}}$, $\vec{S_{\text{D}}}$, as demonstrated e.g. by BICKEL & BAILEY [25] and many others. Clearly, 6 possible polarization settings for both the PSG and the PSA yield 36 setting combinations. It is common to either choose the mathematical minimum of 16 setting combinations for improved speed; or to over-determine the linear equation system using all 36 setting combinations for a more intuitive understanding of tissue effects and less error propagation within the results. Chapter 3 further investigates the experimental measurement and evaluation of the Müller matrix.

2.2.3 Calibration of a Müller Polarimeter

When an unknown sample M is measured with a non-ideal Müller polarimeter, deviations from the optimal settings within the PSG and PSA influence the measured raw data matrix B

$$B = AMW \tag{2.35}$$

Here, the unknown 4×4 Müller matrices A and W sum up the non-ideal optical deviations of the PSA and PSG, respectively. Calibrating a Müller polarimeter means finding the matrices A and W using designated calibration samples with known properties. COMPAIN ET AL. [44] developed the *Eigenvalue Calibration Method (ECM)* for Müller polarimetry and suggest optimal calibration samples. Furthermore, they show that the exact azimuthal orientation and the exact retardance of the calibration samples does not matter as long as the employed polarization filters can be assumed as perfect. More specifically, the calibration requires measuring the empty setup (i.e. the Müller matrix of air), a linear polarization filter at two different orientations, and a birefringent plate (for example, but not necessarily, a quarter-wave plate).

The measurement of the empty setup without a sample yields

$$B_0 = AM_0W = AW \qquad M_0 = \mathbb{1} \tag{2.36}$$

where the ideal Müller matrix M_0 for air corresponds to the unit matrix. A measurement of other three samples yields the raw data matrices B_1, B_2 and B_3

$$B_i = AM_iW \qquad i = 1, ..., 3 \tag{2.37}$$

An auxiliary matrix C_i is calculated for each sample using the raw data matrices B_i and the inverse of B_0

$$C_i = B_0^{-1}B_i = W^{-1}M_iW \tag{2.38}$$

Intrinsically, the matrices C_i have the same eigenvalues as M_i regardless of their orientation because rotation does not change the eigenvalues. W is a solution of

$$M_iW - WC_i = 0 \tag{2.39}$$

MACÍAS-ROMERO & TÖROK [110] used the **vec** operator to solve the equation system: The **vec** operator – as introduced by HENDERSON & SEARLE [79] – stacks the columns of a $n \times m$ matrix to to form a $1 \times n \cdot m$ vector. Using **vec**(W), Eq. (2.39) is rewritten as

$$H_i\mathbf{vec}(W) =: (I \otimes M_i - C_i^T \otimes \mathbb{1})\mathbf{vec}(W) = 0 \tag{2.40}$$

with H_i being a 16×16 auxiliary matrix and $\otimes$ denoting the Kronecker product. H_i can be constructed from every raw data matrix B_i and the corresponding ideal matrix M_i (again, the azimuthal rotation of M_i does not matter). A linear combination L yields[11]

$$L\mathbf{vec}(W) = 0 \qquad L = \sum_i^N H_i^T H \tag{2.41}$$

Here, the choice of calibration samples becomes important: W is only unique when the calibration samples have been chosen according to the aforementioned restrictions. Only then, the null space of L is reduced to 1, i.e. there is only one eigenvalue of L that is zero (or very close to zero in practice)

$$0 \approx \lambda_0 \ll \lambda_1 < \lambda_2 ... < \lambda_{15} \tag{2.42}$$

The 1×16 eigenvector associated with the eigenvalue λ_0 corresponds to W and can easily be reshaped into a 4×4 matrix[12]. Finally, A is easily calculated from the inverse of W. The inverse matrix W^{-1} always exists when W is correctly determined

$$A = B_0 W^{-1} \tag{2.43}$$

Now, every raw data matrix B for an unknown sample M can be calibrated with the inverse of A and W

$$M = A^{-1} B W^{-1} \tag{2.44}$$

2.2.4 Lu-Chipman Decomposition

The Müller matrix contains information about all polarization-related properties of the investigated material. LU & CHIPMAN [107] extracted the direction- and polarization-dependent diattenuation, the retardance and the depolarization by performing mathematical operations on the matrix elements. The next paragraph follows their calculations unless stated otherwise.

A polarization element is said to be *homogeneous* when it has two orthogonal eigenpolarizations. It can written as a Jones matrix or a Müller matrix, both of which are then said to be homogeneous. A *diattenuator* is a homogeneous element with zero retardance and a *retarder* is a homogeneous polarization element with no diattenuation.

The *retardance*[13] R is described by a retardance vector $\vec{R}$ along the fast axis $\hat{R}$. The components of $\vec{R}$ hold the *horizontal* (δ_H), the *diagonal* (δ_D) and the *circular* (δ_C) *retardance* component:

$$\vec{R} = R\hat{R} = \begin{pmatrix} R_H \\ R_D \\ R_C \end{pmatrix} \tag{2.45}$$

The *linear retardance* R_L is defined as

$$R_L = \sqrt{R_H^2 + R_D^2} \tag{2.46}$$

[11] Requiring H_i to be Hermitian, which is generally not the case, therefore the multiplication with the transposed matrix to eliminate this issue.

[12] e.g. in Python with the *reshape* function from *numpy* [139], reshaping the vector to a 4×4 matrix 4,4 in Fortran order.

[13] R represents the combined effects of linear and circular retardance. δ, as it was established in Section 2.1.2 and is measured with 3D-PLI in Section 3.2, is the linear retardance.

It follows that

$$R = \sqrt{R_H^2 + R_D^2 + R_C^2} = \sqrt{R_L^2 + R_C^2} = |\vec{R}| \tag{2.47}$$

The *diattenuation* D is described accordingly by a diattenuation vector $\vec{D}$ along the axis with the larger transmittance $\hat{D}$

$$\vec{D} = D\hat{D} = \begin{pmatrix} D_H \\ D_D \\ D_C \end{pmatrix} \tag{2.48}$$

The *linear diattenuation* D_L is defined as

$$D_L = \sqrt{D_H^2 + D_D^2} \tag{2.49}$$

and accordingly

$$D = \sqrt{D_H^2 + D_D^2 + D_C^2} = \sqrt{D_L^2 + D_C^2} = |\vec{D}| \tag{2.50}$$

A *linear diattenuator* has no circular diattenuation just like a *linear retarder* has no circular retardance. Likewise, a *circular diattenuator* (or retarder) has no *linear diattenuation* (or retardance). Furthermore, the diattenuation vector $\vec{D}$ and the retardance vector $\vec{\delta}$ are parallel for homogeneous elements.

When an experimental Müller matrix M with matrix elements $m_{i,j}$ is given, the *maximum* and *minimum transmittance* $T_{\max}$ and $T_{\min}$ are completely determined by its first row

$$T_{\max,\min} = m_{00} \pm \sqrt{m_{01}^2 + m_{02}^2 + m_{03}^2} \tag{2.51}$$

The diattenuation D and the diattenuation vector $\vec{D}$ are given by

$$D = \frac{T_{\max} - T_{\min}}{T_{\max} + T_{\min}} = \frac{1}{m_{00}} \sqrt{m_{01}^2 + m_{02}^2 + m_{03}^2} \in [0, 1] \tag{2.52}$$

$$\vec{D} = \frac{1}{m_{00}} \begin{pmatrix} m_{01} \\ m_{02} \\ m_{03} \end{pmatrix} = \begin{pmatrix} D_H \\ D_D \\ D_R \end{pmatrix} \tag{2.53}$$

Furthermore, the first row – when normalized – directly corresponds to the *horizontal diattenuation* D_H, the *diagonal diattenuation* D_D and the *circular diattenuation* D_C as defined in Eq. (2.48). Analogously to the diattenuation, the polarizance P (the ability to polarize unpolarized light) is given by

$$P = \frac{1}{m_{00}} \sqrt{m_{10}^2 + m_{20}^2 + m_{30}^2} \in [0, 1] \tag{2.54}$$

So far, Eq. (2.51) - (2.54) are valid both for depolarizing and non-depolarizing systems. However, when an experimental Müller matrix M is given, it is usually necessary to separate the depolarizing effects from the diattenuating and retarding effects to interpret the result. GIL & BERNABEU [67] derived a necessary and sufficient criterion to determine whether an optical system described by a Müller matrix M has depolarizing properties

$$Tr(M^T M) = 4m_{00}^2 \tag{2.55}$$

When equality is given, the system is non-depolarizing. The *Lu-Chipman decomposition* rewrites M as the matrix product

$$M = M_\Delta M_R M_D \tag{2.56}$$

with M_Δ the *depolarization matrix*, M_R the *retardance matrix* and M_D the *diattenuation matrix*. The decomposition of the retardance and the depolarizing matrix includes solving an eigenvalue problem for the depolarizing matrix and was demonstrated in detail by LU& CHIPMAN [107][14].

When M is decomposed according to Eq. (2.56), the Müller matrix of depolarization M_Δ yields the *total depolarization* Δ

$$\Delta = 1 - \frac{|Tr(M_\Delta|)}{3} \qquad 0 \leq \Delta \leq 1 \tag{2.57}$$

with $Tr(M_\Delta)$ denoting the trace of the matrix. A value of 1 indicates complete depolarization. A value of 0 indicates that no depolarization occurs. Analogously, AHMAD ET AL. [3] employed the *linear depolarization* Δ_L defined by only the diagonal matrix elements that are associated with linearity

$$\Delta_L = 1 - \frac{|m_{\Delta,11} + m_{\Delta,22}|}{2} \qquad 0 \leq \Delta \leq 1 \tag{2.58}$$

The *eigenpolarizations* of a retarding Müller matrix M_δ are along the fast axes and slow axes, i.e. the total retardance δ and the elements r_i of the retardance vector can be obtained by

$$R = \cos^{-1}\left(\frac{tr(M_R)}{2} - 1\right) \tag{2.59}$$

and

$$r_i = \frac{1}{2\sin(R)} \sum_{j,k=1}^{3} \epsilon_{ijk}(m_R)_{jk} \qquad \text{with} \qquad M_R = \begin{pmatrix} 1 & \vec{0}^T \\ \vec{0} & m_R \end{pmatrix} \tag{2.60}$$

with $Tr(M_R)$ denoting the trace of the matrix and ϵ_{ijk} the Levi-Civita permutation symbol [102]. The total retardance R can be separated into an *optical rotation* of magnitude Ψ and the *linear retardance* δ. MANHAS ET AL. [111] and GHOSH ET AL. [66] expressed the linear retardance δ as

$$\delta = \cos^{-1}\left(\sqrt{\left([m_{R,11} + m_{R,22}]^2 + [m_{R,21} + m_{R,12}]^2\right)} - 1\right) \tag{2.61}$$

the orientation of the fast axis with respect to the horizontal axis θ by

$$\phi_R = \frac{1}{2}\tan^{-1}(\frac{r_3}{r_2}) = \frac{1}{2}\tan^{-1}(\frac{m_{R,12} - m_{R,21}}{m_{R,13} - m_{R,31}}) \tag{2.62}$$

and the optical rotation Ψ (i.e. the rotation of the axis of linear polarization around an angle Ψ; the effect of a circular retarder) by

$$\Psi = \tan^{-1}\left(\frac{m_{R,21} - m_{R,12}}{m_{R,11} + m_{R,22}}\right) \tag{2.63}$$

[14] In Chapter 4, the Lu-Chipman decomposition is implemented with functions from *pySCATMECH*.

2.3 Anatomy and Optical Properties of Brain Tissue

The human brain consists of about 86 billions of neurons that form a highly complex network of cells and nerve fiber pathways [80]. This chapter gives a basic overview of the human brain anatomy. The focus is set on characteristic well-known fiber structures that are used to compare and validate measurement results in subsequent chapters. Optical properties of brain tissue are explored, such as birefringence, absorption, scattering, and depolarization, thus directly linking tissue properties to the optical phenomena introduced in Section 2.1. Moreover, the impact of neurodegenerative diseases on light-tissue-interaction is discussed.

The anatomical explanations follow ZILLES [215], SNELL [177] and TREPEL [194].

2.3.1 Anatomy of the Human Brain

The brain and the spinal cord are considered parts of the *central nervous system* (CNS). The brain is further categorized into the *forebrain* (*cerebrum/telencephalon* and *diencephalon*), the *midbrain* (also *mesencephalon*) and the *hindbrain* (*medulla oblongata*, *pons* and *cerebellum*).

The medulla oblongata, pons and midbrain form together the *brainstem* that links the cerebrum to the *spinal cord*. The two *hemispheres* of the cerebrum are connected by a broad commissure, the *corpus callosum*. The cerebral cortex covering the whole surface exhibits a convoluted shape characterized by *gyri* (folds) and *sulci* (fissures).

Figure 2.6a shows a a typical human brain and the three anatomical planes (coronal, sagittal, horizontal). Figure 2.6b illustrates characteristic white matter structures in the coronal plane that are discussed later in further detail.

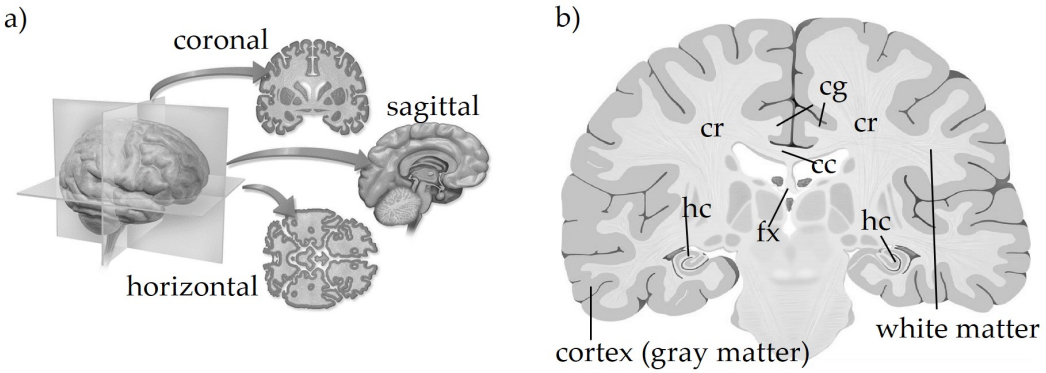

FIGURE 2.6: Characteristic anatomical structures in a coronal section. a) The three neuroanatomical planes in the brain (coronal, sagittal, horizontal), shown exemplary for a human brain. Image adapted and modified from Blausen Medical [26] (CC BY 3.0). b) Schematic depiction of a coronally sectioned human brain. The *corpus callosum* (cc) is a white matter structure of mostly parallel fiber bundles that connects the two brain hemispheres. The *corona radiata* (cr) is constituted by multiple interwoven crossing fiber bundles. The *fornix* (fx) is a C-shaped structure (when seen from the sagittal plane) of mostly parallel fiber bundles on each side that arise from the *hippocampus* (hc) and join beneath the corpus callosum. The *cingulum* (cg) is a nearly ring-shaped sagittal fiber bundle around the corpus callosum.

At the cellular level, the nervous system is composed of *neurons* which are excitable nerve cells that are supported by *glial cells*, but also blood vessels and connective tissue.

Neurons receive, process, and transmit information in the form of electrical stimuli, while various types of glial cells provide essential support functions, including nutrition, protection, and electrical insulation, as shown in Figure 2.7a. There are five to ten times more glial cells than neurons in the human body, with about 86 billion neurons in the human brain alone [80]. *Oligodendrocytes* are a type of glial cell that provides support and insulation. *Astrocytes*, among other functions, provide nutrients to the nervous tissue. *Microglia* are part of the immune system of the nervous system.

Depending on its cellular composition, brain matter is classified into *gray matter* and *white matter* that differ optically and structurally. Gray matter consists of nerve cells embedded in *neuroglia* whereas white matter consists of their axonal processes embedded in *oligodendroglia*. While the cortices of the cerebrum and cerebellum are predominantly gray matter, the interior is primarily white matter.

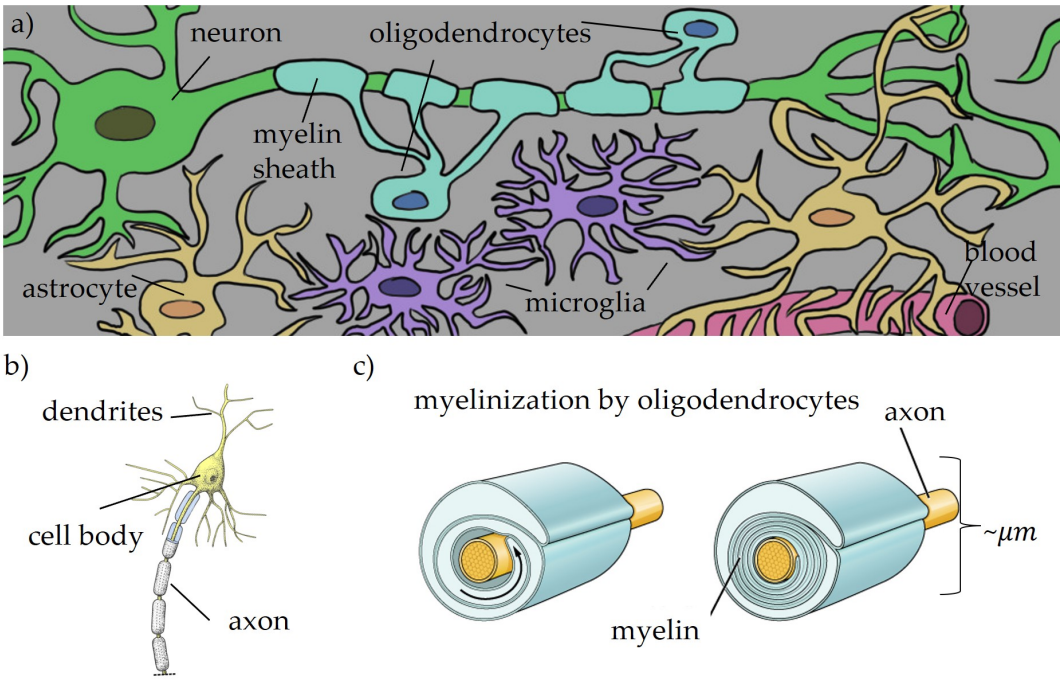

FIGURE 2.7: Cells in the central nervous system (CNS). a) Overview of cell types in the CNS. The major components of the CNS are nerve cells (the *neurons*), *glial cells*, and blood vessels. *Oligodendrocytes* form the *myelin sheath*. *Astrocytes*, among other functions, provide nutrients to the nervous tissue. *Microglia* are part of the immune system of the CNS. Image inspired by PUHL ET AL [148]. b) Anatomy of a typical nerve cell. Electric stimuli are received via *synapses*, located on the *dendrite* tree of the cell. Excitatory and inhibitory stimuli are integrated at the axon hillock (a part of the cell body) and transmitted via the myelinated axon. c) A myelinated nerve fiber. The myelin sheath is made up by many windings of lipid bilayers with an overall diameter in the order of the wavelength of visible light. In the CNS, it is formed by oligodendrocytes. The myelin sheaths wrap around the axons and induce an optical anisotropy leading to uniaxial birefringence and diattenuation due to their radially oriented structure of fatty acid tails. Image modified from OpenStax [140] (CC BY 4.0).

A sketch of a typical neuron is shown in Figure 2.7b. Neurological information is coded as an electric signal: Excitatory and inhibitory stimuli are received via the many *dendrites* (antennae of the nerve cell) and then integrated at the *axon hillock*, a

part of the cell body. If a threshold potential is reached, the *action potential* is generated and propagates along a single long nerve cell extension called the *axon*.

The axon is typically covered in *myelin* – made up by many windings of lipid bilayers produced by the oligodendrocytes – providing electrical insulation and significantly accelerating signal transmission through *saltatoric excitation*[15]. The myelin sheath is shown in Figure 2.7c. White matter consists mainly of myelinated nerve fibers whereas gray matter mainly contains tightly packed nerve cell bodies and dendrites, which are not myelinated. Therefore, white matter has a higher lipid content compared to gray matter, with 54.9 % in human white matter and 32.7% in human gray matter. Inversely, the protein content in white matter is lower with 39.0 % in human white matter and 55.3 % in human gray matter [149]. LIEWALD ET AL. [104] mentioned the white matter fiber diameters in human brains to range from 0.16 µm to 9µm, with most of the average values below 1 µm diameter. Neurons appear in a wide variety of shapes and sizes, with the cell body size ranging from 5 µm up to 135 µm in diameter.

Corpus Callosum The *corpus callosum* (cc) is the white matter commissure that connects the two brain hemispheres and is indicated in Figure 2.6b. It consists of mostly parallel bundles of nerve fibers. In a coronal section, the nerve fibers run in-plane whereas in a sagittal section, the fibers are vertical to the sectioning plane. ABOITIZ ET AL. investigated the regional fiber composition of the human corpus callosum using light microscopy and electron microscopy [1]: They found that myelinated fiber sizes range from 0.2 µm up to more than 10 µm in diameter and fibers larger than 1 µm represent about 20% of the total fibers counted. Unmyelinated fibers are scarce in most callosal regions. The fiber density varies along the corpus callosum. The corpus callosum serves as a model region of parallel (in-plane) fibers within the scope of this thesis.

Corona Radiata The *corona radiata* (cr) is characterized by several crossing nerve fiber bundles. In a coronal section, two major fiber bundles are crossing in-plane with a third major bundles crossing vertically to the sectioning plane. WEDEEN ET AL. [201] mapped and visualized the crossing fibers of e.g. the corona radiata based on MRI data. The corona radiata serves as a model region for crossing fibers.

Fornix The *fornix cerebri* or simply *fornix* (fx) is a C-shaped bundle (seen from the sagittal plane) of white matter arising from the *hippocampus* (hc) of each side and joining beneath the corpus callosum. CATANI ET AL. [36] virtually dissected and visualized the three-dimensional fiber structure of the fornix. In the coronal plane, the fiber direction forms an inclined angle with the sectioning plane. Thus, the fornix is used as a model region for inclined fiber (usually in comparison to the in-plane fibers of the corpus callosum).

Cingulum The *cingulum* (cg) is a nearly ring-shaped fiber bundle around the corpus callosum (when seen from the sagittal plane). In the coronal plane, the fiber bundles are oriented nearly vertically to the sectioning plane, thus serving as a model region for steep fibers. BUBB ET AL. [29] illustrated how various minor fiber structures lead towards or away from the major fiber direction.

[15] An action potential traveling continuously along an unmyelinated axon would not be very fast: Its traveling speed is only about 2 m/s. The myelinization of axons quickens the propagation so a speed of up to 120 m/s is reached [105].

2.3.2 Animal Models in Neuroanatomy

Animal models, particularly primates such as the vervet monkey, are commonly used in neuroscience. CARLSSON ET AL. [34] provided an overview over nonhuman primates as neurological models for the human brain. TAKEMURA ET AL. [184] investigated the structure of fiber pathways in the vervet monkey brain. WOODS ET AL. [207] presented a web-based brain atlas for the vervet monkey, from which the images in Figure 2.8 were selected. The atlas includes photos of vervet monkey brains during cryo-sectioning (the cryo-sectioning process is illustrated in Section 3.1.2) and the corresponding *Magnetic Resonance Imaging (MRI)* measurement. Notable white matter structure such as the corpus callosum, the corona radiata, the cingulum, and the fornix also exist in vervet monkey brains even though there are species-related anatomical differences to the human brain. Figure 2.8a shows an overview of a coronal vervet monkey brain with the cingulum (cg), corona radiata (cr), corpus callosum (cc) and fornix (fx) indicated. Figure 2.8b presents the corresponding MRI image.

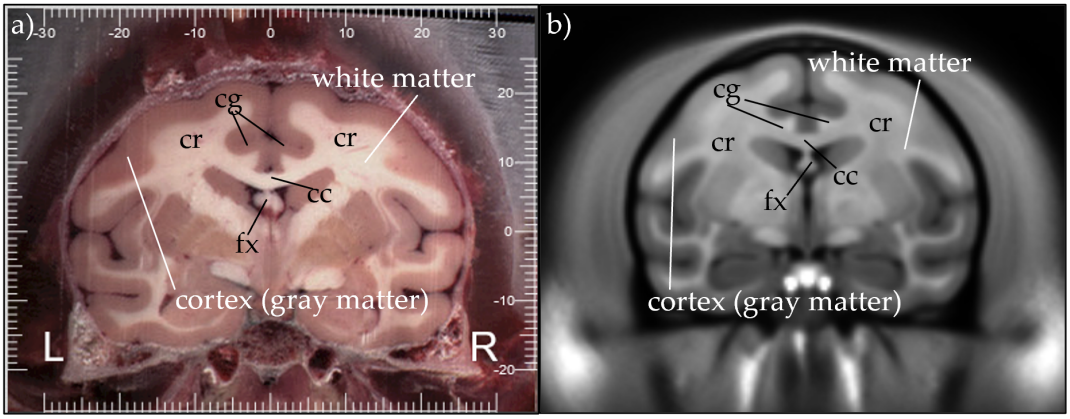

FIGURE 2.8: Coronal section of vervet monkey brain. White and gray matter areas can be distinguished by their brightness. Selected white matter matter are marked: the corona radiata (cr), the corpus callosum (cc), the fornix (fx), and the cingulum (cg). Images adapted and modified from the Vervet Atlas Viewer of the UCLA Brain Mapping Center [198]. a) Photography of the coronal vervet monkey brain cryo-section, indicating the left (L) and right (R) hemisphere (brain atlas X, Y, Z coordinates: 289, 307, 265). b) Magnetic Resonance Imaging (MRI) of the corresponding anatomical plane (MRI atlas X, Y, Z coordinates: 97, 103, 89).

2.3.3 Optical Properties of Brain Tissue

In biological tissue, polarimetric changes arise from tissue microstructures, i.e. linear retardance and diattenuation arising from uniaxial linear birefringent and dichroic microstructures or optical activity (circular retardance and circular diattenuation) arising from chiral structures [150]. Many tissues show optical anisotropies, primarily a result of fibrous cell structures as stated by KOIKE-TANI ET AL. [95].

The optical anisotropy of brain fibers is a result of the radially symmetric highly-layered *myelin sheaths* wrapped around an axon and were already described in 1913 by GÖTHLIN [72]. In brain tissue, the myelin sheaths exhibit positive uniaxial birefringence that is mainly caused by the lipid molecules. However, polarimetry encounters certain difficulties in biological tissue: Multiple scattering events in optically thick turbid matter might alter the polarization or even cause strong depolarization. It is

still challenging to use polarimetry in bulk tissue, as stated by GHOSH ET AL. [65], which is one reason why the methods in Chapter 3 are limited to thin tissue slices of post-mortem brains (about 60 µm)).

ZHANG ET AL. [214] set up a Müller matrix to model birefringent fibrous tissue in the context of *Polarization-Sensitive Optical Coherence Tomography (PS-OCT)* (for Müller matrix calculus, s. Section 2.2.2). [16]. The tissue is characterized by a local fiber direction ϕ and retardance δ (which is linked to the fiber inclination, s. Section 3.2), i.e. it is modeled as a rotated retarder

$$M_{\text{tissue}}(\phi, \delta) = R(\phi) \cdot M(\delta) \cdot R(-\phi) \tag{2.64}$$

$$= \begin{pmatrix} 1 & 0 & 0 & 0 \\ 0 & w_\phi^2 + v_\phi^2 \cos\delta & w_\phi v_\phi (1 - \cos\delta) & -v_\phi \sin\delta \\ 0 & w_\phi v_\phi (1 - \cos\delta) & v_\phi^2 + w_\phi^2 \cos\delta & +w_\phi \sin\delta \\ 0 & v_\phi \sin\delta & -w_\phi \sin\delta & \cos\delta \end{pmatrix} \tag{2.65}$$

with $v_\phi = \sin(2\phi)$, $w_\phi = \cos(2\phi)$. A minimum of only two measurements is required to determine the two unknown variables. The derivation is shown in Appendix A.1 and expanded there to include the diattenuation.

Generally, brain tissue is both scattering and absorbing [137]. CHUE-SANG ET AL. [41] explained how scattering is generally high in biological media due to the high density and large variety of sub- and extracellular components. SINGH ET AL. [175] stated that scattering is usually more considered as a hindrance in biomedical polarimetry due to bulk tissue depolarization. In white matter, scattering is mainly caused by the layered myelin structure and thus, white matter appears darker in transmission image due to its larger attenuation coefficient. However, the same anisotropy that leads to birefringence also leads to diattenuation in brain tissue. MEHTA ET AL. [113] measured the linear and circular diattenuation and illustrated the connection between birefringence and diattenuation. Depolarization is primarily the result of scattering and other randomization effects. Many tissues, particularly bulk tissue, are turbid and birefringent, alongside potential optical activity, linear/circular dichroism, and other second-order effects. Müller polarimetry can provide a deep understanding of all optical properties. However, a Müller polarimeter (i.e. a complete polarimeter) is not always required: Often, crossed polarizers or other incomplete polarimeters can already extract the relevant optic parameters, as detailed by SINGH ET AL. [175].

Typical refractive indices of gray matter and white matter from a rat brain were measured by SUN ET AL. [181] using *Optical Coherence Tomography* (OCT) at a wavelength of 1310 nm, yielding an average refractive index of $n = 1.369 \pm 0.014$ for gray matter and $n = 1.407 \pm 0.015$ for white matter from the corpus callosum. The refractive indices of myelin, axons and the surrounding tissue were estimated by MENZEL [115] from values for the refractive index of cytoplasm, cell membranes and nerve fibers. YAROSLAVSKY ET AL. [210] determined absorption coefficients, the scattering coefficients and the anisotropy factors in white matter, gray matter, cerebellum and brainstem tissue in the spectral range between 360 nm and 1100 nm. White matter had an absorption coefficient of $\mu_{\text{abs}} = 0.1\,\text{mm}^{-1}$, gray matter had a slightly lower absorption coefficient of $\mu_{\text{abs}} = 0.04\,\text{mm}^{-1}$, both for a wavelength of 510 nm, i.e. green light. The scattering coefficient for white matter was with $\mu_{\text{scat}} = 42.6\,\text{mm}^{-1}$ four times larger than $\mu_{\text{scat}} = 10.6\,\text{mm}^{-1}$ for gray matter. However, optical properties also depend on the tissue preparation process [125, 206].

[16] MENZEL ET AL. [114] presented a birefringent tissue model based on Jones calculus for 3D-PLI.

2.3.4 Pathological Changes

Pathological alterations of brain tissue affect its optical properties: Structural changes, vascularization and change of water content affect scattering, absorption and refraction. GENINA ET AL. [59] investigated optical parameters such as absorption coefficient, scattering coefficient, and scattering anisotropy factor in healthy rats and rats with C6-glioma and notice e.g. changes in water content, marked by an increased absorption coefficient, and a complex dependence of the scattering properties throughout different tumor stages. Furthermore, the highly ordered structure of healthy white matter differs from brain tumor tissue where cells grow in a largely chaotic way, thus leading to changes in depolarization, retardance, and change of the fast optical axis in polarimetry, as investigated by NOVIKOVA ET AL. [138]. SCHUCHT ET AL. [169] used reflective Müller polarimetry to detect tumor borders by measuring these optical phenomena. LEE ET AL. [100] investigated structural changes due to Alzheimer's disease by measuring scattering parameters of brain tissue. WONG ET AL. [205] described the myelin dysfunction and subsequent neurodegeneration in *Multiple System Atrophy* (MSA), a neurodegenerative disease caused by the abnormal aggregations of *alpha-synuclein protein* in the myelin-producing *oligodendrocytes* (healthy oligodendrocytes are shown in Figure 2.7).

Chapter 3

Methods and Materials

Transmission-based optical measurement techniques investigate the optical properties of biomedical samples from macroscopic to mesoscopic scales. Each method exploits certain optical tissue properties, visualizes specific tissue features, and requires adequate tissue preparation to support the measurement and to sustain tissue properties over a long period. The methods in this chapter all work in the visible spectrum and image the nerve fiber architecture in thin sections of brain tissue.

First, the following chapter introduces two procedures for **brain tissue preparation**, i.e. *paraffin-embedded sectioning* and *cryo-sectioning*. Moreover, it outlines **four methods for the imaging of long-distance dense white matter nerve fibers with micrometer resolution in thin post-mortem brain sections**, namely the polarimetric methods *three-dimensional polarized light imaging (3D-PLI)*, *diattenuation imaging*, *Müller polarimetry*, and the scattering-based technique *computational scattered light imaging (ComSLI)*. Additionally, this chapter provides the **technical specifications of microscopes** such as the *Large-Area Polarimeter (LAP)*, *LMP1*, and *LMP3D* for 3D-PLI, and the *ComSLI setup* for scattering-based imaging.

3.1 Tissue Preparation

Paraffin-embedded sectioning and cryo-sectioning are procedures used to obtain very thin tissue sections, their thicknesses typically ranging from 10 to 100 micrometers, e.g. for neuroimaging. After preparation, these tissue samples can be stored for years without notable decay. Most tissue samples used in this thesis were cryo-sectioned. Section 7.1 investigates the application of ComSLI on formalin-fixed paraffin-embedded samples. All brains were obtained in accordance with legal and ethical requirements. Unless stated otherwise, the samples were prepared in the laboratory of the Institute of Neuroscience and Medicine (INM-1, Forschungszentrum Jülich GmbH, Germany) by the team of Markus Cremer.

3.1.1 Formalin-Fixed Paraffin-Embedded Sectioning

Formalin-fixation and paraffin-embedding (FFPE) is a standard procedure employed in both clinical and research histology. Tissues preserved in paraffin blocks can be sectioned using a microtome and subsequently stained with various dyes [213, 182, 2]. FFPE blocks can be stored at room temperature for years [162]. The brain is removed from the skull within 24 hours post-mortem. The tissue undergoes fixation in a buffered 4% aqueous formaldehyde solution and then dehydrated in an increasing series of alcohols starting with 70%, then 80%, 90%, 96% and then nearly 100%, each for about a week. A solvent like chloroform is used as an intermediate to mix with

both alcohol and paraffin [165]. In the paraffin-embedding process, the tissue is permeated with a heated paraffin solution and then poured over with liquid paraffin to solidify as a paraffin block. After the paraffin has cooled down, the block can be stored to be cut with a microtome (here: *Leica SM2500*). A typical section thickness is 20 µm. The slice is mounted on a glass slide. The removal of paraffin is accomplished through an intermediate and a series of alcohols with descending concentration, rendering the sections ready for staining.

Nissl staining with *Cresyl violet* is a standard method to highlight neuronal cell bodies by staining nuclei and Nissl bodies [172, 2]. The method is commonly used for cell counting. Another stain for cell bodies is *Silver (Ag) Nissl*. The preparation follows the protocol of MERKER ET AL [124] (based on the procedure by GALLYAS ET AL. [58]) where the black pigment improves the visibility and the localization of cytoarchitectonic boundaries, particularly when an image analysis system is used. The advantages of Cresyl violet Nissl versus Silver staining are discussed by UYLINGS ET AL. [199]. In particular, the Ag Nissl stain has been used by AMUNTS ET AL. for the *BigBrain 3D Human Brain Model* [7]. After staining, the sections are embedded in a cover medium and a cover glass, thereby creating slides that last for years. The sections can be scanned and digitized for further evaluation. Three more stains are investigated briefly in Section 7.1. *Hematoxylin and eosin stain* (H&E) is the most widely used stain in medical diagnosis [193] and stains cell nuclei in blue and the extracellular matrix and cytoplasm in pink [37]. *Perls' Iron*, also known as *Perls' Prussian Blue* and often enhanced with diaminobenzidine (DAB), is used to evaluate the occurrence of iron, e.g. in hematological diseases [106]. The *Tau stain* addresses the tau protein that is involved in the stabilization of cellular proteins in the brain [202] and can be combined with a hematoxylin stain.

3.1.2 Cryo-Sectioning

Preserving the birefringent properties is crucial during the processing of brain tissue for polarization-based imaging. The clinical standard technique of embedding tissue in paraffin for high-quality cutting of histological sections as described in Section 3.1.1 disturbs the layered lipid structure of the myelin sheaths, primarily due to the use of alcohol (an organic hydrophobic solvent) during the initial dehydration phase [92, 35]. Therefore, brain sections intended for polarization-based imaging undergo an alternative procedure known as cryo-sectioning.

First, the brain is removed from the skull within 24 hours after death. Subsequently, it undergoes fixation using a buffered 4% formaldehyde solution to prevent decay and is stored at room temperature for several days or weeks. The storage time depends on the species. Subsequently, the brain is deep-frozen for storage and sectioning, thus requiring previous cryoprotection [146]: The formation of ice crystals in the tissue is prevented by immersing the brain in a solution of 10% glycerin and then 20% glycerin (each for several days) [160]. Finally, the brain is dipped in isopentane at roomtemperature for some minutes and frozen in -80°C isopentane for nearly a hour. In this deep-frozen state, the brain can be stored for months. A large-scale cryostat microtome (here: *CM3600 (Leica)*) is used to cut the frozen brain into thin sections. AXER ET AL. have investigated the optimal thickness for polarization-based imaging [13]: The maximum section thickness goes up to about 120 µm before the slice is too thick. The lower limit is given by the tissue's tendency to rip at a minimum thickness of about 20 µm (for small brains such as rat brains). The default section thickness is 60 µm. During sectioning, deformations and ruptures of the tissue

may occur. Therefore, a so-called "blockface image" of the brain block surface is taken before each cut to support image registration as depicted by AXER ET AL. [17]. The brain sections are mounted onto glass slides, embedded in 20% glycerin, cover-slipped, weighted, and – after air bubbles have emerged from the solution – sealed with nail polish. Tissue staining is possible but not required for polarization- or scattering-based imaging.

The transmittance of cryo-sectioned brain tissue changes over time because scattering within the tissue decreases, likely due to evaporation of the embedding medium[1]. Therefore, polarization-based measurements are usually done right after the preparation process. However, MENZEL ET AL. [117] found that scattering-based measurements can actually benefit from the decreased transmittance due to a higher contrast of scattering peaks. Accordingly, scattering-based measurements of cryo-sectioned tissue are ideally performed several weeks or even months after their preparation.

3.2 Three-Dimensional Polarized Light Imaging (3D-PLI)

Polarized light imaging (PLI) uses the birefringence of brain tissue as initially described by GÖTHLIN [72] in 1913, s. Section 2.3.3. AXER ET AL. [12] located and visualized the orientation of long myelinated fiber tracts. MYKLOSSY ET AL. [127] studied the structural degeneration of myelin using this method. Furthermore, AXER ET AL. [15, 16] have introduced *three-dimensional polarized light imaging* (3D-PLI) to map the nerve fiber orientations of post-mortem brain sections with a sub-millimeter resolution and reconstruct the threedimensional nerve fiber architecture from measuring multiple subsequent sections. This part follows AXER ET AL. [15, 17].

3.2.1 Setup and Measurement

Figure 3.1a illustrates the experimental configuration for 3D-PLI. An unpolarized, incoherent light source emits light in the visible spectrum, usually green light. A narrow wavelength spectrum is required due to the wavelength-dependence of the retardance $\delta = \delta(\lambda)$, as introduced in Section 2.1.2, and can be achieved with a spectral filter. Incorporating a diffuser plate ensures spatial homogeneity of the light source. The light is polarized by passing through a linear polarization filter (LP) that is rotated azimuthally in equidistant steps ρ during the measurement. The linearly polarized light passes through a thin sample of cryo-sectioned brain tissue (with a typical thickness of 60 - 100 µm, s. Section 3.1.2). The optical anisotropy of the myelinized nerve fibers introduces a phase shift that depends on the local nerve fiber orientations within this image pixel and the polarization changes to elliptical. To analyze the phase shift, a quarter-wave plate (QWP) converts the polarization from elliptical to linear. Here, the polarization angle depends on the phase of the former elliptical polarization. Finally, the linearly polarized light passes through a second LP and reaches the camera. The pixelwise light intensity at the camera depends on the angle between the transmission axis angle of the second LP with the pixel-specific polarization angle according to Malus' law, s. Section 2.1.3.

For a 3D-PLI measurement, the optical components are simultaneously rotated to equidistant angles ρ while the brain section is fixed in the setup. The pixelwise evaluation is depicted in Figure 3.1b. The light intensity $I(\rho)$ of every image pixel is

[1] Revitalization, i.e. re-embedding an old sample in glycerin solution, can increase the contrast again.

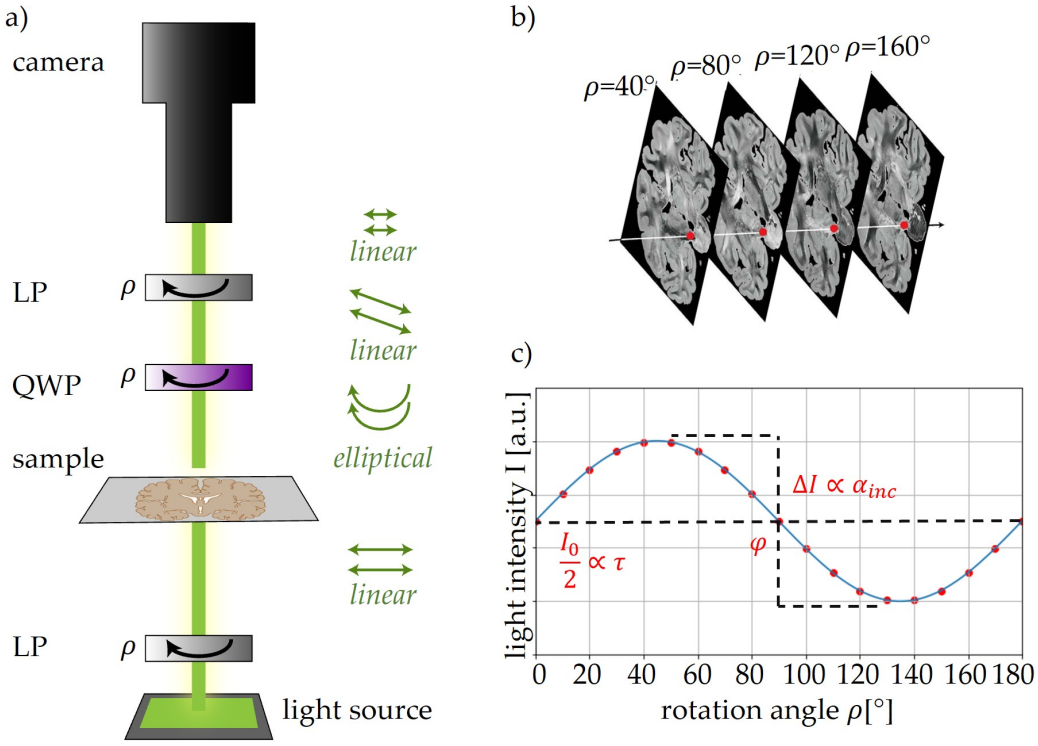

FIGURE 3.1: Three-dimensional polarized light imaging (3D-PLI). a) Light emitted by a large-area green LED panel is polarized by a linear polarization filter (LP). The light passes through a tissue sample that introduces a phase shift depending on local nerve fiber orientations. A quarter-wave plate (QWP) converts the polarization from elliptical to linear. Finally, the linear polarized light passes through a second LP and a camera detects the light intensity. b) During the measurement, the LPs and the QWP are rotated azimuthally. Images are taken at equidistant angular steps ρ, yielding a intensity curve $I(\rho)$ per image pixel. Image adapted from AXER ET AL. [17]. c) The light intensity $I(\rho)$ of every image pixel is a sinusoidal curve. Its normalized amplitude is related to the retardation $|\sin(\delta)|$ with δ the retardance, i.e. to the fiber inclination α_{inc}. The phase ϕ_{dir} is related to the in-plane fiber direction. Image inspired by AXER ET AL. [17].

described by

$$I(\rho) = \frac{I_0}{2} \cdot (1 + \sin(2\rho - 2\phi_{\text{dir}}) \cdot \sin(\delta)) \tag{3.1}$$

where δ is the retardance, $\sin(\delta)$ is the retardation, ρ is the transmission axis angle of the first LP and ϕ_{dir} is the fiber direction angle (projected onto the brain section plane with respect to the zero position of the setup)[2]. The local fiber inclination (i.e, the out-of-plane angle) α_{inc} is connected to the local retardance[3]

$$\delta = \frac{2\pi d}{\lambda} \Delta n \cos^2(\alpha_{\text{inc}}) \tag{2.9}$$

and is linked to the amplitude ΔI of the intensity curve $I(\rho)$ via $\Delta I \propto |\sin(\delta|$. The phase of $I(\rho)$ is determined by the fiber direction (i.e. the in-plane angle) ϕ_{dir}. Figure 3.1c depicts a typical intensity curve.

[2]The intensity curve is derived with Müller matrix calculus in Appendix A.3.1.

[3]However, the 3D-PLI setup cannot differentiate between δ_L and δ as introduced in Section 2.2.4 and the influence of optical rotation Ψ is neglected.

3.2.2 Parameter Maps

Following the calculation by GLAZER ET AL. [70], a discrete harmonic Fourier decomposition allows the evaluation of the curve $I(\rho)$

$$I(\rho) = \frac{I_0}{2} \cdot (1 + \sin(2\rho - 2\phi_{\text{dir}}) \cdot \sin(\delta)) = a_0 + a_2 \cdot \sin(2\rho) + b_2 \cdot \cos(2\rho) \tag{3.2}$$

with the coefficients

$$a_0 = \frac{I_0}{2}, \qquad a_2 = \frac{I_0}{2} \cdot \sin(\delta) \cdot \cos(2\phi_{\text{dir}}), \qquad b_2 = \frac{I_0}{2} \cdot \sin(\delta) \cdot \sin(2\phi_{\text{dir}}) \tag{3.3}$$

The Fourier coefficients a_0, a_2 and b_2 are calculated for each pixel from the individual light intensity I_i for all equidistant angles ρ_i for N sampled angular steps i

$$a_0 = \frac{1}{N} \sum_{N}^{i=1} I_i \qquad a_2 = \frac{2}{N} \sum_{N}^{i=1} I_i \sin(2\rho_i) \qquad b_2 = \frac{2}{N} \sum_{N}^{i=1} I_i \cos(2\rho_i) \tag{3.4}$$

From the Fourier coefficients, a set of parameter maps is generated to evaluate the nerve fiber architecture of the investigated tissue sample: The *transmittance map*, the *retardation map*, the *fiber inclination map*, the *fiber direction map* and the *fiber orientation map (FOM)* as shown in Figure 3.2 [17]. The *transmittance map* corresponds to birefringence-independent light extinction. White and gray matter have distinct attenuation coefficients in the optical regime, s. Section 2.3.3, with the attenuation through white matter being generally larger due to higher absorption and scattering. The transmittance τ is calculated pixelwise from the Fourier coefficients as

$$I_0 = \tau = 2a_0 \tag{3.5}$$

The *retardation map* shows the parameter $|\sin(\delta)| = \Delta I / I_0$, i.e. the normalized amplitude of the light intensity profile. The retardation $|\sin(\delta)|$ is given by

$$|\sin(\delta)| = \frac{\sqrt{a_2^2 + b_2^2}}{a_0} \in [0, 1] \tag{3.6}$$

The *fiber inclination map* visualizes the out-of-plane fiber angle α_{inc} and can be calculated from the retardation via Eq. (2.9) if the wavelength λ, the local birefringence Δn and the sample thickness d are known. AXER ET AL. [15] presented an approach for the calculation of fiber inclination maps if those parameters are unknown (which is usually the case) based on the relative thickness t_{rel}: This is the ratio of the actual section thickness and the section thickness at which an in-plane fiber $a_{\text{inc}} = 0°$ acts as an ideal quarter-wave plate [153], leading to

$$|\sin(\delta)| = |\sin(\frac{\pi}{2} t_{\text{rel}} \cdot \cos^2(\alpha_{\text{inc}}))| \tag{3.7}$$

If the section has a thickness of exactly a quarter wavelength, then $|\sin(\delta)| = 1$. In practice, t_{rel} can be determined from the measured retardation of in-plane fibers $|\sin(\delta)|_{\alpha=0°}$. The fiber inclination α_{inc} is then given by

$$\alpha_{\text{inc}} = \arccos\left(\sqrt{\frac{\arcsin(|\sin(\delta)|)}{\arcsin(|\sin(\delta)|_{\alpha=0°})}}\right) \tag{3.8}$$

However, the fiber inclination has a sign ambiguity that can only be resolved by tilting the specimen stage or the angle of light incidences, as discussed by WIESE ET AL. [204]. The *fiber direction map* shows the azimuthal (in-plane) angle ϕ_{PLI} of each fiber given by

$$\phi_{\text{PLI}} = 180^\circ \cdot \frac{\arctan 2(-a_2, b_2)}{2\pi} \in [-90^\circ, 90^\circ] \tag{3.9}$$

and shifted by 90° to be in the angular range $\in [0^\circ, 180^\circ]$.

By combining information about the inclination and the direction of the nerve fibers, a color-coded *fiber orientation map* (FOM) is generated. The nerve fiber orientations are visualized in *Hue Saturation Value (HSV)* color space. The hue encodes the fiber direction ϕ_{PLI} and the saturation defines α_{inc}, ranging from maximum saturation ($\alpha_{\text{inc}} = 0^\circ$) to no saturation ($\alpha_{\text{inc}} = 90^\circ$).

Three-dimensional fiber orientations are derived from serial sections of an entire brain, overall yielding a z-resolution that depends on the section thickness, and an xy-resolution that depends on the camera and objective lens. Image registration aided by *blockface imaging* assembles the 2D images and eliminates spatial distortions, following PALM ET AL. [143]. AXER ET AL. [15] reconstruct a fiber model from the *pons* area using an algorithm based on the *Euler method* [128].

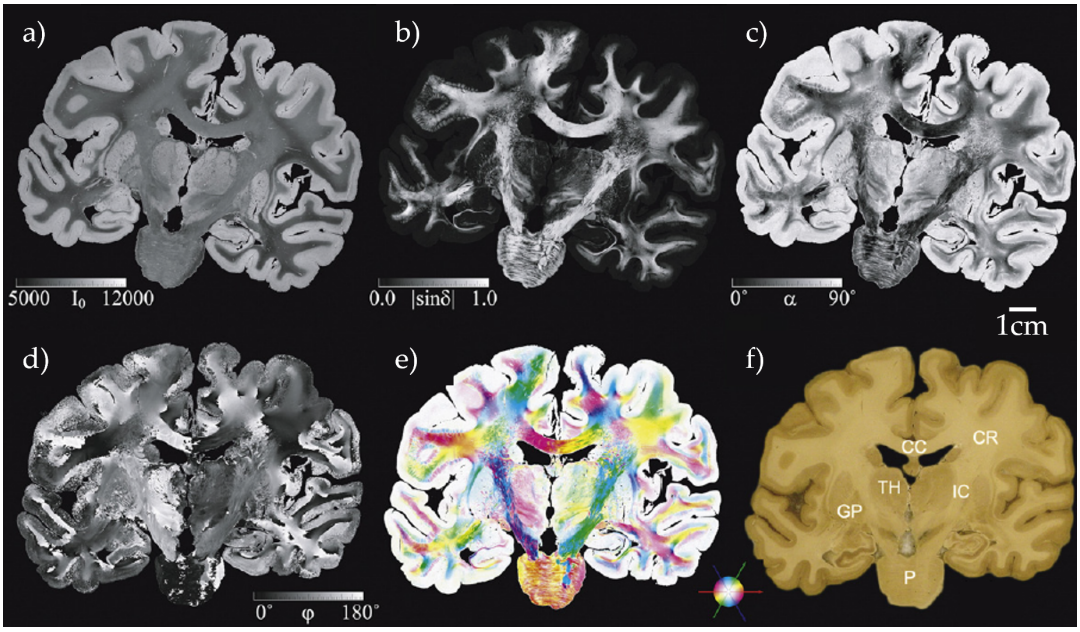

FIGURE 3.2: Parameter maps in 3D-PLI. The parameter maps are generated from the sinusoidal intensity curve for each pixel. a) Transmittance map. The transmittance is the birefringence-independent attenuation. White matter appears darker. b) Retardation map. The retardation $|\sin(\delta)|$ (with δ the retardance) corresponds to the normalized amplitude of the sinusoidal curve. c) Fiber inclination map. The fiber inclination α_{inc} is calculated from the retardation. d) Fiber direction map. The fiber direction corresponds to the phase of the sinusoidal curve. e) Color-coded fiber orientation map (FOM). The hue represents the direction, the saturation encodes the inclination. f) Block-face image with anatomical regions indicated: Corpus callosum (cc), corona radiata (cr), internal capsule (ic), thalamus (th), globus pallidus (gp), pons (p). Image adapted from AXER ET AL. [17].

3.3 Diattenuation Imaging (DI)

The same optical anisotropy of the myelin sheath that causes birefringence also causes diattenuation in brain tissue. While the impact of brain tissue diattenuation on 3D-PLI fiber orientation measurements is minimal (less than 4% in rat brain), MENZEL ET AL. [118, 117] proposed *diattenuation imaging* (DI) as an extension to 3D-PLI to reveal previously undetected anatomical tissue differences. This text passage follows mainly MENZEL ET AL. [118, 117] unless stated otherwise.

3.3.1 Setup and Measurement

Figure 3.3a presents the experimental configuration for DI. In comparison with the 3D-PLI setup shown in Figure 3.1a, the DI setup excludes the quarter-wave plate (QWP) and the second linear polarization filter (LP). Similar to 3D-PLI, the first LP is rotated to equidistant angular positions ρ. As polarized light passes the brain section, the anisotropies of myelinated nerve fibers result in diattenuation. The pixelwise intensity curve $I(\rho)$ is influenced by fiber orientations, fiber size, myelin sheath thickness, and embedding time [117]. In particular, the fiber direction angle ϕ_{dir}, the diattenuation D and the transmittance τ are described by the sinusoidal equation

$$I(\rho) = \tau \frac{I_0}{2} \cdot (1 + D\cos(2\rho - 2\phi_{\text{dir}})) \tag{3.10}$$

where δ is the retardance and ϕ_{dir} is the fiber direction angle (projected onto the brain section plane with respect to the zero position of the setup)[4]. Figure 3.3b depicts an exemplary intensity curve $I(\rho)$ in direct comparison to the typical corresponding 3D-PLI curve.

3.3.2 Parameter Maps

As discrete harmonic Fourier analysis yields the parameters as coefficients of a Fourier series

$$I(\rho) = a_0 + a_2 \cdot \cos(2\rho) + b_2 \cdot \cos(2\rho) \tag{3.11}$$

with the Fourier coefficients

$$a_0 = \tau \frac{I_0}{2}, \qquad a_2 = \tau D \frac{I_0}{2} \cos(2\phi_{\text{dir}}), \qquad b_2 = \tau D \frac{I_0}{2} \sin(2\phi_{\text{dir}}) \tag{3.12}$$

The Fourier coefficients a_0, a_2 and b_2 can be calculated from the individual light intensity I_i of each pixel over all equidistant angles ρ for N sampled data points i

$$a_0 = \frac{1}{N} \sum_{N}^{i=1} I_i \qquad a_2 = \frac{2}{N} \sum_{N}^{i=1} I_i \sin(2\rho_i) \qquad b_2 = \frac{2}{N} \sum_{N}^{i=1} I_i \cos(2\rho_i) \tag{3.13}$$

Analogous to 3D-PLI, the tissue parameters can be visualized by calculating the pixelwise transmittance, diattenuation and fiber directions following MENZEL ET AL. [118].

The *transmittance map* shows the intensity I_0, corresponding to diattenuation-independent light attenuation where white and gray matter have distinct extinction coefficients in the optical regime. The transmittance is calculated pixelwise from the

[4]The intensity curve is derived with Müller matrix calculus in Appendix A.4.1.

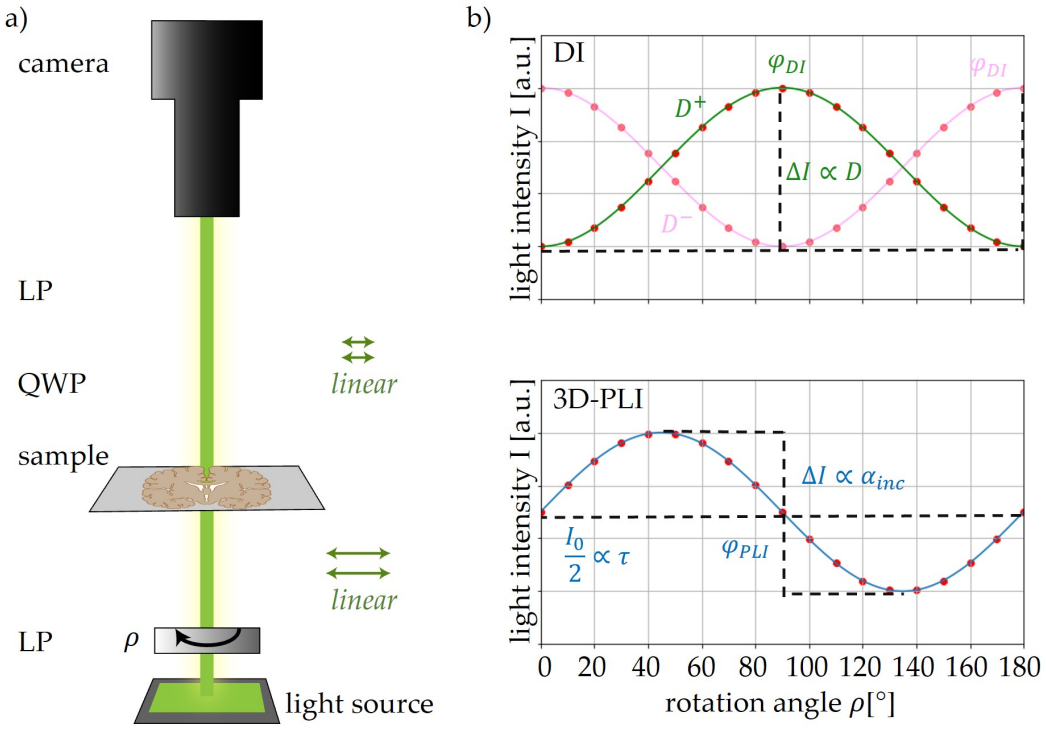

FIGURE 3.3: Diattenuation imaging (DI). DI can serve as an extension to 3D-PLI. a) A homogeneous large-area light source emits unpolarized, incoherent, green light with a narrow spectral bandwidth. The light undergoes polarization through by a linear polarization filter (LP). Subsequently, the linearly polarized light passes through a brain section. The optical anisotropy of the brain tissue leads to diattenuation that depends on the local nerve fiber structure within the tissue. A camera detects the attenuated light intensity. During the measurement, the LP is azimuthally rotated. Images are taken at equidistant angular steps ρ, yielding a characteristic intensity curve $I(\rho)$ per image pixel. b) The light intensity $I(\rho)$ of every image pixel describes a sinusoidal curve. The amplitude of the curve is related to the diattenuation. The phase ϕ_{dir} is related to the in-plane fiber direction. When $\phi_{\text{DI}} = \phi_{\text{PLI}}$, the tissue is called D^+ tissue (green curve). When $\phi_{\text{DI}} = \phi_{\text{PLI}} + 90°$, the tissue is called D^- tissue (magenta curve). For comparison, the typical corresponding 3D-PLI curve is depicted below. Image inspired by MENZEL ET AL. [117].

Fourier coefficients as

$$I_0 = \tau = 2a_0 \tag{3.14}$$

The *diattenuation map* shows the diattenuation which is the amplitude of the normalized intensity profile

$$D = \frac{\sqrt{a_2^2 + b_2^2}}{a_0} \tag{3.15}$$

The *fiber direction map* shows the azimuthal (in-plane) angle ϕ_{DI} of each fiber. In contrast to 3D-PLI, the fiber direction is defined by the angle of maximum transmittance

$$\phi_{\text{DI}} = 180° \cdot \frac{\arctan 2(b_2, a_2)}{2\pi} \in [0°, 180°] \tag{3.16}$$

3.3.3 Fiber Direction Shift between 3D-PLI and DI

A comparison between 3D-PLI and DI direction maps reveals differences between the fiber directions ϕ_{DI} and ϕ_{PLI}. Specifically, certain brain regions exhibit a 90° angular shift in their fiber direction. This perceived mismatch corresponds to tissue structures where light transmission reaches a minimum rather than a maximum, leading to a mathematical, though not anatomical, alteration in the fiber directions. Two tissue types are discernible: D^+ (where the intensity is maximal) and D^- (where the intensity is minimal), named D^+ *tissue* and D^- *tissue* for brevity within the context of this thesis. Regions with a strong negative diattenuation D^- indicate strongly myelinated, small, straight, in-plane fibers, as shown by *Finite-Difference Time-Domain (FDTD)* simulations performed by MENZEL ET AL. [117]. Figure 3.4 depicts regions of D^+ and D^- in sagittal sections of a vervet brain.

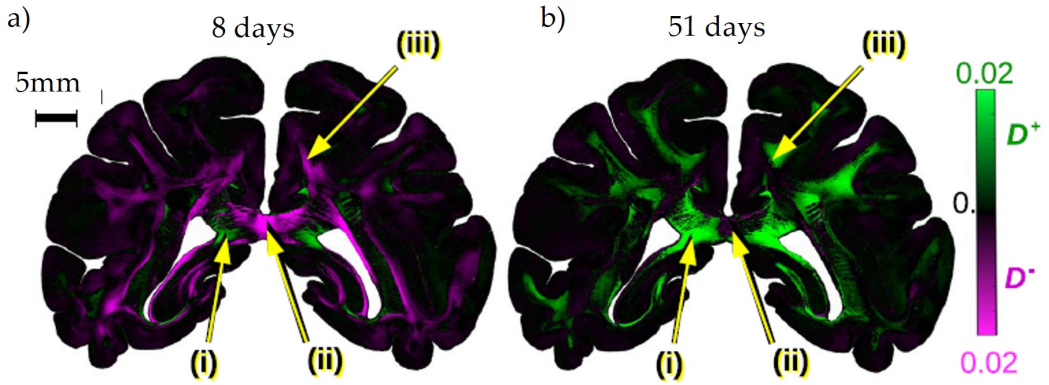

FIGURE 3.4: D^+/D^- tissue in DI. A comparison between 3D-PLI and DI fiber directions reveals local phase shifts of 90° in the fiber directions ϕ_{dir}. Regions with a strong negative diattenuation D^- (i.e. a perceived phase shift) indicate strongly myelinated, small, straight, in-plane fibers whereas strong positive diattenuation D^+ (i.e. 3D-PLI and DI yielding the same fiber direction) indicates the opposite. The appearance of D^+ and D^- also depends on the time after embedding: a) After 8 days, D^- regions are dominant, e.g. for the indicated regions (ii) and (iii). Region (i) shows D^+ tissue. b) After 51 days, D^+ tissue is also found for (iii). Parameter maps adapted from MENZEL ET AL. [117].

Furthermore, experiments have revealed the influence of time on the distribution of D^+ and D^- tissue: Both D^+ and D^- are measured within days after embedding, but after several weeks, D^- has changed to D^+ for most regions. Consequently, the timing of measurements is crucial for the interpretation of DI results. Figure 3.4a shows a coronal vervet monkey section 8 days after embedding. Figure 3.4b displays the same section 51 days after embedding, demonstrating how some regions previously identified as D^- now have D^- behavior.

Experimental observations suggest the coexistence of both anisotropic absorption and anisotropic scattering phenomena within brain tissue sections because the diattenuation signal is not proportional to the retardation signal. In contrast to 3D-PLI and DI, a Scattering Polarimeter, as constructed in Chapter 4, has the capability to differentiate between anisotropic absorption and scattering.

3.4 Müller Polarimetry

Müller polarimetry, also *ellipsometry*, is a widely employed tool in biomedicine and material science and the direct application of the theory introduced in Section 2.2. The first measurement on human tissue were performed by DREHER ET AL. [49] in 1992, measuring the polarization effects in nearly transparent ocular media in human eyes post-mortem. By now, wide-field Müller polarimetry is applicable in clinical diagnosis, e.g. for tumor border identification as demonstrated by SCHUCHT ET AL. [169] and near-real-time during neurosurgical intervention as presented by MORICONI ET AL. [129].

3.4.1 Setup and Measurement

Generally, Müller polarimeters are constructed either with mechanically rotating elements, with mechanically fixed but voltage-controlled variable retarders or with a combination of both. Mechanically rotating elements yield a higher optical precision because all optic elements can be matched to the illuminating wavelength, but suffer from a lower speed and a lack of flexibility (e.g. the use of a different wavelength). Voltage-controlled variable retarders offer speed and flexibility but have a lower optical precision in direct comparison.

Figure 3.5 displays typical configurations in transmission mode. The Scattering Polarimeter constructed in Chapter 4 employs variable retarders while the polarization-based setups described in Section 3.6 are incomplete versions of the mechanically rotating type. In this context, "incomplete" means that not all elements of the Müller matrix can be measured with them.

By setting the PSG and PSA to all possible combinations of the basic Stokes polarization states and measuring the transmitted intensity, the Müller matrix elements are calculated from 36 measurements s. Table 3.1a, as shown e.g. by GHASSEMI ET AL. [64]. Mathematically, only 16 measurements are required to solve the linear equation system for the 16 matrix elements, as suggested e.g. by LOPEZ-TELLÉZ ET AL. [108], s. Table 3.1b. A Müller polarimeter can be calibrated with the eigenvalue calibration method (ECM) by COMPAIN ET AL. [44], s. Section 2.2.3, for which only a set of well-known calibration samples is required.

Because experimentally determined Müller matrices are influenced by statistical errors, DEL HOYO ET AL. [82] presented criteria for error filtering based on a list of conditions a physically realizable Müller matrix must satisfy, along with transformations that ensure those conditions are not violated[5]

$$m_{00} \geq 0 \qquad m_{00} \longrightarrow -m_{00} \tag{3.17a}$$

$$m_{00} \leq 1 \qquad m_{ij} \longrightarrow m_{ij}/m_{00} \tag{3.17b}$$

$$m_{ij} \leq m_{00} \qquad m_{ij} \longrightarrow m_{00} \tag{3.17c}$$

$$P \leq m_{00} \qquad m_{i>0j} \longrightarrow m_{i>0j}/P \tag{3.17d}$$

$$D \leq m_{00} \qquad m_{i>0j} \longrightarrow m_{ij>0}/D \tag{3.17e}$$

[5] In a shortened version, as required in the context of this thesis. The complete criteria list is provided by DEL HOYO ET AL. [82].

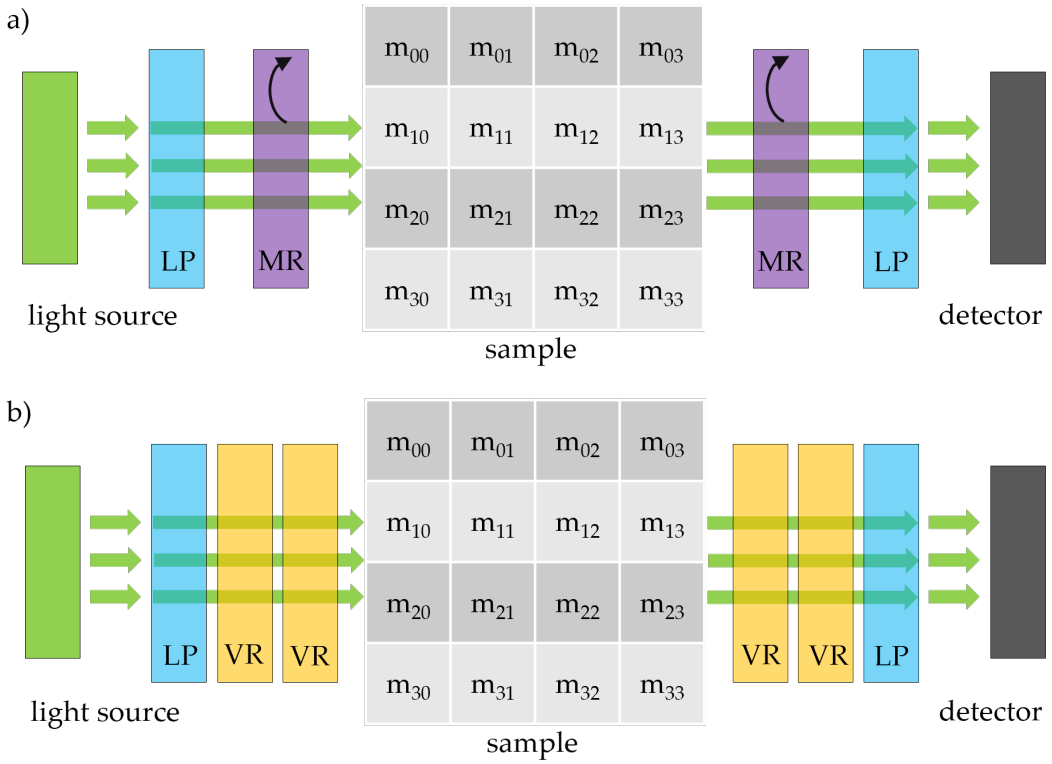

FIGURE 3.5: Typical configurations for transmission-based Müller polarimeters. Other configurations are possible. a) Müller Polarimeter based on rotating retarders. The *polarization state generator* (PSG) and *analyzer* (PSA) both combine a linear polarizer (LP) with a mechanically rotatable retarder (MR), usually a quarter-wave plate (QWP). A disadvantage is the comparably low speed of the mechanical rotation and the low flexibility to vary the illumination parameters, e.g. the use of different wavelengths. b) Müller Polarimeter based on variable retarders (VR) with their slow axes set at different azimuthal angles. An advantage of such a system is the high flexibility for other measurements or also other wavelengths, the high speed in comparison to mechanical rotation. A disadvantage is the overall lower chance for component optimization. Image inspired by GOLDSTEIN [71].

3.4.2 Signal-to-Noise Ratio

It must be noted that the best theoretically possible signal-to-noise ratio (SNR) in a real setup is not achieved with the six "basic" Stokes polarization states (horizontal H, vertical V, diagonal D and antidiagonal A linear polarization and left- L and right-handed RC circular polarization): AZZAM ET AL. [18, 19] showed that the signal-to-noise ratio is highest when the employed polarization states are at the vertices of a tetrahedron inscribed inside the Poincaré sphere. SABATKE ET AL. [161] calculated the corresponding settings for a Müller polarimeter consisting of a linear polarization filter with fixed azimuthal angle and a rotatable retarder. They found exactly two possible ways to inscribe a regular tetrahedron within the Poincaré sphere for their investigated experimental setting. In contrast, TYO ET AL. [196] showed that a Müller polarimeter based on variable retarders has many possible optimal configurations, rendering those systems more suitable for some applications.

Consequently, DE MARTINO ET AL. [46] proposed the following settings for the retardance δ_i and the azimuthal angles θ_i for the two variable retarders of the PSG: $\delta_1 = 315° + p90°$, $\delta_2 = 135° + p90°$ with p being the same integer, $\theta_1 = \epsilon 27.4° + r90°$

TABLE 3.1: Calculation of Müller matrix elements from 36 and 16 measurements. I_{HV} refers to a settings where the PSG is set to generate horizontal polarization and the PSA is set to transmit vertical polarization etc., where H horizontal polarization, V vertical polarization, D diagonal polarization, A antidiagonal polarization, R right-handed circular polarization and L left-handed circular polarization. LOPEZ-TELLÉZ ET AL. [108] proposed a solution to the linear equation system where only 16 measurements are required. Other solutions are possible.

a)

$I_{HH} + I_{HV} + I_{VH} + I_{VV}$	$I_{HH} + I_{HV} - I_{VH} - I_{VV}$	$I_{DH} + I_{DV} - I_{AH} - I_{AV}$	$I_{RH} + I_{RV} - I_{LH} - I_{LV}$
$I_{HH} - I_{HV} + I_{VH} - I_{VV}$	$I_{HH} - I_{HV} - I_{VH} + I_{VV}$	$I_{DH} - I_{DV} - I_{AH} + I_{AV}$	$I_{RH} - I_{RV} - I_{LH} + I_{LV}$
$I_{HD} - I_{HA} + I_{VD} - I_{VA}$	$I_{HD} - I_{HA} - I_{VD} + I_{VA}$	$I_{DD} - I_{DA} - I_{AD} + I_{AA}$	$I_{RD} - I_{RA} - I_{LD} + I_{LA}$
$I_{HR} - I_{HL} + I_{VR} - I_{VL}$	$I_{HR} - I_{HL} - I_{VR} + I_{VL}$	$I_{DR} - I_{DL} - I_{AR} + I_{AL}$	$I_{LL} - I_{RL} - I_{LR} + I_{RR}$

b)

$I_{HH} + I_{HV} + I_{VH} + I_{VV}$	$I_{HH} + I_{HV} - I_{VH} - I_{VV}$	$2\left(\frac{m_{00}}{2} - I_{AH} - I_{AV}\right)$	$2\left(\frac{m_{00}}{2} - I_{LH} - I_{LV}\right)$
$I_{HH} - I_{HV} + I_{VH} - I_{VV}$	$I_{HH} - I_{HV} - I_{VH} + I_{VV}$	$2\left(\frac{m_{10}}{2} - I_{AH} + I_{AV}\right)$	$2\left(\frac{m_{10}}{2} - I_{AH} + I_{AV}\right)$
$2\left(I_{LD} + I_{VD} - \frac{m_{00}}{2}\right)$	$2\left(I_{HD} - I_{VD} - \frac{m_{01}}{2}\right)$	$m_{00} - m_{02} + m_{20} - 4I_{AD}$	$m_{00} - m_{03} + m_{20} - 4I_{LD}$
$2\left(\frac{m_{00}}{2} - I_{HL} - I_{VL}\right)$	$2\left(\frac{m_{01}}{2} - I_{HL} + I_{VL}\right)$	$4I_{AL} - m_{00} + m_{02} + m_{30}$	$4I_{LL} - m_{00} + m_{03} + m_{30}$

and $\theta_2 = \epsilon 72.4^\circ + r90^\circ$ where p and r are any integers, not necessarily equal, and $\epsilon = \pm 1$ but same for both values. The PSA settings are symmetrical. LAUDE-BOULESTEIX ET AL. [99], among others, constructed and investigated such a system.

3.4.3 Parameter Maps

To investigate the optical properties of a spatially inhomogeneous sample such as brain tissue, the Müller matrix is calculated separately for each image pixel. Then, the pixelwise Müller matrix is normalized with the respective element m_{00} of this image pixel. The resulting 4×4 images visualize the Müller matrix for the whole sample and can be investigated, e.g. for symmetries. For further analysis, a Lu-Chipman decomposition as introduced in Section 2.2.4 can separate diattenuation, retardance and the depolarization. Notable among the measurable parameter maps are the transmittance maps for $T_{\min}$ and $T_{\max}$, the diattenuation map (both the complete diattenuation D and the separated linear and circular diattenuation maps), the retardance maps (i.e. the complete retardance R, the linear retardance δ and circular retardance/optical rotation Ψ), the direction map that shows the direction of the fast axis of retardance, the direction map that shows the axis of diattenuation, and the depolarization map.

3.5 Computational Scattered Light Imaging (ComSLI)

Computational scattered light imaging (ComSLI) was introduced under the name *scattered light imaging* (SLI) by MENZEL ET AL. [119, 120]. ComSLI is a scattering-based technique for determining white matter nerve fiber orientations in post-mortem brain sections with oblique illumination. Unlike Müller polarimetry, 3D-PLI and DI, ComSLI does not rely on polarization. Here, two subtypes of ComSLI illumination and their evaluation are introduced. ComSLI is proficient in detecting in-plane nerve fiber directions, out-of-plane nerve fiber inclinations, and measuring fiber crossings with multiple fiber directions. So far, tissue preparation in ComSLI brain sections has been the same as for 3D-PLI (i.e. unstained cryo-sectioning). Section 7.1 evaluates the application of ComSLI for *formalin-fixed paraffin-embedded (FFPE)* stained tissue sections.

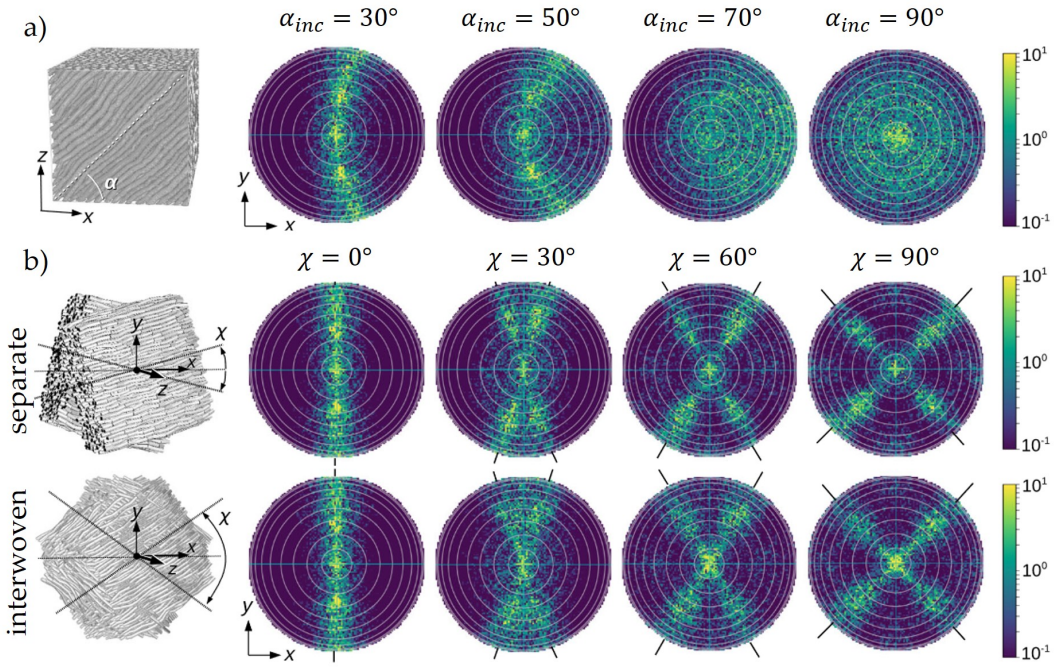

FIGURE 3.6: Simulated scattering patterns for various fiber architectures. a) Parallel in-plane (i.e. non-inclined) fibers show a bar-shaped scattering pattern which exhibits an increasing curvature towards a higher fiber inclination α_{inc}.b) A crossing of two fibers (separate or interwoven) corresponds to an X-shaped scattering pattern depending on the fiber crossing angle χ and fiber inclination α_{inc}. Image adapted from MENZEL ET AL. [122].

Finite-Difference Time-Domain (FDTD) simulations (as presented by TAFLOVE ET AL. [183]) by MENZEL ET AL. [122] have shown that light scattering at nerve fiber bundles can reveal nerve fiber orientations in transmission microscopy with micrometer resolution using wavelengths in the visible spectrum. The characteristic *scattering pattern* contains information about nerve fiber orientations, but also about crossing fiber bundles. Parallel in-plane (i.e. non-inclined) fibers show a bar-shaped scattering pattern which exhibits an increasing curvature towards a higher fiber inclination α_{inc}, as shown in Figure 3.6a. A crossing of two fibers corresponds to an X-shaped scattering pattern depending on the fiber crossing angle χ and fiber inclination α_{inc}, demonstrated for separate and interwoven crossings in Figure 3.6b. The mechanism

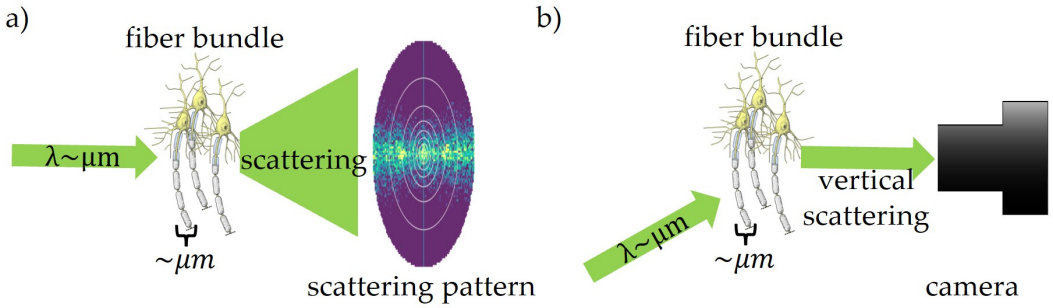

FIGURE 3.7: Light scattering at nerve fiber bundles. a) Light scattering of visible light at nerve fiber bundles reveals nerve fiber orientations. When a tissue sample is scanned with a coherent light beam, the characteristic scattering patterns contains information about nerve fiber orientations for each scanning point. b) In ComSLI, the light path is inverted: Instead of measuring the full scattering pattern for a limited amount of grid points, the whole sample is illuminated at once but from different angles using a large-area incoherent light source. The vertically scattered light is detected for each illumination angle. Then, the scattering pattern for each image pixel is reconstructed.

of light scattering at nerve fiber bundles is shown in Figure 3.7a, exemplary for parallel fiber bundles.

MENZEL & PEREIRA [116] performed *Coherent Fourier Scatterometry* to determine the scattering patterns for brain tissue. In this imaging technique, a laser beam raster scans the sample and the transmitted diffraction is measured for each grid point (compare Section 2.1.5). However, the resolution in Coherent Fourier scatterometry is limited by the density of scanned points and the beam diameter of the laser beam.

In ComSLI, the light path is inverted, as shown in Figure 3.7b: Instead of measuring the full scattering pattern for a limited amount of grid points, the whole sample is illuminated at once but from different angles with a large-area incoherent light source. The vertically scattered light is detected. The intensity becomes maximum when the incident light beam (projected to the plane) forms a 90° angle with the fiber direction. A scattering pattern emerges for each image pixel. In ComSLI, the resolution is not limited by the scanning resolution but by the wavelength of the light[6]. Experimentally measured scattering patterns for various fiber architectures are shown in Figure 3.9c.

Two subtypes of ComSLI can be distinguished, distinct in their illumination technique: Scatterometry ComSLI and angular ComSLI. Figure 3.8b shows the faster angular illumination compared with the more extensive scatterometry illumination in Figure 3.8a. Section 7.4 further introduces compressed sensing illumination as a variant of scatterometry ComSLI.

3.5.1 Scatterometry Illumination

Scatterometry ComSLI measures the scattering pattern for each image pixel. Within the illumination sequence, the whole sample is illuminated under various azimuthal and polar angles with N×N subsequent illumination squares [121]. The resolution of the scattering patterns is determined by the number of squares that constitute

[6]Shorter wavelengths such as X-ray scatter at the single lipid layers of the myelin sheaths as shown by MENZEL ET AL. [123] and GEORGIADIS ET AL. [62].

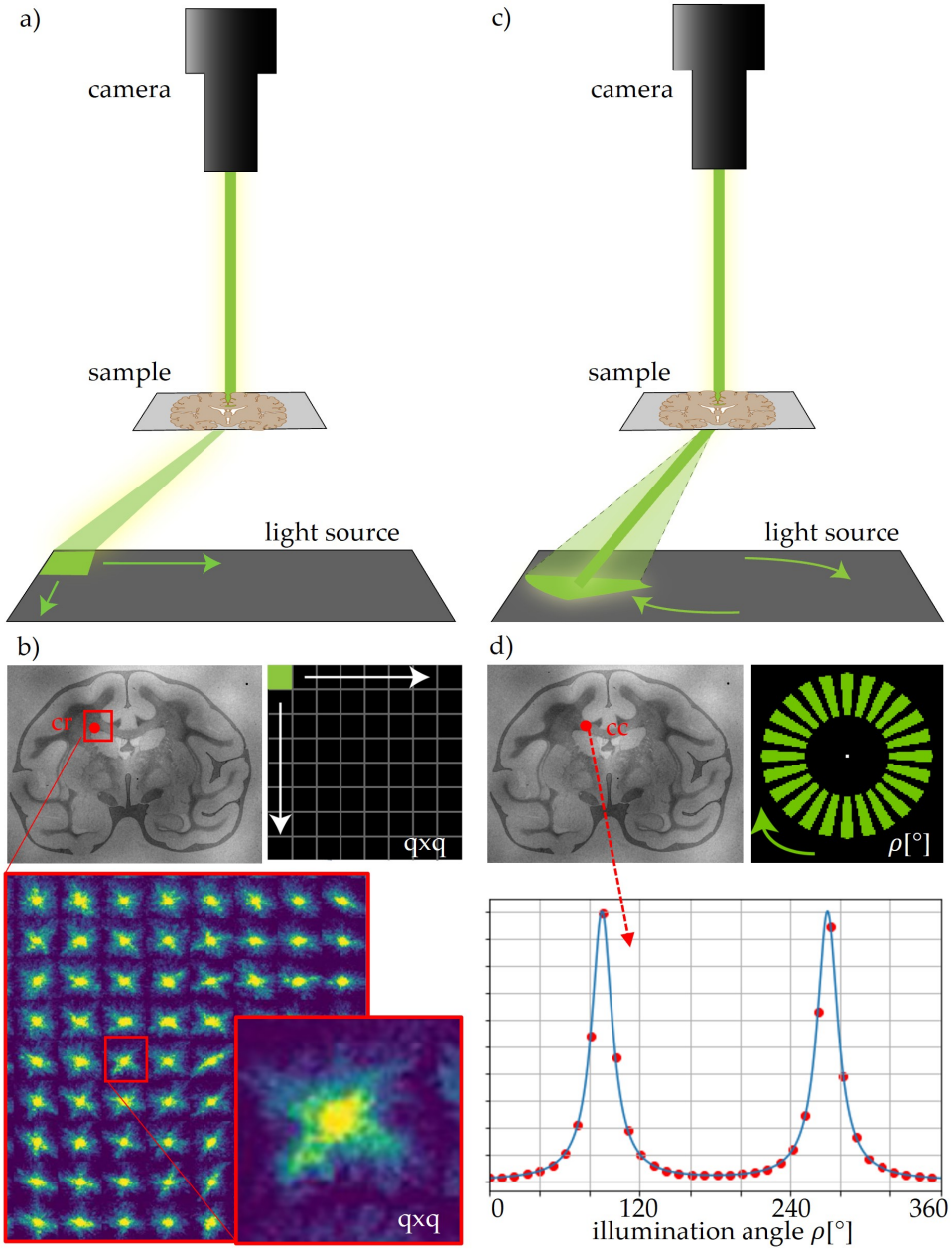

FIGURE 3.8: Computational scattered light imaging (ComSLI). A large-area light source emits unpolarized, incoherent light in the visible spectrum (usually green or white) to illuminate the brain section under various angles. The vertically scattered light is detected by the camera. The intensity becomes maximum when the incident light beam (projected to the plane) forms 90° angle with the fiber direction. a) Scatterometry ComSLI measures the scattering pattern for each image pixel by illuminating the whole sample with q×q subsequent illumination squares. b) Per image pixel, a q×q scattering pattern is assembled from the q×q measurement images. The scattering pattern contains information about fiber orientations and crossings. A bar-shaped pattern corresponds to parallel fiber orientations, an X-shape to crossing fibers. c) Angular ComSLI is performed with oblique illumination under constant illumination angles in discrete equidistant azimuthal positions ρ around a circle of 360°. d) For each image pixel, an intensity profile $I(\rho)$ referred to as the "line profile" is obtained. The peak position is directly related to the fiber orientations. Two peaks correspond to single fibers, four or six peaks correspond to two or three crossing fibers. The peak distance holds information about the fiber inclination. In-plane fibers have the maximum peak distance of 180°.

the N×N illumination grid, typically 64×64 = 4096 illumination squares. Thus, the illumination sequence yields 4096 images of the whole FOV illuminated under 4096 different azimuthal and polar angles. When the 64×64 intensities for each image pixel are rearranged into a grid of 64×64 intensity pixels, the scattering pattern is generated for each image pixel within the examined brain section as shown in Figure 3.9 [120]. Scatterometry ComSLI can be evaluated by using tools from the *Scatterometry Toolbox* (ScatBox) provided by REUTER.

Generally, the scattering patterns contain extensive information about the tissue structure beyond just the fiber orientation. However, scatterometry ComSLI is very time-consuming: The comparatively small but many illumination segments result in a longer exposure time and a significantly longer measurement. Compressed sensing ComSLI as an approach to reduce time and data is investigated in Section 7.4.

The characteristic line profiles of angular ComSLI, s. Section 3.5.2, can be retrieved from the scattering patterns by choosing intensity values along a circle or by integrating the intensity values around a circle. Thus, scatterometry ComSLI enables the calculation of line profiles with a higher resolution. Furthermore, artifacts from asymmetric illumination at image borders are easier detected and corrected in scatterometry ComSLI [120].

3.5.2 Angular Illumination

In angular ComSLI, the measurement is performed with oblique illumination under constant illumination angles in discrete equidistant azimuthal positions ρ around a circle of 360° [119, 120]. Typically, the illumination angle is $\approx 50°$. A typical azimuthal step width is $\Delta\rho = 15°$ (24 angles) or $\Delta\rho = 5°$ (72 angles). For each image pixel, an intensity profile $I(\rho)$ referred to as the "line profile" is obtained. The line profile is the pixel intensity over all azimuthal angles and contains information about fiber directions, crossings, and inclinations. Specifically, peaks in the line profile indicate the presence of a fiber bundle orthogonal to the illumination direction (when projected onto the plane), causing maximal light scattering vertically into the camera. Consequently, an in-plane fiber bundle manifests as a line profile with two peaks separated by a 180° angle, as shown in Figure 3.8d and Figure 3.9c. When two in-plane fiber bundles intersect, the line profile exhibits four peaks, forming two pairs with a 180° separation. Inclined fibers yield line profiles where two peaks converge until they merge into a single broad peak for steeper fibers.

Angular ComSLI measurement images are automatically evaluated using the open source software *SLI ToolboX (SLIX)* implemented by REUTER ET AL. [157, 158]. SLIX computes various parameter maps and visualizes the nerve fiber orientations either as a *fiber orientation map (FOM)* or a *vector map*: In the color-coded *fiber orientation map (FOM)*, each image pixel is represented by a 2×2 color matrix that contains all fiber directions within that image pixel, compare Figure 3.9a. The color-coded vector map shows fiber orientations as vectors layered on top of the tissue, see Figure 3.9b. Usually, the vectors are only shown for every n-th pixel for depiction purposes. SLIX can compute up to 12 parameter maps that provide insight into tissue properties. In the context of this thesis, the focus is on the following parameter maps:

The *average map* shows the average intensity for each line profile. Regions with high scattering are brighter while regions with low scattering are darker. The *high prominence peak map*, *low prominence peak map* and *average peak prominence map* display

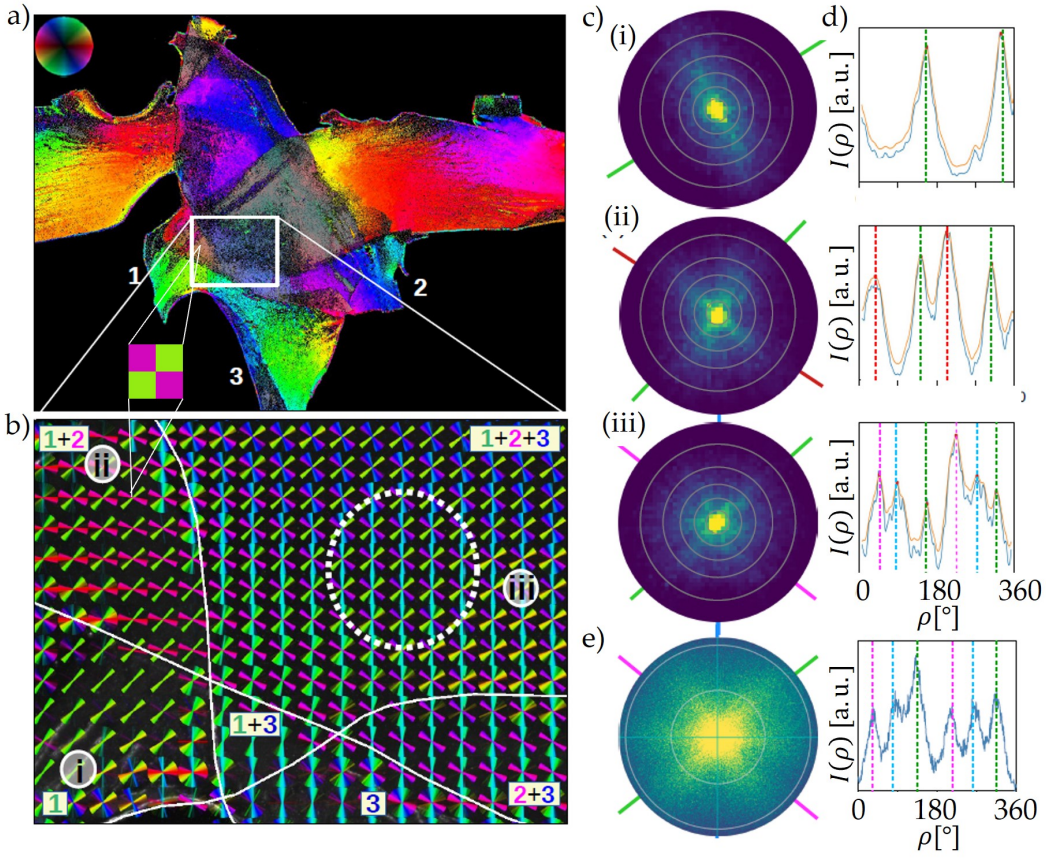

FIGURE 3.9: *Fiber orientation map (FOM)* in ComSLI. Artificial defined fiber crossings were created by layering two parts of the optic chiasm, s. Section 5.1 a) FOM of artificial fiber crossings. Each image pixel is represented by a color-coded 2×2 matrix visualizing the in-plane fiber directions as colored squares. b) Vector map. The fiber directions are displayed as color-coded vectors on top of each other. c) Scattering patterns for exemplary image pixels. The scattering pattern corresponds to the fiber orientations. d) Line profiles for the displayed scattering patterns. The fiber directions are given by the minima between the peak positions. e) Comparison with a scattering pattern obtained with Coherent Fourier Scatterometry. Parameter maps adapted from MENZEL ET AL. [121].

the number of prominent peaks, non-prominent peaks and the average peak prominence for each image pixel. The position of the high prominence peaks is used to calculate the fiber directions. The number of low prominence peaks is related to the signal-to-noise ratio (SNR) and should ideally be zero. The three *direction angle maps* contain information about the in-plane orientations of fiber bundles within individual image pixels. Each pixel can show up to three distinct directions. The calculation of in-plane direction angles occurs only when the line profile exhibits one, two, four, or six prominent peaks, with pairwise distances within the range of $(180 \pm 35)^\circ$. To determine the direction angle, the mid-position of a peak pair is considered, or in the case of a single peak, the position of that peak itself. All direction angles are in degrees, with 0° being along the positive x axis and 90° along the positive y-axis [157, 156].

3.6 Experimental Setups

The *Large Area Polarimeter (LAP)* measures 3D-PLI and DI for an entire human brain section at once. The *LMP1* and its successor, the *LMP3D*, perform high-resolution 3D-PLI measurements by scanning multiple tiles of the imaging area. The *ComSLI setup* can conduct angular and scatterometry ComSLI measurements. All these microscopes are located at the Institute of Neuroscience and Medicine (INM-1, Forschungszentrum Jülich, Germany) and are used for reference measurements in Chapter 5. Chapter 7 discusses hardware upgrades to the ComSLI setup shown here.

3.6.1 Large Area Polarimeter (LAP)

The Large Area Polarimeter (LAP) for 3D-PLI was introduced by AXER ET AL. [17] and subsequently characterized by RECKFORT ET AL. [153, 154]. The LAP features an imaging area of up to 24 cm in diameter, hence the term "large area". A *charge-coupled device (CCD)* camera (*Zeiss AxioCam HRc*) is mounted above the sample at a distance of approximately 1 m and detects the transmitted light with an object pixel size of 20-60 µm^2 (dependent on the setup configuration for different section sizes). With a sensor dimension of 1388×1040 pixels, the resulting field of view is 140×100 mm^2 for the objective lens *APO-Rodagon-N* (depending on the free working distance and the focal length, here 50 mm), which is large enough to fit human brain samples.

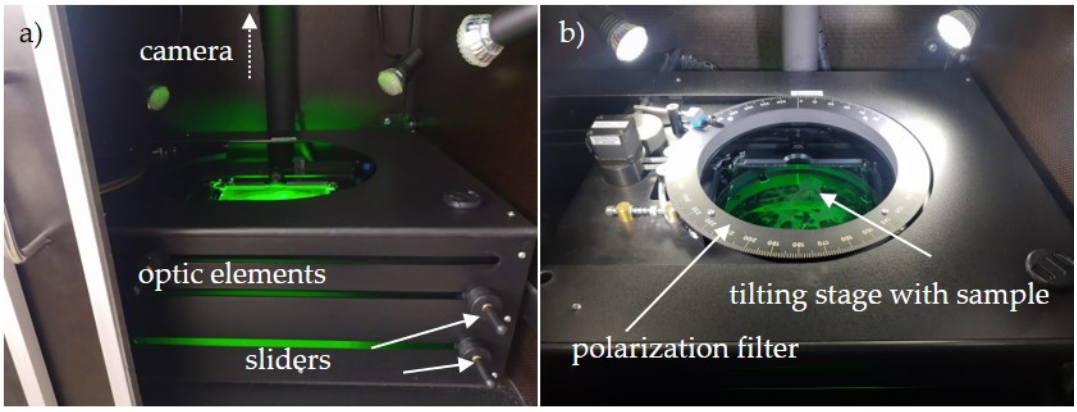

FIGURE 3.10: The Large Area Polarimeter (LAP). The LAP can measure whole human brain sections with sample tilting to resolve the inclination ambiguity. When the quarter-wave plate and the second linear polarization filter are removed, the LAP can perform DI. a) Stack with polarization filters, quarter-wave plate, and sample holder. All elements (apart from the sample holder) can be removed from the setup by sliding them to the left side. b) Top view of the optic elements and a tissue sample. Here, the setup is illuminated with supplementary lamps that are turned off during the measurement.

The customized narrow-band LED light source (*FZJ-SSQ300-ALK-G, iiM-AG*) consists of a 2D-array of 1296 diodes, each with a central wavelength of $\lambda = 525$ nm (green light), covered by a diffuser plate. The LAP contains two large-area linear polarization filters (*XP38, ITOS* [50]), furthermore a large-area quarter-wave plate (*WP140, ITOS* [50]) optimized for the transmitted wavelength. The principal axes form an angle of 45° with the transmission axes of the two crossed linear polarization filters. The linear polarization filters and the quarter-wave plate are simultaneously rotated around the stationary sample stage in steps of $\rho = 10°$, resulting in 18 measurement angles. To measure the diattenuation signal, the quarter-wave plate and the second

linear polarization filter are removed. The specimen stage can tilt the sample in all four directions with tilting angles of $|\tau| \leq 8°$. Sample tilting resolves the sign ambiguity of the fiber inclination as proposed by KLEINER ET AL. [93], calculated by WIESE ET AL. [204] and optimized by SCHMITZ ET AL. [167]. Thus, tilted measurements allow fiber bundle tracking across neighboring brain sections by determining the fiber inclination without ambiguity. The measurement (including one measurement without tilting of the sample holder and four tilted measurements) takes about 15 minutes. Pixel- and angle-wise calibration factors $g_{x,y,\rho}$ are obtained through an empty calibration measurement. The measurement images are calibrated according to

$$I_{x,y,\rho} = g_{x,y,\rho} \cdot I'_{x,y,\rho} \tag{3.18}$$

with $I'_{x,y,\rho}$ and $I_{x,y,\rho}$ being the intensity before and after calibration, respectively. Furthermore, a spatial independent component analyses (ICA) as suggested by DAMMERS ET AL. [45] and further developed by BENNING ET AL. [23] decreases artifacts such as dust and noise; thereby enhancing the signal and allowing to construct 18 high quality images in the post-processing.

3.6.2 LMP1 and LMP3D

Other than the LAP, the LMP1 (*Taorad GmbH, Germany*) comprises a motorized XY scanning stage with a tile size of $2.7 \times 2.7 \dot{\text{m}}\text{m}^2$. The measurement of a larger section can take up to 24 hours. The LMP1 employs the *Retiga 4000R* CCD camera with 2048×2048 sensor pixels in combination with the *Nikon 5x, NA 0.15* objective lens that yields an object pixel size of $1.3\,\mu\text{m}^2$. A white LED light source combined with a wavelength filter with $\lambda = (550 \pm 5)\,\text{nm}$ serves as the light source. During measurement, the first polarization filter is rotated to equidistant angular positions, typically with an angular step width of $\Delta\rho = 10°$ or $\Delta\rho = 20°$. The quarter-wave retarder ($\lambda = 545\,\text{nm}$) and the second polarization filter are located below the sample and remain fixed during the measurement.

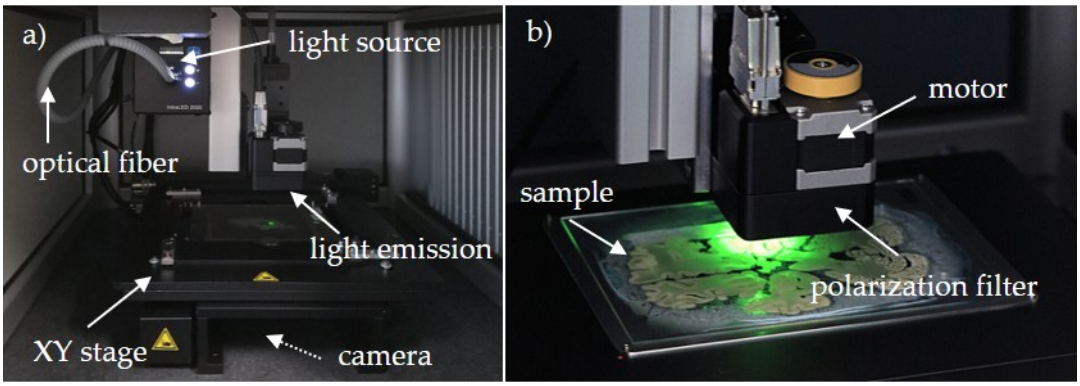

FIGURE 3.11: The LMP1 microscope. The LMP3D is the next generation of the LMP1. Photos taken from taorad.com [185]. a) Overview of the setup. The white light source is combined with a spectral filter for a green wavelengths. The LMP1 comprises a motorized XY stage to scan the sample. The camera, its objective lens, the second polarization filter, and the quarter-wave plate are located below the XY stage. b) The tissue sample is illuminated from above. During the measurement, the indicated stepper motor rotates the first polarization filter.

The *LMP3D* microscope (*Taorad GmbH, Germany*) is the next generation of the LMP1 microscope. Not sample tilting but oblique illumination is employed to solve the

sign ambiguity of the inclination. The LMP3D accelerates the image acquisition in comparison to the LMP1 and measures a larger section in only 6 hours [136]. The microscope setup employs the *SVS Vistek evo4070 GigE* CCD camera with a sensor dimension of 2048×2048 pixels combined with a *Nikon 4x (NA 0.2)* lens, thus achieving an object pixel size of 1.85 µm^2. The light source has a wavelength of $\lambda = (520 \pm 20)$ nm and is combined with a wavelength filter with $\lambda = (532 \pm 5)$ nm. The first polarization filter is rotated to equidistant angular positions with $\Delta\rho = 20°$ during measurement [61]. Similar to the LMP1, the quarter-wave plate ($\lambda = 532$ nm) and the second polarization filter are fixed. A motorized XY stage scans the imaging area in tiles of 3.8×3.8 mm^2.

3.6.3 ComSLI Setup

The ComSLI setup is built on a breadboard measuring 60×60 cm^2. A vertical aluminum rail at the rear of the breadboard is used to mount the upper elements. Illumination is provided by a controllable LED panel, specifically the *Absen Polaris 3.9pro In/Outdoor LED Cabinet* [98], featuring 128×128 LEDs (R, G, B) with an LED pitch of 3.9 mm and an overall brightness of 5000 cd/m^2. The LED panel measures 50×50 cm^2. A sample holder is positioned 17 cm above the light source, thereby offering a maximum illumination angle of $\tan^{-1}(25/18) \approx 54°$. The dimensions of the Scattering Polarimeter in Chapter 4 are based on these sizes.

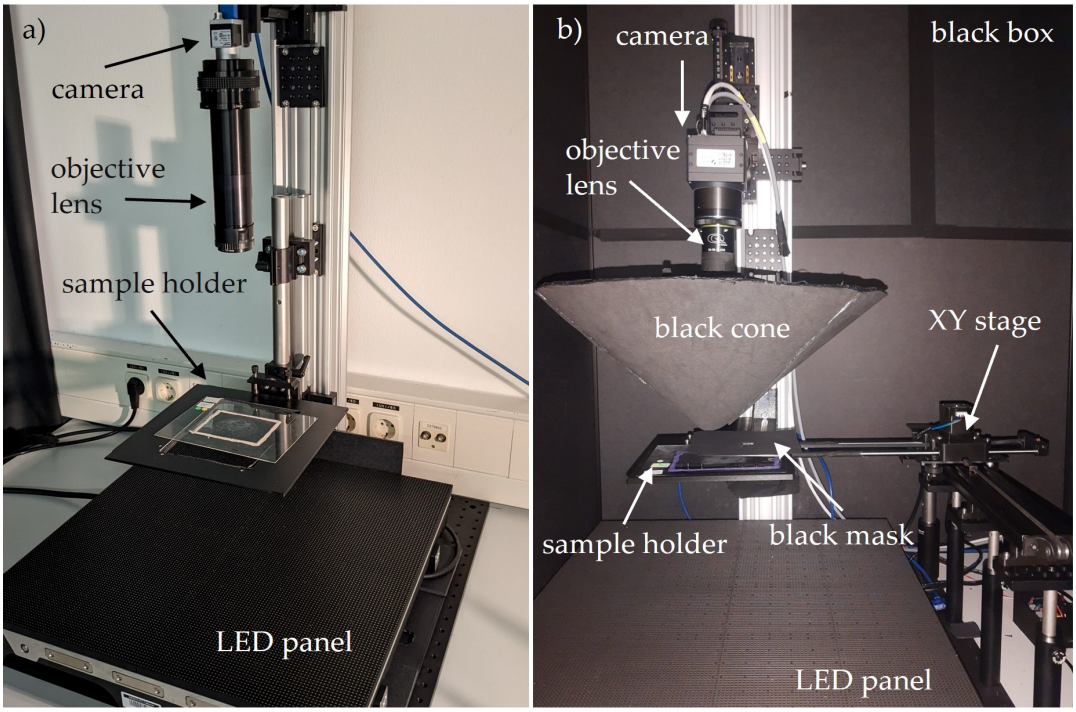

FIGURE 3.12: The ComSLI setup without and with light shielding. a) ComSLI setup without light shielding. Oblique illumination is achieved with a large-area LED panel. A camera detects the vertically scattered light. The depicted camera is the *Basler acA5472-17uc*. b) Extensive light shielding prevents unwanted reflections and stray light to enter the camera tube. In particular, this includes a black protective casing for the setup, a black cone to prevent oblique reflections into the objective lens, and a black cardboard mask placed on top of the tissue sample. This photo already shows the high-sensitivity camera *SVS-VISTEK HR455CXGE* described in Section 7.2 and the XY stage described in Section 7.3.

The *Basler acA5472-17uc* [21] CCD camera is located centrally above the sample holder. The camera employs a *Sony IMX183 CMOS* sensor [178] with a sensor dimension of $13.1 \times 8.8\,\mathrm{mm}^2$, a sensor pixel size of $2.4 \times 2.4\,\mu\mathrm{m}^2$ and 5472×3648 pixels. It can operate at a maximum of 17 frames per second and provides either a color depth of 10 bit for 10-bit high-speed all-pixel readout or a color depth of 12 bit for 12-bit high-resolution readout. In this configuration, the *Rodenstock Apo-Rodagon-D120* objective lens yields a field of view of $1.6 \times 1.1\,\mathrm{cm}^2$ and a resolution in object space of $3.5 \times 3.5\,\mu\mathrm{m}^2$ at a focal length of 120 mm [51]. The setup without light shielding is depicted in Figure 3.12a. To ensure high measurement quality, the ComSLI setup incorporates thorough shielding against external light and internal reflections. A casing made from black light-absorbing cardboard and a blackout curtain shield the setup from external light sources. A black cone made out of Ethylene-vinyl acetate (EVA) foam covers the light path between the sample and the camera, preventing reflections within the objective lens tube. Reflective surfaces inside the casing are covered with black masking tape where applicable. The setup without light shielding is depicted in Figure 3.12b, already including the high-sensitivity camera *SVS-VISTEK HR455CXGE* described in Section 7.2 and the XY stage described in Section 7.3.

In Chapter 7, the capabilities of the ComSLI setup are expanded through the integration of new hardware, its application on differently prepared tissue sections, and through the use of an illumination strategy based on compressed sensing.

Chapter 4

The Scattering Polarimeter

Imaging the nerve fiber architecture of the human brain is a major goal in neuroscience. Müller polarimetry, three-dimensional polarized light imaging (3D-PLI), diattenuation imaging (DI) and computational scattered light imaging (ComSLI) employ visible, mostly incoherent light to achieve a micrometer in-plane resolution in the investigation of long-range fiber pathways in histological brain sections. The four techniques were detailed in Chapter 3.

The **combination of Müller polarimetry, 3D-PLI, DI and ComSLI within a single setup** – a multi-modal high-speed *Scattering Polarimeter* – opens up the possibility for pixelwise mapping, cross-validation of fiber orientations and the usage of unique advantages from each technique. This chapter documents its **construction from scratch to a fully operational device**. As far as known, such a device has never been built before. First, the conceptual sketch for the device is presented. Suitable optical and mechanical hardware are introduced, including a routine to adjust the novel device. The duration of the measurement is estimated based on the custom measurement software. The **liquid crystal variable retarders (LCVRs)** play a major role within the Scattering Polarimeter, and thus, their thorough characterization is crucial to a successful device operation, especially the determination of correct voltage settings for all modalities. Finally, this chapter presents a fully operational device and includes suggestions on future development.

4.1 Concept and Design

The design of the Scattering Polarimeter is shown in Figure 4.1a. Two light paths are indicated in green[1], the vertical light path for Müller polarimetry, 3D-PLI, and DI, and an exemplary angular segment of oblique illumination for ComSLI. The two linear polarization filters (LP) are marked in gray. The voltage-controlled liquid crystal variable retarders (LCVRs) are displayed in pink and blue, depending on the azimuthal orientation of their slow axis (45° or 0°, respectively).

LP 1 has its transmission axis at an azimuthal angle of 0°. LCVR 1 has its slow axis at 45° and LCVR 2 at 0°. Together, the LP 1, LCVR 1 and LCVR 2 form the *polarization state generator* (PSG). The *polarization state analyzer* (PSA) mirrors the optic components of the PSG: Here, LCVR 3 with its slow axis at 0° is followed by LCVR 4 with its slow axis at 45° that again is followed by LP 2 with its transmission axis at 0°. The tissue sample is located between the PSG and the PSA. With this configuration, the PSG can generate any polarization state, and the PSA can analyze any polarization state. The

[1]The choice of color represents the typically green illumination wavelength.

LCVRs can operate as a classic Müller polarimeter but also perform 3D-PLI and DI measurements by generating linear polarization with equidistant angles ρ and using the PSA as a circular analyzer for left- and right-circular polarization.

A large-area light source, e.g. a panel with separately controllable LEDs, can display ComSLI illumination patterns but can also illuminate the sample directly from below. Furthermore, the illumination color can be changed within the range of RGB colors, thus adding the possibility for wavelength-dependent measurements to the setup. The response of the LCVRs depends on the wavelength, thus the light source spectrum should be narrowed by a matching spectral filter positioned on top of the light source in the vertical light path.

The overall setup demands stability, precision, and effective shielding from external light interference. The sample holder can be stationary but preferably contains an XY stage allowing scanning of the sample[2]. The finished device is shown in Figure 4.1b.

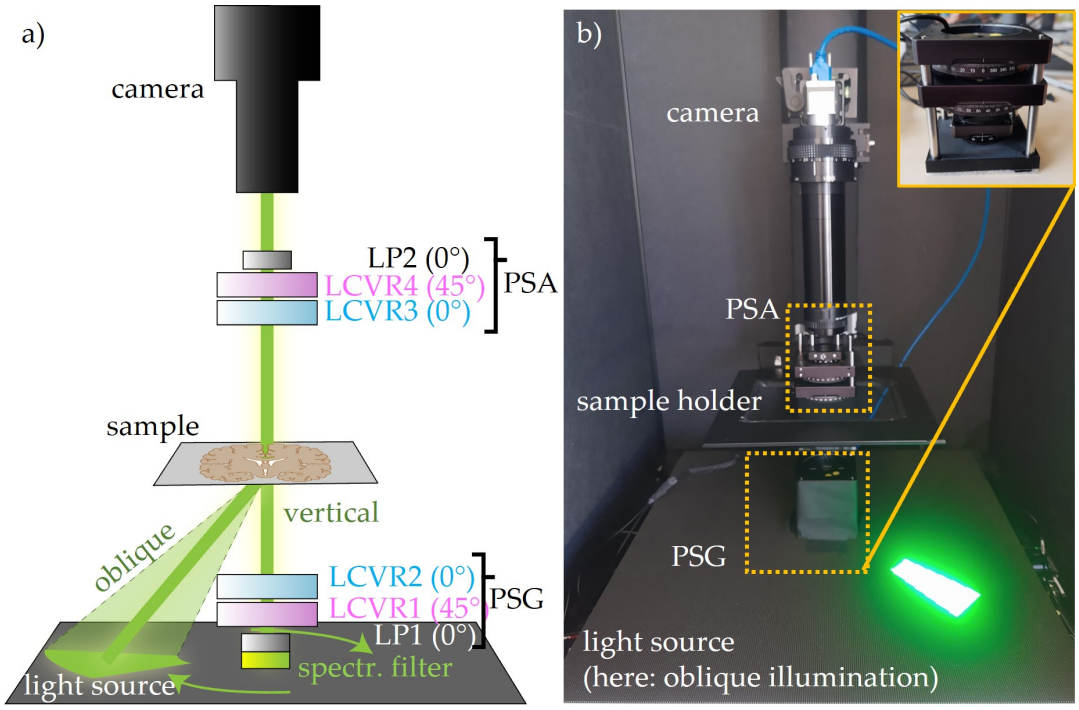

FIGURE 4.1: Sketch and prototype of the Scattering Polarimeter. a) The Scattering Polarimeter is realized as a (modified) Müller polarimeter with two high-quality linear polarizers (LPs) and four voltage-controlled liquid crystal variable retarders (LCVRs) for the polarization state generator (PSG) and analyzer (PSA), and a large-area light source suitable for vertical and oblique illumination (indicated in green). LP 1 and LP 2 have their transmission axes at an azimuthal angle of 0°. For the LCVRs, blue and pink represent their azimuthal orientations, with blue having the slow axis at an angle of 0° and pink at 45°. The sketch is not to scale. b) Picture of the device. An exemplary angular illumination segment for ComSLI is displayed on the LED panel. The components of the PSG are shown in the upper right corner.

[2]A suitable custom-built XY stage for the ComSLI setup is presented in Section 7.3 that is also compatible with the Scattering Polarimeter.

4.2 Optical Components

The Scattering Polarimeter contains a camera and a suitable objective lens, a large-area light source plus a spectral filter, two high-quality LPs and four voltage-controlled LCVRs. The chosen hardware components are presented in the following.

4.2.1 Camera and Objective Lens

The *Basler acA5472-17uc* CCD camera[3] uses a *Sony IMX183 CMOS* sensor with a size of $13.1 \times 8.8\,\mathrm{mm}^2$, a sensor pixel size of $2.4 \times 2.4\,\mu\mathrm{m}^2$ and 5472×3648 pixels, i.e. a resolution of 20 megapixels. It operates at maximum of 17 frames per second and provides either a color depth of 10 bit for 10-bit high-speed all-pixel readout or a color depth of 12 bit for 12-bit high-resolution readout [21, 178].

The geometry of the setup imposes restrictions on the objective lens: The field of view should be as large as possible without the LCVR apertures causing vignetting or other border effects. Especially the apertures of the lower optical components (i.e. the PSG) need to be considered. Furthermore, the minimum free working distance needs to accommodate the elements of the PSA (LCVR 3, LCVR 4, and LP 2, overall forming a stack of about 7 cm). The choice of the objective lens further depends on the camera sensor.

The *QIOPTIQ APO-RODAGON-D 1X 75/4,0* [51] objective lens must match the setup geometry and the camera sensor as shown in Figure 4.2. The calculations were made with the free software *MachVis* [52]. The field of view is $8 \times 5\,\mathrm{mm}^2$ and the optical resolution $2.2 \times 2.2\,\mu\mathrm{m}^2$ (determined with a United States Air Force (USAF) chart). The camera aperture is at its maximum value of 5.6 for maximum light incidence.

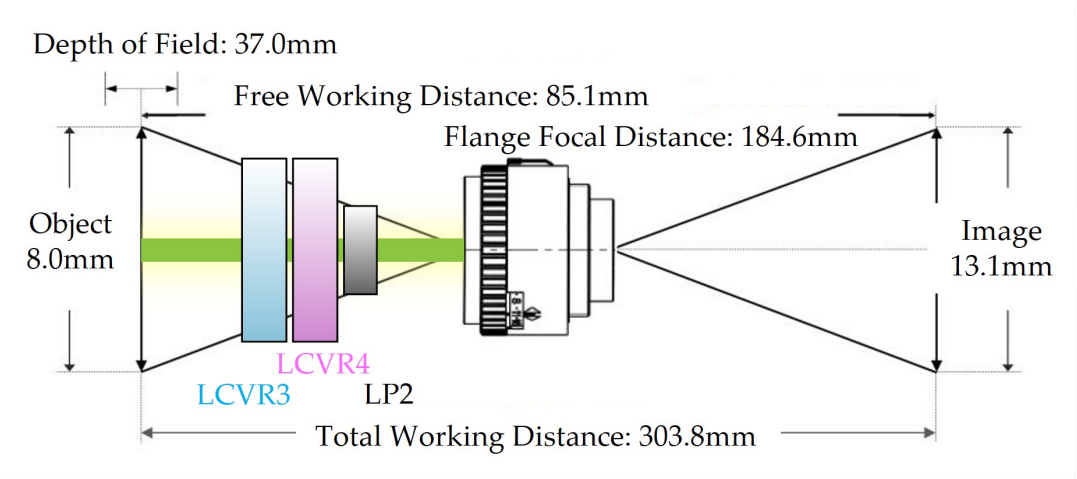

FIGURE 4.2: Imaging properties of the objective lens. The geometry of the setup limits the maximum field of view through the apertures of the lower optical components. The minimum free working distance needs to accomodate the PSA (LCVR 3, LCVR 4, LP 2, overall forming a stack of about 7 cm). Furthermore, the choice of the objective lens depends on the camera sensor. Parameters for the *APO-RODAGON-D 1X 75/4,0* were calculated with the free software *MachVis* [52].

[3]The performance of a high-sensitivity camera, the *SVS-VISTEK HR455CXGE* CCD camera, is addressed in Section 7.2 for ComSLI.

4.2.2 Linear Polarization Filters (LPs)

Two *Thorlabs LPVISC100* linear polarization filters with a diameter of 25 mm serve as the lower LP 1 and the upper LP 2. These nanoparticle LPs consist of prolate ellipsoid nanoparticles embedded in sodium-silicate glass. According to the manufacturer, the polarization filters provide an extinction ratio of 1000:1 in the range of visible light from 510 to 800 nm and and extinction ratio of 10000:1 in the range from 520 nm to 740 nm [192]. Crossed and parallel configuration measurements yielded an extinction ratio of 3274:1 (exposure time of 2 seconds, central wavelength $\lambda_0 = 520$ nm, FWHM $= 10$ nm bandpass filter, averaged over 7 images).

4.2.3 Light Source and Spectral Filter

Generally, the signal-to-noise ratio (SNR) benefits from a bright light source. A brighter light source can also shorten the exposure time, and thus reduce the overall measurement time. The light-emitting diode (LED) panel *INFiLED s1.8 LE Indoor LED Cabinet* serves as a large-area light source [11]. The panel consists of 256×256 LEDs (R, G, B) with an LED pitch of 1.8 mm and a view angle of 120°. It has a size of 46.56×46.56 cm². The overall brightness is 1000 cd/m². The LED panel control is connected to the measurement computer as an additional monitor, allowing for easy switching between ComSLI illumination patterns and vertical illumination, as well as enabling changes in illumination color.

A spectral wavelength filter with a diameter of 25 mm on top of the LED panel can narrow the illumination wavelength spectrum but also decreases the transmitted light intensity. The transmission and bandwidth of two hard-coated bandpass filters were investigated and compared to the unfiltered spectrum. The spectral filter *Thorlabs FBH515-10* has a central wavelength of $\lambda_0 = 514.5$ nm and a full width half maximum (FWHM) of 10 nm [190]. The *Thorlabs FBH515-3* spectral filter has a smaller FWHM of 3 nm and a $\lambda_0 = 514.5$ nm. The spectrum was measured with the *Thorlabs Compact CCD Spectrometer CCS100/M* [188] and integrated over 5 seconds.

Figure 4.3 shows the spectrum before and after filtering. The wavelength-dependent intensity $I(\lambda)$ was fitted with a Gaussian curve

$$I(\lambda) = I_0 \cdot \exp\left(-\frac{(\lambda - \bar{\lambda})^2}{2\sigma^2}\right) \tag{4.1}$$

where $\bar{\lambda}$ is the central wavelength and σ the standard deviation, linked to the FWHM

$$\text{FWHM} = 2\sqrt{2\ln(2)} \cdot \sigma \approx 2.355\sigma \tag{4.2}$$

The spectral bandwidth of the LED panel is centered at a wavelength of λ =(520.9±0.1) nm with an FWHM of (35.1±0.2) nm. The 10 nm bandwidth filter with a fitted central wavelength of λ =(513.4±0.1) nm and an FWHM of (14.1±0.3) nm offers a good compromise between wavelength precision and transmitted light intensity. The 3 nm filter with a fitted central wavelength of λ =(511.2±0.5) nm and an FWHM of (7.7±1.1) nm yields a considerably lower light intensity that barely peaks above background noise and is therefore unsuitable for high-speed applications with a short exposure time. The offset from the central wavelength of the light source results in an even lower light transmission. The fitted values slightly deviate from those given by the manufacturer, especially for the noise-influenced third fit.

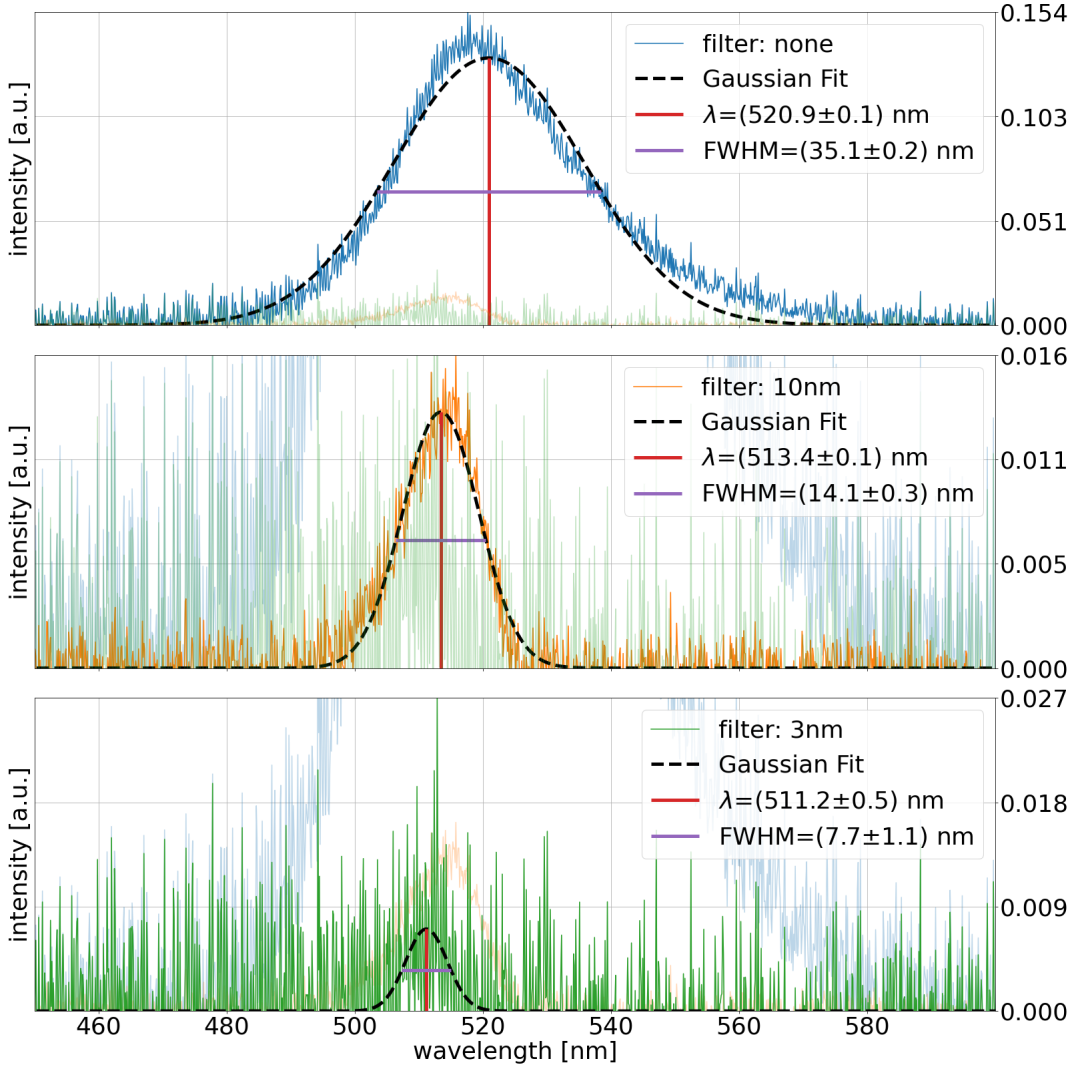

FIGURE 4.3: Light source spectrum with and without spectral filters. For each spectrum, the depiction shows the two other spectra with lowered opacity for easier comparison. Top: Spectrum without spectral filter. The central wavelength is 520 nm and the full width half maximum (FWHM) is 35 nm. Middle: Spectrum with 10 nm spectral filter. This spectral filter was chosen for the Scattering Polarimeter. Bottom: Spectrum with 3 nm spectral filter. The transmitted intensity is very low. The fitted values deviate slightly from those given by the manufacturer, especially for the noise-influenced third fit.

4.2.4 Liquid Crystal Variable Retarders (LCVRs)

Four *Thorlabs LCC1223-A* full-wavelength LCVRs with a 20 mm large clear aperture were chosen for the polarization state generator and analyzer [189]. The diameter of 20 mm was the largest commercially available diameter and limits the imaging area for the Scattering Polarimeter. Previous experiments with custom large-area LCVRs encountered issues due to an inhomogeneous area [75]. The LCVRs are antireflection (AR)-coated to work best in a wavelength range from 350 nm to 700 nm. According to the manufacturer, the switching speed is typically a rise time of 59.6 ms and a fall time of 1.45 ms at room temperature (22 °C)[4]. Instead of reaching true zero for the

[4]The switching speed must be considered when the exposure time has a similar duration. However, this is not the case here because typical exposure times are 10 to 100 times as long.

maximum voltage, the LCVRs have a residual retardance of $\approx 30\,\text{nm}$ at the largest applicable voltage of 25 V. It is possible to purchase devices that compensate the residual retardance, however, this results in a slightly degraded retardance uniformity. Uncompensated LCVRs were chosen for the Scattering Polarimeter because spatial homogeneity is crucial. Nevertheless, the achievable retardance range of more than a full wavelength is sufficient for the Scattering Polarimeter because zero retardance is equivalent to the retardance of one wavelength in all desired applications. Adequate voltage settings for the LCVRs were identified in Section 4.5.

The LCVRs are controlled with four separate *KLC101 K-Cube* controllers [191]. The K-Cube provides square-wave voltage from 0 to $\pm 25\,\text{V}$ with frequencies from 500 Hz to 10 kHz. The frequency can be adjusted to avoid interference with other signals or – when used for operation with off-brand LCVRs – to match a given operation frequency. The K-Cubes are connected to the computer via USB and controlled either with a graphical user interface (GUI) or by integrating the provided software development kit (SDK) into a custom measurement software.

4.3 Construction of the Scattering Polarimeter

The mechanical elements of the Scattering Polarimeter involve aluminum rails and various mounts plus suitable screws and nuts. Custom components were designed in the Computer-Aided Design (CAD) program *Autodesk Fusion* and 3D-printed in polylactide (PLA) filament [10, 174]. Furthermore, extensive light shielding actions were taken, as illustrated in the following.

4.3.1 Mechanical Construction

A breadboard of size $60 \times 60\,\text{cm}^2$ forms the base of the Scattering Polarimeter. Positioned at the back of the breadboard is an aluminum mounting rail with a height of 1 m, allowing for height-variable mounting of the optical elements. During construction, the LED panel was pushed back against the aluminum rail so that its backside aligns with the front plane of the rail, ensuring that the LED panel, and therefore the PSG components, align correctly with the Cartesian coordinate system of the setup.

The sample holder was attached to the aluminum rail at a height of 16 cm above the LED panel, in focus distance of the camera. The camera was mounted centrally above the LED panel and focused on the sample plane. The camera height can be roughly adjusted by moving it up or down the aluminum rail. Precise focusing is achieved by rotating the focus wheel of the camera objective. The LPs and LCVRs were mounted in rotation mounts to enable precise azimuthal adjustment. The four K-Cubes for controlling the LCVRs were positioned beside the LED panel with their displays deactivated to avoid stray light within the setup. The LED panel controller, the camera, and the K-Cubes were connected to the measurement computer via HDMI and USB-A, respectively.

The PSG is composed of LP 1 and two LCVRs with their slow axes set to azimuthal angles of $\theta = 45^\circ$ (LCVR 1) and $\theta = 5^\circ$ (LCVR 2). The PSG elements were vertically stacked and fastened within a 3D-printed custom base with a suitable cutout compatible with a cage system of 6 mm aluminum rods. The PSG stack also incorporates the spectral filter, placed directly on top of the light source. The complete stack is shown in Figure 4.1b, upper right corner. In ComSLI measurements, it is crucial not to cover any angular illumination segments with, e.g. a mounting rod. Therefore,

the lower element stack was not attached to the mounting rail but placed loosely on top of the LED panel and secured in place with small strips of black masking tape. The square-shaped base of the stack aligns with the LEDs, allowing precise angular adjustment as long as the LED panel also aligns with the mounting rail. The two slim LCVR cables were directed towards the side of the LED panel and secured to lie flat between two ComSLI illumination segments, thereby minimizing obstruction caused by the cables. The height of the PSG limits the LED panel area in ComSLI illumination (both angular ComSLI and scatterometry ComSLI) by forming a dead angle: LEDs within that area cannot be used for scattered light imaging because their light path is covered by the PSG. Angular illumination patterns take the dead angle into account by choosing an inner radius of 50 LEDs of the illumination segments. The outer radius is limited by the LED panel size.

The PSA was secured in place between sample holder and camera. Its components mirror the PSG: The slow axis of LCVR 3 was set to $\theta = 0°$, the slow axis of LCVR 4 to $\theta = 45°$ and the transmission axis of LP 2 at $\theta = 0°$. LCVR 3, LCVR 4 and LP 2 were placed into rotation mounts for precise and quick adjustment and secured using a cage system of 6 mm rods. An aluminum rod connects the cage system with the mounting rail.

A black cardboard box shields the Scattering Polarimeter from external light. Inside the box, reflecting surfaces like the mounting rail were covered with black masking tape. Furthermore, the PSG elements were wrapped in black cardboard. The LED display controller was placed outside the box, with its connective cables leading inside the box. The K-Cubes had to be placed within the box due to the short LCVR cable length, so their displays were switched off. During measurement, the sample should be covered with a black mask with a rectangular cut-out slightly larger than the imaging area to avoid unwanted reflections, which is especially important in ComSLI.

4.3.2 Azimuthal Adjustement Routine

The azimuthal adjustment of LPs and LCVRs followed a scheme starting with a single LP placed inside the setup and successively adding more optical components. The routine required an additional polarization filter (preferably rectangular for convenience) with a known transmission axis. An exceptional quality for the reference polarization filter was not necessary because only the relative transmission was relevant. Here, a square-shaped piece of polarization film with its transmission axis aligned with one of the rectangle sides serves as the reference sample.

For all steps, a live view of the camera image was required, e.g. with the free software *Pylon Viewer* [22], s. Section 4.4. For a comprehensive overview, the azimuthal adjustment scheme is presented step by step.

1. The central LEDs below the camera were illuminated, e.g. by displaying a green circle on the LED display.
2. The reference polarization filter was placed on top of the LED panel with its sides aligning with the LED array. This aligned the polarization filter with the Cartesian coordinate system of the Scattering Polarimeter.
3. LP 2 was added to the system and rotated until the transmitted intensity is at its minimum or maximum. This defined the azimuthal angle $\theta = 0°$. In the

context of this thesis, $\theta = 0°$ is parallel to the front edge of the LED panel and corresponds to the angle of horizontal linear polarization (H).

4. The reference polarization filter was removed. The 3D-printed base plate for the lower elements was installed in its position below the camera and aligned with the LED array. The spectral filter and LP 1 were placed into the base plate. LP 1 was rotated until the position of maximum transmission relative to LP 2 was found, indicated by the camera image showing maximum light intensity. Thus, LP 1 and LP 2 were parallel.

5. LCVR 1 was added to the base plate with its optic axis at $\approx 0°$. The voltage for LCVR 1 was varied with the K-Cube control software provided by the manufacturer, s. Section 4.4. Generally, the visible shifts in intensity in the camera image are lowest[5] for $\theta = 0°$. After the azimuthal zero position for LCVR 1 was found, the LCVR was set to $\theta = 45°$ to measure the retardance voltage curve as demonstrated in Section 4.5.

6. LCVR 1 was removed and step 4 was repeated for LCVR 2, including the measurement of the retardance voltage curve. Then, LCVR 2 was removed and step 4 was repeated for LCVR 3 and LCVR 4.

7. Now the azimuthal axes were identified correctly and all LCVRs were characterized. All LCVRs were put back into the setup and – in case of LCVR 2 and LCVR 3 – set to their correct azimuthal orientation $\theta = 0°$.

4.4 Software and Measurement Routine

The measurement computer controls the K-Cubes, the camera, and the LED display controller. While the LED display is addressed as an additional monitor via an HDMI connection, the K-Cube and the camera both come with a graphical user interface (GUI) but can also be integrated into custom measurement routines via their software development kits (SDKs) provided by the manufacturers. The GUIs, the custom measurement software, and the illumination sequence for ComSLI are presented in the following and the minimum time for a complete measurement sequence is estimated.

4.4.1 Graphical User Interfaces

The *Thorlabs KLC101* software [191] sets the voltage and the frequency of the K-Cubes, i.e. the LCVR s. The GUI can be opened for each of the four LCVRs separately. Each time, the corresponding LCVR has to be chosen via its unique identification number that is written on the device. The software comes with an SDK that can be integrated via Python or C++ into a custom measurement software.

Basler Pylon Viewer [22] provides a camera live image which is especially useful during positioning of the sample. Instead of directly working with the SDK, the Python module *pypylon* [69] can be integrated into custom Python code to access the camera during an automatized measurement routine.

[5] Ideally: non-existent

4.4.2 Custom Measurement Software

A custom Python measurement software was written in the context of this thesis for a complete measurement sequence that includes all four modalities. The camera, the LED panel and the K-Cubes were integrated as objects of their own class, allowing to exchange all devices without changing the main code. The routine accesses the camera via *pypylon* and the K-Cubes via their SDK that is also available for Python. Furthermore, the measurement software displays custom illumination patterns onto the LED display.

The user can choose the measured modality (Müller polarimetry, 3D-PLI, DI and/or ComSLI) or any combination or all of them. When only DI is chosen, a 3D-PLI measurement with the PSA set to left-handed circular analysis (LC) and a 3D-PLI measurement with the PSA set to right-handed circular analysis (RC) is performed as required for DI, s. Section 5.3. Camera parameters such as exposure time, gain, color depth, color channel, averaging etc. can be set with an input JSON file. Furthermore, the input file includes information about the sample and defines the LCVR-specific voltages for all major retardance values, i.e. $2\pi = 0$ or 1λ (no retardance), $\frac{\pi}{2}$ or 0.25λ (operation as a positive quarter-wave plate), π or 0.5λ (operation as a half-wave plate), $3\frac{\pi}{2}$ or 0.75λ (operation as a negative quarter-wave plate).

The measured images are averaged over all repetitions and saved as TIFF images in a user-specified folder along a descriptive JSON file with all measurement parameters. The user can choose to save the raw data or to only keep the averaged images (if desired, with the corresponding standard deviation). The software can do a sweep over equidistant voltages (as required for the retardance voltage curve or the PSG characterization, s. Section 4.5), or use an array of custom voltages that correspond to steps of equidistant linear polarization angles generated by the PSG. The software allows the potential integration of an XY stage even though a scanning stage is not yet implemented.

4.4.3 Illumination Sequence

The illumination patterns that are displayed during the measurement routine are referred to as the *illumination sequence*. The illumination sequence starts with a central circle with the diameter of roughly the PSG apertures (a diameter of about 10 LEDs) that serves as the light source for vertical illumination (in Müller polarimetry, 3D-PLI and DI). Then, the angular illumination segments for ComSLI illumination follow one after each other.

Display images of the central circle and the angular patterns are given by a sequence of TIFF images that are progressively named and contained within the same folder. Before the measurement, the illumination sequence was centered on the LED display by determining an x- and y-position on the monitor that centers the central circle within the camera image. The angular segments were generated similar to those used for regular ComSLI measurements. They are defined by their inner and outer radius (in pixels), the number of segments, the azimuthal segment size and their color (green as a default). Apart from the angular illumination sequence, also scatterometry ComSLI is possible by switching the illumination patterns correspondingly.

4.4.4 Time Estimation

The complete measurement sequence of the Scattering Polarimeter comprises two 3D-PLI measurements (left-handed circular (LC) and right-handed circular (RC) setting for the PSA), Müller polarimetry with 36 measurements[6] and an angular ComSLI measurement with steps of 15°. The DI measurement is obtained later by adding up the two 3D-PLI measurements. For the time estimation, 3D-PLI measurements with a default angular step of $\Delta\rho = 10°$ are considered, thus requiring 2×18 images[7]. The default ComSLI illumination pattern is a green angular pattern with steps of 15°, therefore consisting of 24 images.

The complete default measurement consists of 96 measurement images, multiplied by the number of repetitions N. Technically, a further small reduction of the measurement time is possible because four images are taken twice: When the PSG generates linear polarization with an angle of 0° (angular steps of 10°) and the PSA is set to LC for 3D-PLI, this is equivalent to a measurement during Müller polarimetry where the PSG generates H and the PSA analyzes L. The same holds for 90° and RC, and combinations of those. This synergy can be implemented into future versions of the measurement software.

The exposure time for vertical t_{vert} and angular illumination t_{obl} is usually different and can be set separately. With 2×18 images for 3D-PLI, 36 for Müller polarimetry and 24 images for ComSLI, the estimated time for a full measurement t_{meas} is therefore

$$t_{\text{meas}} = N \cdot [(2 \cdot 18 + 36) \cdot t_{\text{vert}} + 24 \cdot t_{\text{obl}}] + N \cdot (2 \cdot 18 + 36 + 24) \cdot t_{\text{data}} \tag{4.3}$$

The time for data processing t_{data} strongly depends on the hardware (camera and computer) but also on the software implementation for data processing.

Section 5.1.3 introduces exposure times that have proven to be effective for the various techniques. With a typical exposure time of $t_{\text{vert}} = 2$ seconds, $t_{\text{obl}} = 4$ seconds and $N = 4$ repetitions, the minimum measurement time is estimated to $t_{\text{meas}} > 960$ seconds≈ 16 minutes. An important goal in context of high-speed scattering polarimetry is to decrease measurement time by mathematical, technical, and methodological means. The estimation does not take t_{data} into account because it strongly depends on the hardware of the specific measurement computer (e.g. camera, computer) and can therefore not be generalized.

4.5 Characterization of Variable Retarders

The LCVRs as major components of the Scattering Polarimeter are each characterized by their unique retardance voltage curve, i.e. the behavior of the LCVR when a certain voltage is applied. Müller polarimetry, 3D-PLI and DI require specific combinations of retardance settings to achieve the desired polarization state. Thus, the corresponding voltage settings need to be determined prior to any measurements.

4.5.1 Retardance Voltage Curve

In LCVRs, the retardance $\delta = \delta(V)$ depends on the applied voltage V in a non-linear way. To determine the relation between voltage and retardance, an LCVR is usually

[6] The measurement with a reduced number of 16 images is explored in Section 5.4.2.

[7] A successful further reduction of measurement images is demonstrated in Section 5.2.5

placed between two crossed polarizers and the average transmitted light intensity $I(V)$ is determined for an array of voltages. Intensity maxima correspond to voltages where the PSG rotates the initial polarization around 90° whereas intensity minima indicate voltages where the LCVR does not rotate the polarization angle (which is equivalent to a rotation of 180°).

Mathematical Derivation Jones matrix calculus as introduced in Section 2.2.1 yields the transmitted amplitude $\vec{A}(\delta)$ based on the retardance δ

$$\vec{A}(\delta) = M_{\mathrm{LP}}(\theta = 90^\circ) \cdot M_{\mathrm{LCVR}}(\theta = 45^\circ) \cdot M_{\mathrm{LP}}(\theta = 0^\circ) \tag{4.4}$$

$$= \begin{pmatrix} 0 & 0 \\ 0 & 1 \end{pmatrix} e^{i\frac{\delta}{2}} \begin{pmatrix} \cos(\delta/2) & i\sin(\delta/2) \\ i\sin(\delta/2) & \cos(\delta/2) \end{pmatrix} \begin{pmatrix} 1 & 0 \\ 0 & 0 \end{pmatrix} \begin{pmatrix} A_x \\ A_y \end{pmatrix} \tag{4.5}$$

$$= A_y e^{i\frac{\delta}{2}} \begin{pmatrix} 0 \\ i\sin(\delta/2) \end{pmatrix} \tag{4.6}$$

The intensity is the squared absolute value

$$I(\delta) = |A_y|^2 = \sin(\delta/2) \tag{4.7}$$

The retardance voltage curve $\delta(V)$ is determined from Eq. (4.7) and the measured $I(V)$ curve:

$$\delta(V) = 2\sin^{-1}(I) \tag{4.8}$$

Eq. (4.8) has four possible solutions due to the mathematical features of $\sin^{-1}$ and properties of square root. However, the correct physical solution is a continuous curve. Therefore the solutions of the equation must be calculated interval-wise where the minima and maxima form the interval boundaries.

Furthermore, the measured intensity must be normalized within each interval with the local maximum before calculation of the retardance voltage curve. The interval-wise normalization is crucial, or else, gaps and distortions occur in the retardance voltage curve. In literature, this calculation is called *phase-unwrapping* and was discussed in detail by LÓPEZ-TÉLLEZ & BRUCE [109] and SCHNOOR ET AL. [168].

Measurement with the Scattering Polarimeter The retardance voltage curve depends on the wavelength λ but also on the applied square voltage frequency. The curve was measured for two spectral filters (FWHM = 10 nm, FWHM = 3 nm) and for the unfiltered spectrum (FWHM = 35 nm). The two spectral filters were introduced in Section 4.2.3. Furthermore, three different frequencies were investigated ($f = 2\,\mathrm{kHz}$, $f = 5\,\mathrm{kHz}$, $f = 10\,\mathrm{kHz}$).

All retardance voltage curves $\delta(V)$ were measured in a crossed-polarizer configuration. The characterization took place within the Scattering Polarimeter. All LCVRs – apart from the investigated LCVR – were removed from the setup. The transmission axis of the lower linear polarization filter was set to an azimuthal angle of $\theta = 0^\circ$. The transmission axis of the upper linear polarization filter was rotated to an azimuthal angle of $\theta = 90^\circ$, thereby forming the crossed-polarizer configuration. The slow axis of the LCVR was set to an azimuthal angle of $\theta = 45^\circ$. The retardance voltage curve was sampled in voltage steps of 0.02 V from 0.8 V to 5.0 V at an exposure time of 2 seconds. Every image was recorded two times for averaging.

Theoretically, the LCVR can operate with voltages up to 25 V, but at higher voltages, the curve is nearly flat (even though the retardance never reaches zero because the LCVRs are not retardance-compensated, s. Section 4.2.4. However, the LCVR covered a retardance range of more than one wavelength which is sufficient for the application in the polarization-based imaging techniques 3D-PLI, DI and Müller polarimetry.

Spectral Filter Figure 4.4 shows the $I(V)$ and $\delta(V)$ curves for LCVR 1 for different spectral bandwidth. The maxima and minima of the three retardance voltage curves do not deviate considerably from each other. However, the intensity for FWHM $=$ 3 nm is so low that it suffers from a cut-off. High transmission is generally desirable for a better signal-to-noise-ratio and the use of lower exposure times. Therefore, the spectral filter FWHM $=$ 3 nm is not a good choice for the Scattering Polarimeter. On the other hand, while the unfiltered retardance voltage curve (FWHM $=$ 40 nm) reaches the highest maximum intensity, the minimum does not reach zero: Due to the wavelength deviation at the spectral borders, the light contains elliptical polarization that passes the second linear polarization filter. The intensity offset is not caused by residual light within the setup, or else the retardance voltage curve for FWHM $=$ 10 nm would show the same offset. The spectral filter with FWHM $=$ 10 nm is a good compromise between wavelength precision and high transmission.

Square Voltage Frequency The operating square voltage frequency f can be changed to avoid eventual cross-talk with other hardware components. Figure 4.5 exemplary shows the $I(V)$ and $\delta(V)$ curves for LCVR 1 for three different operating frequencies ($f = 2$ kHz, $f = 5$ kHz, $f = 10$ kHz). The curves deviate from each other but do not show a difference in quality, thus any chosen frequency is valid. All subsequent measurement employed the manufacturer's default setting of $f = 2$ kHz.

Spatial Homogeneity In Figure 4.4 and Figure 4.5, the standard deviation of the averaged intensity is visualized as error bars in Figure 4.5. The standard deviation remains at about 5 % of the mean intensity value over the measured voltage range, indicating a sufficient spatial homogeneity with no voltage-dependent fluctuations. Consequently, small local deviations are easily corrected with spatial calibration.

Overall, the measured curves are in accordance with the reference curves provided by the manufacturer (s. Appendix C, Figure C.1) within the expected small device-specific range of deviations. The $I(V)$ and $\delta(V)$ curves for the other LCVRs are presented in Appendix B.1 in Figure B.1–B.2.

4.5.2 Generation of Equidistant Polarization Angles

To replicate the mechanical rotation of a linear polarization filter for 3D-PLI and DI, the PSG needs to generate linear polarization at equidistant azimuthal steps ρ within the range of 180°. For this purpose, the voltage of LCVR 1 was varied while LCVR 2 operated as a quarter-wave plate, thus turning the elliptical polarization generated by LCVR 1 into linear polarization with an azimuthal angle ρ that is determined by the retardance δ_1 of LCVR 1. LCVR 3 and LCVR 4 were removed from the setup[8]. Then, ρ was measured in a crossed-polarizer configuration[9].

[8] Alternatively, they could have been set to $\delta_3 = \delta_4 = 0$.

[9] A parallel-polarizer would have been possible as well, directly corresponding to Malus' law.

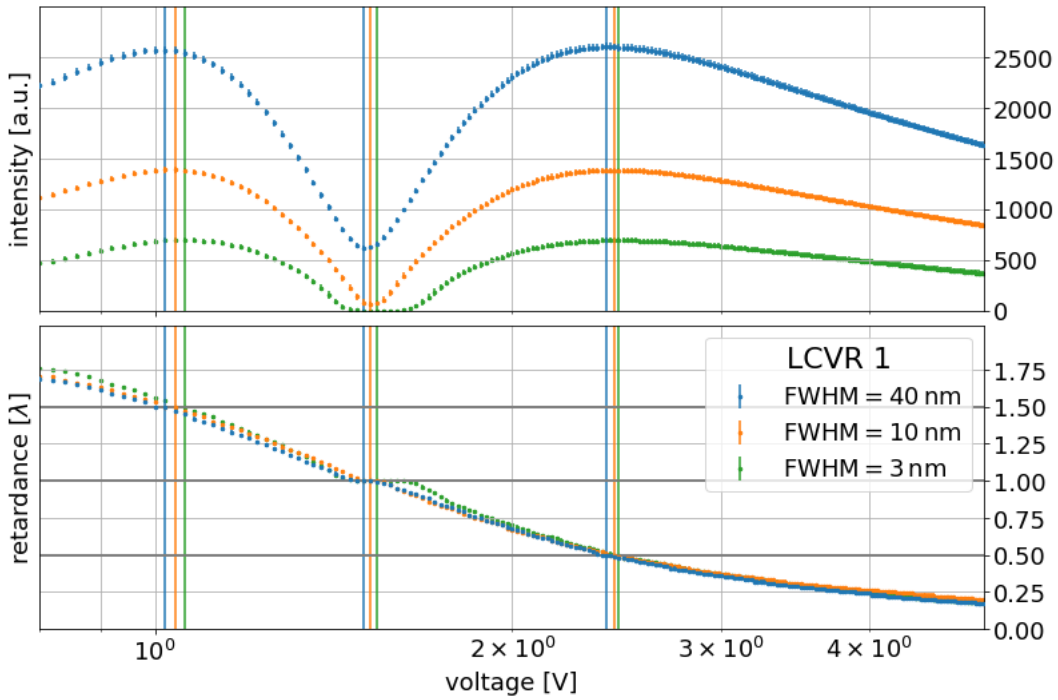

FIGURE 4.4: Bandwidth dependence of liquid crystal variable retarder 1 (LCVR 1). The curve was obtained from a crossed-polarizer configuration. The curve of the unfiltered light source spectrum (central wavelength $\lambda = 520\,\text{nm}$, FWHM $= 40\,\text{nm}$) is compared to two spectral filters of FWHM $= 10\,\text{nm}$ and FWHM $= 3\,\text{nm}$. Overall, the spectral filter with FWHM $= 10\,\text{nm}$ is a good compromise between wavelength precision and high intensity transmission.

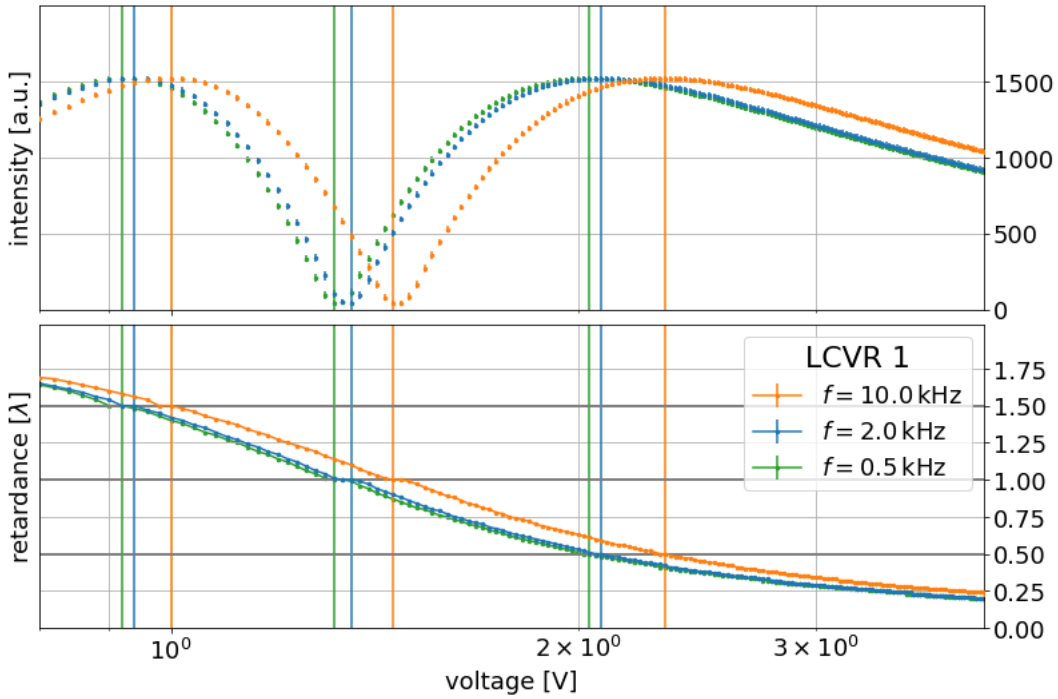

FIGURE 4.5: Frequency-dependence of LCVR 1. The curve was obtained from a crossed-polarizer configuration. The operating square voltage frequency f can be changed to avoid eventual crosstalk with other hardware components. The curves deviate from each other but do not show a difference in quality, meaning that any choice of frequency is valid.

Mathematical Derivation Jones calculus yields for parallel polarizers

$$\vec{J}(\delta) = M_{\mathrm{LP}}(\theta = 90°) \cdot M_2(\theta = 0°, \delta = \frac{\pi}{2}) \cdot M_1(\theta = 45°, \delta = \delta_1) \cdot \vec{J}_H \tag{4.9}$$

$$= E_{x0} \begin{pmatrix} 1 & 0 \\ 0 & 0 \end{pmatrix} \begin{pmatrix} 1 & 0 \\ 0 & e^{i\delta_2} \end{pmatrix} e^{i\frac{\delta_1}{2}} \begin{pmatrix} \cos(\delta_1/2) & i\sin(\delta_1/2) \\ i\sin(\delta_1/2) & \cos(\delta_1/2) \end{pmatrix} \begin{pmatrix} 1 \\ 0 \end{pmatrix} \tag{4.10}$$

$$= E_{x0} e^{i\frac{\delta_1}{2}} \begin{pmatrix} \cos(\delta_1/2) \\ 0 \end{pmatrix} \tag{4.11}$$

The intensity is given by squared absolute value

$$I(\delta) = |E_x|^2 = I_0 \cos^2(\delta/2) \tag{4.12}$$

The transmitted intensity is equivalent to Malus' law in Eq. (2.17). Maxima and minima correspond to polarization angles of 0° or 90°, respectively. The retardance voltage curve $\delta(V)$ of the whole system can be calculated from the normalized intensities using Eq. (4.8), again taking phase-unwrapping into account. The first measured polarization angle in 3D-PLI measurements is arbitrary as long as a range of 180° is covered and the starting angle is considered for the relative fiber directions.

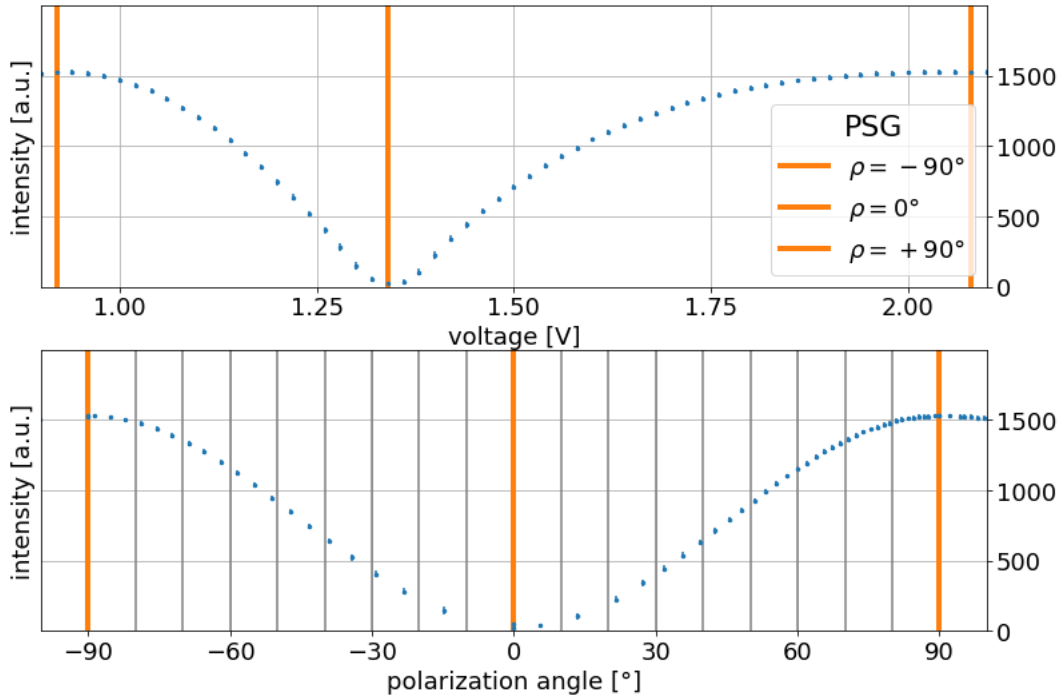

FIGURE 4.6: Generation of equidistant polarization angles. ρ was determined in a parallel-polarizer configuration. The PSG covers a range of more than 180° with linear polarization angles ρ. Maxima and minima correspond to polarization angles of 0° or 90°, respectively. Angular steps of $\Delta\rho = 10°$ are indicated by gray lines.

Measurement with the Scattering Polarimeter The curve in Figure 4.6 was sampled in steps of 0.02 V from 0.8 V to 4.0 V at an exposure time of 2 seconds. Every image was recorded four times for averaging. Angular steps of $\Delta\rho = 10°$ were chosen as the default (corresponding to the typical step size in 3D-PLI, s. Section 3.2) with the first angle (i.e. the lowest voltage) at $\rho = -90°$ relative to the coordinate system of the system, yielding a set of non-equidistant set of 18 voltages for LCVR 1.

4.5.3 LCVR Settings for All Modalities

The output polarization state of the PSG is determined only by the retardances of the two LCVRs, δ_1 and δ_2, and their azimuthal orientation (45° and 0°, respectively).

Mathematical Derivation With the matrices for various optical elements from Table 2.2 and the in-going Stokes vector of horizontal linear polarization (already comprising the first linear polarization filter), the Stokes vector of the output polarization state is given by Müller calculus

$$\begin{pmatrix} S_0 \\ S_1 \\ S_2 \\ S_3 \end{pmatrix} = \begin{pmatrix} 1 & 0 & 0 & 0 \\ 0 & 1 & 0 & 0 \\ 0 & 0 & \cos(\delta_2) & \sin(\delta_2) \\ 0 & 0 & -\sin(\delta_2) & \cos(\delta_2) \end{pmatrix} \begin{pmatrix} 1 & 0 & 0 & 0 \\ 0 & \cos(\delta_1) & 0 & -\sin(\delta_1) \\ 0 & 0 & 1 & 0 \\ 0 & \sin(\delta_1) & 0 & \cos(\delta_1) \end{pmatrix} \begin{pmatrix} 1 \\ 1 \\ 0 \\ 0 \end{pmatrix} \tag{4.13}$$

$$= \begin{pmatrix} 1 \\ \cos(\delta_1) \\ \sin(\delta_1)\sin(\delta_2) \\ \sin(\delta_1)\cos(\delta_2) \end{pmatrix} = \begin{pmatrix} 1 \\ H-V \\ D-A \\ R-L \end{pmatrix} \tag{4.14}$$

with δ_1 being the retardance of LCVR 1 and δ_2 being the retardance of LCVR 2. The six basic polarization states $\vec{S}_\mathrm{H}$, $\vec{S}_\mathrm{V}$, $\vec{S}_\mathrm{D}$, $\vec{S}_\mathrm{A}$, $\vec{S}_\mathrm{R}$ and $\vec{S}_\mathrm{L}$ can be achieved by choosing δ_1 and δ_2 so that the product of the $\sin(\delta_i)$ and $\cos(\delta_i)$ functions yield ± 1 or 0. In some cases, multiple combinations lead to the desired polarization state.

TABLE 4.1: Liquid Crystal Variable Retarder (LCVR) settings. The settings for all basic polarization states are given both as a retardance δ_i and as a fraction of the wavelength λ (QWP = quarter-wave plate, HWP = half-wave plate). Other combinations are possible. The PSG and PSA mirror each other and can be combined into 36 different setting combinations for Müller polarimetry.

PSG	LCVR 1	LCVR 2	LCVR 3	LCVR 4	PSA
H	2π λ	$\frac{3\pi}{2}$ -QWP	$\frac{3\pi}{2}$ +QWP	2π λ	H
V	π HWP	$\frac{3\pi}{2}$ -QWP	$\frac{3\pi}{2}$ -QWP	π HWP	V
D	$\frac{3\pi}{2}$ -QWP	$\frac{3\pi}{2}$ -QWP	$\frac{3\pi}{2}$ -QWP	$\frac{3\pi}{2}$ -QWP	D
A	$\frac{\pi}{2}$ +QWP	$\frac{3\pi}{2}$ -QWP	$\frac{3\pi}{2}$ -QWP	$\frac{\pi}{2}$ +QWP	A
R	$\frac{3\pi}{2}$ -QWP	2π λ	2π λ	$\frac{3\pi}{2}$ -QWP	R
L	$\frac{3\pi}{2}$ -QWP	2π λ	2π λ	$\frac{3\pi}{2}$ -QWP	L

Table 4.1 shows how to achieve each basic polarization state in terms of the LCVR settings, written both as a retardance δ_i and as a fraction of the wavelength λ (QWP = quarter-wave plate, HWP = half-wave plate). The PSG and PSA mirror each other and can be combined into 36 different setting combinations for Müller polarimetry. True zero cannot be achieved as discussed in Section 4.2.4, therefore a retardance of one wavelength λ is denoted with a retardance of 2π. Retardance values of 0, π and $\pm\frac{\pi}{2}$ for each LCVR can be determined from the retardance voltage curves.

In ComSLI, LCVR 1 and LCVR 2 are bypassed by the oblique light incidence. LCVR 3 and LCVR 4 are set to a retardance of $\delta_3 = \delta_4 = 0$ to exclude any possible polarization dependency of the scattered light. However, the investigation of such a dependency is theoretically possible with different settings.

4.6 Future Hardware Upgrades

The Scattering Polarimeter has successfully advanced from the prototypical stage to a fully operational multi-modal device. The novel device integrates oblique illumination for ComSLI and vertical illumination for 3D-PLI, DI, and Müller polarimetry into a single, multi-modal system that has maintained the flexibility to realize illumination with different wavelengths or the use of other polarization states. In the following, the hardware performance of the Scattering Polarimeter is discussed in detail and the potential for high-speed multi-modal scattering polarimetry is evaluated. Suggestions for further improvements are also outlined.

4.6.1 Light Source

An LED panel serves as the large-area light source, suitable for both vertical and oblique illumination. Since the coherence of the light source is irrelevant to the measurement, using an LED panel has proven effective. However, the transmitted light intensity is reduced by the four LCVRs, the two polarization filters, and the spectral filter, all of which are crucial to the device. Therefore, implementing a brighter LED panel is strongly recommended. So far, no upper limit for illumination brightness has been identified for the four modalities, so the brightest available LED panel can be used, possibly combined with a cooling system to prevent undesired wavelength fluctuations of the LEDs due to overheating. A bright light source combined with a high-sensitivity camera can also shorten the exposure times and improve the signal-to-noise ratio.

Furthermore, a custom light source can be built, mainly to benefit the ComSLI measurement. In the current setup, the PSG elements block the oblique light path for LEDs in the center of the panel, affecting not only the covered LEDs but also those in the "dead angle" of the PSG stack. Ideally, the LCVR mounts would be smaller in diameter while maintaining their aperture size. Integrating the PSG into the light source to create a flat top surface would serve ComSLI measurements, particularly in context of scatterometry illumination. This adjustment would also solve the issue of the LCVR cables obstructing the light source. Angular ComSLI measurements are not visibly influenced by the LCVR cables due to the large illumination segment size compared to the very thin cable diameter (about 1 mm), but scatterometry and compressed sensing ComSLI might encounter issues. The construction of a custom light source can be considered in future versions of the Scattering Polarimeter.

4.6.2 Camera

Camera and objective lens were optimized for the limiting apertures of the LCVRs, and in fact, no vignetting was observed. Therefore, the objective lens and camera can be deemed suitable in geometrical terms. The camera captures a field of view of $8\times5\,\mathrm{mm}^2$ and an optical resolution of $2.2\times2.2\,\mu\mathrm{m}^2$ which enables the visualization of intricate fiber structures. The resolution and field of view are in the same size order as for the ComSLI setup, the LMP3D, and the LMP1 (with minor device-specific differences). A high-sensitivity camera, e.g. the Vistek camera shown in Section 7.2, can improve the signal-to-noise ratio for tissue regions with a lower signal.

For convenience, the mechanical stability of the camera can be improved by implementing a micro-meter screw to vary the camera height with micrometer precision. Currently, using the focus screw on the side of the camera tends to rotate the lens tube which changes the imaging area and can even require a new spatial calibration measurement. Instead, a micrometer screw for adjusting the camera height with micrometer precision without touching the camera tube itself is recommended. This improvement is easily realizable.

4.6.3 XY Stage

The current camera resolution is comparable to other single-mode setups, but the imaging area is relatively small considering that automatic scanning is not possible yet. Using a different objective lens is not recommended due to potential vignetting from optical apertures. Integrating an XY scanning stage would allow the scanning of whole brain tissue samples. The design of the scanning stage as presented in Section 7.3 is compatible with the Scattering Polarimeter even though the size of the shielding box needs to be expanded to accommodate the rails.

4.6.4 LCVRs

The LCVRs cover a range of more than one wavelength for green light at 520 nm and show a good spatial homogeneity. If needed, the LCVRs can be azimuthally adjusted within their rotation mounts, e.g. to employ elliptical polarization states for an optimal signal-to-noise ratio in Müller polarimetry as illustrated in Section 3.4.2. Furthermore, the LCVRs can operate across the full visible spectrum even though only green light has been investigated so far. This flexibility allows for wavelength-dependent birefringence measurements with red or blue light.

The aperture of the LCVRs, despite being the largest commercially available, would ideally be even larger to yield a larger field of view and reduce the risk of accidental vignetting due to minor misalignment. However, previous experiments with custom large-area LCVRs have shown issues with spatial homogeneity [75], therefore a suitable large-are LCVR should be of very high quality.

4.6.5 Software

The developed software measures all four modalities sequentially, with the option to only measure some of them. However, data processing during the measurement is not yet optimized. Currently, the camera waits for the images to be saved before taking the next image, a process that could be parallelized which would decrease measurement time. For convenience, a graphical user interface with a live viewer could be developed based on the measurement software.

Chapter 5

Single-Mode Performance

The Scattering Polarimeter can perform **Müller polarimetry, three-dimensional polarized light imaging, diattenuation imaging, and computational scattered light imaging within a multi-modal measurement**. In the following, the performance across all modalities is investigated qualitatively and quantitatively by measuring a set of representative samples, i.e. well-known optical elements and tissue samples with characteristic fiber structures. Reference measurements and mathematical considerations provide a deep understanding of the device features from both a mathematical and an experimental perspective.

Error propagation caused by imperfect optical components in the device is investigated using Müller calculus. Custom **error correction and signal processing** routines are developed to improve the signal, depending on the unique properties of the setup. Where applicable, the measured parameter maps are compared with **literature values** and **reference measurements** obtained with the single-mode setups introduced in Section 3.6. The **unique strengths and limitations of each modality** of the Scattering Polarimeter are discussed, providing a quantitative and qualitative evaluation of the performance for each modality.

5.1 Investigated Samples

A quantitative performance evaluation requires samples with well-known optical properties. The simplest way to evaluate the setup is with an empty measurement because air does not affect the polarization properties of light[1]. However, high-quality optical elements, such as polarization filters, quarter-wave plates, and diffuser plates, are commercially available and their optical properties are typically provided by the manufacturer. These components are generally assumed to be spatially homogeneous and maintain their optical properties over time (in contrast to biological tissue), making them suitable for the Eigenvalue Calibration Method (ECM) in Müller polarimetry.

Qualitatively, the measurement of well-characterized tissue samples provides deeper insights into the complex interplay of retardation, attenuation, and depolarization, thereby illustrating the strengths and limitations of the Scattering Polarimeter in various fiber architectures and tissue compositions. Given the optical properties of tissue samples can change over time, up-to-date comparative measurements for each modality with the available single-mode setups introduced in Section 3.6 are crucial.

[1] For the low intensities and visible wavelengths in the given context.

5.1.1 Optical Elements

The flexible polarization filter film *Edmund Optics XP38* [50] has a thickness of 0.19 mm and an extinction ratio of up to up to 7500:1 for visible light according to the manufacturer. The transmission axis of the square-shaped polarization filter is indicated by a notch. Furthermore, a birefringent polymer plate *Newport 10RP34-532* [134] achieves a retardance close to a quarter-wave plate (QWP): The central wavelength where the birefringent plate introduces a phaseshift of a quarter wave is at 532 nm. The retardance for 520 nm (which is 98% of 532 nm) is 0.255 instead of 0.25, as shown in Appendix C.4. However, for the ECM, the birefringent element can deviate from an exact QWP as explained in Section 2.2.

5.1.2 Brain Tissue

The investigated human and animal brain tissue samples contain gray and white matter, distinct anatomical regions with characteristic fiber structures (in-plane parallel fibers, out-of-plane fibers, crossing fibers, as described in Section 2.3.1, but also artifacts such as crystallization of the embedding medium and bubbles within the medium. All samples were cryo-sectioned as described in Section 3.1. For improved readability, the samples are referenced as follows:

Broca *Broca* is a 50 µm sagittal section (s454) from the human brain (female, 80 years, no neurological diseases) that includes the *Broca's region* with areas of gray and white matter. Broca's region is associated with language production and articulation [208], but the fiber architecture of the Broca's region is not well understood yet [6]. The section was embedded in 2023 (less than a year old at the time of measurement), making it very new compared to the other samples. There are no crystallization artifacts. The transmittance is comparatively low while the scattering is high. *Broca-A*, *Broca-B*, and *Broca-C* refer to different regions within the sample, all containing white and gray matter. Broca-A also contains a small area without tissue.

Vervet1818 *Vervet1818* is a 60 µm coronal section (s506) from the center of a vervet monkey brain (monkey 1818, male, 2.4 years old, no neurological diseases). Most noticeably, the sample contains the corona radiata, the fornix, the cingulum and the corpus callosum, but also gray matter in the cortex. The section was embedded in 2012 (i.e. 12 years ago) and the embedding medium has started to crystallize at the tissue borders. Compared to more recently embedded samples, the transmittance is higher. Vervet1818 contains a variety of representative fiber configurations in close proximity that fit well in the field of view of the Scattering Polarimeter. Three regions were measured: *Vervet1818-CC* contains the corpus callosum (in-plane fibers) and the cingulum (nearly orthogonal fiber bundles). *Vervet1818-CR* shows the border region between corona radiata (crossing fibers) and corpus callosum (in-plane fibers). *Vervet1818-FX* contains the fornix (inclined fibers), a part of the corpus callosum, and an area without tissue. Section 2.3.2 discusses the applications of animal models in neuroimaging.

ChiasmX2 *ChiasmX2-7* and *ChiasmX2-15* are artificially assembled fiber crossings. The samples were previously measured by MENZEL ET AL. [119, 120] to investigate fiber crossing with 3D-PLI and ComSLI. To examine fibers at a well-defined crossing angle, two optic tracts of a 30 µm thin section of a human optic chiasm were overlaid, with a crossing angle of approximately $\chi = 90°$ for ChiasmX2-15 and an angle of

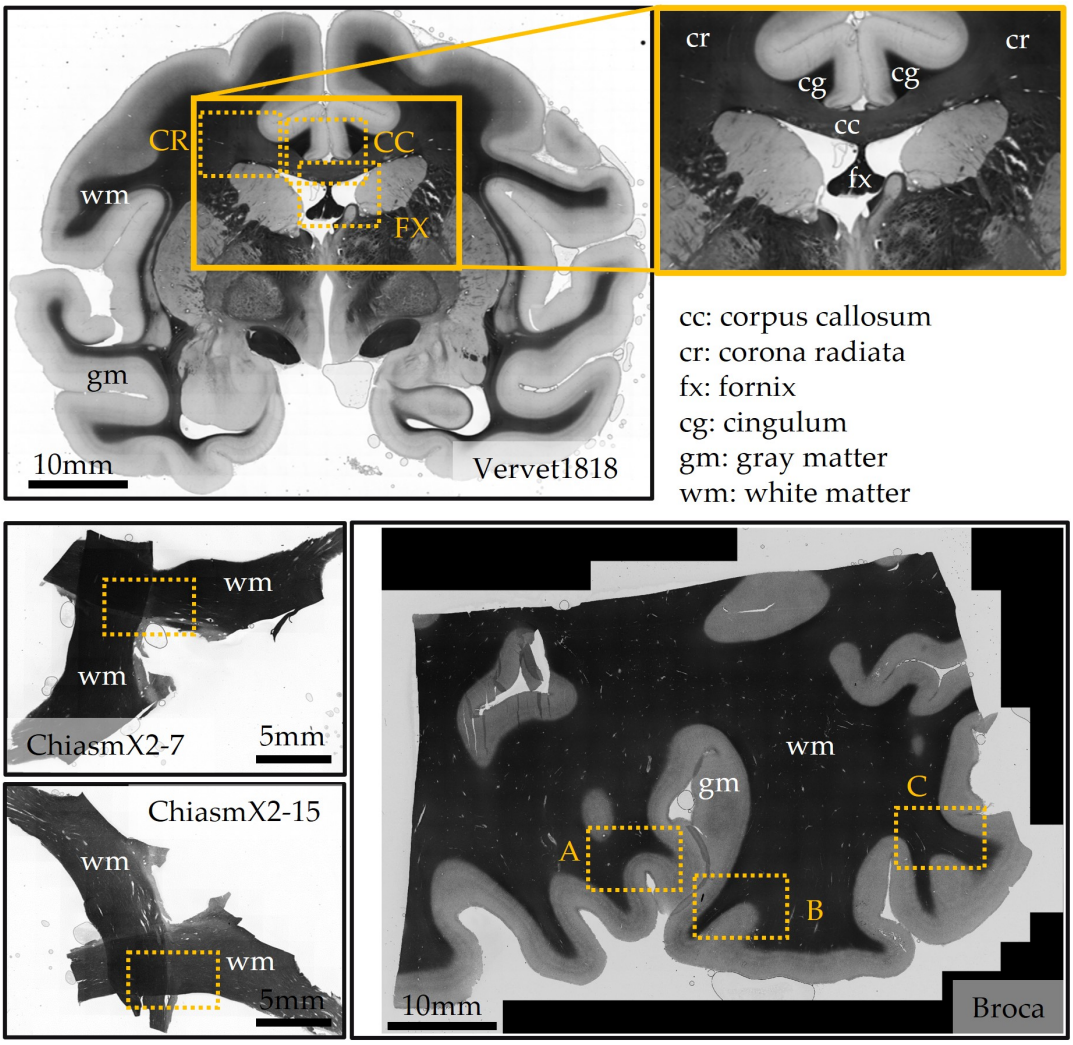

FIGURE 5.1: Overview of brain tissue samples. *Vervet1818* is a 60 µm coronal section (s506) from the center of a vervet monkey brain. *ChiasmX2-7* and *ChiasmX2-15* are artificially assembled fiber crossings. *Broca* is a 50 µm sagittal section (s454) from the human brain that includes the Broca's region. The investigated regions are indicated in the overview images that are based on transmittance maps obtained with the LMP1 (ChiasmX2-7, ChiasmX2-15, Vervet1818) and the LMP3D (Broca). White matter appears darker than gray matter.

approximately $\chi = 60°$ for ChiasmX2-7. The crossing angle can be seen in Figure 5.1. Optic tracts contain mainly parallel white matter fibers with well-defined orientations. The sample was embedded in a solution of 20% glycerin and cover-slipped in 2019 (5 years ago). Within the context of this thesis, the samples are referred to as ChiasmX2-7 and ChiasmX2-15[2], corresponding to the labels on the specimen slides. Both samples also contain areas without tissue.

Figure 5.1 gives an overview of the samples based on 3D-PLI transmittance maps that were obtained with the LMP1 (ChiasmX2-7, ChiasmX2-15, Vervet1818) and the LMP3D (Broca). White matter appears darker than gray matter in the transmittance maps. The investigated regions are indicated with orange squares.

[2]However, ChiasmX2-15 is influenced by artifacts that show up especially in the 3D-PLI and DI transmittance maps. The stripe-shaped effects are possibly caused by scratches or a contamination of the object carrier.

5.1.3 Measurement Parameters

The exposure times for polarimetric measurements and scattering-based measurements had to be short enough to avoid overexposure and keep the overall measurement time as short as possible. Scattering at artifacts can lead to overexposure for short exposure times; however, this effect was not taken into account. On the other hand, the exposure time needed to be sufficiently long for a good signal-to-noise-ratio. The exposure times for polarimetric measurements was chosen to be 2 seconds, the exposure time for scattering-based measurements was 4 seconds. No gain was used because doing so would have also amplified the noise. Only the green camera channel was evaluated. All images were measured four times and averaged.

For ComSLI, green illumination patterns with 15° angular steps (i.e. 24 measurement angles), a segment width of 12°, an inner radius of 50 LEDs, and an outer radius of 90 LEDs were used. This illumination sequence has comparatively large illumination segments for maximum brightness while maintaining a sufficiently precise angular discretization.

5.2 3D-PLI

The Scattering Polarimeter realizes a 3D-PLI measurement by generating linear polarization with equidistant polarization angles ρ. During the 3D-PLI measurement, the polarization state analyzer (PSA) operates as a circular analyzer, i.e. a quarter-wave plate (QWP) plus a linear polarization filter. Each image pixel yields a sinusoidal intensity curve $I(\rho)$, which is evaluated using the Fourier coefficient fit method introduced in Section 3.2. The *Large Area Polarimeter (LAP)*, the *LMP1* and the *LMP3D* as introduced in Section 3.6 employ steps of $\Delta\rho = 10°$ or $\Delta\rho = 20°$, respectively, and a left-handed circular analyzer.

Generally, the Scattering Polarimeter can operate with larger or smaller $\Delta\rho$ and a right-handed circular analyzer. The various options are only determined by the retardance settings of the liquid crystal variable retarders (LCVRs). This flexibility allows the investigation of alternative settings for high-speed and high-quality measurements with the Scattering Polarimeter.

However, LCVRs typically introduce more systematic errors compared to specialized rotating optic elements which can be modeled and understood using Müller calculus and Taylor approximations. Accordingly, custom correction methods and filtering routines are investigated in the following. Reference measurements conducted with the LMP3D and LMP1 are compared with the Scattering Polarimeter measurements. Section 5.6 summarizes the overall performance of 3D-PLI in context with the other three modalities.

Within the following, color-coded direction maps show the in-plane fiber direction. If not indicated otherwise, the fiber inclination is shown as a separate map. This simplifies the visual comparison of fiber directions in regions with low retardation when judging the performance, i.e. for inclined fibers or in gray matter.

5.2.1 Fourier Coefficient Fit

Section 3.2 introduced the Fourier fit routine in 3D-PLI. The Fourier coefficients a_0, a_2 and b_2 were calculated for every single image pixel. To uncover statistical and

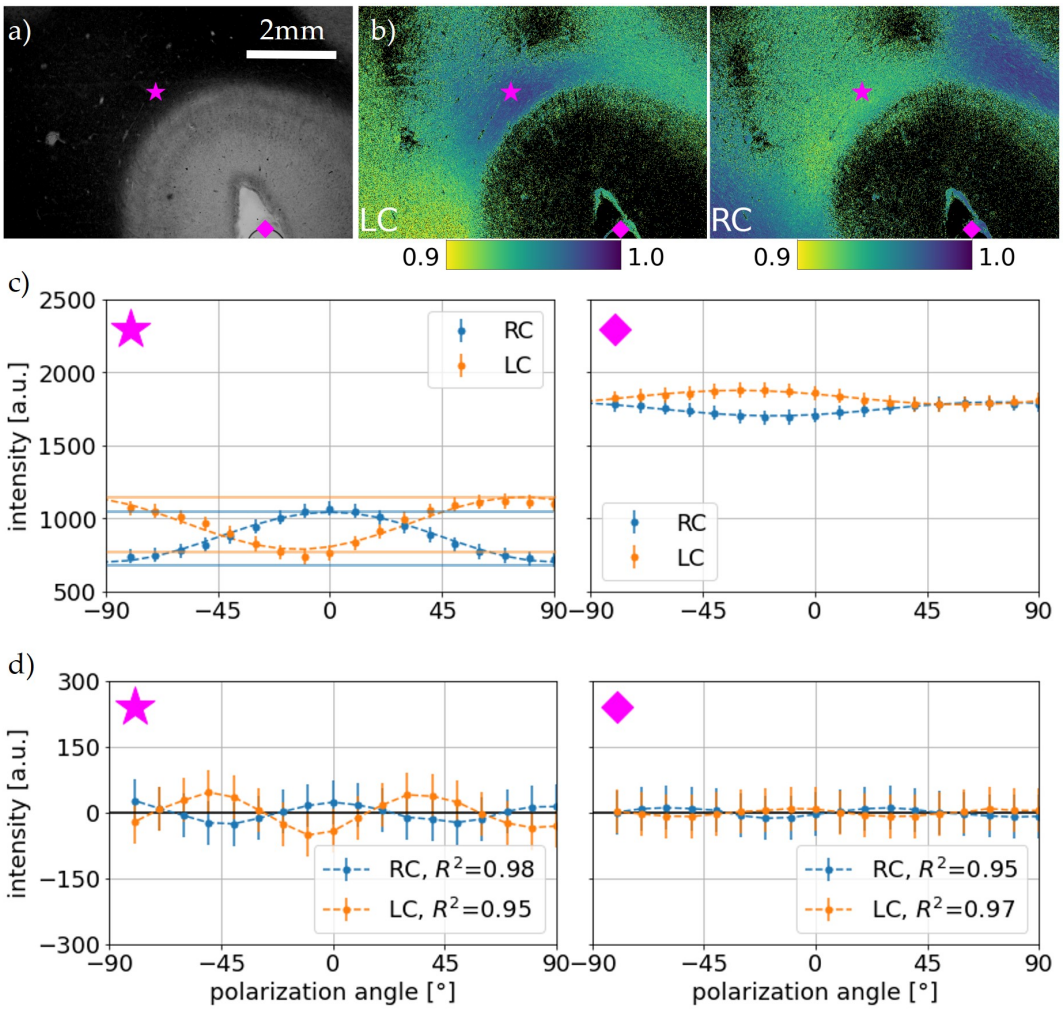

FIGURE 5.2: 3D-PLI: Pixelwise Fourier coefficient fit. The fit is shown for the left-circular (LC) and right-circular (RC) analyzer setting a) Transmittance map for Broca-A with exemplary white matter area (magenta star) and background (magenta diamond) indicated. b) Pixelwise coefficient of determination R^2 for LC and RC. The closer R^2 to 1, the more successful the fit. c) The Fourier coefficient fit yields sinusoidal curves for LC and RC. Horizontal lines mark the maximum and minimum intensity for both curves. d) The residuals indicate a systematic error.

systematic errors within the setup, image pixels from two characteristic regions in Broca-A were investigated in detail.

Exemplary Intensity Curve Figure 5.2a shows the transmittance map for Broca-A with two locations marked: one in white matter (magenta star), where a sinusoidal curve with high retardation (i.e. large amplitude) but comparatively low transmittance is expected. Reference measurements indicated parallel fibers in the chosen white matter area. The phase of the sinusoidal curve depends on the fiber direction but also on the circular analyzer setting. The right-handed circular analyzer (RC) setting results in a 90° shift compared to the left-handed circular analyzer (LC). This shift must be accounted for in the correct mathematical evaluation of fiber directions but has no other consequences. Furthermore, a region without tissue (magenta diamond) was investigated, accordingly with high transmittance and only statistical noise, both due to the absence of birefringent tissue.

Figure 5.2c displays the raw intensities averaged over 20×20 image pixels, thus limiting the impact of single pixel artifacts, blood vessels, or crystals within the embedding medium. The statistical error σ_I=17 a.u. was estimated from the average standard deviation of 4 raw images. The sinusoidal curve is displayed for the right-circular (RC, blue) and left-circular (LC, orange) setting. A dashed line indicates the fitted sinusoidal curve. Figure 5.2d shows the corresponding residuals. The coefficient of determination R^2 (a statistical quantity, not to be confused with the retardance R) indicates the fit quality for each image pixel

$$R^2 = 1 - \frac{\sum(y_i - f_i)^2}{\sum(y_i - \bar{y})^2} \in [0, 1] \tag{5.1}$$

where y_i represents the measured data points (here, intensity in arbitrary units), f_i the fitted data, and $\bar{y}$ the mean value of the measured data. The closer R^2 is to 1, the better the fit quality typically is. Figure 5.2b displays $R^2 \geq 0.9$ for each image pixel, both for LC and RC. $R^2 < 0.9$ is displayed in black and mostly coincides with the background area and gray matter (areas with few or no birefringent fibers). Appendix B.2 shows corresponding results for Vervet1818-FX in Figure B.3.

5.2.2 Influence of Systematic Errors

With a coefficient of determination R^2 close to 1, the Fourier coefficient fit can generally be considered successful, especially for white matter areas. However, Müller matrix calculus provides further insight into the observed systematic errors.

Transmittance Asymmetry The mean amplitude (i.e. transmittance) differs slightly between RC and LC, indicating a polarization dependency of transmittance. This phenomenon is not based on any physical tissue properties (as confirmed by the reference measurements in Section 5.2.7) but caused by minor ellipticities within the Scattering Polarimeter, i.e. unintended elliptical deviations from the ideal circular or linear polarization.

A non-ideal PSG deviates from the ideal values for δ_1 and δ_2, usually because of a minor voltage offset for LCVR 1 and LCVR 2. While a deviation from δ_1 only results in a global phase shift, a deviation of δ_2 causes elliptical polarization that propagates through the whole system. When $(\delta_2 - \pi/2) = h_2 \approx 0$, a Taylor approximation to the 1st order describes the Stokes vector $\vec{S}_{\text{real}}$ as a sum of the ideal vector $\vec{S}_{\text{PSG}}$ and a deviation $\vec{S}_{h2}$ caused by LCVR 2

$$\vec{S}_{\text{real}} = \begin{pmatrix} 1 \\ \cos\delta_1 \\ \sin\delta_1 \sin\delta_2 \\ \sin\delta_1 \cos\delta_2 \end{pmatrix} \approx \begin{pmatrix} 1 \\ \cos\delta_1 \\ \sin\delta_1 \\ 0 \end{pmatrix} - \begin{pmatrix} 0 \\ 0 \\ 0 \\ h_2 \sin\delta_1 \end{pmatrix} = \vec{S}_{\text{PSG}} + \vec{S}_{h2} \tag{5.2}$$

The ideal Stokes vector $\vec{S}_{\text{PSG}}$ for the PSG is derived in Appendix A.2.1. The non-ideal Stokes vector $\vec{S}_{\text{PLI}'}$ of the 3D-PLI signal can be calculated from Müller matrix multiplication using M_{tissue} as established in Section 2.3.3. The Müller matrix M_{PSA} for an ideal PSA is calculated in Appendix A.2.3. The measured 3D-PLI intensity $I_{\text{PLI}'}$ for a non-ideal PSG and ideal PSA is given by the first element of the Stokes vector

$$I_{\text{PLI}'} = \frac{1}{2}\left(1 \pm \sin\delta \sin(\delta_1 - 2\phi)\right) \pm \frac{h_2}{2} \cos\delta \sin(\delta_1) \tag{5.3}$$

The detailed derivation is shown in Appendix A.3.2. The first term corresponds to the ideal 3D-PLI signal. The second term is an offset that depends on the local fiber retardance δ, the setting of LCVR 1 δ_1, and the setting of the PSA, based on the sign, but not on the fiber direction ϕ. This matches the observation that the transmittance and retardance show an asymmetry that is inverted for LC and RC but the fiber direction is not influenced. Therefore, the transmittance asymmetry is most likely caused by a small offset of LCVR 2. Furthermore, the intensity profile for background pixels shows not only statistical noise but a sinusoidal curve, likely caused by the same asymmetry within the Scattering Polarimeter. An appropriate retardation correction (as discussed in Section 5.2.3) can partially compensate this effect and lead to anatomically correct results.

Higher Frequency Signal The residuals indicate a systematic error in the shape of a higher-frequency sinusoidal curve. This systematic error is relatively small compared to the maximum amplitude of the signal in white matter and even smaller for the background signal, suggesting that the higher-frequency curve either originates from the tissue itself or is enhanced through interaction with the tissue.

Müller calculus shows that the effect is likely caused by non-ideal deviations in the PSA. A non-ideal PSA can deviate from the ideal values for δ_3 and δ_4, usually because of a minor voltage offset for LCVR 3 and LCVR 4. When $(\delta_4 - \pi/2) = h_4$ and $(\delta_3 - \pi/2) = h_3$, a Taylor approximation to the 1st order describes the non-ideal PSA via M_{real} as a sum of two Müller matrices, one for the ideal PSA M_{PSA} and one for a deviation $M_{h3,h4}$ caused by LCVR 3 and LCVR 4. The non-ideal Stokes vector $\vec{S}_{\text{PLI}'}$ of the 3D-PLI signal can be calculated from Müller matrix multiplication using M_{tissue} as established in Section 2.3.3 for an ideal PSG and a non-ideal PSA. Here, the abbreviation $v_\phi = \sin 2\phi$, $w_\phi = \cos 2\phi$ is used

$$\vec{S}_{\text{PLI}'} = (M_{\text{PSA}} + M_{h3,h4}) \cdot M_{\text{tissue}} \cdot \vec{S}_{\text{PSG}} \tag{5.4}$$

$$= \vec{S}_{\text{PLI}} \mp \frac{h_4}{2} \begin{pmatrix} \cos\delta_1 w_\phi^2 + v_\phi^2 \cos\delta + w_\phi v_\phi (1-\cos\delta)\sin\delta_1 \\ \cos\delta_1 w_\phi^2 + v_\phi^2 \cos\delta + w_\phi v_\phi (1-\cos\delta)\sin\delta_1 \\ 0 \\ 0 \end{pmatrix} \tag{5.5}$$

$$+ \frac{h_3}{2} \begin{pmatrix} w_\phi v_\phi (1-\cos\delta)\cos\delta_1 + v_\phi^2 + w_\phi^2 \cos\delta \sin\delta_1 \\ w_\phi v_\phi (1-\cos\delta)\cos\delta_1 + v_\phi^2 + w_\phi^2 \cos\delta \sin\delta_1 \\ 0 \\ 0 \end{pmatrix} \tag{5.6}$$

$$= \vec{S}_{\text{PLI}} + \vec{S}_{\text{LCVR3}}(\phi, \delta, \delta_1) + \vec{S}_{\text{LCVR4}}(\phi, \delta, \delta_1) \tag{5.7}$$

The detailed derivation is shown in Appendix A.3.3. The measured 3D-PLI intensity $I_{\text{PLI}'}$ is given by the first element of the Stokes vector: The ideal 3D-PLI intensity curve is modulated by two functions with amplitudes h_3 and h_4 that depend on the fiber retardance δ, the retardance of LCVR 1 δ_1, and fiber direction ϕ

$$I_{\text{PLI}'} = \frac{1}{2}\left(1 \pm \sin\delta \sin(\delta_1 - 2\phi)\right) \tag{5.8}$$

$$\mp \frac{h_4}{2}\left(\cos\delta_1 w_\phi^2 + v_\phi^2 \cos\delta + w_\phi v_\phi (1-\cos\delta)\sin\delta_1\right) \tag{5.9}$$

$$\pm \frac{h_3}{2}\left(w_\phi v_\phi (1-\cos\delta)\cos\delta_1 + v_\phi^2 + w_\phi^2 \cos\delta \sin\delta_1\right) \tag{5.10}$$

With $v_\phi^2 = \sin^2 2\phi = \frac{1}{2}(1 - \cos 4\phi)$ and $w_\phi^2 = \cos^2 2\phi = \frac{1}{2}(1 + \cos 4\phi)$, a higher-order frequency is introduced into the signal that depends on the fiber direction.

Even though the offset is minor, it is important to be aware of the effect. Figure B.4 in Appendix B.2 depicts how a higher frequency signal influences tissue with the same transmittance but a different retardation. For a high retardation (i.e. in-plane parallel fibers), deviations from the ideal sinusoidal curve are minor. However, in case of a low retardation (i.e. out-of-plane parallel fibers), the curve is strongly distorted. In the schematic depiction, the magnitude of the higher frequency signal is strongly exaggerated compared to the real measurements. It is important to be aware that fibers with a strong inclination can be affected by this phenomenon.

Prevention and Correction of Systematic Errors In subsequent analyses, systematic errors do not significantly affect the evaluation of strong fiber signals, such as those in white matter. However, they may interfere with weak signals, hindering evaluation of the low density fibers in gray matter, and possibly of strongly inclined fibers. Compensating for unwanted ellipticities with a dedicated calibration method (like the ECM in Müller polarimetry) is not feasible[3]: Even if the matrices A and W are obtained for PSA and PSG[4], an analytical correction of the sinusoidal signal with the matrix coefficients is inherently not possible. The complex dependencies of the 3D-PLI intensity curve from non-ideal Müller matrix coefficients cannot be solved without previous knowledge of the fiber parameters. The calculation is provided in Appendix A.5.

Therefore, it is crucial to determine the voltage settings as precisely as possible for 3D-PLI to minimize non-ideal effects, and to carefully align the optical components. The azimuthal orientation significantly influences the resulting polarization, but also vertical misalignment (i.e. a rotation away from the horizontal plane) of optical elements can cause polarization shifts. Therefore, precise alignment of LCVRs and linear polarization filters parallel to the light source is of great importance.

5.2.3 Retardation Correction

AXER ET AL. [15] suggested normalization of the retardation with its maximum value $|\sin(\delta)|_{\alpha=0^\circ}$ which is found for in-plane, parallel fibers to obtain correct fiber inclinations. Figure 5.3a shows the retardation $|\sin(\delta)|_{\text{raw}}$ obtained directly from the Fourier coefficient fit for Broca-B and Vervet1818-FX. Reference measurements (s. Section5.2.7) indicated that Broca-B partially contains parallel in-plane fibers. In Vervet1818-FX, parallel in-plane fibers are located in the corpus callosum.

Figure 5.3b displays the impact of normalization on $|\sin(\delta)|_{\text{norm}}$. Now, in-plane parallel fibers have a retardation of $|\sin(\delta)|_{\text{norm}} = 1$, thus yielding an inclination of $\alpha_{\text{inc}} = 0^\circ$. This approach is sufficient for typical 3D-PLI samples such as Broca with a high contrast in the transmittance. However, the residual retardation, which is most visible in background areas, is also increased by normalization. As a result, signals are further distorted in regions without tissue and in gray matter. Thus, an alternative approach is suggested for correcting the retardation in low contrast samples such as Vervet1818.

[3] Spatial calibration to homogenize the field of view remains possible and is performed before all other evaluation steps.

[4] In principle, this is possible for the Scattering Polarimeter but not for a classical 3D-PLI setup that is typically an incomplete polarimeter.

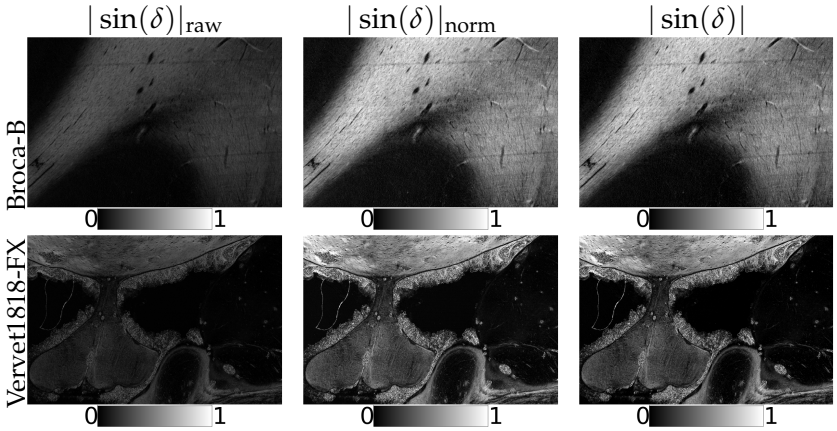

FIGURE 5.3: 3D-PLI: Retardation correction for the Scattering Polarimeter. First row: Broca-B, where reference measurements indicated areas with parallel in-plane fibers. Second row: Vervet1818-FX which contains parts of the corpus callosum, characterized by parallel in-plane fibers. First column: The measured retardation $|\sin(\delta)|_{raw}$. Second column: $|\sin(\delta)|_{raw}$ is normalized with the expected retardation of in-plane parallel fibers to $|\sin(\delta)|_{norm}$. Third column: Alternative retardation correction: Before the normalization, the background retardation is subtracted. The effect is best observed in the background for Vervet1818-FX. No visible changes occur for Broca, indicating that the original retardation correction in b) is already sufficient.

First, the residual retardation $|\sin(\delta)|_{min}$ is determined from an area without tissue. $|\sin(\delta)|_{min}$ is subtracted from the raw retardation $|\sin(\delta)|_{raw}$. Then, $|\sin(\delta)|_{max}$ is given by the (mean) retardation of pixels from, e.g. the corpus callosum. When the correction causes the retardation $|\sin(\delta)|$ to exceed the interval from 0 to 1 (which, due to statistical reasons, can happen for some pixels), $|\sin(\delta)|$ is automatically set to 0 or 1, respectively

$$|\sin(\delta)| = \frac{|\sin(\delta)|_{raw} - |\sin(\delta)|_{min}}{|\sin(\delta)|_{\alpha=0^\circ} - |\sin(\delta)|_{min}} \quad 0 \leq |\sin(\delta)| \leq 1 \tag{5.11}$$

Figure 5.3c presents the corrected retardation, using correction values of $|\sin(\delta)|_{min}$ =0.015 for Broca and Vervet1818, $|\sin(\delta)|_{\alpha=0^\circ}$ =0.4 for Broca and $|\sin(\delta)|_{\alpha=0^\circ}$ =0.45 for Vervet1818. The minor difference to Figure 5.3b is best observed in the background for Vervet1818-FX, but also in the fornix which appears slightly darker after the correction. No visible changes occur for Broca-B. $|\sin(\delta)|_{min}$ is constant among the different samples because the retardation for a region without tissue only depends on properties of the embedding medium and the object carrier, both of which are minor effects. The retardation correction yields parameter maps that agree with the reference measurements with the LMP3D (s. Figure 5.12), thus the correction is deemed successful and applied to all subsequent parameter maps.

5.2.4 Background Masking

For a typical 3D-PLI sample such as Broca, background areas are characterized by their relatively high intensity in the transmittance map because there is no attenuation by tissue. For Broca-A, the process of background identification and masking based on the transmittance map is illustrated in Figure 5.4. The first image presents the measured transmittance. In the second image, background pixels characterized by a transmittance $I_T > 4100$ a.u. are displayed in white, indicating the maximum light

transmission in background areas. The specific threshold value is influenced by measurement parameters such as exposure time and gain. The third image displays the measured fiber directions. The minor background retardation as discussed in Section 5.2.1 appears as falsely detected red/pink fiber directions in background areas. The fourth image shows the fiber directions with the background masked in black.

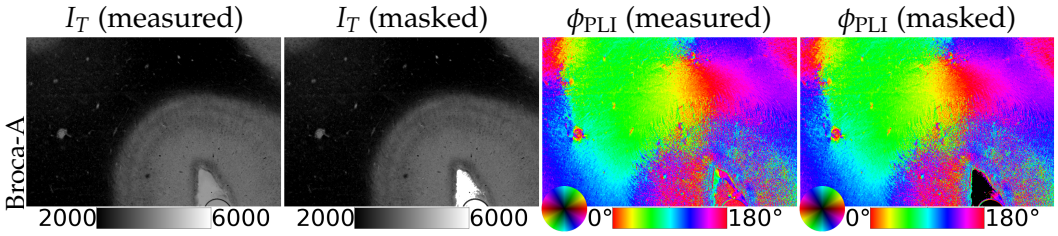

FIGURE 5.4: 3D-PLI: Background masking based on the transmittance. First column: The measured transmittance map for Broca-A. The transmittance is given in arbitrary units. Second column: All pixels with a a transmittance $I_T > 4100$ a.u. are identified as part of the background and displayed in white. Third column: The measured fiber directions for Broca-A. The residual retardation manifests as pink fiber directions in areas without tissue. Fourth column: The transmittance-based threshold is applied: Image pixels with a transmittance $I_T > 4500$ a.u. are displayed in black.

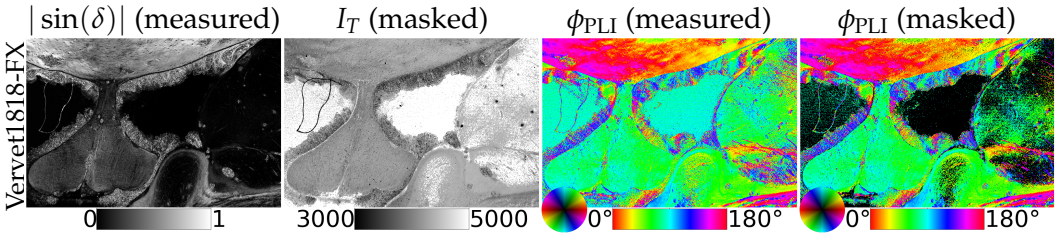

FIGURE 5.5: 3D-PLI: Background masking based on the retardation. In cases where the contrast in the transmittance map is insufficient, such as with older samples like Vervet1818, an alternative approach can be used for approximate background identification. First column: Retardation map for Vervet1818-FX. Areas with a retardation below a threshold $|\sin(\delta)| \leq 0.015$ are identified as part of the background. Second column: The transmittance [a.u.] map with a correspondingly masked background. Background pixels are displayed in white. Third column: The measured fiber directions for Vervet1818-FX. The residual retardation manifests as blue/green fiber directions in areas without tissue. Fourth column: A retardation-based threshold is applied: Background pixels are displayed in black.

It is important to note that Vervet1818, due to the comparatively long time since its embedding, is not a typical 3D-PLI sample. The contrast in the transmittance map is not distinct enough to identify background areas. However, an alternative approach can be employed for background masking: Given the significantly lower contrast in the transmittance map, it is more effective to set a threshold based on the retardation $|\sin(\delta)|$. Figure 5.5 demonstrates the application of a threshold value for $|\sin(\delta)| \leq 0.015$. The first image displays the retardation, already corrected as discussed in Section 5.2.3. The second image presents the transmittance map, with background pixels displayed in white. The third image shows the measured fiber directions. The residual retardation manifests as blue fiber directions in areas without tissue. The fourth image shows the fiber directions with the background masked in black. Stricter filtering can also remove (potentially distorted) gray matter signals depending on the selected threshold for $|\sin(\delta)|$, this method is less precise compared

to the transmittance-based approach for Broca. In Section 6.1, improved automatic background masking based on multi-modal parameter analysis is developed.

5.2.5 Polarization State Generator: Number of Angular Steps

By default, the polarization state generator (PSG) generates 18 equidistant polarization angles in steps of $\Delta\rho = 10°$ between $\rho = 90°$ and $\rho = -90°$, as determined in Section 4.5.2. However, $\Delta\rho$ can be changed without major changes in the software and evaluation routine. A larger step size with fewer steps is of particular interest for a high-speed device. To investigate the influence of $\Delta\rho$ on the parameter maps, a reduced measurement was simulated: First, the measurement with 18 images and $\Delta\rho$ =10° was performed. Then, a subset of images was evaluated that corresponded to steps of $\Delta\rho = 20°$ (9 images), $\Delta\rho = 30°$ (6 images) and $\Delta\rho = 60°$ (3 images). Figure 5.6 demonstrates the changes in the transmittance, the retardation, and the fiber direction for Vervet1818-CC with $\Delta\rho$ increasing from left to right.

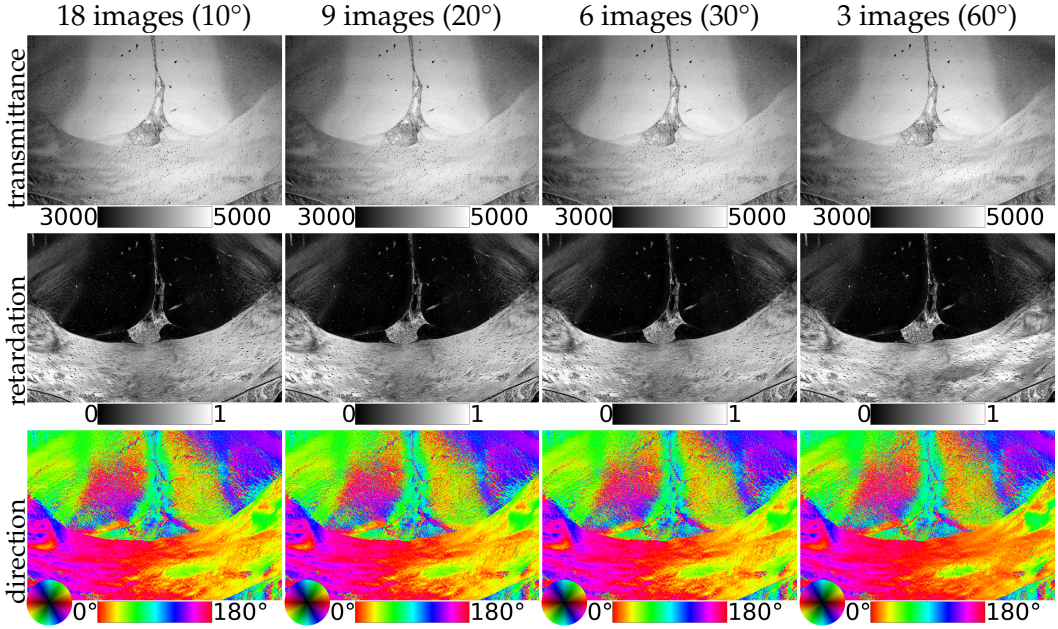

FIGURE 5.6: 3D-PLI: Reduced number of measurement images. From top to bottom: Transmittance [a.u.], retardation, fiber direction. In pursuit of a high-speed measurement, the number of polarization angles, i.e. the number of required measurement images, is decreased while the angular step size between equidistant angles of linear polarization $\Delta\rho$ increases. From left to right: 18 images, 9 images, 6 images, 3 images. The parameter maps are stable up to $\Delta\rho = 30°$. The fiber directions start to deviate for $\Delta\rho = 60°$ (indicated by the migration of the orange direction to the right).

While the transmittance and retardation remain nearly unchanged, differences in the fiber direction become noticeable at $\Delta\rho = 60°$ where the orange fiber direction starts to migrate towards the right side of the corpus callosum. However, the parameter maps remain stable up to $\Delta\rho = 30°$. Although the subsequent evaluations were still performed with the default setting $\Delta\rho = 10°$ (like in the LAP and the LMP1 measurements), future high-speed measurements can safely consider reducing the number of images to 6 which decreases their number by a factor of 3.

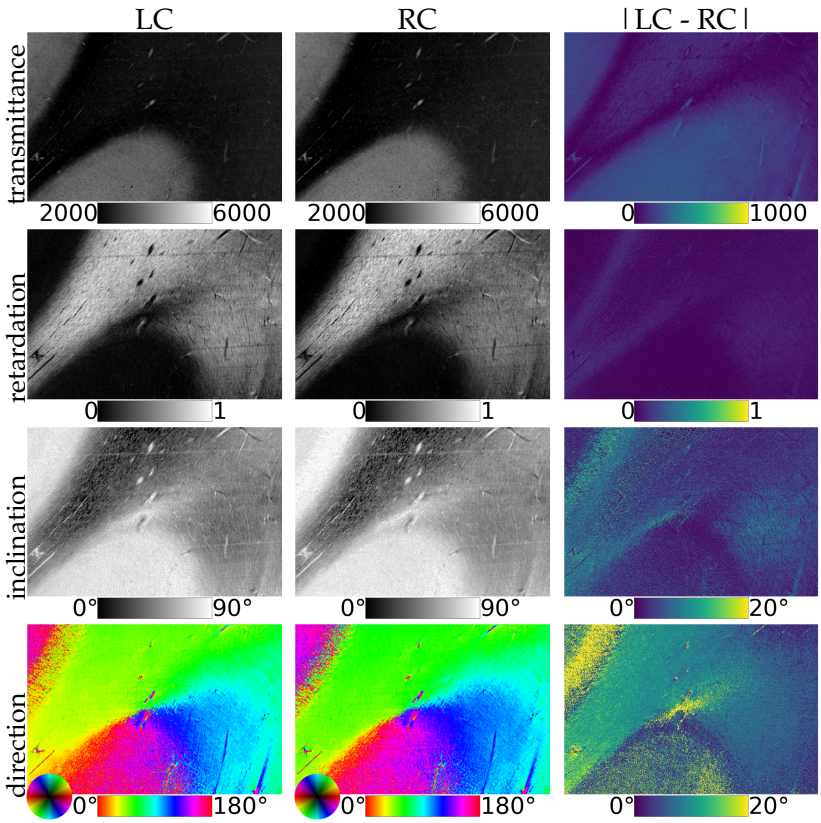

FIGURE 5.7: 3D-PLI: Influence of circular analyzer. From top to bottom: Transmittance [a.u.], retardation, inclination, fiber direction. When performing 3D-PLI measurements, the PSA can be set to operate a left-circular (LC) or right-circular analyzer (RC). Theoretically, the parameter maps for Broca-B should not differ between LC and RC, apart from a phase shift of 90° in the fiber direction. The third column shows the difference (absolute value) between LC and RC.

5.2.6 Polarization State Analyzer: Circular Analyzer

Within the Scattering Polarimeter, LCVR 4 has the flexibility to operate as a quarter-wave plate (QWP) in two ways: by analyzing right- or left-handed circular polarized light, depending on the sign of the phase shift introduced by LCVR 4. Theoretically, this does not make a difference, apart from a phase shift of exactly 90° in the sinusoidal intensity curve. Figure 5.7 shows the transmittance, retardation, inclination and fiber direction maps for LC and RC. The third column presents the absolute value differences for Broca-B. The retardation map is already corrected, and the fiber direction background is masked as discussed earlier. The transmittance map exhibits a direction-dependent deviation, thus showing the asymmetry already observed in the Fourier coefficient fit in Section 5.2.1. The retardation is slightly influenced by the asymmetry, showing minor offsets towards the borders from gray to white matter. Differences in the fiber direction are around 10° and can be higher for gray matter, where the signal-to-noise ratio is generally lower. Appendix B.2 shows the comparison for Vervet1818, Broca-A, and Broca-C in Figure B.5–B.10.

The parameter maps for Vervet1818-CC underline that LC is the better choice for 3D-PLI measurements, as indicated by a more symmetric appearance of the parameter maps (especially visible in the retardation and inclination maps). The slightly better performance of LC agrees with an observation from Section 4.5.1: The retardance voltage curve is steeper for lower voltages (e.g. the voltage for LCVR 4 to obtain RC)

and rather flat for higher voltages. Hence, higher voltages (e.g. the voltage for LCVR 4 for LC) are less prone to differ from the ideal voltage setting.

Even though the PSA settings are a choice in 3D-PLI, it is important to be aware of the asymmetries between LC and RC: In diattenuation imaging (DI), LC and RC are added up to obtain the complete transmitted intensity per incident polarization angle ρ. Visible error propagation into the already small DI signal must be expected and is investigated in Section 5.3.1.

5.2.7 Reference Measurements

With the measurement parameters for the Scattering Polarimeter (LC, $\Delta\rho = 10°$) and signal correction algorithms established, the 3D-PLI parameter maps obtained with the Scattering Polarimeter can be compared to reference measurements with the LMP3D and LMP1, s. Section 3.6.2. For Broca and Vervet1818, the reference measurements were performed with the LMP3D. For ChiasmX2-7 and ChiasmX2-15, reference measurements from the LMP1 are shown in Appendix B.2 in Figure B.11.

The transmittance map has arbitrary units that depend on factors like the brightness of the light source, the camera, and the exposure time. To allow for visual comparison, the minimum and maximum values of the visualization range were chosen so that the reference transmittance map resembles the contrast of the Scattering Polarimeter maps. Furthermore, the pre-processed direction maps from the LMP3D (s. Section 3.2) were rotated by flipping and/or transposing the data array so that the image orientation matches the images from the Scattering Polarimeter. If required, a global direction offset ϕ_{off} was added to match the relative fiber directions $\phi_{\text{PLI}} = \phi_{\text{off}} + \phi'_{\text{PLI}}$.

Broca Figure 5.8 - 5.10 show the transmittance map, retardation map and fiber direction map for Broca. The inclination map is not shown because it provides the same information as the retardation map. The regions Broca-A, Broca-B and Broca-C are indicated in the reference measurement and the corresponding parameter maps from the Scattering Polarimeter are displayed below.

As the most recently embedded sample, Broca exhibits excellent contrast between gray and white matter in the transmittance map, which aligns well with the reference measurement. Unlike Vervet1818, Broca does not show asymmetries, even though asymmetries may be concealed by the larger range of transmittance values and consequently, the better contrast. The retardation map agrees with the reference measurement and displays even minor local differences in white matter but also in gray matter, especially close to the white matter border where low retardation fiber bundles can be discerned. The correction of residual retardation proves to be successful and yields an accurate retardation map that agrees with the reference measurement. Fiber directions are accurately identified in white matter and, for many areas, in gray matter as well. Given the significantly lower fiber density in gray matter, these fibers typically produce a low 3D-PLI signal. Accordingly, the capability of the Scattering Polarimeter to resolve these fibers demonstrates its high performance for 3D-PLI measurements.

Vervet1818 Figure 5.11 - 5.13 show the transmittance map, retardation map and fiber direction map for Vervet1818. The regions measured with the Scattering Polarimeter are indicated in the reference measurement, and the corresponding parameter maps from the Scattering Polarimeter are displayed below. The transmittance exhibits

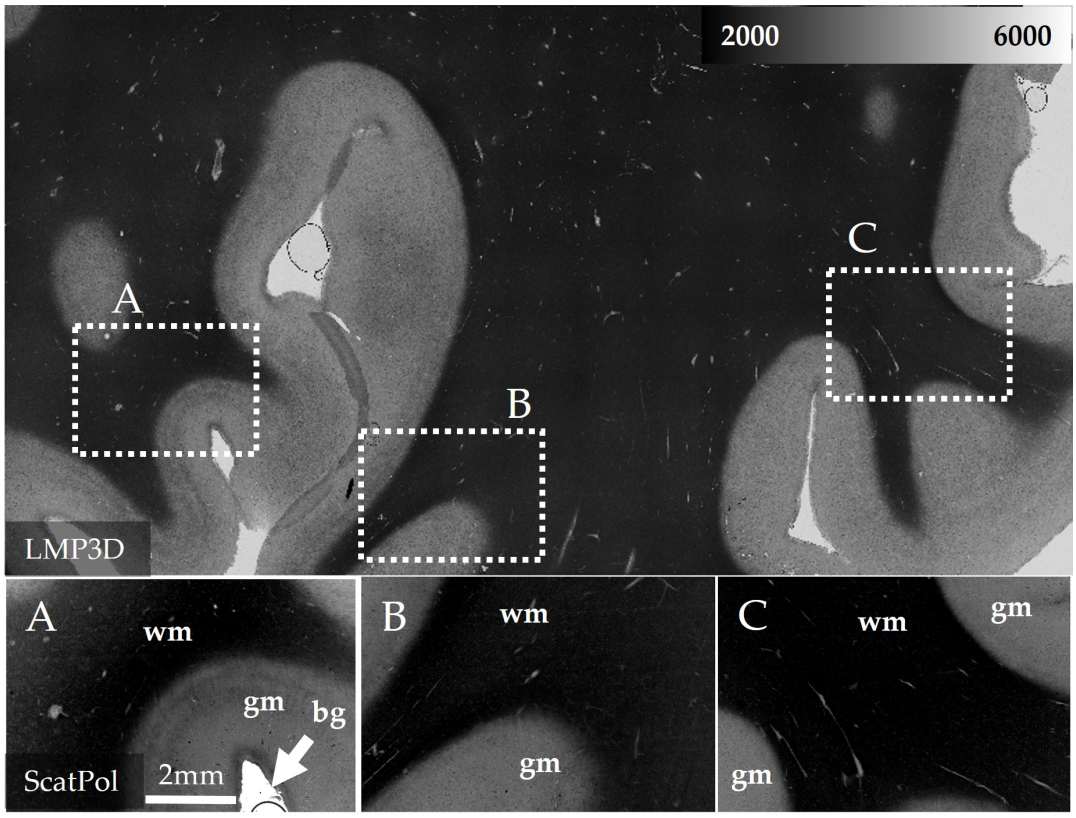

FIGURE 5.8: 3D-PLI: Broca transmittance map compared to LMP3D reference. The regions measured with the Scattering Polarimeter are indicated in the reference measurement. Broca shows an excellent contrast between gray matter (gm) and white matter (wm).

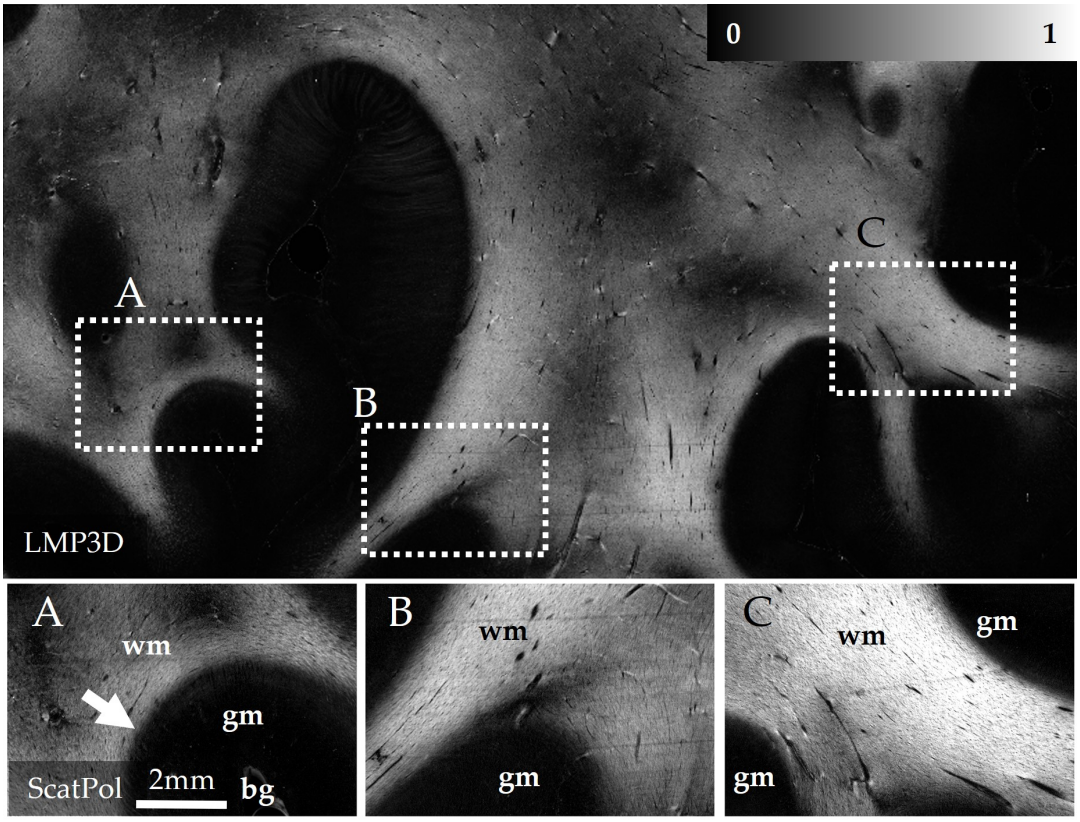

FIGURE 5.9: 3D-PLI: Broca retardation map compared to LMP3D reference. The regions measured with the Scattering Polarimeter are indicated in the reference measurement. The retardation maps are in accordance and the Scattering Polarimeter even resolves gray matter (gm) fibers (white arrows).

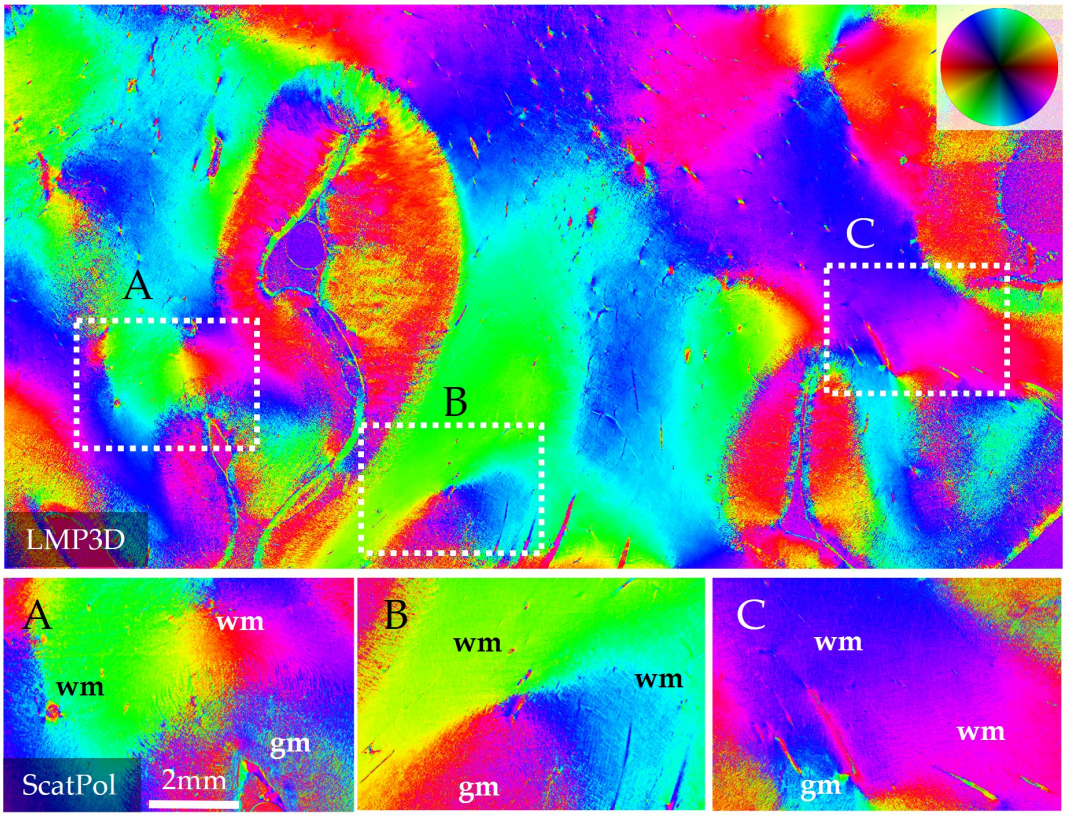

FIGURE 5.10: 3D-PLI: Broca direction map compared to LMP3D reference. The regions measured with the Scattering Polarimeter are indicated in the reference measurement. The Scattering Polarimeter identifies fiber directions correctly in white matter (wm) and even for low density gray matter (gm) fibers.

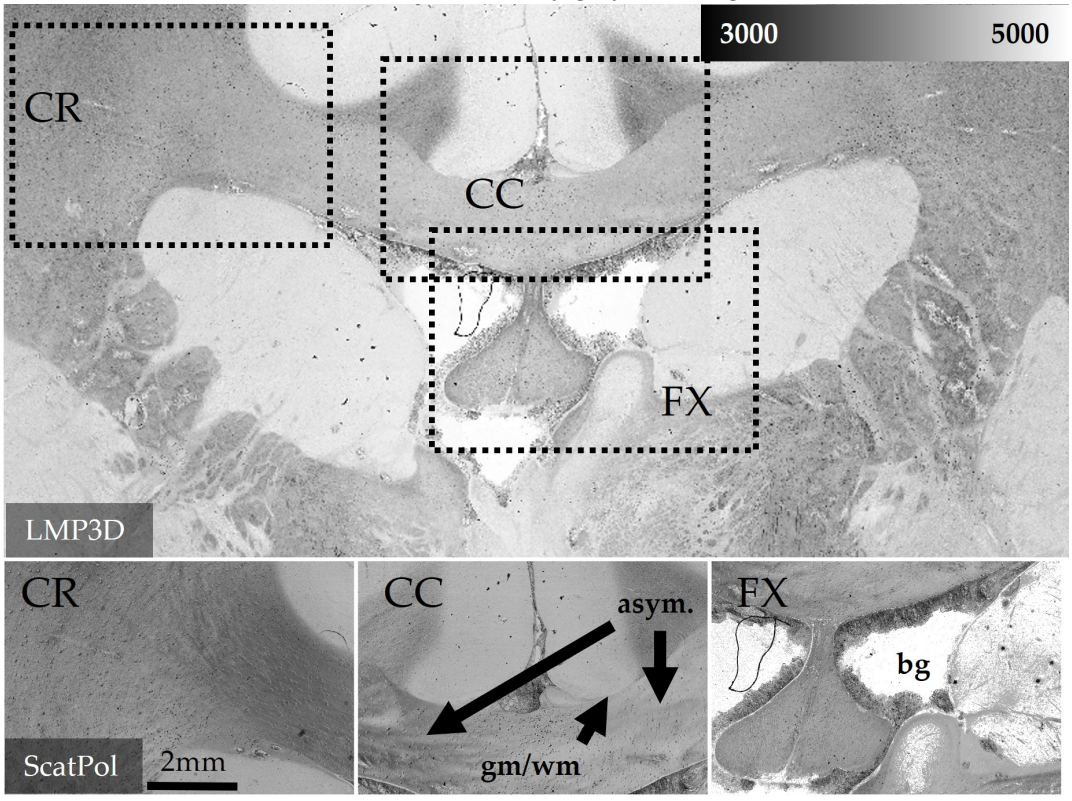

FIGURE 5.11: 3D-PLI: Vervet1818 transmittance map compared to LMP3D reference. The regions measured with the Scattering Polarimeter are indicated in the reference. The transmittance asymmetry is an artifact of the Scattering Polarimeter measurement. The border between white (wm) and gray matter (gm) is less pronounced.

contrasts between gray matter, white matter, and the background, that are comparable to the reference measurement. However, the reference measurement demonstrates that the observed transmittance asymmetry is an artifact of the Scattering Polarimeter measurement and most likely caused by the influence of minor ellipticities in the LCVRs. It appears more striking in Vervet1818 than in, e.g. Broca: The lower contrast between gray and white matter (gm/wm) in Vervet1818 – due to the longer time since embedding of the sample – requires an adequate choice of the visualized intensity range which, however, visually enhances the asymmetry.

Nevertheless, the retardation map agrees with the reference measurement, thereby also indicating a successful retardation correction. The retardation map demonstrates the sensitivity of the Scattering Polarimeter to small local variations. As expected, the cingulum and the fornix show a lower retardation than the corpus callosum. Minor retardation differences, such as an area of slightly lower retardation in the center of the corpus callosum – indicated by a darker shade of gray – are displayed correctly.

The fiber direction map aligns with the reference measurement for the corpus callosum and the cingulum. Even in the highly complex fibers of the corona radiata, the Scattering Polarimeter yields the same predominant fiber directions as the reference measurement. Fiber directions in white matter are determined with great success. Correct fiber directions in gray matter are detected well for many pixels but not as reliable in comparison. Similar to the Scattering Polarimeter, the LMP3D shows a residual retardation in areas without tissue, indicated by the blue background color in the fiber direction map. The influence of the residual retardation on gray matter fibers can be well observed in the gray matter area of Vervet1818-CC where the sinusoidal signals are shifted towards the phase of the residual retardation, i.e. the blue background direction.

ChiasmX2-7 and ChiasmX2-15 As for Vervet1818, the transmittance map shows a comparatively low contrast. Furthermore, the transmittance map of ChiasmX2-15 is influenced by stripe-shaped artifacts, possibly caused by scratches or a contamination of the object carrier that has occurred during the reference measurement and the measurement with the Scattering Polarimeter. However, the retardation and fiber direction map are in good agreement for both samples.

Summary The Scattering Polarimeter shows an excellent performance for Broca. Even fibers in regions with low fiber density such as gray matter are resolved correctly. 3D-PLI measurements are usually performed on recently embedded tissue and benefit from the lower transmittance and the consequently better contrast. For highly transmitting older samples such as Vervet1818, the Scattering Polarimeter reaches its limits concerning the transmittance map, even though fiber directions and retardation are still mostly correct. In future research, detailed parameter studies should identify the optimal measurement parameters, e.g. the ideal exposure time. Automatic scanning of the sample can measure the parameter maps for entire samples while maintaining high resolution.

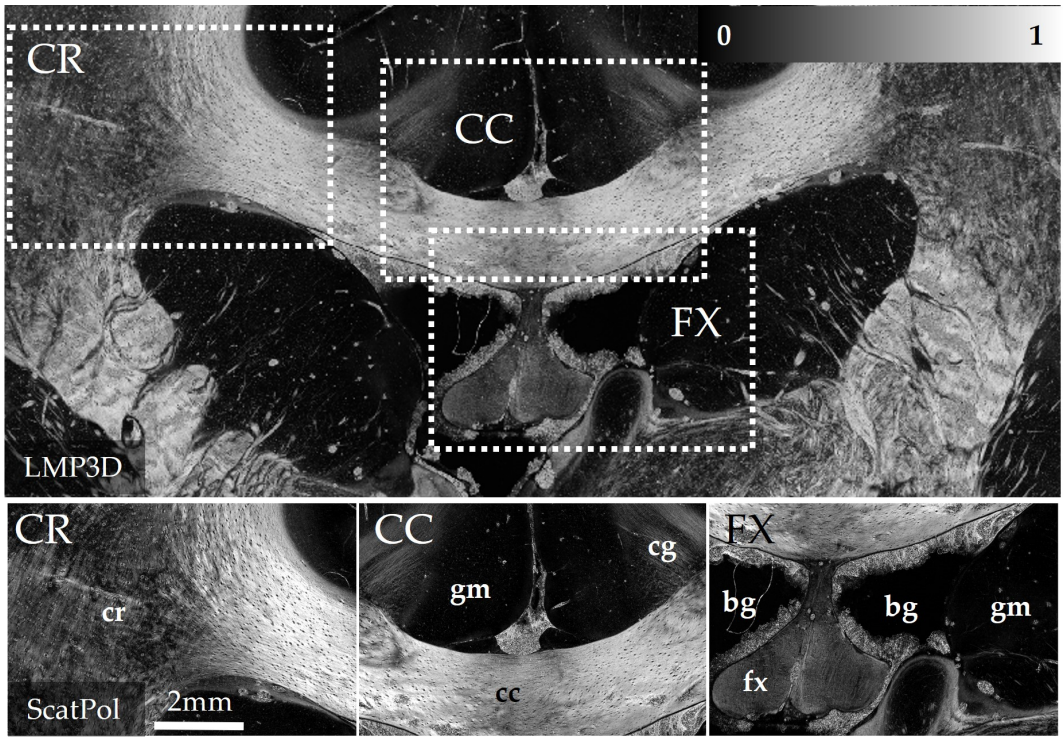

FIGURE 5.12: 3D-PLI: Vervet1818 retardation map compared to LMP3D reference. The regions measured with the Scattering Polarimeter are indicated in the reference measurement. As expected, the Scattering Polarimeter detects a lower retardation in the fornix (fx), the cingulum (cg), and in the corona radiata (cr).

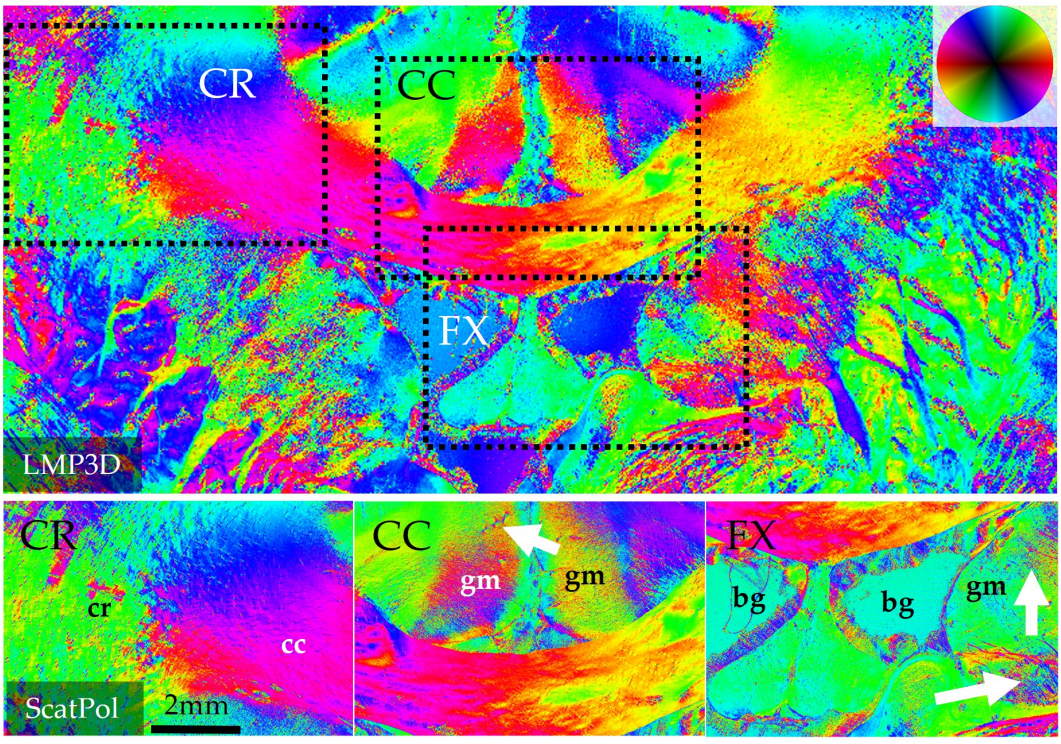

FIGURE 5.13: 3D-PLI: Vervet1818 direction map compared to LMP3D reference. The regions measured with the Scattering Polarimeter are indicated in the reference measurement. The Scattering Polarimeter is less sensitive to signals in gray matter (gm). Fiber directions in white matter (wm) are successfully detected, e.g. in the corpus callosum (cc) and the dominant direction in the corona radiata (cr).

5.3 DI

The Scattering Polarimeter measures the diattenuation by performing two 3D-PLI measurements; one with a left-handed circular analyzer (LC) and one with a right-handed circular analyzer (RC) for the PSA. The intensities for each polarization angle ρ are added up. DI represents an initial step towards multi-modal parameter analysis: In combination with 3D-PLI and through comparison of the fiber direction maps obtained from both techniques, two tissue types labeled as D^+ and D^- can be distinguished. The distribution of D^+ and D^- is investigated for Vervet1818 and Broca. Error propagation from the two 3D-PLI measurements into the DI signal is a primary focus of the subsequent section.

This part uses the same 3D-PLI data as in Section 5.2. Reference measurements were performed with the LAP, s. Section 3.6.1. Section 5.6 presents the characteristics of DI in context with Müller polarimetry, 3D-PLI, and ComSLI.

5.3.1 Error Propagation from 3D-PLI into DI Signal

Section 5.2 extracted reliable 3D-PLI fiber orientations especially in white matter despite systematic errors in the raw signal. However, the diattenuation signal is typically much lower than the retardation signal (MENZEL ET AL. [118] found diattenuation to be less than 4% for comparable brain tissue samples). Systematic and statistical errors propagate into the DI signal when LC and RC are added up and impair the signal-to-noise ratio and the fit quality.

Exemplary Analysis of Intensity Curve Figure 5.14a displays the 3D-PLI sinusoidals and the summarized DI signal for the same pixels from Broca-A as in Section 5.2.1, i.e. for white matter (magenta star) and for a background area (magenta diamond). For visualization purposes, the diattenuation signal is divided by 2 to simplify direct comparison with the LC and RC signals. Dashed lines indicate the fitted sinusoidal curves. Figure 5.14b shows the residuals of the fitted diattenuation signal. Appendix B.2 shows corresponding results for Vervet1818-FX in Figure B.12.

The Fourier coefficients for DI can be obtained in one of two ways: Either by summing up the raw intensity data (thus, 2×18 data points for each image pixel) from LC and RC and performing a Fourier coefficient fit on the resulting 18 new data points; or by calculating the Fourier fit of both LC and RC separately (as done in 3D-PLI) and summing up the curves, meaning that the DI Fourier coefficients are given by the sum of the 3D-PLI Fourier coefficients

$$a_{0,\,\mathrm{DI}} = a_{0,LC} + a_{0,RC} \quad a_{2,\mathrm{DI}} = a_{2,LC} + a_{2,RC} \quad b_{2,\,\mathrm{DI}} = b_{2,LC} + b_{2,RC} \tag{5.12}$$

Mathematically, both techniques are equivalent but the second option is usually computationally faster when the 3D-PLI coefficients have already been calculated.

The parameter maps can be calculated from the Fourier coefficients, s. Section 3.3. The diattenuation signal has a very low amplitude compared to the 3D-PLI signals. The residuals show a systematic error in the form of a sinusoidal-like curve with higher frequency with an amplitude comparable to the signal amplitude. Here, an issue becomes apparent: This distortion prevents a clear distinction between retardance and diattenuation.

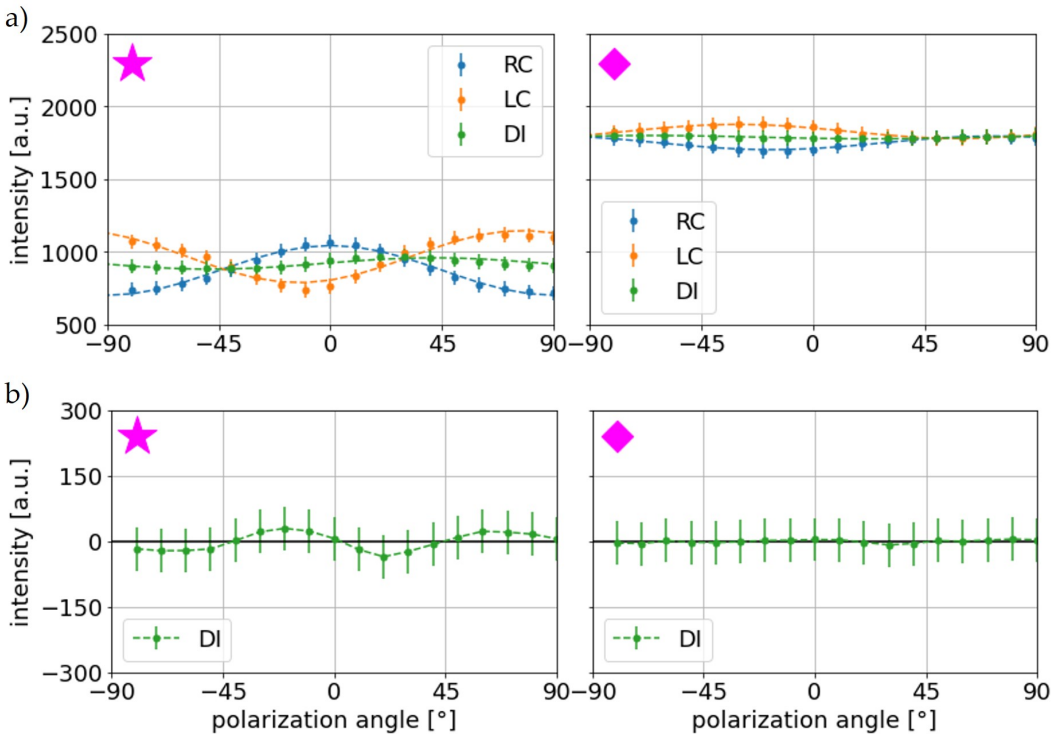

FIGURE 5.14: DI: Pixelwise Fourier coefficient fit. The fit is performed for the same areas of Broca-A as in Section 5.2.1, Figure 5.2. a) The Fourier coefficient fit for a white matter area (magenta star) and for background (magenta diamond) yields two sinusoidal curves for LC and RC. The dashed orange and blue lines indicate the Fourier fit for the 3D-PLI curves. When added up, the diattenuation signal (green) emerges. Here, the diattenuation intensity is divided by 2 for visualization purposes. b) The residuals of the diattenuation signal indicate a systematic error.

Error Propagation due to LCVR 4 When $(\delta_4 - \pi/2) = h_4$ and $(\delta_3 - \pi/2) = h_3$, a Taylor approximation to the 1st order describes the non-ideal PSA via M_{real} as a sum of two Müller matrices, one for the ideal PSA M_{PSA} and one for a deviation $M_{h3,h4}$ caused by LCVR 3 and LCVR 4. The non-ideal Stokes vector $\vec{S}_{\text{PLI}',\pm}$ of the left- and right-circular 3D-PLI signal is calculated from Müller matrix multiplication using $v_\phi = \sin 2\phi$, $w_\phi = \cos 2\phi$

$$\vec{S}_{\text{PLI}',\pm} = (M_{\text{PSA}} + M_{h3,h4}) \cdot M_{\text{tissue}} \cdot \vec{S}_{\text{PSG}} \tag{5.13}$$

$$= \vec{S}_{\text{PLI},\pm} \mp \frac{h_4}{2} \begin{pmatrix} 1 + D\cos(\delta_1 - 2\phi) \mp \sqrt{1 - D_L^2}\sin(\delta)\sin(\delta_1 + 2\phi) \\ 1 + D\cos(\delta_1 - 2\phi) \mp \sqrt{1 - D_L^2}\sin(\delta)\sin(\delta_1 + 2\phi) \\ 0 \\ 0 \end{pmatrix} \tag{5.14}$$

$$\pm \frac{h_3}{2} \begin{pmatrix} 1 + D\cos(\delta_1 - 2\phi) \mp \sqrt{1 - D_L^2}\sin(\delta)\sin(\delta_1 + 2\phi) \\ 1 + D\cos(\delta_1 - 2\phi) \mp \sqrt{1 - D_L^2}\sin(\delta)\sin(\delta_1 + 2\phi) \\ 0 \\ 0 \end{pmatrix} \tag{5.15}$$

$$= \vec{S}_{\text{PLI},\pm} + \vec{S}_{\text{LCVR3}}(\phi, \delta, \delta_1) + \vec{S}_{\text{LCVR4}}(\phi, \delta, \delta_1) \tag{5.16}$$

The complete derivation is provided in Appendix A.4.4. It is important to note that h_4 is not necessarily equal for $\vec{S}_{\text{PLI},+}$ and $\vec{S}_{\text{PLI},-}$ because two different voltage settings are applied to LCVR 4. Thus, not every term cancels out when adding up the intensities

$$I_{DI'} = I_{\text{PLI}',+} + I_{\text{PLI}',-} \tag{5.17}$$
$$= 1 + D_L \cos(\delta_1 - 2\phi) \tag{5.18}$$
$$\mp (h_{4,+} - h_{4,-}) \left(1 + D_L \cos(\delta_1 - 2\phi) \mp \sqrt{1 - D_L^2} \sin(\delta) \sin(\delta_1 + 2\phi)\right) \tag{5.19}$$

The successful measurement of the comparatively small diattenuation signal D_L depends on its magnitude compared to $(h_{4,+} - h_{4,-})$. Here, the practical results indicate that the diattenuation signal cannot be reliably retrieved because higher-order frequencies dominate the signal.

Transmittance Map It is worth noting that the DI transmittance map can be a valuable asset to differentiate gray and white matter in old samples with high transmittance, such as Vervet1818. Asymmetries in the 3D-PLI transmittance cancel out in the DI transmittance map. Appendix A.4.3 demonstrates how asymmetries caused by the LCVR 2 cancel out in the diattenuation signal. Figure 5.15 shows the asymmetric transmittance maps from RC and LC in the Vervet1818-CC, and the summarized transmittance map. The improved distinction between white and gray matter by brightness value can have practical implications in the context of multimodal parameter analysis in Chapter 6 because the diattenuation transmittance map can serve as a criterion for tissue distinction.

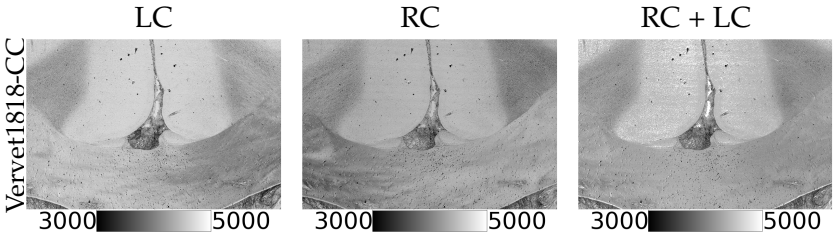

FIGURE 5.15: DI: Symmetry of the transmittance map. The transmittance maps from 3D-PLI for Vervet1818-CC were measured either with a left-circular setting (LC) of the PSA or with a right-circular (RC) setting. For DI, the two measurements were added up. Here, the diattenuation transmittance map was divided by 2 for visualization purposes. The transmittance is given in arbitrary units. While the two 3D-PLI transmittance maps (LC and RC) show deviations in the symmetric structure of the corpus callosum area in Vervet1818-CC, the asymmetries in the summarized transmittance map (LC+RC) cancel each other out. This simplifies the differentiation between gray and white matter in old samples with a high transmittance such as Vervet1818. The improved distinction by brightness value is valuable in the context of multimodal parameter analysis in Chapter 6.

5.3.2 Background Masking

For Broca-A, the process of background identification and masking using the transmittance map is illustrated in Figure 5.4. The first image presents the measured transmittance. In the second image, background pixels characterized by a transmittance $I_T > 4100$ a.u. are displayed in white, indicating the maximum light transmission in

background areas. The specific threshold value is influenced by measurement parameters such as exposure time and gain. The third image displays the measured fiber directions. The minor background retardation as discussed in Section 5.2.1 appears as falsely detected red/pink fiber directions in background areas. The fourth image shows the fiber directions with the background masked in black.

Analogously to the background masking in 3D-PLI discussed in Section 5.2, background areas can be identified based on the transmittance. Other than in 3D-PLI, transmittance-based background masking is also feasible for Vervet1818 despite the lower contrast because the transmittance has a more symmetric appearance, as discussed in Section 5.3.1. For Broca-A and Vervet1818, transmittance-based background masking is illustrated in Figure 5.16.

The first row presents the measured transmittance. In the second row, pixels with a transmittance higher than the threshold are displayed in white, indicating the maximum light transmission in background areas. Thresholds of $I_T > 4100$ a.u. for Broca-A and $I_T > 4550$ a.u. for Vervet1818 were chosen[5]. The specific threshold value is influenced by measurement parameters such as exposure time and gain. The third image displays the measured fiber directions.

The minor background retardation as discussed in Section 5.2.1 propagates into the diattenuation signal and appears as falsely detected fiber directions in background areas. The fourth image shows the fiber directions with the background masked in black. In Section 6.1, improved automatic background masking based on multi-modal parameter analysis is developed.

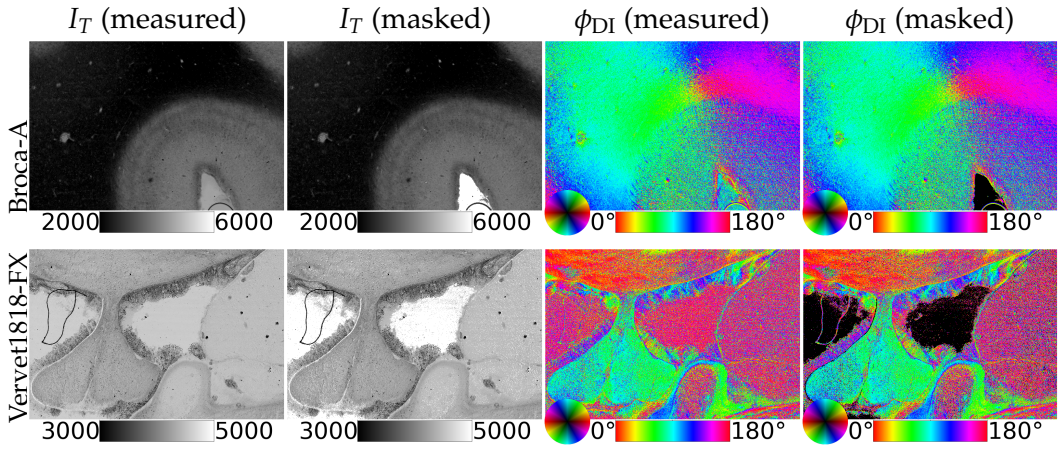

FIGURE 5.16: DI: Background masking based on the transmittance map. First row: Broca-A. Second row: Vervet1818-FX. First column: The measured transmittance map. The transmittance is given in arbitrary units. Second column: All pixels with a a transmittance $I_T > 4100$ a.u. for Broca-A and $I_T > 4550$ a.u. for Vervet1818-FX are identified as part of the background and displayed in white. Third column: The measured fiber directions. The residual retardation propagates into the diattenuation signal and appears as falsely detected fiber directions in areas without tissue. Fourth column: The transmittance-based threshold is applied: Masked image pixels are displayed in black.

[5] $I_T > 4100$ a.u. for ChiasmX2-7 and $I_T > 4800$ a.u. for ChiasmX2-15 in subsequent depictions. However, background masking is not very reliable for ChiasmX2-15 due to the generally low contrast and the additional occurrence of artifacts, possibly caused by scratches or a contamination of the object carrier.

5.3.3 Fiber Direction Maps from 3D-PLI and DI

While the multi-modal analysis of parameter maps is primarily explored in Chapter 6, the main purpose of DI is to distinguish between two tissue types, D^+ and D^- by comparing the fiber direction maps from 3D-PLI and DI. Therefore, the comparison of fiber directions between 3D-PLI and DI is addressed here. Given that Vervet1818 is an older sample (i.e. the time since embedding is way longer than for Broca), D^+ tissue is expected in the investigated regions, meaning that 3D-PLI and DI yield the same fiber direction. Broca, being relatively new, may still show a mix of D^+ and D^-. However, MENZEL ET AL. [117] reported that D^- tissue is barely detected anymore after several weeks, i.e. D^+ tissue is expected to be dominant, potentially being the only tissue type present.

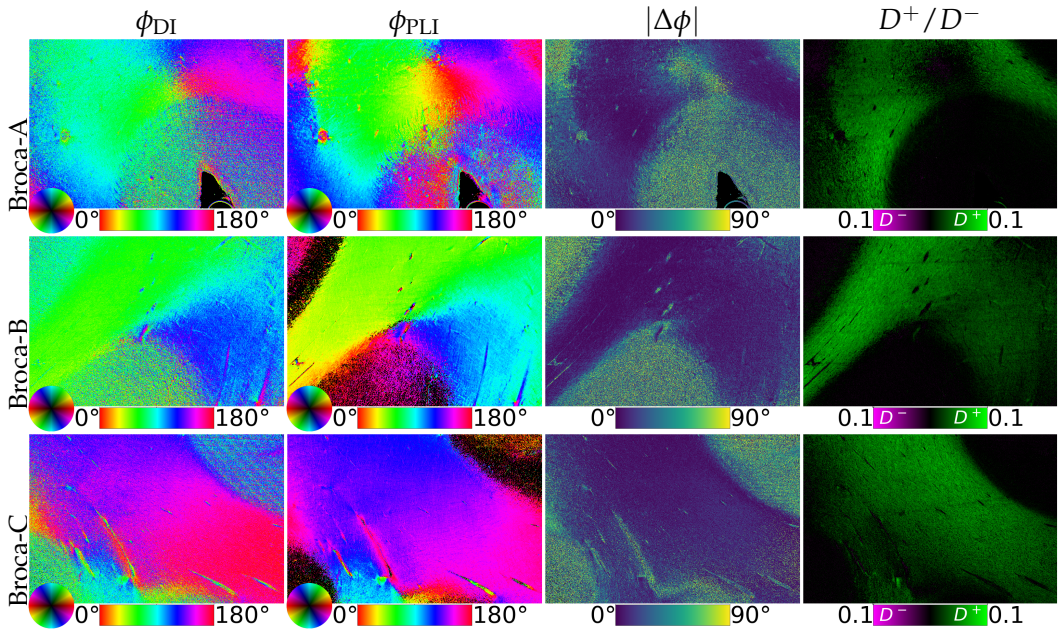

FIGURE 5.17: DI: Direction maps from 3D-PLI and DI for Broca. From left to right: Fiber direction from DI ϕ_{DI}, fiber direction from 3D-PLI ϕ_{PLI}, relative directional difference $|\Delta\phi| = |\phi_{DI} - \phi_{PLI}|$ between the fiber direction angles, D^+/D^- tissue distribution weighed with the maximum absolute diattenuation $D = 0.1$. Tissue with D^+ is depicted in green, with D^- in magenta. From top to bottom: Broca-A, Broca-B, Broca-C.

Figure 5.18 and Figure 5.17 compare the fiber direction maps derived from DI (first column) and 3D-PLI (second column) for Vervet1818 and Broca, respectively. The third columns displays the relative difference $|\Delta\phi| = |\phi_{DI} - \phi_{PLI}|$ between the fiber direction angles. The last column presents the binary distribution of D^+/D^- tissue. Pixels with $|\Delta\phi| \leq 20°$ are labeled as D^+ and visualized in green. When $|\Delta\phi - 90°| \leq 20°$, the pixel is labeled as D^- (magenta). The color value is weighed with the diattenuation D, with a fully saturated image pixel indicating the sample-dependent maximum value (or even a higher value, although this occurs mostly for artifacts in Vervet1818) and lower values indicating a lower diattenuation strength. Black pixels indicate regions where no reliable fiber direction is detected in one or both modalities, where $\Delta\phi$ falls outside the defined ranges, or when the diattenuation $D = 0$. Then, the distinction of D^+/D^- tissue is not possible.

Naturally, the 3D-PLI direction maps generally exhibit stronger signals compared to the DI direction maps, resulting in fewer black pixels in tissue areas. The diattenuation

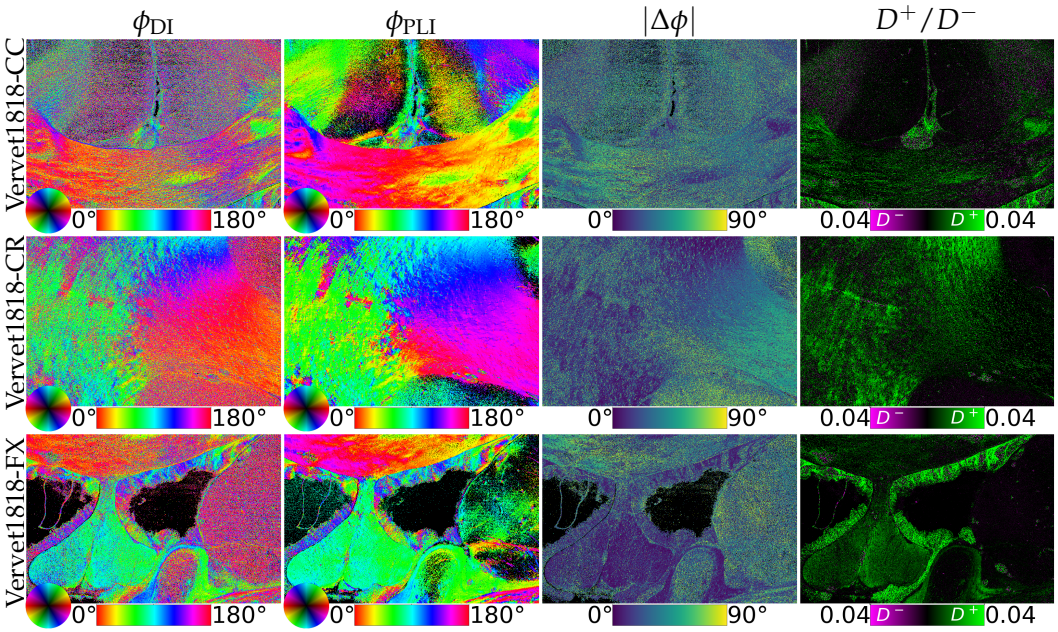

FIGURE 5.18: DI: Direction maps from 3D-PLI and DI for Vervet1818. From left to right: Fiber direction from DI ϕ_{DI}, fiber direction from 3D-PLI ϕ_{PLI}, relative directional difference $|\Delta\phi| = |\phi_{DI} - \phi_{PLI}|$ between the fiber direction angles, D^+/D^- tissue distribution weighed with the maximum absolute diattenuation $D = 0.04$. Tissue with D^+ is depicted in green, D^- in magenta. From top to bottom: Vervet1818-CC, Vervet1818-CR, Vervet1818-FX.

signal in the gray matter of Broca is below the chosen threshold, indicating that the fiber directions are unreliable in gray matter. In white matter, the detected DI fiber directions agree well with the 3D-PLI directions, as indicated by the relative directional differences rarely exceeding 20° for Broca. Even Vervet1818, which is more influenced by artifacts due to its lower transmittance, shows many pixels where 3D-PLI and DI agree within an acceptable difference range of 20°. The distribution of D^+/D^- supports these observations, with most identified pixels being D^+, as expected. D^- occurs mostly in the unstructured artifacts of Vervet1818.

However, due to the asymmetries between LC and RC, the diattenuation axis is not reliable: Future research should include measurements on freshly embedded tissue samples to verify if D^- can indeed be reliably measured. It is crucial to ensure that the phase of the DI intensity curve is actually defined by diattenuation and not influenced by the birefringence-related phase of one of the two original 3D-PLI signals. Furthermore, DI can benefit from an improved signal-to-noise ratio, particularly to enhance the measurement of gray matter diattenuation.

The corresponding maps for ChiasmX2-7 and ChiasmX2-15 are depicted in Appendix B.2 in Figure B.13. In the artificial samples ChiasmX2-7 and ChiasmX2-15, mainly D^+ is expected due to the longer time since embedding. However, the diattenuation is generally very low: The single optic tracts only have thickness of 30 µm and thus, the diattenuation signal is even weaker than for Vervet1818 and Broca. However, ChiasmX2-7 shows fiber orientations from the diattenuation measurement that are in agreement with the 3D-PLI measurement, and a diattenuation signal for the single optic tracts. In the crossing regions, the two axes of diattenuation are expected to cancel out, an effect that is actually observed for ChiasmX2-7.

5.3.4 Reference Measurements

The required 3D-PLI measurement was performed with the LAP as described in Section 3.6.1. To perform a DI measurement with the LAP, the quarter-wave plate and the second linear polarization filter were removed from the setup. The PLI measurement was performed with an exposure time of 70 ms and averaged over 10 images. The DI measurement was performed with an exposure time of 30 ms and averaged over 20 images.

Broca In 3D-PLI, Broca showed a reliable signal in white and gray matter. Figure 5.19 displays the strength of diattenuation measured with the LAP and with the Scattering Polarimeter, furthermore the direction maps and the distribution of D^+/D^- tissue obtained with both devices. When examining the fiber directions and the D^+/D^- map, the obtained white matter fiber directions are in good agreement. The distribution of D^+/D^- is as expected, with a strong dominance of D^+ (indicated in green). However, it is evident that the diattenuation is noticeably stronger in the Scattering Polarimeter measurement than for the reference measurement, as indicated by the different visualization scale. This observation suggests that the diattenuation signal is influenced by residual retardation, indicating that the low diattenuation signal is affected by systematic errors resulting from the asymmetries between LC and RC. Consequently, the diattenuation signal is determined by birefringence and should not be considered reliable.

Vervet1818 Vervet1818 exhibited a very robust signal for 3D-PLI in white matter and accurately detected fiber orientations even in gray matter areas. However, the transmittance in 3D-PLI showed asymmetries that propagate into the diattenuation signal. Figure 5.20 shows the strength of diattenuation measured with the LAP, with the corresponding diattenuation measured with the Scattering Polarimeter below, furthermore the fiber directions and distribution of D^+/D^-. Similar to Broca, the diattenuation is visibly stronger in the Scattering Polarimeter measurement, with artifacts appearing very bright, especially when compared to the reference measurement. In areas with low fiber density, the diattenuation signal is expected to be low, as seen in the reference measurement, but gray matter areas show a higher diattenuation in the Scattering Polarimeter. This is likely due to the previously discussed error propagation. Thus, the diattenuation signal should not be considered reliable. Additionally, the Scattering Polarimeter has limitations for highly transmitting samples such as Vervet1818. In the corpus callosum, the fiber directions show a strong deviation on the left side, displaying purple instead of orange, whereas the reference measurement mostly shows the same fiber directions as the 3D-PLI measurements.

Summary While the fiber directions and D^+/D^- map mostly agree with the reference measurement, the preliminary results should be interpreted with caution. Future research should focus on reducing systematic errors and finding methods to distinguish actual diattenuation from birefringence dependence. For instance, performing diattenuation measurements by analyzing horizontal and vertical polarization with the PSA, rather than summing two 3D-PLI measurements (LC and RC), could reduce the influence of circular components. However, with this approach, the synergy with the 3D-PLI measurement is lost – meaning that two additional measurements are required on top of the 3D-PLI measurement – which would increase the overall measurement time.

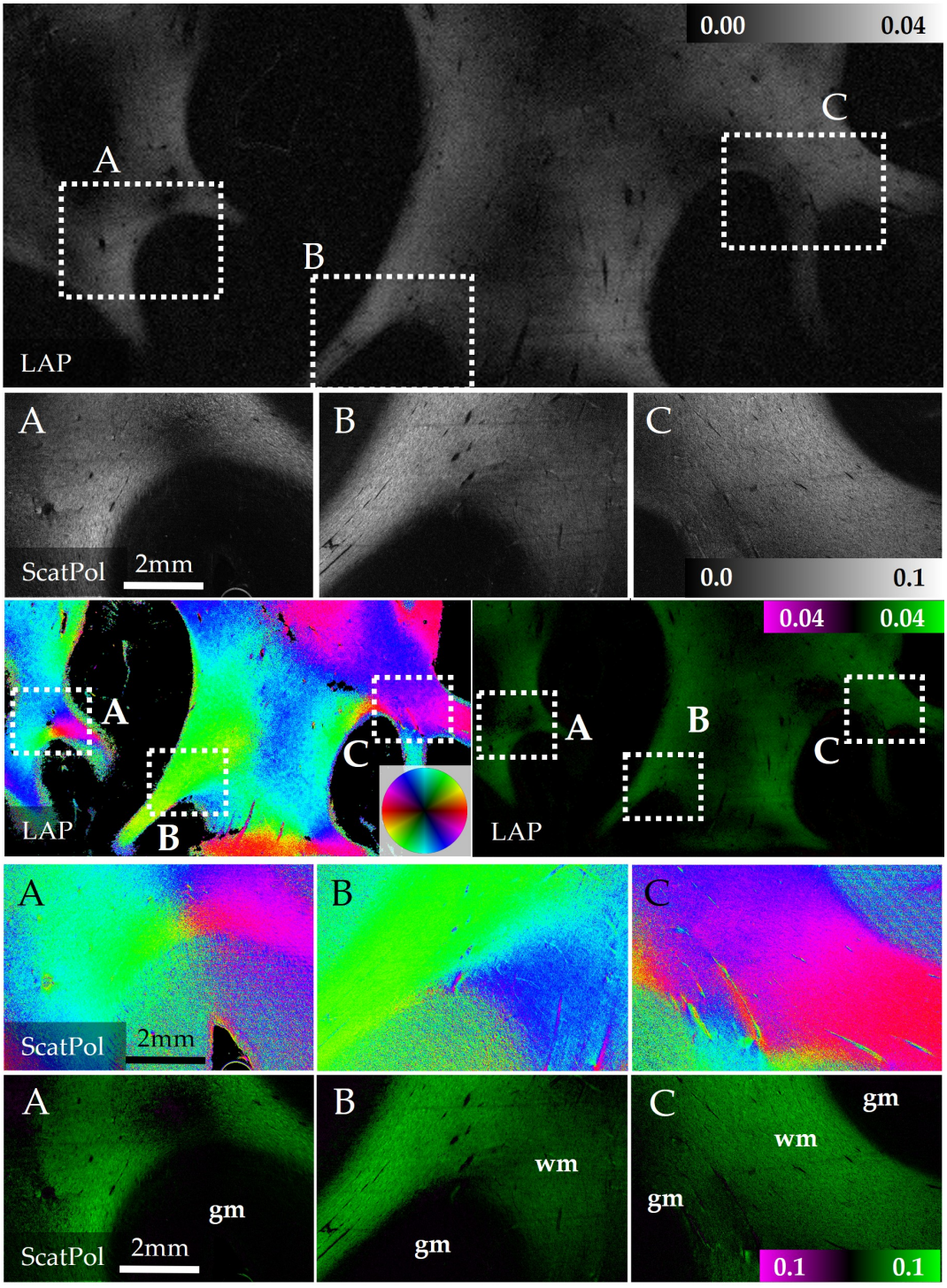

FIGURE 5.19: DI: Broca diattenuation maps compared to LAP reference. First row: The LAP diattenuation map. The regions measured with the Scattering Polarimeter are indicated. Second row: The Scattering Polarimeter diattenuation map (visualization with a different scale). Third row: The fiber direction map obtained from the LAP diattenuation measurement (left) and the D^+ (green) and D^- (magenta) distribution weighed with the diattenuation D (right). Fifth row: Fiber directions obtained with the Scattering Polarimeter. Last row: The distribution of D^+/D^- measured with the Scattering Polarimeter weighed with the diattenuation D. Overall, the Scattering Polarimeter shows the expected D^+/D^- distribution but a considerably stronger diattenuation.

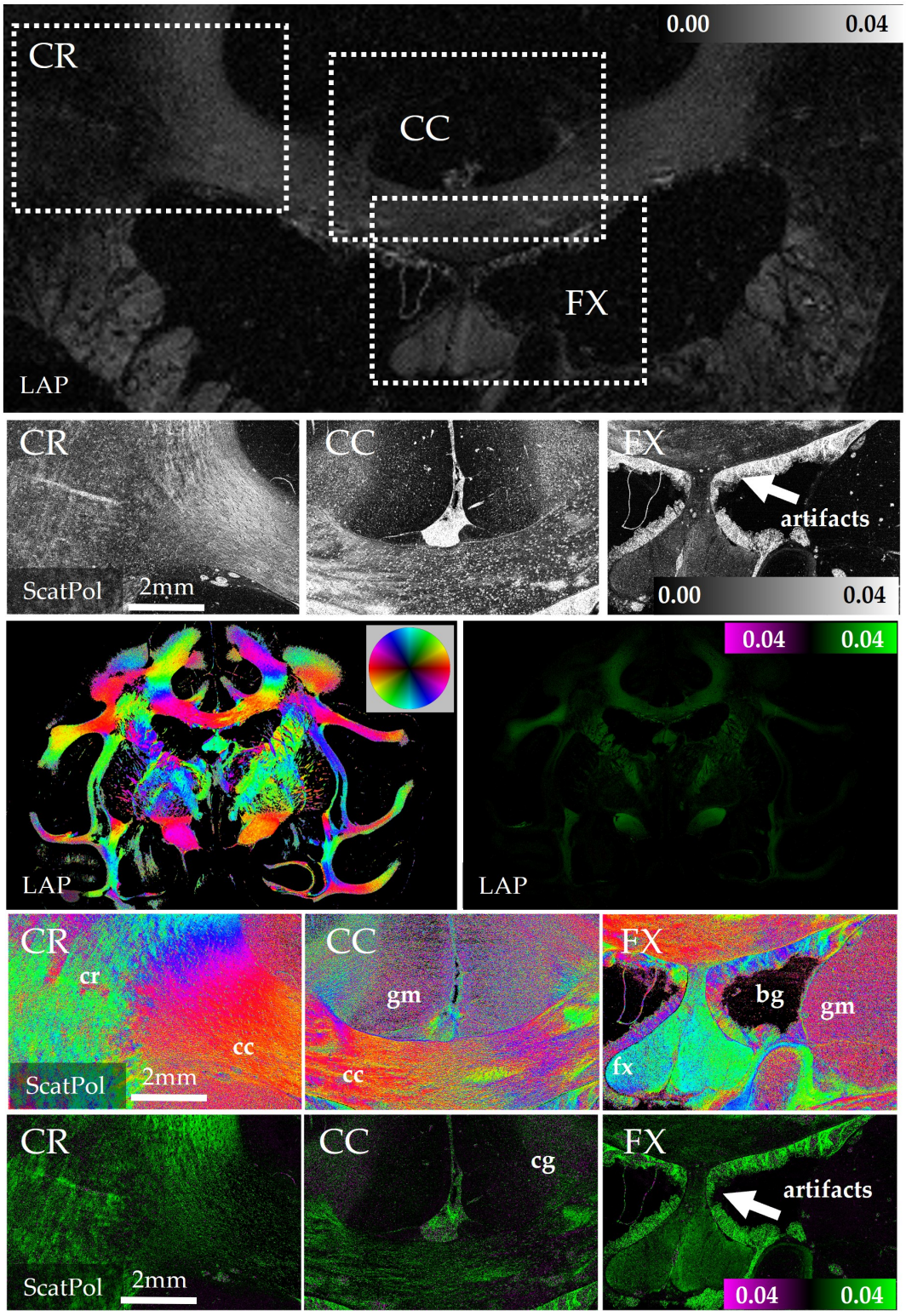

FIGURE 5.20: DI: Vervet1818 diattenuation maps compared to LAP reference. First row: The LAP diattenuation map. The regions measured with the Scattering Polarimeter are indicated. Second row: The Scattering Polarimeter diattenuation map. Third row: The fiber direction map obtained from the LAP diattenuation measurement (left) and the D^+ (green) and D^- (magenta) distribution weighed with the diattenuation D (right). Fifth row: Fiber directions obtained with the Scattering Polarimeter. Last row: The distribution of D^+/D^- measured with the Scattering Polarimeter weighed with the diattenuation D. D^+ tissue (green) is dominant over D^- tissue (magenta). Overall, the Scattering Polarimeter shows a considerably stronger diattenuation.

5.4 Müller Polarimetry

Müller polarimetry calculates the Müller matrix for each pixel in an image. In the following, the performance of Müller polarimetry with the Scattering Polarimeter is explored. Unless specified otherwise, all investigations are based on 36 measurements, covering all possible combinations of basic polarization states. From the Müller matrix, parameters such as retardation, diattenuation, and depolarization are derived. The application of the eigenvalue calibration method (ECM) for Müller polarimeters is demonstrated, and the precision of the Scattering Polarimeter is assessed using well-known optical elements. Parameter maps are generated to visualize pixelwise tissue characteristics. Additionally, signal processing and error filtering routines are developed to enhance the anatomical accuracy of these parameter maps. Strengths and limitations are analyzed, along with recommendations for future research and development. Section 5.6 discusses the performance of Müller polarimetry in direct comparison with the other three modalities 3D-PLI, DI, and ComSLI.

5.4.1 Application of Eigenvalue Calibration Method

The *eigenvalue calibration method* (ECM) is a standard calibration algorithm for Müller polarimeters, such as the Scattering Polarimeter and was detailed in Section 2.2.3. The ECM requires four samples with known optical properties to determine the calibration matrices A and W, which account for the non-ideal features of the polarization state analyzer (PSA) and the polarization state generator (PSG), respectively. B_0 is the Müller matrix of air, obtained by measuring with an empty setup. The Müller matrices B_1 and B_2 are acquired with the *Edmund Optics XP38* polarization filter at two different azimuthal angles ($\theta \approx 0°$, $\theta \approx -45°$). Exact azimuthal positioning is not required for the ECM, which simplifies its practical application. B_3 is determined with the *Newport 10RP34-532* birefringent plate, which operates near quarter-wave retardance for the specific wavelength used. However, neither exact azimuthal positioning at $\theta = 45°$ nor a retardance of precisely $\delta = \pm\frac{\pi}{2}$ are needed for the ECM.

Measurement of ECM Matrices Measurements were performed with an exposure time of 2 seconds and averaged over two images. Results were derived from the average intensity over all 3568×5472 pixels of the measurement images under the assumption of spatial homogeneity. The ECM yields

$$A = \begin{pmatrix} \mathbf{1.000} & -0.021 & 0.175 & -0.002 \\ 0.012 & \mathbf{0.875} & -0.051 & -0.001 \\ 0.033 & -0.024 & \mathbf{0.754} & -0.045 \\ 0.002 & -0.022 & 0.002 & \mathbf{0.851} \end{pmatrix} \tag{5.20}$$

and

$$W = \begin{pmatrix} \mathbf{1.000} & -0.019 & -0.103 & -0.005 \\ 0.02 & \mathbf{0.693} & 0.089 & 0.106 \\ -0.045 & -0.02 & \mathbf{0.766} & 0.01 \\ 0.038 & -0.078 & -0.026 & \mathbf{0.668} \end{pmatrix} \tag{5.21}$$

In an ideal setup, both A and W would be unit matrices. The diagonal elements are highlighted with a bold font to indicate the positions of 1 in an ideal setup. A and W were used to calibrate each pixelwise Müller matrix obtained from raw measurement data.

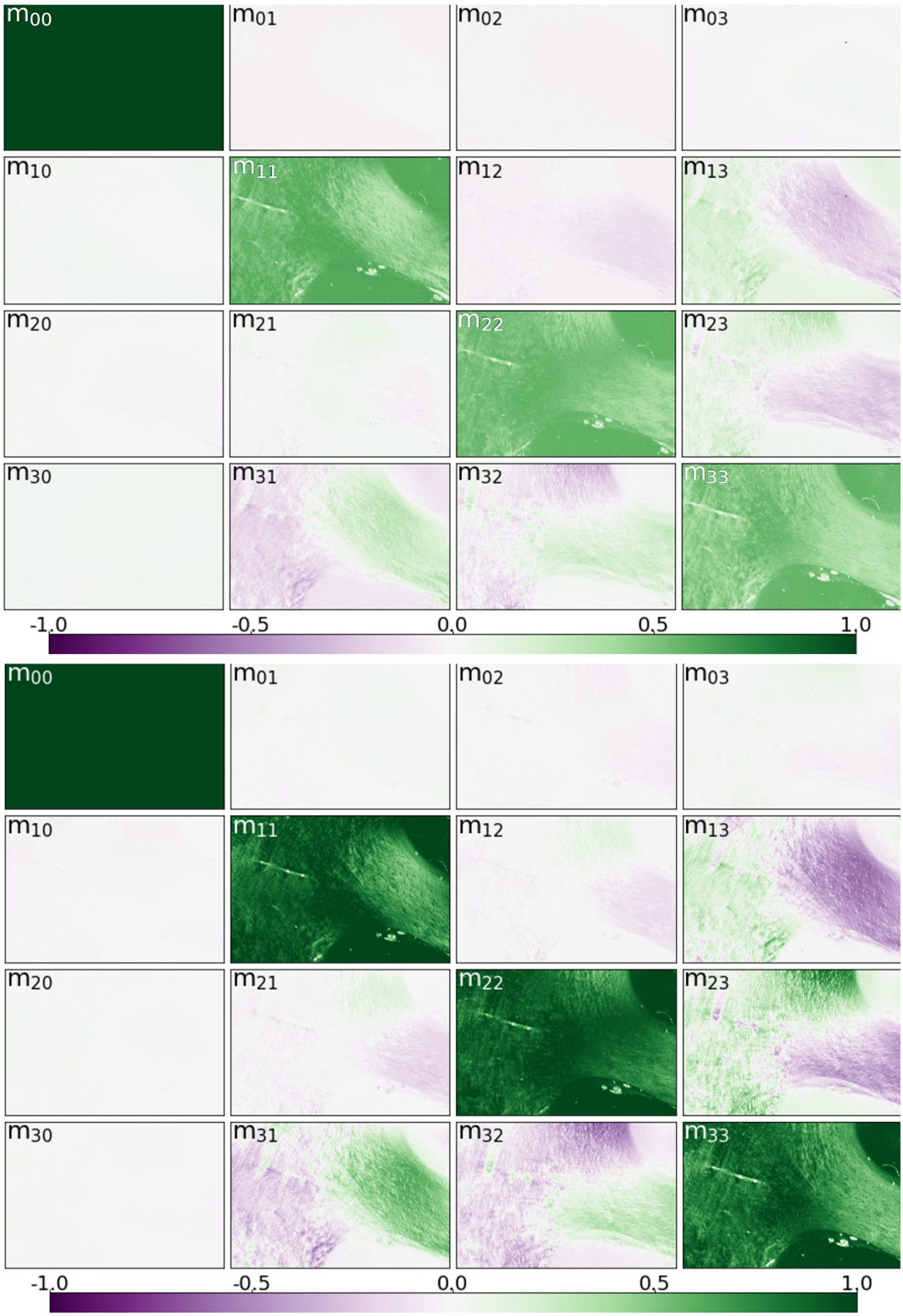

FIGURE 5.21: Müller polarimetry: Vervet1818-CR before (top) and after calibration (bottom). Each image pixel yields a 4×4 Müller matrix, therefore the subplots visualize 5472×3648 Müller matrices that provide a spatial overview over the sample. Gray matter is a good indicator for a successful calibration: Here, the diagonal matrix elements are expected to approximate 1 whereas the off-diagonal elements should be close to zero because gray matter is less turbid, less absorbing and less birefringent than white matter.

Measurement of Optical Elements The measurement of well-known samples provides information about the success of the calibration. The Müller matrices of the empty setup, the linear polarization filter *Edmund Optics XP38* ($\theta = 0°$) and the *Newport 10RP34-532* birefringent plate ($\theta = 45°$), were measured and then calibrated with A and W. The normalized calibrated Müller matrix M_{air} for the empty setup would ideally be a unit matrix and was measured to be

$$M_{\text{air}} = \begin{pmatrix} \mathbf{1.0000} & 0.0009 & -0.0017 & -0.0018 \\ -0.0004 & \mathbf{0.9978} & -0.0023 & -0.0004 \\ 0.0000 & 0.0027 & \mathbf{0.9971} & 0.0047 \\ -0.0004 & 0.0042 & -0.0035 & \mathbf{0.9967} \end{pmatrix} \tag{5.22}$$

The matrix elements are in accordance with the theoretical values down to the third or even fourth decimal place.

The normalized calibrated Müller matrix $M'_{\text{LP},0°}$ for the linear horizontal polarization filter was measured to be

$$M'_{\text{LP},0} = \begin{pmatrix} \mathbf{1.0000} & \mathbf{0.9904} & 0.1171 & -0.0001 \\ \mathbf{1.0349} & \mathbf{0.9910} & 0.1192 & 0.0068 \\ 0.0174 & 0.0209 & -0.0059 & -0.0312 \\ 0.0032 & -0.0064 & 0.0301 & 0.0201 \end{pmatrix} \tag{5.23}$$

Here, the pre-factor of 0.5 was disregarded as it does not contain additional information regarding the calibration quality. In this case, the Müller matrix does not yet make sense from a physical point of view because the matrix element m_{10} is larger than m_{00}. This can happen when solving the linear equation system with actual measurement data due to statistical fluctuations. To address this issue, the criteria suggested by DEL HOYO ET AL. [82] were applied, s. Section 3.4, resulting in the physically correct Müller matrix $M_{\text{LP},0°}$

$$M'_{\text{LP},0°} = \begin{pmatrix} \mathbf{1.0000} & \mathbf{0.9904} & 0.1171 & -0.0001 \\ \mathbf{1.0000} & \mathbf{0.9910} & 0.1192 & 0.0068 \\ 0.0174 & 0.0209 & -0.0059 & -0.0312 \\ 0.0032 & -0.0064 & 0.0301 & 0.0201 \end{pmatrix} \tag{5.24}$$

The matrix elements mostly deviate in the second decimal place. As an additional quantitative criterion, the eigenvalues of the Müller matrix can be investigated: Completely precise azimuthal alignment of the linear polarization filter to $\theta = 0°$ can neither be guaranteed nor verified, however, eigenvalues are invariant under rotation. The theoretical Müller matrix has the eigenvalues

$$\lambda = \quad 1 \quad ; \quad 0 \quad ; \quad 0 \quad ; \quad 0 \tag{5.25}$$

whereas the measured Müller matrix has eigenvalues

$$\lambda \approx \quad 0.9965 \quad ; \quad 0.0028 + 0.0139i \quad ; \quad 0.0028 - 0.0139i \quad ; \quad 0.0000 \tag{5.26}$$

The eigenvalues deviate in the third or even fourth decimal place from the theoretical value, thus underlining the successful application of the ECM.

The expected Müller matrix $M'_{\text{B,-45°}}$ for the birefringent plate at an azimuthal angle of $\theta = 45°$ is

$$M'_{\text{B,-45°}} \approx \begin{pmatrix} 1 & 0 & 0 & 0 \\ 0 & -0.03 & 0 & -1 \\ 0 & 0 & 1 & 0 \\ 0 & 1 & 0 & -0.03 \end{pmatrix} \tag{5.27}$$

in which the birefringent plate is modeled as a phase retarder of $\delta = 0.255$, i.e.

$$\cos(2 \cdot \pi \cdot 0.255) \approx -0.03 \quad ; \quad \sin(2 \cdot \pi \cdot 0.255) \approx 1 \tag{5.28}$$

hence taking the offset from the ideal quarter-wave plate into account by using a phaseshift of 0.255 instead of 0.25 (as indicated by the manufacturer's datasheets, s. Appendix C.4). The normalized calibrated Müller matrix $M'_{\text{B,-45°}}$ was measured to be

$$M'_{\text{B,-45°}} \approx \begin{pmatrix} \mathbf{1.0000} & 0.0203 & 0.0131 & 0.0222 \\ -0.0136 & -0.0518 & 0.1114 & \mathbf{-0.8284} \\ -0.0014 & 0.055 & \mathbf{0.8889} & 0.0561 \\ 0.0138 & \mathbf{0.8910} & -0.0990 & -0.0601 \end{pmatrix} \tag{5.29}$$

The theoretical Müller matrix has the complex eigenvalues

$$\lambda = \quad 1 \quad ; \quad 1 \quad ; \quad (-0.03 + i) \quad ; \quad (-0.03 - i) \tag{5.30}$$

whereas measured matrix has the eigenvalues

$$\lambda \approx \quad 1.0279 \quad ; \quad 0.8885 \quad ; \quad -0.0697 + 0.8641i \quad ; \quad -0.0697 - 0.8641i \tag{5.31}$$

BUENO ET AL. [31] achieved comparable precision using a combination of liquid crystal variable retarders and a removable quarter-wave plate, reporting deviations from theoretical matrix elements in the third decimal place for air and in the second decimal place for a horizontal linear polarizer and a quarter-wave plate. Similarly, BABA ET AL. [20] found deviations in the third decimal place for air and in the second decimal place for a horizontal linear polarizer in reflection mode, using a combination of variable and rotating retarders. Thus, the Scattering Polarimeter demonstrates precision similar to setups with comparable components. However, the birefringent plate exhibits greater deviations from the expected Müller matrix compared to air and the linear polarization filter, suggesting that elements associated with linearity are more accurately determined than those associated with circularity.

Moreover, an inherent limit is imposed to the ECM by the non-ideal natures of the samples: During the calculation of A and W and also during the subsequent evaluations, the samples were assumed to be perfect. Accordingly, improvement to the ECM can be realized by using samples of higher manufacturing quality, although a truly ideal calibration can never be achieved.

Measurement of Brain Tissue Figure 5.21 illustrates the influence of calibration exemplary for Vervet1818-CR: The 4×4 subplots correspond the 4×4 Müller matrix elements of 3648×5427 Müller matrices, one for each image pixel. Notably, matrix elements show increased absolute values and enhanced contrast between gray and white matter. Gray matter and areas without tissue can indicate a successful calibration: Gray matter – as established in Section 2.3.3 – is less turbid, less absorbing and less birefringent than white matter, largely due to the lower content of myelinated fibers. Therefore, gray matter has a lower influence on the optical properties of

the transmitted light, and consequently, diagonal matrix elements are expected to approximate 1 in areas with gray matter, while off-diagonal elements should be close to zero. These expected anatomy-based features align with the observations. Overall, both quantitative and qualitative analyses validate the successful calibration.

5.4.2 High-Speed Müller Routine with 16 Images

The Müller matrices can be calculated with fewer than 36 measurements: Only 16 measurements are required to solve the linear equation system for the 16 matrix elements. However, the minimal measurement routine shown in Section 3.4 unavoidably introduces a propagation of errors across the matrix elements, e.g. BABA ET AL. [20] achieved a lower precision with 16 measurements. For direct comparison, the measurement of 16 images was simulated by taking only those 16 measurements from a set of 36 images that are required to solve the linear equation system shown in Section 3.4. With only 16 measurements, the ECM matrices A and W were found to be

$$A = \begin{pmatrix} \mathbf{1.00} & -0.114 & -0.732 & 0.065 \\ -0.141 & \mathbf{0.751} & 0.3101 & -0.311 \\ -0.549 & 0.554 & \mathbf{1.349} & 0.045 \\ 0.143 & -0.322 & -0.171 & \mathbf{0.951} \end{pmatrix} \tag{5.32}$$

and

$$W = \begin{pmatrix} \mathbf{1.00} & -0.190 & 0.337 & -0.164 \\ -0.089 & \mathbf{0.633} & -0.307 & 0.176 \\ 0.542 & -0.317 & \mathbf{0.683} & -0.066 \\ -0.187 & 0.113 & -0.17 & \mathbf{0.229} \end{pmatrix} \tag{5.33}$$

Figure 5.22 visualizes the Müller elements obtained from 16 measurements for Vervet1818-CR after calibration. Differences to Figure 5.21 become more visible with the propagation of errors towards the lower right corner: m_{33} shows severe deviations from the expected results. To avoid error propagation through the matrix elements, the measurement with 36 images was deemed more reliable and employed for all subsequent investigations.

5.4.3 Transmittance, Diattenuation and Polarizance Maps

Before performing the Lu-Chipman decomposition, several basic parameter maps can be computed from the Müller matrix: The first row of the Müller matrix defines the minimum and maximum transmittance T_{min} and T_{max} of a sample (s. Section 2.2), and thereby provide the diattenuation D. Conversely, the first column of the Müller matrix is associated with the polarizance P, i.e. the ability to polarize previously unpolarized light. Figure 5.23 displays these parameters maps for Vervet1818, Broca, and the artificial crossings of ChiasmX2-7 and ChiasmX2-15.

Minimum and Maximum Transmittance The transmittance highlights regions of gray matter and white matter: In T_{max}, gray matter appears lighter due to higher transmittance, while white matter appears darker because of the lower transmittance[6]. This effect is evident in all tissue samples that contain gray matter (Vervet1818, Broca). Additionally, an increase in transmittance related to the embedding time is expected: Broca (the most recently embedded sample) shows a more distinct separation between

[6] $T_{\text{max}} = \tau$ as defined in 3D-PLI.

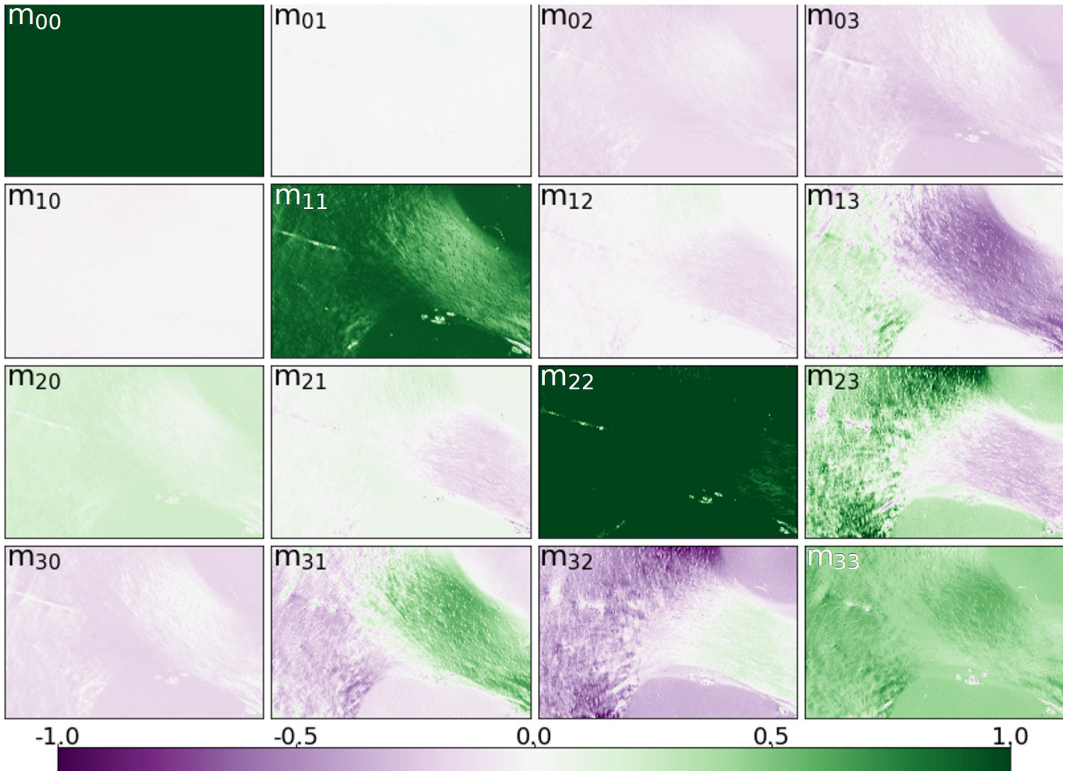

FIGURE 5.22: Müller polarimetry: Vervet1818-CR from 16 measurements. Differences to the measurement with 36 images become more visible with the propagation of errors towards the lower right corner: m_{33} shows severe deviations from the expected results. Thus, the measurement with 36 images is employed for all further investigations.

gray and white matter compared to the older sample Vervet1818. Particularly in the older sample Vervet1818, little contrast is evident between gray matter and inclined or crossing white matter fibers, although strong signals arise from crystallization artifacts. Lower transmittance in the crossing regions of ChiasmX2-7 and ChiasmX2-15 is expected due to the presence of not only one but two tissue layers.

Diattenation and Polarizance The diattenuation D as a composition of linear and circular diattenuation is discussed later in greater detail. Nevertheless, it is already evident that the diattenuation in thin samples is relatively low – yet detectable – when compared with, e.g. an ideal linear polarization filter (D =1). As expected, the diattenuation is significantly stronger in white matter tissue compared to gray matter tissue. Similarly, the polarizance P is also low (compared to 1 for an ideal linear polarization filter). Nonetheless, the symmetrical structure of in-plane parallel white matter fibers operates as a non-ideal linear polarization filter and exhibits a higher polarizance than the surrounding gray matter tissue. Consequently, the polarizance and diattenuation are considerably lower in the crossing regions of ChiasmX2-7 and ChiasmX2-15.

Overall, transmittance, diattenuation, and polarizance map already offer insights into the samples that align with expected optical effects influenced by tissue anatomy. For an in-depth analysis of fiber structure, Lu-Chipman decomposition provides further quantitative information.

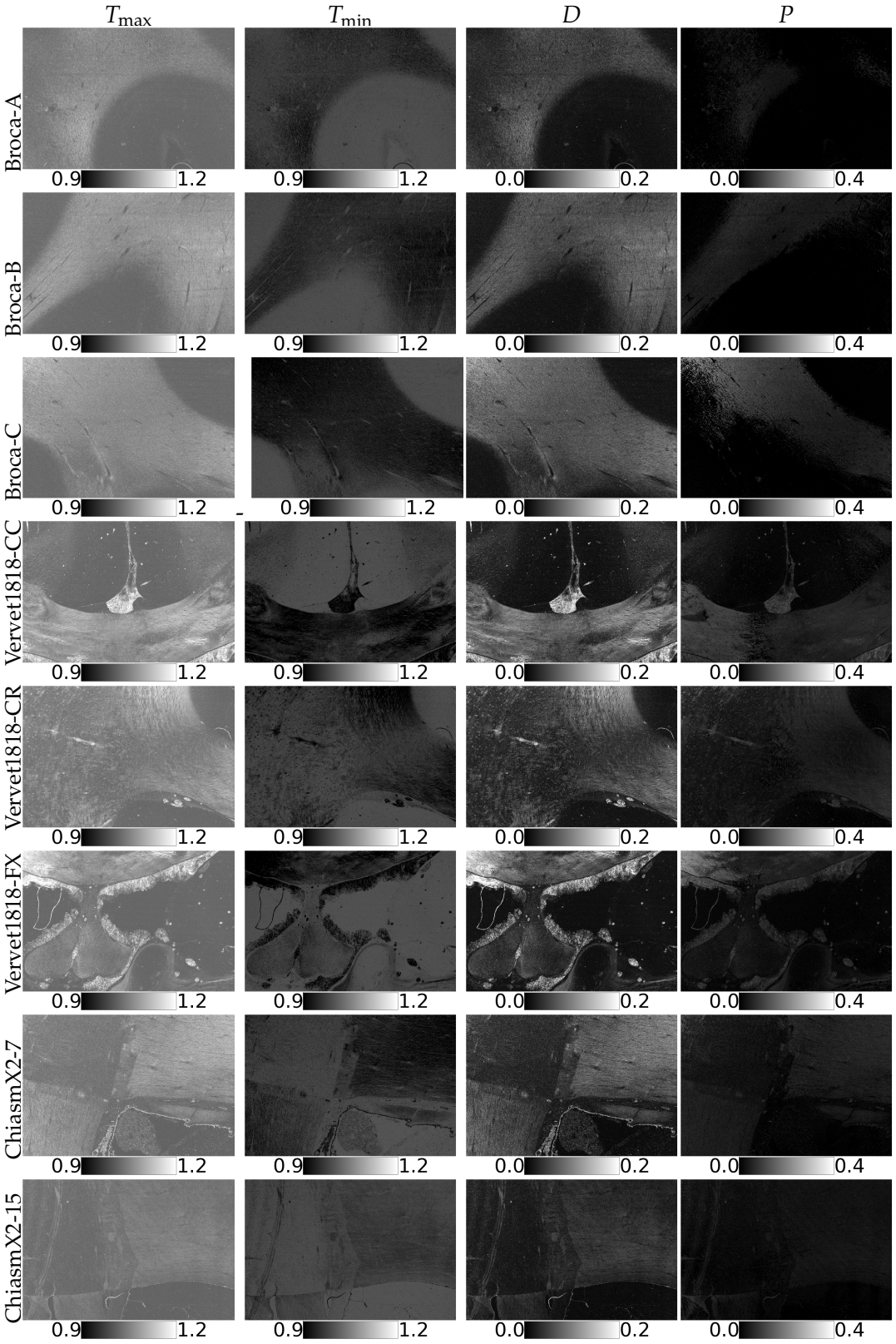

FIGURE 5.23: Müller polarimetry: Transmittance, diattenuation, and polarization maps. From left to right: Maximum transmittance, minimum transmittance, diattenuation, polarizance. From top to bottom: Broca-A, Broca-B, Broca-C, Vervet1818-CC, Vervet1818-CR, Vervet1818-FX, ChiasmX2-7, and ChiasmX2-15.

5.4.4 Lu-Chipman Decomposition

The Lu-Chipman decomposition breaks down a Müller matrix into a retardance matrix, a diattenuation matrix and a depolarization matrix. This decomposition was performed for each image pixel using the Python module *pySCATMECH* [63], which can also automatically calculate most of the scalar optical parameters introduced in Section 2.2.4. Additionally, the depolarization coefficient Δ and the linear depolarization coefficient Δ_L were calculated from the corresponding matrix elements (s. Section 2.2.4).

Decomposed Matrices Figure 5.25–5.26 depict the pixelwise matrices of Vervet1818-CR, calculated from the calibrated Müller matrices in Figure 5.21. All pixels in the upper left subplot take values of 1 because this subplot corresponds to the matrix elements m_{00} which are used for normalization. Theoretically, matrix elements can take values in the range from -1 to 1. The displayed scale is decreased for a better visual contrast of the diattenuation matrices in Figure 5.25 and the depolarization matrices in Figure 5.26. Appendix B.2 shows the decomposition matrices for all samples in Figure B.26–B.42.

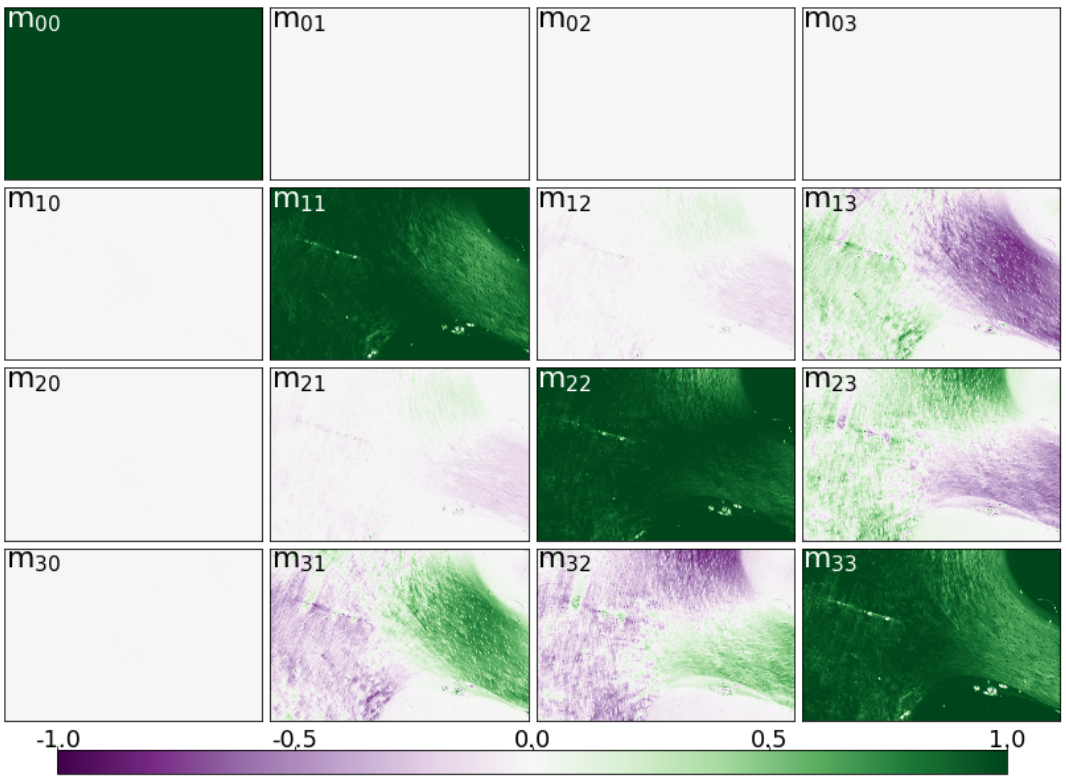

FIGURE 5.24: Lu-Chipman retardance matrix for Vervet1818-CR. The anti-symmetrical corpus callosum area directly indicates the fiber anatomy.

By definition, the diagonal elements of the diattenuation matrix are equal to 1, and the first row is identical to the first column in Figure 5.25. The absolute values of the non-zero off-diagonal elements are relatively low due to the low diattenuation of a thin tissue sample. In contrast, the retardance-related effects are more prominent, as shown by the retardance matrix in Figure 5.24: The anti-symmetry of retardance in the third row and column (associated with circular polarization) is particularly visible in the anti-symmetrical corpus callosum area. By definition, the off-diagonal

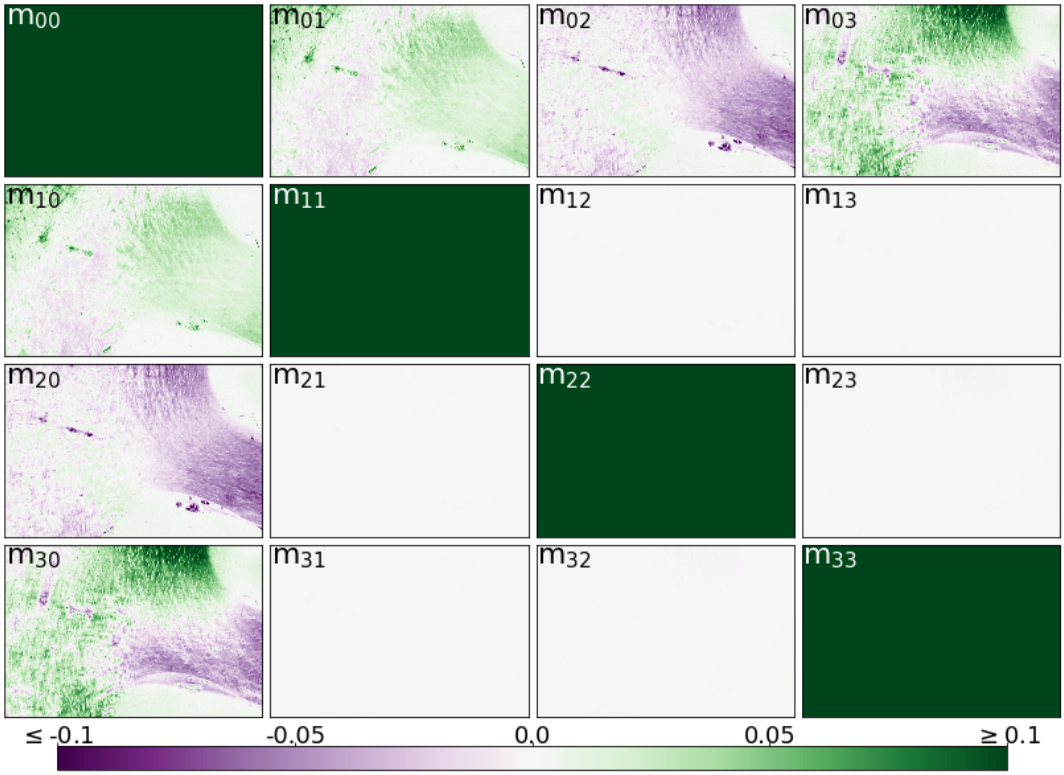

FIGURE 5.25: Lu-Chipman diattenuation matrix for Vervet1818-CC. By definition, the diagonal elements of the diattenuation matrix are equal to 1, and the first row is identical to the first column. The absolute values of the non-zero off-diagonal elements are relatively low due to the low diattenuation of a thin tissue sample.

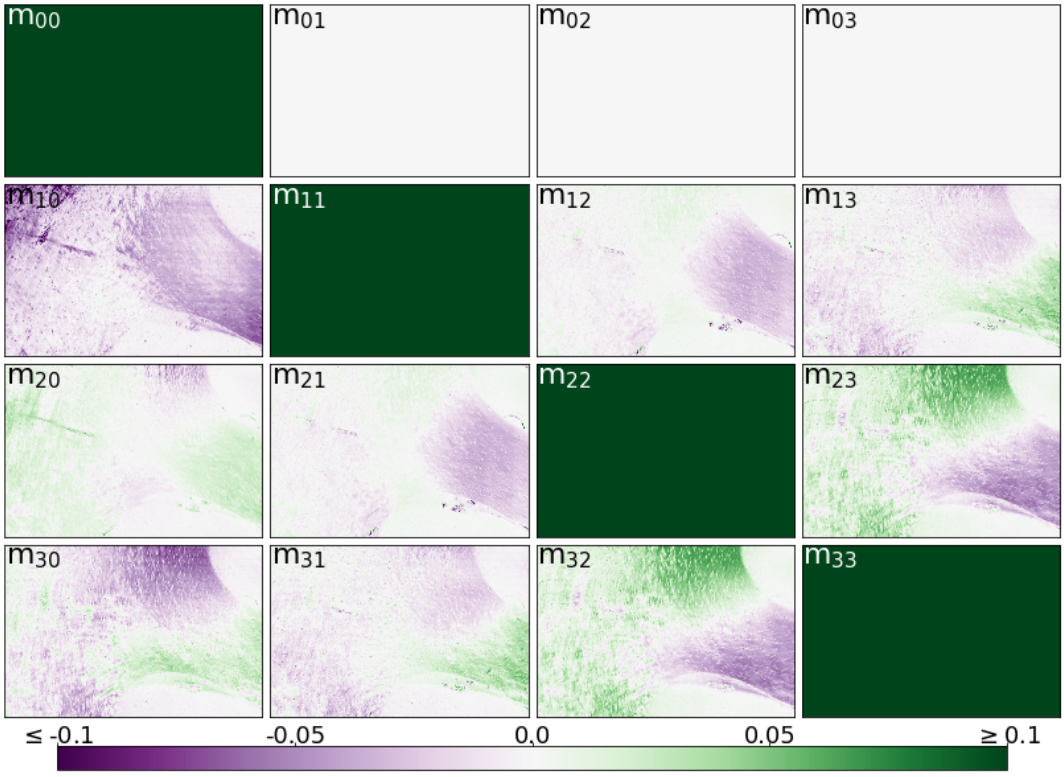

FIGURE 5.26: Lu-Chipman depolarization matrix for Vervet1818-CR. The depolarization-related phenomena are strongest for the crystallized artifacts.

elements of the first row and column in the retardance matrix are zero. The depolarization matrices in Figure 5.26 has a symmetrical structure within its 3×3 lower right submatrix and the off-diagonal matrix elements of the first row are equal to zero by definition. The depolarization-related phenomena are strongest for the crystallized artifacts. Generally, gray matter has comparatively lower retardance, diattenuation, and depolarization, resulting in values close to zero in all matrix elements except for the diagonal elements.

Calculation of Parameter Maps To quantify the observed optical effects, the optical parameters were calculated for every image pixel as introduced in Section 2.2.4, resulting in a set of parameter maps for every sample. In the following, the parameter maps are sorted into diattenuation-related phenomena, retardance-related phenomena and depolarization-related phenomena, each derived from the corresponding matrices. The retardance-related parameter maps are discussed first and later referred to during the discussion of diattenuation-related phenomena.

5.4.5 Retardance Parameter Maps

The retardance R and the linear retardance δ take values between -1 and 1 (for the definition, s. Section 2.2.4). The magnitude of the optical rotation is given in radians within a range from $[-\frac{\pi}{2}, \frac{\pi}{2}]$, i.e. $[-90°, 90°]$. Apart from a phase shift of 90°, the fast axis of retardance directly corresponds to the fiber direction ϕ_{PLI} in 3D-PLI as introduced in Section 3.2. For a corresponding visualization, ϕ'_R was translated into degrees and shifted from the range $[-90, 90]$ to $[0, 180]$ to match the established HSV colormap, yielding the fiber direction angle ϕ_R

$$\phi_R = \frac{180}{\pi}\phi'_R + 90° \qquad \begin{cases} +180° & \text{if } \phi_R \in [-90°, 0°] \\ & \text{if } \phi_R \in [0°, 90°] \end{cases} \tag{5.34}$$

Noise Filtering for the Fiber Orientation Map Two filters were applied to remove noise from the gray matter, again demonstrated for Broca-A and Vervet1818-FX in Figure 5.27: Pixels with a value of exactly 0°, 90° and 180° are displayed in black: Here, the argument x of $\arctan 2(x)$ is $\pm\infty$ or 0, indicating that $m_{R,01}$ or $m_{R,02}$ are exactly zero, respectively. Mathematically, this only happens for pixels with a signal that is too low to detect. This typically occurs for pixels with signals too weak to reliably detect. Being the youngest sample, Broca still exhibits low transmittance, resulting in a lower signal-to-noise ratio compared to Vervet1818, and a major part of the sample is affected. With the adequate filtering, only meaningful signals are displayed. Optionally, pixels below a threshold retardance can be displayed in black, thus masking noise especially in gray matter and background areas, if required. Here, the effect of a threshold of $R < 0.08$ is demonstrated. The effect is best observed in Vervet1818-FX.

Discussion of Parameter Maps Figure 5.28 shows the retardance parameter maps. Linear retardance δ and total retardance R are very similar and furthermore in good agreement with the parameter maps obtained with 3D-PLI as discussed in Section 5.2.7. The magnitude of optical rotation Ψ is generally only a few degrees, despite optical rotation theoretically ranging from -90° to 90°. This is expected, as there are no anatomical structures within brain tissue that would cause optical rotation. Furthermore, the measurements align with the findings from FELGER ET AL. [53]

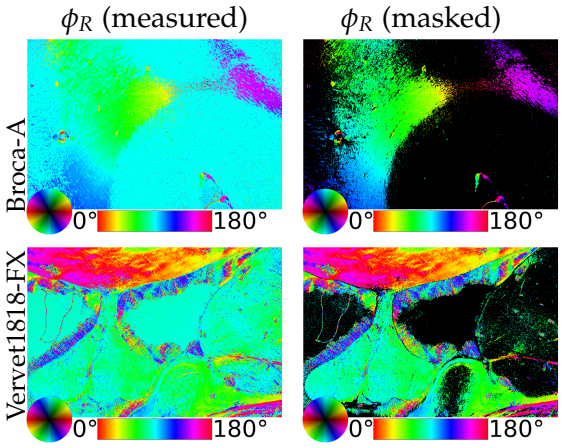

FIGURE 5.27: Müller polarimetry: Retardance-based mask. Pixels with a value of exactly 0°, 90° and 180° are displayed in black to remove mathematical artifacts of the arctan 2(x) function. The effect shows well in Broca-A (first row) where the signal-to-noise ratio is lower. Furthermore, pixels with a retardance $R < 0.08$ can be displayed in black to filter noise especially in gray matter and background areas. The mask covers background and gray matter and is best observed in Vervet1818-FX (second row). However, both filters are applied on both samples.

who found that the average linear retardance[7] is higher in white matter than in gray matter.

Fiber directions are reliable for most pixels, even to some extent in the gray matter of Vervet1818-CC, where fewer nerve fibers are present. However, the less transmitting Broca suffers from a lower signal in its gray matter area. Fiber directions in white matter regions are not as reliably determined as in 3D-PLI. These results are consistent with the parameter maps obtained using 3D-PLI discussed in Section 5.2.7, even though 3D-PLI detects signals in regions where the signal-to-noise ratio in Müller polarimetry is insufficient, especially in gray matter. Future research should aim to improve the signal-to-noise ratio, for example, by utilizing a brighter light source or a more sensitive camera.

5.4.6 Diattenuation Parameter Maps

Technically, the diattenuation D, the linear diattenuation D_L, the circular diattenuation D_C and the axis of diattenuation ϕ'_D can already be identified from the original Müller matrix because the first row of the diattenuation matrix is equal to the first row of the original matrix[8]. The azimuthal axis of (linear) diattenuation in radians is

$$\phi'_D = \frac{1}{2} \arctan 2(m_{D,01}, m_{D,02}) \tag{5.35}$$

This is the angle of maximum transmittance. It directly corresponds to the definition of fiber direction ϕ_{DI} in DI as introduced in Section 3.3. For visualization purposes, ϕ'_D was translated into degrees and shifted from the range $[-90, 90]$ to $[0, 180]$ to match

[7] And depolarization.
[8] This is not obvious from the visualization in Figure 5.25 and Figure 5.21 due to the chosen scale.

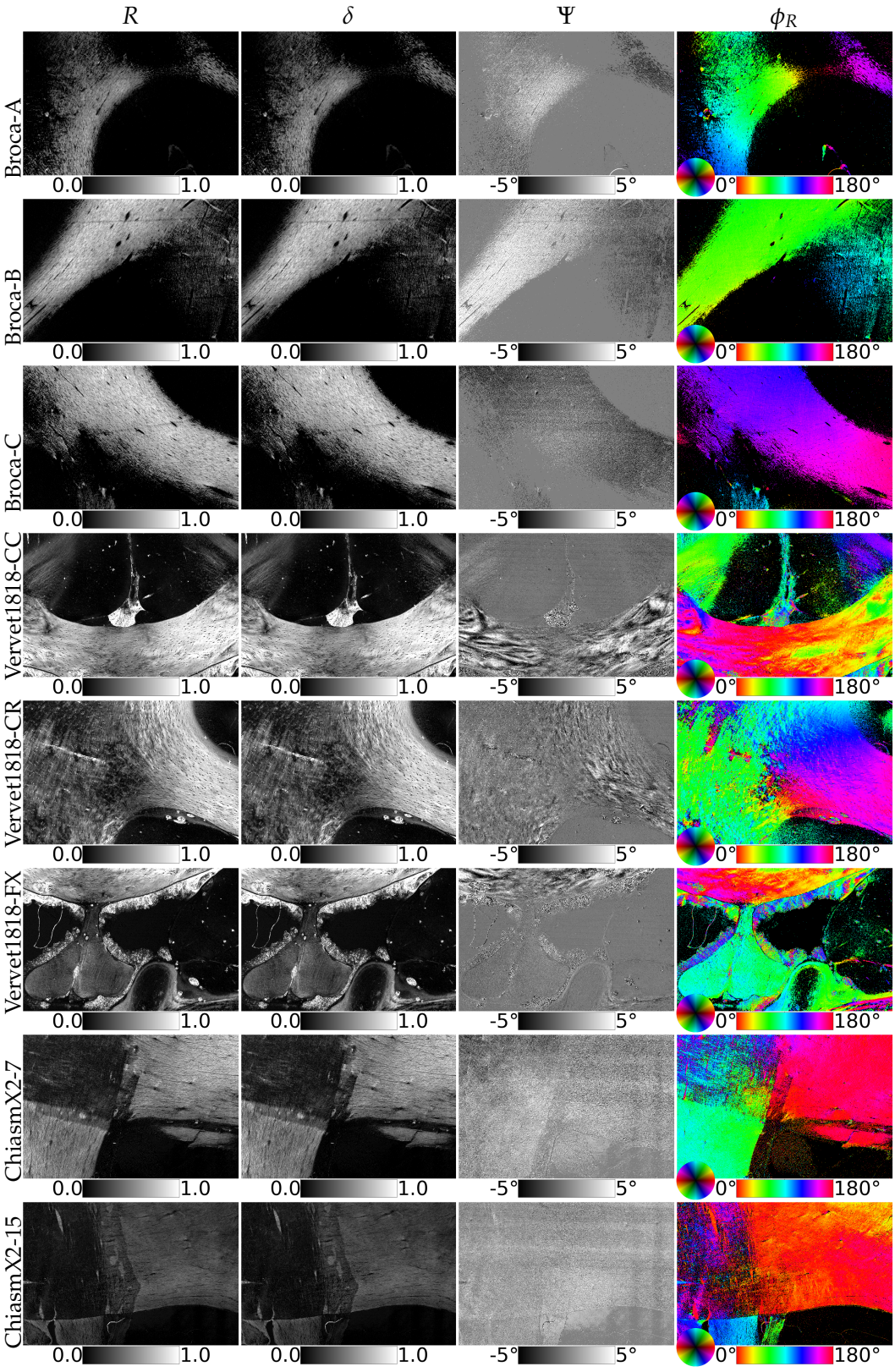

FIGURE 5.28: Müller polarimetry: Retardance maps. From left to right: Retardance R, linear retardance δ, magnitude of optical rotation Ψ, masked fiber direction ϕ_R. From top to bottom: Broca-A, Broca-B, Broca-C, Vervet1818-CC, Vervet1818-CR, Vervet1818-FX, ChiasmX2-7, and ChiasmX2-15.

the established HSV colormap, yielding the fiber direction angle ϕ_D

$$\phi_D = \frac{180}{\pi}\phi'_D \qquad \begin{cases} +180° & \text{if } \phi_D \in [-90°, 0°] \\ & \text{if } \phi_D \in [0°, 90°] \end{cases} \tag{5.36}$$

Noise Filtering for the Fiber Orientation Map Similarly to the retardance filter, two filters were applied to remove noise from the gray matter as demonstrated for Broca-A and Vervet1818-FX in Figure 5.29: Pixels with a value of exactly 0°, 90° and 180° are displayed in black: Here, the argument x of $\arctan 2(x)$ is $\pm\infty$ or 0, indicating that $m_{D,01}$ or $m_{D,02}$ are exactly zero, respectively. This typically occurs for pixels with signals too weak to detect. Broca-A as the youngest sample has still a low transmittance, thus the signal-to-noise ratio is worse than for Vervet1818 and a major part of the sample is affected. With the adequate filtering, only meaningful signals are displayed. Optionally, pixels with a diattenuation $D < 0.02$ can be displayed in black, thus masking noise especially in gray matter and background areas, if required. The effect is best observed in Vervet1818-FX.

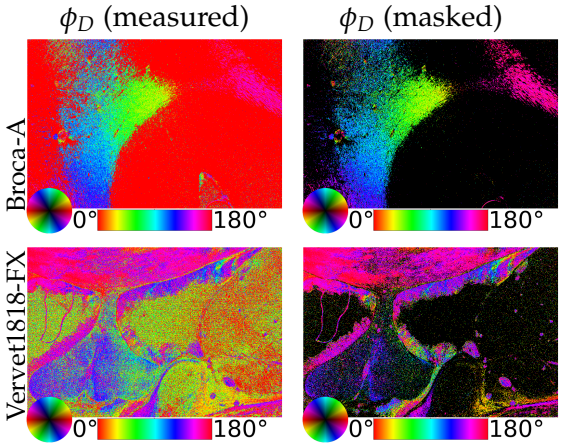

FIGURE 5.29: Müller polarimetry: Diattenuation filters. Pixels with a value of exactly 0°, 90° and 180° are displayed in black to remove mathematical artifacts of the $\arctan 2(x)$ function. The effect shows well in Broca-A (first row) where the signal-to-noise ratio is lower. Furthermore, pixels with a diattenuation $D < 0.02$ are displayed in black to filter noise especially in gray matter and background areas. The mask covers background and gray matter and is best observed in Vervet1818-FX (second row). However, both filters are applied on both samples.

Discussion of Parameter Maps Figure 5.30 displays the diattenuation D, the linear diattenuation D_L, the circular diattenuation D_C and the fiber angle direction ϕ_D (i.e. the angle of maximum transmittance). As expected, diattenuation is generally higher in regions with parallel in-plane fibers. Areas with crossed fibers as in Vervet1818-CR or the overlapping areas in ChiasmX2-7 and ChiasmX2-15 express a lower diattenuation compared to unidirectional fibers because each fiber direction defines its own axis of diattenuation. The total diattenuation D and linear diattenuation D_L are similar in regions with parallel fibers, such as the corpus callosum, the single optic tracts in the artifical crossings and within a large part of Broca-B. However, the crossings and inclined fibers exhibit circular diattenuation to some degree. Circular diattenuation in fiber crossings has not been investigated in literature yet and is low compared to other phenomena. Here, it is unclear whether the observed

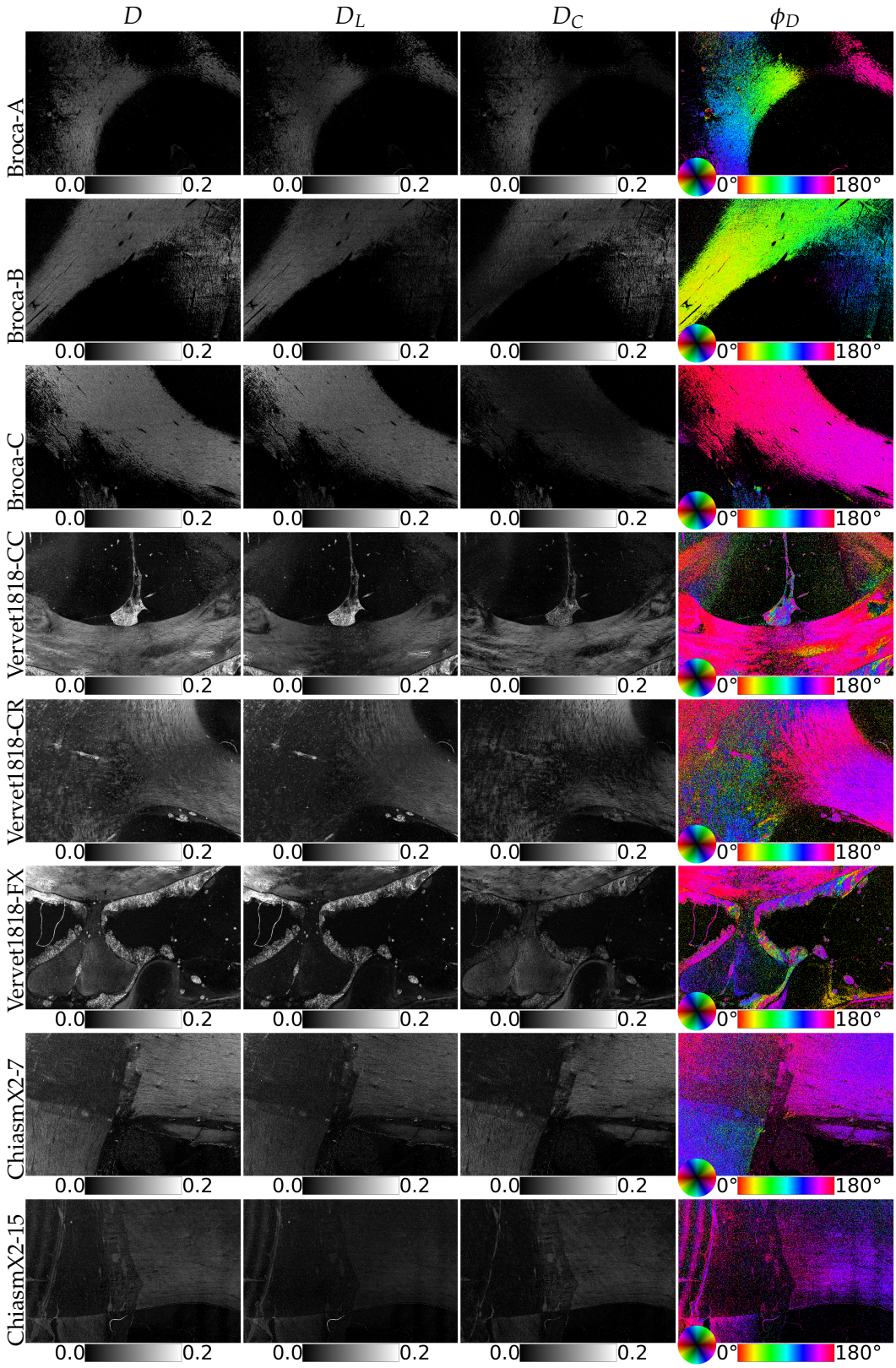

FIGURE 5.30: Müller polarimetry: Diattenuation maps. From left to right: Diattenuation D, linear diattenuation D_L, circular diattenuation D_R, masked fiber direction (i.e. the angle of maximum transmittance) ϕ_D. From top to bottom: Broca-A, Broca-B, Broca-C, Vervet1818-CC, Vervet1818-CR, Vervet1818-FX, ChiasmX2-7, and ChiasmX2-15.

circular diattenuation represents an actual effect or a measurement artifact. Circular diattenuation can be addressed in future research with the Scattering Polarimeter.

MENZEL ET AL. [117] explained how the axis of diattenuation and the fast axis of retardance are related to the fiber direction, and how D^- tissue leads to the observed 90° shift between the fast axis of retardance and the axis of diattenuation [117]. The direct comparison with the fiber directions obtained from the retardance matrix shows similarities and differences: In Vervet1818, directions displayed in magenta/purple dominate most of the tissue for ϕ_D, however, ϕ_R is in good accordance with the expected fiber directions. ϕ_D has no visible connection to the actual fiber directions. Similarly, ChiasmX2-15 is mostly dominated by the same magenta/purple direction as Vervet1818. It is unclear whether ChiasmX2-7 is also affected because the major magenta/purple region actually has this fiber direction. The diattenuation signal is known to be small: It is likely that Vervet1818, ChiasmX2-15 and probably ChiasmX2-7 suffer from a bad signal-to-noise ratio and a yet unidentified effect becomes dominant, possibly even caused by, e.g. the object carrier. For Broca, however, the directions obtained from ϕ_D and ϕ_R agree with each other. Furthermore, ϕ_D agrees also with the diattenuation reference measurement for Broca in Section 5.3.4 performed with the LAP, even though far less pixels are evaluated. The successful evaluation of Broca indicates that the measurement is not flawed in general.

Overall, the study of diattenuation in brain tissue is still a young field of research and holds many open questions. The causes of diattenuation in brain tissue, but also of the object carrier, the embedding medium, and the age-related change of diattenuation need to be studied more in the future. Similar to retardance measurements, improving the signal-to-noise ratio through brighter light sources or more sensitive cameras can improve measurement precision in diattenuation studies.

5.4.7 Depolarization Parameter Maps

The total depolarization Δ and the linear depolarization Δ_L both range from 0 to 1. Complete depolarization is indicated by values of 1, and no depolarization by 0. However, Δ and Δ_L take similar values, as shown in Figure 5.31. Depolarization can differentiate between gray and white matter, as demonstrated by SCHUCHT ET AL. [169], RODRÍGUEZ NÚNEZ ET AL. [159] and FELGER ET AL. [53]: the cell-dense cortex shows less depolarization compared to white matter because there is more light scattering in white matter, as established in Section 2.3. These observations align with the measurements obtained here. Artifacts exhibit particularly high depolarization due to chaotic scattering structures.

Discussion of Parameter Maps Figure 5.31 presents binary maps that differentiate gray and white matter by setting a threshold of $\Delta > 0.01$ to identify white matter. Generally, the threshold-based differentiation agrees with the anatomical distribution of white and gray matter. However, distinguishing between gray and white matter remains challenging in certain areas, especially where fiber crossings occur, as observed in Vervet1818-CR, ChiasmX2-7, and ChiasmX2-15. Furthermore, background areas and gray matter cannot be distinguished because both exhibit a close-to-zero depolarization. Additionally – and similar to its retardance and diattenuation maps – Broca could benefit from an improved signal-to-noise ratio to improve the detection of white mater regions. A more refined distinction between white and gray matter or even various white matter fiber architectures requires information from additional parameter maps and is developed in Chapter 6.

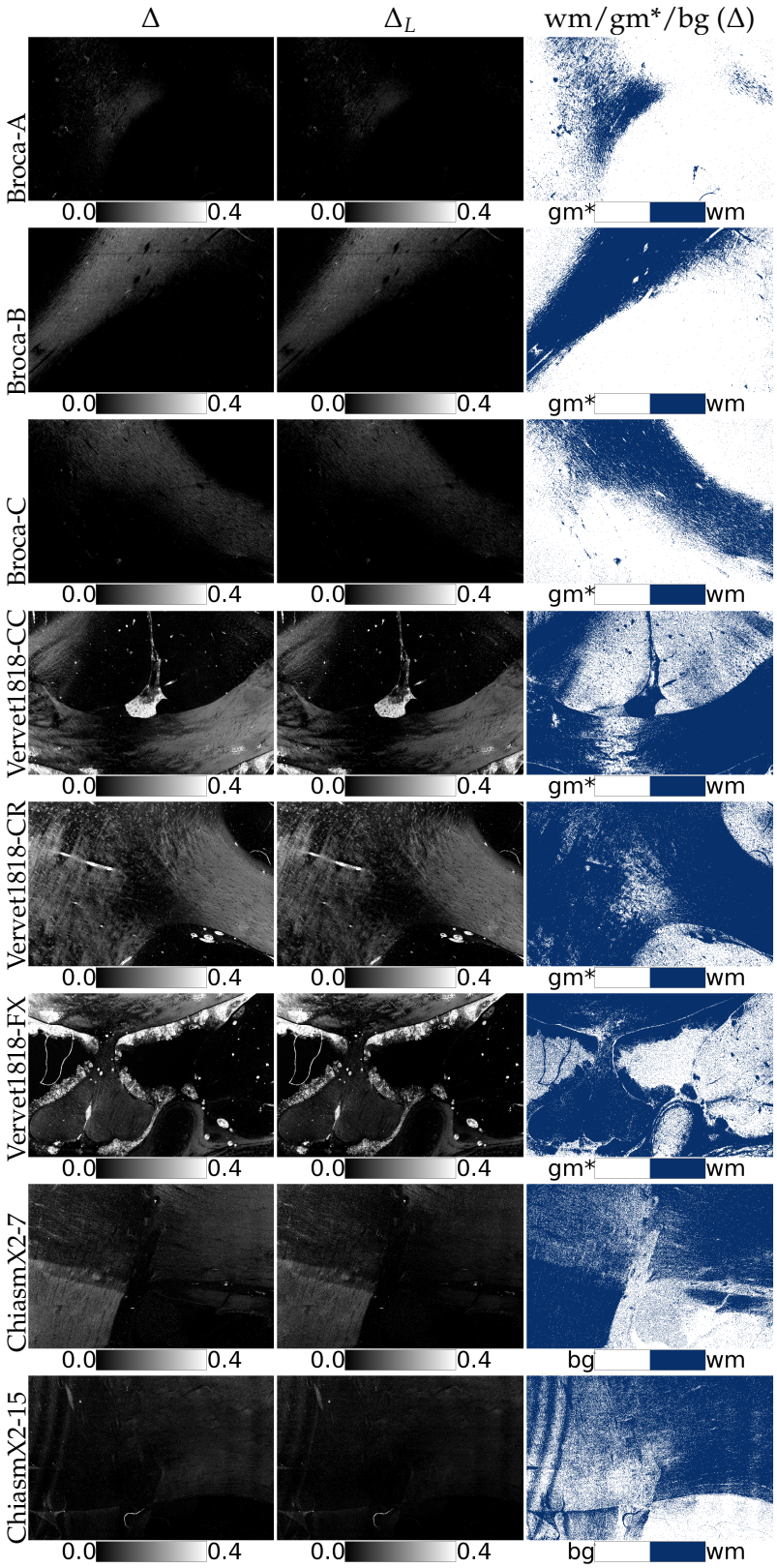

FIGURE 5.31: Müller polarimetry: Depolarization maps. From left to right: Depolarization Δ, linear depolarization Δ_L, mask for white matter (wm) and gray matter (gm*) or wm and background (bg) based on the Δ. gm* indicates that gray matter and background cannot be distinguished because both exhibit a close-to-zero depolarization. From top to bottom: Broca-A, Broca-B, Broca-C, Vervet1818-CC, Vervet1818-CR, Vervet1818-FX, ChiasmX2-7 and ChiasmX2-15.

5.4.8 Müller Polarimetry with Elliptical Polarization States

As established in Section 3.4.2, Müller polarimetry achieves the best signal-to-noise ratio when the employed polarization states are at the vertices of a tetrahedron inscribed inside the Poincaré sphere, rather than using the 6 basic polarization states. This was shown by AZZAM ET AL. [18, 19]. DE MARTINO ET AL. [46] proposed settings for the retardance δ_i and the azimuthal angles θ_i. Those settings can be adapted for the Scattering Polarimeter, however, this fundamentally changes the generation of linear polarization states for 3D-PLI. With $\theta_1 = 27.4°$ and $\theta_2 = 72.4°$, the output polarization state of the PSG is given by Müller calculus as

$$\vec{S}_{\text{PSG}} = M(\theta = 72.4°, \delta) \cdot M(\theta = 27.4°, \delta) \cdot \vec{S}_H \tag{5.37}$$

$$\approx \begin{pmatrix} 1 \\ 0.03 - 0.70\cos\delta_1 + 0.12\cos\delta_2 + 0.39\cos\delta_1\cos\delta_2 - 0.43\sin\delta_1\sin\delta_2 \\ 0.20 + 0.65\cos\delta_1 - 0.02\cos\delta_2 + 0.43\cos\delta_1\cos\delta_2 + 0.70\sin\delta_1\sin\delta_2 \\ 0.05\cos\delta_1\sin\delta_2 + 0.57\sin\delta_2 - 0.82\cos\delta_2\sin\delta_1 \end{pmatrix} \tag{5.38}$$

The full calculation is provided in Appendix A.6. DE MARTINO ET AL. [46] provided the settings for δ_1 and δ_2 for Müller polarimetry as $\delta_1 = 315° + p90°$, $\delta_2 = 135° + p90°$ with p being the same integer. However, the settings for 3D-PLI have become significantly more complex. For linear polarization, S_3 must be equal to 0, and S_1 and S_2 must achieve equidistant polarization angles. While an appropriate set of δ_1 and δ_2 can be calculated to meet these requirements, the error calculations performed in Section 5.2.2 are no longer applicable.

5.5 ComSLI

The Scattering Polarimeter realizes ComSLI measurements by displaying angular illumination patterns on a large-area light source, thus bypassing the elements of the polarization state generator (PSG). The vertically scattered light is detected by the camera. Within this section, only angular ComSLI is investigated. Image data was pre-processed with the SLI Toolbox (SLIX), generating initial parameter maps.

The main advantage of ComSLI is the measurement of fiber crossings. Consequently, the feasibility of distinguishing multiple fiber directions per image pixel is investigated, especially in Vervet1818-CR and the artificial fiber crossings of ChiasmX2-7 and ChiasmX2-15. Furthermore, no additional false directions should be detected in regions with parallel fibers. Reference measurements were performed with the ComSLI setup as presented in Section 3.6.3. Section 5.6 summarizes the performance of ComSLI in direct comparison with the other three modalities.

5.5.1 Average Maps and Peak Prominence Maps

In the context of the Scattering Polarimeter, the ComSLI average map reveals different fiber architectures through variations in brightness. Figure 5.32 displays the average maps for Vervet1818 and Broca. The brightness values distinguish gray matter, background, and various white matter fiber structures: the background appears dark, gray matter shows less scattering than white matter, and specific fiber arrangements (e.g. steep and crossing fibers) appear brightest in the average map.

Average Map In Vervet1818, inclined, crossing, and in-plane parallel fibers can be identified by their distinct brightness levels. Notably, in Vervet1818-CC, the steep fibers of the cingulum exhibit a bright contrast against both the surrounding gray matter and the corpus callosum. Similarly, in Vervet1818-CR, the crossing fibers in the corona radiata appear brighter than the corpus callosum. However, gray matter and in-plane white matter fibers are less distinctly separated based on brightness in Vervet1818 compared to Broca, likely due to the old age of the sample, which generally results in reduced scattering. In contrast, Broca, being newer, exhibits much higher overall scattering, as indicated by the chosen value range for visualization. The average map separates background areas without fibers from both gray matter and white matter. Furthermore, the distinction between gray and white matter is more prominent. Therefore, the average map serve as a solid foundation for tissue classification in the following.

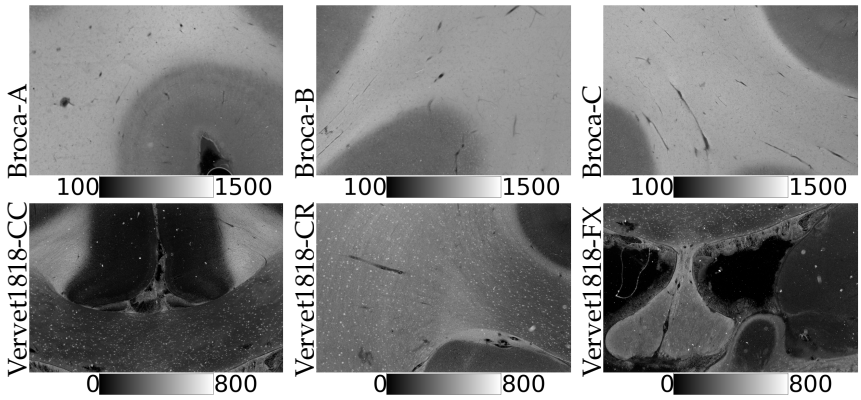

FIGURE 5.32: ComSLI: Average maps for Broca and Vervet1818. First row: Broca-A, Broca-B, Broca-C. Second row: Vervet1818-CC, Vervet1818-CR, Vervet1818-FX. Gray matter, background and various white matter fiber structures can be distinguished by their brightness value. The scattering is lower in Vervet1818 compared to Broca due to the different time since embedding of the samples.

Peak Prominence Map The signal strength in ComSLI is indicated by the peak prominence map, which represents the ratio of high peaks to low peaks. Low prominence peaks typically indicates noise, therefore the peak prominence map directly corresponds to the signal-to-noise ratio. Crossing fibers inherently have lower peak prominence, although the peak prominence is still higher than statistical noise. Figure 5.33 displays the peak prominence: In-plane parallel fibers (such as those in the corpus callosum) and inclined parallel fibers (such as those in the fornix) generally show higher peak prominence compared to crossing fibers (like in the corona radiata). Gray matter and background exhibit lower peak prominence values.

Threshold-Based Tissue Classification When combining features from the average map and the peak prominence map, fiber structures can be roughly classified by their distinct appearance: In-plane parallel fibers show weaker scattering in the average map (however, stronger than in gray matter) but a high peak prominence. Inclined parallel fibers are defined by strong scattering and a high peak prominence. Crossing fibers have stronger average scattering but a lower peak prominence. A tissue classification based on both the average maps and the peak prominence maps is used in Chapter 6.

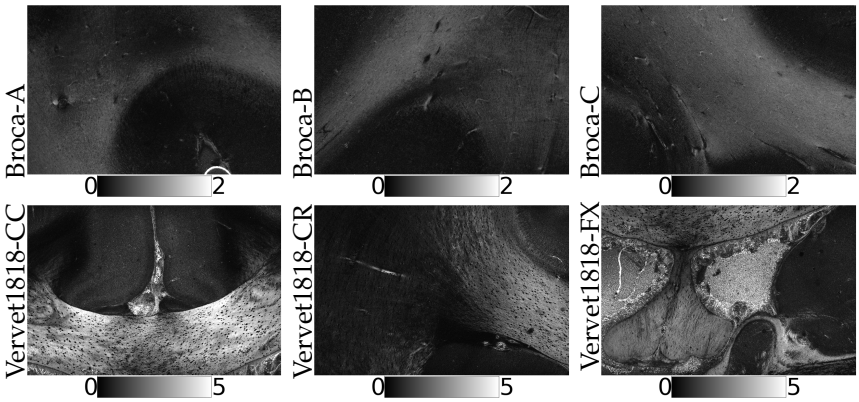

FIGURE 5.33: ComSLI: Peak prominence maps for Broca and Vervet1818. First row: Broca-A, Broca-B, Broca-C. Second row: Vervet1818-CC, Vervet1818-CR, Vervet1818-FX. White matter fiber structures can be distinguished by their brightness value in the peak prominence map. The peak prominence is generally higher for in-plane parallel fibers (corpus callosum) or inclined parallel fibers (fornix) compared to crossing fibers (corona radiata). Gray matter and background have a lower peak prominence.

5.5.2 Background Masking

Due to statistical effects in the line profiles, SLIX sometimes identifies noise as fiber directions. The false directions appear as single colored pixels in regions that are otherwise displayed in black, e.g. in background areas without tissue and in gray matter where the signal from potential fibers is typically so low that these regions mainly consist of noise with no preferred directions. By setting thresholds based on the average map, false directions can be filtered out and the corresponding pixels are displayed in black.

The actual threshold values for the average map depend on the sample, especially its age and thickness, as these factors significantly influence scattering intensity. Figure 5.34 displays the average map, the measured fiber orientation map and the masked fiber orientation map for Vervet1818-FX and ChiasmX2-7. For Vervet1818, average scattering $\geq$200. For Broca, average scattering $\geq$800 (used in subsequent sections). For ChiasmX2-7 and ChiasmX2-15, average scattering $\geq$100.

5.5.3 Reference Measurements

Reference measurements were performed with the ComSLI setup using green angular illumination in steps of 15° (segment width: 9°, inner radius: 28 LEDs, outer radius: 69 LEDs) and the following settings: Vervet1818 was measured with an exposure time of 500 ms, a gain of 3 dB and 4 repetitions. ChiasmX2-7 and ChiasmX2-15 were measured with an exposure time of 2 seconds, a gain of 0 dB and 4 repetitions and already with the new high-sensitivity camera introduced in Section 7.2. Broca was measured with an exposure time of 5 seconds, a gain of 0 dB and 4 repetitions, also with the new camera, aiming at the best possible signal with an already comparatively long exposure time for the highly scattering sample.

Fiber directions were obtained with SLIX, and FOMs and vector maps were calculated from the three directions. Background masking was not used to compare statistical background noise and noise in gray matter for both setups. All displayed vector lengths in vector maps are weighed with the corresponding average map. Vector

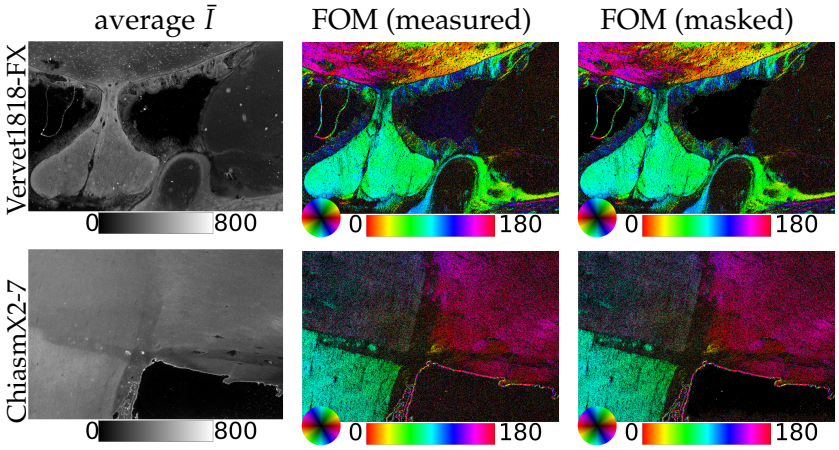

FIGURE 5.34: ComSLI: Background masking based on the average map. From left to right for Vervet1818-FX (top) and ChiasmX2-7 (bottom): Average map $\bar{I}$ a.u, measured (unmasked) FOM, masked FOM. A threshold based on the average map can cover false fiber directions caused by statistical noise. False fiber directions appear as pixels in various colors in background areas of the unmasked FOM. The masked FOM displays those pixels in black.

maps for the Scattering Polarimeter are displayed with a thinout of 20 (i.e. only showing every 20-th vector), vector maps from the ComSLI setup either have a thinout of 10 (Vervet1818) or 20 (ChiasmX2-7, ChiasmX2-15) which is chosen to approximately match the vector maps from the Scattering Polarimeter and depends on the camera sensor pixels and the objective lens.

Vervet1818 Figure 5.35 compares the fiber orientation maps (FOMs) of Vervet1818 with the reference measurement from the ComSLI setup. Overall, the Scattering Polarimeter provides comparable fiber directions and crossings, with only minor deviations. Fiber crossings in the corona radiata are resolved similarly to those in the ComSLI setup. The boundary between parallel fibers in the corpus callosum (bold colors) and crossing fibers in the corona radiata (pastel colors, caused by the 2×2 visualization pixels with different colors in crossing regions) follows the same path as in the reference measurement, indicating similar resolution for fiber crossings in both setups.

As expected, tissue borders are significantly influenced by artifacts that scatter light chaotically. Background noise levels are similar in both setups. Fiber directions in the gray matter and the cingulum are not resolved in either the reference measurement or the Scattering Polarimeter measurement: The fiber density in gray matter is very low and the fiber bundles of the cingulum are nearly orthogonal to the sectioning plane which is why the directional signal is low compared to statistical noise. The required exposure time for a clear signal is much longer for the Scattering Polarimeter (4 seconds vs. 500 ms). A generally lower signal-to-noise ratio for the Scattering Polarimeter is indicated by the presence of more dark pixels in the FOM, where no fiber direction is detected, such as in the center of the corpus callosum.

Vector maps for exemplary subregions in Figure 5.36 suggest that the signal-to-noise ratio is slightly worse, especially for the crossing fibers in the corona radiata. The two crossing fiber directions in the exemplary region are detected but appear noisier (i.e. containing false directions, mostly visualized as yellow or blue vectors overlaying the original two directions) in the Scattering Polarimeter. The in-plane parallel fibers

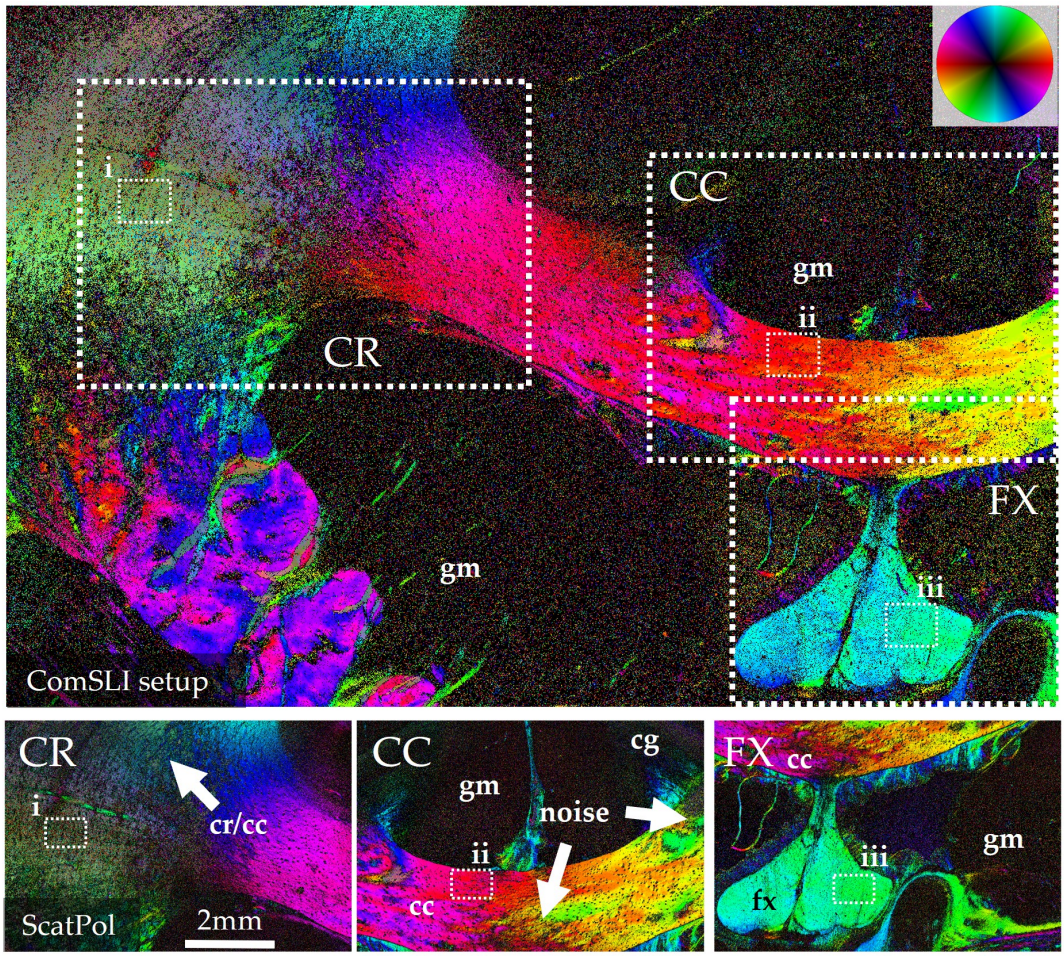

FIGURE 5.35: ComSLI: Vervet1818 FOM compared to reference. In the reference measurement with the ComSLI setup (upper FOM), the regions measured with the Scattering Polarimeter (FOMs in the second row) are indicated. Smaller rectangles marked with i, ii, iii indicate the regions for which the vector maps are compared in Figure 5.36. The Scattering Polarimeter has a worse signal-to-noise ratio indicated by more dark pixels, e.g. in the corpus callosum (cc). The border between parallel fibers (bold colors) and crossing fibers (cr/cc border) has the same course for both setups. Fiber directions in gray matter (gm) are not resolved in any of the setups.

of the corpus callosum are detected with comparable precision. Local artifacts—most likely from the embedding medium—manifest as rainbow-colored "wheels" and are independent of the setup, although in the white matter, these artifacts are typically limited to single pixels. The inclined parallel fibers of the fornix show a dominant direction (blue/green) plus a minor secondary direction (red/magenta) for both the ComSLI setup and the Scattering Polarimeter.

ChiasmX2-7 and ChiasmX2-15 Measuring ChiasmX2-7 and ChiasmX2-15 can demonstrate the ability of the Scattering Polarimeter to measure and distinguish regions with parallel and crossing fibers. The FOMs in Figure 5.37 and the exemplary vector maps in Figure 5.38 confirm the observation that the signal-to-noise ratio is lower for the Scattering Polarimeter compared to the ComSLI setup.

White matter regions appear darker due to more unresolved pixels and more falsely identified fiber directions. In fact, the vector maps show one additional direction

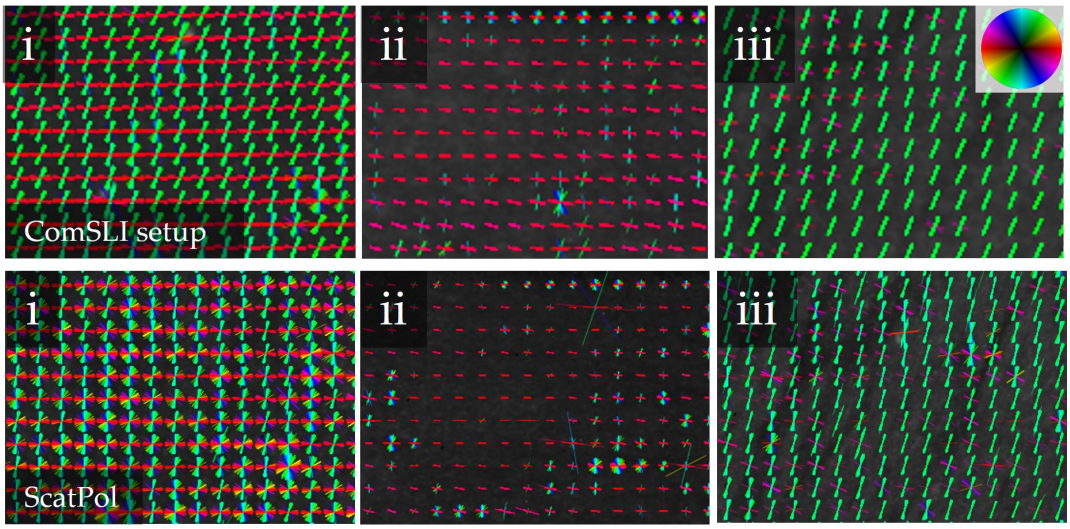

FIGURE 5.36: ComSLI: Vervet1818 vector map compared to reference. First row: Vector maps obtained with the ComSLI setup. Second row: Vector maps for the same regions obtained with the Scattering Polarimeter. Color-coded vectors display the detected fiber directions for exemplary regions with characteristic fiber architectures, indicated in Figure 5.35. i) The two crossing fiber directions of the corona radiata appear noisier (i.e. more than two colors) for the Scattering Polarimeter. ii) The in-plane parallel fibers of the corpus callosum are detected with comparable precision. iii) The inclined parallel fibers of the fornix show a minor secondary direction for both the ComSLI setup and the Scattering Polarimeter.

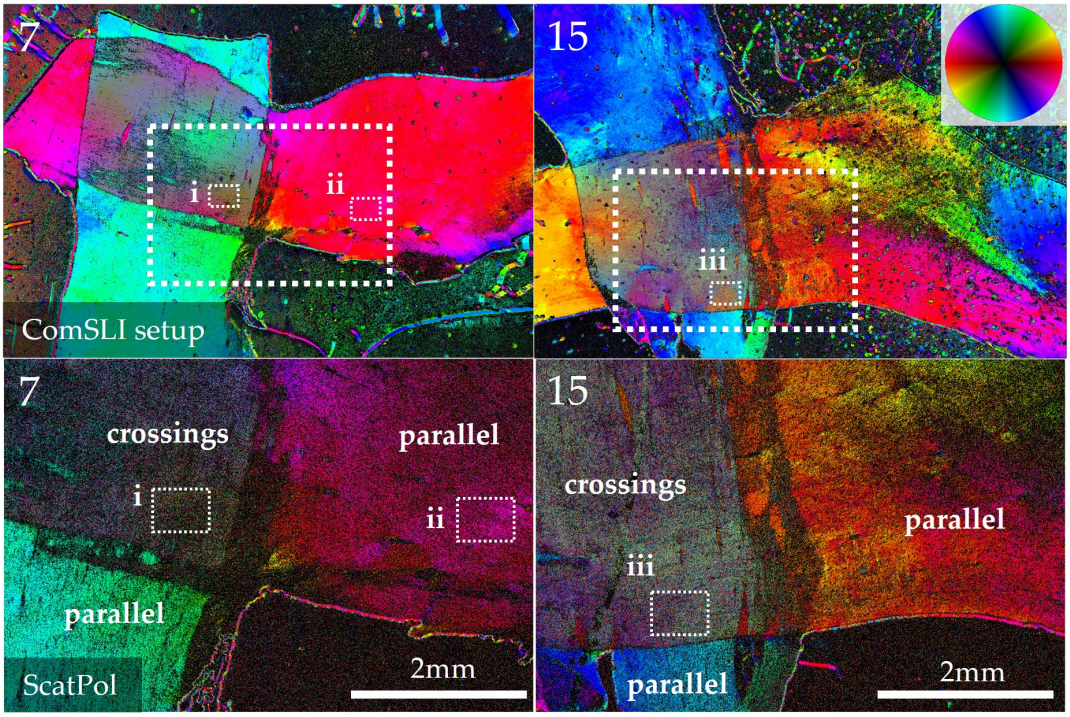

FIGURE 5.37: ComSLI: ChiasmX2-7 and ChiasmX2-15 FOM compared to reference. In the reference measurement with the ComSLI setup (upper FOM), the regions measured with the Scattering Polarimeter (FOMs in the second row) are indicated. The signal-to-noise ratio is worse for the Scattering Polarimeter, indicated by more dark pixels both for parallel fiber directions and crossings.

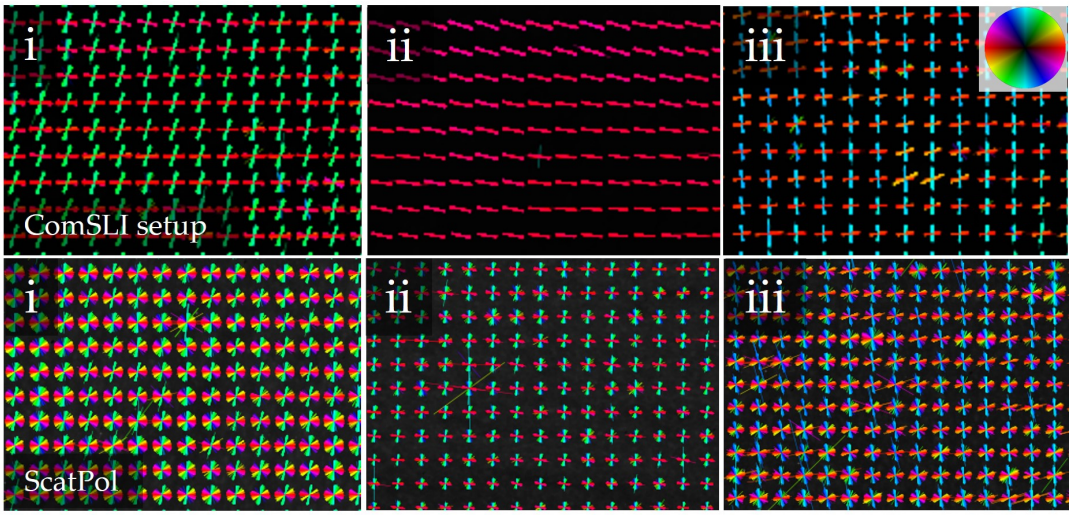

FIGURE 5.38: ComSLI: ChiasmX2-7 and ChiasmX2-15 vector maps compared to reference. First row: Vector maps obtained with the ComSLI setup. Second row: Vector maps for the same regions obtained with the Scattering Polarimeter. Zoom-ins for two crossing regions and one area with parallel fiber bundles are shown, as indicated in Figure 5.37. Major fiber directions are correctly detected. However, the signal from the Scattering Polarimeter suffers from noise, as indicated by additional wrong fiber directions.

for in-plane parallel fibers and noisy directional signals for crossing fibers. Despite these issues, the major fiber directions are still correctly identified. Refining the measurement routine with an optimized exposure time etc. and employing a more sensitive camera, as discussed in Section 7.2, could improve the stable detection of fiber directions.

Broca Increased scattering in the Broca region results from the shorter time since tissue embedding, leading to a lower signal-to-noise ratio that prevents the fiber directions in some white matter areas from being detected. Specifically, the indicated area (white arrow) and its surroundings in Broca-A show predominantly noise, which is more pronounced in the Scattering Polarimeter measurement compared to the reference measurement. Conversely, Broca-B exhibits an area with improved pixel evaluation in the indicated tissue regions. Therefore, performance varies depending on the underlying tissue.

Despite long exposure times, both setups reach their limits for Broca, with the ComSLI setup performing only slightly better. Both the reference and Scattering Polarimeter measurements show almost no signal in gray matter. The light source in the Scattering Polarimeter is less bright than that in the ComSLI setup, where a brighter light source contributes to better signal quality. Upgrading the Scattering Polarimeter with a brighter light source could enhance the signal-to-noise ratio and overall performance.

Summary The Scattering Polarimeter performs best for Vervet1818 due to the high transmittance in the sample. However, the Scattering Polarimeter suffers from noise in the directional signals, indicated by more black pixels in the FOM and additional fiber directions or only statistical noise in the vector maps, especially in crossing regions. Detecting fiber directions in gray matter remains challenging for both setups.

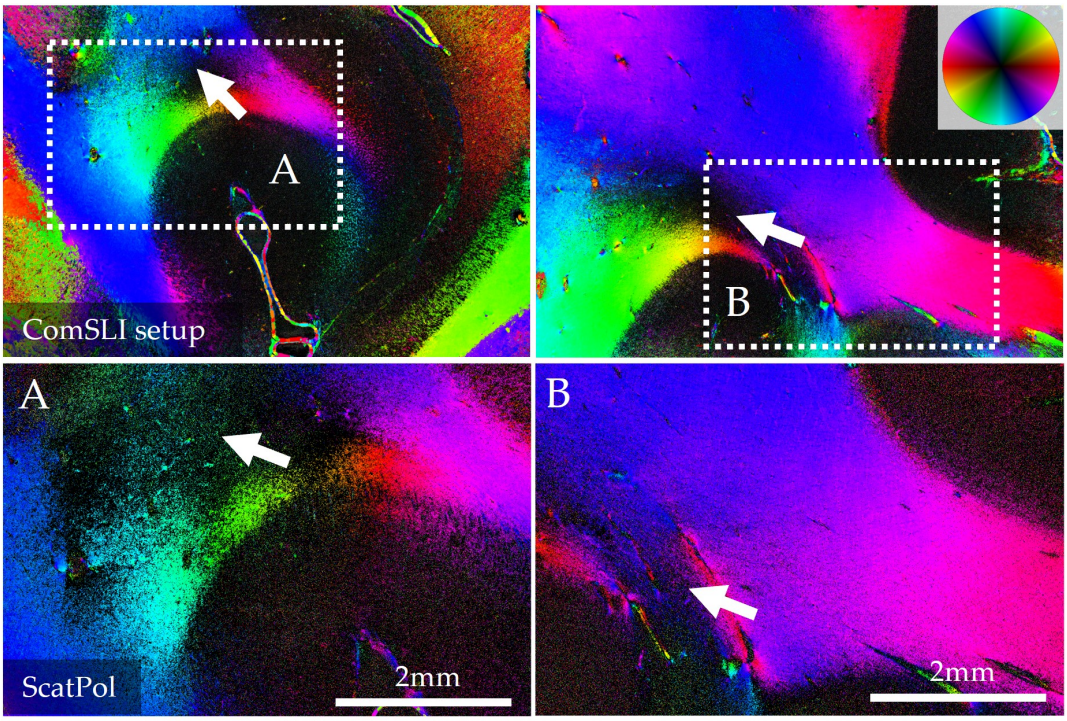

FIGURE 5.39: ComSLI: Broca FOM compared to reference. In the reference measurement with the ComSLI setup (upper FOM), the regions measured with the Scattering Polarimeter (FOMs in the second row) are indicated. More scattering occurs in Broca. This results in a lower signal-to-noise ratio, preventing the indicated white matter areas (white arrow) from being resolved in Broca-A. Broca-B exhibits an area with the opposite effect, with slightly more pixels being evaluated in the indicated tissue regions. Thus, performance varies depending on the underlying tissue. However, both setups reach their limit for the low transmittance sample Broca.

ComSLI measurements are typically performed on tissue that has been embedded long enough for transmittance to decrease. For relatively freshly embedded samples, both the Scattering Polarimeter and the ComSLI setup reach their limits. High light source brightness and long exposure times are necessary for obtaining a sufficient signal.

In Section 6.2, a multi-modal FOM is presented that improves the directional signal with information obtained from 3D-PLI which enhances specifically the signal in gray matter. Future studies should focus on improving performance in gray matter and low transmittance samples by enhancing the signal-to-noise ratio with a brighter light source.

5.6 Summary of All Modalities

Scattering Polarimetry seeks to optimally combine 3D-PLI, DI, Müller polarimetry, and ComSLI to make use of the strengths and compensate the weaknesses of each modality. This chapter concludes with a discussion of the strengths and limitations of each technique, also mentioning which are specific to the Scattering Polarimeter and which are inherent to the modality itself. For clarity, the main characteristics of each technique are summarized in bullet points before delving into more detailed analysis. All modalities can benefit from a brighter light source, a more sensitive camera and

a thorough parameter study to determine optimal measurement settings for each modality.

5.6.1 3D-PLI

Parameters: Inclination (retardation), direction, transmittance
Strengths: Stable for weak signals, even gray matter, speed-up possible
Weaknesses: No analytical calibration

3D-PLI provides reliable measurements of fiber directions and inclinations when adequate retardation normalization is applied. The Fourier fit effectively smooths statistical noise and stabilizes the signal, allowing the detection of weak signals even in gray matter, where the fiber density is comparatively low. Additionally, measurement speed can be increased by a larger angular step size $\Delta\rho$, resulting in fewer measurement images. The experiments have shown that inclinations and directions are retrieved using as few as 6 measurement images, compared to the 36 images required for Müller polarimetry. This stability of the 3D-PLI signal is a great advantage for the Scattering Polarimeter. However, 3D-PLI has a limitation due to the lack of retardation calibration which becomes apparent for low contrast samples such as Vervet1818 and when using 3D-PLI signals for DI. Any elliptical deviation introduced by the system can distort the transmittance and, to a lesser extent, the retardation. This issue is inherent to the method: Even though the Scattering Polarimeter specifically allows to determine the Müller matrix for the PSG and PSA – because the Scattering Polarimeter is a complete polarimeter, unlike classical 3D-PLI setups – the modified formula for the 3D-PLI intensity curve cannot be solved without previous knowledge about tissue parameters. This problem is more apparent for the Scattering Polarimeter because the LCVRs are less precise than rotating mechanical elements.

5.6.2 DI

Parameters: Diattenuation, D^+/D^- (in combination with 3D-PLI), transmittance
Strengths: Transmittance map
Weaknesses: Error propagation from 3D-PLI

The diattenuation signal is inherently low, making it difficult to measure accurately even with a specialized setup. Statistical noise and systematic deviations hinder the evaluation. In the Scattering Polarimeter routine, errors from 3D-PLI propagate and distort the summarized DI signal. This distortion makes it impossible to clearly distinguish between retardance and diattenuation. Although DI and 3D-PLI may appear to yield the same directions (indicating D^+ tissue, as expected), the amplitude is highly influenced by the retardance, not by the actual diattenuation. Ideally, diattenuation imaging should be performed using ECM-calibrated results from Müller polarimetry, despite requiring more measurement images than standard DI. In the DI transmittance map, the transmittance asymmetries from LC and RC cancel out. Therefore, the DI transmittance map has still a practical application and can potentially replace the 3D-PLI transmittance map in multi-modal parameter analysis where tissue transmittance is investigated. Research should aim to reduce systematic errors and develop methods to distinguish actual diattenuation from birefringence dependence. For example, performing diattenuation measurements by analyzing horizontal and vertical polarization with the PSA, instead of summing two 3D-PLI

measurements (LC and RC), could minimize the influence of circular components. However, this approach loses the previous synergy with the 3D-PLI measurement, requiring two additional measurements within the measurement routine.

5.6.3 Müller Polarimetry

Parameters: Everything (except for fiber crossings) including depolarization
Strengths: Analysis of all optic properties, Eigenvalue Calibration Method
Weaknesses: Sufficient signal-to-noise ratio required, gray matter, speed-up limited

Müller polarimetry, in principle, can determine all the optical properties that 3D-PLI and DI measure, specifically diattenuation and its axis, and retardation and its axis, with the axes hold direct information about the fiber direction. Unlike 3D-PLI and DI, Müller polarimetry can also distinguish between linear and circular retardation/diattenuation. Moreover, Müller polarimetry measures depolarization, which can be used to differentiate between white and gray matter and between healthy and tumorous (disordered, chaotically growing) fibers. The Eigenvalue Calibration Method provides a theoretically ideal calibration routine, with the primary limiting factor being the quality of calibration samples. This leads to more precise results which is particularly important for the relatively weak diattenuation signal. However, Müller polarimetry requires a good signal-to-noise ratio, i.e. a long exposure time, a bright light source, a high sensitivity camera and sufficient repetitions because each Müller coefficient is determined by a sum of only four images. In contrast, 3D-PLI uses Fourier fitting to stabilize and smooth the signal, reducing the overall number of images down to six. In Müller polarimetry, the image number can mathematically be reduced only to 16, and the investigations of this chapter have shown it should not be decreased below 36. Therefore, Müller polarimetry is less suitable for high-speed measurements compared to 3D-PLI.

5.6.4 ComSLI

Parameters: Multiple fiber directions, scattering properties
Strengths: Fiber crossing, independence from retardance deviations
Weaknesses: Sufficient signal-to-noise ratio required

ComSLI is the only method that can measure multiple fiber directions within a single image pixel. Furthermore, scattering is nearly independent from polarization[9], so it does not suffer from retardance deviations in the Scattering Polarimeter. The average map generated by ComSLI is highly reliable for tissue classification for both older and newer tissue. However, ComSLI has a lower signal-to-noise ratio compared to 3D-PLI, which is particularly noticeable in gray matter and more recently embedded (i.e. less transmittive and more scattering) tissue. The signal-to-noise ratio can be enhanced for the Scattering Polarimeter by implementing a brighter light source, larger illumination segments, a more sensitive camera and – if time is not a factor – using a longer exposure time and more repetitions. Good light-shielding is crucial because reflections negatively influence the signal. With these improvements, ComSLI can effectively measure multiple fiber crossings especially in white matter.

[9]There is a slight polarization dependency in scattering, but it is negligible within this context.

Chapter 6

Multi-Modal Parameter Analysis

Chapter 5 initiated the first steps towards multi-modal parameter analysis: Diattenuation imaging (DI) inherently requires fiber directions obtained from three-dimensional polarized light imaging (3D-PLI) to distinguish D^+/D^- tissue. In this chapter, the **parameter maps are combined** to leverage the advantages of each modality and to compare differences between parameter maps. This chapter showcases the potential of multi-modal parameter analysis and provides suggestions for further multi-modal routines.

Automatic classification is crucial to a multi-modal analysis. Here, a threshold-based multi-modal classification is demonstrated for two samples with different transmitting and scattering properties. The method identifies anatomically different regions, i.e. areas of gray matter, white matter, background area and – to some extent – crystallization artifacts in the embedding medium. Additionally, white matter fiber architectures such as in-plane parallel fibers, inclined fibers, and crossing fibers are differentiated based on multi-modal parameter maps.

Furthermore, a **combined fiber orientation map** is assembled from ComSLI and 3D-PLI. The multi-modal map displays the most reliable directional signal per pixel and visualizes up to three fiber crossings per image pixel. Briefly, the **correlation between the ComSLI peak distance and the 3D-PLI fiber inclination** is investigated. Finally, the chapter provides further suggestions for **future research on multi-modal imaging** with the Scattering Polarimeter.

6.1 Matter and Fiber Classification

Within the following, "matter classification" refers to the differentiation of gray matter, white matter and – where applicable – artifacts, and background areas. "Fiber classification" refers to the classification of different fiber configurations in white matter, such as crossing or parallel fibers. By strategically combining parameter maps from several modalities, the identification becomes more reliable than the purely depolarization-based classification in Section 5.4.7. While this classification can only be an approximation due to the anatomical complexity of the nerve fiber network, the resolution limit of the imaging process, and the presence of several nerve fiber layers even within a thin section, it remains effective for the subsequent analysis of multimodal data, e.g. in Section 6.2– 6.3.

To avoid overly restrictive classification, identification only employs as few parameter maps as absolutely needed. A basic classification approach sets a brightness threshold on one or multiple parameter maps. Where applicable, the classification sets a lower

or upper value limit per parameter map instead of a range of values, thereby minimizing the number of required thresholds. Other combinations of parameter maps than those presented can achieve similar results. More advanced approaches are discussed later, e.g. automatic threshold-identification based on brightness histograms.

The applicability of a threshold-based classification is demonstrated in Broca and Vervet1818. Due to the different time since embedding, Broca shows a low transmittance and a high scattering, Vervet1818 a high transmittance and lower scattering. Both samples present unique challenges for characterization: Vervet1818 shows more local deviations in its parameter maps due to the overall lower contrast, while Broca-A suffers from a lower signal-to-noise ratio in some parameter maps that manifests as pixels not being evaluated at all. However, threshold-based classification is more challenging for Vervet1818 due to the lower contrast and the occurrence of artifacts. Thus, Vervet1818 illustrates the limitations of the threshold-based approach.

6.1.1 White Matter, Gray Matter, Background and Artifacts

Anatomically different regions exhibit distinct brightness values across the selected parameter maps that are shown for Broca, Vervet1818, ChiasmX2-7, and ChiasmX2-15 in Figure 6.1. ChiasmX2-7 and ChiasmX2-15 only contain white matter fibers and background areas and are shown for comparison.

The optical properties that lead to scattering, absorption, retardation, and depolarization were established in Section 2.3.3 and can be observed here: The average map from ComSLI provides a scattering-based distinction, although with a better contrast for Broca: White matter leads to stronger scattering than gray matter. The transmittance map from DI exhibits a lower transmittance for white matter due to the stronger light absorption and increased internal scattering. This map can differentiate gray matter, white matter, and background areas, and is less sensitive to systematic asymmetries than the 3D-PLI transmittance map, as discussed in Section 5.3.1.

The depolarization map from Müller polarimetry was discussed in detail in Section 5.4.7. In white matter, there is stronger depolarization as more scattering occurs. However, the maps from Müller polarimetry suffer from a lower signal-to-noise ratio especially in Broca. Additionally, the retardation map from 3D-PLI (or Müller polarimetry) highlights white matter nerve fibers by their higher retardation values even though the distinction between steeply inclined fibers and the less densely packed nerve fibers in the more transmitting gray matter regions is limited.

Broca White and gray matter in Broca can be well distinguished either from the average map $\bar{I}$ (ComSLI) or the transmittance map τ (DI). In Appendix B.3 in Fig B.46, the minor differences are exemplary shown for the identification of gray matter and are mostly limited to the border area between white and gray matter. Figure 6.2 presents the successful classification based only on the average map $\bar{I}$ (ComSLI) for Broca. The thresholds were chosen as follows: Background $\bar{I} \leq 500$ a.u., gray matter 500a.u. $< \bar{I} \leq 800$ a.u., white matter: 800 a.u. $< \bar{I}$. Pixels that were recognized as part of the indicated are displayed in blue. The results are in accordance with the expected distribution of gray and white matter and correctly identifies the small background area in Broca-A.

Vervet1818 The classification of Vervet1818 requires a more strategic combination of the average map, the depolarization map, and the retardation map. Structures

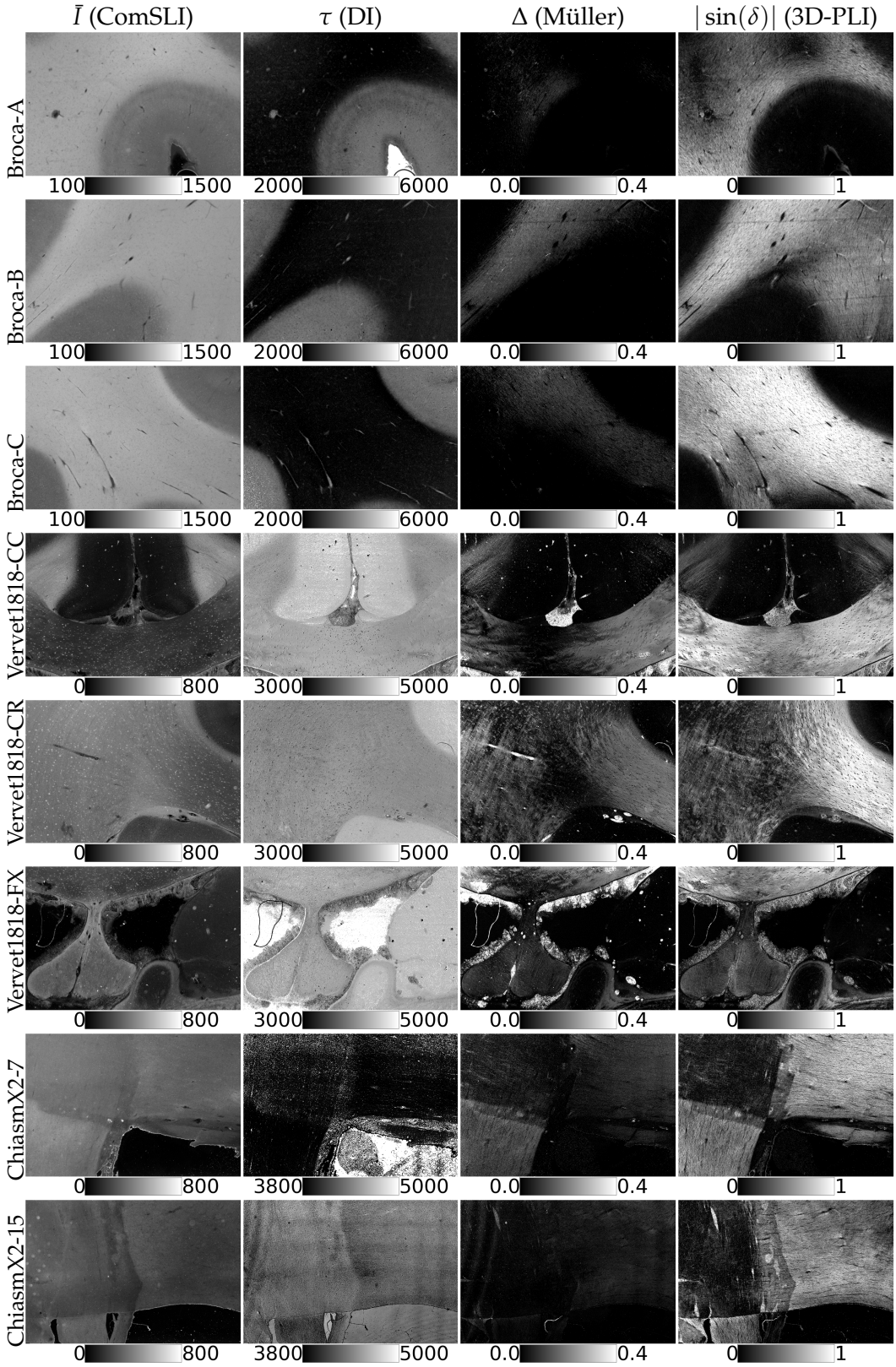

FIGURE 6.1: Parameter maps for matter classification. From left to right: Average map $\bar{I}$ (ComSLI, [a.u.]), transmittance map τ (DI, [a.u.]), depolarization map Δ (Müller polarimetry), retardation map $|\sin(\delta)|$ (3D-PLI). From top to bottom: Broca-A, Broca-B, Broca-C, Vervet1818-CC, Vervet1818-CR, Vervet1818-FX, ChiasmX2-7, and ChiasmX2-15. For Broca (low transmittance, high scattering), $|\sin(\delta)|$ or $\bar{I}$ are sufficient to differentiate gray matter, white matter, and background. For Vervet1818 (high transmittance, low scattering), various maps can be combined.

like crystallization artifacts in the embedding medium exhibit significantly higher depolarization than anatomical structures. Consequently, the depolarization map was used to filter out the most pronounced crystallization artifacts. Strong artifacts were identified by a depolarization $\Delta \geq 0.3$. The conditions to identify background pixels areas were set as follows: 1) The pixel was not already identified as an artifact. 2) The threshold on the average map from ComSLI was chosen as $\bar{I} \leq 20$ a.u. because background areas do not scatter light. Then, the following conditions were used to identify gray matter pixels: 1) The pixel was not already identified as an artifact or as part of the background. 2) The threshold on the retardation map from 3D-PLI was chosen to be $|\sin(\delta)| < 0.07$. All areas that are neither background, artifacts, nor gray matter were automatically identified as white matter without the need for additional information. The result is shown in Figure 6.3. Due to the characteristics of Vervet1818, the classification is less accurate compared to Broca. Nevertheless, major tissue regions are identified correctly. The most prominent artifacts can be identified based on their depolarization, however, less prominent artifacts are often mistakenly classified as white or gray matter.

Discussion The identification of white matter, gray matter, and background is successful for Broca. Broca is a typical 3D-PLI sample in terms of tissue preparation, the comparatively short time since embedding and the resulting high contrast between gray and white matter, and the lack of crystallization artifacts. Here, tissue classification is trivial but it is still noteworthy that two fundamentally different methods (ComSLI and 3D-PLI) yield the same result. Due to the transmitting and scattering properties of Vervet1818, the classification is less accurate in comparison. The most prominent artifacts can be identified based on their depolarization, however, less prominent artifacts are often mistakenly classified as white matter. Furthermore, the distinction between crossing fibers in the corona radiata and gray matter is not exact. Nevertheless, major tissue regions are identified correctly despite the suboptimal sample conditions.

6.1.2 White Matter Fiber Structures

Based on their geometrical configuration within a brain section, nerve fibers can be roughly categorized into in-plane crossing fibers, in-plane parallel fibers, inclined parallel fibers, and steep fibers, each configuration showing a unique fingerprint of optical properties across the many parameter maps. They can be identified based on e.g. the ComSLI average map and the ComSLI peak prominence map. These parameter maps are shown in Appendix B.3 in Figure B.47.

Threshold values for peak prominence and average scattering were extracted from comparison with known anatomical regions. Future research should focus on automatic threshold determination. Complex structures such as inclined crossing fibers but also nerve fibers in gray matter were neglected in the approach.

In-Plane Parallel Fibers Here, in-plane parallel fibers are defined as fibers with an inclination $\alpha_{\text{inc}} \leq 30°$, i.e. a (normalized) retardation $|\sin(\delta)| \geq 0.68$. In-plane parallel fibers, such as in the corpus callosum, were identified by the following criteria: 1) They were part of the previously identified white matter regions, and 2) the retardation from 3D-PLI was $|\sin(\delta)| \geq 0.68$ (which corresponds to the chosen upper inclination angle). The inclination map from 3D-PLI or the corresponding maps from Müller polarimetry could have been used for similar results. Furthermore,

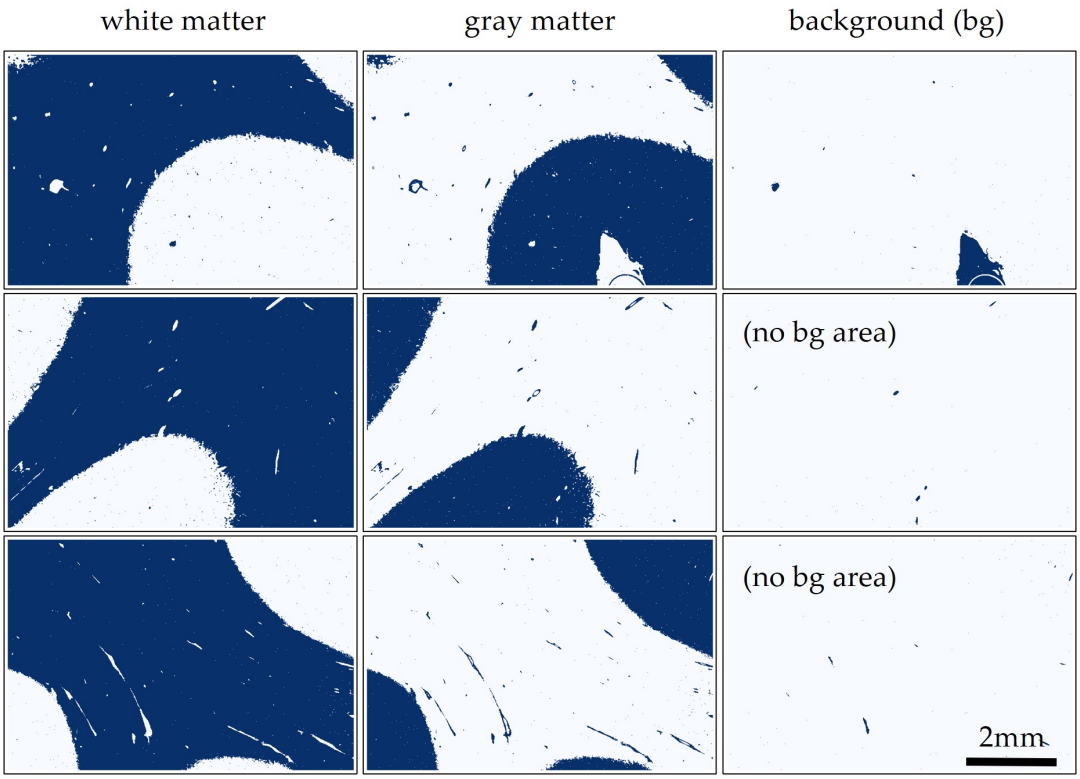

FIGURE 6.2: Broca matter classification. From top to bottom: Broca-A, Broca-B, Broca-C. Blue indicates the identified regions of white matter, gray matter, and background (bg), respectively. The classification is based on the average map (ComSLI). A classification based on the transmittance map (DI) would have been possible.

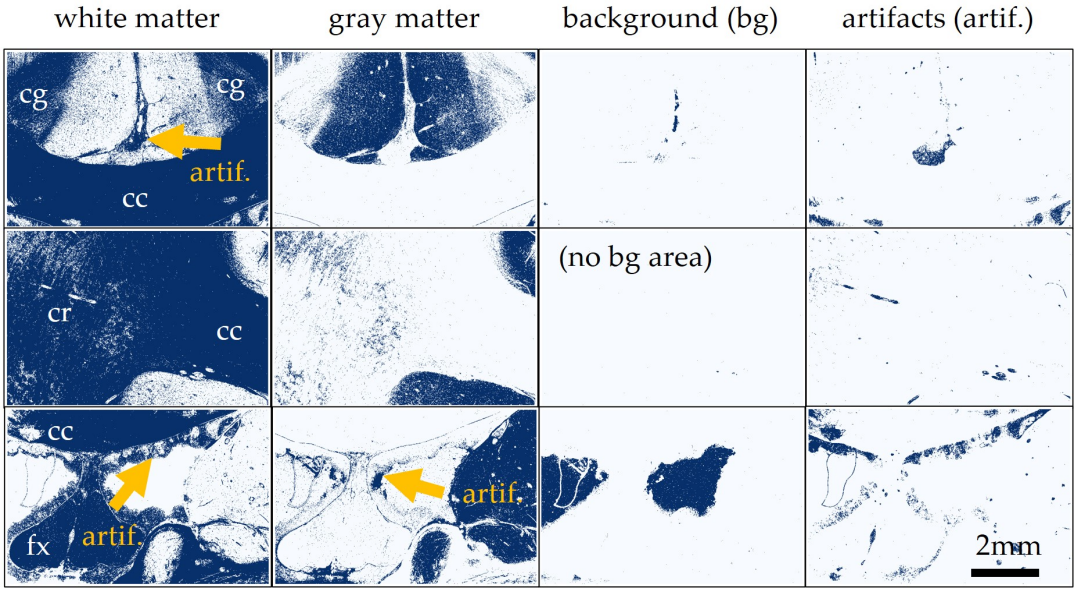

FIGURE 6.3: Vervet1818 matter classification. From top to bottom: Vervet1818-CC, Vervet1818-CR, Vervet1818-FX. Blue indicates the identified regions of white matter, gray matter, background (bg), and artifacts, respectively. Characteristic white matter structures are marked: Corpus callosum (cc), corona radiata (cr), cingulum (cg), fornix (fx). The most prominent artifacts can be identified based on their depolarization, however, less prominent artifacts are often mistakenly classified as white or gray matter (some of them exemplary indicated by yellow arrows).

in-plane parallel fibers have a comparatively high peak prominence. However, the use of an additional criterion was not required. Figure 6.4 – 6.5 (first column) shows the identified pixels in blue.

Inclined Parallel Fibers Here, inclined fibers have an inclination in the range $30° < \alpha_{\text{inc}} < 65°$, i.e. a retardation in the range $0.17 < |\sin(\delta)| < 0.68$. Inclined parallel fibers cannot be differentiated from crossing fibers alone from their retardation: A lower retardation signal can indicate a stronger inclination but also a sum of signals from crossing fibers in which the individual intensity curves cancel out. However, the peak prominence from ComSLI is higher for parallel fibers than for crossing fibers. Inclined parallel fibers, such as in the fornix, were identified by the following criteria: 1) They were part of the previously identified white matter regions but not already classified as in-plane parallel fibers, 2) the retardation from 3D-PLI was within the given range and 3) the peak prominence from ComSLI was comparatively high, here ≥ 0.3 for Broca and ≥ 1.0 for Vervet1818.[1] Figure 6.4 – 6.5 (second column) shows the identified pixels in blue.

Steep Fibers In this context, steep fibers have an inclination $\alpha_{\text{inc}} \geq 65°$ which corresponds to a retardation $|\sin(\delta)| \leq 0.17$. The differentiation of steep fibers – i.e. strongly inclined fibers that are nearly orthogonal to the sectioning plane – from crossing fibers is challenging. Both have a comparatively low retardation and a low peak prominence (the latter due to a low signal-to-noise ratio in steep fibers). However, steep fibers like in the cingulum appear extraordinary bright in the average map from ComSLI due to their strong scattering. Thus, the criteria for steep fibers were chosen as follows: 1) They were part of the previously identified white matter regions but not already classified as in-plane or inclined parallel fibers, 2) the retardation from 3D-PLI was within the given range and 3) the average scattering intensity was $\bar{I} > 1200$ for Broca and $\bar{I} > 430$ for Vervet1818. Figure 6.4 – 6.5 (third column) shows the identified pixels in blue.

Fiber Crossings Crossing fibers, such as in the corona radiata, were identified with the following criterion: 1) They were part of the previously identified white matter regions but not of the already identified in-plane, inclined or steep parallel fiber structures. The logical implication is that the retardation did not matter for the identification, only the (comparatively low) peak prominence and the average scattering. Figure 6.4 – 6.5 (fourth column) shows the identified pixels in blue.

Discussion Clear separation of fibers structures is not expected in real biological tissue, particularly within complex structures like the corona radiata and border regions. Although more complex structures such as inclined crossing fibers were neglected, a rough categorization is achievable and sufficient for the purposes outlined in Section 6.2. However, parts of the cingulum are incorrectly identified as crossing fibers. Although the cingulum does contain minor crossings, as discussed in Section 2.3.1, the noise generated by scattering at the nearly vertical fiber bundles is a major cause for the misidentification as crossing fibers. In Broca – a sample that generally exhibits more noise due to stronger scattering – no steep regions were identified at all with this approach at all, most likely for the same reason.

[1] Vervet1818 exhibits lower overall scattering compared to Broca, therefore more distinct peaks and a higher peak prominence for parallel fibers.

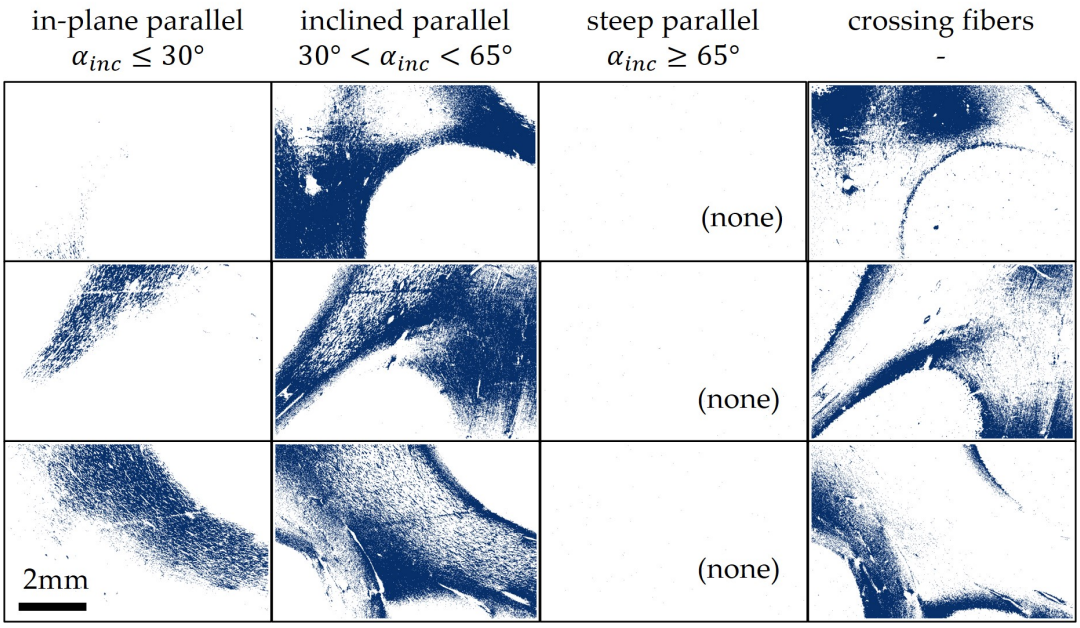

FIGURE 6.4: Classification of white matter fibers for Broca. Top to bottom: Broca-A, Broca-B, Broca-C. Left to right: In-plane parallel fibers, inclined parallel fibers, steep fibers, and fiber crossings. Image pixels belonging to one of those fiber configurations are displayed in blue, respectively.

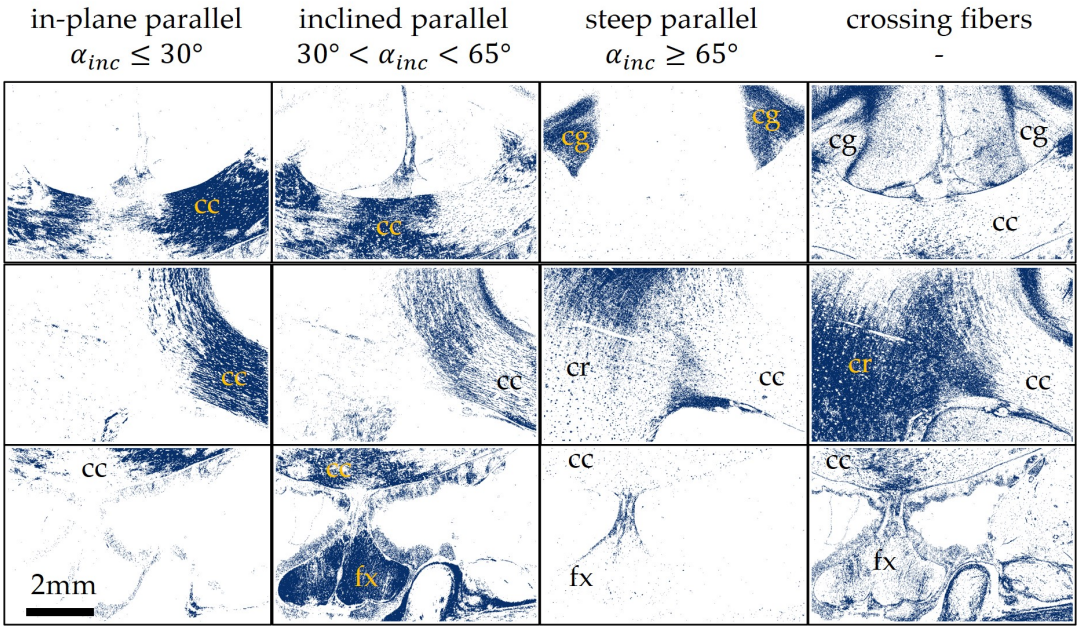

FIGURE 6.5: Classification of white matter fibers. Top to bottom: Vervet1818-CC, Vervet1818-CR, Vervet1818-FX. Left to right: In-plane parallel fibers, inclined parallel fibers, steep fibers, and fiber crossings. Image pixels belonging to one of those fiber configurations are displayed in blue, respectively. Various fiber configurations in the corpus callosum (cc), the corona radiata (cr) and the fornix (fx) are mostly correctly identified. The identification of steep fibers like in the cingulum (cg) remains challenging.

It should be noted that finding more than one fiber direction is currently not a reliable characteristic for distinguishing parallel fibers from crossing fibers, as discussed in Section 5.5.3. Improving the signal-to-noise ratio of the Scattering Polarimeter with a brighter light source and a high-sensitivity camera should be the goal of future research.

However, the algorithm yields a basic categorization of fiber configurations based on their distinct combination of optical properties, thereby demonstrating the strength of multi-modal measurements and its ability to compensate for the limitations of single modalities. The categorization proves to be effective in Section 6.2.

The results for fiber classification for ChiasmX2-7 and ChiasmX2-15 are shown in Appendix B.3 in Figure B.48. The two artificially constructed samples only contain white matter and background areas, therefore, the detection of gray matter was left out. Inclined fibers were identified by setting a threshold to the peak prominence ≥ 0.8. Steep fibers, defined by $\bar{I} > 800$, are not present in the artificial crossings.

6.1.3 Advanced Tissue Classification

Through a strategic combination of parameter maps, classification is achievable, even for highly transmitting (low contrast) samples such as Vervet1818. For a typical 3D-PLI sample like Broca, the distinction between white matter, gray matter, and background is simple. Due to the transmitting and scattering properties of Vervet1818, the distinction is comparatively less accurate. Generally, the classification is less accurate especially at borders between white and gray matter and in presence of crystallization artifacts. However, the investigation of Vervet1818 demonstrates how fiber configurations can be identified even under suboptimal sample conditions, highlighting the strengths of the multi-modal approach. This routine establishes a foundation for the automatic assembly of multi-modal fiber orientation maps in Section 6.2.

Steep fibers like in the cingulum impose challenges to the fiber classification routine and are misidentified due to noise. Future research must focus on distinguishing crossings from noise-influenced steep fibers, especially by improving the signal-to-noise ratio. Ideally, the occurrence of a single fiber direction and multiple directions would be sufficient to differentiate steep fibers from crossing fibers.

A disadvantage of a threshold-based classification routine is the need to determine thresholds individually for each sample, or at least separately for each sample set prepared and measured under the same conditions. Additionally, the algorithm presented here uses previous knowledge about fiber architecture to identify correct thresholds. One potential method to automatically identify suitable thresholds could involve analyzing a brightness histogram to identify brightness ranges. More advanced machine-learning approaches could use multiple parameter maps to perform automatic tissue classification.

6.2 Combined Fiber Orientation Maps

All four modalities of the Scattering Polarimeter – Müller polarimetry, 3D-PLI, DI and ComSLI – yield information about fiber directions. However, ComSLI is based on a fundamentally different mechanism (i.e. scattering, s. Section 3.5) than the three

polarimetric methods. While the diattenuation signal is relatively weak and the measured fiber direction for D^- tissue is shifted from the actual fiber direction, the other modalities are well-suited for providing pixelwise fiber directions. The evaluation of fiber directions for Müller polarimetry, 3D-PLI, and ComSLI was discussed in Chapter 5.

Initially, results from 3D-PLI and Müller polarimetry are compared: both modalities rely on fiber birefringence and ideally yield similar fiber directions. Then, an algorithm based on the fiber classification in Section 6.1.2 is introduced that generates a multi-modal FOM from 3D-PLI and ComSLI to display the most reliable directional signal per pixel from the available modalities. The multi-modal FOM exploits the advantages of the two techniques, increases the total number of evaluated pixels and displays up to three directions.

6.2.1 Comparison of Single-Mode Fiber Directions

Figure 6.6 displays the fiber directions from Müller Polarimetry ϕ_{MP} (first column), 3D-PLI ϕ_{PLI} (second column), ComSLI ϕ_{SLI} (third column, FOM with all directions), and the difference between 3D-PLI and ComSLI $|\phi_{\mathrm{PLI}} - \phi_{\mathrm{SLI}}|$ (fourth column), to be precise, the difference between ϕ_{PLI} and the first direction $\phi_{\mathrm{SLI},1}$ or the second direction $\phi_{\mathrm{SLI},2}$ or the third direction $\phi_{\mathrm{SLI},3}$ from ComSLI, depending on whichever is closest to the fiber direction measured by 3D-PLI.

Müller Polarimetry and 3D-PLI As expected, the fiber directions from Müller polarimetry show only minor deviations from those of 3D-PLI, mainly in gray matter. Broca, however, shows many dark pixels where the signal-to-noise ratio for Müller polarimetry is insufficient due to low transmittance to detect any directions.

The similarities between 3D-PLI and Müller polarimetry confirm that the assumptions made in the 3D-PLI error corrections are reasonable, the residual retardation does not cause significant issues, and the signal-to-noise ratio in Müller polarimetry does not cause deviations for the successfully evaluated pixels. However, 3D-PLI yields a better signal-to-noise ratio and more pixels are evaluated. Thus, 3D-PLI is used as the foundation of the multi-modal FOM.

3D-PLI and ComSLI The difference between the polarimetric modalities and ComSLI are more pronounced: The last column in Figure 6.6 visualizes the differences between 3D-PLI and the closest obtained direction from ComSLI. In the subsequent Section 6.2.2, ComSLI and 3D-PLI are considered to yield the same direction when $|\phi_{\mathrm{PLI}} - \phi_{\mathrm{SLI}}| < \Delta\phi$ and a different direction where $|\phi_{\mathrm{PLI}} - \phi_{\mathrm{SLI}}| > \Delta\phi$. The pixel is displayed in black when one or both modalities do not yield any fiber direction. The threshold value $\Delta\phi$ was estimated from the angular steps of the measurement (15° steps for ComSLI, 10° steps for 3D-PLI): $\Delta\phi = \sqrt{10^2 + 15^2}^\circ \approx 18^\circ$.

In direct comparison, ComSLI obtains similar fiber orientations as 3D-PLI for most white matter regions, as expected for healthy tissue. However, the signal is noisier, indicated by more black pixels. ComSLI detects no fiber directions in gray matter, where the fiber signal is very weak compared to white matter. Furthermore, Broca shows strong scattering due to its shorter time since embedding, making it difficult to evaluate the ComSLI line profiles for many white matter pixels. On the other hand, ComSLI is the only modality that successfully measures more than one fiber direction in regions with crossing fibers.

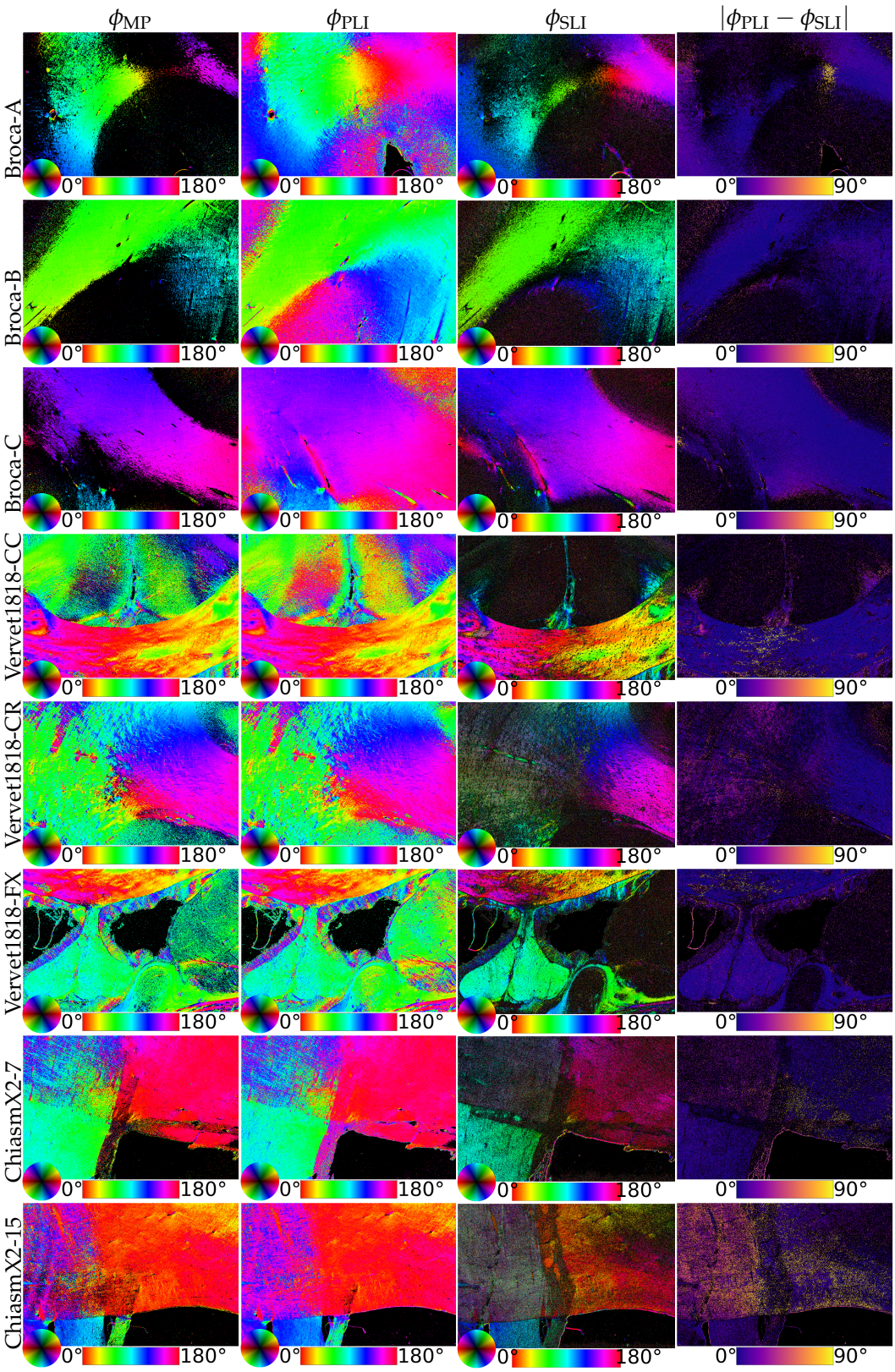

FIGURE 6.6: Comparison of fiber directions from all modalities. Fiber direction obtained from Müller polarimetry, 3D-PLI, and ComSLI (here: only first direction displayed). The fourth column shows the absolute difference in fiber direction between 3D-PLI and ComSLI $|\phi_{PLI} - \phi_{SLI}|$. From top to bottom: Vervet1818-CC, Vervet1818-CR, Vervet1818-FX, Broca-A, Broca-B, Broca-C, ChiasmX2-7 and ChiasmX2-15.

6.2.2 Construction of a Multi-Modal Fiber Orientation Map

A multi-modal FOM combines information from multiple modalities to achieve the most reliable fiber direction per pixel. The reliability of signals from 3D-PLI or ComSLI largely depends on local tissue features, such as fiber architecture, as well as sample properties like the age (i.e. time since embedding) and thickness of the sample.

Step-Wise Construction Process Figure 6.7 illustrates the step-wise procedure used to construct a multi-modal FOM for Vervet1818-CR. This procedure is based on the tissue classification developed in Section 6.1 and the differences between ComSLI and 3D-PLI shown in Figure 6.6. It should be noted that the final FOM does not contain visual information about the inclination. The three direction maps of the multi-modal FOM were assembled as follows:

1. Fiber directions in crossing regions are found more reliably with ComSLI because 3D-PLI cannot differentiate multiple directions and only detects the average signal. For pixels that were identified as part of crossing regions with the routine established in Section 6.1, the directions $\phi_{\text{SLI},1}$, $\phi_{\text{SLI},2}$, or $\phi_{\text{SLI},3}$ were chosen for the respective multi-modal direction map, e.g. in the corona radiata.
2. For each pixel within a white matter region not classified as a crossing region, the direction $\phi_{\text{SLI},1}$, $\phi_{\text{SLI},2}$, $\phi_{\text{SLI},3}$ was selected when the 3D-PLI and a ComSLI direction maps indicate different fiber orientations. This takes into account potential misclassification of border regions that may have been incorrectly identified as non-crossing. Furthermore, it can take into account myelin degradation (e.g. caused by neurodegenerative diseases, s. Section 2.3.4), where changes occur in the birefringence that influence the 3D-PLI signal but not the ComSLI signal.
3. For parallel fibers, the sinusoidal curve of the 3D-PLI signal is typically more stable than the line profiles of the ComSLI signal. Additionally, the angular discretization is lower for 3D-PLI than for ComSLI. For these pixels, ϕ_{PLI} was chosen if it was similar to $\phi_{\text{SLI,i}}$. In this step, changes in the second and third multi-modal direction map were small and limited to statistical fluctuations.
4. Gray matter was treated separately due to its rather low signal that is usually detected more reliably by 3D-PLI than ComSLI. For the first direction, ϕ_{PLI} was chosen when $\phi_{\text{SLI},1}$ was not found. Otherwise, $\phi_{\text{SLI},1}$ was chosen. For the second and third direction, $\phi_{\text{SLI},2}$ or $\phi_{\text{SLI},3}$ were used for the respective direction map, if found.

The three new multi-modal direction maps were assembled as a FOM, where each image pixel is represented by 2×2 color-coded pixels, as described in Section 3.5. All pixels without any detected fiber direction are displayed in black. They are mostly part of the background area or gray matter.

Comparison between Single-Mode and Multi-Modal FOM Figure 6.8 compares the single-mode FOMs from ComSLI and the multi-modal FOMs for Vervet1818. The single-mode and the multi-modal vector maps (vector length weighed with the corresponding average map and vectors visualized with a thinout of 20) are compared in Figure 6.9 for selected areas indicated in the FOMs by asterisks. The multi-modal FOM does not only provide information about multiple fiber directions

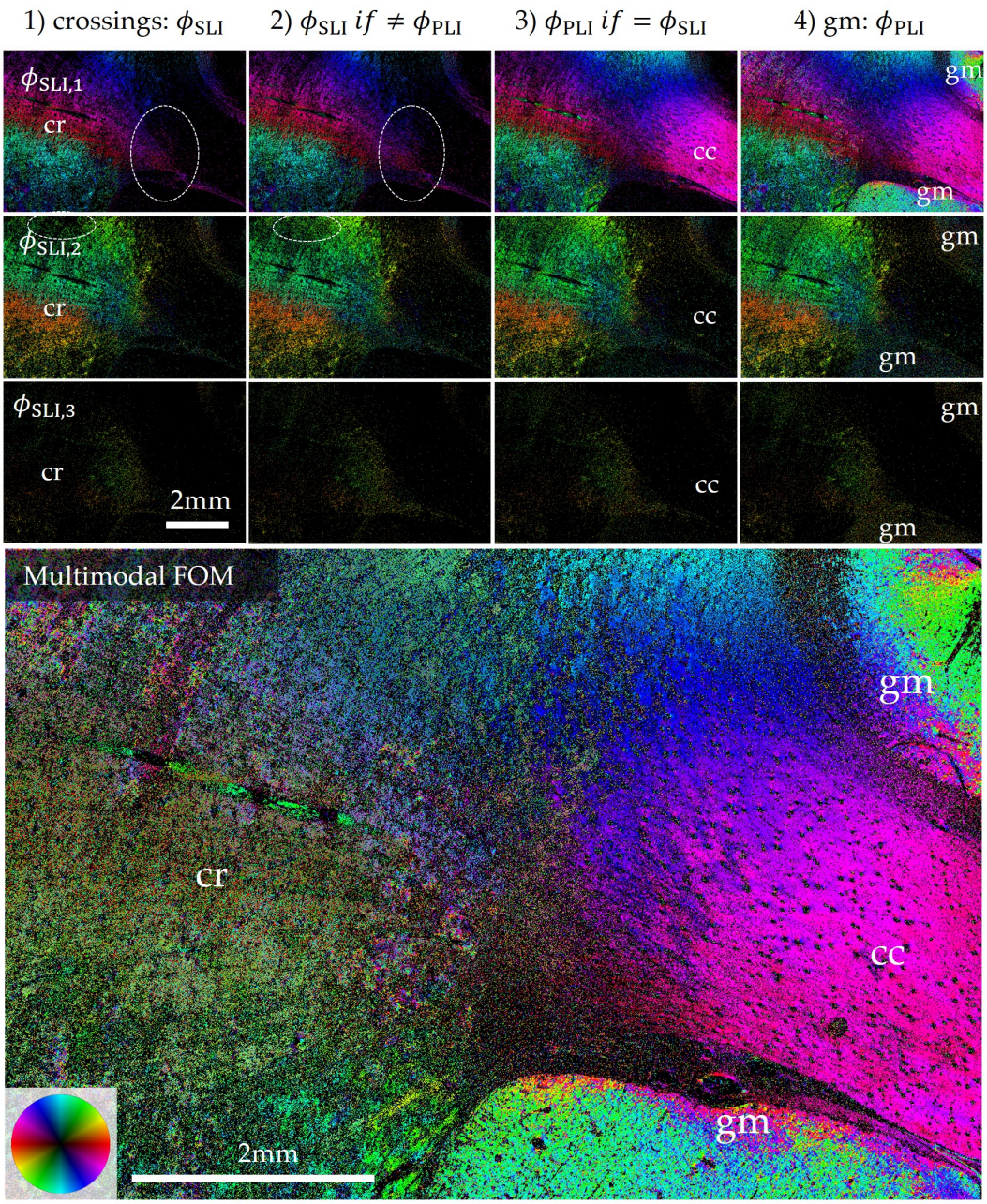

FIGURE 6.7: Step-by-step construction of a multi-modal FOM. The image pixels are filled based on the tissue classification developed in Section 6.1 with the directions ϕ_{PLI} from 3D-PLI and $\phi_{SLI,1}$, $\phi_{SLI,2}$, $\phi_{SLI,3}$ from ComSLI. The construction of each multi-modal direction map based on the best signal is displayed in the three top rows. The multi-modal FOM is displayed below. For each of three directions i, the following algorithm yielded a multi-modal direction map: 1) $\phi_{SLI,\,i}$ was used for white matter crossing regions, e.g. the corona radiata (cr). 2) $\phi_{SLI,i}$ was used in white matter regions when it was dissimilar to ϕ_{PLI}. 3) ϕ_{PLI} if it was similar to $\phi_{SLI,i}$, e.g. the corpus callosum (cc). In this step, changes in the second and third multi-modal direction map were small and limited to statistical fluctuations. 4) For the first direction: ϕ_{PLI} was used in gray matter (gm) regions where $\phi_{SLI,1}$ was not found, otherwise $\phi_{SLI,1}$. For the second and third direction, $\phi_{SLI,2}$ or $\phi_{SLI,3}$ were used respectively, if found. Changes between the steps are highlighted by dashed ellipses in the image.

obtained from ComSLI but also exhibits a better signal-to-noise ratio due the data from 3D-PLI, particularly for parallel fibers and gray matter, compared to the single-mode FOM obtained only with ComSLI. Noticeable improvements are observed in the gray matter, the corpus callosum, and parts of the cingulum in Vervet1818-CC. Additionally, background noise is inherently filtered out by the routine which become clear for Vervet1818-FX.

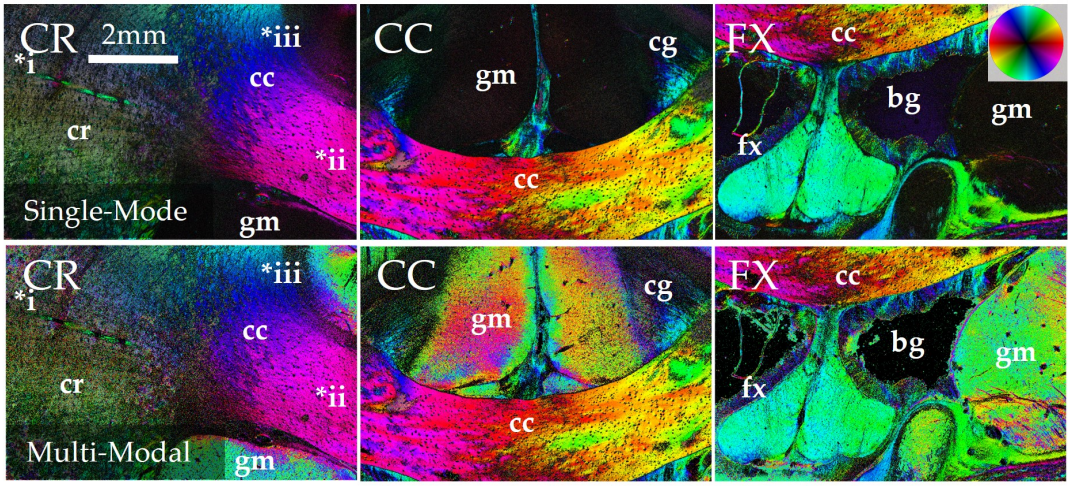

FIGURE 6.8: Single-mode FOM and multi-modal FOM for Vervet1818. Top row: Single-mode FOMs from ComSLI for Vervet1818-CR, Vervet1818-CC, Vervet1818-FX. Bottom row: The corresponding multi-modal FOMs. Vector maps for selected regions indicated with i, ii, iii are shown in Figure 6.9. Compared to the single-mode FOM obtained only with ComSLI (first row), the multi-modal FOM combines up to three fiber directions per pixel and exhibits a noticeably better signal-to-noise ratio. The most obvious improvement is seen in the gray matter (gm), the corpus callosum (cc), and parts of the cingulum (cg) in Vervet1818-CC. Additionally, background (bg) noise is inherently filtered out.

More subtle differences are evident in the vector maps in Figure 6.9: While the crossing regions in *i do not differ significantly between the single-mode and the multi-modal FOM (as expected, as they are all retrieved from the ComSLI directions), the directions of the parallel in-plane fibers in Vervet1818-CC indicated by *ii are more distinct and less affected by noise. Although a second green direction manifests in the single-mode FOM, the multi-modal FOM shows only the dominant magenta direction for most pixels. The parallel fibers of the corpus callosum area bordering the gray matter in *iii are improved even more visibly, nearly removing the additional yellow direction. Overall, the multi-modal FOM is provides more detailed information with improved quality.

However, a notable phenomenon occurs in the cingulum. Here, where the fiber bundles run nearly orthogonal to the sectioning plane, many pixels remain black in the multi-modal FOM, even when 3D-PLI clearly detects a dominant direction. This occurs because ComSLI fails to reliably detect a single or multiple directions. As a result, these pixels are not filled with 3D-PLI data because the 3D-PLI fiber directions are not considered reliable based on information from ComSLI. MENZEL ET AL. [120] discuss how the inclination obtained from 3D-PLI is not necessarily reliable for very steep fibers and how a combination of ComSLI and 3D-PLI can improve the results in this context.

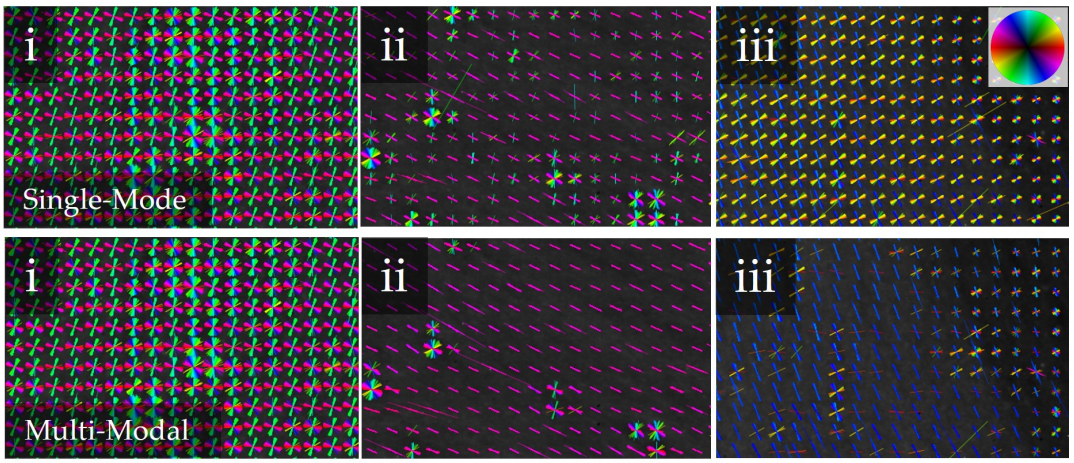

FIGURE 6.9: Single-mode and multi-modal vector maps for Vervet1818. Top row: Single-mode vector maps from ComSLI for Vervet1818-CR, Vervet1818-CC, Vervet1818-FX. Bottom row: The corresponding multi-modal vector maps. The origin region of the vector maps are indicated with *i, *ii, *iii in Figure 6.8. The displayed vector length is weighed with the corresponding average map and vectors are visualized with a thinout of 20. The maps show more subtle differences between the single-mode directions obtained only with ComSLI and the multi-modal directions: Fiber directions are more distinct in the multi-modal vector map and less affected by noise that leads to additional fiber directions in *ii and *iii for parallel fibers in the single-mode vector map. Crossing fibers as in *i do not change significantly because they are mostly retrieved from ComSLI alone.

Future research should aim to accurately determine fiber directions in steep fibers through an optimal combination of 3D-PLI, ComSLI signals, and potentially other modalities. Additionally, future visualization strategies should incorporate information about fiber inclination and overcome the current challenges in determining the inclination of crossing fibers.

6.3 Fiber Inclination

Müller polarimetry and 3D-PLI yield information about the fiber inclination via the retardation. In ComSLI, the peak distance is influenced by the fiber inclination. Here, this relationship is investigated with multi-modal parameter analysis by qualitatively and quantitatively comparing the peak distance maps from ComSLI to the retardation and inclination maps obtained from Müller polarimetry and 3D-PLI.

6.3.1 Qualitative Comparison of Retardation and Peak Distance

In ComSLI, fiber directions are indicated by a peak pair in the line profile, as illustrated in Section 3.5. The peak distance is expected to be about 180° for in-plane parallel fibers and to decrease for inclined fibers, i.e. the two peaks approach each other until they merge into a single peak.[2] MENZEL ET AL. [120] took initial steps to compare fiber inclinations obtained from ComSLI and 3D-PLI using registered samples. However, a direct comparison is challenging: A low retardation from 3D-PLI can indicate strongly inclined fibers but also in-plane crossing fibers.

[2] In SLIX, the peak distance is only defined for pixels where two peaks are found. The peak distance for four or six peaks is theoretically defined but cannot be evaluated with the current version of SLIX.

Qualitative Comparison for Vervet1818 Figure 6.10 shows a qualitative comparison of the retardation maps obtained from 3D-PLI and Müller polarimetry with the peak distance map from ComSLI for Vervet1818. The retardation map is shown instead of the inclination map for easier visual comparison with the peak distance map: Both maps appear bright for in-plane parallel fibers as in the corpus callosum. There are visible similarities between retardation (from both modalities) and peak distance. Major tissue features like the border towards gray matter or prominent blood vessels are reflected in all maps. In-plane parallel fibers are identified as such, showing both a high retardation and a peak distance of about 180°. Prominent local effects occur for both maps, e.g. the center of the corpus callosum being less bright, indicating a lower retardation and a smaller peak distance. However, the fornix does not show a notable contrast to the corpus callosum despite the difference in inclination that is observed in the retardation map. The cingulum shows smaller peak distances, as expected for a region with strongly inclined fibers. Gray matter and crossing fibers are neglected in this investigation: There, peak distances are unidentified or caused by statistical noise.

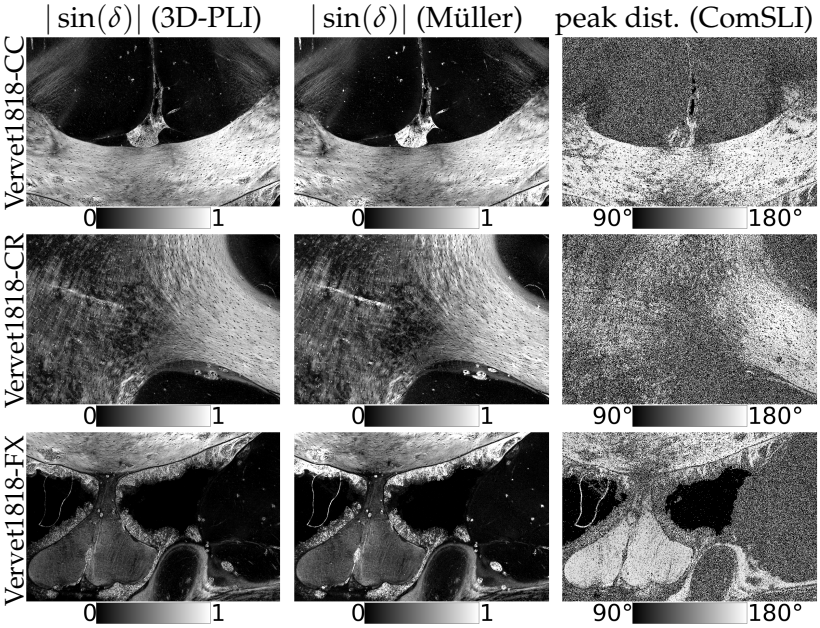

FIGURE 6.10: Retardation maps (3D-PLI, Müller) and peak distance map (ComSLI). From top to bottom: Vervet1818-CC, Vervet1818-CR. From left to right: Retardation $|\sin(\delta)|$ obtained with 3D-PLI, retardation $|\sin(\delta)|$ obtained from Müller polarimetry, peak distance obtained from ComSLI. The retardation map is chosen instead of the inclination map for easier visual comparison of bright and dark areas.

Qualitative Comparison for Broca Broca in Figure 6.11 underlines the observation that in-plane parallel fibers correlate with the expected large peak distance. More complex structures in the retardation map are also reflected by a higher complexity in the peak distance map. Especially at the border between white and gray matter in Broca-B and Broca-C, a gradient from bright to dark can be observed not only in the retardation maps, but also in the peak distance map. Furthermore, even intricate tissue features like blood vessels (dark lines or dots in the white matter) also appear in the peak distance map.

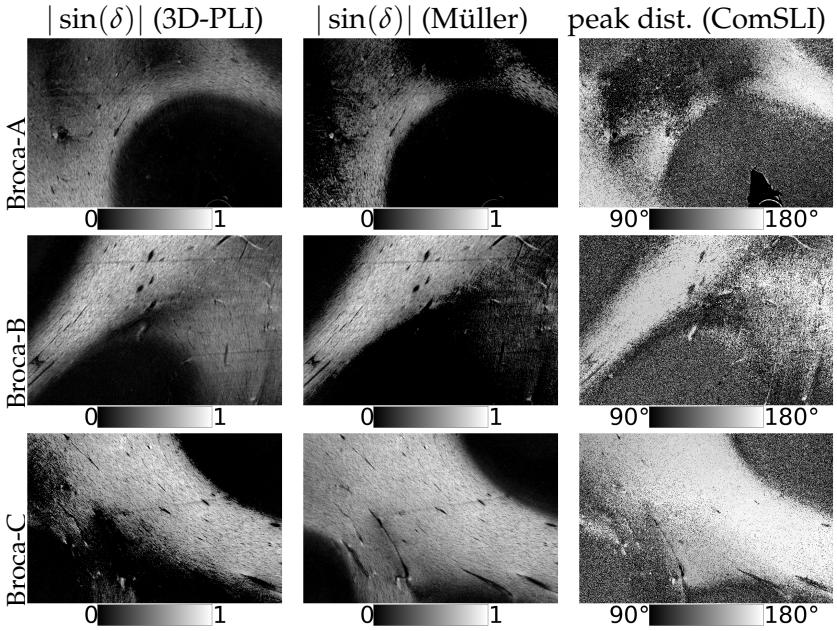

FIGURE 6.11: Retardation maps (3D-PLI, Müller) and peak distance map (ComSLI). From top to bottom: Broca-A, Broca-B, Broca-C. From left to right: Retardation $|\sin(\delta)|$ obtained with 3D-PLI, retardation $|\sin(\delta)|$ obtained from Müller polarimetry, peak distance obtained from ComSLI. The retardation map is chosen instead of the inclination map for easier visual comparison of bright and dark areas.

6.3.2 Correlation of Inclination and Peak Distance

3D-PLI and Müller polarimetry do not differ significantly for the inclination map, as demonstrated in Appendix B.3 in Figure B.49 for Vervet1818 and Broca. Major differences mostly occur where Müller polarimetry has not retrieved any signal due to the low signal-to-noise ratio. In most regions, the inclination differences are around or even below $\Delta\alpha_{\text{inc}} = 10°$. Therefore, only 3D-PLI parameter maps are considered in the following.

The correlation between peak distance and inclination is investigated for a specific subset of pixels based on the tissue classification described in Section 6.1. Only white matter pixels for parallel fibers were taken into account, following the previously developed distinction between in-plane, inclined, and steep fibers. This approach excludes gray matter and background areas but also fiber crossings from the investigation: Those areas are either dominated by noise or the inclination is not defined due to the occurrence of multiple fiber directions. Vervet1818-FX served as an example for the investigation: The sample contains the parallel inclined fiber bundles of the fornix, partially includes the parallel in-plane fiber bundles of the corpus callosum, and lacks major crossing regions. Additionally, Broca-C was analyzed because the retardation map and previous ComSLI results indicate that Broca-C predominantly contains parallel fibers without overly complex structures.

Figure 6.12 shows the correlation for Vervet1818-FX and Broca-C. Each image pixel is displayed as part of a two-dimensional distribution, with peak distance on the x-axis and inclination on the y-axis. For visualization purposes, only every 50-th image pixel is shown. A *detection limit* indicates the inclination which is too steep to be detected, resulting in black pixels. For both samples, a distinct linear correlation cannot be identified. However, an approximate boundary, referred to as the *thinout*

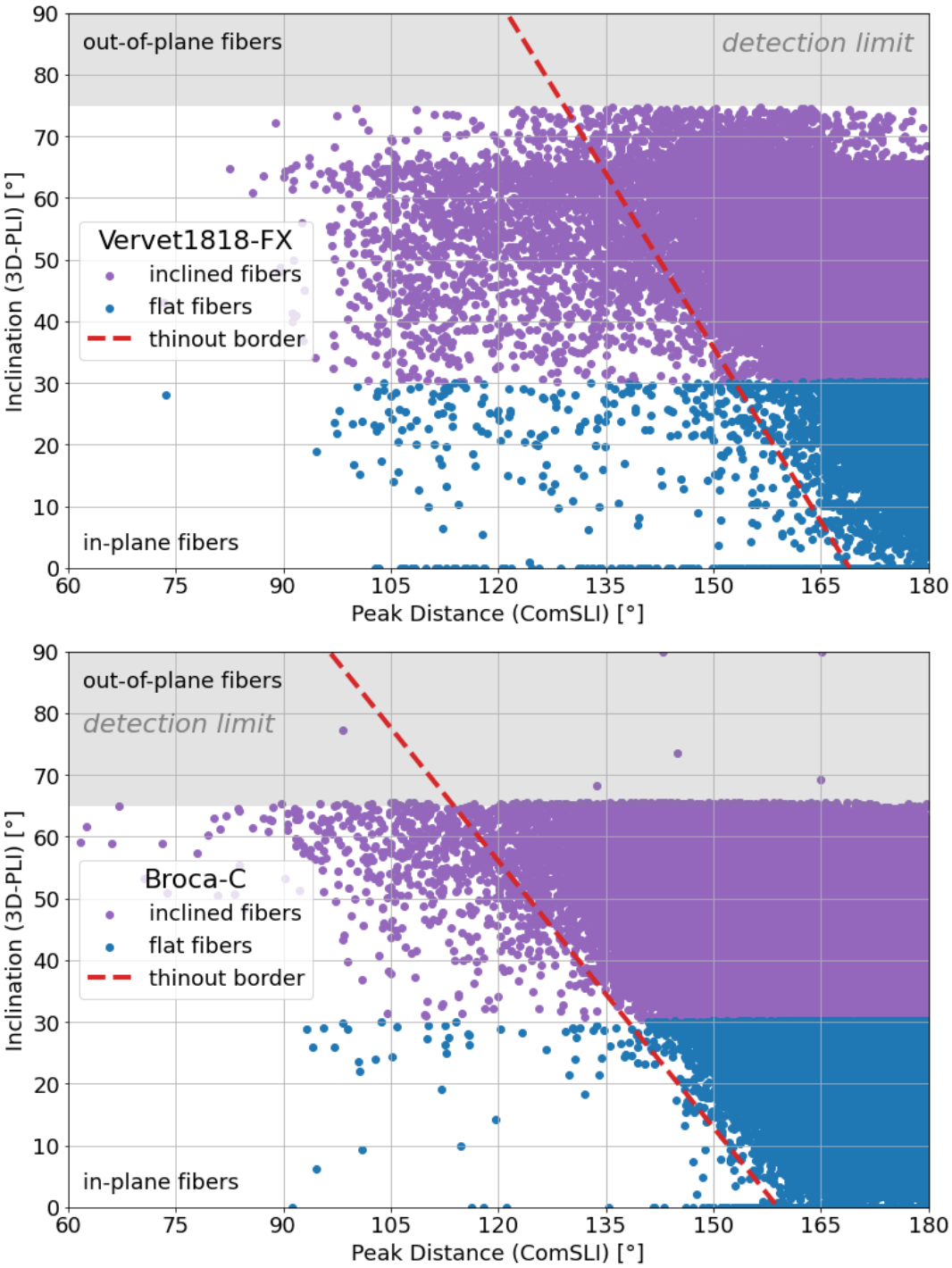

FIGURE 6.12: Peak distance correlation for Vervet1818-FX and Broca-C. The peak distance and inclination of the investigated image pixels are shown in a two-dimensional distribution. For visualization purposes, only every 50-th image pixel is shown. Only image pixels for parallel fibers in white matter were taken into account. This approach excludes fiber crossing, gray matter and background areas. In-plane and inclined fibers were defined like in Section 6.1. A thinout border in the pixel distribution is very distinct for Broca-C and less distinct but visible for Vervet1818-FX. Beyond the detection limit, the retardation is (mostly) too low to be detected.

border, is observed beyond which the density of image pixels rapidly decreases. On the other side of the border, all combinations of inclination and peak distance occur. The approximate course of the thinout border is indicated by a red dashed line. The thinout border is more distinct for Broca-C. Low peak distances are rare due to the discretized angular steps. For steeper fibers, two peaks merge into a single peak and then, the peak distance is not defined anymore. However, it is important to note that the thinout border is diagonal rather than vertical. A vertical border could indicate an issue with detecting peak distances below a certain threshold.

The corresponding depictions for Vervet1818-CC, Vervet1818-CR, Broca-A, and Broca-B are shown in Appendix B.3 in Figure B.50–B.53. Vervet1818 is influenced more by artifacts and statistical noise. Broca displays a distinct thinout border for all samples. The correlation indicates a relation between peak distance and fiber inclination. However, it appears to be more complex than anticipated. Further studies should focus on explaining phenomena that can influence the retardation and the peak distance apart from the geometrical fiber inclination, e.g. by performing appropriate simulations. Different fiber thicknesses and sample conditions should be considered. Experimentally, the angular discretization of ComSLI can be decreased by using smaller angular steps. Finally, the scattering patterns from scatterometry ComSLI should be taken into consideration, as they hold more information about the fiber substructure beyond the fiber orientation: The fiber inclination can be estimated from the radius of curvature of the scattering peak, s. Section 3.5.

6.4 Future Multi-Modal Parameter Analysis

Multi-modal parameter analysis is valuable in many scenarios. Here, an outlook on the future of multi-modal parameter analysis is given, ranging from fundamental research to biomedical applications. In all scenarios, the Scattering Polarimeter can enable rapid measurement of all modalities, thus preventing long breaks in-between measurements in which the tissue condition can change. Additionally, no image registration is required with the Scattering Polarimeter, thus allowing for pixel-exact comparison and cross-validation of parameter maps.

Scattering at Inclined Fibers Section 6.3 demonstrates the complex relationship between scattering and fiber inclination. There is a visible correlation between peak distance and retardation but the results suggest that additional factors must be considered. Thus, future studies should investigate the thinout border and why fibers on one side of the thinout border show any combination of inclination and peak distance. For an in-depth understanding, the effects of crossing fibers and depolarization must be taken into account as well. Additionally, the impact of asymmetric scattering, variations in fiber sizes, and the interaction of scattered light with the surrounding tissue should be investigated. Simulation can aid with both tasks. Furthermore, if the inclination of fibers in crossing regions can be determined, it is mandatory to develop a new type of visualization that shows different inclinations in crossing fibers. A three-dimensional vector visualization could be suitable.

Retardation Normalization with ComSLI In 3D-PLI, the retardation is normalized using the measured retardation of in-plane parallel fibers. However, there might be instances where the sample does not contain in-plane parallel fibers, or their presence is uncertain. In such cases, the peak distance map from ComSLI can be employed to

verify if fibers are indeed in-plane and parallel. This is determined by the presence of two distinct peaks at an approximate distance of 180° on the peak distance map. The corresponding retardation value for these fibers can then be used as a reference. Furthermore, it could be possible to develop a retardation correction based on the peak distance also for cases where there are no in-plane parallel fibers in a sample.

Linear and Circular Components of Diattenuation and Retardation Inherently, 3D-PLI and DI do not distinguish between circular and linear components of retardation and diattenuation. Circular effects are expected to be small due in brain tissue. However, when combined with Müller polarimetry, the possible influence of circular components on 3D-PLI and particularly on the recently developed DI can be explored anyway. This relies on a very good signal-to-noise ratio to possibly detect even the most subtle effects.

Inclusion of Depolarization Within this chapter, the effects of depolarization have been mostly neglected. However, a physical connection between scattering and depolarization is expected. Investigating how depolarization influences other modalities can enhance the evaluation and understanding of 3D-PLI and DI. Moreover, depolarization can indicate tissue degeneration (e.g. caused by tumors or neurodegenerative diseases), so incorporating depolarization and its relationship to birefringent properties can help in understanding pathological alterations.

Observing Pathological Birefringence Changes When myelin degenerates – often in the course of neurodegenerative diseases, s. Section 2.3.4, the consequent birefringence change leads to an apparent change of fiber directions: The existence of myelin leads to a strong negative birefringence. When myelin degenerates, only the remaining axon exhibits a weaker and positive birefringence. However, the fiber directions obtained by ComSLI are not influenced by this phenomenon because scattering is mostly unaffected by the effect, as shown by GEORGIADIS ET AL. [61] and also addressed in Section 7.1. Multi-modal analysis can support the investigation of neurodegenerative diseases by comparing ComSLI and 3D-PLI directions. Furthermore, the differentiation between D^+/D^- fibers obtained from DI could provide valuable insights into the anatomy of pathological tissue.

Artifact Removal and Feature Detection As demonstrated as a proof-of-principle in Section 6.1, artifacts such as crystallization artifacts in the embedding medium show unique features that distinguish them from tissue. An automatic artifact removal based on multi-modal parameter maps can improve the evaluation of measured data in case of low quality or old samples. Furthermore, anatomical features such as blood vessels in the tissue can be detected by their unique combination of optic properties.

Investigation with Different Wavelengths Fibers of various thicknesses can be examined by using light of different wavelengths. Measurements with different wavelengths can be implemented for each of the four modalities. However, investigations are limited to the visible spectrum because the optic components are specialized for this wavelength range. For the polarimetric techniques 3D-PLI, DI, and Müller Polarimetry, an appropriate spectral filter must be incorporated into the setup, thus replacing the green spectral filter, and the LCVRs need to be characterized correspondingly.

Chapter 7

Advancing ComSLI

Computational scattered light imaging (ComSLI) as established in Section 3.5 is still in active development. This chapter delves into various enhancements to the original ComSLI setup and the ComSLI measurement routine.

So far, ComSLI was only applied to cryo-sectioned samples. Here, the **application of ComSLI to formalin-fixed paraffin-embedded (FFPE) sections** is presented, aiming to expand its use from specially prepared sections to a diverse range of histological tissue samples, including FFPE sections with various stains.

As a hardware upgrade to the ComSLI setup introduced in Section 3.6, a **customized XY scanning stage** was developed to accommodate the oblique illumination that is integral to ComSLI. Thus, a high resolution can be achieved during the measurement of a whole sample. Furthermore, the implementation of a **new high-sensitivity camera** has improved the detection of minor intensity differences. These hardware modifications required the development of a new measurement software to integrate the XY stage and the camera into the automatic measurement routine.

The high-sensitivity camera is crucial for the successful **Compressed Sensing illumination**: Rooted in compressed sensing, this novel illumination strategy can substantially shorten the measurement time and the required data storage, aiming towards high-speed measurement of scattering patterns in scatterometry ComSLI.

All enhancements made to hardware, software, and measurement in this chapter are also applicable to the Scattering Polarimeter and can be used for future improvement of the multi-modal setup.

7.1 Formalin-Fixed Paraffin-Embedded Tissue

Unlike polarization-based techniques, ComSLI is independent of birefringence. This leads to the assumption that ComSLI is applicable not only to unstained cryo-sectioned brain tissue, as introduced in Section 3.1, but also to a broad spectrum of stained or unstained histology sections.

Formalin-fixation and paraffin-embedding (FFPE) is the standard method for preparing high-quality tissue sections in both clinical and research histology. In this process, tissue is dehydrated and paraffin-embedded for easier subsequent sectioning with a microtome, as illustrated in Section 3.1.1. During these steps, a large percentage of lipids is removed due to the use of organic solvents, especially hydrophobic solvents like alcohol, during the dehydration step, thereby disturbing the layer nanostructure of myelin and resulting in significant birefringence loss.

Polarization-based techniques cannot be used on FFPE brain sections, as shown by CARRIEL ET AL. [35]. So far, fiber pathways in white matter can only be extracted indirectly from stained FFPE sections, namely by image processing of specific histology stains, for example through *Structure Tensor Analysis* (STA) as shown by BUDDE ET AL. [30] and SCHURR ET AL. [170]. Thus, direct measurement of nerve fiber orientations in densely packed but non-birefringent tissue remains challenging.

The investigations presented here serve as a proof-of-principle and open up the possibility of combining histological insights from cell body distributions of stained FFPE samples with detailed mapping of nerve fiber architecture in brain tissue samples. Parts of the following chapter were published in AUF DER HEIDEN ET AL. [76]. The tissue samples with H&E, Perls' Iron (+ hematoxylin), and Tau staining (+ DAB enhancement) were provided by the Stanford University School of Medicine.

7.1.1 Methods and Materials

As a proof of principle, the direct measurement of fiber orientations in FFPE brain sections is demonstrated. Two human brains (male, 30 and 71 years, no neurological diseases) were formalin-fixed, dehydrated in increasing alcohol series, embedded in paraffin, and coronally cut with a large-scale microtome into 20 µm-thin sections. After deparaffinization, two different stains were applied to highlight neuronal cell bodies: the sections of the first brain were stained with Cresyl violet, the sections of the second one with silver (Ag) Nissl, following the procedures shown in Section 3.1.1.

A section from each brain at approximately the same plane was selected. Figure 7.1a and Figure 7.1b display the investigated samples with a rectangle indicating the imaging area. An area was chosen that contains characteristic fiber structures introduced in Section 2.3, specifically the in-plane parallel fibers of the corpus callosum (cc) and the crossing fibers of the corona radiata (cr). As a reference, Figure 7.1c indicates the expected nerve fiber orientations obtained with 3D-PLI in a comparable imaging area for a cryo-sectioned coronal brain tissue sample (reference FOM provided by AXER & AMUNTS [14]).

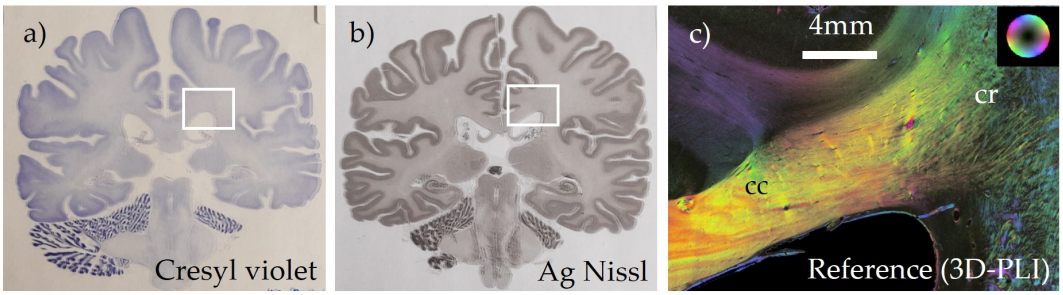

FIGURE 7.1: Formalin-fixed paraffin-embedded (FFPE) brain sections. The sections were stained for cell bodies with a different stain, respectively. a) Picture of FFPE section with Cresyl violet stain. The rectangle indicates the imaging area that was investigated with ComSLI. b) Picture of FFPE section with silver (Ag) Nissl stain. The rectangle indicates the imaging area that was investigated with ComSLI. c) A cryo-sectioned coronal human sample yields the expected fiber orientations in a comparable imaging area with three-dimensional polarized light imaging (3D-PLI) [14].

7.1.2 Birefringence Loss in FFPE Brain Sections

3D-PLI reference measurements (s. Section 3.2) were performed for both samples with the LMP3D s. Section 3.6.2). 3D-PLI could not retrieve any fiber directions from the FFPE sections due to birefringence loss, and the color-coded fiber orientation maps (FOMs) only show statistical noise, as seen in Figure 7.2.

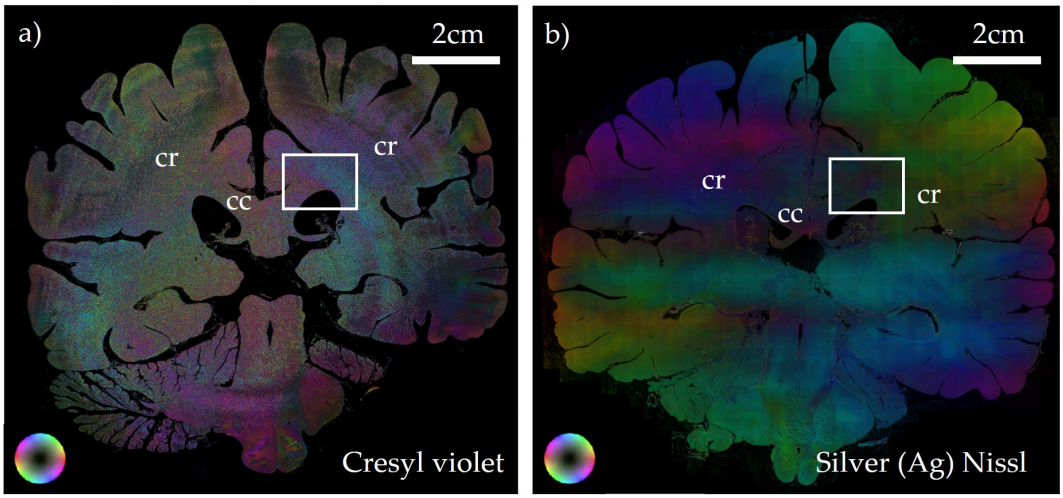

FIGURE 7.2: 3D-PLI FOMs for Cresyl violet stained and silver stained FFPE sections. During the embedding process, the myelin sheaths were disrupted by alcoholic solvents leading to a loss of birefringence. 3D-PLI detected only statistical noise. The in-plane parallel fibers of the corpus callosum (cc) and the crossing fibers of the corona radiata (cr) are indicated for reference. a) Cresyl violet stain b) Silver (Ag) Nissl stain.

7.1.3 Direct Measurement of Fiber Orientations in FFPE Brain Sections

The sections were measured with ComSLI setup (s. Section 3.6.3). During measurement, each section was illuminated by angular illumination (green angular segments in 15° steps, segment width 9°, inner radius 28 LEDs, outer radius 69 LEDs, incidence angle of 47°, Cresyl violet: exposure time 10 seconds, gain[1] x10 ; Ag Nissl: 5 seconds, gain x5; 4 repetitions for both, measured with the Basler camera, s. Section 7.2). The evaluation is performed with the SLI ToolboX (SLIX) as introduced in Section 3.5.

In contrast to the 3D-PLI measurements in Figure 7.2, the ComSLI measurements in Figure 7.3 and Figure 7.4 successfully retrieve the expected nerve fiber directions. The zoom-in displays the corresponding vector maps for two areas, demonstrating how fiber crossings are resolved in the FOM.

The corpus callosum fiber bundles run mostly diagonally in the image plane (green and yellow directions) with some distinct horizontal bundles (red). However, even though fiber crossings in the corona radiata can be resolved, regions with crossing fibers have a lower signal-to-noise ratio. Optimizing measurement parameters, such as brighter illumination or longer exposure time, might help overcome this issue. Overall, the signal from the silver (Ag) Nissl section is stronger than that from the Cresyl-violet section, resulting in more colored pixels in the corresponding FOM.

[1]Here, the gain is not given in dB but as a multiplication factor as it was implemented in the LabView measurement software *SLI-Commander* prior to the Python measurement software *pySLI* developed in Section 7.2.

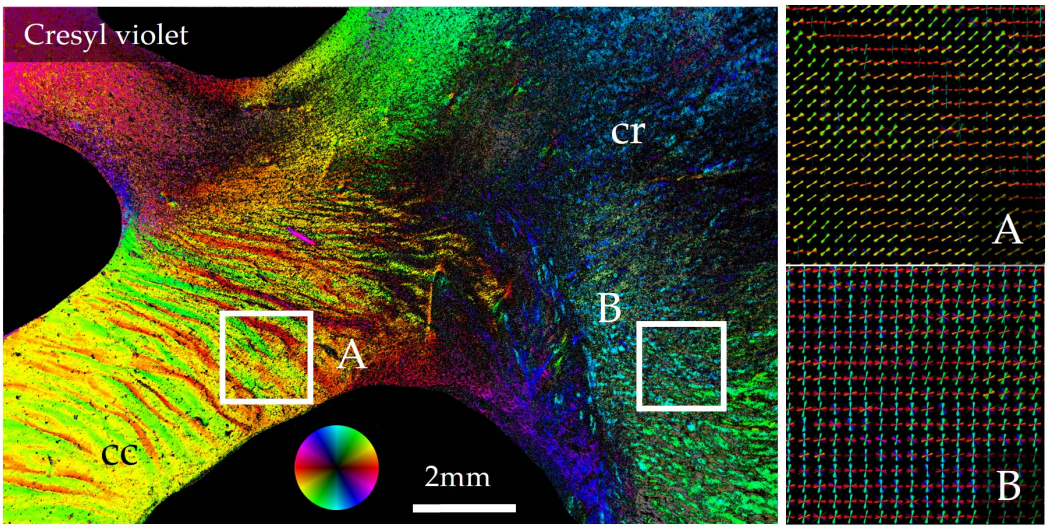

FIGURE 7.3: FOM and vector maps for Cresyl violet stained tissue. The ComSLI fiber orientation map (FOM) of the stained FFPE section (left) shows that fiber directions are detected successfully for the in-plane parallel fiber of the corpus callosum (cc) and for the crossing fiber bundles of the corona radiata (cr). Vector maps (A, B) visualize the fiber orientations for the corpus callosum (A) and corona radiata (B).

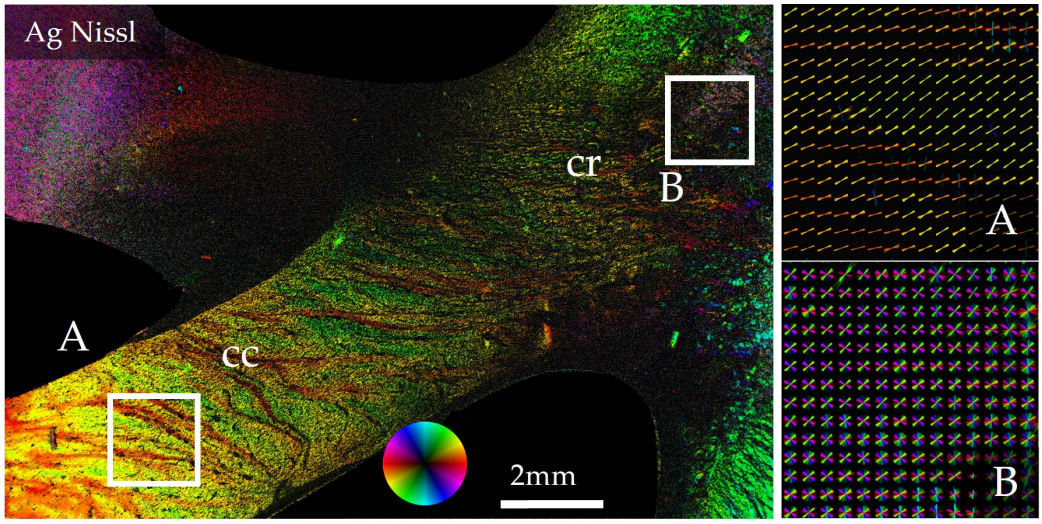

FIGURE 7.4: FOM and vector maps for silver (Ag) Nissl stained tissue. The ComSLI fiber orientation map of the stained FFPE section (left) shows that fiber directions are detected successfully for the in-plane parallel fiber of the corpus callosum (cc) and, to lesser extent, for the crossing fiber bundles of the corona radiata (cr). Vector maps (A, B) visualize the fiber orientations for the corpus callosum (A) and corona radiata (B).

Figure 7.5 shows that ComSLI also retrieves fiber directions for various stains and fiber architectures, here: H&E, Perls' Iron (+ hematoxylin), and Tau staining (+ DAB enhancement) (s. Section 3.1.1). Fiber directions are detected especially well in white matter. The detection of gray matter signals remains challenging.

The investigations showcase the direct measurement of fiber directions in FFPE sections and open up the possibility to combine the measurement of cell body distributions in cell-body stained FFPE brain sections with detailed mapping of the intricate nerve fiber architecture. A wide range of stains and fibrous tissues (e.g. brain tissue, but also muscle tissue) was investigated in a follow-up study by GEORGIADIS ET AL. [61].

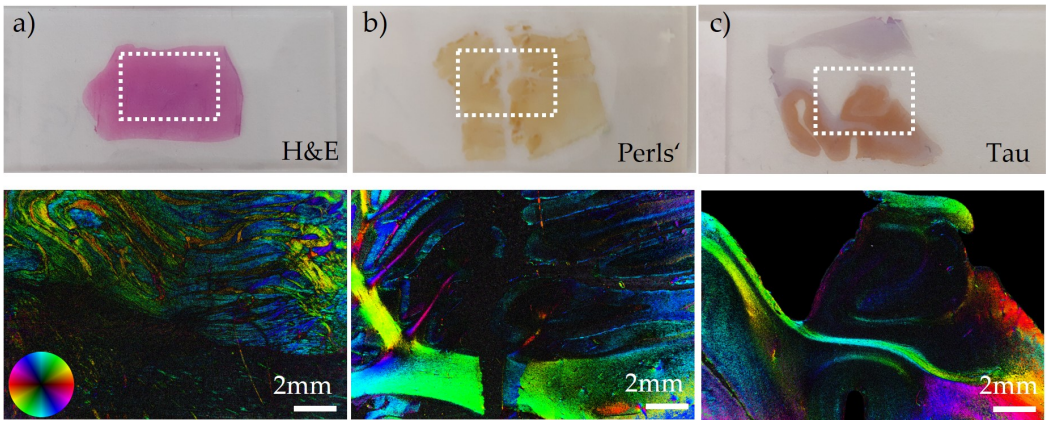

FIGURE 7.5: Fiber directions in brain tissue sections with various histological stains. a) Hematoxylin and eosin (H&E), b) Perls' iron stain, c) Tau stain. A wide range of stains and fibrous tissues was investigated by GEORGIADIS ET AL. [61].

7.2 High-Sensitivity Camera

A more sensitive camera allows for a shorter exposure time, thereby increasing measurement speed while maintaining or even improving the signal-to-noise ratio. Scatterometry ComSLI, and especially the more advance illumination strategy based on compressed sensing in Section 7.4 greatly benefit from a camera capable of detecting minor differences in light intensity.

7.2.1 Camera Specifications

Originally, the *BASLER acA5472-17uc* CCD camera (only referred to as *Basler* for simplicity) was installed in the ComSLI setup, as presented in Section 3.6. The same model of the Basler camera is currently also installed in the Scattering Polarimeter, s. Section 4.2. To investigate the performance of a higher-sensitivity camera, the Basler camera was replaced in the ComSLI setup by the *SVS-VISTEK HR455CXGE* CCD camera, or simply *Vistek*. The Vistek camera has a significantly larger sensor dimension and pixel size, resulting in enhanced sensitivity for low light measurements but also the ability to differentiate small intensity differences in medium and bright light settings. The area of a single sensor pixel is nearly 2.5 times larger and the entire sensor area is nearly 7.5 times larger than that of the Basler camera. Correspondingly, the number of image pixels increases as well.

The Vistek camera was paired with the *Qioptiq OPTEM Lower Lens 1.25/160mm*, thus keeping a field of view comparable to the previous objective lens *Rodenstock Apo-Rodagon-D120* [51]. Table 7.1 compares the two cameras in combination with their respective objective lenses. The resolution was measured with the standardized USAF (United States Air Force) test target.

7.2.2 Software Interface

The camera manufacturer provides a software development kit (SDK) in C++ that can be integrated into a measurement software. In this case, a fundamentally new measurement software called *pySLI* was developed in Python to replace the former LabView-based software *SLI-Commander*, thus offering open-source accessibility and improved versioning. The new software integrates the SDK using the Python module *ctypes* [78]. Just like the light source and the XY stage developed in Section 7.3, the camera was implemented into the routine as an object, allowing for easier interchangeability between different cameras. Apart from the camera access via *ctypes*, the software closely resembles the program introduced in Section 4.4 but without an LCVR interface.

camera	Vistek	Basler
sensor pixel size	$3.76 \times 3.76\,\mu m^2$	$2.4 \times 2.4\,\mu m^2$
sensor dimension	$36.0 \times 24.0\,mm^2$	$13.1 \times 8.8\,mm^2$
pixel number	9568×6380 px	5472×3648 px
resolution	$3.1 \times 3.5\,\mu m^2$	$3.5 \times 3.5\,\mu m^2$
field of view	$14 \times 10\,mm^2$	$16 \times 11\,mm^2$

TABLE 7.1: Comparison of Basler and Vistek camera specifications. The *SVS-VISTEK HR455CXGE* (in short: *Vistek*) camera replaced the *BASLER acA5472-17uc* (*Basler*) camera in the ComSLI setup. The Vistek camera offers a larger sensor and sensor pixel size while maintaining a similar field of view, thus achieving greater sensitivity for low light measurements and the ability to differentiate small intensity differences.

7.2.3 Comparative Measurement

Figure 7.6 displays the fiber orientation map (FOM) for Vervet1818 as calculated from a measurement with the Basler camera (left) and with the Vistek camera (right). Both measurements were taken with the same measurement parameters (angular green illumination in 15° steps, segment width 9°, inner radius 28 LEDs, outer radius 69 LEDs, exposure time 500 ms, 4 repetitions, gain 3 dB). Generally, the FOMs show

similar directions and crossing for both cameras. Directions in the cingulum or gray matter fibers are not resolved by any of the two cameras. However, the Vistek camera has nearly twice the pixel number in both dimensions compared to the Basler camera. In the FOM, fewer pixels are dark, indicating an improved signal-to-noise ratio. The better signal can be observed in nearly all white matter regions, such as the corona radiata, corpus callosum, and fornix. Additionally, gray matter areas are less affected by noise when using the Vistek camera. The vector maps from the border area between the corpus callosum and corona radiata, shown below the FOMs, underline the higher sensitivity of the Vistek camera, as indicated by a higher density of successfully evaluated vectors.

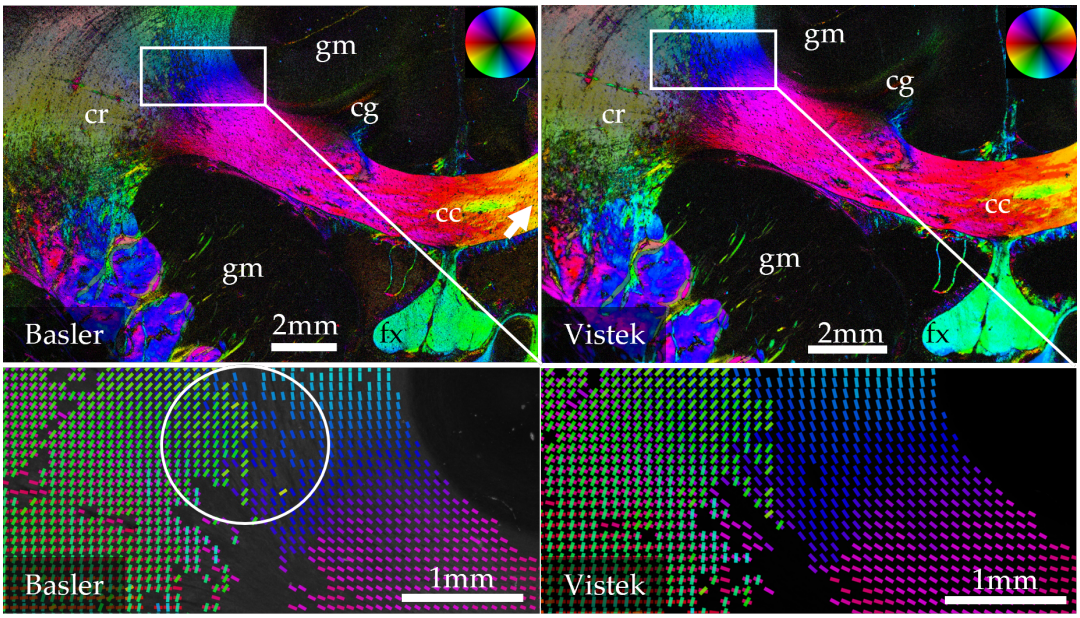

FIGURE 7.6: FOM and vector map comparison between Basler and Vistek cameras. Vervet1818 was measured with the Basler camera and the higher-sensitivity Vistek camera. Top: FOMs for Basler (left) and Vistek (right). Bottom: Vector maps for selected area (indicated by a rectangle in the FOMs) for Basler (left) and Vistek (right). Both measurements were taken with the same measurement parameters and yield similar directions and crossing for Vervet1818. However, the Vistek camera has nearly twice the pixel number in both dimensions. In the FOM, less pixels are dark, indicating a better signal-to-noise ratio in the corona radiata (cr), the corpus callosum (cc), and the fornix (fx), but also in the gray matter (gm) that shows less noise for the Vistek camera. The cingulum (cg) is not resolved well with either camera. The vector maps show a higher density of evaluated vectors for the Vistek camera, e.g., within the region marked with a circle.

7.2.4 Gamma Correction

The gamma value γ of an imaging system describes the relation between an input value I_{in} and an encoded output value I_{out}. Gamma correction accommodates for the non-linear human perception of intensities [155]. γ is defined by

$$I_{\text{out}} \propto I_{\text{in}}^{\gamma} \tag{7.1}$$

In the case of the ComSLI imaging system, the gamma correction factor γ connects the color value detected by the camera with the color value displayed by the LED

panel that is used light source. Gamma characterization is not required for angular or scatterometry ComSLI, where illumination is monochromatic and typically uses only one color (usually green or white light at maximum intensity). However, it is crucial when intensity gradients are employed, especially to calculate the correct transformation coefficients in compressed sensing ComSLI (s. Section 7.4).

To determine γ for the ComSLI setup, 256 images of linearly increasing gray values – from black with a gray value of 0 up to white with a gray value of 255 – were displayed on the LED panel and their brightness was measured (exposure time 350 ms, 2 repetitions, gain 3 dB). When γ is 0, the slope is linear. Otherwise, the curve shows exponential behavior. The results were fitted to Eq. (7.1) and shown in Figure 7.7. Overexposed gray values show clipping, while underexposed gray values remain zero. The fitting range excluded those values. The imaging system has a gamma value of $\gamma = (2.641 \pm 0.008)$.

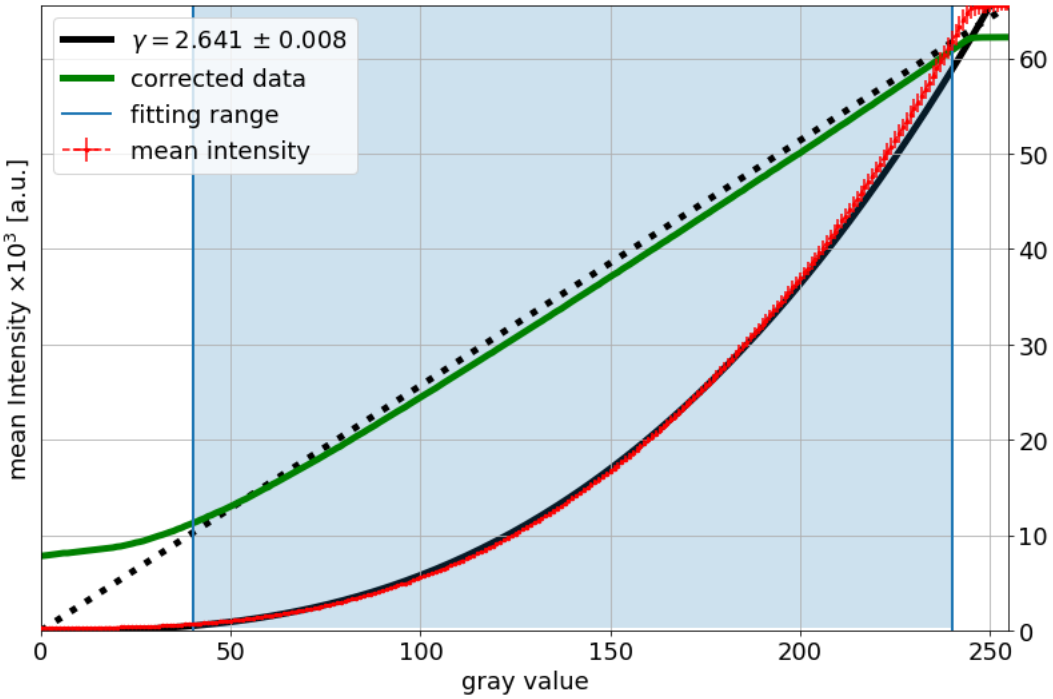

FIGURE 7.7: Gamma correction of the Vistek camera. The dashed line indicates a linear slope, i.e. $\gamma = 0$. The gamma correction γ connects the color value detected by the camera with the color value displayed by the light source. Fitting a power-law function to the detected intensity for each displayed intensity value yields $\gamma = (2.641 \pm 0.008)$. Fitting only data points within the indicated fitting range excludes over- and underexposed intensity values. As a control, the green curve displays the intensity curve after gamma correction which restores the (nearly) linear slope. Gamma correction does not need to be considered for angular or scatterometry ComSLI, but is crucial in the context of compressed sensing ComSLI s. Section 7.4.

7.3 Automatized High-Resolution Scan

A typical coronal section of the human brain, taken from its center, measures approximately 14 cm in diameter. However, the ComSLI setup has a much smaller field of view of about $14 \times 10\,\mathrm{cm}^2$. While using a different objective lens with a larger numerical aperture would increase the imaging area, this would result in a loss of resolution

and furthermore introduce a gradient of uneven illumination across the section[2]. To address this issue, a custom XY stage was integrated into the ComSLI setup. An advanced version of the 3D-printed sample holder was developed by Stefan Schiffer from the Institute of Neuroscience and Medicine (INM-1, Forschungszentrum Jülich GmbH, Germany).

7.3.1 Construction

The rail design is inspired by the *Cartesian Plotter v3* developed by SLEIGH [176] but was customized for the application. The scanning stage hardware consists of two stepper motors mounted on two crossing rails. The stepper motors are controlled by an *Arduino Uno Rev 3* [9] combined with the *joyIT CNC Shield* and two suitable motor drivers *A4988* [88]. The CNC (*computerized numerical control*) shield can drive up to 4 *NEMA 23* (*National Electrical Manufacturers Association*) bipolar stepper motors by utilizing an external voltage source of 25 V [89]. The stepper motors operate within a voltage range from 12 V to 36 V and generate a torque of 3 Nm each, which is sufficient for the lightweight low-friction scanning stage.

Each full step of a stepper motor corresponds to a 1.8° rotation, allowing for 200 discrete steps per revolution. *Microstepping* reduces noise and smooths the rotation, thereby preventing vibrations. An electrical connection between designated contacts on the CNC shield enables microstepping with various substeps. The smallest microstep has a fraction of 1/32 of the original step size, i.e. a 0.5625° rotation per microstep. The corresponding contacts were soldered together.

Gears translate the motor rotation into a linear movement in X and Y direction. The first motor moves a sleigh along a rail via a belt, while the second motor, placed atop the sleigh, pulls a second belt, thereby enabling movement in both directions. Custom parts, including a sample holder, connective elements, and a protective case for the Arduino and CNC shield, were 3D-printed from polylactic acid (PLA). To minimize reflections, the reflective components of the XY stage were covered with black masking tape where applicable. Figure 7.8 shows the finished XY stage.

7.3.2 Integration into Measurement Software

The Arduino firmware, written in C and uploaded via the Arduino IDE, awaits serial input from the measurement computer. It interprets two types of signals: movement in the X and Y directions. Both functions support positive and negative values for forward and backward movements. The conversion from rotation steps to movement distance depends on the gears and is calculated based on the gear circumference and the number of (micro-) steps

$$\frac{\text{steps}}{\text{distance}} = \frac{200 \cdot 32}{\pi \cdot d_{\text{gear}}} \tag{7.2}$$

With gear diameters d_{gear} of 30 mm (Y axis) and 20 mm (X axis), the required steps per distance are 68 $\frac{\text{steps}}{\text{mm}}$ (X axis) and 102 $\frac{\text{steps}}{\text{mm}}$ (X axis). The conversion is already established within the Arduino firmware, meaning that the Arduino awaits a distance given in millimeters. When the stage movement is finished, the applied voltage is set to zero to reduce noise. The XY scanning stage is integrated into the measurement

[2] e.g. rendering the left side of the illuminated section much brighter when it is illuminated from the left, and vice versa.

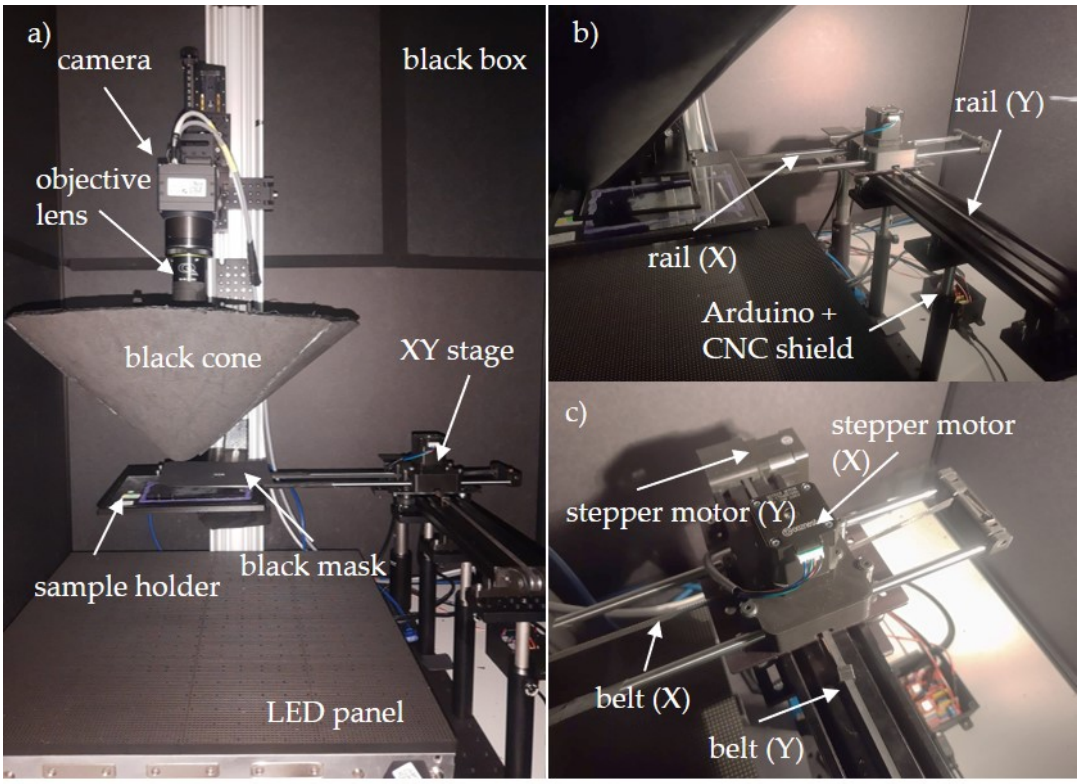

FIGURE 7.8: XY scanning stage and Arduino with CNC shield. a) Overview of the ComSLI setup. The setup comprises also the new camera introduced in Section 7.2. b) The XY scanning stage. The rail design is inspired by the *Cartesian Plotter v3* but customized for the application [176]. The scanning stage hardware consists of two stepper motors mounted on two crossing rails, an Arduino with a CNC Shield and an external voltage source of 25 V. The Arduino is connected to the stepper motors, the computer and the external voltage source and kept in a protective case. c) Close-up of the previous photo.

software with a serial connection using the Python module *pyserial* [103]. Now, the XY stage can scan a sample tile-wise by implementing the measurement routine into a for-loop for movement in X and Y direction. The overlap between tiles is set to 1 mm on each side to facilitate stitching.

7.3.3 Stitched Fiber Orientation Map

Figure 7.9 shows the fiber orientation map (FOM) for Vervet1818 from 5×5 angular ComSLI measurements (downscaled by a factor of 10 for visualization purposes) obtained with the Vistek camera. Here, the stitching was performed by the automatic stitching routine within the imaging software *Fiji (ImageJ)* [68]. The routine assembled a single image from 5×5 measurement images, each of them with the 24 measurement angles of a 15° angular measurement, thus generating a set of 24 complete images.

The SLI ToolboX (SLIX) evaluated the image set and generated the FOM as detailed in Section 3.5. For more image tiles, the use of a specialized stitching routine for large data sets is recommended.

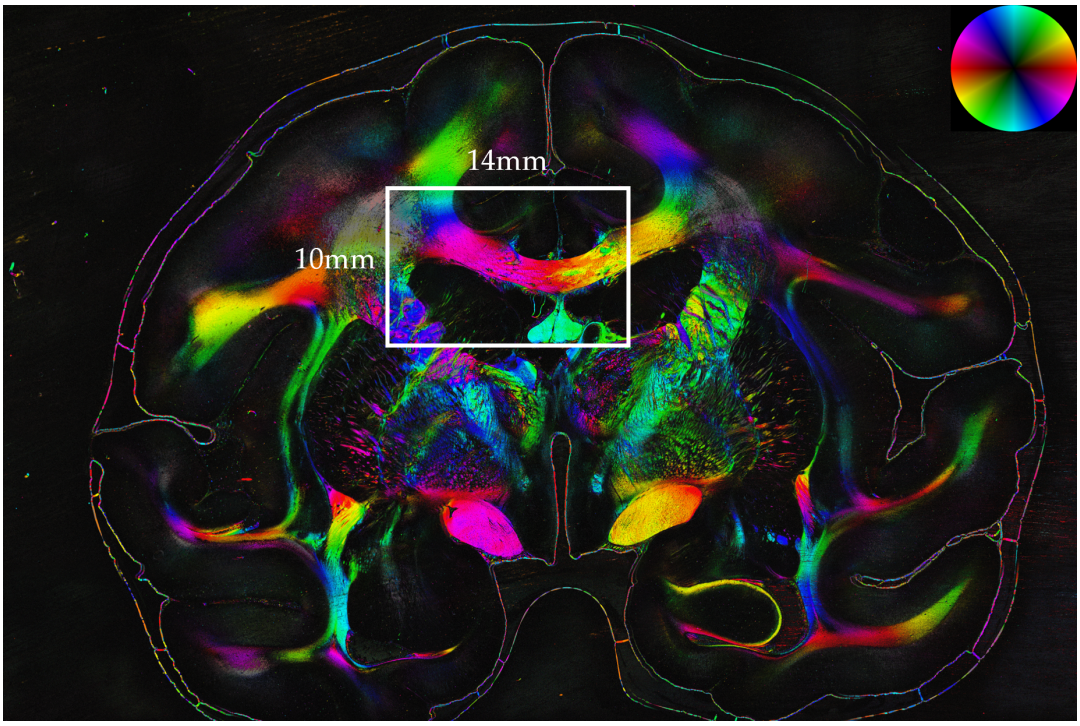

FIGURE 7.9: Stitched FOM obtained from XY scan. The complete sample area of Vervet1818 was stitched together from 5×5 angular ComSLI measurements with the Vistek camera. Here, the stitching was performed by the automatic stitching routine from *Fiji (ImageJ)* [68]. The SLI ToolboX (SLIX) evaluated the set of 24 stitched angular images and generated the FOM for visualization. The size of the field of view is indicated for the Vistek camera.

7.4 High-Speed Compressed Sensing Illumination

Integrating compressed sensing into scatterometry ComSLI can achieve a significant speed-up of the measurement. A highly sensitive camera is integral to the measurement and the integration of such a camera was detailed in Section 7.2. Partially, the following results were published in AUF DER HEIDEN ET AL. [77]. First investigations on the topic of Compressed Sensing in scatterometry ComSLI were made by Oliver Münzer from the Institute of Neuroscience and Medicine (INM-1, Forschungszentrum Jülich GmbH, Germany). The line profiles were calculated by Simon van Staalduine from the Department of Imaging Physics at the Delft University of Technology.

7.4.1 Compressed Sensing in ComSLI

Compressed sensing reconstructs a signal from fewer measurements than required by the *Shannon-Nyquist theorem* [171], under the condition that the signal is *sparse* (as described by CANDES ET AL. [33]). Approximately sparse signals, i.e. *compressible* signals, can nearly be recovered. By following a non-linear method called *Compressed Sensing* and measuring only those coefficients that have the highest impact on the recovery of the actual signal, measurement efforts can be reduced drastically with no or little perceptual loss as shown by DONOHO ET AL. [48]. In scatterometry ComSLI, the sparsity condition is fulfilled: The illumination grid as introduced in Section 3.5 can be interpreted as a matrix with a gridsize N×N that contains only zeros except for one non-zero entry, representing the single illuminated square. The complete illumination sequence forms a mathematical basis of N×N matrices that is referred

to as *Euclidean illumination* to distinguish it from compressed sensing illumination. To obtain a compressible set of matrices, the Euclidean matrices are transformed into the frequency domain by applying a *discrete cosine transformation* (DCT) of type II (DCT-II) [4, 180]. The DCT-II coefficients f_0 and f_k are defined as

$$f_0 = \frac{\sqrt{2}}{N} \sum_{n=0}^{N-1} x_n \tag{7.3}$$

$$f_k = \frac{2}{N} \sum_{n=0}^{N-1} x_n \cos\left[\, \frac{\pi}{N} \left(n + \frac{1}{2}\right) k \,\right] \qquad \text{for } k = 1, \ldots N-1 \tag{7.4}$$

Then, the two-dimensional DCT-II coefficients are

$$f_{k_1,k_2} = \sum_{n_1=0}^{N_1-1} \left(\sum_{n_2=0}^{N_2-1} x_{n_1,n_2} \cos\left[\frac{\pi}{N_2}\left(n_2 + \frac{1}{2}\right) k_2\right]\right) \cos\left[\frac{\pi}{N_1}\left(n_1 + \frac{1}{2}\right) k_1\right] \tag{7.5}$$

$$= \sum_{n_1=0}^{N_1-1} \sum_{n_2=0}^{N_2-1} x_{n_1,n_2} \cos\left[\frac{\pi}{N_1}\left(n_1 + \frac{1}{2}\right) k_1\right] \cos\left[\frac{\pi}{N_2}\left(n_2 + \frac{1}{2}\right) k_2\right] \tag{7.6}$$

The obtained matrices represent a new illumination sequence characterized by periodic fluctuations in intensity (different gray values) with increasing frequency. It is important to note that these matrices may contain both positive and negative entries. Light intensity can inherently only take positive values; therefore the positive and the negative part of the matrix are measured separately, resulting in two illumination matrices per transformed matrix and thus 2×N×N required measurements. This approach may appear counter-intuitive since it doubles the number of required measurements. However, during compressed sensing, only the low-frequency illumination matrices need to be measured, such as the lowest 2×8×8 coefficients in a 64×64 grid. Assuming the signal is compressible, higher coefficients can be assumed to be zero. Therefore, this approach is still beneficial and reduces the number of required measurements from 4096 to 128, which is a reduction by a factor of 32. The calculated matrix entries are upscaled to 255 so that the LED intensities cover the full available display range from 0 to 255. Figure 7.10 shows exemplary illumination matrices.

It should be mentioned that instead of using a DCT, a *discrete Fourier transformation* (DFT) could have been employed. The advantage of using a DCT is the faster decrease of the coefficients than the corresponding DFT coefficients. Furthermore, the DFT requires twice as many measurements to consider not only the negative parts, but also the positive and negative imaginary parts of the calculated matrices.

7.4.2 Generation and Reconstruction of Scattering Patterns

The measured images are processed as established in Section 3.5: The scattering patterns for every pixel are generated by arranging the measured intensities in a 64×64 grid, corresponding to the order in the measurement. The shape of the scattering pattern corresponds directly to the fiber orientations.

In case of the DCT illumination, the positive and negative image sets are initially treated separately and rearranged to positive and negative patterns in the DCT space. The results are 2×64×64 patterns per evaluated kernel, one derived from the positive DCT illumination, one derived from the negative DCT illumination that

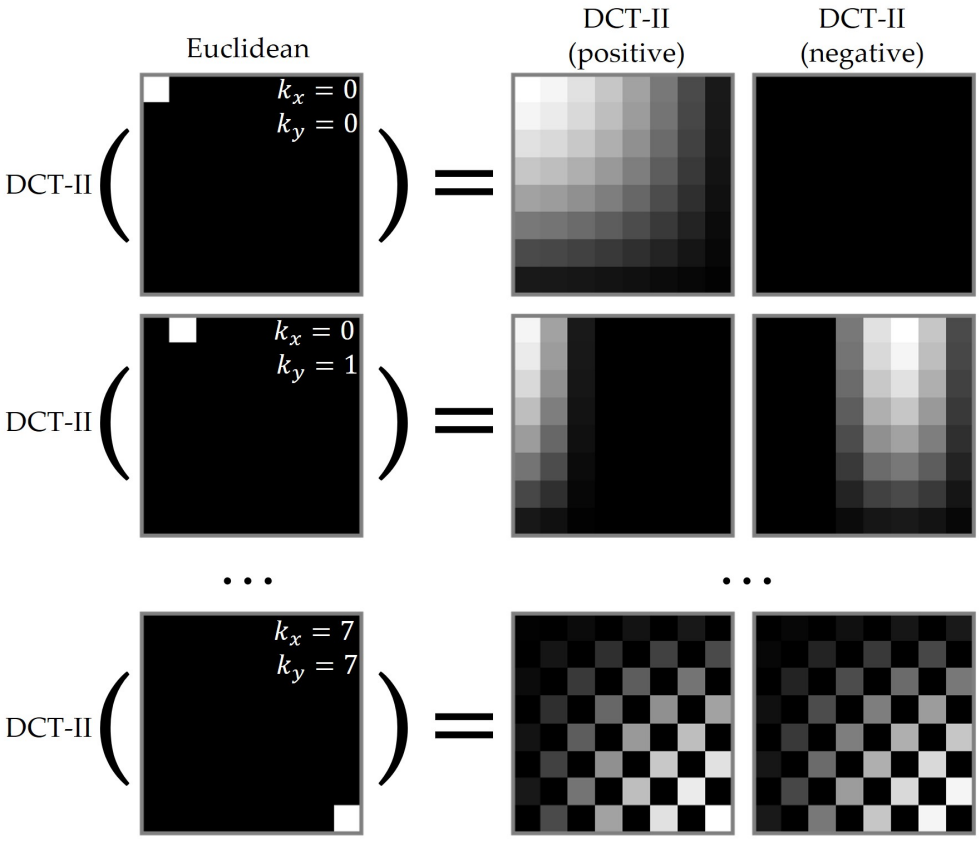

FIGURE 7.10: Discrete cosine transformation (DCT) of illumination patterns. The effect of the DCT-II on the Euclidean matrices is illustrated for 8×8 coefficients. Each Euclidean matrix yields two Compressed Sensing matrices, one representing the positive coefficients and one representing the negative coefficients. When the measurement is compressed, the higher-order coefficients have a low impact on the recovered signal and are not measured but assumed to be zero. The matrices represent how the LED panel is illuminated with different periodic gray values between 255 and 0.

contain both negative and positive values. Figure 7.11 illustrates the reconstruction of the real-space scattering patterns for an exemplary scattering pattern from the corpus callosum (in-plane parallel fibers, bar-shaped scattering pattern): The intensity values of the negative DCT image are subtracted from the intensity values of the positive DCT image, resulting in an image that corresponds to the DCT transform of a scattering pattern obtained with Euclidean illumination. In compressed sensing, the main objective is the reduction of required measurements, i.e. omitting higher-order illumination matrices from the measurement, i.e. setting the coefficients to zero.

An inverse two-dimensional DCT-II retrieves the corresponding real-space scattering pattern

$$x_{k_1,k_2} = \sum_{n_1=0}^{N_1-1} \left(\sum_{n_2=0}^{N_2-1} f_{n_1,n_2} \cos\left[\frac{\pi}{N_2} \left(n_2 + \frac{1}{2} \right) k_2 \right] \right) \cos\left[\frac{\pi}{N_1} \left(n_1 + \frac{1}{2} \right) k_1 \right] \tag{7.7}$$

$$= \sum_{n_1=0}^{N_1-1} \sum_{n_2=0}^{N_2-1} f_{n_1,n_2} \cos\left[\frac{\pi}{N_1} \left(n_1 + \frac{1}{2} \right) k_1 \right] \cos\left[\frac{\pi}{N_2} \left(n_2 + \frac{1}{2} \right) k_2 \right] \tag{7.8}$$

Theoretically, the scattering patterns should contain only positive intensity values. In practice, the calculated scattering patterns contain a portion of negative values. Therefore, only the positive intensity values are taken into account for the subsequent analysis and all negative values are set to zero. Furthermore, the center of the scattering pattern shifts depending on the scattering pattern position in the field of view. For the correct calculation of the line profiles, this offset is corrected based on the distance between consecutively lit LED squares, and the pixel pitch of the optical setup. A polar integral is used to calculate the line profiles by summing up the pixel intensities going from an inner circle with diameter d_1 towards an outer diameter d_2. The inner circle is large enough to contain the either dark (for compressed sensing illumination) or overexposed (for Euclidean illumination) pixels that are directly below the camera. The scattering pattern is sampled for 360 consecutive angles as shown in Figure 7.11, starting at an angle $\phi_0 = 0°$ and going counterclockwise around a circle.

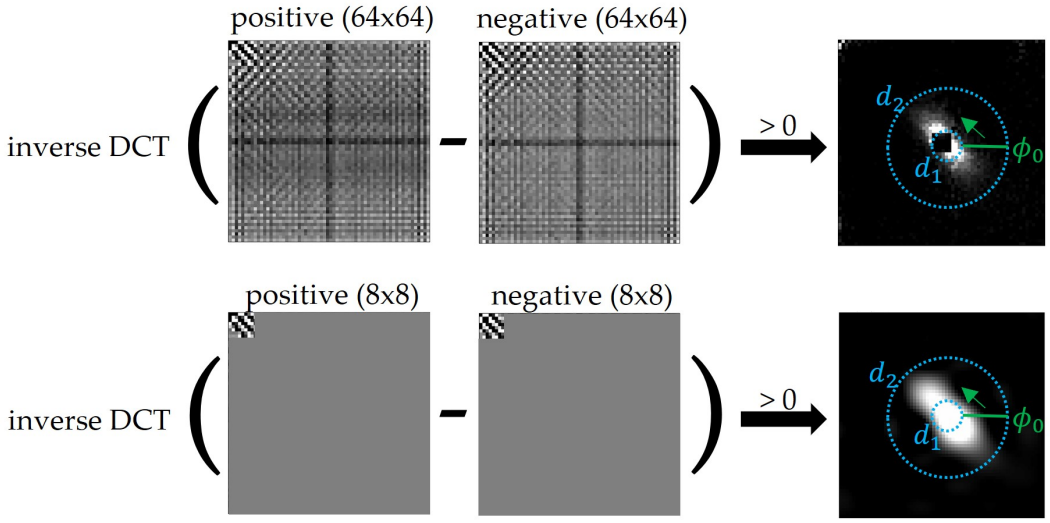

FIGURE 7.11: Reconstruction of Euclidean scattering patterns from DCT images. Two transformed scattering patterns of size 64 ×64 can be reconstructed from the DCT illumination, one from the positive illumination images and one from the negative illumination images. The negative coefficients are subtracted from the positive coefficients. Then, an inverse DCT-II reconstructs the scattering patterns. In case of compression, all coefficients except for the first N× N (here: $N = 8$) are zero, resulting in a blurred scattering pattern. A polar integral is used to calculate the line profiles, leaving out the innermost and outer pixels (radii d_1 and d_2).

7.4.3 Experimental Proof of Principle

Vervet1818 was introduced in Section 5.1. To demonstrate the applicability of compressed sensing to scatterometry ComSLI, an imaging area that contains parts of the corpus callosum (cc), the corona radiata (cr) and the fornix (fx) was chosen, s. Figure 7.12. These regions are exemplary for typical fiber orientations encountered in ComSLI, i.e. in-plane, parallel fibers in the corpus callosum (cc), crossing fibers in the corona radiata (cr) and parallel, inclined fibers in the fornix (fx). For the Euclidean illumination, an exposure time of 1 second was used. For the Compressed Sensing illumination, the exposure time can generally be lower because a greater part of the

LED panel is illuminated. Therefore, an exposure time of 400 ms was chosen, a value where the brightest illumination was not yet overexposed.

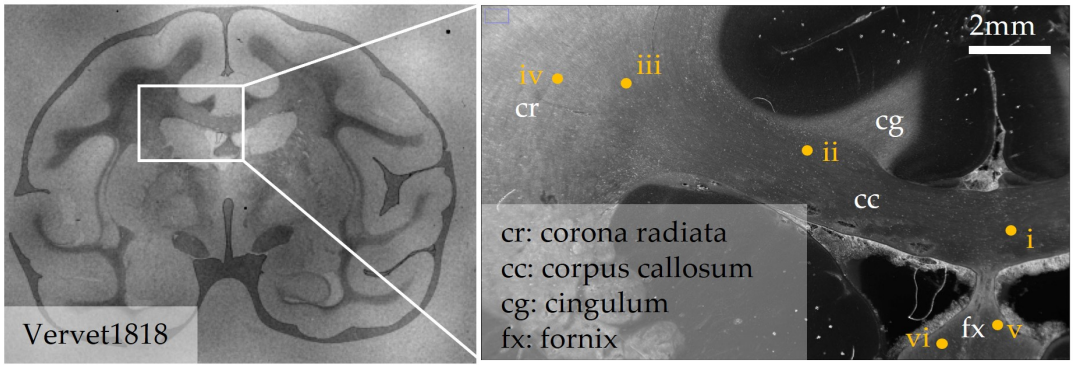

FIGURE 7.12: Imaging area of Vervet1818 for compressed sensing illumination. Left: Overview image (3D-PLI transmittance map) of Vervet1818 with imaging area indicated by a rectangle. Right: A region that contains parts of the corpus callosum (cc), the corona radiata (cr) and the fornix (fx) was chosen to demonstrate Compressed Sensing in ComSLI. Scattering patterns from six positions labeled with lowercase Roman numbers are presented as examples in Figure 7.13.

Two measurement sequences were performed with the ComSLI setup: One with 4096 images in Euclidean base, one with 8192 images in the uncompressed compressed sensing base. The scattering patterns were reassembled as described above and evaluated for every 50-th pixel while averaging over a kernel of the 10×10 surrounding pixels. In case of the Euclidean illumination, the resulting 64×64 images represented the real-space scattering patterns for every evaluated kernel. To simulate the acquisition of measurements with fewer illumination matrices, all coefficients except for the first $N\times N$ coefficients were set to zero, being equivalent to a compressed measurement with a reduced number of illumination matrices. To demonstrate the capabilities of compressing, this was done for 64×64 coefficients (that is, a full uncompressed measurement), 32×32, 16×16 and 8×8 coefficients. The real space scattering patterns were retrieved by applying the inverse DCT in the Python module *scipy.fft* [187] and the line profiles were calculated. To enable a comparison of the obtained line profiles, the intensity values were normalized using

$$I_{\text{norm}} = \frac{I - I_{\text{min}}}{I_{\text{max}} - I_{\text{min}}} \tag{7.9}$$

Subsequently, the line profiles were visualized by plotting the normalized intensity values against the corresponding angles ϕ, ranging from 0° to 360° in steps of 1°. Since the line profiles for each image pixel or evaluated kernel were known now, the fiber orientation map (FOM) was calculated to visualize the fiber orientations in the complete field of view.

7.4.4 Compressed Scattering Patterns and Fiber Orientation Maps

The corpus callosum (cc), the corona radiata (cr) and the fornix (fx) were chosen as test regions with well-known and distinct nerve fiber orientations (s. Section 2.3). These scattering patterns serve as examples for typical fiber orientations encountered in ComSLI, i.e. flat fibers, crossing fibers and inclinated fibers, and as a demonstration of both the potential and the current limits of compressed sensing ComSLI. As a

reference, the first column in Figure 7.13 shows the scattering patterns obtained through the Euclidean illumination patterns. Subsequent columns exhibit increasing degrees of compression, starting with the uncompressed DCT measurement (64×64) up to a highly compressed measurement with only 8×8 coefficients. Notably, the scattering patterns acquired from the DCT measurement feature a dark square in the image center corresponding to the cut-out in the original DCT illumination images. The intensity values are displayed in the *viridis* color map for better visualization. Additionally, line profiles for each scattering pattern in various stages of compression are provided in Figure 7.14.

The corpus callosum primarily contains flat, parallel, in-plane fiber bundles. The characteristic scattering patterns manifest as bar-shaped structures, with the long axis of the bar orthogonal to the fiber direction. The two different directions in the left and right part of the corpus callosum are visible for the Euclidean illumination, but also up to the highest degree of compression. Although the bar blurs increasingly towards higher degrees of compression, the angular direction persists. This observation is supported in the line profiles where the two peaks broaden but keep their angular position at a distance of $\approx 180°$, as expected for in-plane, parallel fibers. At higher compression levels, cross-shaped periodic artifacts along the x- and y-axis become visible but do not significantly influence the overall results.

The corona radiata is characterized by several crossing fiber bundles. The scattering patterns of a coronal brain section are dominated by two crossing in-plane fiber bundles that become visible as an X-shape. The two X-bars correspond again to two fiber directions that are orthogonal to the long axis of each bar. The crossing angle matches up to the fiber bundles' crossing angle. The X-shaped configuration is discernible by the naked eye up to the highest compression levels even though the 8×8 scattering pattern has nearly lost its major directions. Yet, the evaluation of line profiles decreases in precision as the X-shape blurs, the peaks broaden and start to merge and shift as a result of blurriness. Again, artifacts associated with the compression become visible as periodic patterns along the x- and y-axis.

The fornix consists of inclined fibers, i.e. fiber orientations with an out-of-plane component. This manifests as a curvature of the bar-shaped scattering pattern that is characteristic for parallel in-plane fiber bundles. Two scattering patterns are shown where one exhibits a stronger curvature than the other one. As seen in the corpus callosum, the shape of the scattering pattern is stable in its general features such as direction and curvature. The curvature can be observed with the naked eye even up to the highest stage of compression. The line profiles yield distinct and similar peaks, with their distance deviation from 180° reflecting the curvature of the scattering pattern and thereby inclination. Again, the peaks broaden towards higher compression levels but the overall angular position remains stable. As before, compression artifacts are present.

The fiber orientation map (FOM) for each compression stage is calculated from the line profiles as established in Section 3.5. Figure 7.15 shows the results.

7.4.5 Discussion

Initial results for various scattering patterns suggest that compressed sensing based on a DCT-II base is applicable in ComSLI and feasible even for the highest investigated compression level of 8×8. Fiber characteristics are retrieved even from the most compressed scattering patterns. The major directions in the corpus callosum are

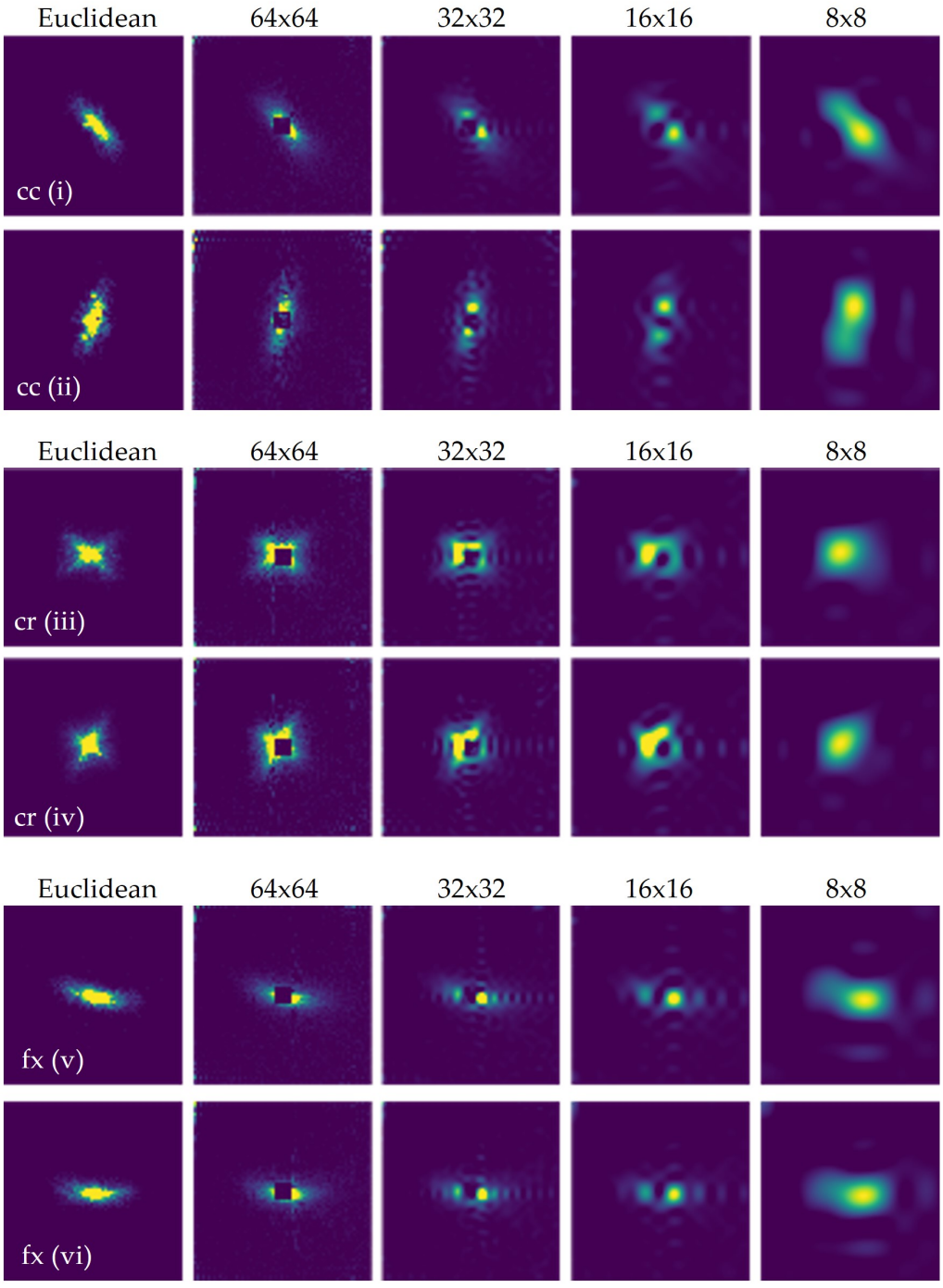

FIGURE 7.13: Selected scattering patterns with increasing compression. The scattering pattern obtained with Euclidean illumination are shown as reference. Row 1-2: Corpus callosum (cc). A bar-shaped scattering pattern is characteristic for in-plane, parallel fibers. The long axis is orthogonal to the fiber direction. Row 3-4: Corona radiata (cr). The characteristic scattering patterns for in-plane crossing fibers have an X-shape where the long axis of each crossing bar is orthogonal to one fiber direction. Row 5-6: Fornix (fx). The characteristic scattering pattern for out-of-plane (i.e. inclined) parallel fibers shows a curvature that increases with higher inclination angles. The curvature is visible up to the highest level of compression.

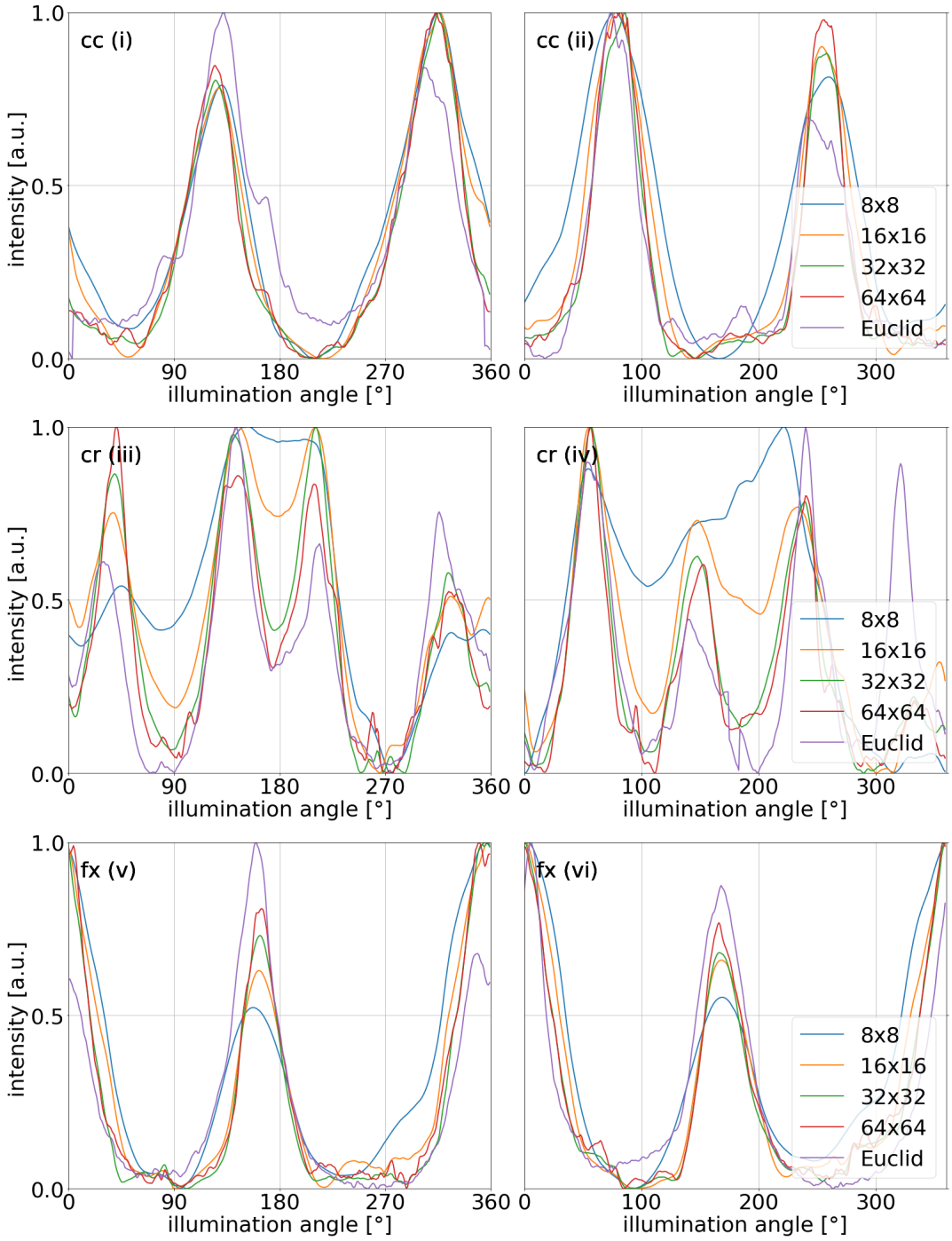

FIGURE 7.14: Selected line profiles with increasing compression. Row 1: Corpus callosum (cc). Two peaks are obtained from the bar-shaped structure; the distance between the two peaks is ≈180°. The minima between the two peaks correspond to the fiber direction. The peaks broaden towards higher levels of compression but their angular position remains stable. Row 2: Corona radiata (cr). Four peaks correspond to the X-shaped scattering pattern and represent the two crossing fibers. Their angular position shifts and merges for higher levels of compression. Row 3: Fornix (fx). Two peaks correspond to the curved bar shape; the distance between the two peaks deviates from 180° and is related to the out-of-plane inclination of the fiber. The peaks broaden towards higher levels of compression but their angular position remains stablee.

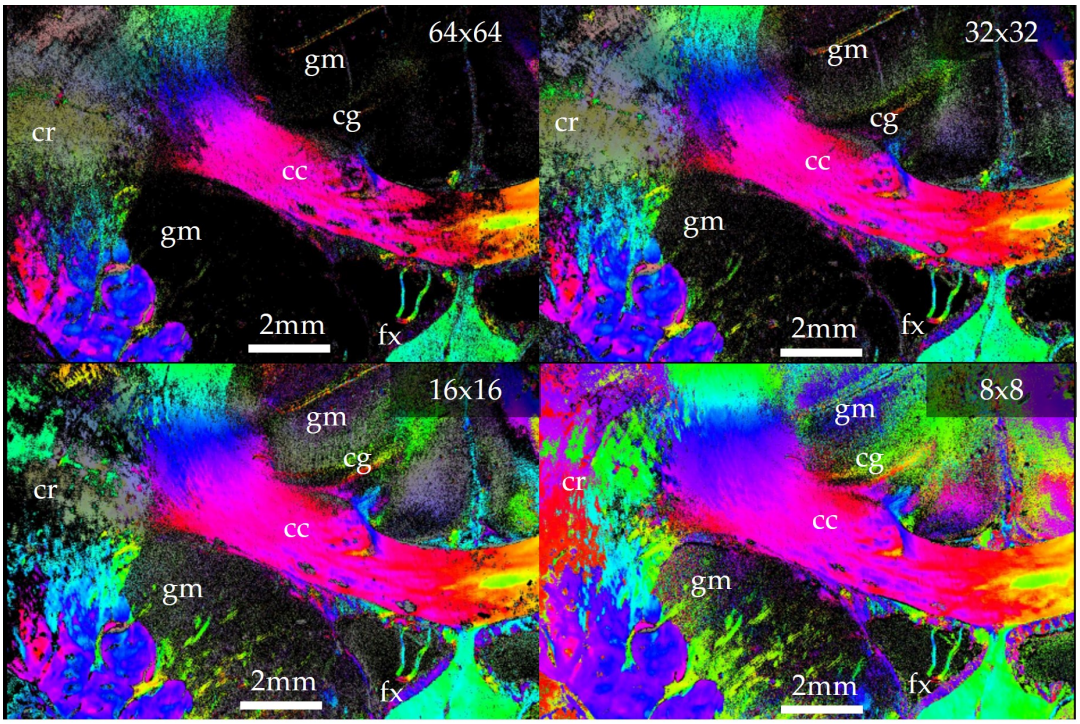

FIGURE 7.15: FOMs with increasing compression. For lower compression levels, compressed sensing smooths the signal and yields fiber directions even in the gray matter (gm). At some point, the compression becomes counter-productive by blurring the crossings and generating false signals in areas without fibers. Corona radiata (cr), cingulum (cg), fornix (fx), corpus callosum (cc).

extracted up the highest compression stage. Interestingly, noise levels decrease at higher compression stages due to the smoothing effect of the blurred scattering pattern, making it easier to extract the fiber direction and even improving the signal compared to the Euclidean illumination. This phenomenon is observed in the fornix as well. Crossings in the corona radiata are discernible up to a compression stage of 16×16 but become increasingly noisy. In the highest compression stage, the algorithm fails to find a crossing and only discovers as single direction, as indicated by the bolder colors in the FOM.

Furthermore, fiber directions are detected in the gray matter and the empty space around the tissue. The first phenomenon shows the potential to extract even low signals (there are considerably less fibers in gray matter, as illustrated in Section 2.3 but the second effect illustrates the risk of generating additional false signals. To some degree, compressed sensing is beneficial by increasing the signal and yielding fiber directions but at some point, the compression becomes counter-productive by blurring the crossings to much and generating fake fiber directions. It must also be considered at which stage the blurred scattering patterns contain less (or less reliable) information about the tissue compared to the faster angular ComSLI method. Furthermore, the compressed sensing approach presents some hardware-related drawbacks: A camera with a high-sensitivity is crucial to distinguish the subtle variations in intensity in the illuminated sample. Previous experiments with a lower-quality camera (*BASLER acA5472-17uc*) have not been successful. Furthermore, a bright display and a profound shielding from external light is absolutely required.

Speed and Data The main reason for a compressed sensing approach in ComSLI is the reduction of measurement time and stored data. Given that the scattering patterns are discernible at least by the naked eye up to the highest compression level and that there is still room to improve the quantitative evaluation of line profiles, even an 8×8 compression seems a realistic goal. However, it may be of interest to initially consider a less compressed measurement. Table 7.2 provides an overview of the required time and data for all stages of compression. For the DCT-II, twice as many measurements as coefficients are required for the reconstruction of scattering patterns, rendering an uncompressed (64×64) measurement pointless in comparison to the Euclidean measurement. Yet, a compressed measurement with 32×32 images or less starts to become beneficial. The factor 2 is taken into account in the second column of the table.

TABLE 7.2: Measurement time and data for various compression levels. The DCT-II requires twice as many measurements. However, the overall speed-up is still beneficial for 32×32 images or less. The total measurement time assumes that only one measurement image is taken per illumination image and no time is required to process and store the image on the hard drive.

Compression	Images	Exposure Time	Total Time	Data Stored
Euclidean	4096	1000 ms	68 minutes	≈ 500 GB
64×64	8192	400 ms	55 minutes	≈ 1000 GB
32×32	2048	400 ms	14 minutes	≈ 250 GB
16×16	512	400 ms	3 minutes	≈ 62.5 GB
8×8	128	400 ms	> 1 minute	≈ 15.6 GB

The total measurement time is calculated under the assumption that only one measurement image is taken per illumination image (repetitions = 1), with no time required to process and store the image on the hard drive. Therefore, the total measurement time is an ideal lower limit. The actual measurement time depends on the measurement software and processing hardware. The real measurement time for the current setup is roughly twice as long as the theoretical lower limit. The total stored data assumes a single-channel image with a bit depth of 16 bit and an image size of 9568×6380 pixels. Lossless compression of the measured images (e.g. an LZW (Lempel-Ziv-Welch) algorithm [203]) is not yet considered.

The highest compression stage of 8×8 only requires 3% of data storage. In terms of total measurement time, the benefit is even higher: Due to the brighter DCT illumination, the exposure time can be decreased, lowering the required measurement

time down to only 1.5% of the original measurement time. Even an uncompressed 64 $\times$ 64 is – in theory – quicker than the original Euclidean measurement.

Outlook Fiber directions and crossings can already be reliably identified using the faster angular ComSLI method. Therefore, future research on compressed sensing ComSLI should focus on determining which fiber properties can only be obtained through scatterometry ComSLI and how to extract these features despite compression. Machine learning approaches can be applied to enhance recognition of scattering patterns that pose challenges for analytical evaluation due to their compression-induced blurriness.

Subsequent studies should explore the source of compression artifacts, which show as periodic cross structures in the reconstructed compressed scattering patterns. These artifacts may stem from the central black cut-out in the illumination. Furthermore, the small amount of negative values in the reconstructed scattering pattern needs to be investigated. If these negative values are a result of noise, a measurement with more repetitions may reduce them. Otherwise, setting them to zero does not appear to cause problems in the signal analysis. Further research can include experimenting with different illumination grids and alternative mathematical bases. Additionally, studies should explore the feasibility of conducting Compressed Sensing ComSLI with less specialized hardware, as the relatively low hardware requirements have been an advantage of ComSLI thus far.

Chapter 8

Discussion and Outlook

This chapter is a **summary and discussion** of the results obtained in the previous chapters, beginning with the mechanical construction of the Scattering Polarimeter and covering the performance evaluation, the multi-modal parameter analysis, and the advancements made to ComSLI. Here, results are presented in the global context of the development of Scattering Polarimetry. Furthermore, this chapter discusses the **methodology** used in this thesis. An emphasis is set on the development and improvement of the various measurement techniques. The following discussion includes **outlooks and suggestions on future research**. Detailed discussions of the results can be found in the corresponding chapters, while this chapter highlights only the most significant concepts.

8.1 The Scattering Polarimeter

The Scattering Polarimeter has successfully advanced from the prototypical stage to a fully operational multi-modal device. The novel device integrates oblique illumination for ComSLI and vertical illumination for 3D-PLI, DI, and Müller polarimetry into a single, multi-modal system that has maintained the flexibility to realize illumination with different wavelengths or the use of other polarization states. Software for measurement and evaluation were developed. The liquid crystal variable retarders (LCVRs) were thoroughly characterized.

8.1.1 Hardware Upgrades for Improved Illumination

Possible upgrades to the hardware were discussed in Section 4.6. Among those, the most urgent one is a brighter LED light source. Especially the ComSLI reference measurements (s. Section 5.5.3) indicated that measurements with a brighter light source lead to a better signal and less noise. Additionally, the comparatively long exposure time could be shortened with a brighter light source. The integration of a new LED panel into the setup would be very easy because the hardware can be exchanged quickly. The development of a custom light source with integrated polarization state generator (PSG) is optional but must be considered when scatterometry ComSLI or compressed sensing ComSLI become part of the routine measurement.

Furthermore, the current Basler camera can be swapped with a high-sensitivity camera as long as the corresponding objective lens matches the setup geometry that is limited by the LCVR apertures as outlined in Section 4.2.1. Minor modifications to the camera mount could enhance mechanical stability and improve the overall usability of the system.

Lastly, integrating an XY stage is highly recommended. In the context of this thesis, the measurement of whole brain sections was of secondary interest. However, for future applications, the Scattering Polarimeter must be capable of measuring entire human brain sections.

8.1.2 High-Speed Measurement

Currently, the measurement software is fully operational. The upgrades suggested in Section 4.6 aim mostly at a more convenient user experience. However, the software needs to be optimized for quick data processing for a high-speed measurement. Section 4.4 estimated the measurement time to scan a typical human brain sample with all four modalities to about 18 hours as an upper limit. With a brighter light source, a more sensitive camera, and a reduced number of 3D-PLI images as discussed in Section 5.2, the measurement time could be significantly reduced. Optimized data processing can speed up the measurement further. It seems realistic to decrease the measurement time for a whole human coronal section down to a few hours. For reference: The LMP3D takes around 13 hours to measure an entire brain section with 3D-PLI, according to the manufacturer [136], with the resolution given in Section 3.6. A parameter study to determine the optimal measurement parameters for the Scattering Polarimeter is mandatory.

8.2 Single-Mode Performance

The Scattering Polarimeter successfully measured the four modalities – 3D-PLI, DI, Müller polarimetry, and ComSLI – within its measurement routine. The performance of each modality was investigated both qualitatively and quantitatively using four representative tissue samples. Sources of statistical and systematic errors were identified and suggestions for further improvement were made. In the following, the key findings for each modality are discussed.

8.2.1 Choice of Tissue Samples

Scattering polarimetry was demonstrated for samples with notably different optical properties. The exemplary tissue samples Broca, Vervet1818, ChiasmX2-7, and ChiasmX2-15 represent a broad range of cryo-sectioned samples, each distinct in its scattering and transmittive properties. Broca is the sample that most closely resembles common measurement conditions: In 3D-PLI, samples are measured days after embedding. In ComSLI, it is beneficial to wait several weeks or even month until the transmittance has increased but it is uncommon to measure a sample that was embedded years earlier like Vervet1818. However, cases occur where an older sample is re-measured. The artificially assembled samples ChiasmX2-7 and ChiasmX2-15 would rarely be investigated in context of neuroimaging, but proved useful for the characterization of the new device.

The spectrum of tissue samples revealed the strength and limitations of each measurement modality, and has highlighted potential challenges that can arise with different tissue properties. A parameter study could now identify the optimal measurement parameters for routine scattering polarimetry of common tissue samples. The primary goal would be to determine the default exposure time and required number of repetitions for all modalities to obtain a good signal-to-noise-ratio.

Recently embedded tissue required relatively longer exposure times to yield a sufficient signal, especially for ComSLI and Müller polarimetry. The optimal time for a multi-modal measurement after embedding should be investigated through a long-term study. This is especially important if DI is included in the measurement because D^- tissue can only be measured within a short time frame after embedding.

8.2.2 3D-PLI

The Scattering Polarimeter showed an excellent performance for the Broca sample. Even fibers in regions with low fiber density, such as gray matter, were correctly resolved. For highly transmitting older samples such as Vervet1818, the limits of the Scattering Polarimeter became visible in the transmittance map, even though fiber directions and retardation in white matter were still detected correctly. Comparison with the reference measurement from the LMP3D shows excellent agreement for Broca. Results for the highly transmitting Vervet1818 deviate slightly from the reference measurements due to an asymmetry in the transmittance; however, fiber directions and retardation are still determined accurately, apart from minor deviations in some gray matter areas where fiber density is low. 3D-PLI measurements are usually performed on recently embedded tissue and benefit from lower transmittance and consequently a better contrast between white and gray matter. Thus, Broca is a typical 3D-PLI sample. As long as the user is aware of the limitations for more transmittive samples, 3D-PLI with the Scattering Polarimeter performs very well.

Fourier Fit and Calibration The accuracy of the Fourier fit for 3D-PLI was investigated for two exemplary locations as well as across the entire imaging area of Broca-A, using the coefficient of determination R^2 as a measure of fit quality. The results showed a high overall accuracy of the Fourier fit. Additionally, the Fourier fit smooths statistical noise and stabilizes the signal which enabled reliable signal detection even in gray matter where fiber density was low and the 3D-PLI signal was comparatively weak.

Two systematic errors occurred and were successfully analyzed using Müller matrix calculus: First, an ellipticity in LCVR 2 caused an asymmetry between the left-circular (LC) and right-circular setting of the PSA. This asymmetry affected the transmittance map and impacted the retardation map through normalization with the transmittance. The fiber direction was not affected. Using Müller matrix calculus combined with a Taylor approximation, it was possible to identify the main sources of these deviations: The calculations indicated that LCVR 2 was responsible for this effect, likely due to a minor voltage offset. The asymmetry was more prominent in the highly transmitting Vervet1818 which exhibited weaker contrast between gray and white matter. Additionally, this ellipticity caused a low-amplitude sinusoidal signal in background areas where otherwise only statistical noise would be expected.

Second, a higher frequency signal became visible in the Fourier fit residuals. Again, Müller matrix calculations were able to identify the main source of this signal, i.e. minor deviations in LCVR 3 and LCVR 4. Although this systematic offset was very low compared to the 3D-PLI signal, simulations indicate it could influence the signal of strongly inclined white matter fibers. These systematic offsets did not cause significant issues in 3D-PLI but generally propagate into the already weak DI signal. Müller matrix calculations demonstrated why analytical calibration is inherently not possible. However, a retardance correction was developed that achieved signals that agreed with reference measurements.

Generally, the Taylor approximation did not take higher-order effects into account. However, the low-order deviations should be addressed first before the signal can be further refined. Future studies should focus on further reducing ellipticities by fine-tuning voltage values. The retardance voltage curve can be sampled around the expected voltage values in the smallest possible step size to identify the optimum voltage. If the ellipticites still occur, an iterative correction algorithm should be developed.

Retardation Correction The Scattering Polarimeter specifically allows to determine the non-ideal Müller matrix for the PSG and PSG. However, the modified formula for the 3D-PLI intensity curve cannot be solved without previous knowledge about tissue parameters. Therefore, analytical calibration for the retardation is not possible. This problem is more apparent for the Scattering Polarimeter than for, e.g. the LMP3D because LCVRs are generally less precise than rotating mechanical elements. Here, a retardation correction based on the highest and lowest expected retardation was suggested. Normalization with the retardation of in-plane parallel fibers was established by AXER ET AL. [15]. To compensate for background retardation caused by minor ellipticities, the subtraction of the background retardation was added to the routine. Comparison with reference measurements showed the success of the developed routines.

During the correction routine, the values of maximum and minimum retardation were entered manually into the correction algorithm. A more refined algorithm could find these values based on a histogram of intensity values, thereby choosing adequate values automatically. Alternatively, a multi-modal approach can determine the correct values: The presence of two peaks at a 180° distance in the ComSLI line profiles indicates in-plane parallel fibers. The retardation of the corresponding pixels in the 3D-PLI retardation map can serve as the normalization value. In the future, the automatic detection of the highest and lowest retardation should be added for a fully automatized evaluation of the retardation map.

Angular Step Size The Fourier fit yielded stable results for the transmittance map, the retardation map and the direction map even for step sizes of 30° instead of 10°. Correspondingly, fiber orientations can be retrieved correctly from using as few as 6 measurement images instead of 18, and possibly even fewer. This demonstrated the strength of 3D-PLI, especially in comparison with the 36 images required for Müller polarimetry.

In the context of high-speed imaging, the smallest possible number of measurements (i.e. the largest angular step size) should be determined. The goal should be steps of 45°, i.e. 4 measurement images per 3D-PLI cycle. This step size has the advantage that the corresponding measurements have a synergy with Müller polarimetry because the 3D-PLI images would directly correspond to eight of the Müller polarimetric measurements (HL, DL, VL, AL, HR, DR, VR, AR). The result is a further reduction of measurement time.

Circular Analyzer Setting The PSA was set to analyze left-circular (LC) or right-circular (RC) light. The retardance-voltage curve is steeper for the voltage that yields RC, making it more likely to have an offset from the ideal voltage. In fact, LC yielded slightly better results for 3D-PLI. Therefore, for a standard 3D-PLI measurement, the

LC setting is recommended. However, the minor difference between LC and RC influence the already low diattenuation signal, as discussed in the following.

8.2.3 Diattenuation Imaging

The diattenuation signal is inherently low in brain tissue, making it difficult to measure accurately in the presence of statistical and systematic errors. Here, a strategy for Diattenuation Imaging was used that has synergies with the 3D-PLI routine, thus benefiting the goal of a high-speed measurement. The results from the Scattering Polarimeter showed the expected distribution of D^+/D^- tissue. However, Müller matrix calculations predicted that propagation of systematic errors from 3D-PLI prevents the correct identification of fiber directions. With the developed routine, diattenuation and residual retardation cannot be reliably distinguished. Thus, it is mandatory to develop a different routine for Diattenuation Imaging.

Error Propagation During the evaluation routine, systematic errors from the 3D-PLI signal propagated and distorted the summarized DI signal. Using Müller matrix calculus and appropriate Taylor approximations, the sources of systematic were identified and separated from each other. Consequently, it was possible to demonstrate why the transmittance map obtained from DI was more reliable than the transmittance maps from 3D-PLI, as asymmetries stemming from LCVR,2 canceled out. However, ellipticities from the PSA, specifically from LCVR,4, did not cancel out and distorted the signal which made it impossible to clearly distinguish between retardation and diattenuation. Reference measurements showed that the diattenuation obtained with the Scattering Polarimeter was stronger than expected, indicating that the signal amplitude was actually caused by residual retardation. Therefore, the diattenuation signal derived from two 3D-PLI measurements should not be deemed reliable until the ellipticities in the device are corrected. Nonetheless, the DI transmittance map has practical applications and can potentially replace the 3D-PLI transmittance map in multi-modal parameter analysis where tissue transmittance is investigated.

Alternative Implementations of Diattenuation Imaging The studies highlighted why the reduction of systematic errors is mandatory for the challenging measurement of diattenuation. Alternative methods should be tested to distinguish actual diattenuation from residual retardation. Performing diattenuation measurements by analyzing horizontal and vertical polarization with the PSA, instead of summing two 3D-PLI measurements (LC and RC), could minimize the influence of circular components. However, this approach loses its synergy with the 3D-PLI measurement and requires up to 36 additional measurements (depending on the intended angular step size). Alternatively, the optical elements of the PSA can be removed manually from the setup, which is obviously not compatible with a fully automatic measurements and may furthermore inhibit pixelwise comparison if the image is spatially influenced by the LCVRs (which theoretically should not be the case, but this has not been investigated yet). Lastly, DI can be performed using ECM-calibrated results from Müller polarimetry, provided that measurement parameters for Müller polarimetry are optimized for an ideal signal-to-noise ratio. Overall, the investigations indicated that the last option is the most promising.

Measuring D^- Tissue The measured tissue samples were not expected to contain D^- tissue. Once the measurement routine is improved and the diattenuation signal

can be reliably determined, the first step should be to verify whether D^- tissue can be measured in samples where it is expected to occur, i.e. recently embedded samples.

8.2.4 Müller Polarimetry

Müller polarimetry was directly compared to 3D-PLI and DI, in the context of this thesis. The successful application of the Eigenvalue Calibration Method (ECM) was demonstrated for well-known optical samples. The Lu-Chipman decomposition was performed exemplary to showcase the parameter maps that can be obtained with Müller polarimetry.

Eigenvalue Calibration Method The application of the Eigenvalue Calibration Method (ECM) to the measurement results of the Scattering Polarimeter was demonstrated. After calibration, the obtained Müller matrices provided accurate results with precision the second or even third decimal place for the Müller matrix elements. With this, the Scattering Polarimeter demonstrated precision similar to setups with comparable components, as discussed in Section 5.4.1. For tissue measurements, the measured optical features aligned with the expected anatomy. Overall, both quantitative and qualitative analyses validate the successful calibration.

However, an inherent limit was imposed by the non-ideal natures of the calibration samples: During the calculation of the calibration matrices and also during the subsequent performance measurements, the samples were assumed to be perfect. Accordingly, improvement to the ECM could be realized by using samples of even higher manufacturing quality, although a truly ideal calibration can never be achieved. To make the calibration routine more convenient, calibration samples should be quickly removable from the setup.

Lu-Chipman Decomposition The Lu-Chipman decomposition is essential to extract parameter maps from the Müller matrix of a sample. Computationally, the decomposition was performed using the pySCATMECH module. However, the evaluation process is currently time-intensive because pySCATMECH needs to apply the eigenvalue decomposition to every pixel. Using multiprocessing and/or a more powerful computer, the evaluation could be sped up significantly.

Although the Lu-Chipman decomposition is the most common matrix decomposition in literature, there are other decomposition routines. MORIO & GOUDAIL [130] investigated various orders of the depolarization matrix, the diattenuation matrix and the retardation matrix in the decomposition. ORTEGA-QUIJANO & ARCE-DIEGO [141] discussed a decomposition based on the differential formulation of Müller calculus and state that this routine is particularly well-suited for samples in which several polarization effects take place simultaneously. In context of scattering polarimetry, the investigation of other decomposition routines apart from the default could serve an improved evaluation.

Speed-Up In Section 5.4.2, the measurement of 36 images was deemed more reliable than a measurement with 16 images and then employed for all subsequent investigations. Theoretically, the Müller matrices can be calculated with fewer than 36 measurements: Only 16 measurements are required to solve the linear equation system for the 16 matrix elements. However, the minimal measurement routine unavoidably introduces a propagation of errors across the matrix elements. Instead

of reducing the number of measurements for Müller polarimetry, the aim should be to find synergies with the 3D-PLI measurements as already discussed.

Signal-to-Noise Ratio Comparison with reference measurements from 3D-PLI indicated that Müller polarimetry struggled to evaluate signals with a lower transmittance for the Broca sample. Thus, an extensive parameter study should determine the optimal exposure time. The exposure time is expected to be larger than for 3D-PLI. Furthermore, the measurement can benefit from a brighter light source and a high-sensitivity camera.

Section 3.4.2 illustrated how Müller polarimetry has the optimal signal-to-noise ratio when the Stokes vectors form a tetrahedron within the Poincaré sphere, i.e. when elliptical polarization states are employed. This was not taken into account in favor of the more intuitive circular and linear polarization states that are also compatible with 3D-PLI. For an optimal signal-to-noise ratio, the LCVRs need to be rotated to the ideal azimuthal angles of 27.4° and 72.4°, respectively. However, this makes the generation of linear polarization angles for 3D-PLI much more complex, as demonstrated in Section 5.4.8. Future studies could experiment with the alternative elliptical LCVR settings and determine the respective voltage settings for 3D-PLI.

Reference Measurements for Depolarization So far, reference measurements were only performed with 3D-PLI and DI. The retardance-based parameter maps can be assumed to be very similar to the 3D-PLI reference measurements: Although Müller polarimetry distinguishes circular retardance from linear retardance, other than 3D-PLI, the effect of circular retardance is expected to be very low for brain tissue. The same holds for diattenuation. However, reference measurements with wide-field Müller polarimetry need to be performed with a suitable device at some point for a better understanding of depolarization.

Diattenuation Imaging with Müller Polarimetry DI based on 3D-PLI remains inherently challenging with the Scattering Polarimeter due to the lack of a calibration routine like the ECM for Müller polarimetry. However, successful evaluation of Broca in accordance with the reference measurements showed that diattenuation can be measured with Müller polarimetry, although the signal for e.g. Vervet1818 was hidden by artifacts in the measurement. As soon as the signal-to-noise ratio is improved so that diattenuation can be measured reliably for all image pixels, Müller polarimetry is a valuable alternative foundation for DI. The axis of diattenuation can be compared to the fast axis of retardation, thus yielding the desired information about D^+/D^- tissue, and – theoretically – even differentiating between the linear and circular effects, although the latter are expected to very small.

Furthermore, circular diattenuation could be addressed in future research with the Scattering Polarimeter. Overall, the study of diattenuation in brain tissue is still a young field of research and holds many open questions. The causes of diattenuation in brain tissue, but also of the object carrier, the embedding medium, and the age-related change of diattenuation, need to be studied more in the future. Similar to retardance measurements, improving the signal-to-noise ratio through brighter light sources or more sensitive cameras can improve measurement precision in diattenuation studies.

8.2.5 ComSLI

ComSLI measurements successfully identified the major directions in agreement with the reference measurement. However, the signal quality was lower compared to the reference measurement, which utilized a brighter light source and a high-sensitivity camera. With corresponding hardware enhancements, ComSLI measurements are expected improve significantly in the future.

Statistical Noise Fiber crossings are sometimes misidentified as statistical noise and therefore not evaluated, e.g. in gray matter but also in the cingulum. Conversely, additional fiber directions are incorrectly identified in parallel fibers due to statistical noise. While dominant directions are already well recognized, there is a need for more accurate determination of fiber crossings for each pixel. To address these challenges, it is essential to improve the hardware to achieve less noisy measurements. As a second step, adequate signal interpolation can aid with extracting correct fiber directions.

Scatterometry ComSLI The integration of scatterometry ComSLI into the Scattering Polarimeter was not explicitly addressed in this thesis. The current light source already leads to noisy signals for angular ComSLI, suggesting that the signal-to-noise ratio is insufficient for Scatterometry ComSLI, at least without employing very long exposure times. This issue can be addressed with the recommended hardware upgrades, especially a brighter light source.

However, the center pixels of the illumination pattern are obscured by the elements of the polarization state generator. Typically, the scattering patterns are brightest at their center and show the clearest distinction of fiber directions around the center pixels. A systematic evaluation of how much of the middle part can be covered while still achieving reliable extraction of fiber directions (and possibly other features) should be conducted. However, the results from compressed sensing ComSLI in Section 7.4 indicate the feasibility, retrieving information about the fiber directions despite the missing image pixels in the image center.

8.3 Multi-Modal Parameter Analysis

Multi-modal parameter analysis is valuable in various scenarios. Section 6.4 listed a variety of applications. The field of multi-modal parameter analysis is extensive, with the Scattering Polarimeter generating approximately 35 different maps (around 15 for Müller polarimetry, 4 for 3D-PLI, 4 for DI, and 12 from SLIX for ComSLI), covering a wide range of optical parameters, not even including the three-dimensional visualization of fiber orientations and vector maps. This thesis provides a proof-of-principle of how multi-modal parameter analysis serves the imaging of nerve fiber architecture. It is meant to showcase the potential of scattering polarimetry and multi-modal parameter analysis. Of course, for practical application, further development and investigation of these concepts are necessary.

It is important to note that the investigations in Chapter 6 would not require a Scattering Polarimeter if good image registration of different modalities is available. However, pixel-precise alignment of images is crucial for resolving structures of nerve cells that occur at this level of detail. A Scattering Polarimeter inherently guarantees correct and pixel-precise alignment, which is essential for accurate multi-modal analysis.

8.3.1 Tissue and Fiber Classification

Accurate tissue and fiber classification is crucial for multi-modal parameter analysis. However, tissue and fiber classification based on one or several value thresholds have a common issue: the need of prior knowledge about fiber properties to determine meaningful thresholds. Automatic approaches such as histogram-based brightness analysis or machine learning-based methods should be explored to generalize the classification to all sorts of unknown samples.

Tissue Classification Multi-modal analysis is typically unnecessary for differentiating between gray matter, white matter, and background. In both scattering-based and transmittance-based measurements, classification can rely on as few as a single parameter map (such as the average map in ComSLI or the transmittance map in 3D-PLI). However, the strength of multi-modal analysis becomes evident for samples like Vervet1818. Combining multiple maps enables the approximate detection of gray and white matter despite artifacts and low contrast.

To improve contrast in 3D-PLI, revitalizing a sample (i.e. renewing the embedding medium) can enhance contrast, even for old samples, thus improving tissue classification. This method should be preferred where applicable because it yields more precise results, as seen with Broca compared to Vervet1818. However, if an old sample cannot be revitalized, multi-modal parameter analysis can provide the necessary tissue classification.

Fiber Classification The fiber classification performed on Vervet1818 heavily relies on manually set thresholds across various ComSLI and 3D-PLI maps that require prior knowledge of fiber structures. These thresholds depend on several factors, including the sample thickness and exposure time, making it impossible to determine a universal value that holds for every sample and can identify fiber structures for unknown samples. However, when the signal-to-noise ratio in ComSLI is improved, the fiber classification can rely on the ComSLI direction maps instead: detecting more than one fiber direction indicates a crossing region, which is a binary criterion independent of other parameters. In any case, the primary goal is to develop a classification routine applicable to unknown samples.

Artifact Filtering Artifacts in the embedding medium exhibited different optical properties. Therefore, multi-modal parameter analysis could be further developed to remove crystallization artifacts from older samples. This is situational, as it is uncommon in practice to measure rather old samples where the embedding medium has started to crystallize. Nevertheless, artifacts can arise from various causes, even in freshly embedded samples. Therefore, a multi-modal investigation of artifact removal can aid in the evaluation of tissue parameters and improve the visualization quality.

8.3.2 Multi-Modal FOM

A routine to assemble a multi-modal FOM was developed, based on the established FOM from ComSLI. When all measurement techniques are optimized and tissue and fiber classification routines are enhanced, the multi-modal FOM is expected to yield even more valuable results. Future research should focus on developing methods to accurately determine fiber directions in regions with steep fibers by

optimally combining 3D-PLI and ComSLI signals and potentially incorporating other modalities.

Interpolation Although no interpolation of the direction signals was used in this study, implementing a suitable interpolation routine could smooth noisy signals and enhance the evaluation. For example, interpolation could be achieved by averaging the values of surrounding pixels. The simplest approach would be to determine whether the four direct neighbors or a number of the eight surrounding pixels have the same or similar values, and then use this information for interpolation. However, the focus should be on upgrading the hardware (e.g. with a brighter light source) and improving the actual signal before interpolating.

Visualization Future visualization strategies could incorporate information about fiber inclination, despite the current challenges in accurately determining the inclination of crossing fibers. It would also be useful to highlight pixels where ComSLI and PLI yield differing results, as this could indicate potentially degenerated regions. Generally, a visualization of fiber directions must be developed in the future that is easily comprehensible and emphasizes the information that is most important to the user.

8.3.3 Inclination

The relationship between fiber inclination and peak distances was only briefly addressed. Preliminary results indicated that this dependency is more complex than a linear relationship. Future research should begin with simulations that model line profiles and scattering patterns and directly compare these with the retardation caused by the same fiber structures. Then, multi-modal measurements can then be employed to validate results from these simulations. To enhance the accuracy of the peak distance map, the angular discretization of the illumination patterns should be increased. The primary objective should be to identify the cause of the observed thinout border and to understand why all parameter combinations occur exclusively on the right side of this border.

8.4 Advancing ComSLI

The focus of this thesis was the development of a multi-modal high-speed Scattering Polarimeter. However, as ComSLI, one of the measurement techniques, is still under development, it was essential to continue advancing ComSLI while simultaneously developing the multi-modal device. All investigations were performed with the ComSLI setup (s. Section 3.6.3) in order not to interfere with the development of the Scattering Polarimeter. However, the following advancements are all applicable in the context of scattering polarimetry. Especially the hardware upgrades should be incorporated in the future development of the Scattering Polarimeter.

8.4.1 Formalin-Fixed Paraffin-Embedded Tissue

Formalin-fixation and paraffin-embedding (FFPE) is the standard method for preparing high-quality tissue sections in histology, making FFPE samples widely available in many laboratories. Here, the investigations with ComSLI demonstrated the feasibility of directly measuring fiber directions in FFPE sections, where polarimetric

methods like 3D-PLI are not applicable and fiber directions can only be retrieved by indirect mathematical methods such as Structure Tensor Analysis (STA). A follow-up study by GEORGIADIS ET AL. [61] explored a wide range of stains and fibrous tissues, including brain and muscle tissue.

To effectively apply ComSLI on FFPE sections, it is necessary to develop measurement protocols for different stains, determining measurement parameters such as optimal exposure time for common stains and tissue thicknesses. Then, ComSLI enables the combination of cell body distribution measurements with mapping of directly measured fiber architecture. Furthermore, Scattering Polarimetry could be used to directly investigate the loss of birefringence in relation to scattering properties. Potential changes in other optical properties caused by formalin-fixation and paraffin-embedding could be investigated with the combination of Müller polarimetry and ComSLI.

8.4.2 High-Sensitivity Camera

A recurring issue with the Scattering Polarimeter has been the insufficient signal-to-noise ratio. Apart from using a brighter light source, employing a more sensitive camera can reduce exposure time, thereby increasing measurement speed while maintaining or even improving the signal-to-noise ratio. Especially scatterometry ComSLI and the more advanced illumination strategy, compressed sensing ComSLI (s. Section 7.4), greatly benefit from a camera capable of detecting minor differences in light intensity. Section 7.2 demonstrated how the high-sensitivity Vistek camera improved signals in nearly all white matter regions and reduced noise in gray matter areas.

For convenience, a live viewer should be integrated directly into the custom measurement routine for ComSLI. Future research could include experiments with other objective lenses to further optimize the system.

8.4.3 Automatized High-Resolution Scan

Integrating an automated XY scanning stage into the Scattering Polarimeter is essential. Commercial XY stages do not meet the requirements for the large-area light source and typically block the oblique light incidence in some way. Therefore, a custom XY stage was developed, as detailed in Section 7.3, which moves smoothly without vibration due to microstepping and is both easy to operate and stable. The most critical point is the narrow focus length: the sample holder must remain within the focus length across the entire scanning area. After optimizing the sample holder for stability, this criterion was successfully met.

Another challenge is the prevention of reflections. During a ComSLI measurement, a mask of black cardboard (with a cut-out that matches the field of view) is placed on top of the sample to prevent reflections. However, with a moving stage, this is not possible, and reflections occur. To counter this, the mask can be attached to a mounting rod to rest closely above the sample plane while remaining stationary beneath the camera.

When a similar XY stage is integrated into Scattering Polarimeter in the future, the light shielding box needs to be enlarged to accommodate the rail system.

8.4.4 High-Speed Compressed Sensing Illumination

Compressed sensing was successfully adapted for scatterometry ComSLI in Section 7.4. The novel illumination strategy yields correct fiber directions and crossings while achieving a significant speed-up. Initial results suggested that Compressed Sensing based on a DCT-II base is applicable in ComSLI and feasible even at the highest investigated compression level of 8×8. The highest compression level only requires 3% of data storage and the required measurement time decreases down to only 1.5% of the original measurement time. Additionally, due to the shorter exposure time, even an uncompressed 64×64 can be faster than the original Euclidean measurement. Future research could experiment with alternative mathematical bases and different sizes of illumination grids to find the best compromise between a fast measurement and a good resolution of the scattering patterns.

A disadvantage of compressed sensing are the high hardware requirements: a high-sensitivity camera is crucial to distinguish the subtle variations in intensity within the illuminated sample. Additionally, a bright light source is absolutely necessary. Future studies should explore conducting compressed sensing ComSLI with less specialized hardware, as the relatively low hardware requirements have been a significant advantage of ComSLI thus far.

Although compressed sensing ComSLI has been shown to be both mathematically and experimentally feasible in Section 7.4, a scatterometry measurement takes significantly longer compared to Müller polarimetry, DI, 3D-PLI, and angular ComSLI. When only fiber crossings are of interest in context of multi-modal imaging, it is sufficient to measure angular ComSLI in favor of a high-speed measurement. Therefore, research should explore the benefits of measuring scattering patterns in context of multi-modal imaging.

Chapter 9

Conclusion

Understanding the intricate structure of the human connectome is a major objective in neuroscience. Neuroimaging techniques such as Müller polarimetry, three-dimensional polarized light imaging (3D-PLI), diattenuation imaging (DI), and computational scattered light imaging (ComSLI) investigate long-range fiber pathways in histological brain sections using incoherent visible light. While there are ongoing efforts to optimize individual neuroimaging techniques, there is a growing interest in multi-modal imaging to combine the strengths of each technique, allowing for pixel-precise comparison and cross-validation of tissue properties.

This thesis has established the theoretical, experimental, and technical foundation for scattering polarimetry by developing a multi-modal high-speed Scattering Polarimeter that integrates Müller polarimetry, 3D-PLI, DI, and ComSLI within a single novel setup. The development process included hardware selection and the creation of an automated measurement routine, but also a mathematical description with a focus on error analysis, performance evaluation of each modality, and, for demonstration purposes, various multi-modal analyses. The thesis presents a fully operational setup and lays the groundwork for future advancements, suggesting opportunities for improving hardware, software, and overall system performance.

The Scattering Polarimeter was designed as wide-field Müller polarimeter in transmission mode that employs a large-area light source and four voltage-controlled liquid crystal variable retarders (LCVRs). The setup was developed from scratch and transitioned from a prototype to a functional device. Operational routines were established, allowing this thesis to serve as a manual. The performance of each modality was thoroughly investigated on both theoretical and experimental bases, using Müller calculus and reference measurements to evaluate the system performance. Potential opportunities to improve and further speed up the measurements were identified, aiming for high-quality, high-speed multi-modal measurements. Various applications for multi-modal analyses were showcased, demonstrating the benefits of pixel-precise analysis provided by the Scattering Polarimeter. Additionally, advancements were made in ComSLI to improve the detection of fiber crossings, measurement speed, and application range, all of them compatible with the Scattering Polarimeter.

This thesis opens up the possibility for unprecedented multi-modal imaging of the nerve fiber architecture in the human brain. The unification of four imaging techniques on technical, theoretical, and experimental levels is valuable for a variety of applications, ranging from fundamental neuroscience to biomedical research. Consequently, this thesis has advanced multi-modal nerve fiber imaging and contributed to a deeper understanding of the human connectome.

Literature

[1] F. Aboitiz et al. “Fiber composition of the human corpus callosum”. In: *Brain Research* 598.1–2 (Dec. 1992), pp. 143–153. ISSN: 0006-8993. DOI: 10.1016/0006-8993(92)90178-c.

[2] E. Aescht et al. “Färbungen”. In: *Romeis Mikroskopische Technik*. Spektrum Akademischer Verlag, 2010, pp. 181–297. ISBN: 9783827422545. DOI: 10.1007/978-3-8274-2254-5_3.

[3] I. Ahmad et al. “Ex vivocharacterization of normal and adenocarcinoma colon samples by Mueller matrix polarimetry”. In: *Journal of Biomedical Optics* 20.5 (May 2015), p. 056012. ISSN: 1083-3668. DOI: 10.1117/1.jbo.20.5.056012.

[4] N. Ahmed, T. Natarajan, and K. Rao. “Discrete Cosine Transform”. In: *IEEE Transactions on Computers* C–23.1 (Jan. 1974), pp. 90–93. ISSN: 0018-9340. DOI: 10.1109/t-c.1974.223784.

[5] E. Alerstam. “Anisotropic diffusive transport: Connecting microscopic scattering and macroscopic transport properties”. In: *Physical Review E* 89.6 (June 2014), p. 063202. ISSN: 1550-2376. DOI: 10.1103/physreve.89.063202.

[6] K. Amunts and K. Zilles. “Architecture and organizational principles of Broca’s region”. In: *Trends in Cognitive Sciences* 16.8 (Aug. 2012), pp. 418–426. ISSN: 1364-6613. DOI: 10.1016/j.tics.2012.06.005.

[7] K. Amunts et al. “BigBrain: An Ultrahigh-Resolution 3D Human Brain Model”. In: *Science* 340.6139 (June 2013), pp. 1472–1475. ISSN: 1095-9203. DOI: 10.1126/science.1235381.

[8] D. Andrienko. “Introduction to liquid crystals”. In: *Journal of Molecular Liquids* 267 (Oct. 2018), pp. 520–541. ISSN: 0167-7322. DOI: 10.1016/j.molliq.2018.01.175.

[9] Arduino. *UNO R3*. 2023. URL: https://docs.arduino.cc/hardware/uno-rev3 (visited on 10/09/2024).

[10] Autodesk Inc. *Fusion 360. Integrated CAD, CAM, CAE, and PCB software.* 2021. URL: https://www.autodesk.eu/products/fusion-360/overview (visited on 10/09/2024).

[11] AVMS Germany. *LED INFiLED S1.8 indoor*. 2023. URL: https://www.avms-germany.de/wp-content/uploads/2020/04/flyer_s18_web.pdf (visited on 10/09/2024).

[12] H. Axer and D. G. v. Keyserlingk. “Mapping of fiber orientation in human internal capsule by means of polarized light and confocal scanning laser microscopy”. In: *Journal of Neuroscience Methods* 94.2 (Jan. 2000), pp. 165–175. ISSN: 0165-0270. DOI: 10.1016/s0165-0270(99)00132-6.

[13] H. Axer et al. “Quantitative estimation of 3-D fiber course in gross histological sections of the human brain using polarized light”. In: *Journal of Neuroscience Methods* 105.2 (Feb. 2001), pp. 121–131. ISSN: 0165-0270. DOI: 10.1016/s0165-0270(00)00349-6.

[14] M. Axer and K. Amunts. "Scale matters: The nested human connectome". In: *Science* 378.6619 (Nov. 2022), pp. 500–504. ISSN: 1095-9203. DOI: 10.1126/science.abq2599.

[15] M. Axer et al. "A novel approach to the human connectome: Ultra-high resolution mapping of fiber tracts in the brain". In: *NeuroImage* 54.2 (Jan. 2011), pp. 1091–1101. ISSN: 1053-8119. DOI: 10.1016/j.neuroimage.2010.08.075.

[16] M. Axer et al. "Estimating Fiber Orientation Distribution Functions in 3D-Polarized Light Imaging". In: *Frontiers in Neuroanatomy* 10 (Apr. 2016). ISSN: 1662-5129. DOI: 10.3389/fnana.2016.00040.

[17] M. Axer et al. "High-Resolution Fiber Tract Reconstruction in the Human Brain by Means of Three-Dimensional Polarized Light Imaging". In: *Frontiers in Neuroinformatics* 5 (2011). ISSN: 1662-5196. DOI: 10.3389/fninf.2011.00034.

[18] R. M. A. Azzam, I. M. Elminyawi, and A. M. El-Saba. "General analysis and optimization of the four-detector photopolarimeter". In: *Journal of the Optical Society of America A* 5.5 (May 1988), p. 681. ISSN: 1520-8532. DOI: 10.1364/josaa.5.000681.

[19] R. M. A. Azzam and A. G. Lopez. "Accurate calibration of the four-detector photopolarimeter with imperfect polarizing optical elements". In: *Journal of the Optical Society of America A* 6.10 (Oct. 1989), p. 1513. ISSN: 1520-8532. DOI: 10.1364/josaa.6.001513.

[20] J. S. Baba et al. "Development and calibration of an automated Mueller matrix polarization imaging system". In: *Journal of Biomedical Optics* 7.3 (2002), p. 341. ISSN: 1083-3668. DOI: 10.1117/1.1486248.

[21] Basler AG. *acA5472-17uc - Basler ace*. 2021. URL: https://www.baslerweb.com/en/products/cameras/area-scan-cameras/ace/aca5472-17uc/ (visited on 10/09/2024).

[22] Basler AG. *pylon Viewer*. 2021. URL: https://www.baslerweb.com/en/products/software/basler-pylon-camera-software-suite/pylon-viewer/# (visited on 10/09/2024).

[23] K. Benning et al. "Independent Component Analysis for Noise and Artifact Removal in Three-Dimensional Polarized Light Imaging". In: *Brain-Inspired Computing*. Springer International Publishing, 2021, pp. 90–102. ISBN: 9783030824273. DOI: 10.1007/978-3-030-82427-3_7.

[24] M. J. Berg and C. M. Sorensen. "A review and reassessment of diffraction, scattering, and shadows in electrodynamics". In: *Journal of Quantitative Spectroscopy and Radiative Transfer* 210 (May 2018), pp. 225–239. ISSN: 0022-4073. DOI: 10.1016/j.jqsrt.2018.02.002.

[25] W. S. Bickel and W. M. Bailey. "Stokes vectors, Mueller matrices, and polarized scattered light". In: *American Journal of Physics* 53.5 (May 1985), pp. 468–478. ISSN: 1943-2909. DOI: 10.1119/1.14202.

[26] Blausen.com staff. "Medical gallery of Blausen Medical". In: *WikiJournal of Medicine* 1.2 (2014). ISSN: 2002-4436. DOI: 10.15347/wjm/2014.010.

[27] D. Bodian. "A new method for staining nerve fibers and nerve endings in mounted paraffin sections". In: *The Anatomical Record* 65.1 (Apr. 1936), pp. 89–97. ISSN: 1097-0185. DOI: 10.1002/ar.1090650110.

[28] J. F. de Boer et al. "Two-dimensional birefringence imaging in biological tissue by polarization-sensitive optical coherence tomography". In: *Optics Letters* 22.12 (June 1997), p. 934. ISSN: 1539-4794. DOI: 10.1364/ol.22.000934.

[29] E. J. Bubb, C. Metzler-Baddeley, and J. P. Aggleton. "The cingulum bundle: Anatomy, function, and dysfunction". In: *Neuroscience & Biobehavioral Reviews*

92 (Sept. 2018), pp. 104–127. ISSN: 0149-7634. DOI: 10.1016/j.neubiorev.2018.05.008.

[30] M. D. Budde and J. A. Frank. "Examining brain microstructure using structure tensor analysis of histological sections". In: *NeuroImage* 63.1 (Oct. 2012), pp. 1–10. ISSN: 1053-8119. DOI: 10.1016/j.neuroimage.2012.06.042.

[31] J. M. Bueno. "Polarimetry using liquid-crystal variable retarders: theory and calibration". In: *Journal of Optics A: Pure and Applied Optics* 2.3 (May 2000), pp. 216–222. ISSN: 1741-3567. DOI: 10.1088/1464-4258/2/3/308.

[32] U. Bürgel et al. "Histological visualization of long fiber tracts in the white matter of adult human brains". In: *Journal fur Hirnforschung* 38.3 (1997), 397—404. ISSN: 0021-8359. URL: http://europepmc.org/abstract/MED/9350511.

[33] E. J. Candès, J. K. Romberg, and T. Tao. "Stable signal recovery from incomplete and inaccurate measurements". In: *Communications on Pure and Applied Mathematics* 59.8 (Mar. 2006), pp. 1207–1223. ISSN: 1097-0312. DOI: 10.1002/cpa.20124.

[34] H. Carlsson et al. "Use of primates in research: A global overview". In: *American Journal of Primatology* 63.4 (Aug. 2004), pp. 225–237. ISSN: 1098-2345. DOI: 10.1002/ajp.20054.

[35] V. Carriel et al. "Staining Methods for Normal and Regenerative Myelin in the Nervous System". In: *Histochemistry of Single Molecules*. Springer New York, 2017, pp. 207–218. ISBN: 9781493967889. DOI: 10.1007/978-1-4939-6788-9_15.

[36] M. Catani et al. "Virtual in Vivo Interactive Dissection of White Matter Fasciculi in the Human Brain". In: *NeuroImage* 17.1 (Sept. 2002), pp. 77–94. ISSN: 1053-8119. DOI: 10.1006/nimg.2002.1136.

[37] J. K. C. Chan. "The Wonderful Colors of the Hematoxylin–Eosin Stain in Diagnostic Surgical Pathology". In: *International Journal of Surgical Pathology* 22.1 (Jan. 2014), pp. 12–32. ISSN: 1940-2465. DOI: 10.1177/1066896913517939.

[38] S. Chandrasekhar. *Radiative Transfer*. Dover Publications, Incorporated, 2013. ISBN: 9780486318455.

[39] D. B. Chenault and R. A. Chipman. "Measurements of linear diattenuation and linear retardance spectra with a rotating sample spectropolarimeter". In: *Applied Optics* 32.19 (July 1993), p. 3513. ISSN: 1539-4522. DOI: 10.1364/ao.32.003513.

[40] R. A. Chipman, W. S. T. Lam, and G. Young. *Polarized Light and Optical Systems*. Taylor & Francis Group, 2018, p. 982. ISBN: 9781351129121.

[41] J. Chue-Sang et al. "Optical phantoms for biomedical polarimetry: a review". In: *Journal of Biomedical Optics* 24.03 (Mar. 2019), p. 1. ISSN: 1083-3668. DOI: 10.1117/1.jbo.24.3.030901.

[42] K. Chung et al. "Structural and molecular interrogation of intact biological systems". In: *Nature* 497.7449 (Apr. 2013), pp. 332–337. ISSN: 1476-4687. DOI: 10.1038/nature12107.

[43] E. Collett. *Field guide to polarization*. 3. print. SPIE field guides 5. Bellingham, Wash.: SPIE Press, 2012. 134 pp. ISBN: 9780819458681.

[44] E. Compain, S. Poirier, and B. Drevillon. "General and self-consistent method for the calibration of polarization modulators, polarimeters, and Mueller-matrix ellipsometers". In: *Applied Optics* 38.16 (June 1999), p. 3490. ISSN: 1539-4522. DOI: 10.1364/ao.38.003490.

[45] J. Dammers et al. "Signal enhancement in polarized light imaging by means of independent component analysis". In: *NeuroImage* 49.2 (Jan. 2010), pp. 1241–1248. ISSN: 1053-8119. DOI: 10.1016/j.neuroimage.2009.08.059.

[46] A. De Martino et al. “Optimized Mueller polarimeter with liquid crystals”. In: *Optics Letters* 28.8 (Apr. 2003), p. 616. ISSN: 1539-4794. DOI: 10.1364/ol.28.000616.

[47] W. Demtröder. *Experimentalphysik 2. Elektrizität und Optik*. 7. Aufl. 2017. Springer-Lehrbuch. Berlin, Heidelberg: Springer Berlin Heidelberg, 2018. 1449 pp. ISBN: 9783662557907.

[48] D. Donoho. “Compressed sensing”. In: *IEEE Transactions on Information Theory* 52.4 (Apr. 2006), pp. 1289–1306. ISSN: 0018-9448. DOI: 10.1109/tit.2006.871582.

[49] A. W. Dreher, K. Reiter, and R. N. Weinreb. “Spatially resolved birefringence of the retinal nerve fiber layer assessed with a retinal laser ellipsometer”. In: *Applied Optics* 31.19 (July 1992), p. 3730. ISSN: 1539-4522. DOI: 10.1364/ao.31.003730.

[50] Edmund Optics Inc. *Überblick über kundenspezifische Polymerpolarisatoren*. 2023. URL: https://www.edmundoptics.de/capabilities/polarizers/ (visited on 10/09/2024).

[51] EURECA Messtechnik GmbH. *Lenses of the Apo-Rodagon, Rodagon and Rogonar-S series by Qioptiq*. 2021. URL: https://www.eureca.de/4645-1-Apo-Rodagon-Rodagon-Rogonar-S.html#Apo-R-D (visited on 11/07/2023).

[52] Excelitas Technologies Corp. *MachVis Lens Selector*. 2023. URL: https://www.excelitas.com/product/machvis-lens-selector (visited on 11/07/2023).

[53] L. Felger et al. “Robustness of the wide-field imaging Mueller polarimetry for brain tissue differentiation and white matter fiber tract identification in a surgery-like environment: an ex vivo study”. In: *Biomedical Optics Express* 14.5 (May 2023), p. 2400. ISSN: 2156-7085. DOI: 10.1364/boe.486438.

[54] S. Foxley et al. “Multi-modal imaging of a single mouse brain over five orders of magnitude of resolution”. In: *NeuroImage* 238 (Sept. 2021), p. 118250. ISSN: 1053-8119. DOI: 10.1016/j.neuroimage.2021.118250.

[55] L. E. Franken et al. “A Technical Introduction to Transmission Electron Microscopy for Soft-Matter: Imaging, Possibilities, Choices, and Technical Developments”. In: *Small* 16.14 (Mar. 2020). ISSN: 1613-6829. DOI: 10.1002/smll.201906198.

[56] A.-J. Fresnel. “Mémoire sur la diffraction de la lumière”. In: ed. by M. de l’Académie des Sciences. Vol. 5. Crochard, 1826, pp. 339–475.

[57] F. Gallyas. “Silver Staining of Myelin by Means of Physical Development”. In: *Neurological Research* 1.2 (Jan. 1979), pp. 203–209. ISSN: 1743-1328. DOI: 10.1080/01616412.1979.11739553.

[58] F. Gallyas et al. “Golgi-like demonstration of "dark" neurons with an argyrophil III method for experimental neuropathology”. In: *Acta Neuropathologica* 79.6 (Apr. 1990), pp. 620–628. ISSN: 1432-0533. DOI: 10.1007/bf00294239.

[59] E. A. Genina et al. “Optical properties of brain tissues at the different stages of glioma development in rats: pilot study”. In: *Biomedical Optics Express* 10.10 (Sept. 2019), p. 5182. ISSN: 2156-7085. DOI: 10.1364/boe.10.005182.

[60] P.-G. Gennes and J. Prost. *The physics of liquid crystals*. 2. ed., repr. Oxford science publications. Oxford: Clarendon Press, 2013. 597 pp. ISBN: 9780198517856.

[61] M. Georgiadis et al. “Micron-resolution fiber mapping in histology independent of sample preparation”. In: (Mar. 2024). DOI: 10.1101/2024.03.26.586745.

[62] M. Georgiadis et al. “Retrieving neuronal orientations using 3D scanning SAXS and comparison with diffusion MRI”. In: *NeuroImage* 204 (Jan. 2020), p. 116214. ISSN: 1053-8119. DOI: 10.1016/j.neuroimage.2019.116214.

[63] T. A. Germer. *pySCATMECH : A Python Interface to the SCATMECH Library*. National Institute of Standards Technology. Mar. 2023. URL: https://pages.nist.gov/pySCATMECH/index.html\#indices-and-tables (visited on 04/01/2024).

[64] P. Ghassemi and M. H. Miranbaygi. "Towards skin polarization characterization using polarimetric technique". In: *Journal of Zhejiang University SCIENCE B* 10.8 (July 2009), pp. 602–608. ISSN: 1862-1783. DOI: 10.1631/jzus.b0920068.

[65] N. Ghosh. "Tissue polarimetry: concepts, challenges, applications, and outlook". In: *Journal of Biomedical Optics* 16.11 (Nov. 2011), p. 110801. ISSN: 1083-3668. DOI: 10.1117/1.3652896.

[66] N. Ghosh, M. F. G. Wood, and I. A. Vitkin. "Mueller matrix decomposition for extraction of individual polarization parameters from complex turbid media exhibiting multiple scattering, optical activity, and linear birefringence". In: *Journal of Biomedical Optics* 13.4 (2008), p. 044036. ISSN: 1083-3668. DOI: 10.1117/1.2960934.

[67] J. J. Gil and E. Bernabeu. "A Depolarization Criterion in Mueller Matrices". In: *Optica Acta: International Journal of Optics* 32.3 (Mar. 1985), pp. 259–261. ISSN: 0030-3909. DOI: 10.1080/713821732.

[68] *GitHub: Fiji*. 2024. URL: https://github.com/fiji/fiji (visited on 06/21/2023).

[69] *GitHub: pypylon*. 2021. URL: https://github.com/basler/pypylon (visited on 10/09/2024).

[70] A. M. Glazer, J. G. Lewis, and W. Kaminsky. "An automatic optical imaging system for birefringent media". In: *Proceedings of the Royal Society of London. Series A: Mathematical, Physical and Engineering Sciences* 452.1955 (Dec. 1996), pp. 2751–2765. ISSN: 1471-2946. DOI: 10.1098/rspa.1996.0145.

[71] D. H. Goldstein. *Polarized light*. Third edition. Includes bibliographical references and index. Boca Raton, Fla.: CRC Press, 2011. 770 pp. ISBN: 9781439830406.

[72] G. F. Göthlin. *Die doppelbrechenden Eigenschaften des Nervengewebes: Ihre Ursachen und ihre biologischen Konsequenzen*. Ed. by K. S. Vetenskapsakademien. Almqvist & Wiksell, 1913.

[73] M. Hazewinkel, ed. *Encyclopaedia of mathematics*. Unabridged reprint of the original 10-vol. hardbound library ed. An updated and annotated translation of the Soviet "Mathematical encyclopaedia". Dordrecht [u.a.]: Kluwer, 1995. ISBN: 1556080107.

[74] E. Hecht. *Optik*. 7. Auflage. De Gruyter Studium. Berlin: De Gruyter, 2018. 11366 pp. ISBN: 9783110526653.

[75] F. auf der Heiden. "Development of a Scattering Polarimeter for Multi-Modal Neuroimaging of Brain Tissue". MA thesis. Fakultät für Mathematik, Informatik und Naturwissenschaften der RWTH Aachen University, 2021.

[76] F. auf der Heiden et al. "Reconstruction of Nerve Fiber Orientations in Cell-body Stained Histological Brain Sections using Computational Scattered Light Imaging". In: *Biophotonics Congress: Optics in the Life Sciences 2023 (OMA, NTM, BODA, OMP, BRAIN)*. BRAIN. Optica Publishing Group, 2023. DOI: 10.1364/brain.2023.bw1b.3.

[77] F. auf der Heiden et al. "Towards high-speed Computational Scattered Light Imaging by introducing Compressed Sensing for optimized illumination". In: *SPIE)*. UNPUBLISHED. SPIE, 2024.

[78] T. Heller. *ctypes 1.0.2*. 2007. URL: https://pypi.org/project/ctypes/ (visited on 05/10/2022).

[79] H. V. Henderson and S. R. Searle. "Vec and vech operators for matrices, with some uses in jacobians and multivariate statistics". In: *Canadian Journal of Statistics* 7.1 (Jan. 1979), pp. 65–81. ISSN: 1708-945X. DOI: 10.2307/3315017.

[80] S. Herculano-Houzel. "The human brain in numbers: a linearly scaled-up primate brain". In: *Frontiers in Human Neuroscience* 3 (2009). ISSN: 1662-5161. DOI: 10.3389/neuro.09.031.2009.

[81] M. G. Honig and R. I. Hume. "Dil and DiO: versatile fluorescent dyes for neuronal labelling and pathway tracing". In: *Trends in Neurosciences* 12.9 (Jan. 1989), pp. 333–341. ISSN: 0166-2236. DOI: 10.1016/0166-2236(89)90040-4.

[82] J. d. Hoyo, L. M. Sanchez-Brea, and J. A. Gomez-Pedrero. "High precision calibration method for a four-axis Mueller matrix polarimeter". In: *Optics and Lasers in Engineering* 132 (Sept. 2020), p. 106112. ISSN: 0143-8166. DOI: 10.1016/j.optlaseng.2020.106112.

[83] D. Huang et al. "Optical Coherence Tomography". In: *Science* 254.5035 (Nov. 1991), pp. 1178–1181. ISSN: 1095-9203. DOI: 10.1126/science.1957169.

[84] H. C. van de Hulst. *Light scattering by small particles*. Unabridged and corrected republication of the work originally published in 1957 by John Wiley & Sons, Inc., N.Y. Dover books on physics. New York: Dover Publications, Inc., 2018. 10470 pp. ISBN: 9780486642284.

[85] C. Huygens. *Traité de la Lumière: Où sont expliquées les causes de ce qui luy arrive dans la reflexion & dans la refraction*. Pierre van der Aa, 1690.

[86] R. C. Jones. "A New Calculus for the Treatment of Optical SystemsI Description and Discussion of the Calculus". In: *Journal of the Optical Society of America* 31.7 (July 1941), p. 488. ISSN: 0030-3941. DOI: 10.1364/josa.31.000488.

[87] R. C. Jones. "A New Calculus for the Treatment of Optical SystemsI Description and Discussion of the Calculus". In: *Journal of the Optical Society of America* 31.7 (July 1941), p. 488. ISSN: 0030-3941. DOI: 10.1364/josa.31.000488.

[88] Joy-IT. *Motor Control Kit*. 2023. URL: https://joy-it.net/en/products/Ard-CNC-Kit1 (visited on 09/23/2022).

[89] Joy-IT. *NEMA23-03 Bipolar Stepper Motor*. 2023. URL: https://cdn-reichelt.de/documents/datenblatt/A300/NEMA23-03_DB_EN.pdf (visited on 09/23/2022).

[90] S. Kasap. *Springer Handbook of Electronic and Photonic Materials*. Ed. by P. Capper. 2nd ed. Springer Handbooks Ser. Cham: Springer International Publishing AG, 2017. 11537 pp. ISBN: 9783319489339.

[91] N. Kasthuri et al. "Saturated Reconstruction of a Volume of Neocortex". In: *Cell* 162.3 (July 2015), pp. 648–661. ISSN: 0092-8674. DOI: 10.1016/j.cell.2015.06.054.

[92] J. A. Kiernan. "Histochemistry of Staining Methods for Normal and Degenerating Myelin in the Central and Peripheral Nervous Systems". In: *Journal of Histotechnology* 30.2 (June 2007), pp. 87–106. ISSN: 2046-0236. DOI: 10.1179/his.2007.30.2.87.

[93] M. Kleiner et al. "Classification of Ambiguous Nerve Fiber Orientations in 3D Polarized Light Imaging". In: *Lecture Notes in Computer Science*. Springer Berlin Heidelberg, 2012, pp. 206–213. ISBN: 9783642334153. DOI: 10.1007/978-3-642-33415-3_26.

[94] J. Klingler. *Erleichterung der makrokopischen Präparation des Gehirns durch den Gefrierprozess*. Orell Füssli, 1935.

[95] M. Koike-Tani et al. "Polarized light microscopy in reproductive and developmental biology". In: *Molecular Reproduction and Development* 82.7–8 (Aug. 2013), pp. 548–562. ISSN: 1098-2795. DOI: 10.1002/mrd.22221.

[96] J. D. van der Laan et al. "Increasing detection range and minimizing polarization mixing with circularly polarized light through scattering environments". In: *Polarization: Measurement, Analysis, and Remote Sensing XI*. Ed. by D. B. Chenault and D. H. Goldstein. SPIE, May 2014. DOI: 10.1117/12.2050375.

[97] J. D. van der Laan et al. "Evolution of circular and linear polarization in scattering environments". In: *Optics Express* 23.25 (Dec. 2015), p. 31874. ISSN: 1094-4087. DOI: 10.1364/oe.23.031874.

[98] LANG AG. *Absen Polaris 3.9 Pro*. 2023. URL: https://catalogue.lang-ag.com/files/13031/8923.pdf (visited on 10/09/2024).

[99] B. Laude-Boulesteix et al. "Mueller polarimetric imaging system with liquid crystals". In: *Applied Optics* 43.14 (May 2004), p. 2824. ISSN: 1539-4522. DOI: 10.1364/ao.43.002824.

[100] M. Lee et al. "Label-free optical quantification of structural alterations in Alzheimer's disease". In: *Scientific Reports* 6.1 (Aug. 2016). ISSN: 2045-2322. DOI: 10.1038/srep31034.

[101] C. Leuze et al. "Comparison of diffusion MRI and CLARITY fiber orientation estimates in both gray and white matter regions of human and primate brain". In: *NeuroImage* 228 (Mar. 2021), p. 117692. ISSN: 1053-8119. DOI: 10.1016/j.neuroimage.2020.117692.

[102] T. Levi-Civita and E. Persico. *Lezioni di calcolo differenziale assoluto*. Nicola Zanichelli Editore., 1925. URL: https://books.google.de/books?id=0xrOAAAAMAAJ.

[103] C. Liechti. *GitHub: pyserial 3.5*. 2020. URL: https://pypi.org/project/pyserial/ (visited on 10/09/2024).

[104] D. Liewald et al. "Distribution of axon diameters in cortical white matter: an electron-microscopic study on three human brains and a macaque". In: *Biological Cybernetics* 108.5 (Aug. 2014), pp. 541–557. ISSN: 1432-0770. DOI: 10.1007/s00422-014-0626-2.

[105] L. Liqun. *Principles of Neurobiology*. Taylor & Francis Group, 2015, p. 672. ISBN: 9780815345336.

[106] C. Lours et al. "Perls' Stain Guidelines from the French-Speaking Cellular Hematology Group (GFHC)". In: *Diagnostics* 12.7 (July 2022), p. 1698. ISSN: 2075-4418. DOI: 10.3390/diagnostics12071698.

[107] S.-Y. Lu and R. A. Chipman. "Interpretation of Mueller matrices based on polar decomposition". In: *Journal of the Optical Society of America A* 13.5 (May 1996), p. 1106. ISSN: 1520-8532. DOI: 10.1364/josaa.13.001106.

[108] J. M. López-Téllez and N. C. Bruce. "Mueller-matrix polarimeter using analysis of the nonlinear voltage–retardance relationship for liquid-crystal variable retarders". In: *Applied Optics* 53.24 (Aug. 2014), p. 5359. ISSN: 2155-3165. DOI: 10.1364/ao.53.005359.

[109] J. M. López-Téllez and N. C. Bruce. "Stokes polarimetry using analysis of the nonlinear voltage-retardance relationship for liquid-crystal variable retarders". In: *Review of Scientific Instruments* 85.3 (Mar. 2014). ISSN: 1089-7623. DOI: 10.1063/1.4867458.

[110] C. Macías-Romero and P. Török. "Eigenvalue calibration methods for polarimetry". In: *Journal of the European Optical Society: Rapid Publications* 7 (Mar. 2012). ISSN: 1990-2573. DOI: 10.2971/jeos.2012.12004.

[111] S. Manhas et al. "Mueller matrix approach for determination of optical rotation in chiral turbid media in backscattering geometry". In: *Optics Express* 14.1 (2006), p. 190. ISSN: 1094-4087. DOI: 10.1364/opex.14.000190.

[112] J. C. Maxwell. "II. A dynamical theory of the electromagnetic field". In: *Proceedings of the Royal Society of London* 13 (Dec. 1864), pp. 531–536. ISSN: 2053-9126. DOI: 10.1098/rspl.1863.0098.

[113] S. B. Mehta, M. Shribak, and R. Oldenbourg. "Polarized light imaging of birefringence and diattenuation at high resolution and high sensitivity". In: *Journal of Optics* 15.9 (Sept. 2013), p. 094007. ISSN: 2040-8986. DOI: 10.1088/2040-8978/15/9/094007.

[114] M. Menzel et al. "A Jones matrix formalism for simulating three-dimensional polarized light imaging of brain tissue". In: *Journal of The Royal Society Interface* 12.111 (Oct. 2015), p. 20150734. ISSN: 1742-5662. DOI: 10.1098/rsif.2015.0734.

[115] M. Menzel. *Finite-Differenzen-Simulationen im Zeitbereich zur verbesserten Rekonstruktion der Nervenfaserarchitektur des Gehirns durch 3D-Bildgebung mit polarisiertem Licht*. en. Vol. RWTH Aachen University. RWTH Aachen University, 2018, p. 2018. DOI: 10.18154/RWTH-2018-230974.

[116] M. Menzel and S. F. Pereira. "Coherent Fourier scatterometry reveals nerve fiber crossings in the brain". In: *Biomedical Optics Express* 11.8 (July 2020), p. 4735. ISSN: 2156-7085. DOI: 10.1364/boe.397604.

[117] M. Menzel et al. "Diattenuation Imaging reveals different brain tissue properties". In: *Scientific Reports* 9.1 (Feb. 2019). ISSN: 2045-2322. DOI: 10.1038/s41598-019-38506-w.

[118] M. Menzel et al. "Diattenuation of brain tissue and its impact on 3D polarized light imaging". In: *Biomedical Optics Express* 8.7 (June 2017), p. 3163. ISSN: 2156-7085. DOI: 10.1364/boe.8.003163.

[119] M. Menzel et al. "Light Scattering Measurements Enable an Improved Reconstruction of Nerve Fiber Crossings". In: *Biophotonics Congress: Biomedical Optics 2020 (Translational, Microscopy, OCT, OTS, BRAIN)*. BRAIN. Optica Publishing Group, 2020. DOI: 10.1364/brain.2020.bw2c.3.

[120] M. Menzel et al. "Scattered Light Imaging: Resolving the substructure of nerve fiber crossings in whole brain sections with micrometer resolution". In: *NeuroImage* 233 (June 2021), p. 117952. ISSN: 1053-8119. DOI: 10.1016/j.neuroimage.2021.117952.

[121] M. Menzel et al. "Scatterometry Measurements With Scattered Light Imaging Enable New Insights Into the Nerve Fiber Architecture of the Brain". In: *Frontiers in Neuroanatomy* 15 (Nov. 2021). ISSN: 1662-5129. DOI: 10.3389/fnana.2021.767223.

[122] M. Menzel et al. "Toward a High-Resolution Reconstruction of 3D Nerve Fiber Architectures and Crossings in the Brain Using Light Scattering Measurements and Finite-Difference Time-Domain Simulations". In: *Physical Review X* 10.2 (Apr. 2020), p. 021002. ISSN: 2160-3308. DOI: 10.1103/physrevx.10.021002.

[123] M. Menzel et al. "Using light and X-ray scattering to untangle complex neuronal orientations and validate diffusion MRI". In: *eLife* 12 (May 2023). ISSN: 2050-084X. DOI: 10.7554/elife.84024.

[124] B. Merker. "Silver staining of cell bodies by means of physical development". In: *Journal of Neuroscience Methods* 9.3 (Nov. 1983), pp. 235–241. ISSN: 0165-0270. DOI: 10.1016/0165-0270(83)90086-9.

[125] M. Mesradi et al. "Experimental and analytical comparative study of optical coefficient of fresh and frozen rat tissues". In: *Journal of Biomedical Optics* 18.11 (Nov. 2013), p. 117010. ISSN: 1083-3668. DOI: 10.1117/1.jbo.18.11.117010.

[126] G. Mie. "Beiträge zur Optik trüber Medien, speziell kolloidaler Metallösungen". In: *Annalen der Physik* 330.3 (Jan. 1908), pp. 377–445. ISSN: 1521-3889. DOI: 10.1002/andp.19083300302.

[127] J. Miklossy and H. Van der Loss. "The Long-Distance Effects of Brain Lesions: Visualization of Myelinated Pathways in the Human Brain Using Polarizing and Fluorescence Microscopy". In: *Journal of Neuropathology & Experimental Neurology* 50.1 (Jan. 1991), pp. 1–15. ISSN: 1554-6578. DOI: 10.1097/00005072-199101000-00001.

[128] S. Mori and J. Zhang. "Principles of Diffusion Tensor Imaging and Its Applications to Basic Neuroscience Research". In: *Neuron* 51.5 (Sept. 2006), pp. 527–539. ISSN: 0896-6273. DOI: 10.1016/j.neuron.2006.08.012.

[129] S. Moriconi et al. "Near-real-time Mueller polarimetric image processing for neurosurgical intervention". In: *International Journal of Computer Assisted Radiology and Surgery* (Mar. 2024). ISSN: 1861-6429. DOI: 10.1007/s11548-024-03090-6.

[130] J. Morio and F. Goudail. "Influence of the order of diattenuator, retarder, and polarizer in polar decomposition of Mueller matrices". In: *Optics Letters* 29.19 (Oct. 2004), p. 2234. ISSN: 1539-4794. DOI: 10.1364/ol.29.002234.

[131] H. Mueller. "Memorandum on the polarization optics of the photoelastic shutte". In: *Report No. 2 of the OSRDproject OEMsr-576* (1943).

[132] S. Mujumdar and H. Ramachandran. "Imaging through turbid media using polarization modulation: dependence on scattering anisotropy". In: *Optics Communications* 241.1–3 (Nov. 2004), pp. 1–9. ISSN: 0030-4018. DOI: 10.1016/j.optcom.2004.07.012.

[133] I. Muševič. *Liquid Crystal Colloids*. Springer, p. 320. ISBN: 9783319855196.

[134] Newport. *Polymer Zero-Order Quarter-Wave Waveplates*. 2024. URL: https://www.newport.com/f/polymer-zero-order-quarter-wave-plates (visited on 03/04/2024).

[135] M. A. Nielsen and I. L. Chuang. *Quantum computation and quantum information*. 10. printing. Cambridge Univ. Press, 2009. 676 pp. ISBN: 9780521635035.

[136] F. Nienhaus et al. "Polarized Light Imaging in Life Sciences". In: *Imaging & Microscopy* (Mar. 2023). URL: https://analyticalscience.wiley.com/content/article-do/polarized-light-imaging-life-sciences.

[137] T. Novikova et al. "Mueller Polarimetry of Brain Tissues". In: *Polarized Light in Biomedical Imaging and Sensing*. Springer International Publishing, June 2022, pp. 205–229. ISBN: 9783031047411. DOI: 10.1007/978-3-031-04741-1_8.

[138] T. Novikova et al. "Polarimetric Imaging for Cancer Diagnosis and Staging". In: *Optics and Photonics News* 23.10 (Oct. 2012), p. 26. ISSN: 1541-3721. DOI: 10.1364/opn.23.10.000026.

[139] NumPy Developers. *NumPy documentation*. Mar. 2024. URL: https://numpy.org/doc/stable/index.html (visited on 10/09/2024).

[140] OpenStax. *Anatomy and Physiology*. Creative Commons Attribution 4.0 International (CC BY). Creative Commons Attribution 4.0 International (CC BY). 2016. URL: https://openstax.org/books/anatomy-and-physiology/pages/preface (visited on 09/01/2024).

[141] N. Ortega-Quijano and J. L. Arce-Diego. "Mueller matrix differential decomposition". In: *Optics Letters* 36.10 (May 2011), p. 1942. ISSN: 1539-4794. DOI: 10.1364/ol.36.001942.

[142] P. Osten and T. W. Margrie. "Mapping brain circuitry with a light microscope". In: *Nature Methods* 10.6 (May 2013), pp. 515–523. ISSN: 1548-7105. DOI: 10.1038/nmeth.2477.

[143] C. Palm. "Towards ultra-high resolution fibre tract mapping of the human brain - registration of polarised light images and reorientation of fibre vectors". In: *Frontiers in Human Neuroscience* (2010). ISSN: 1662-5161. DOI: 10.3389/neuro.09.009.2010.

[144] S. Palmer. "The optical response of liquid crystal cells to a low frequency driving voltage". In: *Liquid Crystals* 24.4 (Apr. 1998), pp. 587–598. ISSN: 1366-5855. DOI: 10.1080/026782998207064.

[145] F. L. Pedrotti and L. S. Pedrotti. *Optik für Ingenieure. Grundlagen*. Ed. by W. Bausch and H. Schmidt. 4., bearb. Aufl. Berlin, Heidelberg: Springer, 2008. 848 pp. ISBN: 9783540734710.

[146] D. E. Pegg. "The History and Principles of Cryopreservation". In: *Seminars in Reproductive Medicine* 20.1 (2002), pp. 005–014. ISSN: 1526-4564. DOI: 10.1055/s-2002-23515.

[147] H. Poincaré. *Théorie mathématique de la lumière*. Gauthier-Villars, 1892.

[148] D. L. Puhl et al. "Electrospun Fiber Scaffolds for Engineering Glial Cell Behavior to Promote Neural Regeneration". In: *Bioengineering* 8.1 (Dec. 2020), p. 4. ISSN: 2306-5354. DOI: 10.3390/bioengineering8010004.

[149] R. H. Quarles, W. B. Macklin, and P. Morell. "Myelin Formation, Structure and Biochemistry". In: *Basic Neurochemistry*. Ed. by G. J. Siegel. 7th ed. Includes bibliographical references. - Description based on print version record. Amsterdam: Elsevier, 2006. Chap. 4. ISBN: 0080472079.

[150] J. C. Ramella-Roman and T. Novikova, eds. *Polarized Light in Biomedical Imaging and Sensing: Clinical and Preclinical Applications*. Springer International Publishing, 2023. ISBN: 9783031047411. DOI: 10.1007/978-3-031-04741-1.

[151] L. Rayleigh. "X. On the electromagnetic theory of light". In: *The London, Edinburgh, and Dublin Philosophical Magazine and Journal of Science* 12.73 (Aug. 1881), pp. 81–101. ISSN: 1941-5990. DOI: 10.1080/14786448108627074.

[152] S. Ready. *Diffraction of Light and Young's Double Slit Experiment*. Creative Commons. 2024. URL: https://sciencready.com.au/pages/diffraction (visited on 09/01/2024).

[153] J. Reckfort et al. "A multiscale approach for the reconstruction of the fiber architecture of the human brain based on 3D-PLI". In: *Frontiers in Neuroanatomy* 9 (Sept. 2015). ISSN: 1662-5129. DOI: 10.3389/fnana.2015.00118.

[154] J. Reckfort et al. "Extracting the inclination angle of nerve fibers within the human brain with 3D-PLI independent of system properties". In: *Polarization Science and Remote Sensing VI*. Ed. by J. A. Shaw and D. A. LeMaster. SPIE, Sept. 2013. DOI: 10.1117/12.2023198.

[155] E. Reinhard, W. Heidrich, and P. Debevec. *High Dynamic Range Imaging. Acquisition, Display, and Image-Based Lighting*. 2. Aufl. [The Morgan Kaufmann series in computer graphics]. Description based upon print version of record. [s.l.]: Elsevier professional, 2010. 31124672 pp. ISBN: 012374914X.

[156] J. Reuter. *GitHub: SLIX*. 2022. URL: https://github.com/3d-pli/SLIX (visited on 10/09/2024).

[157] J. Reuter and M. Menzel. "SLIX: A Python package for fully automated evaluation of Scattered Light Imaging measurements on brain tissue". In: *Journal of Open Source Software* 5.54 (Oct. 2020), p. 2675. ISSN: 2475-9066. DOI: 10.21105/joss.02675.

[158] J. A. Reuter et al. "Enhanced determination of nerve fiber orientations by introducing iterative thresholds in Computational Scattered Light Imaging". In: *Biophotonics Congress: Optics in the Life Sciences 2023 (OMA, NTM, BODA,*

OMP, BRAIN). BRAIN. Optica Publishing Group, 2023. DOI: 10.1364/brain.2023.bw1b.6.

[159] O. Rodríguez-Núñez et al. "Polarimetric visualization of healthy brain fiber tracts under adverse conditions: ex vivo studies". In: *Biomedical Optics Express* 12.10 (Oct. 2021), p. 6674. ISSN: 2156-7085. DOI: 10.1364/boe.439754.

[160] D. L. Rosene, N. J. Roy, and B. J. Davis. "A cryoprotection method that facilitates cutting frozen sections of whole monkey brains for histological and histochemical processing without freezing artifact." In: *Journal of Histochemistry & Cytochemistry* 34.10 (Oct. 1986), pp. 1301–1315. ISSN: 1551-5044. DOI: 10.1177/34.10.3745909.

[161] D. S. Sabatke et al. "Optimization of retardance for a complete Stokes polarimeter". In: *Optics Letters* 25.11 (June 2000), p. 802. ISSN: 1539-4794. DOI: 10.1364/ol.25.000802.

[162] A. Sadeghipour and P. Babaheidarian. "Making Formalin-Fixed, Paraffin Embedded Blocks". In: *Biobanking*. Springer New York, Dec. 2018, pp. 253–268. ISBN: 9781493989355. DOI: 10.1007/978-1-4939-8935-5_22.

[163] M. Sakamoto et al. "Exploring the influence of wavelength and polarization of illuminating light on polarization imaging for birefringent objects concealed behind scattering structure". In: *Optics Communications* 552 (Feb. 2024), p. 130118. ISSN: 0030-4018. DOI: 10.1016/j.optcom.2023.130118.

[164] M. J. Sanderson et al. "Fluorescence Microscopy". In: *Cold Spring Harbor Protocols* 2014.10 (Oct. 2014), pdb.top071795. ISSN: 1559-6095. DOI: 10.1101/pdb.top071795.

[165] A. V. Sathe. "Use of mixture of ethanol-n butanol-xylene in paraffin method". In: *Experientia* 23.9 (Sept. 1967), pp. 790–790. ISSN: 1420-9071. DOI: 10.1007/bf02154182.

[166] S. N. Savenkov. "Jones and Mueller matrices: structure, symmetry relations and information content". In: *Light Scattering Reviews 4*. Springer Berlin Heidelberg, 2009, pp. 71–119. ISBN: 9783540742760. DOI: 10.1007/978-3-540-74276-0_3.

[167] D. Schmitz et al. "A least squares approach for the reconstruction of nerve fiber orientations from tiltable specimen experiments in 3D-PLI". In: *2018 IEEE 15th International Symposium on Biomedical Imaging (ISBI 2018)*. IEEE, Apr. 2018. DOI: 10.1109/isbi.2018.8363539.

[168] N. P. Schnoor et al. "Calibration of liquid crystal variable retarders using a common-path interferometer and fit of a closed-form expression for the retardance curve". In: *Applied Optics* 59.34 (Nov. 2020), p. 10673. ISSN: 2155-3165. DOI: 10.1364/ao.408383.

[169] P. Schucht et al. "Visualization of White Matter Fiber Tracts of Brain Tissue Sections With Wide-Field Imaging Mueller Polarimetry". In: *IEEE Transactions on Medical Imaging* 39.12 (Dec. 2020), pp. 4376–4382. ISSN: 1558-254X. DOI: 10.1109/tmi.2020.3018439.

[170] R. Schurr and A. A. Mezer. "The glial framework reveals white matter fiber architecture in human and primate brains". In: *Science* 374.6568 (Nov. 2021), pp. 762–767. ISSN: 1095-9203. DOI: 10.1126/science.abj7960.

[171] P. Seibt. *Algorithmic Information Theory. Mathematics of Digital Information*. Springer eBook Collection. Berlin, Heidelberg: Springer Berlin Heidelberg, 2006. 443 pp. ISBN: 9783540332190.

[172] R. A. Sheldon, L. Almli, and D. M. Ferriero. "Copper/Zinc Superoxide Dismutase Transgenic Brain in Neonatal Hypoxia–Ischemia". In: *Redox Cell Biology*

and Genetics Part B. Elsevier, 2002, pp. 389–397. DOI: 10.1016/s0076-6879(02)53063-9.

[173] Y Shi and A. W. Toga. "Connectome imaging for mapping human brain pathways". In: *Molecular Psychiatry* 22.9 (May 2017), pp. 1230–1240. ISSN: 1476-5578. DOI: 10.1038/mp.2017.92.

[174] Simplify3D. *PLA*. 2019. URL: https://www.simplify3d.com/support/materials-guide/pla/ (visited on 10/09/2024).

[175] M. D. Singh, N. Ghosh, and I. A. Vitkin. "Mueller Matrix Polarimetry in Biomedicine: Enabling Technology, Biomedical Applications, and Future Prospects". In: *Polarized Light in Biomedical Imaging and Sensing*. Springer International Publishing, Nov. 2022, pp. 61–103. ISBN: 9783031047411. DOI: 10.1007/978-3-031-04741-1_3.

[176] A. Sleigh. *Cartesian Plotter v3*. 2020. URL: https://www.thingiverse.com/thing:4200863 (visited on 09/23/2022).

[177] R. S. Snell. *Clinical neuroanatomy*. 7. ed. Includes bibliographical references and index. Philadelphia [u.a.]: Wolters Kluwer/Lippincott Williams & Wilkins, 2010. 542 pp. ISBN: 9780781794275.

[178] Sony. *IMX183CLK-J/CQJ-J (CMOS Image Sensor)*. 2023. URL: https://www.sony-semicon.com/files/62/flyer_industry/IMX183CLK-J_CQJ-J_Flyer.pdf (visited on 10/10/2024).

[179] G. G. Stokes. "XXX. On the change of refrangibility of light". In: *Philosophical Transactions of the Royal Society of London* 142 (Dec. 1852), pp. 463–562. ISSN: 2053-9223. DOI: 10.1098/rstl.1852.0022.

[180] G. Strang. "The Discrete Cosine Transform". In: *SIAM Review* 41.1 (Jan. 1999), pp. 135–147. ISSN: 1095-7200. DOI: 10.1137/s0036144598336745.

[181] J. Sun et al. "Refractive index measurement of acute rat brain tissue slices using optical coherence tomography". In: *Optics Express* 20.2 (Jan. 2012), p. 1084. ISSN: 1094-4087. DOI: 10.1364/oe.20.001084.

[182] J. Sy and L.-C. Ang. "Microtomy: Cutting Formalin-Fixed, Paraffin-Embedded Sections". In: *Biobanking*. Springer New York, Dec. 2018, pp. 269–278. ISBN: 9781493989355. DOI: 10.1007/978-1-4939-8935-5_23.

[183] A. Taflove and S. C. Hagness. *Computational electrodynamics. The finite-difference time-domain method*. 3rd ed., [Nachdr.] Artech House antennas and propagation library. Literaturangaben. Boston, Mass. [u.a.]: Artech House, 2010. 1006 pp. ISBN: 1580538320.

[184] H. Takemura et al. "Anatomy of nerve fiber bundles at micrometer-resolution in the vervet monkey visual system". In: *eLife* 9 (Aug. 2020). ISSN: 2050-084X. DOI: 10.7554/elife.55444.

[185] TAORAD GmbH. *Microscopes*. 2024. URL: https://www.taorad.com/microscopes/ (visited on 10/09/2024).

[186] B. Taylor. *Methodus incrementorum directa et inversa*. In Collections: Accademia delle Scienze Torino. London: Typis Pearsonianis prostant apud Gul. Innys ad Insignia Principis in Coemeterio Paulino, 1715.

[187] The SciPy community. *Fourier Transforms (scipy.fft)*. 2023. URL: https://docs.scipy.org/doc/scipy/tutorial/fft.html (visited on 07/21/2023).

[188] Thorlabs Inc. *CCS Series Spectrometer Operation Manual*. 2023. URL: https://www.thorlabs.com/drawings/c089cbd4f12b737e-ADC71EAC-CDFF-BF34-8AC88A58D6D9CBD6/CCS100_M-Manual.pdf (visited on 11/01/2023).

[189] Thorlabs Inc. *Full-Wave Liquid Crystal Variable Retarders / Wave Plates*. 2023. URL: https://www.thorlabs.com/newgrouppage9.cfm?objectgroup_id=6339&pn=LCC1223-A (visited on 11/01/2023).

[190] Thorlabs Inc. *Hard-Coated UV/VIS Bandpass Filters*. 2023. URL: https://www.thorlabs.com/newgrouppage9.cfm?objectgroup_id=1860 (visited on 11/22/2023).

[191] Thorlabs Inc. *K-Cube™ Liquid Crystal Controller*. 2023. URL: https://www.thorlabs.com/newgrouppage9.cfm?objectgroup_id=14074&pn=KLC101 (visited on 11/01/2023).

[192] Thorlabs Inc. *Nanoparticle Linear Film Polarizer*. 2023. URL: https://www.thorlabs.com/newgrouppage9.cfm?objectgroup_id=752 (visited on 11/01/2023).

[193] M Titford. "The long history of hematoxylin". In: *Biotech Histochemistry* 80.2 (Jan. 2005), pp. 73–78. ISSN: 1473-7760. DOI: 10.1080/10520290500138372.

[194] M. Trepel. *Neuroanatomie. Struktur und Funktion*. Ed. by K. Dalkowski. 7th ed. Philadelphia: Urban & Fischer Verlag GmbH & Co. KG, 2017. 1439 pp. ISBN: 9783437180095.

[195] S. Trinkle et al. "Synchrotron X-ray micro-CT as a validation dataset for diffusion MRI in whole mouse brain". In: *Magnetic Resonance in Medicine* 86.2 (Mar. 2021), pp. 1067–1076. ISSN: 1522-2594. DOI: 10.1002/mrm.28776.

[196] J. S. Tyo. "Noise equalization in Stokes parameter images obtained by use of variable-retardance polarimeters". In: *Optics Letters* 25.16 (Aug. 2000), p. 1198. ISSN: 1539-4794. DOI: 10.1364/ol.25.001198.

[197] U. Türe et al. "Fiber Dissection Technique: Lateral Aspect of the Brain". In: *Neurosurgery* 47.2 (Aug. 2000), pp. 417–427. ISSN: 1524-4040. DOI: 10.1097/00006123-200008000-00028.

[198] UCLA Brain Mapping Center. *Vervet Atlas Viewer*. 2014. URL: http://www.bmap.ucla.edu/portfolio/atlasviewer/vervetatlas/index.shtml?X=274&Y=307&Z=247 (visited on 10/09/2024).

[199] H. Uylings, K. Zilles, and G. Rajkowska. "Optimal Staining Methods for Delineation of Cortical Areas and Neuron Counts in Human Brains". In: *NeuroImage* 9.4 (Apr. 1999), pp. 439–445. ISSN: 1053-8119. DOI: 10.1006/nimg.1999.0417.

[200] H. Wang et al. "as-PSOCT: Volumetric microscopic imaging of human brain architecture and connectivity". In: *NeuroImage* 165 (Jan. 2018), pp. 56–68. ISSN: 1053-8119. DOI: 10.1016/j.neuroimage.2017.10.012.

[201] V. Wedeen et al. "Diffusion spectrum magnetic resonance imaging (DSI) tractography of crossing fibers". In: *NeuroImage* 41.4 (July 2008), pp. 1267–1277. ISSN: 1053-8119. DOI: 10.1016/j.neuroimage.2008.03.036.

[202] M. D. Weingarten et al. "A protein factor essential for microtubule assembly." In: *Proceedings of the National Academy of Sciences* 72.5 (May 1975), pp. 1858–1862. ISSN: 1091-6490. DOI: 10.1073/pnas.72.5.1858.

[203] T. A. Welch. "A Technique for High-Performance Data Compression". In: *Computer* 17.6 (June 1984), pp. 8–19. ISSN: 0018-9162. DOI: 10.1109/mc.1984.1659158.

[204] H. Wiese et al. "Polarized light imaging of the human brain: a new approach to the data analysis of tilted sections". In: *Polarization: Measurement, Analysis, and Remote Sensing XI*. Ed. by D. B. Chenault and D. H. Goldstein. SPIE, May 2014. DOI: 10.1117/12.2053305.

[205] J. H. Wong, G. M. Halliday, and W. S. Kim. "Exploring Myelin Dysfunction in Multiple System Atrophy". In: *Experimental Neurobiology* 23.4 (Dec. 2014), pp. 337–344. ISSN: 2093-8144. DOI: 10.5607/en.2014.23.4.337.

[206] M. F. G. Wood et al. "Effects of formalin fixation on tissue optical polarization properties". In: *Physics in Medicine and Biology* 56.8 (Mar. 2011), N115–N122. ISSN: 1361-6560. DOI: 10.1088/0031-9155/56/8/n01.

[207] R. P. Woods et al. "A web-based brain atlas of the vervet monkey, Chlorocebus aethiops". In: *NeuroImage* 54.3 (Feb. 2011), pp. 1872–1880. ISSN: 1053-8119. DOI: 10.1016/j.neuroimage.2010.09.070.

[208] Y. Wu et al. "Association fiber tracts related to Broca's area: A comparative study based on diffusion spectrum imaging and fiber dissection". In: *Frontiers in Neuroscience* 16 (Nov. 2022). ISSN: 1662-453X. DOI: 10.3389/fnins.2022.978912.

[209] G. Wysiadecki et al. "Klingler's method of brain dissection: review of the technique including its usefulness in practical neuroanatomy teaching, neurosurgery and neuroimaging". In: *Folia Morphologica* 78.3 (Aug. 2019), pp. 455–466. ISSN: 0015-5659. DOI: 10.5603/fm.a2018.0113.

[210] A. N. Yaroslavsky et al. "Optical properties of selected native and coagulated human brain tissues in vitro in the visible and near infrared spectral range". In: *Physics in Medicine and Biology* 47.12 (June 2002), pp. 2059–2073. ISSN: 0031-9155. DOI: 10.1088/0031-9155/47/12/305.

[211] A. Yendiki et al. "Post mortem mapping of connectional anatomy for the validation of diffusion MRI". In: *NeuroImage* 256 (Aug. 2022), p. 119146. ISSN: 1053-8119. DOI: 10.1016/j.neuroimage.2022.119146.

[212] T. Young. "I. The Bakerian Lecture. Experiments and calculations relative to physical optics". In: *Philosophical Transactions of the Royal Society of London* 94 (Dec. 1804), pp. 1–16. ISSN: 2053-9223. DOI: 10.1098/rstl.1804.0001.

[213] J. Zhang and H. Xiong. "Brain Tissue Preparation, Sectioning, and Staining". In: *Current Laboratory Methods in Neuroscience Research*. Springer New York, Sept. 2013, pp. 3–30. ISBN: 9781461487944. DOI: 10.1007/978-1-4614-8794-4_1.

[214] J. Zhang et al. "Determination of birefringence and absolute optic axis orientation using polarization-sensitive optical coherence tomography with PM fibers". In: *Optics Express* 11.24 (Dec. 2003), p. 3262. ISSN: 1094-4087. DOI: 10.1364/oe.11.003262.

[215] K. Zilles and B. Tillmann, eds. *Anatomie*. Springer-Lehrbuch. Berlin, Heidelberg: Springer Berlin Heidelberg, 2011. 11022 pp. ISBN: 9783540694830.

List of Symbols

Symbols used in this thesis are listed here. Where required, they can be marked with explanatory subscripts, e.g. specifying the time t as t_{exp} to indicate exposure time. For conciseness, only the most relevant derivative symbols are listed here. Other derivative symbols will be defined as needed in the respective chapters.

a_0	Fourier coefficient of 0th order
a_2	Fourier coefficient of 2nd order
b_2	Fourier coefficient of 2nd order
c	Speed of light
c_0	Speed of light in vacuum
d	Thickness or diameter
d_{gear}	Gear diameter
$\hat{e}_x$, $\hat{e}_y$, $\hat{e}_z$	System of Cartesian unit vectors
f	Frequency
$g_{x,y,\rho}$	Pixel- and angle-specific gain factor
i	Index of sampled data point
k	Wave number
$\vec{k}$	Wave vector
k_0	Wave number in vacuum
k_x, k_y, k_z	Elements of wave vector $\vec{k}$
l	Length
m	Integer number
m_{ij}	Matrix element
n	Refractive index
n_1, n_2 , n_3	Refractive indices in anisotropic material
n_A, n_B	Refractive index of material A or B
n_i	Integer number
n_{real}	Real part of complex refractive index
Δn	Difference in refractive index
Δp	Partial depolarization
px	Index of pixel
q	Number of illuminated pixel rows or columns in ComSLI
r	Particle radius
r_i	Vector elements of $\vec{R}$ in Lu-Chipman decomposition
t	Time
t_{rel}	Relative section thickness
v_ϕ, w_ϕ	Auxiliary function in Section 2.3.3
x	Cartesian coordinate
y	Cartesian coordinate
z	Cartesian coordinate
Δz	Distance in z-direction

A	Matrix of polarization state analyzer (PSA)
A	Anti-diagonal polarization
B_i	Matrix in eigenvalue calibration method (ECM)
C_i	Auxiliary matrix in ECM
D	Total diattenuation
$\vec{D}$	Diattenuation vector along the fast axis $\hat{D}$
$\hat{D}$	Fast axis of diattenuation
D	Diagonal polarization
D_C	Circular diattenuation
D_D	Diagonal diattenuation
D_H	Horizontal diattenuation
D_L	Linear diattenuation
D^+	Type of diattenuation in brain tissue
D^-	Type of diattenuation in brain tissue
DOP	Degree of polarization
$\vec{E}$	Electric field
E_0	Maximum amplitude of electric field
E_x, E_y	Electric field amplitude in x- or y-direction
E_{x0}, E_{y0}	Maximum electric field in x- or y-direction
FOV	Field of view
H	Horizontal polarization
H_i	Auxiliary matrix in ECM
I	Intensity
$\bar{I}$	Mean intensity over an area
$I'_{x,y,\rho}$, $I_{x,y,\rho}$	Pixel- and angle-specific intensity
I_0	Initial intensity; also transmittance in 3D-PLI
I_i	Intensity (i-th data point)
I_{px}	Intensity of a pixel with index px
I_{raw}	Raw intensity
I_{in}, I_{out}	Incident intensity and transmitted intensity
I_{HH}, I_{HV}, ...	Intensities with PSG and PSA settings indicated
ΔI	Difference in intensity
$\vec{J}$	Jones vector in Jones matrix calculus
J_x, J_y	Components of Jones vector
$\vec{J}_H$, $\vec{J}_V$, $\vec{J}_D$, $\vec{J}_A$, $\vec{J}_R$, $\vec{J}_L$	Jones vector for basic polarization states
L	Linear combination of matrices in ECM
L	Left-circular polarization
M	Müller matrix or Jones matrix
M_i	i-th Müller matrix or Jones matrix
M_D	Diattenuation matrix
$M_{\text{[element]}}$	Müller or Jones matrix of optic [element]
M_R	Retardance matrix
M_{tissue}	Müller matrix of brain tissue
M_Δ	Depolarization matrix
N	Number of sample data points i
N_{px}	Number of pixels
P	Polarizance
R	Total retardance
$\vec{R}$	Retardance vector along the fast axis $\hat{R}$
$\hat{R}$	Fast axis of retardance

R	Right-circular polarization
R_C	Circular retardance
R_D	Diagonal retardance
R_H	Horizontal retardance
R_L	Linear retardance (also: δ)
$R(\theta)$	Rotation matrix
R^2	Coefficient of determination
$\vec{S}$	Stokes vector in Müller matrix calculus
S_0, S_1, S_2, S_3	Elements of Stokes vector
$\vec{S}_\mathrm{H}$, $\vec{S}_\mathrm{V}$, $\vec{S}_\mathrm{D}$, $\vec{S}_\mathrm{A}$, $\vec{S}_\mathrm{R}$, $\vec{S}_\mathrm{L}$	Stokes vector for basic polarization states
$\vec{S}_\mathrm{in}$, $\vec{S}_\mathrm{out}$	Incident and transmitted Stokes vector
T_c	Clearing point of temperature in liquid crystals
T_max, T_min	Maximum and minimum transmittance
V	Voltage
V	Vertical polarization
W	Matrix of polarization state generator (PSG)

α_inc	Inclination (out-of-plane) angle of nerve fiber
$\Delta\alpha_\mathrm{inc}$	Inclination difference
β_A	Angle of incidence in material A
β_B	Angle of refraction in material B
δ	Linear retardance
$\lvert\sin(\delta)\rvert$	Retardation
$\lvert\sin(\delta)\rvert_{\alpha=0^\circ}$	Retardation of in-plane fibers
ϵ	Electric permittivity
$\tilde{\epsilon}$	Electric permittivity tensor
$\tilde{\epsilon}'$	Diagonalized electric permittivity tensor
ϵ_0	Electric permittivity in vacuum
ϵ_1, ϵ_2, ϵ_3	Diagonal elements of tensor $\tilde{\epsilon}'$
$\epsilon_{11}, \ldots, \epsilon_{33}$	Elements of tensor $\tilde{\epsilon}$
θ	Azimuthal angle
Δ	Total depolarization
Δ_L	Linear depolarization
$\Delta\theta$	Azimuthal angle difference
κ	Imaginary part of complex refractive index
λ	Wavelength
$\bar{\lambda}$	Mean wavelength
λ_0	Wavelength in vacuum
λ_i	i-th eigenvalue
μ	Magnetic permeability
μ_0	Magnetic permeability in vacuum
μ_abs	Absorption coefficient
μ_att	Attenuation coefficient (synonymous to μ_ext)
μ_ext	Extinction coefficient (synonymous to μ_att)
μ_scat	Scattering coefficient
μ_{xx}, μ_{yy}, μ_{zz}	Elements of direction-dependent μ_scat
τ	Average transmittance
$\Delta\tau$	Difference for average transmittance
φ	Phase of electromagnetic wave
φ_x, ϕ_y	Phase of x- or y-component of wave

ϕ_{PLI}, ϕ_{DI}, ϕ_{SLI}	Fiber direction from various methods
ϕ_{dir}	Fiber direction (in-plane) angle of nerve fiber
ϕ_{off}	Fiber direction offset
ϕ_R	Orientation of fast axis of retardance vector $\vec{R}$
$\Delta\varphi$	Phase difference
χ	Fiber crossing angle
ρ	Azimuthal rotation angle of optic element
ρ_i	Rotation angle of optic element (i-th data point)
σ	Standard deviation
σ_I	Standard deviation of intensity I
$\bar{\sigma}_I$	Mean standard deviation of intensity I
σ_δ	Uncertainty of retardance δ
ψ	Polarization angle
$\Delta\psi$	Difference of polarization angle
ψ_i	Polarization angle (i-th data point)
Ψ	Magnitude of optical rotation
ω	Angular frequency

List of Abbreviations

2D	**2**-**D**imensional
3D	**3**-**D**imensional
3D-PLI	**3**-**D**imensional **P**olarized **L**ight **I**maging
Ag	Silver (**Ag**entum)
AR	**A**nti **R**eflection
CA	**C**ircular **A**nalyzer
CAD	**C**omputer **A**ided **D**esign
CCD	**C**harge **C**oupled **D**evice
CFM	**C**onfocal **F**luorescence **M**icroscopy
CLARITY	**C**lear **L**ipid-exchanged **A**crylamide-hybridized **R**igid **I**maging/ **I**mmunostaining/**I**n situ hybridization-compatible **T**issue-h**Y**drogel
CMOS	**C**harged **M**etal **O**xide **S**emiconductors
CNC	**C**omputerized **N**umerical **C**ontrol
CNS	**C**entral **N**ervous **S**ystem
ComSLI	**Com**putational **S**cattered **L**ight **I**maging
CT	**C**omputed **T**omography
DAB	**DiA**mino**B**enzidine
DC	**D**irect **C**urrent
DCT	**D**iscrete **C**osine **T**ransform
DCT-II	**D**iscrete **C**osine **T**ransform Type **II**
DI	**D**iattenuation **I**maging
DFT	**D**iscrete **F**ourier **T**ransform
dMRI	**d**iffusion-weighted **M**agnetic **R**esonance **I**maging
DOP	**D**egree **O**f **P**olarization
DWI	**D**iffusion-**W**eighed Magnetic Resonance **I**maging
ECM	**E**igenvalue **C**alibration **M**ethod
EVA	**E**thylene-**V**inyl **A**cetate
FDTD	**F**inite-**D**ifference **T**ime-**D**omain
FFPE	**F**ormalin **F**ixation & **P**araffin **E**mbedding
FM	**F**luorescence **M**icroscopy
FOM	**F**iber **O**rientation **M**ap
FOV	**F**ield **O**f **V**iew
FWHM	**F**ull **W**idth **H**alf **M**aximum
FZJ	**F**orschungs**Z**entrum **J**ülich
GUI	**G**raphical **U**ser **I**nterface
HDMI	**H**igh **D**efinition **M**edia **I**nterface
H&E	**H**ematoxylin & **E**osin stain
HSV	**H**ue **S**aturation **V**alue Colorspace
HWP	**H**alf **W**ave **P**late
ICA	**I**ndependent **C**omponent **A**nalysis
IDE	**I**ntegrated **D**evelopment **E**nvironment
INM	**I**nstitute of **N**euroscience and **M**edicine

LAP	**L**arge **A**rea **P**olarimeter
LC	**L**eft-Handed **C**ircular
LED	**L**ight **E**mitting **D**iode
LP	**L**inear **P**olarization Filter
LPH	**L**inear **P**olarizer in **H**orizontal orientation
LPV	**L**inear **P**olarizer in **V**ertical orientation
LCVR	**L**iquid **C**rystal **V**ariable **R**etarder
LZW	**L**empel **Z**iv **W**elch
micro-CT	**Micro**n-scale synchrotron X-ray **C**omputed **T**omography
MR	**M**echanically rotatable **R**etarder
MRI	**M**agnetic **R**esonance **I**maging
NA	**N**umerical **A**perture
NEMA	**N**ational **E**lectrical **M**anufacturers **A**ssociation
OCT	**O**ptical **C**oherence **T**omography
PLA	**P**oly**L**actic **A**cid
PLI	**P**olarized **L**ight **I**maging
PSA	**P**olarization **S**tate **A**nalyzer
PSG	**P**olarization **S**tate **G**enerator
PS-OCT	**P**olarization **S**ensitive **O**ptical **C**oherence **T**omography
QWP	**Q**uarter **W**ave **P**late
RC	**R**ight-Handed **C**ircular
RGB	**R**ed **G**reen **B**lue colorspace
SDK	**S**oftware **D**evelopment **K**it
SNR	**S**ignal-to-**N**oise **R**atio
SLI	**S**cattered **L**ight **I**maging
SLIX	**S**cattered **L**ight **I**maging Toolbo**X**
SNR	**S**ignal to **N**oise **R**atio
STA	**S**tructure **T**ensor **A**nalysis
TEM	**T**ransmission **E**lectron **M**icroscopy
TIFF	**T**agged **I**mage **F**ile **F**ormat
TPFM	**T**wo-**P**hoton **F**luorescence **M**icroscopy
USAF	**U**nited **S**tates **A**ir **F**orce
USB	**U**niversal **S**erial **B**us
VR	**V**ariable **R**etarder

bg	**b**ack**g**round
cc	**c**orpus **c**allosum
cg	**c**in**g**ulum
cr	**c**orona **r**adiata
fx	**f**orni**x**
gp	**g**lobus **p**allidus
hc	**h**ippo**c**ampus
ic	**i**nternal **c**apsule
gm	**g**ray **m**atter
p	**p**ons
th	**th**alamus
wm	**w**hite **m**atter

List of Figures

List of Tables

Appendix A

Supplementary Calculations

A.1 Müller Matrices for Fibrous Brain Tissue

Section 2.2 introduced Müller matrix calculus for the complete polarimetric description of any given sample. In the following, fibrous brain tissue is modeled as a Müller matrix that takes into account the optical properties of white matter nerve fibers as established in Section 2.3. Starting with the model by ZHANG ET AL. [214] that includes the fiber direction and retardance (directly linked to the fiber inclination), the model is expanded to incorporate diattenuation and account for D^+/D^- tissue as found in Diattenuation Imaging, compare Section 3.3. Briefly, the inclusion of depolarization into the model is discussed.

A.1.1 Fiber Inclination and Direction

ZHANG ET AL. [214] modeled fibrous brain tissue with a retardance δ and a fiber direction ϕ as a Müller matrix of a retarder rotated around an azimuthal angle ϕ

$$M_{\text{tissue}} = R(\phi) \cdot M(\delta) \cdot R(-\phi) \tag{A.1}$$

$$= \begin{pmatrix} 1 & 0 & 0 & 0 \\ 0 & \cos(2\phi) & -\sin(2\phi) & 0 \\ 0 & \sin(2\phi) & \cos(2\phi) & 0 \\ 0 & 0 & 0 & 1 \end{pmatrix} \begin{pmatrix} 1 & 0 & 0 & 0 \\ 0 & 1 & 0 & 0 \\ 0 & 0 & \cos\delta & \sin\delta \\ 0 & 0 & -\sin\delta & \cos\delta \end{pmatrix} \begin{pmatrix} 1 & 0 & 0 & 0 \\ 0 & \cos(2\phi) & \sin(2\phi) & 0 \\ 0 & -\sin(2\phi) & \cos(2\phi) & 0 \\ 0 & 0 & 0 & 1 \end{pmatrix} \tag{A.2}$$

$$= \begin{pmatrix} 1 & 0 & 0 & 0 \\ 0 & \cos^2(2\phi) + \sin^2(2\phi)\cos\delta & \cos(2\phi)\sin(2\phi)(1-\cos\delta) & -\sin(2\phi)\sin\delta \\ 0 & \cos(2\phi)\sin(2\phi)(1-\cos\delta) & \sin^2(2\phi) + \cos^2(2\phi)\cos\delta & +\cos(2\phi)\sin\delta \\ 0 & +\sin(2\phi)\sin\delta & -\cos(2\phi)\sin\delta & \cos\delta \end{pmatrix} \tag{A.3}$$

$$= \begin{pmatrix} 1 & 0 & 0 & 0 \\ 0 & w_\phi^2 + v_\phi^2\cos\delta & w_\phi v_\phi(1-\cos\delta) & -v_\phi\sin\delta \\ 0 & w_\phi v_\phi(1-\cos\delta) & v_\phi^2 + w_\phi^2\cos\delta & +w_\phi\sin\delta \\ 0 & +v_\phi\sin\delta & -w_\phi\sin\delta & \cos\delta \end{pmatrix} \tag{A.4}$$

Here, the abbreviations $v_\phi = \sin(2\phi)$, $w_\phi = \cos(2\phi)$ are introduced. Diattenuation and depolarization are neglected.

A.1.2 Diattenuation

CHENAULT & CHIPMAN [39] defined a sample with principal intensity transmittances k_1 and k_2 (equivalent to T_{max}, T_{in} in Section 2.2) and a linear retardance δ. The axes of diattenuation and the fast and slow axes of retardance are coincident and align with

the x and y axes. This can be expressed by a Müller matrix

$$M(D_L,\delta) = \frac{1}{2}\begin{pmatrix} k_1+k_2 & k_1-k_2 & 0 & 0 \\ k_1-k_2 & k_1+k_2 & 0 & 0 \\ 0 & 0 & 2\sqrt{k_1k_2}\cos\delta & \sqrt{k_1k_2}\sin\delta \\ 0 & 0 & -2\sqrt{k_1k_2}\sin\delta & 2\sqrt{k_1k_2}\cos\delta \end{pmatrix} \tag{A.5}$$

$$= \tau\begin{pmatrix} 1 & D_L & 0 & 0 \\ D_L & 1 & 0 & 0 \\ 0 & 0 & \sqrt{1-D_L^2}\cos\delta & \sqrt{1-D_L^2}\sin\delta \\ 0 & 0 & -\sqrt{1-D_L^2}\sin\delta & \sqrt{1-D_L^2}\cos\delta \end{pmatrix} \tag{A.6}$$

with the (linear) diattenuation D_L and transmittance τ defined as

$$D_L = \frac{k_1-k_2}{k_1+k_2} \qquad \tau = \frac{1}{2}(k_1+k_2) \tag{A.7}$$

The meaning of Eq. (A.5) becomes apparent when $\delta = 0$ and $D_L = \pm 1$: Then, it represents a horizontal and a vertical linear polarization filter.

Fibrous brain tissue with a retardance δ, a linear diattenuation D_L, and a fiber direction ϕ can be modeled by rotating the Müller matrix $M(D_L,\delta)$ around an azimuthal angle ϕ

$$M_{\text{tissue}} = R(\phi)\cdot M(D_L,\delta)\cdot R(-\phi) \tag{A.8}$$

$$= \tau\begin{pmatrix} 1 & 0 & 0 & 0 \\ 1 & w_\phi & -v_\phi & 0 \\ 0 & v_\phi & w_\phi & 0 \\ 0 & 0 & 0 & 1 \end{pmatrix}\begin{pmatrix} 1 & D_L & 0 & 0 \\ D_L & 1 & 0 & 0 \\ 0 & 0 & \sqrt{1-D_L^2}\cos\delta & \sqrt{1-D_L^2}\sin\delta \\ 0 & 0 & -\sqrt{1-D_L^2}\sin\delta & \sqrt{1-D_L^2}\cos\delta \end{pmatrix}\begin{pmatrix} 1 & 0 & 0 & 0 \\ 0 & w_\phi & v_\phi & 0 \\ 0 & -v_\phi & w_\phi & 0 \\ 0 & 0 & 0 & 1 \end{pmatrix} \tag{A.9}$$

$$= \tau\begin{pmatrix} 1 & D_Lw_\phi & D_Lv_\phi & 0 \\ D_Lw_\phi & w_\phi^2+\sqrt{1-D_L^2}\cos\delta v_\phi^2 & w_\phi v_\phi(1-\sqrt{1-D_L^2}\cos\delta) & -\sqrt{1-D_L^2}\sin\delta v_\phi \\ D_Lv_\phi & w_\phi v_\phi(1-\sqrt{1-D_L^2}\cos\delta) & v_\phi^2+\sqrt{1-D_L^2}\cos\delta w_\phi^2 & \sqrt{1-D_L^2}\sin\delta w_\phi \\ 0 & \sqrt{1-D_L^2}\sin\delta v_\phi & \sqrt{1-D_L^2}\sin\delta w_\phi & \sqrt{1-D_L^2}\cos\delta \end{pmatrix} \tag{A.10}$$

Here, the abbreviations $v_\phi = \sin(2\phi)$, $w_\phi = \cos(2\phi)$ are used.

When $D_L > 0$, i.e. $k_1 > k_2$, the axis of the larger intensity k_1 aligns with the fast axis of retardance and the matrix describes D^+ tissue as defined in context of Diattenuation Imaging s. Section3.3. When $D_L < 0$, i.e. $k_1 < k_2$, the axis of the smaller intensity k_1 aligns with the fast axis of retardance, causing the axis of the larger intensity k_2 to be shifted by 90° in relation to the fast axis of retardance. Then, the matrix describes D^- tissue.

A.1.3 Depolarization

While both diattenuation and retardance in fibrous brain tissue arise from the uniaxial anisotropy of axons, depolarization results from multiple scattering events, as discussed in Section 2.3. Consequently, the principal axes of the Müller matrix for depolarization do not necessarily align with those for diattenuation and retardance in fibrous brain tissue. However, retardance, diattenuation, and depolarization are included in the Lu-Chipman decomposition presented in Section 2.2, irrespective of any anatomical assumptions about the principal axes.

A.2 Müller Calculus for a Non-Ideal Müller Polarimeter

Ideal and non-ideal Müller polarimeters can be modeled using Müller matrix calculus. In the following, the impact of non-ideal optical properties (usually arising from the non-ideal optical components) within the polarization state generator (PSG) and/or the polarization state analyzer (PSA) in a non-ideal Müller polarimeter is mathematically described. The Müller polarimeter is composed of four variable retarders and two linear polarization filters, oriented in the same manner as in the Scattering Polarimeter discussed in Chapter 4.

A.2.1 Stokes Vector of the Ideal Polarization State Generator (PSG)

With the matrices for an ideal retarder from Table 2.2 at azimuthal angles θ and the Stokes vector of horizontal linear polarization $\vec{S}_H$, the Stokes vector $\vec{S}_{\text{PSG}}$ for the ideal polarization state generator (PSG) is given by

$$\vec{S}_{\text{PSG}} = M(\delta_2, \theta = 0^\circ) \cdot M(\delta_1, \theta = 45^\circ) \cdot \vec{S}_H \tag{A.11}$$

$$= \begin{pmatrix} 1 & 0 & 0 & 0 \\ 0 & 1 & 0 & 0 \\ 0 & 0 & \cos\delta_2 & \sin\delta_2 \\ 0 & 0 & -\sin\delta_2 & \cos\delta_2 \end{pmatrix} \begin{pmatrix} 1 & 0 & 0 & 0 \\ 0 & \cos\delta_1 & 0 & -\sin\delta_1 \\ 0 & 0 & 1 & 0 \\ 0 & \sin\delta_1 & 0 & \cos\delta_1 \end{pmatrix} \begin{pmatrix} 1 \\ 1 \\ 0 \\ 0 \end{pmatrix} \tag{A.12}$$

$$= \begin{pmatrix} 1 & 0 & 0 & 0 \\ 0 & 1 & 0 & 0 \\ 0 & 0 & \cos\delta_2 & \sin\delta_2 \\ 0 & 0 & -\sin\delta_2 & \cos\delta_2 \end{pmatrix} \begin{pmatrix} 1 \\ \cos\delta_1 \\ 0 \\ \sin\delta_1 \end{pmatrix} \tag{A.13}$$

$$= \begin{pmatrix} 1 \\ \cos\delta_1 \\ \sin\delta_1 \sin\delta_2 \\ \sin\delta_1 \cos\delta_2 \end{pmatrix} \tag{A.14}$$

$$\overset{\delta_2 = +\frac{\pi}{2}}{=} \begin{pmatrix} 1 \\ \cos\delta_1 \\ \sin\delta_1 \\ 0 \end{pmatrix} \tag{A.15}$$

with δ_1 the retardance of LCVR 1 and δ_2 the retardance of LCVR 2. When LCVR 2 is set to a retardance of $\delta_2 = +\pi/2$ for 3D-PLI measurements, the generated polarization is linear and its polarization angle spins counter-clockwise with increasing δ_1 around the plane of the Poincaré sphere from Section 2.2.

A.2.2 Stokes Vector of the Non-Ideal Polarization State Generator (PSG)

A non-ideal PSG can deviate from the ideal values for δ_1 and δ_2, usually because of a minor voltage offset for LCVR 1 and LCVR 2. While a deviation from δ_1 only results in a global phase shift, a deviation for δ_2 causes elliptical polarization that propagates through the whole system. In Müller polarimetry, the Eigenvalue Calibration Method (ECM) corrects these errors. However, the results of the ECM cannot be applied to the 3D-PLI signal, as demonstrated in Appendix A.5. For 3D-PLI and Diattenuation Imaging (DI), ellipticities can distort results.

When $(\delta_2 - \pi/2) = h_2 \approx 0$, a TAYLOR [186] approximation to the 1st order with

$$\cos(\delta_2 \approx \frac{\pi}{2}) = -(\delta_2 - \frac{\pi}{2}) + ... \approx -h_2 \tag{A.16}$$

$$\sin(\delta_2 \approx \frac{\pi}{2}) = 1 - ... \approx 1 \tag{A.17}$$

describes the Stokes vector $\vec{S}_{\text{real}}$ as a sum of the ideal vector $\vec{S}_{\text{PSG}}$ and a deviation $\vec{S}_{h2}$

$$\vec{S}_{\text{real}} = \begin{pmatrix} 1 \\ \cos\delta_1 \\ \sin\delta_1 \sin\delta_2 \\ \sin\delta_1 \cos\delta_2 \end{pmatrix} \approx \begin{pmatrix} 1 \\ \cos\delta_1 \\ \sin\delta_1 \\ 0 \end{pmatrix} - \begin{pmatrix} 0 \\ 0 \\ 0 \\ h_2 \sin\delta_1 \end{pmatrix} = \vec{S}_{\text{PSG}} + \vec{S}_{h2} \tag{A.18}$$

A.2.3 Müller Matrix of the Ideal Polarization State Analzyer (PSA)

With the matrices for an ideal retarder and horizontal linear polarization filter from Table 2.2 at azimuthal angles θ, the ideal PSA can be described by

$$M_{\text{PSA}} = M_{\text{LP}}(\theta = 0^\circ) \cdot M(\delta_4, \theta = 45^\circ) \cdot M(\delta_3, \theta = 0^\circ) \tag{A.19}$$

$$= \frac{1}{2} \begin{pmatrix} 1 & 1 & 0 & 0 \\ 1 & 1 & 0 & 0 \\ 0 & 0 & 0 & 0 \\ 0 & 0 & 0 & 0 \end{pmatrix} \begin{pmatrix} 1 & 0 & 0 & 0 \\ 0 & \cos\delta_4 & 0 & -\sin\delta_4 \\ 0 & 0 & 1 & 0 \\ 0 & \sin\delta_4 & 0 & \cos\delta_4 \end{pmatrix} \begin{pmatrix} 1 & 0 & 0 & 0 \\ 0 & 1 & 0 & 0 \\ 0 & 0 & \cos\delta_3 & \sin\delta_3 \\ 0 & 0 & -\sin\delta_3 & \cos\delta_3 \end{pmatrix} \tag{A.20}$$

$$= \frac{1}{2} \begin{pmatrix} 1 & \cos\delta_4 & \sin\delta_4 \sin\delta_3 & -\sin\delta_4 \cos\delta_3 \\ 1 & \cos\delta_4 & \sin\delta_4 \sin\delta_3 & -\sin\delta_4 \cos\delta_3 \\ 0 & 0 & 0 & 0 \\ 0 & 0 & 0 & 0 \end{pmatrix} \tag{A.21}$$

$$\overset{\substack{\delta_3=0 \\ \delta_4=\pm\frac{\pi}{2}}}{=} \frac{1}{2} \begin{pmatrix} 1 & 0 & 0 & \mp 1 \\ 1 & 0 & 0 & \mp 1 \\ 0 & 0 & 0 & 0 \\ 0 & 0 & 0 & 0 \end{pmatrix} \tag{A.22}$$

with $\delta_3 = 0$ and $\delta_4 = \pm\pi/2$ when analyzing either right- or left-circular polarization in 3D-PLI.

A.2.4 Müller Matrix of the Non-Ideal Polarization State Analzyer (PSA)

A non-ideal PSA can deviate from the ideal values for δ_3 and δ_4, usually because of a minor voltage offset for LCVR 3 and LCVR 4, respectively. In Müller polarimetry, the Eigenvalue Calibration Method corrects these errors. However, ellipticities can distort results in 3D-PLI and DI. When $(\delta_4 - \pi/2) = h_4$ and $(\delta_3 - \pi/2) = h_3$, a Taylor approximation to the 1st order with

$$\cos(\delta_4 \approx \pm\frac{\pi}{2}) = \mp(\delta_4 - \frac{\pi}{2}) + ... \approx \mp h_4 \tag{A.23}$$

$$\sin(\delta_4 \approx \pm\frac{\pi}{2}) = \pm 1 - ... \approx \pm 1 \tag{A.24}$$

$$\cos(\delta_3 \approx 0) = 1 - ... \approx 1 \tag{A.25}$$

$$\sin(\delta_3 \approx 0) = (\delta_3 - 0) - ... \approx h_3 \tag{A.26}$$

describes the whole Müller matrix for the PSA M_{real} as a sum of two matrices, one for the ideal matrix M_{PSA} and a deviation $M_{h3,h4}$

$$M_{\text{real}} = M_{\text{LP}}(\theta = 0^\circ) \cdot M(\delta_4, \theta = 45^\circ) \cdot M(\delta_3, \theta = 0^\circ) \tag{A.27}$$

$$= \frac{1}{2} \begin{pmatrix} 1 & \cos\delta_4 & \sin\delta_4 \sin\delta_3 & -\sin\delta_4 \cos\delta_3 \\ 1 & \cos\delta_4 & \sin\delta_4 \sin\delta_3 & -\sin\delta_4 \cos\delta_3 \\ 0 & 0 & 0 & 0 \\ 0 & 0 & 0 & 0 \end{pmatrix} \tag{A.28}$$

$$\approx \frac{1}{2} \begin{pmatrix} 1 & 0 & 0 & \mp 1 \\ 1 & 0 & 0 & \mp 1 \\ 0 & 0 & 0 & 0 \\ 0 & 0 & 0 & 0 \end{pmatrix} + \frac{1}{2} \begin{pmatrix} 0 & \mp h_4 & \pm h_3 & 0 \\ 0 & \mp h_4 & \pm h_3 & 0 \\ 0 & 0 & 0 & 0 \\ 0 & 0 & 0 & 0 \end{pmatrix} \tag{A.29}$$

$$= M_{\text{PSA}} + M_{h3,h4} \tag{A.30}$$

It is important to note that h_4 is not necessarily equal for $\delta_4 \approx \pi/2$ and $\delta_4 \approx -\pi/2$, i.e. can be different for right- and left-circular polarization because different voltage

settings are applied to LCVR 4. However, h_3 remains equal because the setting for LCVR 3 $\delta_3 \approx 0$ is kept for both cases.

A.3 Müller Matrix Calculus for 3D-PLI

In the following, the error propagation in 3D-PLI caused by non-ideal optical elements in a Müller polarimeter is calculated, based on Müller calculus and Taylor approximations of the first order. The Müller polarimeter is composed of four variable retarders and two linear polarization filters, oriented in the same way as in the Scattering Polarimeter discussed in Chapter 4. The mathematical results aid in identifying the sources of non-ideal behavior encountered in Section 5.2.

A.3.1 Ideal Three-Dimensional Polarized Light Imaging

The Müller matrix for brain tissue Eq. (A.1), the ideal Müller matrix of the PSA M_{PSA} and the ideal Stokes vector of the PSG $\vec{S}_{\mathrm{PSG}}$ can be applied to calculate the Stokes vector $\vec{S}_{\mathrm{PLI}}$ for 3D-PLI which directly corresponds to the measured intensity.

In 3D-PLI, δ_1 is variable, $\delta_2 = \pi/2$, $\delta_3 = 0$ and $\delta_4 = \pm\pi/2$.

$$\vec{S}_{\mathrm{PLI}} = M_{\mathrm{PSA}} \cdot M_{\mathrm{tissue}} \cdot \vec{S}_{\mathrm{PSG}} \tag{A.31}$$

$$= M_{\mathrm{PSA}} \begin{pmatrix} 1 & 0 & 0 & 0 \\ 0 & \cos^2(2\phi) + \sin^2(2\phi)\cos\delta & \cos(2\phi)\sin(2\phi)(1-\cos\delta) & -\sin(2\phi)\sin\delta \\ 0 & \cos(2\phi)\sin(2\phi)(1-\cos\delta) & \sin^2(2\phi) + \cos^2(2\phi)\cos\delta & +\cos(2\phi)\sin\delta \\ 0 & +\sin(2\phi)\sin\delta & -\cos(2\phi)\sin\delta & \cos\delta \end{pmatrix} \begin{pmatrix} 1 \\ \cos(\delta_1) \\ \sin(\delta_1) \\ 0 \end{pmatrix} \tag{A.32}$$

$$= \frac{1}{2} \begin{pmatrix} 1 & 0 & 0 & \mp 1 \\ 1 & 0 & 0 & \mp 1 \\ 0 & 0 & 0 & 0 \\ 0 & 0 & 0 & 0 \end{pmatrix} \begin{pmatrix} 1 \\ \cos\delta_1\cos^2(2\phi) + \sin^2(2\phi)\cos\delta + \cos(2\phi)\sin(2\phi)i(1-\cos\delta)\sin\delta_1 \\ \cos(2\phi)\sin(2\phi)(1-\cos\delta)\cos\delta_1 + \sin^2(2\phi) + \cos^2(2\phi)\cos\delta\sin\delta_1 \\ +\sin(2\phi)\sin\delta\cos\delta_1 - \cos(2\phi)\sin\delta\sin\delta_1 \end{pmatrix} \tag{A.33}$$

$$= \frac{1}{2} \begin{pmatrix} 1 \pm \sin\delta\sin(\delta_1 - 2\phi) \\ 1 \pm \sin\delta\sin(\delta_1 - 2\phi) \\ 0 \\ 0 \end{pmatrix} \tag{A.34}$$

The first element of the Stokes vector $\vec{S}_{\mathrm{PLI}}$ is directly equivalent to the intensity curve introduced in Section 3.2 but with $\delta_1 \hat{=} 2\rho$

$$I_{\mathrm{PLI}} = \frac{1}{2}\left(1 \pm \sin\delta\sin(\delta_1 - 2\phi)\right) \tag{A.35}$$

A.3.2 3D-PLI Signal with Non-Ideal LCVR 2

With the Taylor approximation in Eq. (A.18) and the abbreviations $v_\phi = \sin(2\phi)$, $w_\phi = \cos(2\phi)$, the non-ideal Stokes vector $\vec{S}_{\mathrm{PLI}'}$ for a non-ideal PSG and an ideal PSA

can be calculated as

$$\vec{S}_{\mathrm{PLI}'} = M_{\mathrm{PSA}} \cdot M_{\mathrm{tissue}} \cdot (\vec{S}_{PSG} + \vec{S}_{h2}) \tag{A.36}$$

$$= \vec{S}_{\mathrm{PLI}} + M_{\mathrm{PSA}} M_{\mathrm{tissue}} \vec{S}_{h_2} \tag{A.37}$$

$$= \vec{S}_{\mathrm{PLI}} - \frac{1}{2} \begin{pmatrix} 1 & 0 & 0 & \mp 1 \\ 1 & 0 & 0 & \mp 1 \\ 0 & 0 & 0 & 0 \\ 0 & 0 & 0 & 0 \end{pmatrix} \begin{pmatrix} 1 & 0 & 0 & 0 \\ 0 & w_\phi^2 + v_\phi^2 \cos\delta & w_\phi v_\phi (1-\cos\delta) & -v_\phi \sin\delta \\ 0 & w_\phi v_\phi (1-\cos\delta) & v_\phi^2 + w_\phi^2 \cos\delta & +w_\phi \sin\delta \\ 0 & v_\phi \sin\delta & -w_\phi \sin\delta & \cos\delta \end{pmatrix} \begin{pmatrix} 0 \\ 0 \\ 0 \\ h_2 \sin(\delta_1) \end{pmatrix} \tag{A.38}$$

$$= \frac{1}{2} \left[\begin{pmatrix} 1 \pm \sin\delta \sin(\delta_1 - 2\phi) \\ 1 \pm \sin\delta \sin(\delta_1 - 2\phi) \\ 0 \\ 0 \end{pmatrix} \pm \begin{pmatrix} h_2 \cos\delta \sin\delta_1 \\ h_2 \cos\delta \sin\delta_1 \\ 0 \\ 0 \end{pmatrix} \right] \tag{A.39}$$

$$= \vec{S}_{\mathrm{PLI}} + \vec{S}_{LCVR2}(\delta, \delta_1) \tag{A.40}$$

The ideal 3D-PLI intensity curve in Eq. (A.35) is now modulated by a function with an amplitude h_2 that depends on the fiber retardance δ, the retardance δ_1 of LCVR 1 but not the fiber direction ϕ

$$I_{\mathrm{PLI}'} = \frac{1}{2} \left(1 \pm \sin\delta \sin(\delta_1 - 2\phi)\right) \pm \frac{h_2}{2} \cos\delta \sin(\delta_1) \tag{A.41}$$

A.3.3 3D-PLI Signal with Non-Ideal LCVR 3 and LCVR 4

Using the Taylor approximation in Eq. (A.27) and the abbreviations $v_\phi = \sin(2\phi)$, $w_\phi = \cos(2\phi)$, the non-ideal Stokes vector $\vec{S}_{\mathrm{PLI}'}$ for an ideal PSG and a non-ideal PSA can be calculated as

$$\vec{S}_{\mathrm{PLI}'} = (M_{\mathrm{PSA}} + M_{h3,h4}) \cdot M_{\mathrm{tissue}} \cdot \vec{S}_{\mathrm{PSG}} \tag{A.42}$$

$$= \vec{S}_{\mathrm{PLI}} + M_{h3,h4} \cdot M_{\mathrm{tissue}} \cdot \vec{S}_{\mathrm{PSG}} \tag{A.43}$$

$$= \vec{S}_{\mathrm{PLI}} + \frac{1}{2} \begin{pmatrix} 0 & \mp h_4 & \pm h_3 & 0 \\ 0 & \mp h_4 & \pm h_3 & 0 \\ 0 & 0 & 0 & 0 \\ 0 & 0 & 0 & 0 \end{pmatrix} \begin{pmatrix} 1 \\ \cos\delta_1 w_\phi^2 + v_\phi^2 \cos\delta + w_\phi v_\phi (1-\cos\delta) \sin\delta_1 \\ w_\phi v_\phi (1-\cos\delta) \cos(\delta_1) + v_\phi^2 + w_\phi^2 \cos\delta \sin\delta_1 \\ v_\phi \sin\delta \cos\delta_1 - w_\phi \sin\delta \sin\delta_1 \end{pmatrix} \tag{A.44}$$

$$= \vec{S}_{\mathrm{PLI}} \mp \frac{h_4}{2} \begin{pmatrix} \cos\delta_1 w_\phi^2 + v_\phi^2 \cos\delta + w_\phi v_\phi (1-\cos\delta) \sin\delta_1 \\ \cos\delta_1 w_\phi^2 + v_\phi^2 \cos\delta + w_\phi v_\phi (1-\cos\delta) \sin\delta_1 \\ 0 \\ 0 \end{pmatrix} \tag{A.45}$$

$$\pm \frac{h_3}{2} \begin{pmatrix} w_\phi v_\phi (1-\cos\delta) \cos\delta_1 + v_\phi^2 + w_\phi^2 \cos\delta \sin\delta_1 \\ w_\phi v_\phi (1-\cos\delta) \cos\delta_1 + v_\phi^2 + w_\phi^2 \cos\delta \sin\delta_1 \\ 0 \\ 0 \end{pmatrix} \tag{A.46}$$

$$= \vec{S}_{\mathrm{PLI}} + \vec{S}_{LCVR3}(\phi, \delta, \delta_1) + \vec{S}_{LCVR4}(\phi, \delta, \delta_1) \tag{A.47}$$

The ideal 3D-PLI intensity curve in Eq. (A.35) is now modulated by two functions with amplitudes h_3 and h_4 that depend on the fiber retardance δ, the retardance of LCVR 1 δ_1, and fiber direction ϕ

$$I_{\mathrm{PLI}'} = \frac{1}{2} \left(1 \pm \sin\delta \sin(\delta_1 - 2\phi)\right) \tag{A.48}$$

$$\mp \frac{h_4}{2} \left(\cos\delta_1 w_\phi^2 + v_\phi^2 \cos\delta + w_\phi v_\phi (1-\cos\delta) \sin\delta_1 \right) \tag{A.49}$$

$$\pm \frac{h_3}{2} \left(w_\phi v_\phi (1-\cos\delta) \cos\delta_1 + v_\phi^2 + w_\phi^2 \cos\delta \sin\delta_1 \right) \tag{A.50}$$

With $v_\phi^2 = \sin^2(2\phi) = \frac{1}{2}(1 - \cos 4\phi)$ and $w_\phi^2 = \cos^2(2\phi) = \frac{1}{2}(1 + \cos 4\phi)$, a higher-order frequency is introduced into the signal that depends on the fiber direction.

A.3.4 3D-PLI Signal with Non-Ideal LCVR 2 - 4

The transmitted Stokes vector $\vec{S}_{\mathrm{PSA}'}$ for a non-ideal PSG and a non-ideal PSA can be calculated

$$\vec{S}_{\mathrm{out}} = (M_{\mathrm{PSA}} + M_{h3,h4}) \cdot M_{\mathrm{tissue}} \cdot (\vec{S}_{\mathrm{PSG}} + \vec{S}_{h2}) \tag{A.51}$$

$$= \vec{S}_{\mathrm{PLI}} + \vec{S}_{LCVR2} + \vec{S}_{LCVR3} + \vec{S}_{LCVR4} + M_{h3,h4} \cdot M_{\mathrm{tissue}} \cdot \vec{S}_{h2} \tag{A.52}$$

which is the sum of previous results and a higher-order term. However, the multiplication of the very small factors h_2, h_3 and h_4 can be neglected.

A.4 Müller Matrix Calculus for DI

In the following, the error propagation in Diattenuation Imaging (DI) caused by non-ideal optical elements in a Müller polarimeter is calculated, based on Müller calculus and Taylor approximations of the first order. The Müller polarimeter is composed of four variable retarders and two linear polarization filters, oriented in the same way as in the Scattering Polarimeter discussed in Chapter 4. The mathematical results aid in identifying the sources of non-ideal behavior encountered in Section 5.3.

A.4.1 Ideal Diattenuation Imaging

The Müller matrix for retarding and diattenuating brain tissue Eq. (A.5), and the ideal Stokes vector of the PSG $\vec{S}_{\mathrm{PSG}}$ can be applied to calculate the Stokes vector $\vec{S}_{\mathrm{DI}}$ for Diattenuation Imaging under the assumption that the PSA is removed from the Scattering Polarimeter, thereby modeling a measurement, e.g. with the Large-Area Polarimeter s. Section 3.6). The first element of $\vec{S}_{\mathrm{DI}}$ directly corresponds to the measured intensity.

During the measurement, δ_1 is variable, $\delta_2 = \pi/2$, $\delta_3 = 0$ and $\delta_4 = \pm\pi/2$. In the following, the abbreviations $v_\phi = \sin(2\phi)$, $w_\phi = \cos(2\phi)$ are used

$$S_{\mathrm{DI}} = M_{\mathrm{tissue}} S_{\mathrm{PSG}} \tag{A.53}$$

$$= \begin{pmatrix} 1 & w_\phi D_L & v_\phi D_L & 0 \\ w_\phi D_L & w_\phi^2 + \sqrt{1-D_L^2}\cos\delta v_\phi^2 & w_\phi v_\phi(1-\sqrt{1-D_L^2}\cos\delta) & -v_\phi\sqrt{1-D_L^2}\sin\delta \\ v_\phi D_L & w_\phi v_\phi(1-\sqrt{1-D_L^2}\cos\delta) & v_\phi^2 + \sqrt{1-D_L^2}\cos\delta w_\phi^2 & w_\phi\sqrt{1-D_L^2}\sin\delta \\ 0 & v_\phi\sqrt{1-D_L^2}\sin\delta & w_\phi\sqrt{1-D_L^2}\sin\delta & \sqrt{1-D_L^2}\cos\delta \end{pmatrix} \begin{pmatrix} 1 \\ \cos\delta_1 \\ \sin\delta_1 \\ 0 \end{pmatrix} \tag{A.54}$$

$$= \begin{pmatrix} 1 + w_\phi D_L \cos\delta_1 + v_\phi D_L \sin\delta_1 \\ w_\phi D_L + (w_\phi^2 + \sqrt{1-D_L^2}\cos\delta v_\phi^2)\cos\delta_1 + w_\phi v_\phi(1-\sqrt{1-D_L^2}\cos\delta)\sin\delta_1 \\ v_\phi D_L + (w_\phi^2 + \sqrt{1-D_L^2}\cos\delta v_\phi^2)\sin\delta_1 + w_\phi v_\phi(1-\sqrt{1-D_L^2}\cos\delta)\cos\delta_1 \\ v_\phi\sqrt{1-D_L^2}\sin\delta\cos\delta_1 + w_\phi\sqrt{1-D_L^2}\sin\delta\sin\delta_1 \end{pmatrix} \tag{A.55}$$

$$= \begin{pmatrix} 1 + D_L\cos(\delta_1 - 2\phi) \\ w_\phi D_L + (w_\phi^2 + \sqrt{1-D_L^2}\cos\delta v_\phi^2)\cos\delta_1 + w_\phi v_\phi(1-\sqrt{1-D_L^2}\cos\delta)\sin\delta_1 \\ v_\phi D_L + (w_\phi^2 + \sqrt{1-D_L^2}\cos\delta v_\phi^2)\sin\delta_1 + w_\phi v_\phi(1-\sqrt{1-D_L^2}\cos\delta)\cos\delta_1 \\ v_\phi\sqrt{1-D_L^2}\sin\delta\cos\delta_1 + w_\phi\sqrt{1-D_L^2}\sin\delta\sin\delta_1 \end{pmatrix} \tag{A.56}$$

The first element of the Stokes vector $\vec{S}_{\mathrm{DI}}$ is directly equivalent to the measured intensity curve introduced in Section 3.3 with $\delta_1 \hat{=} 2\rho$

$$I_{\mathrm{DI}} = 1 + D_L\cos(\delta_1 - 2\phi) \tag{A.57}$$

A.4.2 Ideal DI with the Scattering Polarimeter

The Müller matrix for retarding and diattenuating brain tissue Eq. (A.5), the ideal Müller matrix of the PSA, M_{PSA}, and the ideal Stokes vector of the PSG, $\vec{S}_{\mathrm{PSG}}$, can be applied to calculate the Stokes vector $\vec{S}_{\mathrm{PLI},\pm}$ for both 3D-PLI measurements that are added up to $\vec{S}_{\mathrm{DI}}$ during Diattenuation Imaging with the Scattering Polarimeter. that directly corresponds to the measured intensity.

During the measurement, δ_1 is variable, $\delta_2 = \pi/2$, $\delta_3 = 0$ and $\delta_4 = \pm\pi/2$

$$\vec{S}_{\mathrm{PLI},\pm} = M_{\mathrm{PSA}} \cdot M_{\mathrm{tissue}} \cdot S_{\mathrm{PSG}} \tag{A.58}$$

$$= M_{\mathrm{PSA}} \begin{pmatrix} 1 & w_\phi D_L & v_\phi D_L & 0 \\ w_\phi D_L & w_\phi^2 + \sqrt{1-D_L^2}\cos\delta v_\phi^2 & w_\phi v_\phi(1-\sqrt{1-D_L^2}\cos\delta) & -v_\phi\sqrt{1-D_L^2}\sin\delta \\ v_\phi D_L & w_\phi v_\phi(1-\sqrt{1-D_L^2}\cos\delta) & v_\phi^2 + \sqrt{1-D_L^2}\cos\delta w_\phi^2 & w_\phi\sqrt{1-D_L^2}\sin\delta \\ 0 & v_\phi\sqrt{1-D_L^2}\sin\delta & w_\phi\sqrt{1-D_L^2}\sin\delta & \sqrt{1-D_L^2}\cos\delta \end{pmatrix} \begin{pmatrix} 1 \\ \cos\delta_1 \\ \sin\delta_1 \\ 0 \end{pmatrix} \tag{A.59}$$

$$= M_{\mathrm{PSA}} \begin{pmatrix} 1 + w_\phi D_L\cos\delta_1 + v_\phi D_L \sin\delta_1 \\ w_\phi D_L + (w_\phi^2 + \sqrt{1-D_L^2}\cos\delta v_\phi^2)\cos\delta_1 + w_\phi v_\phi(1-\sqrt{1-D_L^2}\cos\delta)\sin\delta_1 \\ v_\phi D_L + (w_\phi^2 + \sqrt{1-D_L^2}\cos\delta v_\phi^2)\sin\delta_1 + w_\phi v_\phi(1-\sqrt{1-D_L^2}\cos\delta)\cos\delta_1 \\ v_\phi\sqrt{1-D_L^2}\sin\delta\cos\delta_1 + w_\phi\sqrt{1-D_L^2}\sin\delta\sin\delta_1 \end{pmatrix} \tag{A.60}$$

$$= \frac{1}{2}\begin{pmatrix} 1 & 0 & 0 & \mp 1 \\ 1 & 0 & 0 & \mp 1 \\ 0 & 0 & 0 & 0 \\ 0 & 0 & 0 & 0 \end{pmatrix} \begin{pmatrix} 1 + D_L\cos(\delta_1 - 2\phi) \mp (v_\phi\sqrt{1-D_L^2}\sin\delta\cos\delta_1 + w_\phi\sqrt{1-D_L^2}\sin\delta\sin\delta_1) \\ 1 + D_L\cos(\delta_1 - 2\phi) \mp (v_\phi\sqrt{1-D_L^2}\sin\delta\cos\delta_1 + w_\phi\sqrt{1-D_L^2}\sin\delta\sin\delta_1) \\ 0 \\ 0 \end{pmatrix} \tag{A.61}$$

$$= \frac{1}{2}\begin{pmatrix} 1 + D_L\cos(\delta_1 - 2\phi) \mp \sqrt{1-D_L^2}\sin\delta\sin(\delta_1 + 2\phi) \\ 1 + D_L\cos(\delta_1 - 2\phi) \mp \sqrt{1-D_L^2}\sin\delta\sin(\delta_1 + 2\phi) \\ 0 \\ 0 \end{pmatrix} \tag{A.62}$$

with M_{tissue} the ideal case from above including diattenuation. When adding up, the last term cancels out

$$I_{\mathrm{DI}} = I_{\mathrm{PLI},+} + I_{\mathrm{PLI},-} = 1 + D_L\cos(\delta_1 - 2\phi) \tag{A.63}$$

The resulting equation directly corresponds to Eq. (A.57).

A.4.3 DI Signal with Non-Ideal LCVR 2

With the Taylor approximation in Eq. (A.18) and the abbreviations $v_\phi = \sin(2\phi)$, $w_\phi = \cos(2\phi)$, the non-ideal Stokes vector $\vec{S}_{\mathrm{PLI}',\pm}$ for a non-ideal PSG and an ideal PSA can be calculated for diattenuating retarding brain tissue as

$$\vec{S}_{\mathrm{PLI}',\pm} = M_{\mathrm{PSA}} \cdot M_{\mathrm{tissue}} \cdot (\vec{S}_{\mathrm{PSG}} + \vec{S}_{h2}) \tag{A.64}$$

$$= \vec{S}_{\mathrm{PLI},\pm} + M_{\mathrm{PSA}} \cdot M_{\mathrm{tissue}} \cdot \vec{S}_{h2} \tag{A.65}$$

$$= \vec{S}_{\mathrm{PLI},\pm} - M_{\mathrm{PSA}} \cdot M_{\mathrm{tissue}} \cdot \begin{pmatrix} 0 \\ 0 \\ 0 \\ h_2\sin(\delta_1) \end{pmatrix} \tag{A.66}$$

$$= \frac{1}{2}\begin{pmatrix} 1 + D\cos(\delta_1 - 2\phi) \mp \sqrt{1-D_L^2}\sin\delta\sin(\delta_1 + 2\phi) \\ 1 + D\cos(\delta_1 - 2\phi) \mp \sqrt{1-D_L^2}\sin\delta\sin(\delta_1 + 2\phi) \\ 0 \\ 0 \end{pmatrix} \pm \frac{1}{2}\begin{pmatrix} h_2\sqrt{1-D_L^2}\cos\delta\sin(\delta_1) \\ h_2\sqrt{1-D_L^2}\cos\delta\sin(\delta_1) \\ 0 \\ 0 \end{pmatrix} \tag{A.67}$$

$$= \vec{S}_{\mathrm{PLI},\pm} \pm \vec{S}_{LCVR2} \tag{A.68}$$

However, the offset $\vec{S}_{LCVR2}$ caused by the non-ideal LCVR 2 cancels out when the two 3D-PLI signals are added up

$$I_{\mathrm{DI}'} = I_{\mathrm{PLI}',+} + I_{\mathrm{PLI}',-} = 1 + D_L \cos(\delta_1 - 2\phi) = I_{\mathrm{DI}} \tag{A.69}$$

Hence, the diattenuation signal is not influenced by deviations of LCVR 2.

A.4.4 DI Signal with Non-Ideal LCVR 3 and LCVR 4

Using the Taylor approximation in Eq. (A.27) and the abbreviations $v_\phi = \sin(2\phi)$, $w_\phi = \cos(2\phi)$, the non-ideal Stokes vector $\vec{S}_{\mathrm{PLI}',\pm}$ for an ideal PSG and a non-ideal PSA can be calculated as

$$\vec{S}_{\mathrm{PLI}',\pm} = (M_{\mathrm{PSA}} + M_{h3,h4}) \cdot M_{\mathrm{tissue}} \cdot \vec{S}_{\mathrm{PSG}} \tag{A.70}$$

$$= \vec{S}_{\mathrm{PLI},\pm} + M_{h3,h4} \cdot M_{\mathrm{tissue}} \cdot \vec{S}_{\mathrm{PSG}} \tag{A.71}$$

$$= \vec{S}_{\mathrm{PLI},\pm} + \frac{1}{2} \begin{pmatrix} 0 & \mp h_4 & \pm h_3 & 0 \\ 0 & \mp h_4 & \pm h_3 & 0 \\ 0 & 0 & 0 & 0 \\ 0 & 0 & 0 & 0 \end{pmatrix} \begin{pmatrix} 1 + D\cos(\delta_1 - 2\phi) \mp \sqrt{1 - D_L^2}\sin(\delta)\sin(\delta_1 + 2\phi) \\ 1 + D\cos(\delta_1 - 2\phi) \mp \sqrt{1 - D_L^2}\sin(\delta)\sin(\delta_1 + 2\phi) \\ 0 \\ 0 \end{pmatrix} \tag{A.72}$$

$$= \vec{S}_{\mathrm{PLI},\pm} \mp \frac{h_4}{2} \begin{pmatrix} 1 + D\cos(\delta_1 - 2\phi) \mp \sqrt{1 - D_L^2}\sin(\delta)\sin(\delta_1 + 2\phi) \\ 1 + D\cos(\delta_1 - 2\phi) \mp \sqrt{1 - D_L^2}\sin(\delta)\sin(\delta_1 + 2\phi) \\ 0 \\ 0 \end{pmatrix} \tag{A.73}$$

$$\pm \frac{h_3}{2} \begin{pmatrix} 1 + D\cos(\delta_1 - 2\phi) \mp \sqrt{1 - D_L^2}\sin(\delta)\sin(\delta_1 + 2\phi) \\ 1 + D\cos(\delta_1 - 2\phi) \mp \sqrt{1 - D_L^2}\sin(\delta)\sin(\delta_1 + 2\phi) \\ 0 \\ 0 \end{pmatrix} \tag{A.74}$$

$$= \vec{S}_{\mathrm{PLI},\pm} + \vec{S}_{LCVR3}(\phi, \delta, \delta_1) + \vec{S}_{LCVR4}(\phi, \delta, \delta_1) \tag{A.75}$$

It is important to note that h_4 is not necessarily equal for $\vec{S}_{\mathrm{PLI},+}$ and $\vec{S}_{\mathrm{PLI},-}$ because different voltage settings are applied to LCVR 4. However, h_3 remains equal because the voltage setting for LCVR 3 $\delta_3 \approx 0$ is kept for both cases. Therefore, not every term cancels out when adding up the intensities

$$I_{DI'} = I_{\mathrm{PLI}',+} + I_{\mathrm{PLI}',-} \tag{A.76}$$

$$= 1 + D_L \cos(\delta_1 - 2\phi) \tag{A.77}$$

$$\mp (h_{4,+} - h_{4,-}) \left(1 + D_L \cos(\delta_1 - 2\phi) \mp \sqrt{1 - D_L^2}\sin(\delta)\sin(\delta_1 + 2\phi)\right) \tag{A.78}$$

How well the comparatively small diattenuation signal D_L can be measured depends on its magnitude compared to the amplitude $(h_{4,+} - h_{4,-})$ of the modulating signal.

A.5 3D-PLI Calibration

The Eigenvalue Calibration Method by COMPAIN ET AL. [44] determines the matrices A and W that describe non-idealities of the PSA and PSG, respectively. A and W are used to calibrate the measured Müller matrices as illustrated in Section 3.4. However, the knowledge of A and W cannot be simply used to calibrate a 3D-PLI signal obtained with the Scattering Polarimeter. Here, the propagation of the matrix elements of A and W into the measured 3D-PLI signal is investigated using Müller matrix calculus. $\vec{S}_{\mathrm{PLI}'}$ is the Stokes vector of the 3D-PLI signal. The first element directly corresponds to the measured intensity.

The Müller matrix for brain tissue Eq. (A.1), the ideal Müller matrix of the PSA M_{PSA}, the ideal Stokes vector of the PSG, $\vec{S}_{\text{PSG}}$, and the matrices A and W (obtained from a previously performed ECM routine) can be applied to calculate the non-ideal Stokes vector $\vec{S}_{\text{PLI}'}$ for 3D-PLI which directly corresponds to the measured intensity. In 3D-PLI, δ_1 is variable, $\delta_2 = \pi/2$, $\delta_3 = 0$ and $\delta_4 = \pm\pi/2$. The abbreviations $v_\phi = \sin(2\phi)$ and $w_\phi = \cos(2\phi)$ are used in the following

$$
\begin{aligned}
\vec{S}_{\text{PLI}'} =& M_{\text{PSA}} A M_{\text{tissue}}(\phi,\delta) W \vec{S}_{\text{PSG}} \\
=& M_{\text{PSA}} A M_{\text{tissue}}(\phi,\delta) \begin{pmatrix} m_{W,00} & m_{W,01} & m_{W,02} & m_{W,03} \\ m_{W,10} & m_{W,11} & m_{W,12} & m_{W,13} \\ m_{W,20} & m_{W,21} & m_{W,22} & m_{W,23} \\ m_{W,30} & m_{W,31} & m_{W,32} & m_{W,33} \end{pmatrix} \begin{pmatrix} 1 \\ \cos\delta_1 \\ \sin\delta_1 \\ 0 \end{pmatrix} \\
=& \frac{1}{2} \begin{pmatrix} 1 & 0 & 0 & \mp 1 \\ 1 & 0 & 0 & \mp 1 \\ 0 & 0 & 0 & 0 \\ 0 & 0 & 0 & 0 \end{pmatrix} \begin{pmatrix} m_{A,00} & m_{A,01} & m_{A,02} & m_{A,03} \\ m_{A,10} & m_{A,11} & m_{A,12} & m_{A,13} \\ m_{A,20} & m_{A,21} & m_{A,22} & m_{A,23} \\ m_{A,30} & m_{A,31} & m_{A,32} & m_{A,33} \end{pmatrix} \\
& \cdot \begin{pmatrix} 1 & 0 & 0 & 0 \\ 0 & w_\phi^2 + v_\phi^2 \cos\delta & w_\phi v_\phi (1-\cos\delta) & -v_\phi \sin\delta \\ 0 & w_\phi v_\phi (1-\cos\delta) & v_\phi^2 + w_\phi^2 \cos\delta & +w_\phi \sin\delta \\ 0 & +v_\phi \sin\delta & -w_\phi \sin\delta & \cos\delta \end{pmatrix} \begin{pmatrix} m_{W,00} + m_{W,01}\cos\delta_1 + m_{W,02}\sin\delta_1 \\ m_{W,10} + m_{W,11}\cos\delta_1 + m_{W,12}\sin\delta_1 \\ m_{W,20} + m_{W,21}\cos\delta_1 + m_{W,22}\sin\delta_1 \\ m_{W,30} + m_{W,31}\cos\delta_1 + m_{W,32}\sin\delta_1 \end{pmatrix}
\end{aligned}
$$

The measured intensity $I_{\text{PLI}'}$ is equivalent to the first element of the Stokes vector $\vec{S}_{\text{PLI}'}$ and has a highly complex dependency from A and B. An iterative algorithm could approximate the fiber direction ϕ and retardance δ, however, they cannot be determined analytically

$$
\begin{aligned}
I_{\text{PLI}'} =& \frac{1}{2} \cdot [m_{A,00} \mp m_{A,30}] \cdot [m_{W,00} + m_{W,01}\cos\delta_1 + m_{W,02}\sin\delta_1] \\
&+ \frac{1}{2} \cdot [m_{A,01} \mp m_{A,31}] \\
&\quad \cdot [(w_\phi^2 + v_\phi^2 \cos\delta)(m_{W,10} + m_{W,11}\cos\delta_1 + m_{W,12}\sin\delta_1) \\
&\quad + (w_\phi v_\phi (1-\cos\delta))(m_{W,20} + m_{W,21}\cos\delta_1 + m_{W,22}\sin\delta_1) \\
&\quad + (-v_\phi \sin\delta)(m_{W,30} + m_{W,31}\cos\delta_1 + m_{W,32}\sin\delta_1)] \\
&+ \frac{1}{2} \cdot [m_{A,02} \mp m_{A,32}] \\
&\quad \cdot [(w_\phi v_\phi (1-\cos\delta))(m_{W,10} + m_{W,11}\cos\delta_1 + m_{W,12}\sin\delta_1) \\
&\quad + (v_\phi^2 + w_\phi^2 \cos\delta)(m_{W,20} + m_{W,21}\cos\delta_1 + m_{W,22}\sin\delta_1) \\
&\quad + (w_\phi \sin\delta)(m_{W,30} + m_{W,31}\cos\delta_1 + m_{W,32}\sin\delta_1] \\
&+ \frac{1}{2} \cdot [m_{A,03} \mp m_{A,33}] \\
&\quad \cdot [(+v_\phi \sin\delta)(m_{W,10} + m_{W,11}\cos\delta_1 + m_{W,12}\sin\delta_1) \\
&\quad + (-w_\phi \sin\delta)(m_{W,20} + m_{W,21}\cos\delta_1 + m_{W,22}\sin\delta_1) \\
&\quad + \cos\delta(m_{W,30} + m_{W,31}\cos\delta_1 + m_{W,32}\sin\delta_1)]
\end{aligned}
$$

When the PSA and the PSG are ideal, all diagonal matrix elements become 1 and all off-diagonal matrix elements are 0. In this case, the only remaining terms yield the ideal 3D-PLI signal

$$
\begin{aligned}
I_{\text{PLI}'} =& \frac{1}{2} \cdot m_{A,00} \cdot m_{W,00} \mp \frac{1}{2} m_{A,33} (m_{W,11} v_\phi \sin\delta\cos\delta_1 - m_{W,11} w_\phi \sin\delta\sin\delta_1) \\
=& \frac{1}{2} (1 \pm \sin\delta \sin(\delta_1 - 2\phi))
\end{aligned}
$$

A.6 Linear Polarization Angles with Müller Polarimeter

Equidistant polarization angles as required for 3D-PLI and DI can also be generated with the PSG when the LCVRs are set to different azimuthal angles than 0° or 45°. Müller matrix calculus yields the matrix for a retarder at an azimuthal angle θ

$$M_{LCVR} = R(\theta)M(\delta)R(-\theta) \tag{A.79}$$

$$= \begin{pmatrix} 1 & 0 & 0 & 0 \\ 0 & \cos 2\theta & -\sin 2\theta & 0 \\ 0 & \sin 2\theta & \cos 2\theta & 0 \\ 0 & 0 & 0 & 1 \end{pmatrix} \begin{pmatrix} 1 & 0 & 0 & 0 \\ 0 & 1 & 0 & 0 \\ 0 & 0 & \cos\delta & \sin\delta \\ 0 & 0 & -\sin\delta & \cos\delta \end{pmatrix} \begin{pmatrix} 1 & 0 & 0 & 0 \\ 0 & \cos(2\theta) & \sin(2\theta) & 0 \\ 0 & -\sin(2\theta) & \cos(2\theta) & 0 \\ 0 & 0 & 0 & 1 \end{pmatrix} \tag{A.80}$$

$$= \begin{pmatrix} 1 & 0 & 0 & 0 \\ 0 & \cos(2\theta) & -\sin(2\theta) & 0 \\ 0 & \sin(2\theta) & \cos(2\theta) & 0 \\ 0 & 0 & 0 & 1 \end{pmatrix} \begin{pmatrix} 1 & 0 & 0 & 0 \\ 0 & \cos(2\theta) & \sin(2\theta) & 0 \\ 0 & \cos\delta\sin(2\theta) & \cos\delta\cos(2\theta) & \sin\delta \\ 0 & \sin\delta\sin(2\theta) & -\sin\delta\cos(2\theta) & \cos\delta \end{pmatrix} \tag{A.81}$$

$$= \begin{pmatrix} 1 & 0 & 0 & 0 \\ 0 & \cos^2(2\theta) - \cos\delta\sin^2(2\theta) & \cos(2\theta)\sin(2\theta)(1-\cos\delta) & -\sin(2\theta)\sin\delta \\ 0 & \cos(2\theta)\sin(2\theta)(1+\cos\delta) & \cos^2(2\theta) + \cos\delta\sin^2(2\theta) & \cos(2\theta)\sin\delta \\ 0 & \sin(2\theta)\sin\delta & -\cos(2\theta)\sin\delta & \cos\delta \end{pmatrix} \tag{A.82}$$

Müller polarimetry achieves the best signal-to-noise ratio with azimuthal angles $\theta_2 = 72.4°$ and $\theta_1 = 24.7°$, as illustrated in Section 3.4.2. The Stokes vector $\vec{S}_{\mathrm{PSG}}$ generated by the PSG is then given by

$$\vec{S}_{\mathrm{PSG}} = M(\theta = 72.4°, \delta) \cdot M(\theta = 27.4°, \delta) \cdot \vec{S}_H \tag{A.83}$$

$$\approx \begin{pmatrix} 1 & 0 & 0 & 0 \\ 0 & 0.73 - 0.27\cos\delta_2 & -0.45 \cdot (1 - \cos\delta_2) & -0.52\sin\delta_2 \\ 0 & -0.45 \cdot (1 + \cos\delta_2) & 0.73 + 0.27\cos\delta_2 & -0.85\sin\delta_2 \\ 0 & 0.52\sin\delta_2 & 0.85\sin\delta_2 & \cos\delta_2 \end{pmatrix} \tag{A.84}$$

$$\cdot \begin{pmatrix} 1 & 0 & 0 & 0 \\ 0 & 0.33 - 0.67\cos\delta_1 & 0.47 \cdot (1 - \cos\delta_1) & -0.82\sin\delta_1 \\ 0 & 0.47 \cdot (1 + \cos\delta_1) & 0.33 + 0.67\cos\delta_1 & 0.58\sin\delta_1 \\ 0 & 0.82\sin\delta_1 & -0.58\sin\delta_1 & \cos\delta_1 \end{pmatrix} \begin{pmatrix} 1 \\ 1 \\ 0 \\ 0 \end{pmatrix} \tag{A.85}$$

$$= \begin{pmatrix} 1 & 0 & 0 & 0 \\ 0 & 0.73 - 0.27\cos\delta_2 & -0.45 \cdot (1 - \cos\delta_2) & -0.52\sin\delta_2 \\ 0 & -0.45 \cdot (1 + \cos\delta_2) & 0.73 + 0.27\cos\delta_2 & -0.85\sin\delta_2 \\ 0 & 0.52\sin\delta_2 & 0.85\sin\delta_2 & \cos\delta_2 \end{pmatrix} \begin{pmatrix} 1 \\ 0.33 - 0.67\cos\delta_1 \\ 0.47 \cdot (1 + \cos\delta_1) \\ 0.82\sin\delta_1 \end{pmatrix} \tag{A.86}$$

$$\approx \begin{pmatrix} 1 \\ 0.03 - 0.70\cos\delta_1 + 0.12\cos\delta_2 + 0.39\cos\delta_1\cos\delta_2 - 0.43\sin\delta_1\sin\delta_2 \\ 0.20 + 0.65\cos\delta_1 - 0.02\cos\delta_2 + 0.43\cos\delta_1\cos\delta_2 + 0.70\sin\delta_1\sin\delta_2 \\ 0.05\cos\delta_1\sin\delta_2 + 0.57\sin\delta_2 - 0.82\cos\delta_2\sin\delta_1 \end{pmatrix} \tag{A.87}$$

The last element of $\vec{S}_{\mathrm{PSG}}$ (associated with circular polarization) must be zero for purely linear polarization. To achieve equidistant linear polarization as required for 3D-PLI, value sets for δ_1 and δ_2 must be chosen accordingly.

Appendix B

Supplementary Figures

B.1 Supplementary Figures to Chapter 4

The measurement of the retardance voltage curve for the first liquid crystal variable retarder (LCVR) in the setup, LCVR 1, is shown in Section 4.5 in dependence from the spectral bandwidth of the light source and in dependence from the operating frequency of the applied square-wave voltage. For the other LCVRs, the retardance-voltage curves are shown here.

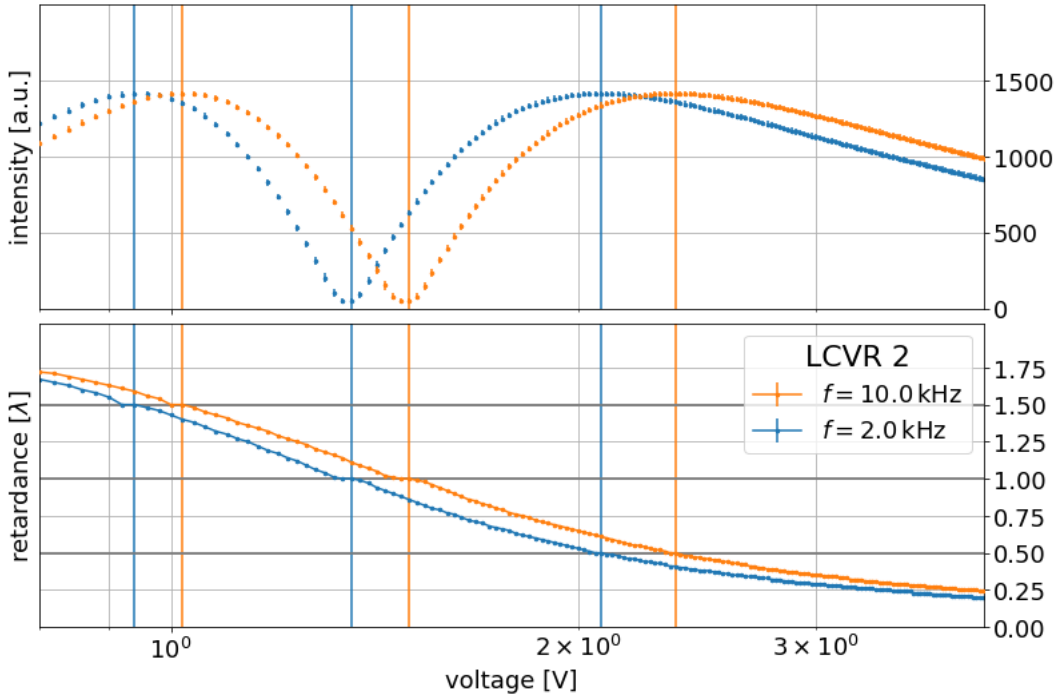

FIGURE B.1: Frequency dependence of LCVR 2. LCVR 2 is part of the polarization state generator (PSG) in the Scattering Polarimeter. The retardance voltage curve is obtained in a crossed-polarizer configuration and depends on the operating frequency of the applied square-wave voltage. Two different frequencies are investigated. $f = 2\,kHz$ is the manufacturer's default setting. $f = 10\,kHz$ is the highest allowed frequency. The retardance voltages curves are measured in combination with the spectral filter with FWHM= 10 nm that was also installed for all subsequent investigations.

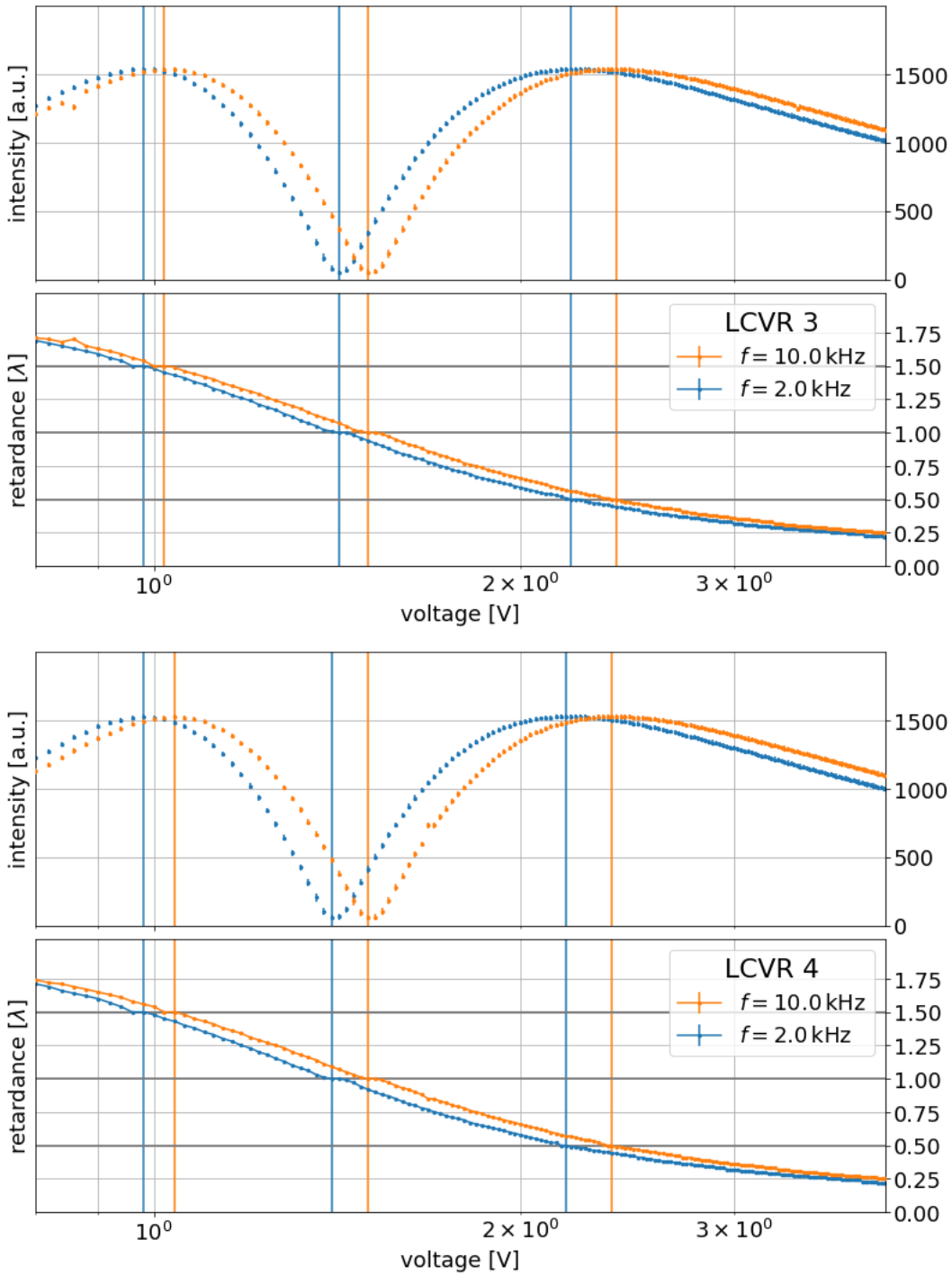

FIGURE B.2: Frequency dependence of LCVR 3 and LCVR 4. LCVR 4 and LCVR 3 are part of the polarization state analyzer (PSA) in the Scattering Polarimeter. The retardance voltage curve is obtained in a crossed-polarizer configuration and depends on the operating frequency of the applied square-wave voltage. Two different frequencies are investigated. $f = 2\,kHz$ is the manufacturer's default setting. $f = 10\,kHz$ is the highest allowed frequency. The retardance voltages curves are measured in combination with the spectral filter with FWHM= 10 nm that was also installed for all subsequent investigations.

B.2 Supplementary Figures to Chapter 5

Section 5.2.1 investigates the performance of the Scattering Polarimeter for 3D-PLI exemplary for two areas in Broca-A. Here, the corresponding depictions for Vervet1818-FX are shown. The asymmetric feature in the curves are more apparent in Vervet1818 due to the lower contrast in the transmittance.

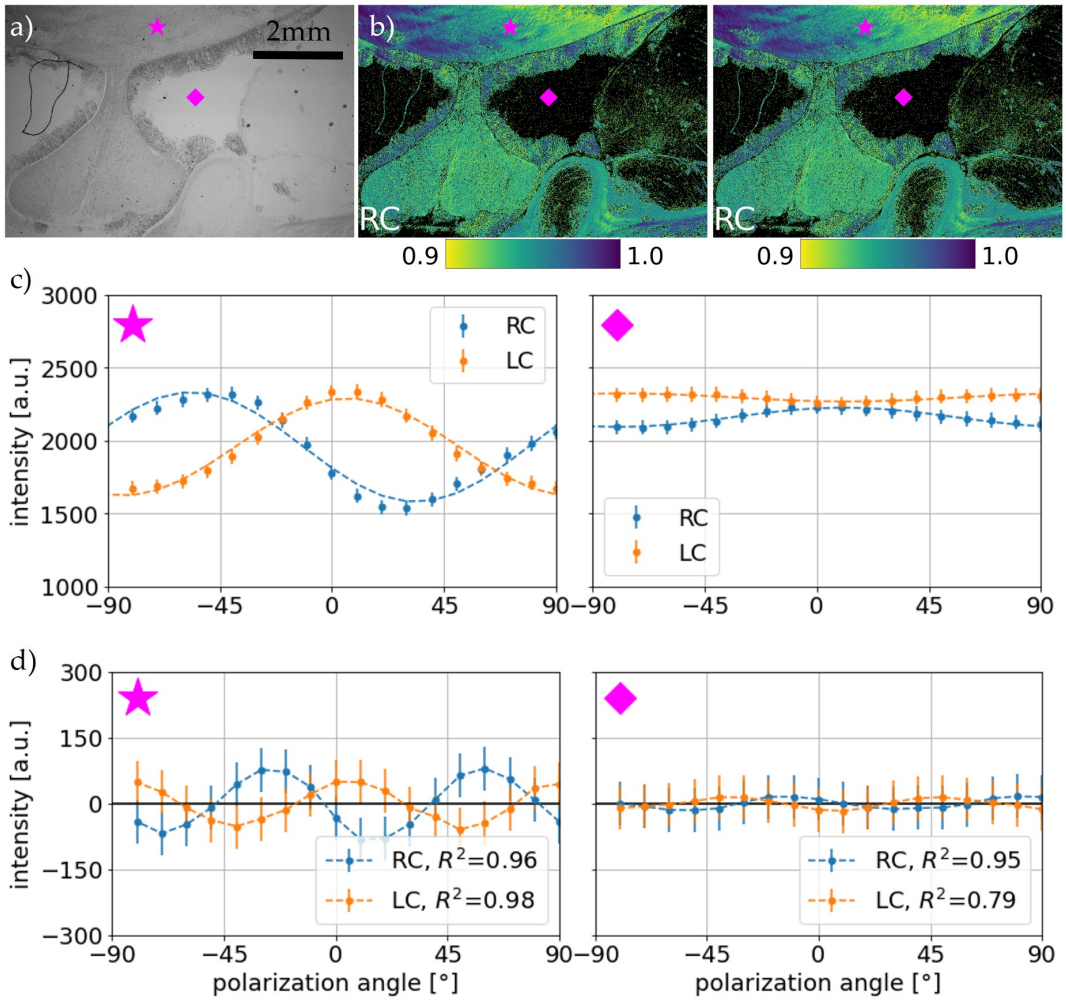

FIGURE B.3: Pixelwise Fourier coefficient fit in 3D-PLI for Vervet1818. The fit is shown the for left-circular (LC) and right-circular (RC) analyzer setting. a) Transmittance map for Vervet1818 with exemplary white matter area (magenta star) and background (magenta diamond) indicated. b) Pixelwise coefficient of determination R^2 for LC and RC. The closer R^2 to 1, the more successful the fit. c) The Fourier coefficient fit yields sinusoidal curves for LC and RC. Horizontal lines mark the maximum and minimum intensity for both curves. d) The residuals indicate a systematic error. Overall, the transmittance asymmetry is stronger than in Broca due to the lower contrast.

In Section 5.2.2, a higher-frequency signal is observed in the 3D-PLI signal. Müller calculus combined with Taylor approximations (s. Appendix A.3.1) show that minor deviations in the PSA can cause this behavior. Even though the systematic offset is small compared to the signal amplitude, it is important to be aware of the effect as it can distort the 3D-PLI signal. Figure B.4 shows the ideal signal modulated with an offset for a simulated signal.

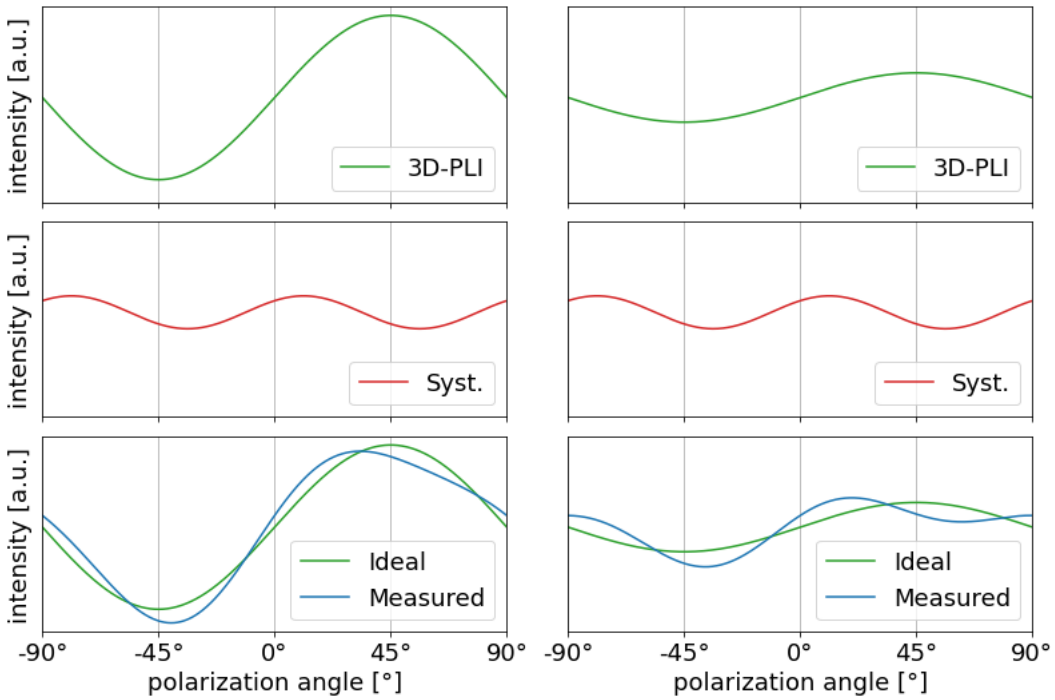

FIGURE B.4: Influence of a higher frequency signal on the 3D-PLI signal. Two 3D-PLI signals are shown (first row) that are different in their amplitude, i.e. their retardation. A small systematic error with twice the frequency (second row) is used to model the influence of a higher frequency signal on the original 3D-PLI signals (third row). The magnitude of the higher frequency signal is strongly exaggerated compared to the real measurements for depiction purposes. However, for a high retardation (i.e. in-plane parallel fibers), deviations from the ideal sinusoidal curve are minor. In case of a low retardation (i.e. out-of-plane parallel fibers), the curve is strongly distorted.

Within the Scattering Polarimeter, LCVR 4 can either analyze right- (RC) or left-handed circular (LC) polarized light, depending on its voltage setting. The influence of the circular analyzer settings on the 3D-PLI measurement is explored in Section 5.2.6 exemplary for Broca-B. In the following, the differences in transmittance, retardation, inclination, and direction are shown for all investigated areas in Broca and Vervet1818.

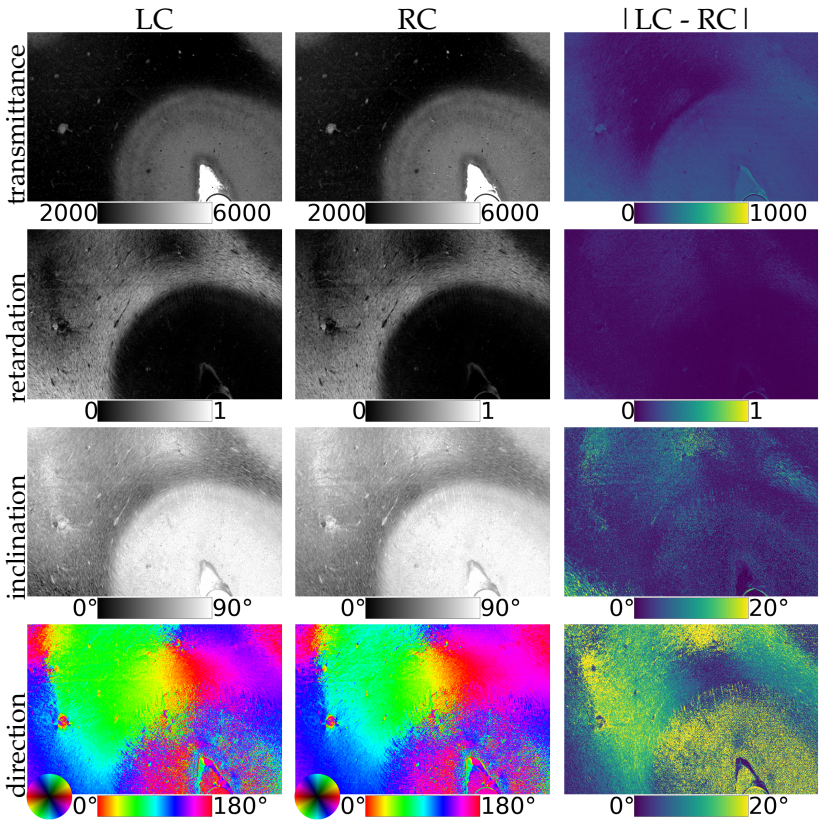

FIGURE B.5: Influence of circular analyzer in 3D-PLI on Broca-A. From top to bottom: Transmittance [a.u.], retardation, inclination, fiber direction. From left to right: Left-circular (LC) setting, right-circular (RC) setting, their absolute difference.

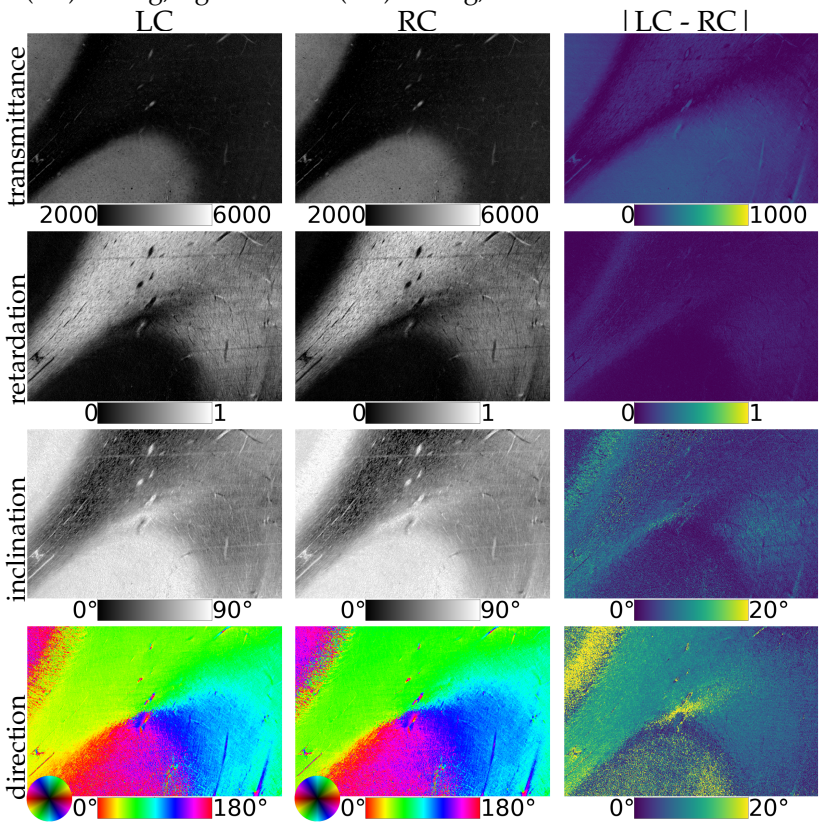

FIGURE B.6: Influence of circular analyzer in 3D-PLI on Broca-B. From top to bottom: Transmittance [a.u.], retardation, inclination, fiber direction. From left to right: Left-circular (LC) setting, right-circular (RC) setting, their absolute difference.

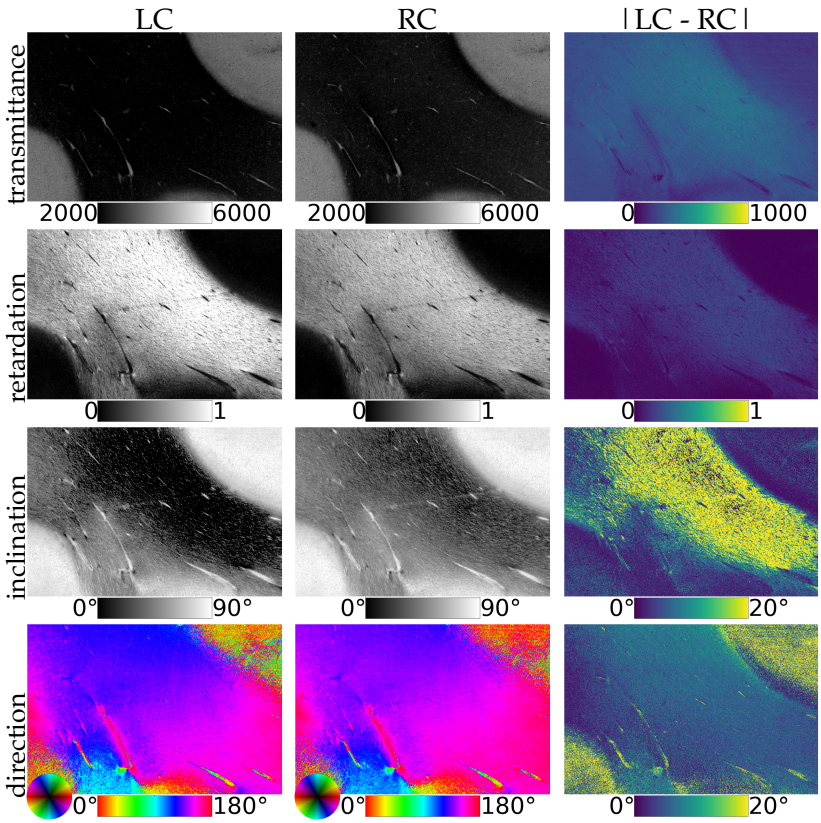

FIGURE B.7: Influence of circular analyzer in 3D-PLI on Broca-C. From top to bottom: Transmittance [a.u.], retardation, inclination, fiber direction. From left to right: Left-circular (LC) setting, right-circular (RC) setting, their absolute difference.

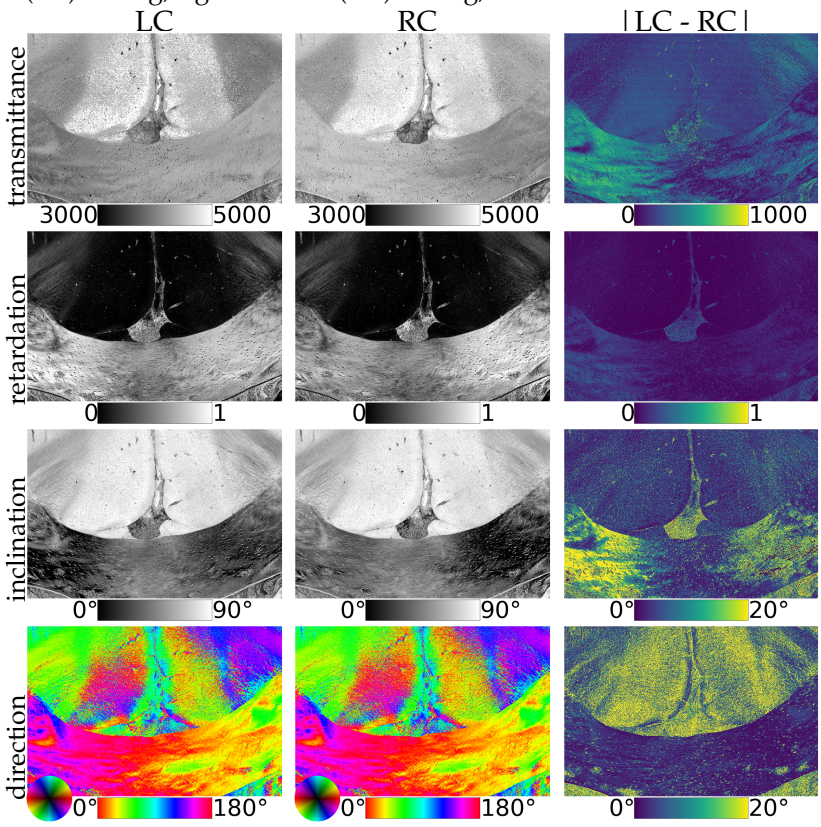

FIGURE B.8: Influence of circular analyzer in 3D-PLI on Vervet1818-CC. From top to bottom: Transmittance [a.u.], retardation, inclination, fiber direction. From left to right: Left-circular (LC) setting, right-circular (RC) setting, their absolute difference.

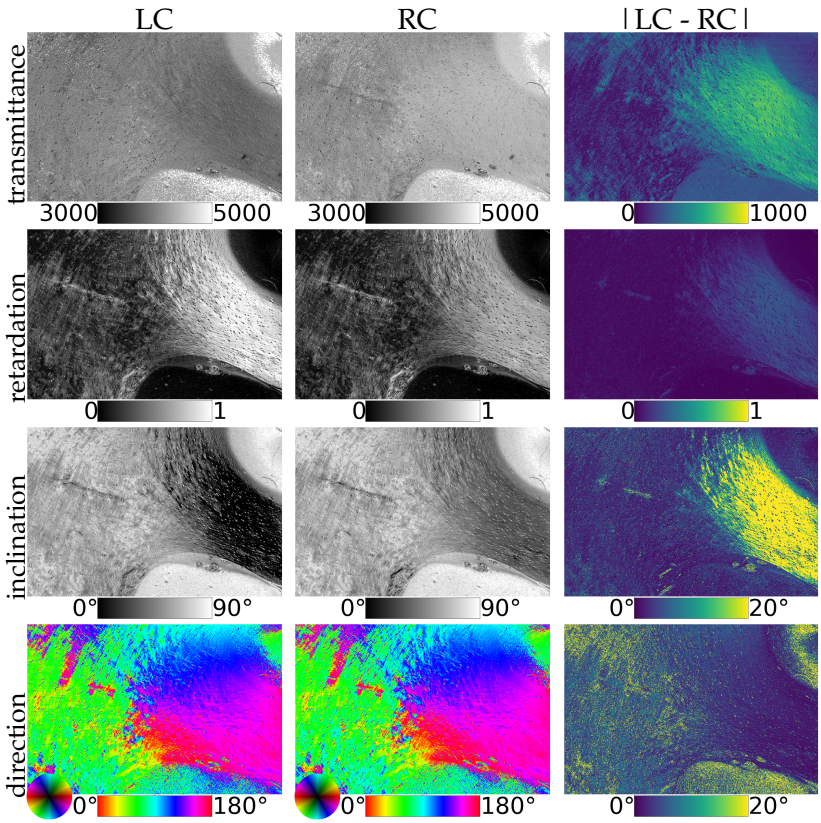

FIGURE B.9: Influence of circular analyzer in 3D-PLI on Vervet1818-CR. From top to bottom: Transmittance [a.u.], retardation, inclination, fiber direction. From left to right: Left-circular (LC) setting, right-circular (RC) setting, their absolute difference.

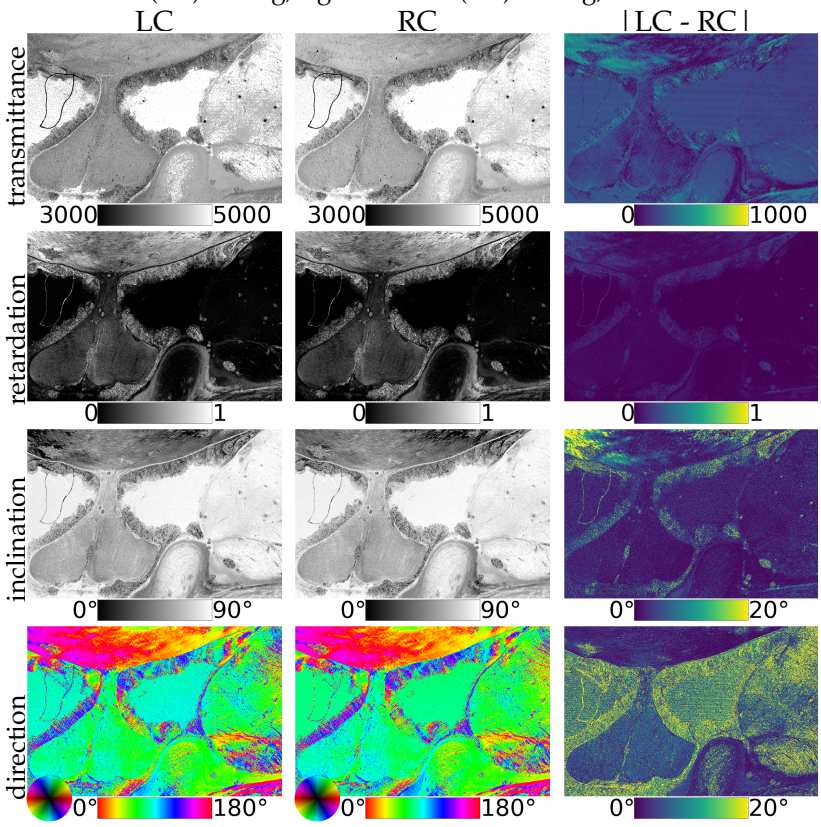

FIGURE B.10: Influence of circular analyzer in 3D-PLI on Vervet1818-FX. From top to bottom: Transmittance [a.u.], retardation, inclination, fiber direction. From left to right: Left-circular (LC) setting, right-circular (RC) setting, their absolute difference.

Reference measurements for 3D-PLI with the LMP3D microscope (s. Section 3.6.2) for Vervet1818 and Broca are shown in Section 5.2.7. Reference measurements with the LMP1 for ChiasmX2-7 and ChiasmX2-15 were available in the database of the Institute of Neuroscience and Medicine (INM-1) at the Forschungszentrum Jülich GmbH and are shown in Figure B.11.

ChiasmX2-15 is influenced by stripe-shaped artifacts that show up in the transmittance map, mainly visible on the left side. They have possibly been caused by scratches or a contamination of the object carrier that has occurred during the reference measurement and the measurement with the Scattering Polarimeter. Otherwise, the parameter maps from the Scattering Polarimeter are in accordance with the reference parameter maps apart from asymmetries in the transmittance map as discussed in Section 5.2.7.

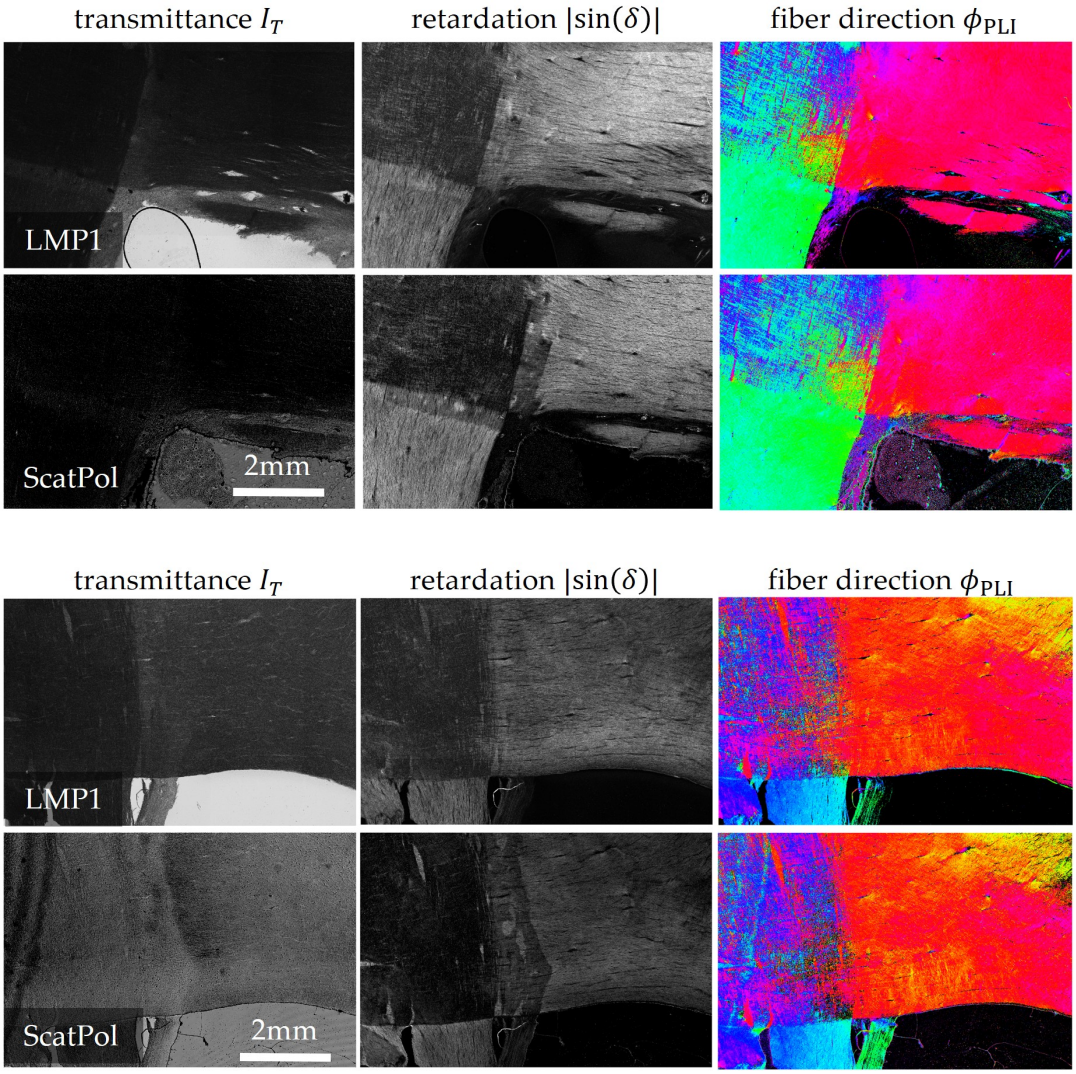

FIGURE B.11: Reference measurements for ChiasmX2-7 and ChiasmX2-15. Direct comparison between parameter maps for ChiasmX2-7 (first and second row) and ChiasmX2-15 (third and fourth row) obtained with the LMP1 (upper row for each) and the Scattering Polarimeter (lower row for each). From left to right: Transmittance map, retardation map, fiber direction map.

Section 5.3.1 investigates the performance of the Scattering Polarimeter for DI exemplary for two areas in Broca-A. Here, the corresponding depictions for Vervet1818-FX are shown. Overall, the transmittance asymmetry is more prominent for Vervet1818 due to the lower contrast.

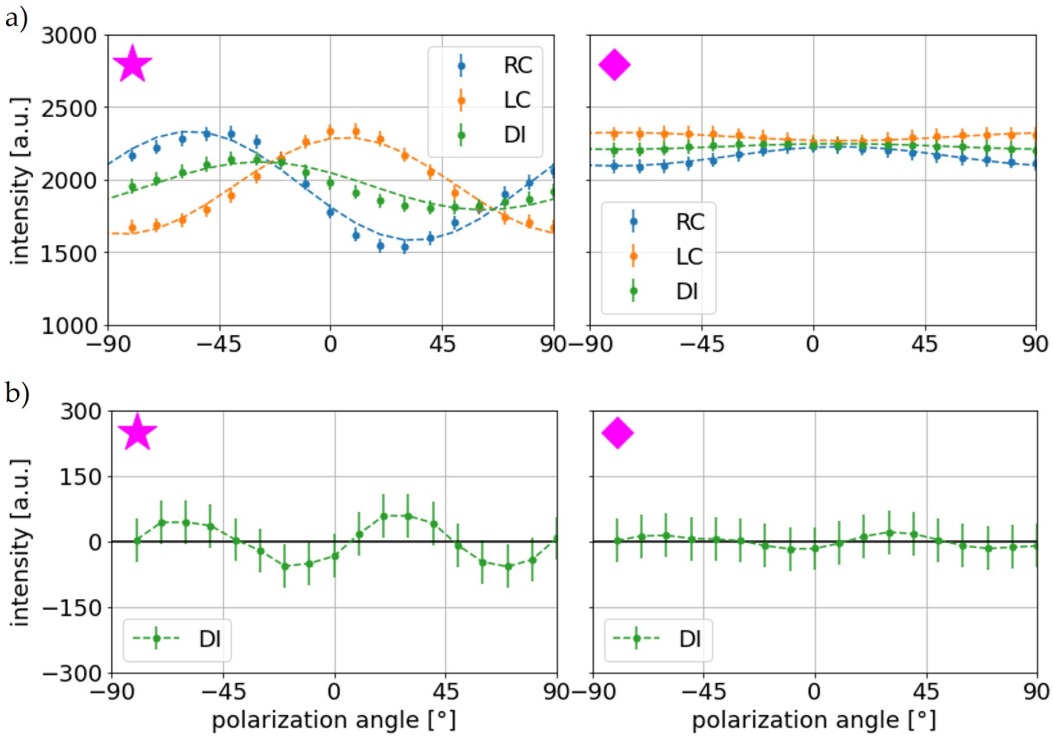

FIGURE B.12: Pixelwise Fourier coefficient fit in DI and 3D-PLI for Vervet1818. a) The Fourier coefficient fit for a white matter area (magenta star) and for background (magenta diamond) yields two sinusoidal curves for LC and RC. The dashed orange and blue lines indicate the Fourier fit for the 3D-PLI curves. When added up, the diattenuation signal (green) emerges. Here, the diattenuation intensity is divided by 2 for visualization purposes. b) The residuals of the diattenuation signal indicate a systematic error.

Section 5.3.3 investigates the distribution of D^+ / D^- in brain tissue by comparing the fiber direction maps from 3D-PLI and DI for Broca and Vervet. Here, the corresponding maps for ChiasmX2-7 and ChiasmX2-15 are presented. ChiasmX2-15 is influenced by the occurrence of artifacts, possibly caused by scratches or a contamination of the object carrier. Mainly D^+ is expected for both samples due to the longer time since embedding. The diattenuation is generally very low: The single optic tracts only have a thickness of 30 µm and thus, the diattenuation signal is even weaker than for Vervet1818 and Broca. However, ChiasmX2-7 shows fiber orientations from the diattenuation measurement that are in agreement with the 3D-PLI measurement, and a diattenuation signal for the single optic tracts. In the crossing regions, the two axes of diattenuation are expected to cancel out, an effect that is actually observed for ChiasmX2-7.

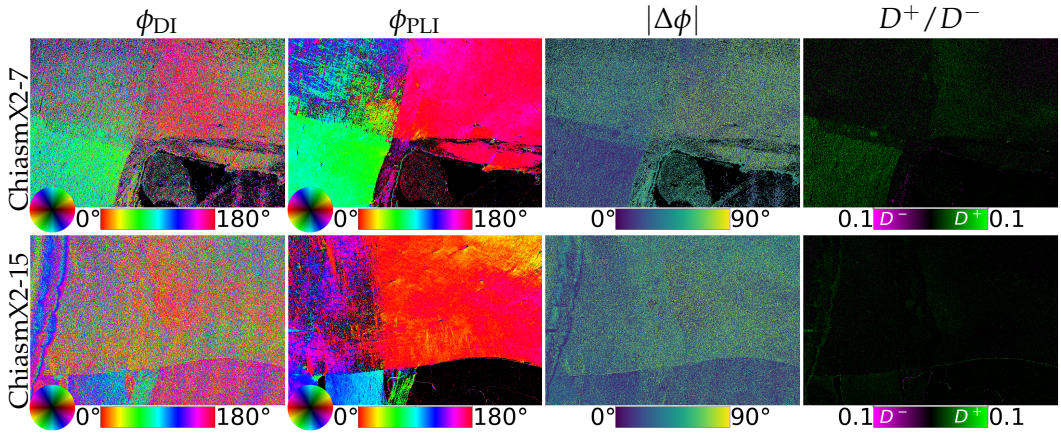

FIGURE B.13: Fiber direction maps from 3D-PLI and DI. From top to bottom: ChiasmX2-7, ChiasmX2-15. From left to right: Fiber direction from DI ϕ_{DI}, fiber direction from 3D-PLI ϕ_{PLI}, relative directional difference, D^+ / D^- tissue distribution weighed with the absolute diattenuation D.

Section 5.4 demonstrates the application of the Lu-Chipman decomposition to obtain a diattenuation matrix, a retardance matrix, and a depolarization matrix from the measured (and calibrated) Müller matrix, but only Vervet1818-CR is shown for brevity. The Müller matrices and the three decomposed matrices for Broca, Vervet1818, ChiasmX2-7, and ChiasmX2-15 are presented in the following. To be precise, each image pixel yields a 4×4 Müller matrix, thus the subplots show 5472×3648 Müller matrices, directly corresponding to the number of image pixels, and thereby providing a spatial overview of the samples.

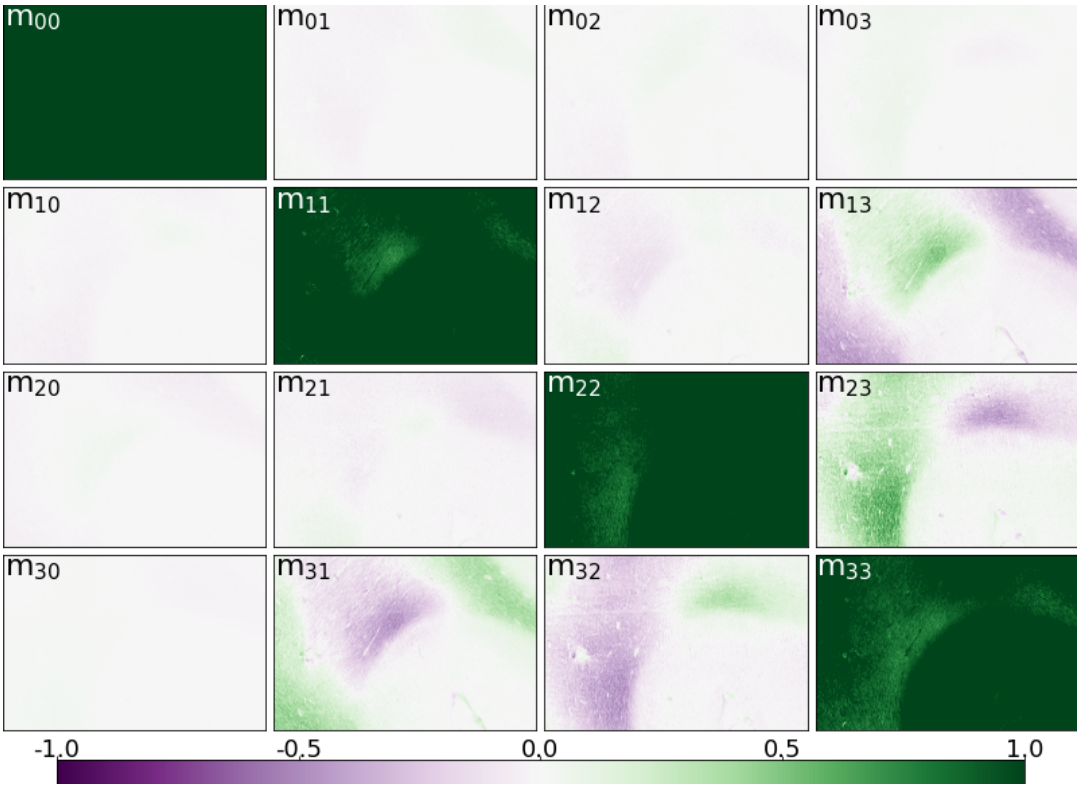

FIGURE B.14: Müller matrices for Broca-A. Each image pixel yields a 4×4 Müller matrix, therefore the subplots visualize 5472×3648 Müller matrices that provide a spatial overview over the sample.

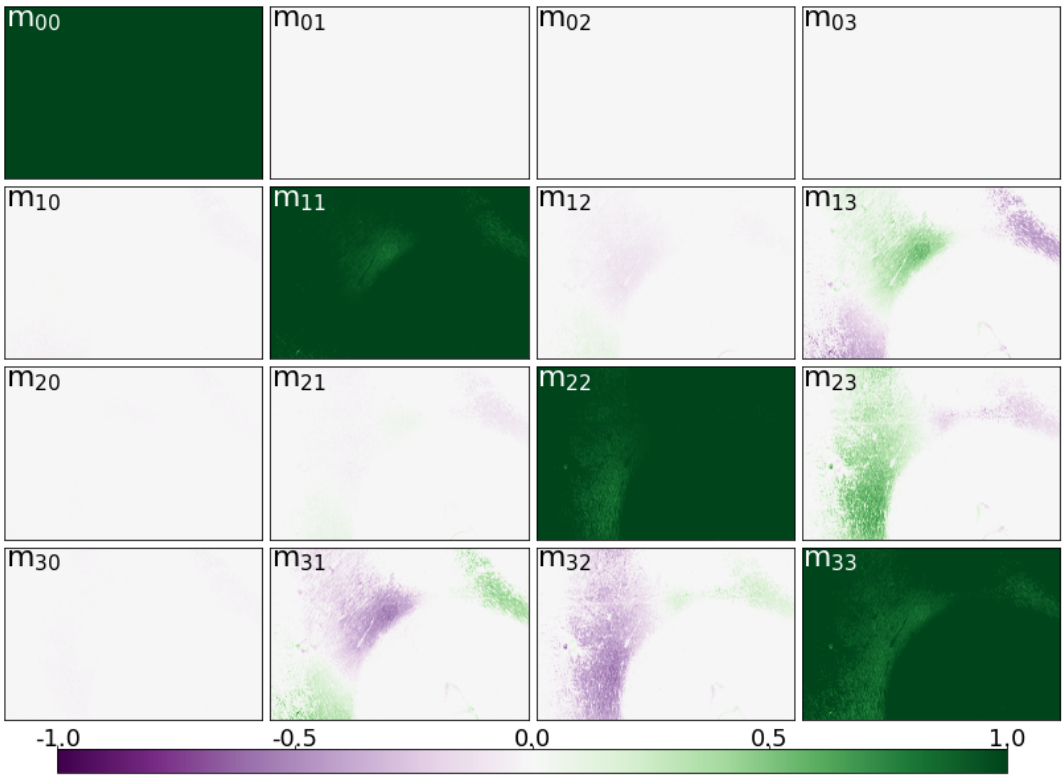

FIGURE B.15: Lu-Chipman retardance matrices for Broca-A. Each image pixel yields a 4×4 Müller matrix, therefore the subplots visualize 5472×3648 Müller matrices that provide a spatial overview over the sample.

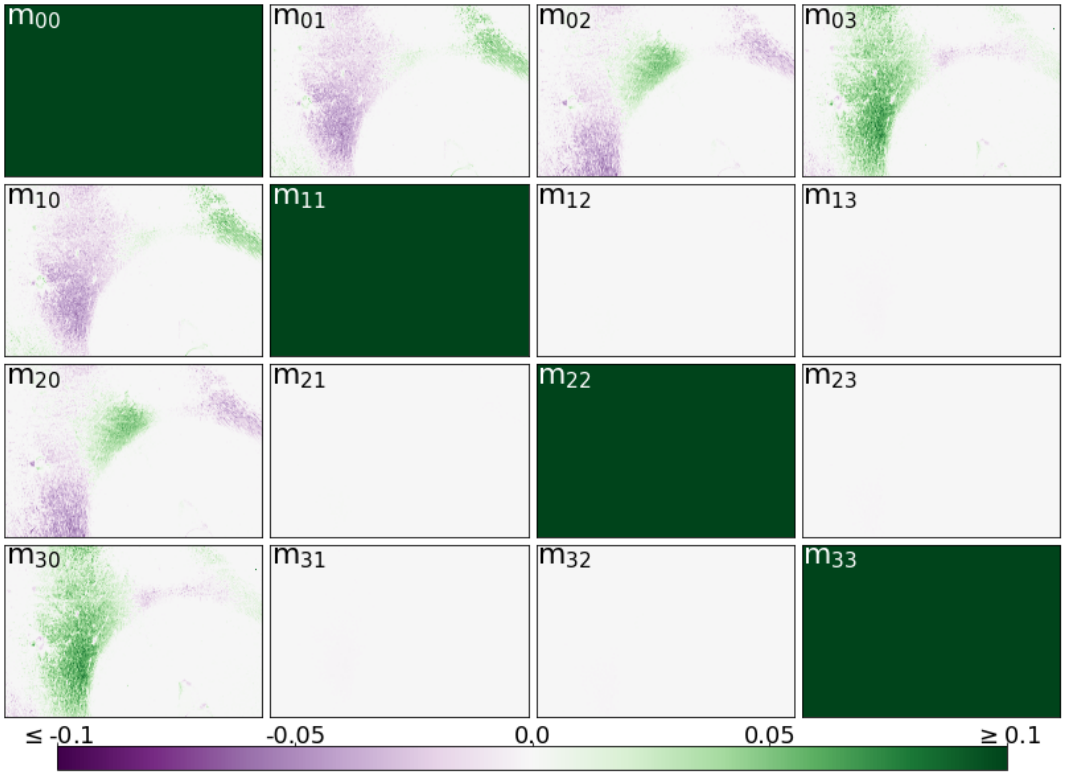

FIGURE B.16: Lu-Chipman diattenuation matrices for Broca-A. Each image pixel yields a 4×4 Müller matrix, therefore the subplots visualize 5472×3648 Müller matrices that provide a spatial overview over the sample.

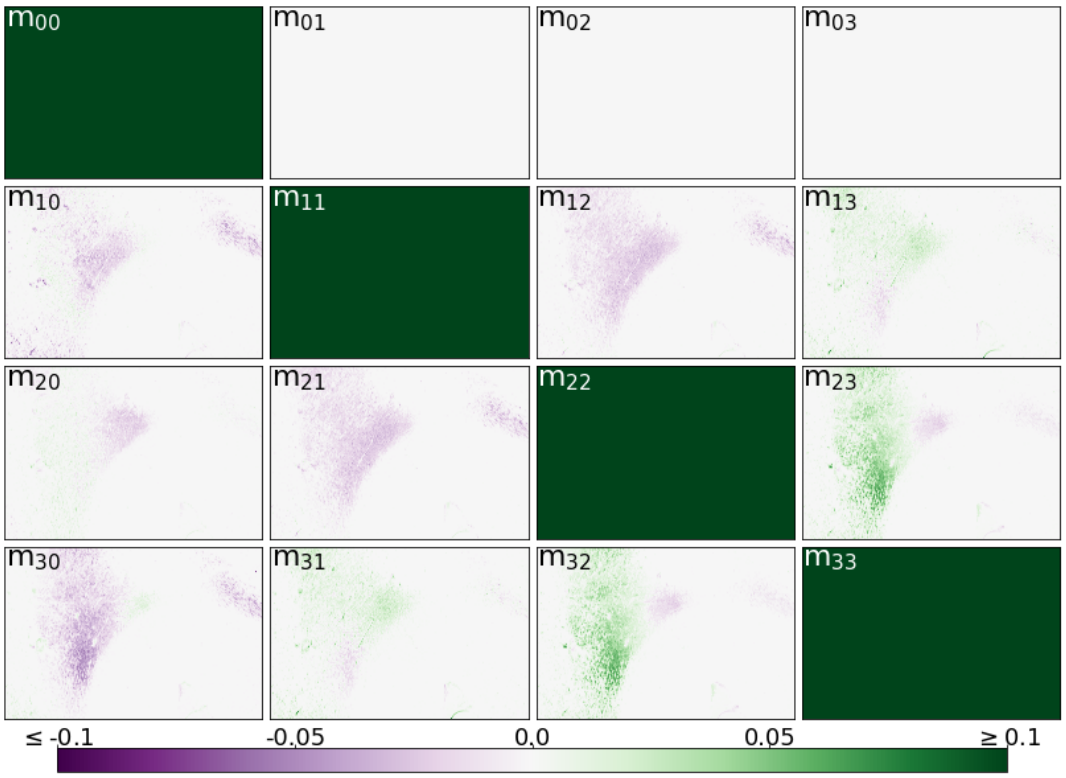

FIGURE B.17: Lu-Chipman depolarization matrices for Broca-A. Each image pixel yields a 4×4 Müller matrix, therefore the subplots visualize 5472×3648 Müller matrices that provide a spatial overview over the sample.

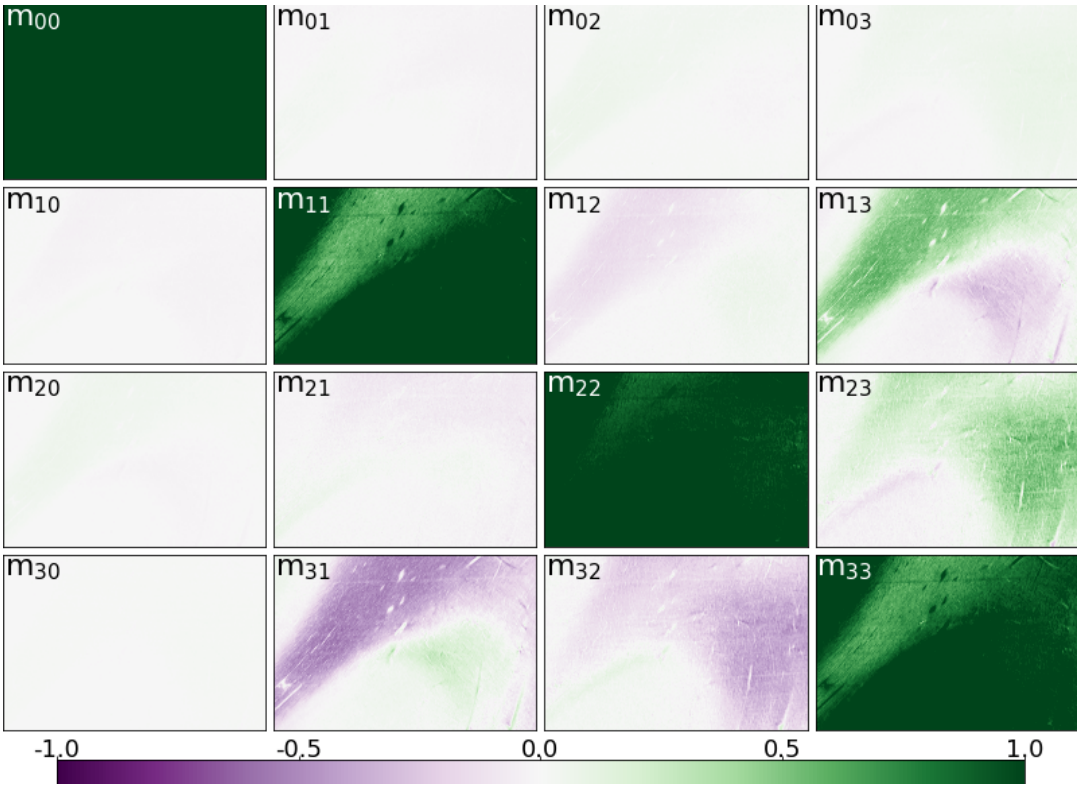

FIGURE B.18: Müller matrices for Broca-B. Each image pixel yields a 4×4 Müller matrix, therefore the subplots visualize 5472×3648 Müller matrices that provide a spatial overview over the sample.

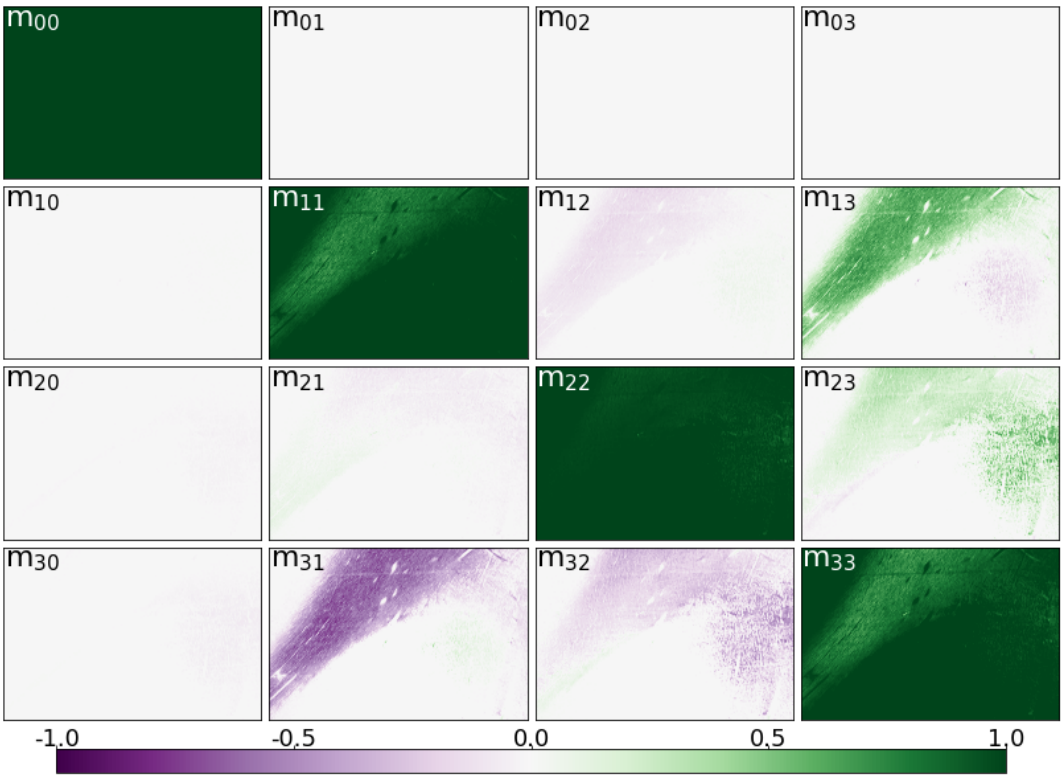

FIGURE B.19: Lu-Chipman retardance matrices for Broca-B. Each image pixel yields a 4×4 Müller matrix, therefore the subplots visualize 5472×3648 Müller matrices that provide a spatial overview over the sample.

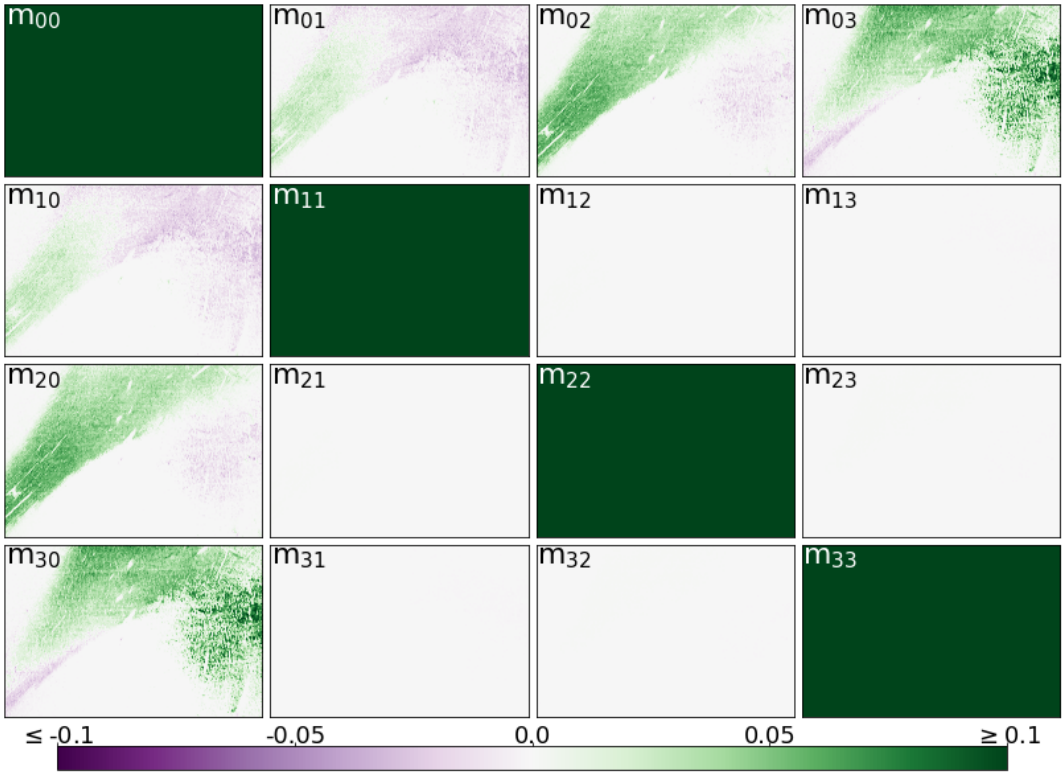

FIGURE B.20: Lu-Chipman diattenuation matrices for Broca-B. Each image pixel yields a 4×4 Müller matrix, therefore the subplots visualize 5472×3648 Müller matrices that provide a spatial overview over the sample.

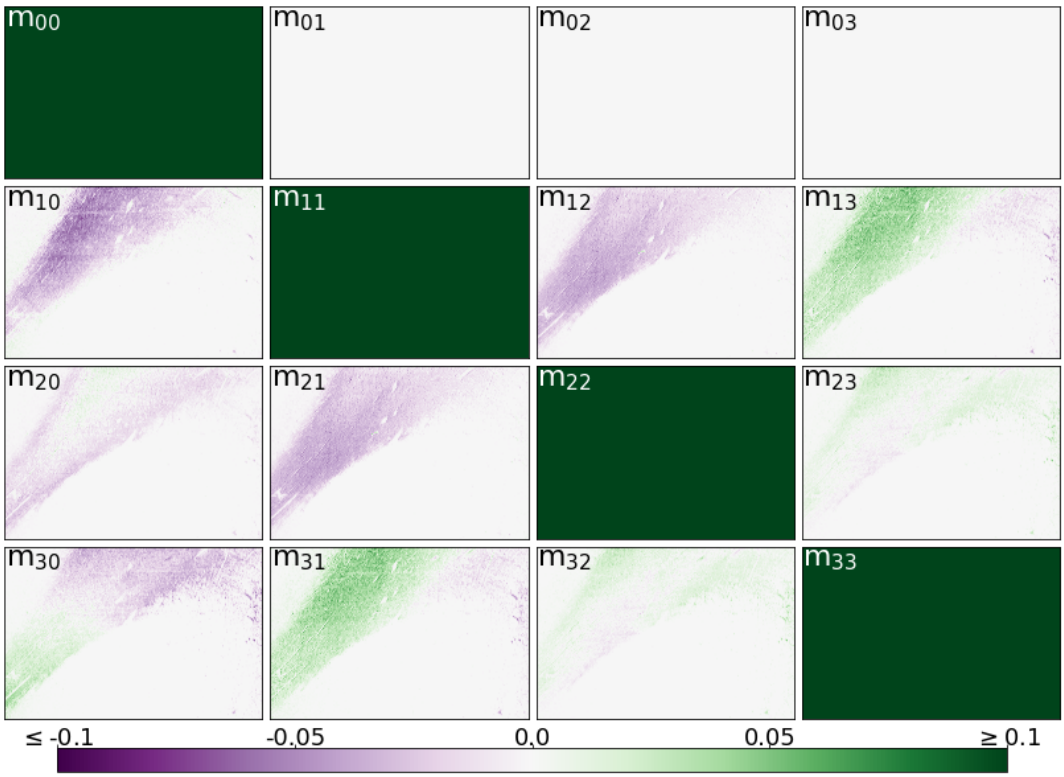

FIGURE B.21: Lu-Chipman depolarization matrices for Broca-B. Each image pixel yields a 4×4 Müller matrix, therefore the subplots visualize 5472×3648 Müller matrices that provide a spatial overview over the sample.

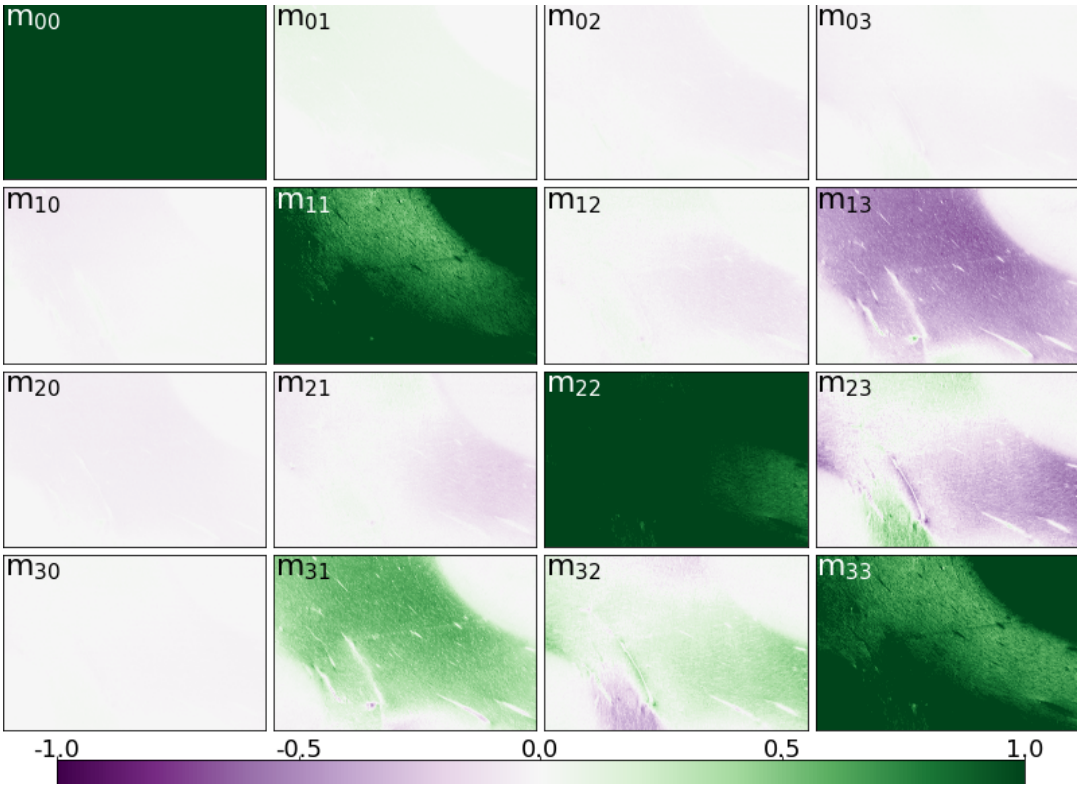

FIGURE B.22: Müller matrices for Broca-C. Each image pixel yields a 4×4 Müller matrix, therefore the subplots visualize 5472×3648 Müller matrices that provide a spatial overview over the sample.

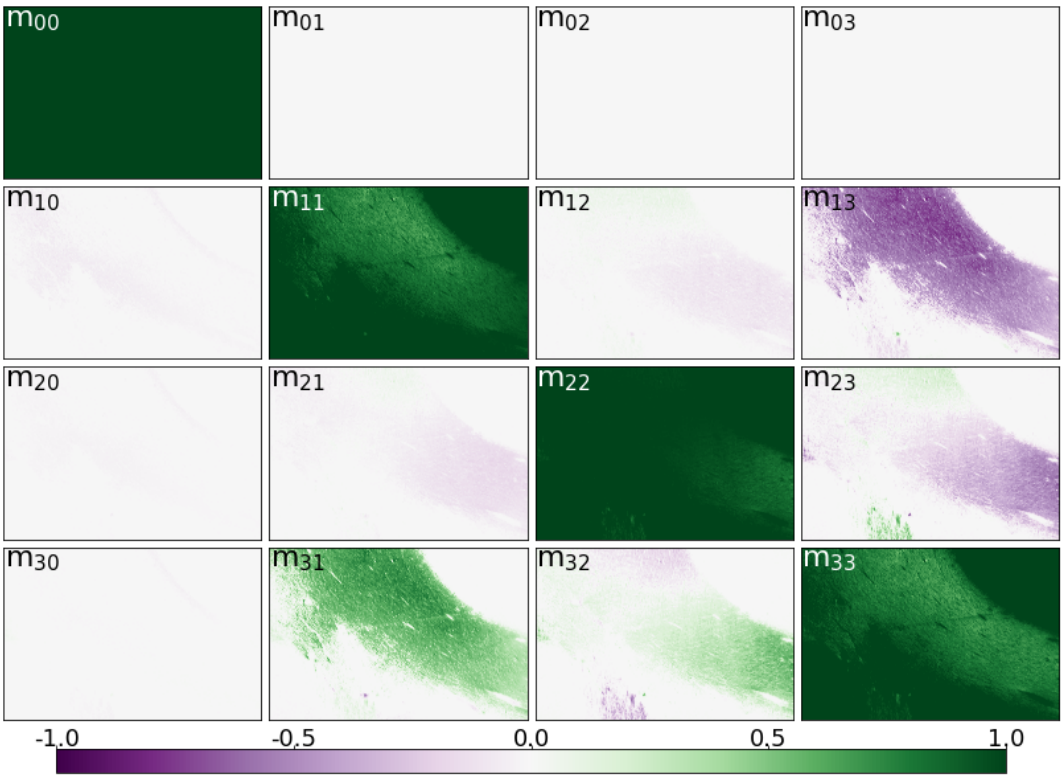

FIGURE B.23: Lu-Chipman retardance matrices for Broca-C. Each image pixel yields a 4×4 Müller matrix, therefore the subplots visualize 5472×3648 Müller matrices that provide a spatial overview over the sample.

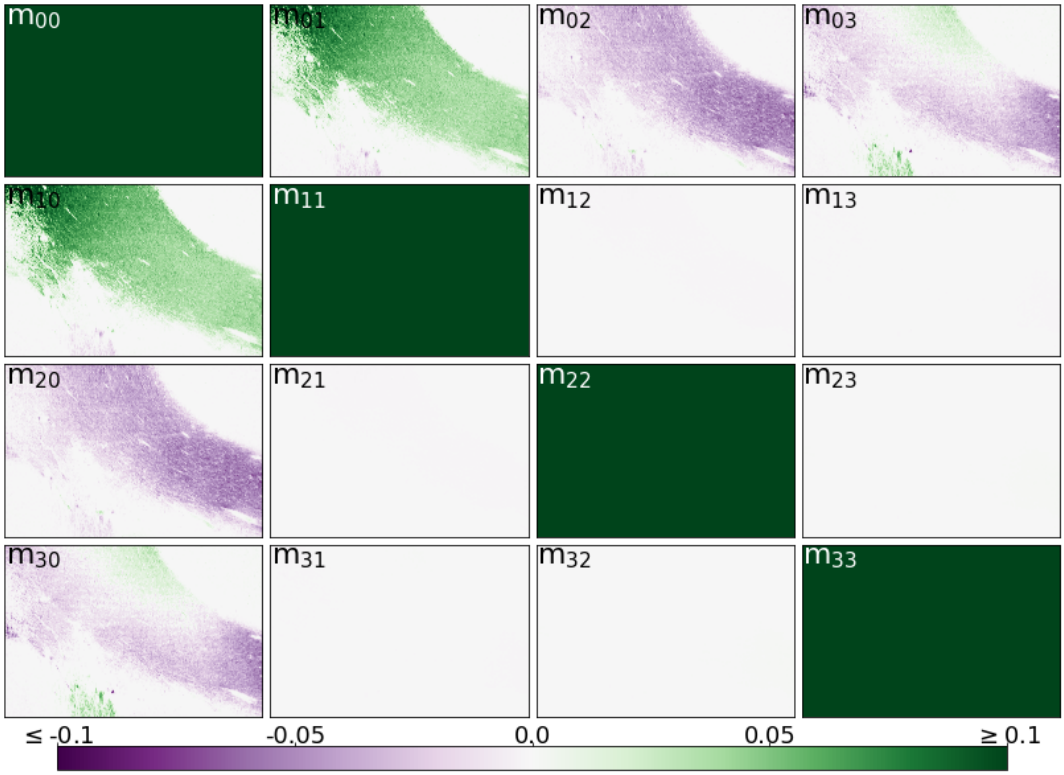

FIGURE B.24: Lu-Chipman diattenuation matrices for Broca-C. Each image pixel yields a 4×4 Müller matrix, therefore the subplots visualize 5472×3648 Müller matrices that provide a spatial overview over the sample.

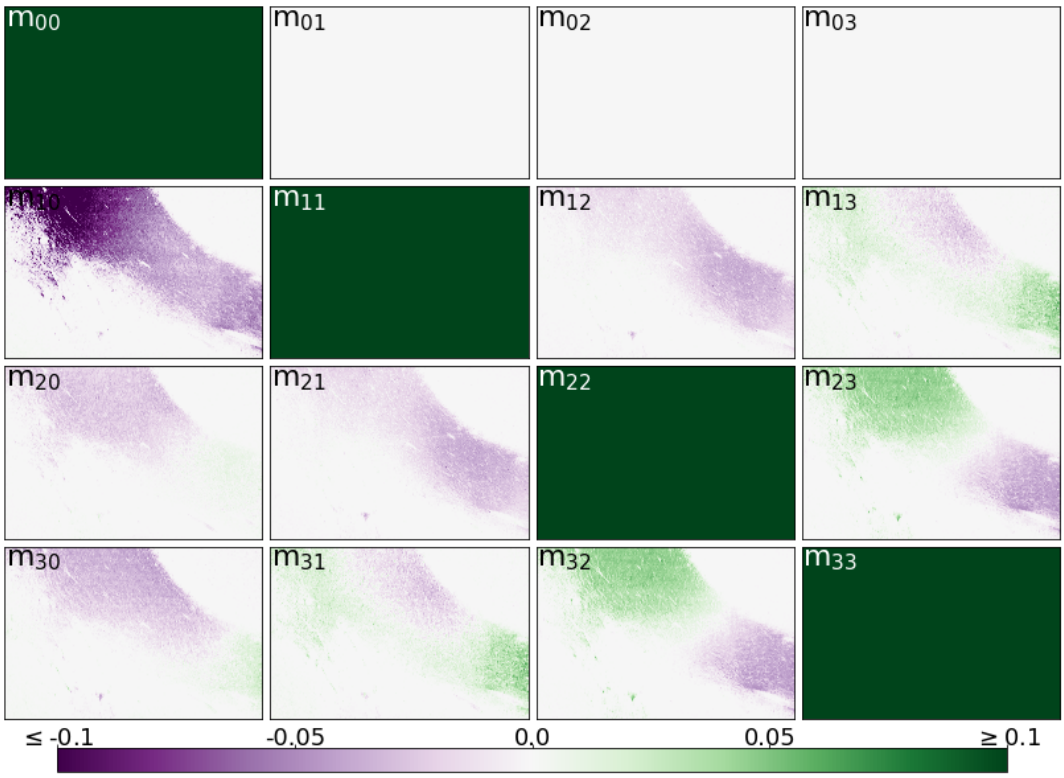

FIGURE B.25: Lu-Chipman depolarization matrices for Broca-C. Each image pixel yields a 4×4 Müller matrix, therefore the subplots visualize 5472×3648 Müller matrices that provide a spatial overview over the sample.

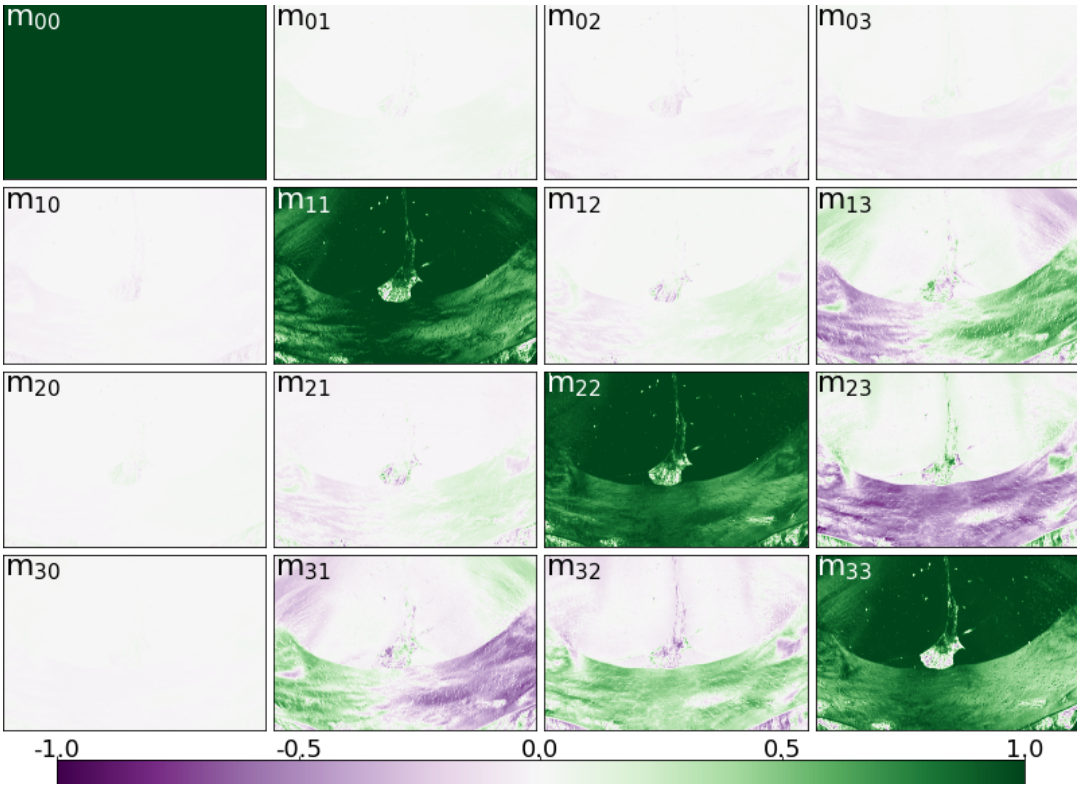

FIGURE B.26: Müller matrices for Vervet1818-CC. Each image pixel yields a 4×4 Müller matrix, therefore the subplots visualize 5472×3648 Müller matrices that provide a spatial overview over the sample.

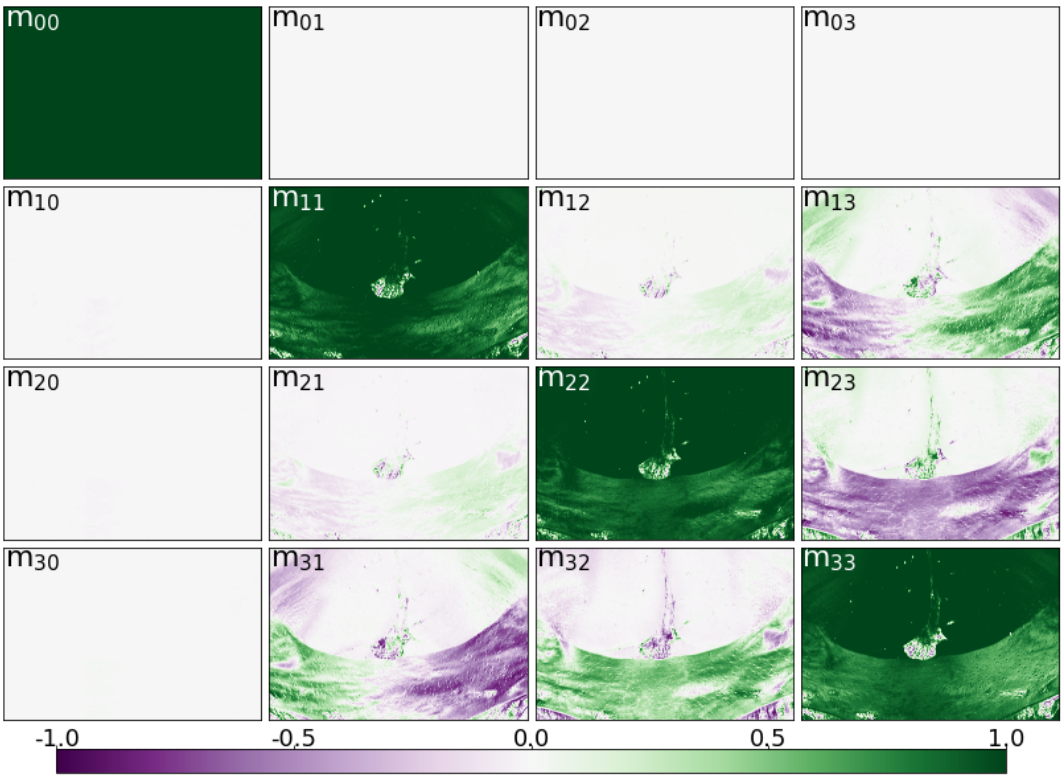

FIGURE B.27: Lu-Chipman retardance matrices for Vervet1818-CC. Each image pixel yields a 4×4 Müller matrix, therefore the subplots visualize 5472×3648 Müller matrices that provide a spatial overview over the sample.

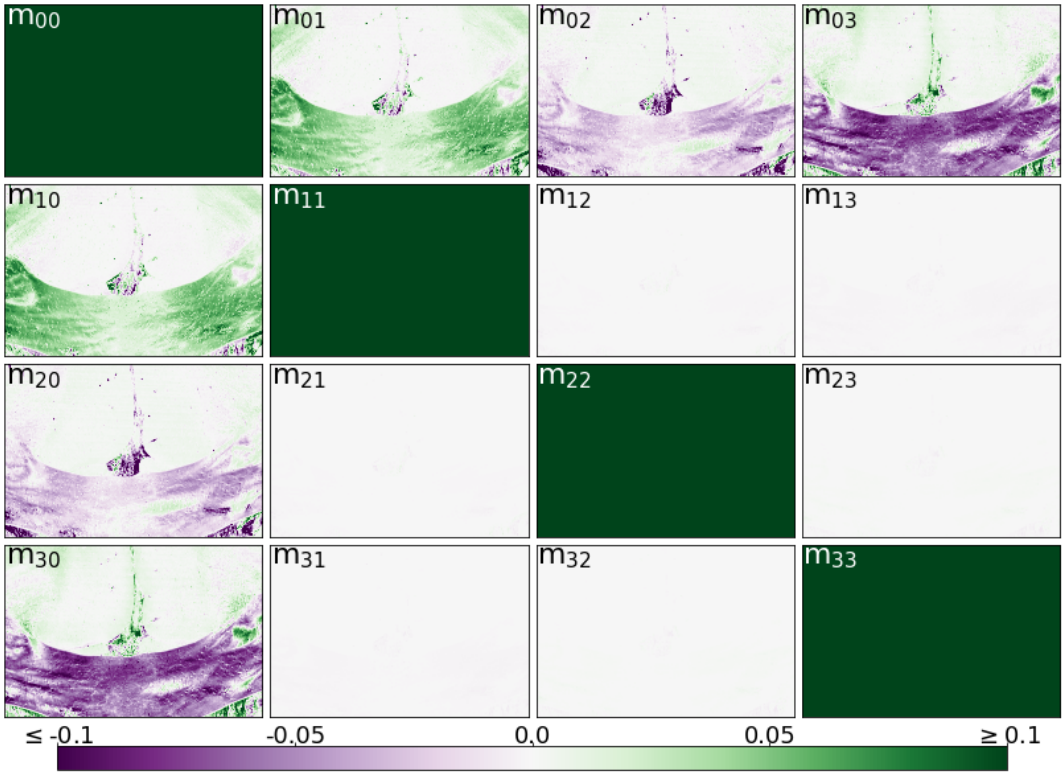

FIGURE B.28: Lu-Chipman diattenuation matrices for Vervet1818-CC. Each image pixel yields a 4×4 Müller matrix, therefore the subplots visualize 5472×3648 Müller matrices that provide a spatial overview over the sample.

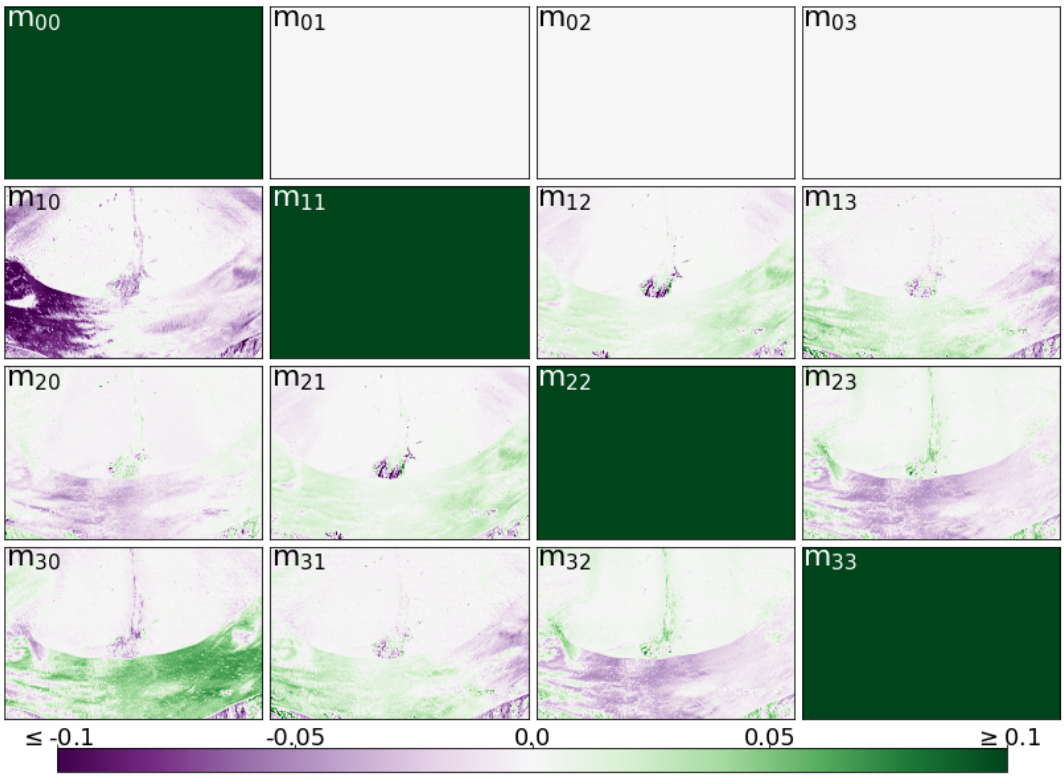

FIGURE B.29: Lu-Chipman depolarization matrices for Vervet1818-CC. Each image pixel yields a 4×4 Müller matrix, therefore the subplots visualize 5472×3648 Müller matrices that provide a spatial overview over the sample.

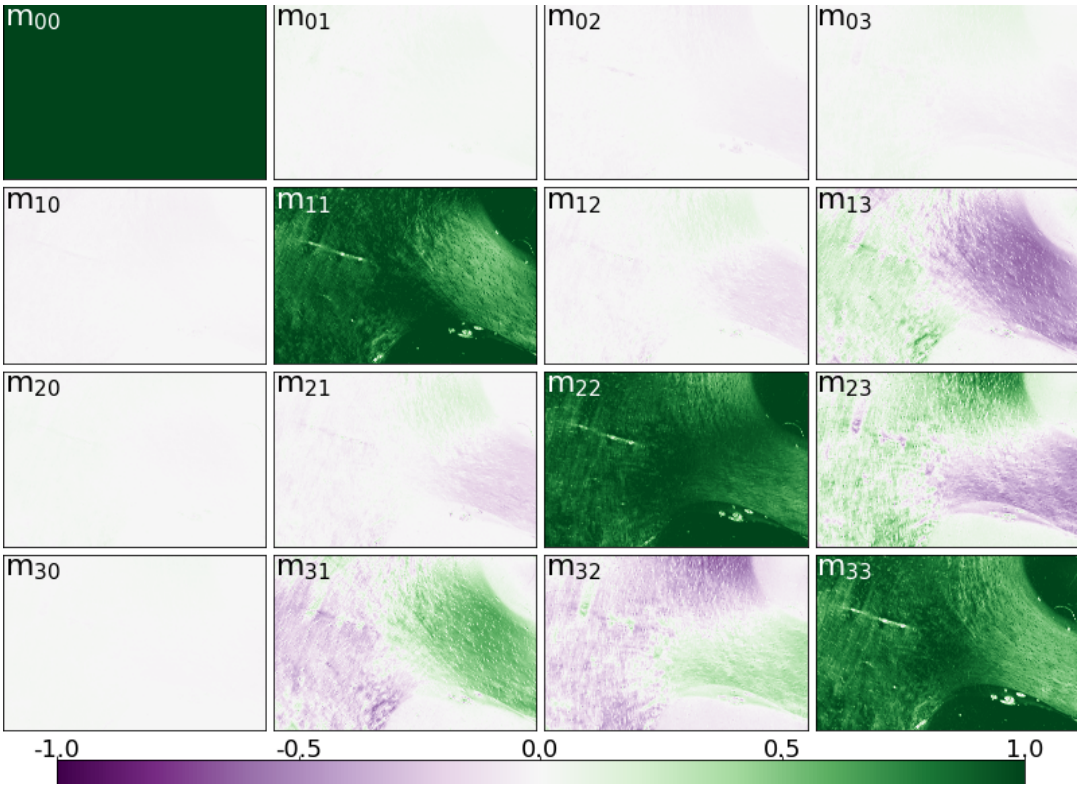

FIGURE B.30: Müller matrices for Vervet1818-CR. Each image pixel yields a 4×4 Müller matrix, therefore the subplots visualize 5472×3648 Müller matrices that provide a spatial overview over the sample.

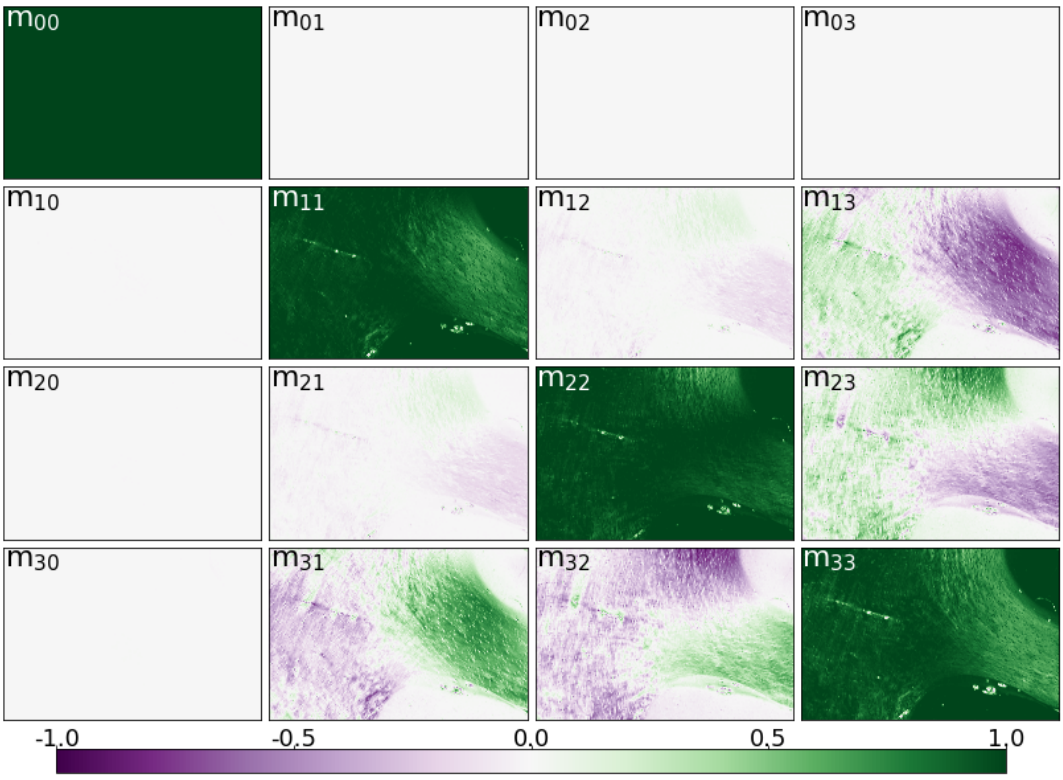

FIGURE B.31: Lu-Chipman retardance matrices for Vervet1818-CR. Each image pixel yields a 4×4 Müller matrix, therefore the subplots visualize 5472×3648 Müller matrices that provide a spatial overview over the sample.

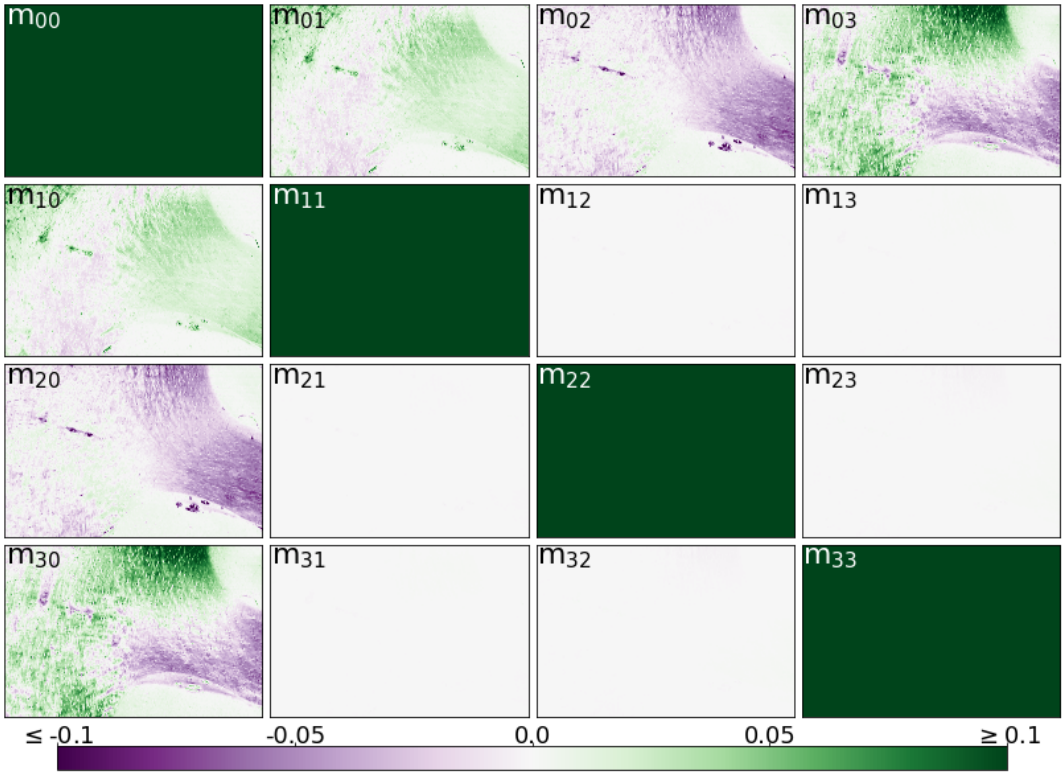

FIGURE B.32: Lu-Chipman diattenuation matrices for Vervet1818-CR. Each image pixel yields a 4×4 Müller matrix, therefore the subplots visualize 5472×3648 Müller matrices that provide a spatial overview over the sample.

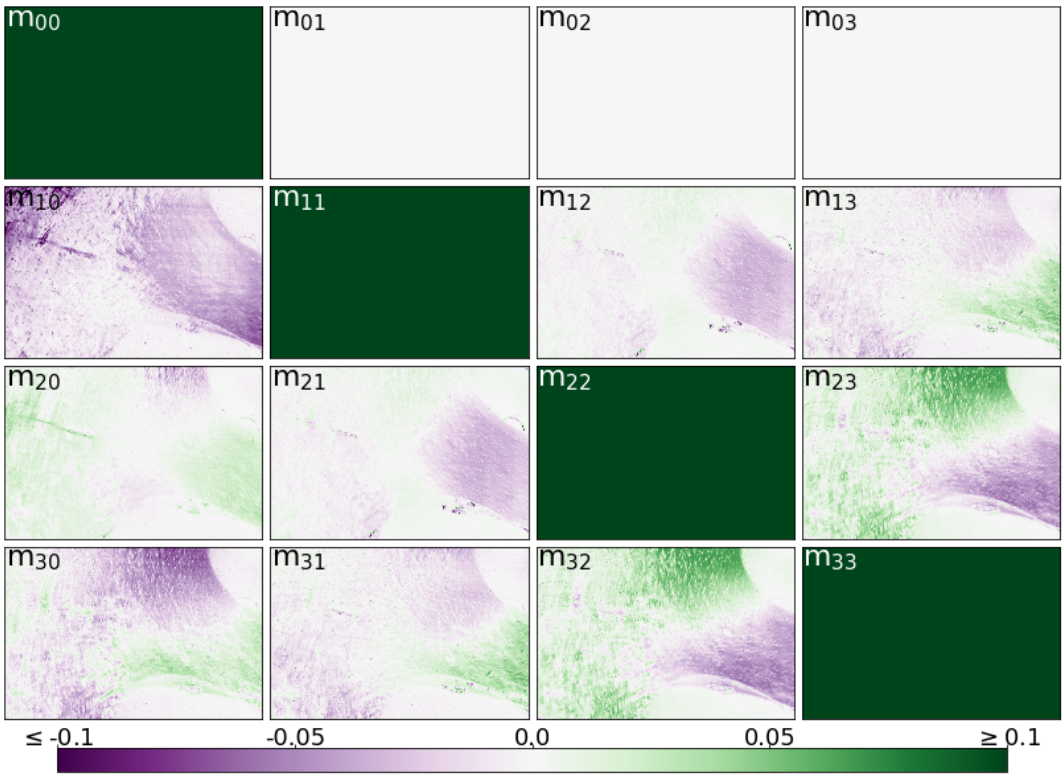

FIGURE B.33: Lu-Chipman depolarization matrices for Vervet1818-CR. Each image pixel yields a 4×4 Müller matrix, therefore the subplots visualize 5472×3648 Müller matrices that provide a spatial overview over the sample.

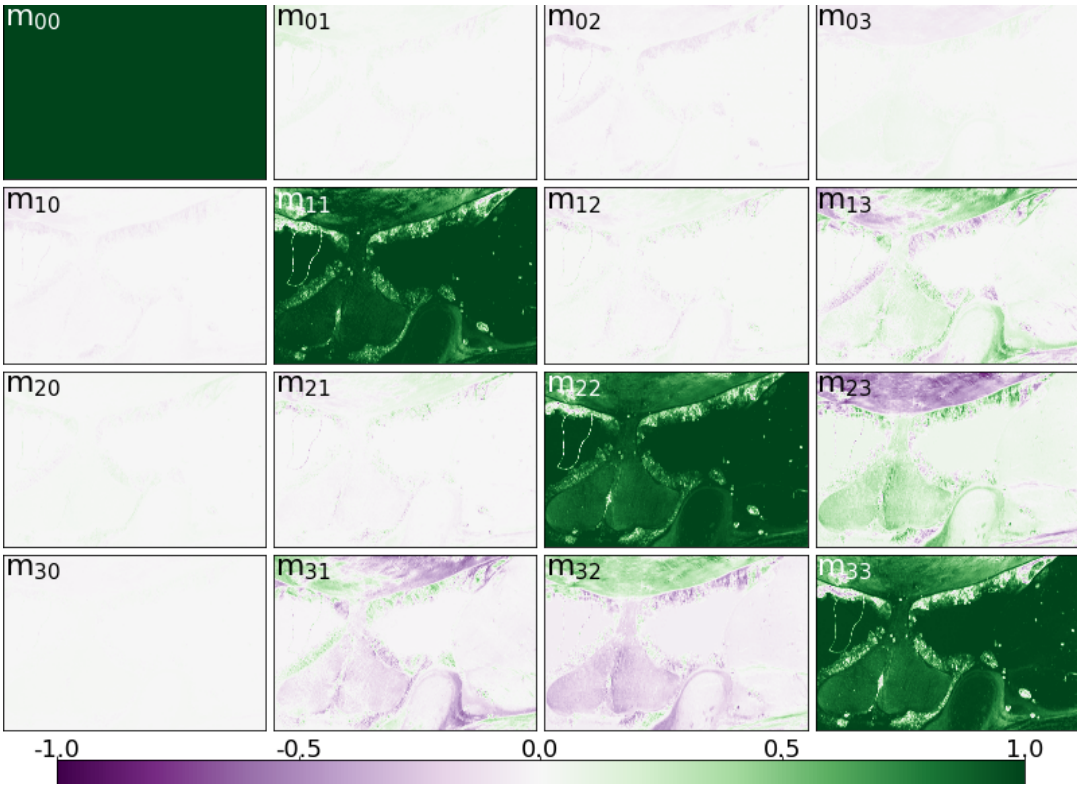

FIGURE B.34: Müller matrices for Vervet1818-FX. Each image pixel yields a 4×4 Müller matrix, therefore the subplots visualize 5472×3648 Müller matrices that provide a spatial overview over the sample.

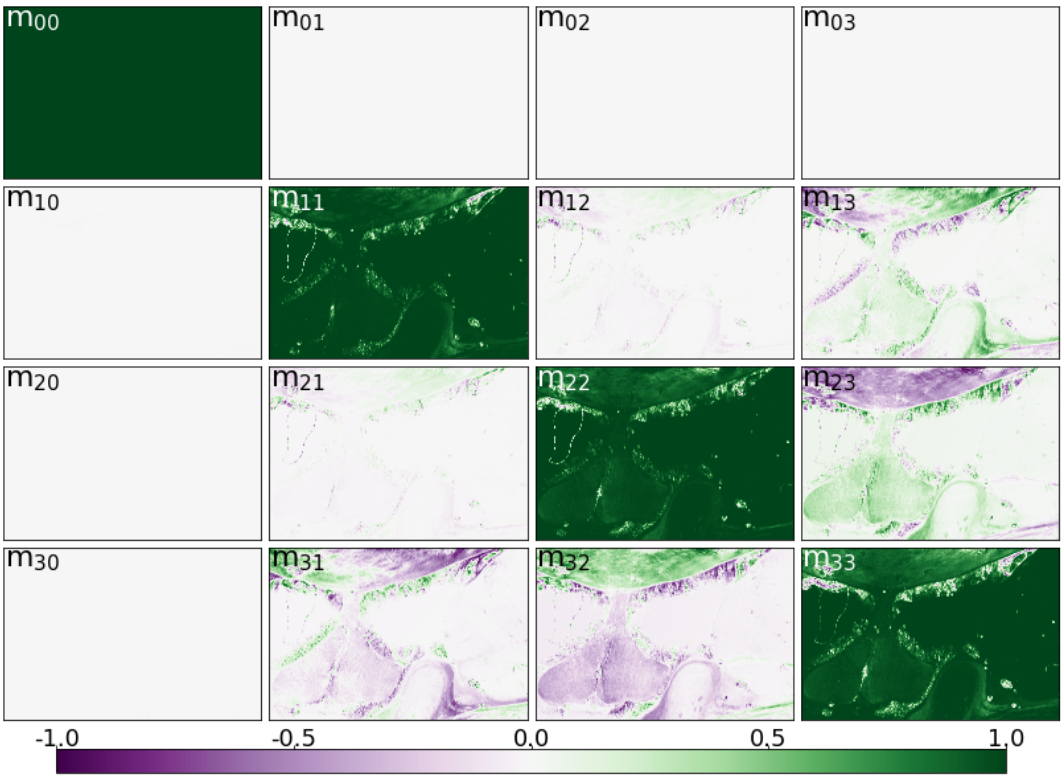

FIGURE B.35: Lu-Chipman retardance matrices for Vervet1818-FX. Each image pixel yields a 4×4 Müller matrix, therefore the subplots visualize 5472×3648 Müller matrices that provide a spatial overview over the sample.

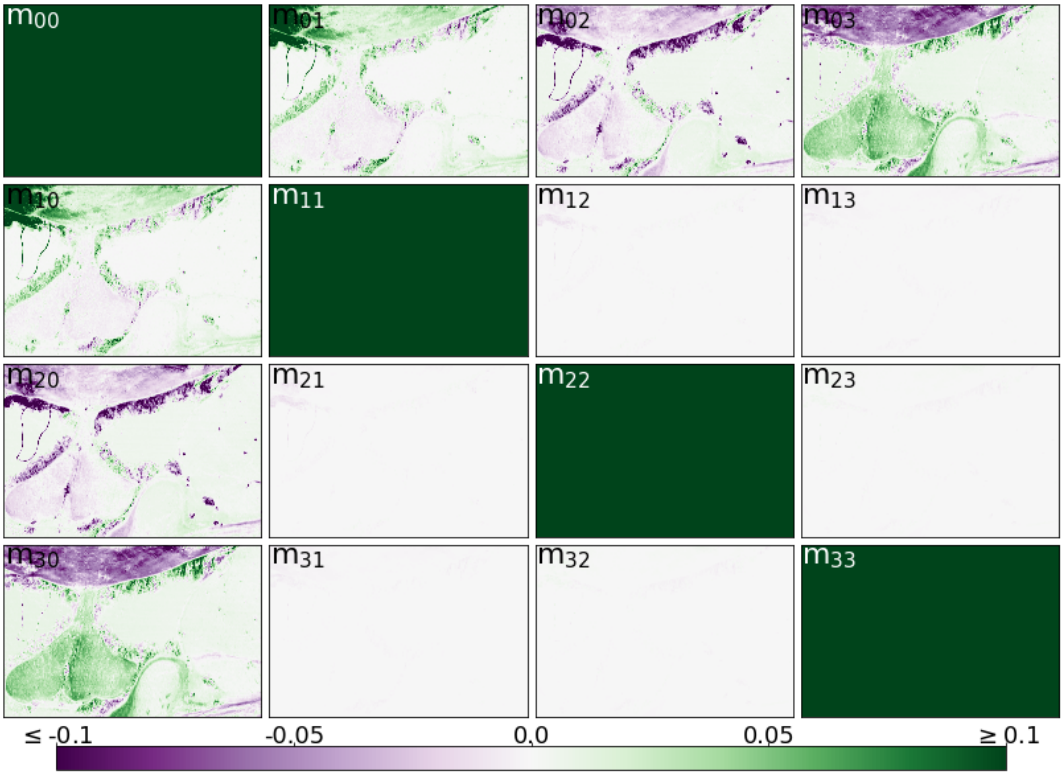

FIGURE B.36: Lu-Chipman diattenuation matrices for Vervet1818-FX. Each image pixel yields a 4×4 Müller matrix, therefore the subplots visualize 5472×3648 Müller matrices that provide a spatial overview over the sample.

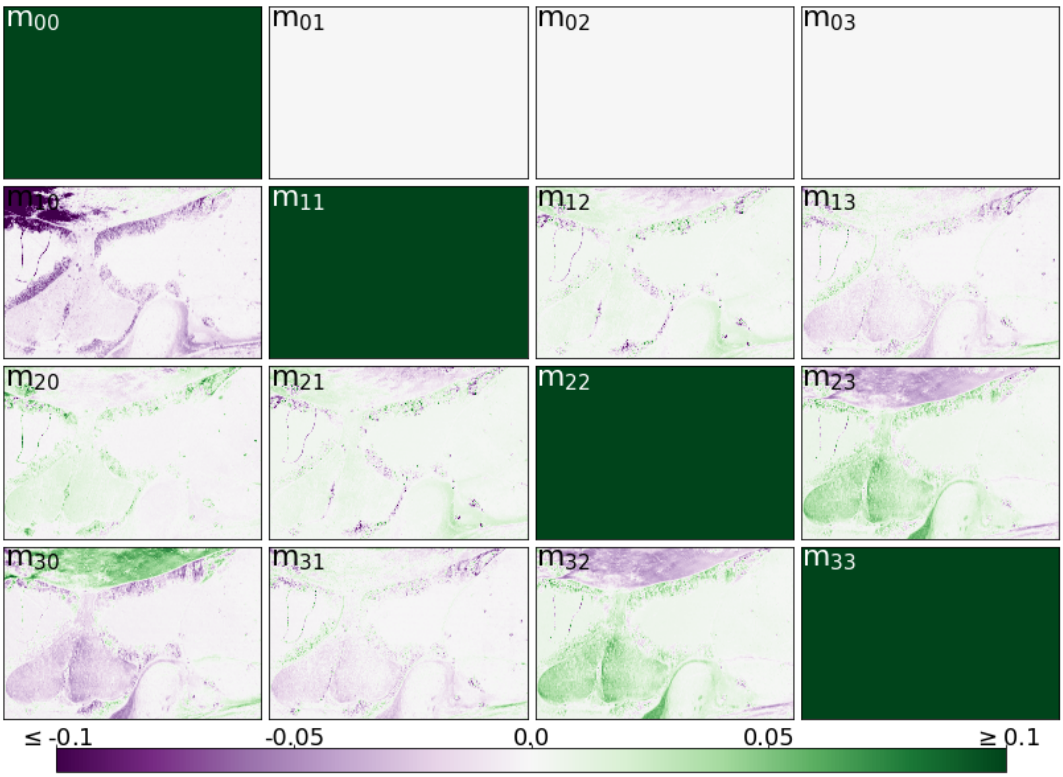

FIGURE B.37: Lu-Chipman depolarization matrices for Vervet1818-FX. Each image pixel yields a 4×4 Müller matrix, therefore the subplots visualize 5472×3648 Müller matrices that provide a spatial overview over the sample.

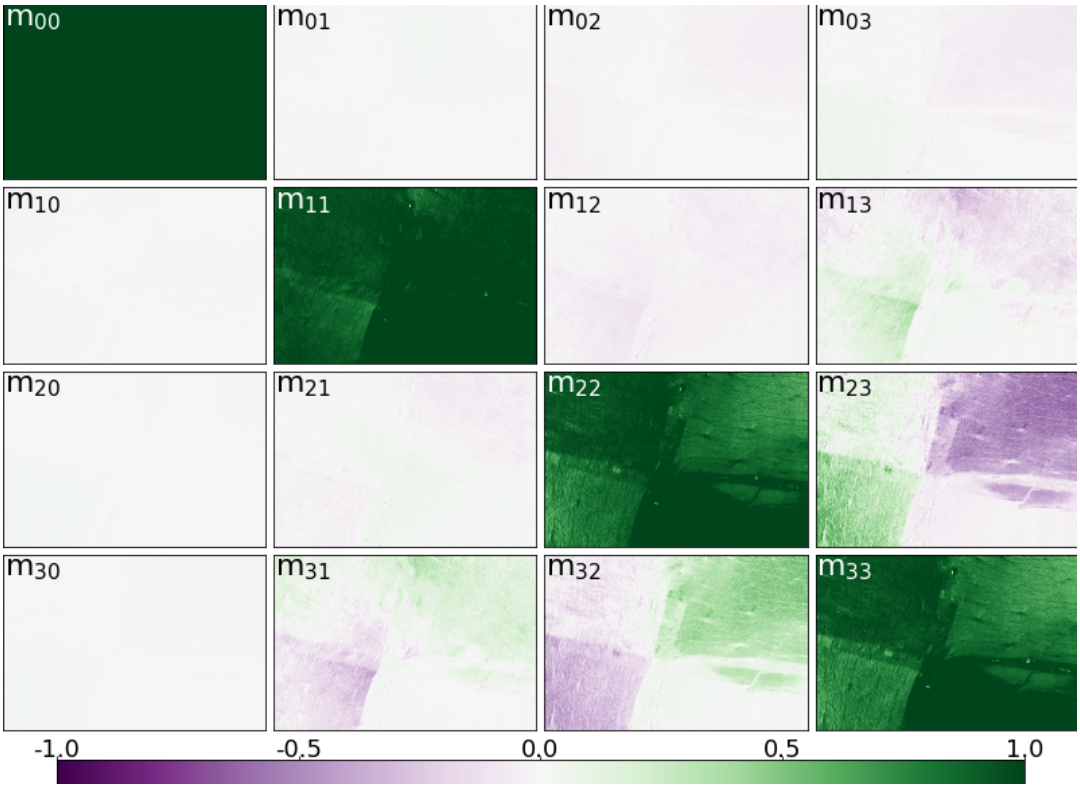

FIGURE B.38: Müller matrices for ChiasmX2-7. Each image pixel yields a 4×4 Müller matrix, therefore the subplots visualize 5472×3648 Müller matrices that provide a spatial overview over the sample.

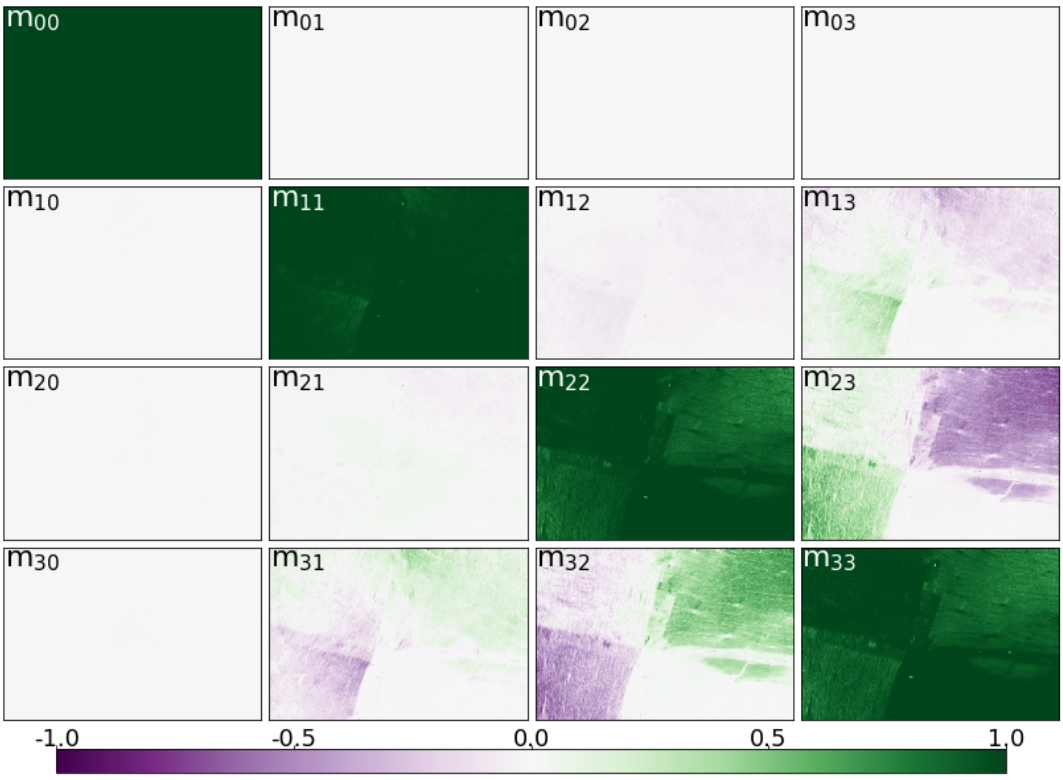

FIGURE B.39: Lu-Chipman retardance matrices for ChiasmX2-7. Each image pixel yields a 4×4 Müller matrix, therefore the subplots visualize 5472×3648 Müller matrices that provide a spatial overview over the sample.

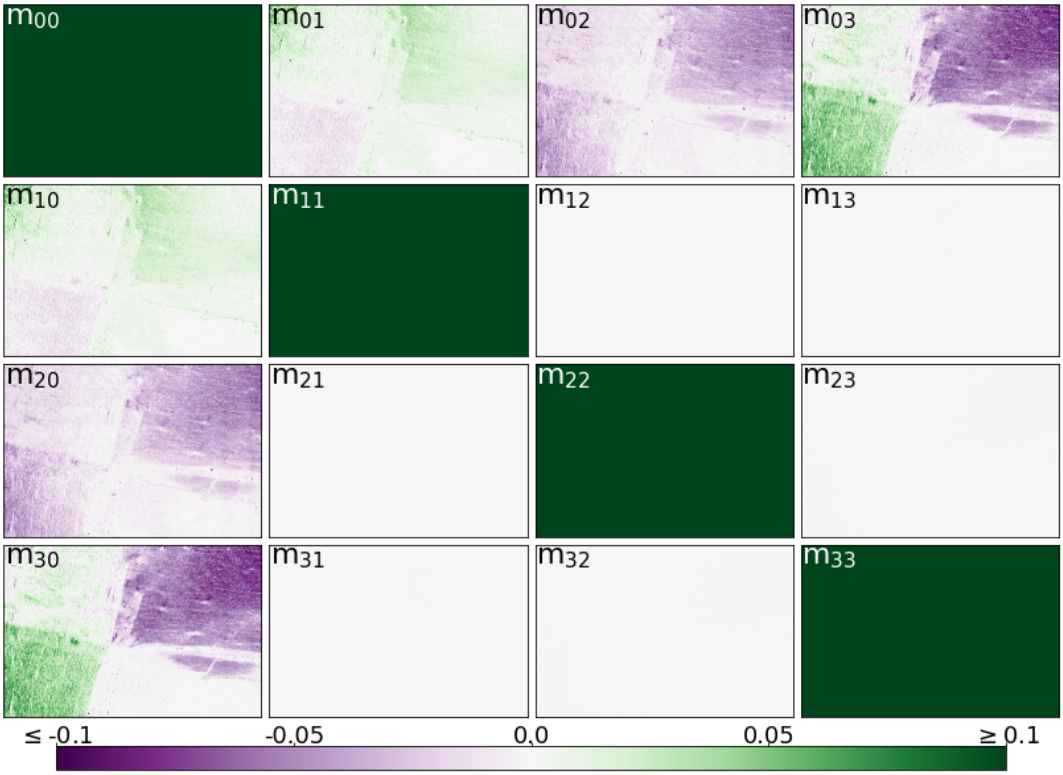

FIGURE B.40: Lu-Chipman diattenuation matrices for ChiasmX2-7. Each image pixel yields a 4×4 Müller matrix, therefore the subplots visualize 5472×3648 Müller matrices that provide a spatial overview over the sample.

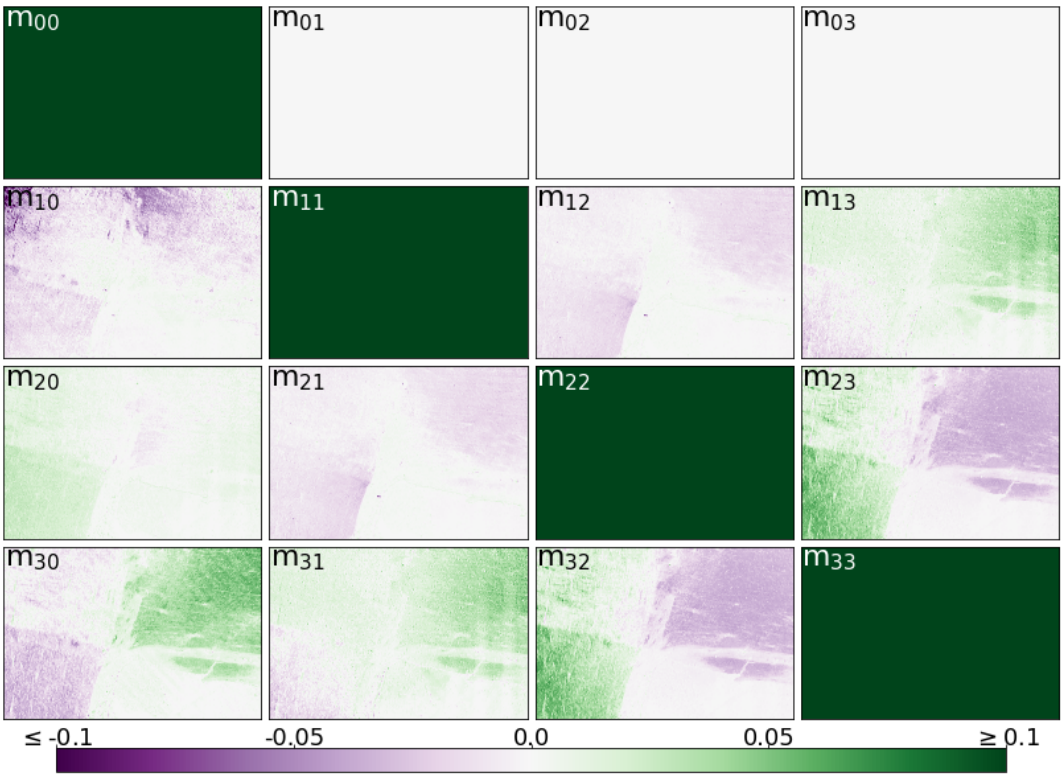

FIGURE B.41: Lu-Chipman depolarization matrices for ChiasmX2-7. Each image pixel yields a 4×4 Müller matrix, therefore the subplots visualize 5472×3648 Müller matrices that provide a spatial overview over the sample.

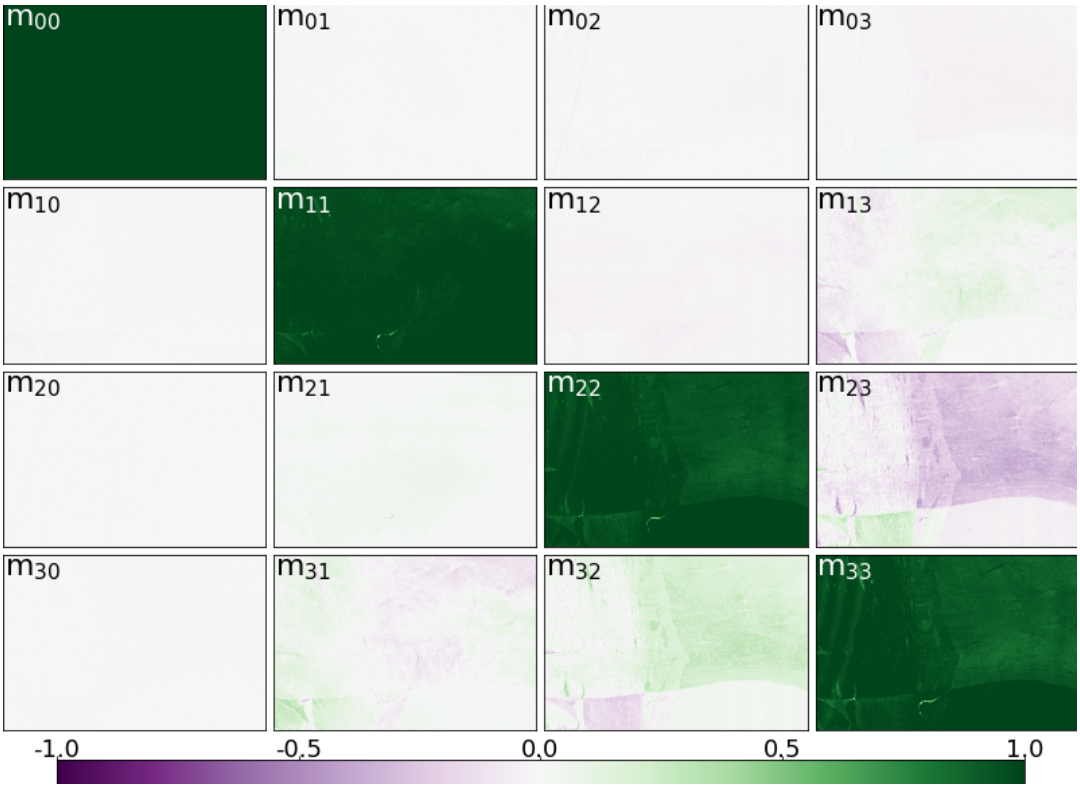

FIGURE B.42: Müller matrices for ChiasmX2-15. Each image pixel yields a 4×4 Müller matrix, therefore the subplots visualize 5472×3648 Müller matrices that provide a spatial overview over the sample.

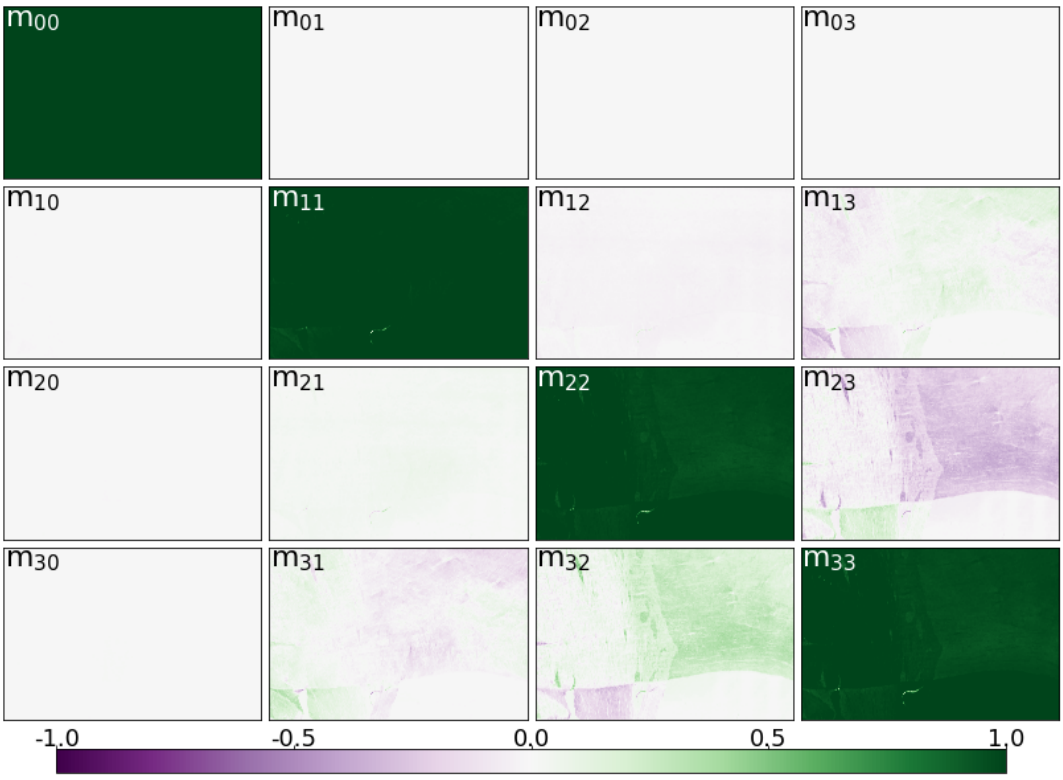

FIGURE B.43: Lu-Chipman retardance matrices for ChiasmX2-15. Each image pixel yields a 4×4 Müller matrix, therefore the subplots visualize 5472×3648 Müller matrices that provide a spatial overview over the sample.

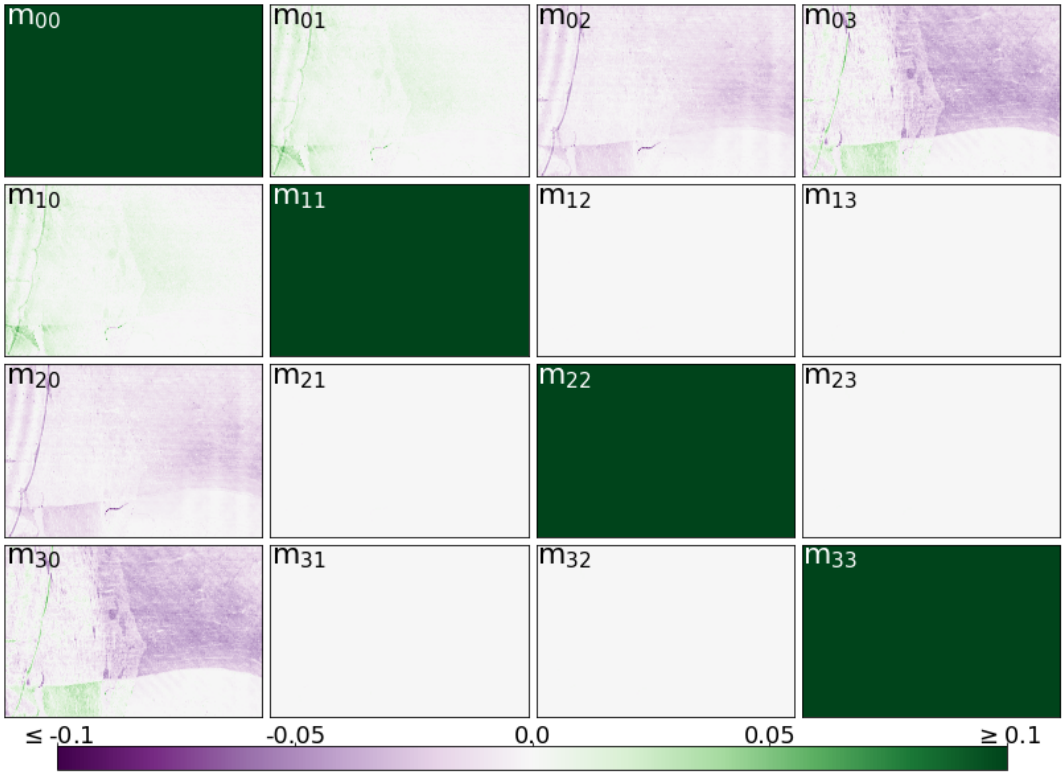

FIGURE B.44: Lu-Chipman diattenuation matrices for ChiasmX2-15. Each image pixel yields a 4×4 Müller matrix, therefore the subplots visualize 5472×3648 Müller matrices that provide a spatial overview over the sample.

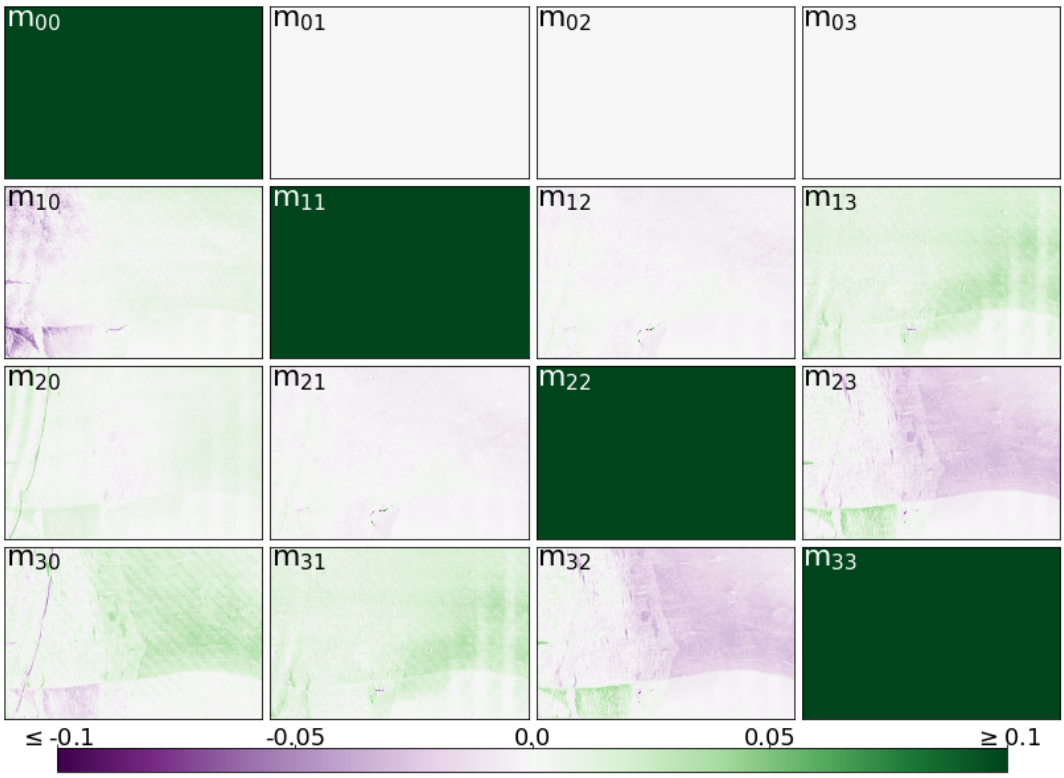

FIGURE B.45: Lu-Chipman depolarization matrices for ChiasmX2-15. Each image pixel yields a 4×4 Müller matrix, therefore the subplots visualize 5472×3648 Müller matrices that provide a spatial overview over the sample.

B.3 Supplementary Figures to Chapter 6

The classification of matter (gray matter, white matter, but also background regions) based on a multi-modal parameter map analysis is introduced in Section 6.1.1. For Broca, there is more than one option to distinguish gray and white matter based on a single parameter map. Below, the identification of gray matter based on the average map from ComSLI and the transmittance map from DI is exemplary displayed. Apart from minor differences for blood vessels and at boundaries between white and gray matter, most identified pixels are similar between the two options.

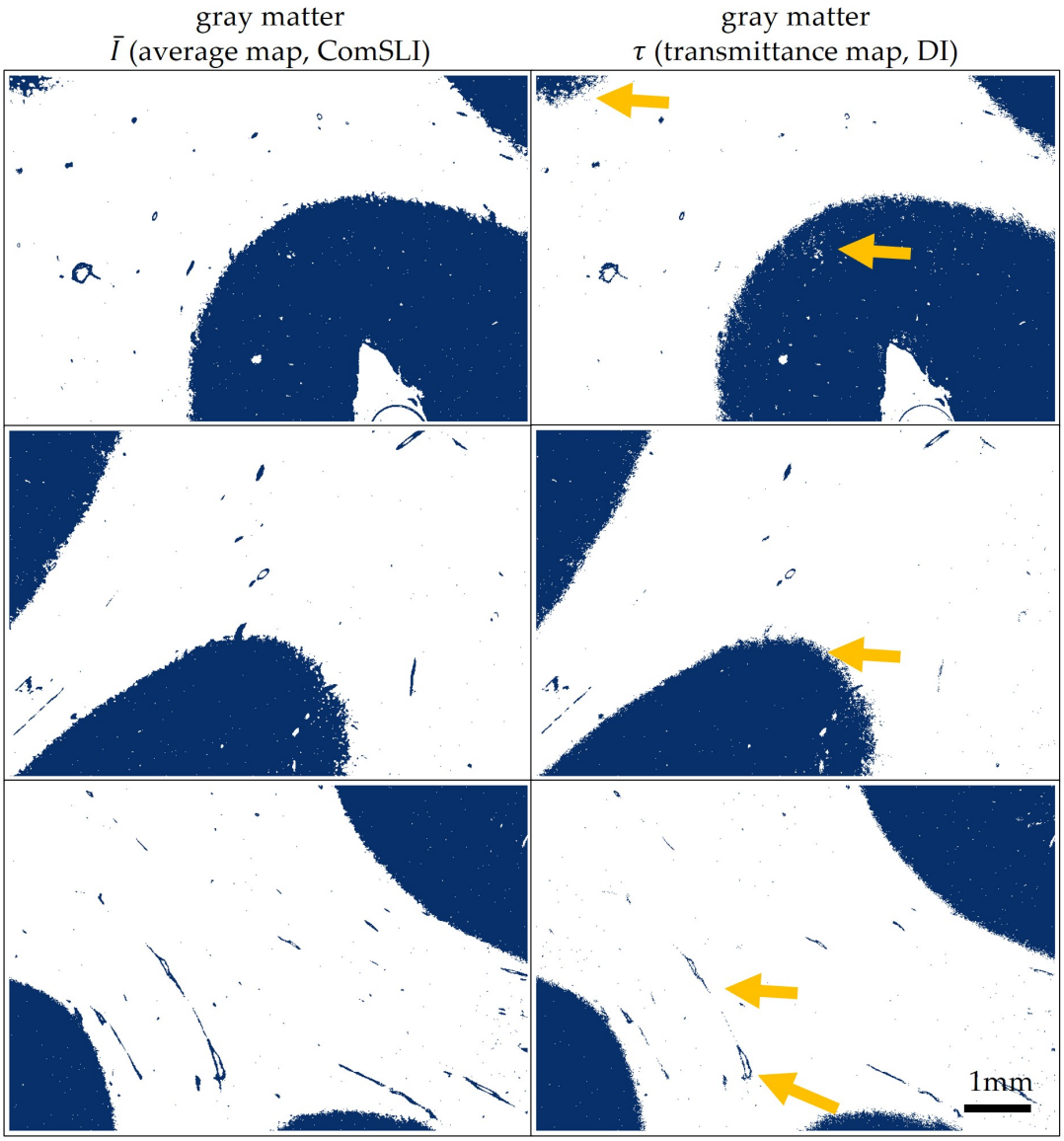

FIGURE B.46: Identification of gray matter by average or transmittance map. Top to bottom: Broca-A, Broca-B, Broca-C. The average map (ComSLI) and the transmittance map (DI) are both suitable for a successful distinction between white and gray matter. The blue pixels indicate the identified gray matter regions. Minor differences are indicated by yellow arrows, especially for blood vessels and at the border between white and gray matter.

As a proof-of-principle, the identification of different fiber configurations in Broca and Vervet1818 is demonstrated in Section 6.1.2. The fiber classification for Broca and Vervet1818 is based on the peak prominence from ComSLI and the retardation obtained from 3D-PLI. Below, these parameter maps are depicted next to each other to highlight differences and similarities.

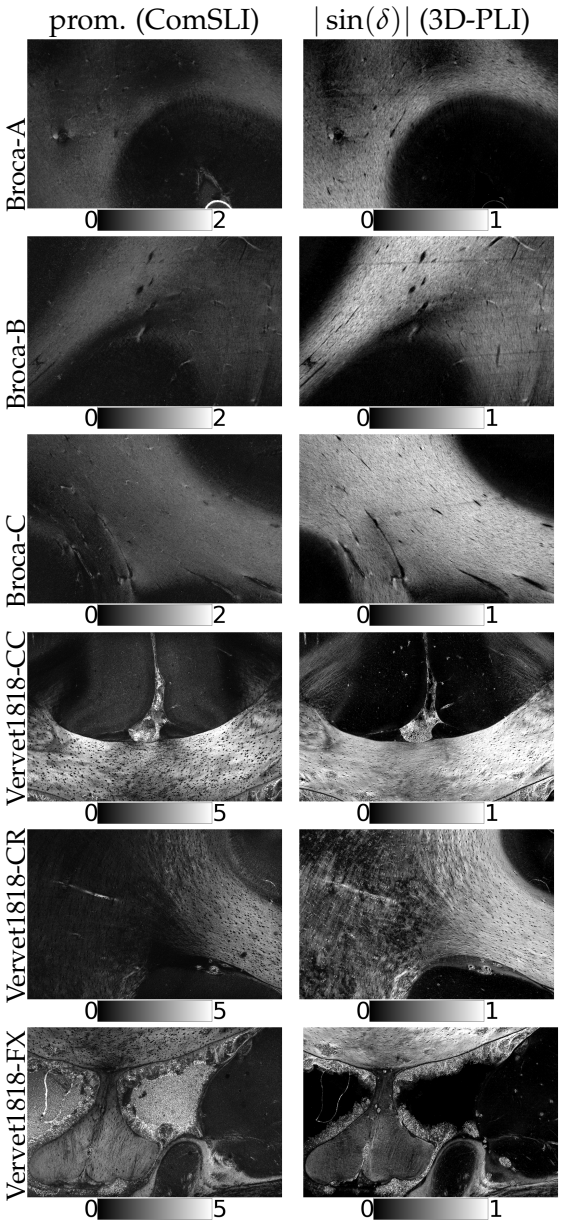

FIGURE B.47: Parameter maps for fiber classification. From left to right: Peak prominence (prom.) obtained with ComSLI, retardation $|\sin(\delta)|$ from 3D-PLI. From top to bottom: Broca-A, Broca-B, Broca-C, Vervet1818-CC, Vervet1818-CR, Vervet1818-FX. In-plane parallel fibers, inclined fibers, steep fibers, and crossing fibers exhibit a set of unique optical properties across various parameter maps.

Section 6.1.2 introduces a matter and fiber classification for Broca and Vervet1818 based on various multi-modal parameter maps. Here, the corresponding classification is shown for the artificial fiber crossings ChiasmX2-7 and ChiasmX2-15. Those two samples do not contain any gray matter areas, only white matter and background areas. Crossings can be separated from parallel fibers for many image pixels pixels.

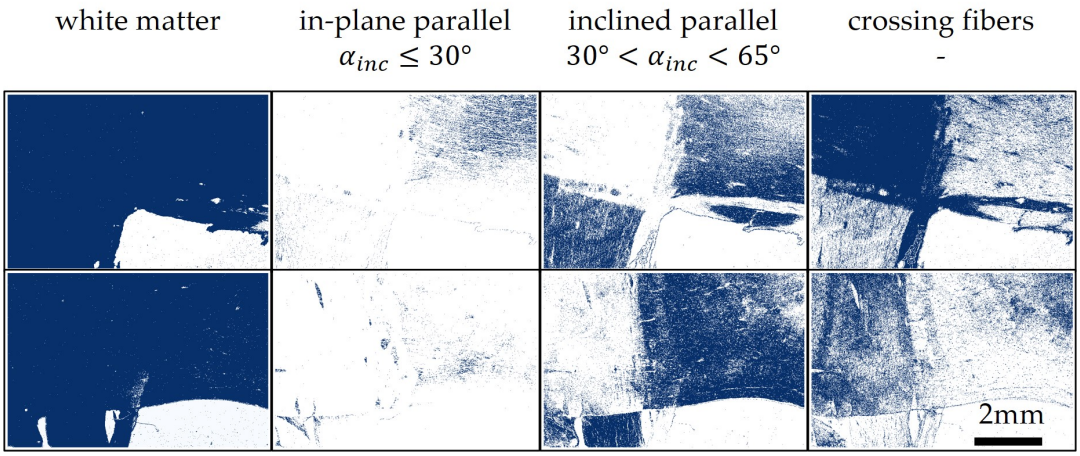

FIGURE B.48: Classification of white matter fibers for ChiasmX2-7 and ChiasmX2-15. The identified pixels for the identified fiber structures are displayed in blue, respectively, for ChiasmX2-7 (top) and ChiasmX2-15 (bottom). Both artificially assembled samples only contain white matter and background areas, therefore, the detection of gray matter is skipped during matter classification. Inclined fibers are identified by setting the threshold for peak prominence to ≥ 0.8. Steep fibers, defined by $\bar{I} > 800$, are not present in the artificial crossing, so this threshold only indirectly affects the identification of crossing fibers.

Section 6.3 explores the complex correlation between the fiber inclination (out-of-plane angle) and the peak distance as determined in ComSLI. The fiber inclination is calculated from the retardance which can be determined from either Müller polarimetry or from 3D-PLI. Here, the results from both techniques are compared for all investigated samples. Major differences occur where Müller polarimetry has not retrieved any signal, mostly in Broca. Otherwise, differences are usually below $\Delta\alpha_{\text{inc}} = 20°$.

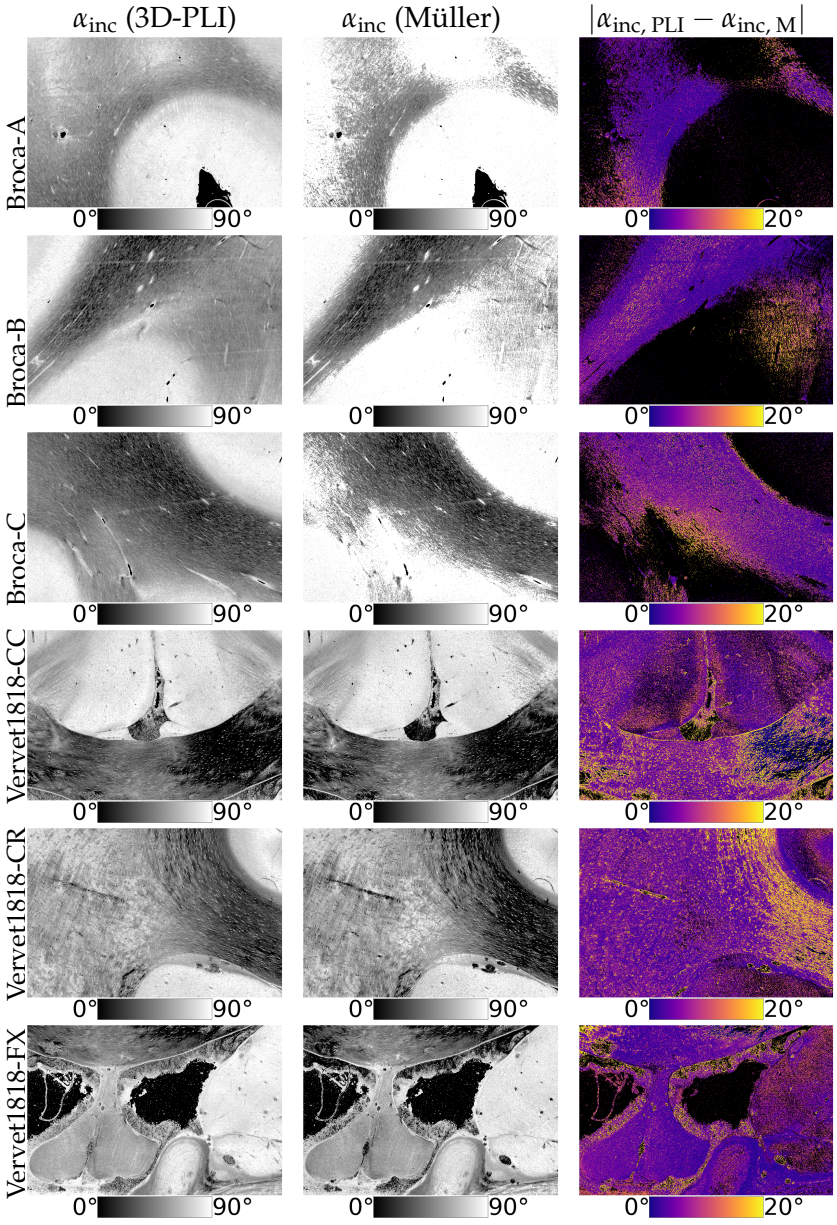

FIGURE B.49: Inclination Maps from 3D-PLI and Müller polarimetry. From top to bottom:Broca-A, Broca-B, Broca-C, Vervet1818-CC, Vervet1818-CR, Vervet1818-FX. From left to right: Inclination α_{inc} measured with 3D-PLI, inclination α_{inc} obtained from Müller polarimetry, absolute difference between the inclination angles from 3D-PLI and Müller polarimetry $|\alpha_{\text{inc, PLI}} - \alpha_{\text{inc, M}}|$.

The correlation between peak distance and inclination is depicted for Broca and Vervet1818. The thinout border is only indicated for Broca-A, Broca-B, and Broca-C where it is very distinct, and for Vervet1818-FX as discussed in Section 6.3.1.

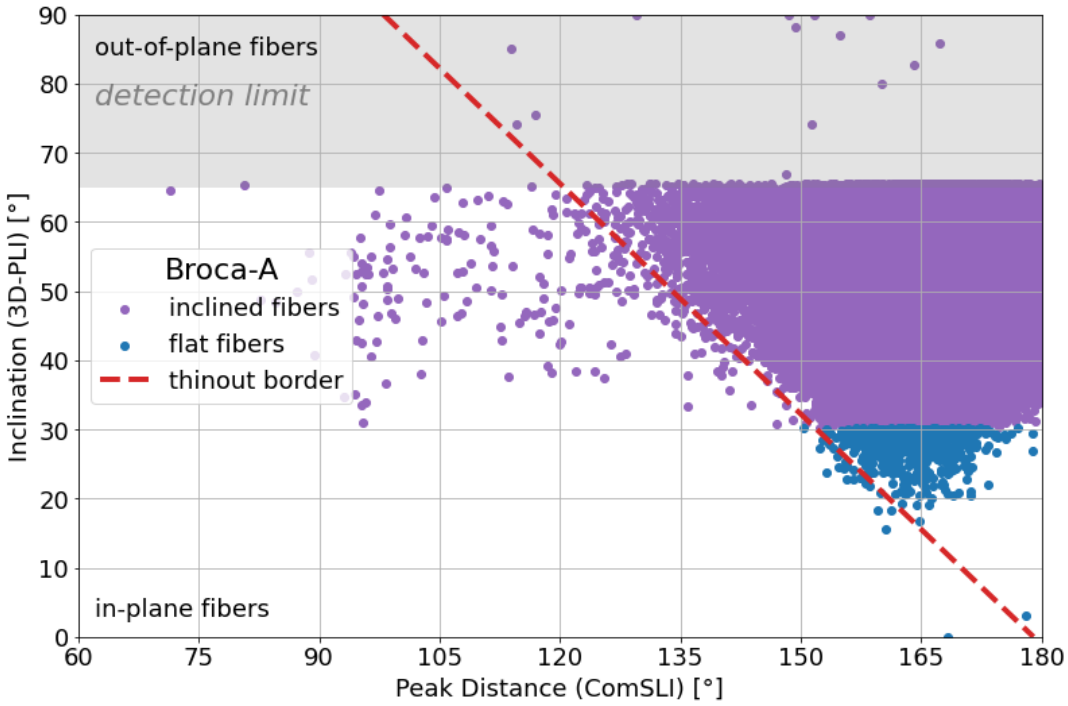

FIGURE B.50: Peak distance correlation for Broca-A. The peak distance and inclination of the investigated image pixels are plotted in a two-dimensional distribution. For visualization purposes, only every 50-th image pixel is shown. Only image pixels for parallel fibers in white matter are taken into account. This approach excludes fiber crossing, gray matter and background areas. The thinout border is very distinct. Beyond the detection limit, the retardation is (mostly) too low to be detected.

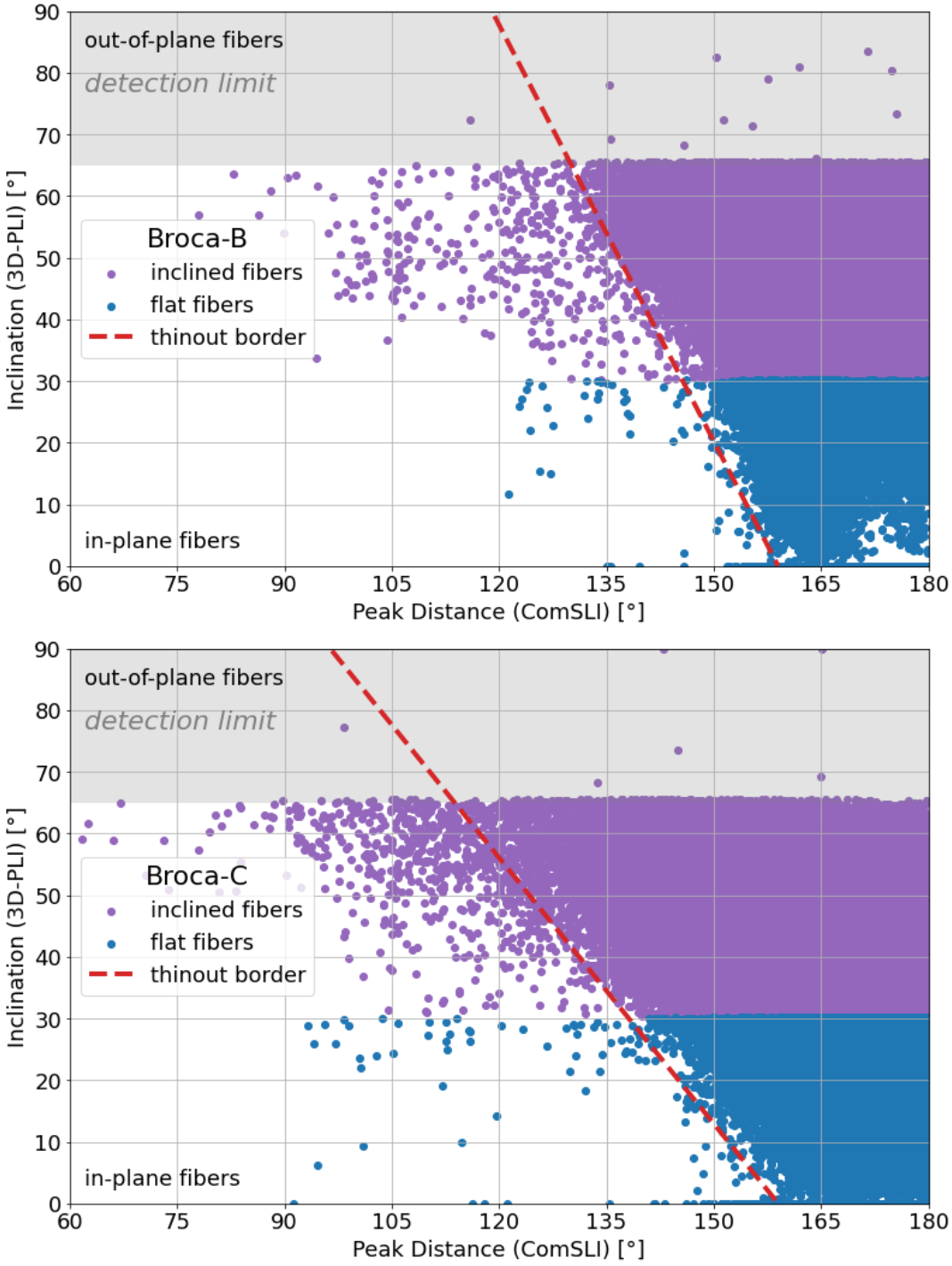

FIGURE B.51: Peak distance correlation for Broca-B and Broca-C. The peak distance and inclination of the investigated image pixels are plotted in a two-dimensional distribution. For visualization purposes, only every 50-th image pixel is shown. Only image pixels for parallel fibers in white matter are taken into account. This approach excludes fiber crossing, gray matter and background areas. The thinout border is very distinct. Beyond the detection limit, the retardation is (mostly) too low to be detected.

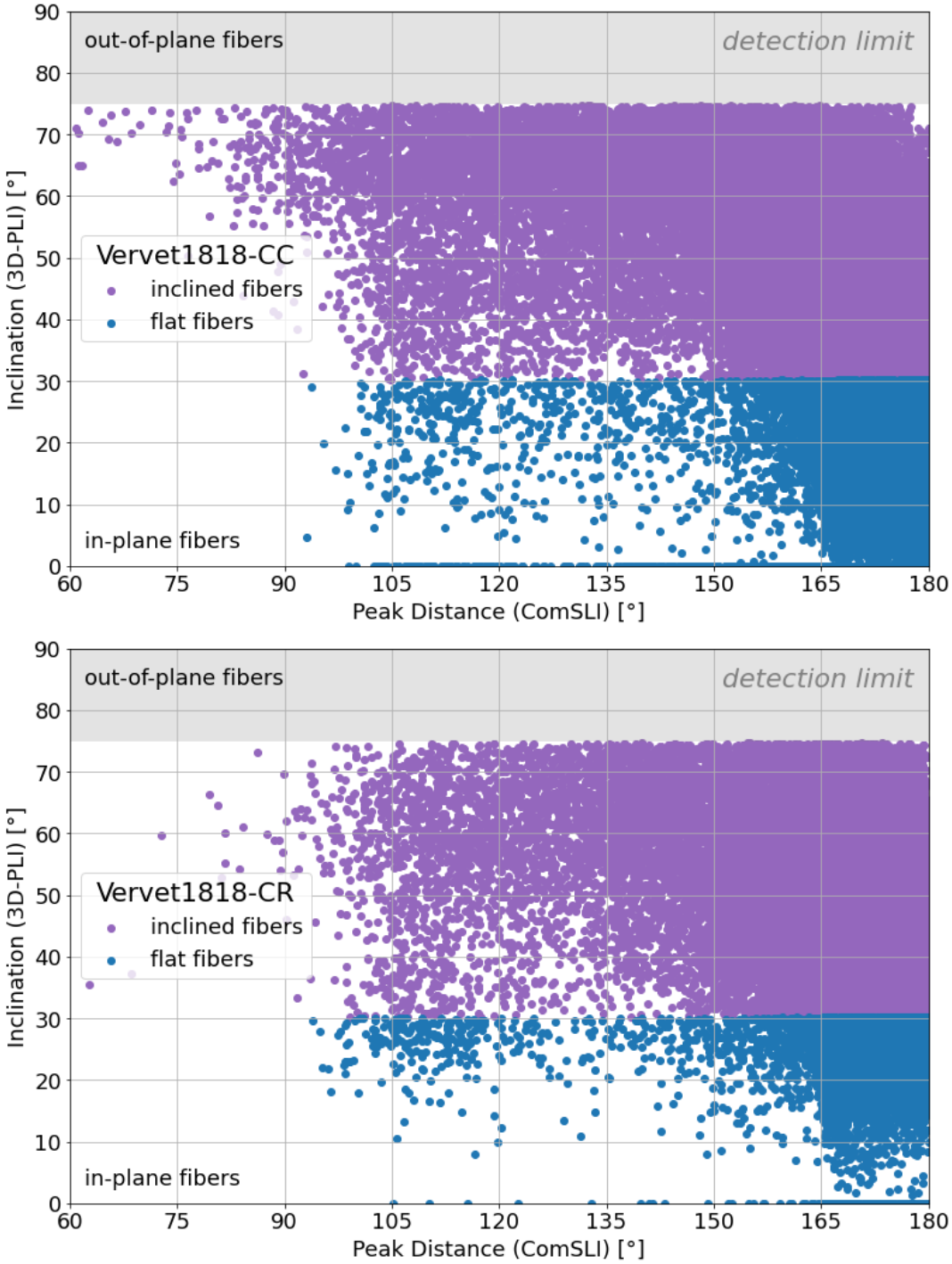

FIGURE B.52: Peak distance correlation for Vervet1818-CC and Vervet1818-CR. The peak distance and inclination of the investigated image pixels are plotted in a two-dimensional distribution. For visualization purposes, only every 50-th image pixel is shown. Only image pixels for parallel fibers in white matter are taken into account. This approach excludes fiber crossing, gray matter and background areas. The thinout border is less distinct (yet observable) and therefore not indicated. Beyond the detection limit, the retardation is too low to be detected.

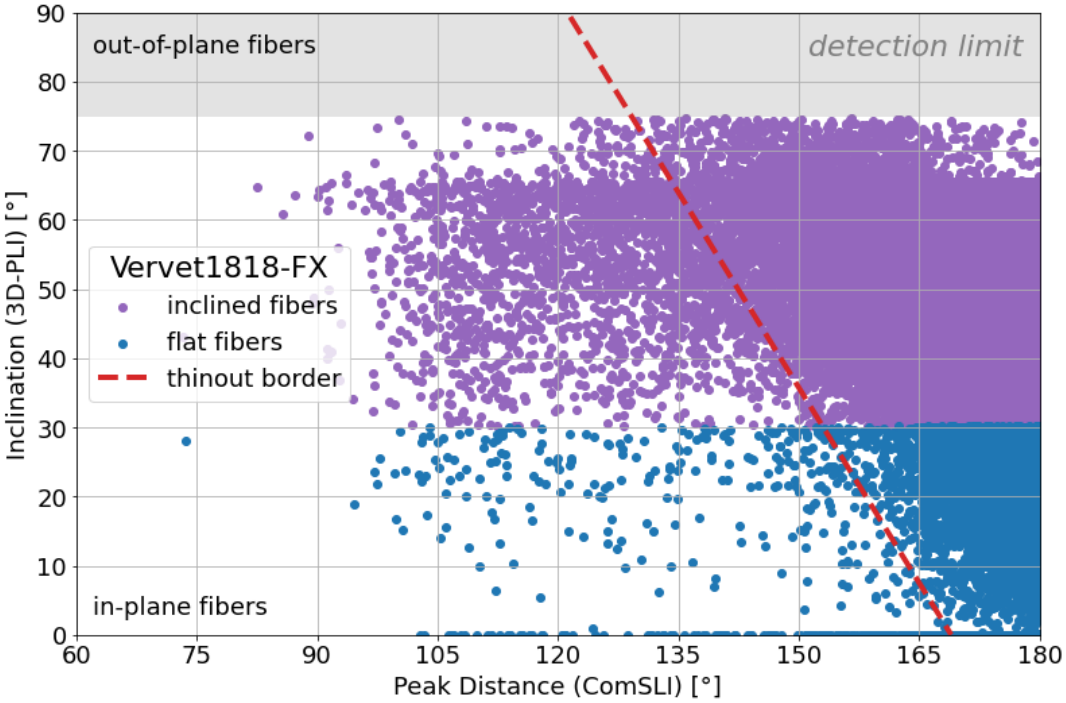

FIGURE B.53: Peak distance correlation for Vervet1818-FX. The peak distance and inclination of the investigated image pixels are plotted in a two-dimensional distribution. For visualization purposes, only every 50-th image pixel is shown. Only image pixels for parallel fibers in white matter are taken into account. This approach excludes fiber crossing, gray matter and background areas. The thinout border is indicated as illustrated in Section 6.3.1. Beyond the detection limit, the retardation is too low to be detected.

Appendix C

Supplementary Data Sheets

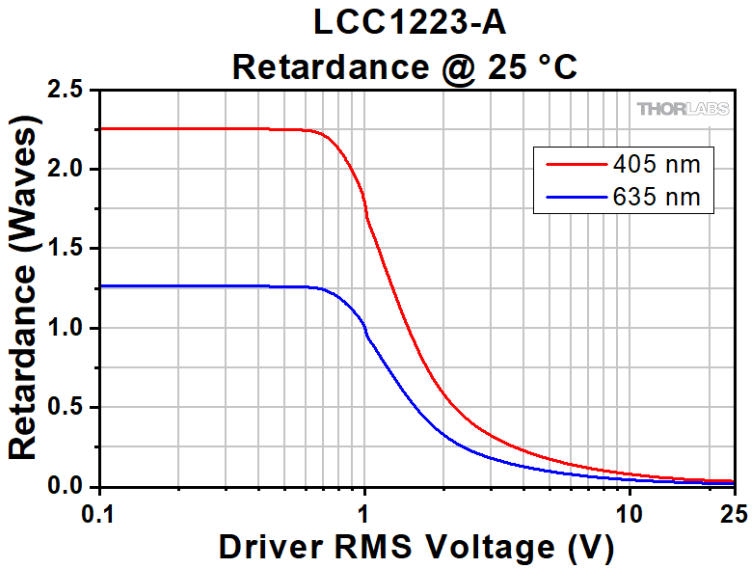

FIGURE C.1: Retardance voltage curve of LCVR. The LCVR is operated at a wavelength of 520 nm. Taken from thorlabs.com [189].

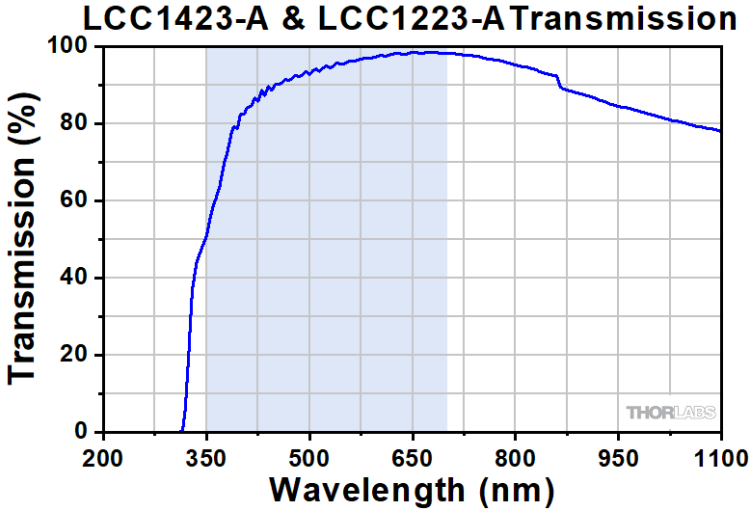

FIGURE C.2: Wavelength-dependent transmission curve of LCVR. The LCVR is operated at a wavelength of 520 nm. Taken from thorlabs.com [189].

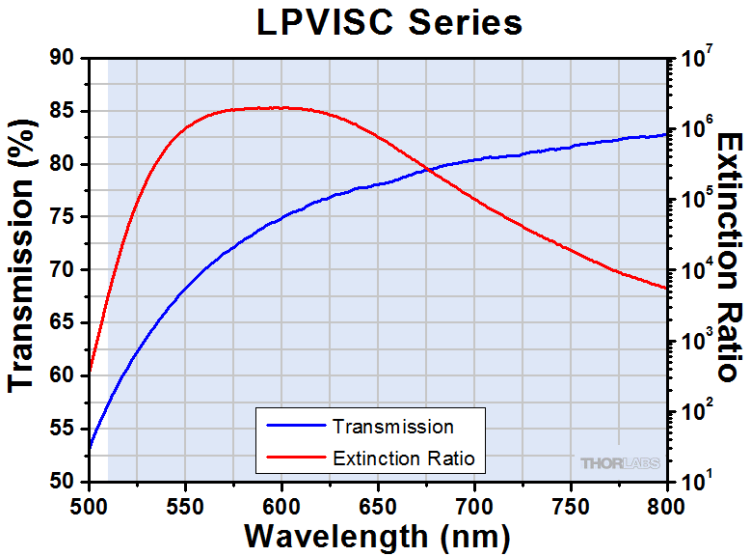

FIGURE C.3: Wavelength-dependent transmission curve of linear polarizer filter (LP). The LP is operated at a wavelength of 520 nm. Taken from thorlabs.com [189].

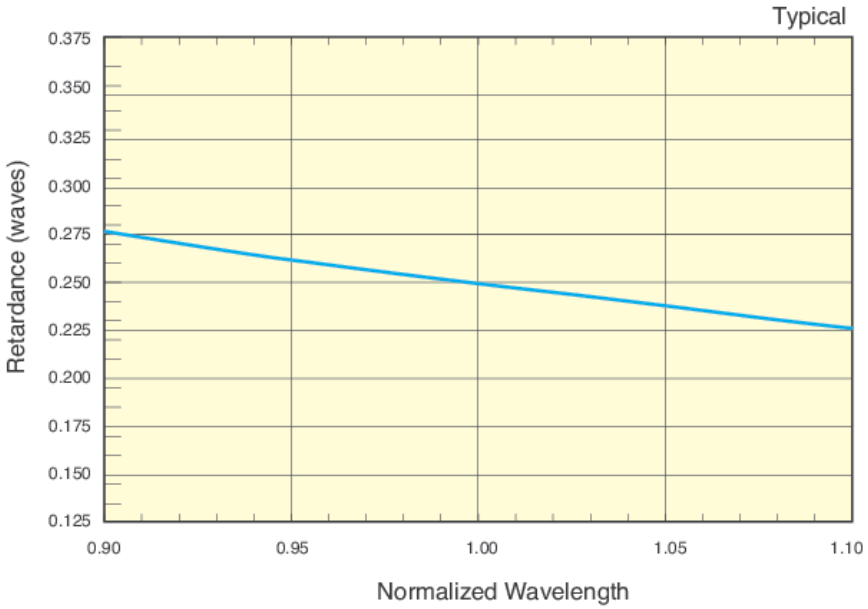

FIGURE C.4: Wavelength-dependent retardance of zero-order quarter-wave plate (QWP). The QWP is operated at a wavelength of 520 nm. Taken from newport.com [134].

Uncompensated Full-Wave LC Retarders

Item #	LCC1513-A	LCC1223-A	LCC1513-B	LCC1223-B	LCC1513-C	LCC1223-C	LCC1113-D	LCC1113-MIR
Wavelength Range	350 - 700 nm[a]		650 - 1050 nm		1050 - 1700 nm		1650 - 3000 nm	3600 - 5600 nm
Retardance Range	~30 nm to >λ							
Clear Aperture	Ø10 mm	Ø20 mm	Ø10 mm	Ø20 mm	Ø10 mm	Ø20 mm	Ø10 mm	Ø10 mm
Housing Outer Dimensions	Ø1"[b] (Ø25.4 mm)	Ø2"[c] (Ø50.8 mm)	Ø1"[b] (Ø25.4 mm)	Ø2"[c] (Ø50.8 mm)	Ø1"[b] (Ø25.4 mm)	Ø2"[c] (Ø50.8 mm)	Ø1"[b] (Ø25.4 mm)	Ø1"[b] (Ø25.4 mm)
Liquid Crystal Material	Nematic Liquid Crystal							
Surface Quality	40-20 Scratch-Dig						60-40 Scratch-Dig	
Parallelism	<5 arcmin							
Switching Time (Rise/Fall, Typical)[d]	16.60 ms / 0.35 ms @ 25 °C, 635 nm	59.6 ms / 1.45 ms @ 25 °C, 635 nm	28.00 ms / 0.69 ms @ 25 °C, 780 nm	124 ms / 2.94 ms @ 25 °C, 780 nm	65.03 ms / 1.46 ms @ 25 °C, 1550 nm	236 ms / 4.89 ms @ 25°C, 1550 nm	586 ms / 7 ms @ 25.6 °C, 2200 nm	4.4 s / 94 ms @ 25.6 °C, 4400 nm
Operating Voltage (Max)[e]	25 V							
Damage Threshold, Pulsed (ns)	2.04 J/cm² (532 nm, 10 Hz, 8 ns, Ø200 µm)		3.56 J/cm² (810 nm, 10 Hz, 7.6 ns, Ø234 µm)		2.5 J/cm² (1542 nm, 10 Hz, 10 ns, Ø458 µm)		0.082 J/cm² (2000 nm, 10 Hz, 6.5 ns, Ø292 µm)	N/A
Damage Threshold, Pulsed (fs)	0.024 J/cm² (532 nm, 100 Hz, 76 fs, Ø162 µm)		0.023 J/cm² (800 nm, 100 Hz, 36.4 fs, Ø189 µm)		0.161 J/cm² (1550 nm, 100 Hz, 70 fs, Ø145 µm)		0.05 J/cm² (2000 nm, 100 Hz, 100 fs, Ø220 µm)	N/A
AR Coating	R_{avg} < 0.5%[f]							R_{avg} < 1.0%[f]
Wavefront Distortion	≤λ/4 (@ 635 nm)						-	
Retardance Uniformity (RMS)[g]	<λ/50 @ 400 nm		<λ/50 @ 650 nm		<λ/50 @ 1050 nm		<λ/10 @ 1650 nm	<λ/10 @ 3600 nm
Housing Thickness	8.0 mm (0.32")	13 mm (0.51")	8.0 mm (0.32")	13 mm (0.51")	8.0 mm (0.32")	13 mm (0.51")	8.0 mm (0.32")	8.0 mm (0.32")
Storage Temperature	-30 to 70 °C							
Operation Temperature	-20 to 45 °C							

a. Liquid crystal is more susceptible to damage when exposed to light sources close to UV wavelengths. Our tests show that our liquid crystal variable retarders deteriorate when exposed to a 395 nm, 6 W/cm² light source for four hours. Using a 365 nm, 40 mW/cm² light source, damage occurs within 15 minutes. We recommend using this product with light sources having wavelengths of 400 nm or longer. For use with shorter wavelengths, power should be kept low and exposure duration limited. The shorter the wavelength, the more susceptible the liquid crystal is to damage.
b. Recommended Mounts: RSP1 (RSP1/M), CRM1T (CRM1T/M), CRM1PT (CRM1PT/M)
c. Recommended Mounts: RSP2 (RSP2/M), LCRM2 (LCRM2/M)
d. Switching speed is highly dependent on several factors, including voltage change and cell temperature. See the *Switching Time* tab for more details.
e. Voltages greater than 25 V can damage the device. See the Performance Tab for device-specific voltage recommendations.
f. At Both Air-to-Glass Surfaces for the Specified Wavelength Range.
g. Specified Over the Entire Clear Aperture

FIGURE C.5: Datasheet of uncompensated full-wave LCVR. Within the context of this thesis, model LCC1223-A is used. Taken from thorlabs.com [189].

Appendix D

Publications

The papers and proceedings published in the scope of this doctoral thesis are listed in chronological order, along with a brief summary of their content and the authors' contributions. The authors' contributions were adapted from the respective publications, where available. Chapters in which these publications have been referenced or incorporated are indicated in the following.

[61] Micron-resolution fiber mapping in histology independent of sample preparation: Marios Georgiadis, **Franca auf der Heiden**, Hamed Abbasi, Loes Ettema, Jeffrey Nirschl, Hossein Moein Taghavi, Moe Wakatsuki, Andy Liu, William Hai Dang Ho, Mackenzie Carlon, Michail Doukas, Sjors A. Koppes, Stijn Keereweer, Raymond A. Sobel, Kawin Setsompop, Congyu Liao, Katrin Amunts, Markus Axer, Michael Zeineh, Miriam Menzel. *Preprint available on bioRxiv, DOI: 10.1101/2024.03.26.586745* (2024)

- The paper explores the capability of ComSLI to determine fiber orientations and crossings across a range of samples, including brain tissue and other fibrous tissues such as muscle and bone. It demonstrates the success of ComSLI with various histological stains, preparation protocols, species, and to pathological samples with altered fiber structures. The study highlights the wide range of applications for which ComSLI can accurately determine fiber architecture, including formalin-fixed paraffin-embedded brain tissues which cannot be analyzed with 3D-PLI.
- Section 7.1 refers to the paper as an extensive follow-up study to [76] and presents the successfully retrieved fiber architectures for H&E, Tau, and Perl's stain.
- F.H. optimized the measurement parameters and hardware of the LED-display setup, performed first measurements of the FFPE whole brain sections, measured and analyzed the myelin-stained human brain section, and contributed to a figure. Other author contributions are listed in detail in the paper. All authors contributed to revision and editing of the manuscript.
- The paper is currently under review.

[77] Towards high-speed Computational Scattered Light Imaging by introducing Compressed Sensing for optimized illumination: **Franca auf der Heiden**, Oliver Münzer, Simon van Staalduine, Katrin Amunts, Markus Axer, Miriam Menzel. *Proc. SPIE 12853, High-Speed Biomedical Imaging and Spectroscopy IX, 1285303* (2024)

- The conference proceeding presents a novel illumination strategy for scatterometry ComSLI that uses compressed sensing algorithms to enable high-speed measurement and data reduction. By integrating Compressed Sensing into scatterometry ComSLI, the approach achieves a reduction in measurement time down to just 1.5% of the original duration at the highest compression level.
- Section 7.4 presents compressed sensing for ComSLI in context of high-speed ComSLI measurements and discusses its integration into the Scattering Polarimeter. The content of the proceeding is expanded upon the FOMs from the compressed measurement (calculated by S.v.S.).
- F.H. optimized the measurement parameters and hardware of the ComSLI setup for compressed sensing, conducted the experiments, analyzed the data, prepared the figures, and wrote the manuscript. O.M. conducted the initial investigations to adapt compressed sensing for ComSLI, which this study further expands upon. S.v.S. calculated the line profiles. K.A. and M.A. contributed to supervision and provided tissue samples. M.M. initially proposed the use of compressed sensing for ComSLI and contributed to the study design, data interpretation, and supervision. All authors participated in revising and editing the manuscript.
- The findings outlined in this proceeding were presented in a talk at the *SPIE Photonics West* (San Francisco 2024).

[76] Reconstruction of Nerve Fiber Orientations in Cell-body Stained Histological Brain Sections using Computational Scattered Light Imaging: **Franca auf der Heiden**, Marios Georgiadis, Michael Zeineh, Katrin Amunts, Markus Axer, Miriam Menzel. *Optics in the Life Sciences 2023, Technical Digest Series (Optica Publishing Group, 2023), paper BW1B.3* (2023)

- The conference proceeding investigates the direct imaging of nerve fiber architecture in formalin-fixed paraffin-embedded (FFPE) histological brain sections with ComSLI. As a proof-of-concept, the study demonstrates the measurement of nerve fiber architecture and crossings for Cresyl violet and silver Nissl stained human brain sections. The preliminary findings presented in this proceeding are further expanded upon in [61].
- Section 7.1 presents the results of the proceeding. There, the proceeding's findings are expanded by the 3D-PLI reference images for the Cresyl violet and Ag Nissl stained tissue. Furthermore, the fiber orientations for additional stained brain tissue samples are shown (H&E, Tau, and Perl's stain, provided by M.G. and M.Z.).
- F.H. optimized the measurement parameters for FFPE sections with various stains, conducted the experiments, analyzed the data, prepared the figures, and wrote the manuscript. M.G. and M.Z. provided tissue samples and contributed to the study design. K.A. provided the BigBrain sections. M.A. contributed to supervision especially in context of 3D-PLI. M.M. contributed to the study design, data interpretation, and supervision. All authors participated in revising and editing the manuscript.
- The findings outlined in this proceeding were presented in a talk at the *Optica Biophotonics Congress: Optics in the Life Sciences* (Vancouver 2023).